Petroleum and Coal

Review **Open Access**

NOVEL METHODS OF DEEP DESULFURIZATION: A REVIEW

M. Aslam Abdullah[1], Nagamalleswara Rao[2], Aruna Singh[1]*

[1] *Department of Chemical Engineering, SCHEME, VIT University, Vellore, Tamil Nadu, Republic of India*
[2] *Centre for Disaster Management and Mitigation, VIT, Vellore, Tamilnadu, Republic of India*

Received March 12, 2019; Accepted May 23, 2019

Abstract

In order to meet the defined standards of sulfur emission, it is an inevitability to develop varied models based on indispensable concepts. Such models can only be created after having robust knowledge about the issue and setups involved in desulfurization. This review presents various criteria for Hydrodesulfurization (HDS) and novel Non-HDS processes with comprehensive information of the catalysts and reactor set up data. In addition, radiation theory concepts and material on novel biocatalyst employed in the process of desulphurization are also elucidated. The recent advancements are in emerging stage, so making feasible improvements on the factors would support the petroleum processes to release a reduced amount of sulfur in the atmosphere. A concerted integrated approach will surely lead the way for a safer and rapid way for the production of zero-sulfur fuels.

***Keywords**: Desulfurization; Catalysts; HDS and Non-HDS; Reactor setup.*

1. Introduction

The rising environmental concerns around the globe have enforced almost all the petroleum process industries to remove the pollutants as much as possible from the light oils. Research on science and technology of deep desulfurization gained momentum during the last decade, due to strict compliance of the standards fixed by the Environmental Protection Agency (EPA) for quality of the fuels that says a minimum allowable sulfur quantity should be < 30ppm. Stringent European standards stipulated a sulfur content of lesser than 10ppm [1-2]. Almost all legislations during the late 1990s were focussing on the removal of sulfur from varied compounds since it has a myriad number of deleterious effects over human lives, variety of refinery equipment, and also on the environment.

The refineries all around the world are developing novel processes to reduce sulfur levels in transportation fuels in order to satisfy the regulations. The research on the removal of sulfur is a primary concern in the process industries. The sulfur basically has adverse effects on engine parts, and metallic joints present in the equipment in addition to the increased corrosion of relevant mechanical parts of the distillation columns. Pollution, greenhouse effect, acid rains are various other reasons behind the removal of it from the fuels.

The removal of sulfur by oxidation is a core process. The experiments presented paradigms for the fact that all the sulfur compounds can be easily converted into separable oxides [3]. The oxidation process has history, which involves the presence of NO_2 was proposed in 1974. Peroxidation of sulfur compounds is one of the best methods used where both adsorption and extraction are followed. The process described as purification of liquid oil in 1988, which was further developed as oxidative desulphurization in 2000 is considered as the most prominent approach for the removal of dibenzothiophene (DBT) and its derivatives at lower temperature and pressure which are complex forms of sulfur and hard to remove by general hydro-desulfurization (HDS). The complexity in treating DBT is due to the substitution of sulfur on the 4 and 6 positions that result in steric hindrance [1]. The hydrogen paucity is majorly responsible for cost rise of ultra-deep desulfurization, which is focused on meeting the need of the ultra-clean fuels.

In recent times, more concerted research through biological route is gaining momentum. One promising short term application of biotechnology is the production of biopetrochemicals from oil. Biodesulfurization of oil was made with resting cells of *Pseudomonas delafieldii* R-8, where the resting cells in the late logarithmic phase harvested from the cultural broth were used [5]. Similarly, Sumedha and Durlubh stated the importance of thermophilic *Klebsiella sp.* as sulfur removing bacteria, which may eventually help biocatalysts to independently desulfurize petroleum oil. *Nocardia globerula R-9* had also shown the potential to remove sulfur content from diesel [6-7].

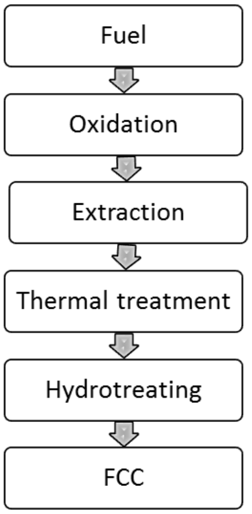

Fig.1. Basic desulfurization process flow

Recent advances in desulfurization involve nanotechnology and polymer sciences. Catalytic properties of the tungsten oxide bronze (TOB) nanoparticles is similar to that of hydrogen peroxide in making a fine desulfurized product [8]. Some compounds of cobalt and molybdenum are used as the metallic catalyst base. Hydroxyl-terminated polybutadiene/ acrylonitrile (HTBN) polymer material was chosen for deep desulphurization of LPG using the solubility parameter method. Despite the fact,that new method developed are unable to compete with traditional desulfurization due to the sturdy nature of the same, various new methods are reported that reduce the production cost and improve the process performance. Basic desulfurization module is illustrated in Fig.1.

2. Fuel components

Nearly 70-80% of the refinery outlets constitute gasoline, diesel, and other non-transportation fuels. These products are under severe investigation for the removal of sulfur [2]. Since oxides of sulfur coming out of various automobiles are noxious, countries like Germany, USA is aiming to squelch these gaseous emissions. Major target is to achieve zero sulfur content of the fuels due to the fact that high content of sulfur hampers the performance of the fuels by a change in the basic intrinsic properties of the fuels like oxygen content, vapor pressure, benzene content and polynuclear aromatic content. Liquid Petroleum Gas (LPG) is one of the most important fractions used all over the world as household and transportation fuel. The LPG obtained from FCC unit or delayed coking process usually contain various kinds of sulfur compounds, including carbonyl sulfide (COS), mercaptan, carbon disulfide (CS_2), dimethyl sulfide (DMS) and dimethyl disulfide (DMDS) and so forth. Out of those DMS and DMDS are intricately dovetailed with the other components, hence very difficult to remove. Gasoline is also treated using the FCC to reduce the sulfur content, but the reduction below 30ppm is very unconventional. The removal of sulfur from straight run diesel is a major concern basically to stabilize the properties like cetane number, density and polyaromatic composition [2] by employing some process that usually reduces sulfur up to 1.5-2.5% by weight. In the case of non-transportation fuels, these factors are not stringent as much as the others.

3. Basic HDS and other processes

Oxidation of the sulfur components is the arcane process, which is simplified and presented using Fig.2. Air is used in various industries for the oxidation process due to its cheap rate and abundance. .The maintenance of 300-380°C temperature under the reaction pressure of 15-90 bar in the reactor is the basic requirement in the HDS process, where the feed gets separated easily as per the component sensitivity. Solvent extraction is developed in sequence with HDS, where the solvent can dissolve and remove up to 90% of the sulfur.

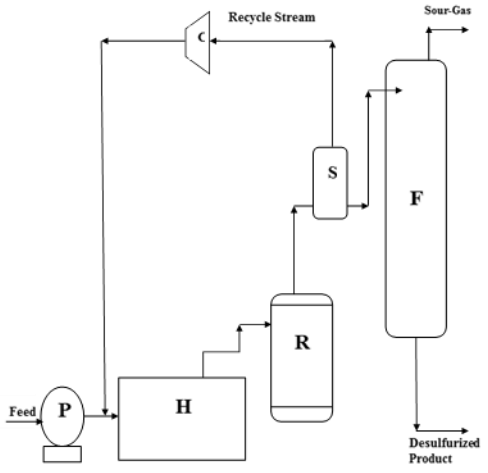

Fig.2. HDS process with catalyst
P - Pump; H - Heat treatment; R - Reactor; S - Separator; F - Fractionator; C- Compressor

Transfer of sulfur from light oil to aqueous polar solvent is the simple step involved. The removal of a very little amount of sulfur present in light oil requires highly extreme temperature, pressure, and catalyst conditions. Hence the development of a cost-effective process with high specificity was the necessity. The Hydrogenation process in the presence of special catalysts combined with irradiation techniques need essential metal supports like Ce; Mo has been used to remove SOx from the gas in petroleum and H_2S from natural gas [9]. A process used tungsten catalysts to convert sulfur compounds to sulfone in the presence of H_2O_2. The catalyst used is tungstophosphoric acid in n-octane and acetonitrile, which has a biphasic system. BDT was quantitatively oxidized within minutes in the presence of tetra octylammonium bromide and phosphor-tungstic acid at 75°C under the influence of ultrasound irradiation [8,10-11]. Application of any form of irradiation has shown positive effects on the process outputs. Atmospheric pressure laser ionization is one of the novel analytical methods employed in the late 2000s for process evaluation. Further research leads to the ESI method, but it was not favoured due to limitations like component polarity and ionization factors. Nowadays, APLI is used to analyse complex crude components and temperature sensitive constituents. APLI effectively detects even non or low polarity compounds such as hydrocarbons, sulfur species, and oxygen species that lead to more advancements in desulfurization processes [12].

NON HDS processes:

3.1. Shifting of boiling point by alkylation

Separation of the sulfur component from the lighter ones simply uses variations in the boiling point, which is derived from British Petroleum using olefin alkylation of the thiophenic sulfur technique [13] (OATS). A general process flowchart is illustrated in Fig.3.

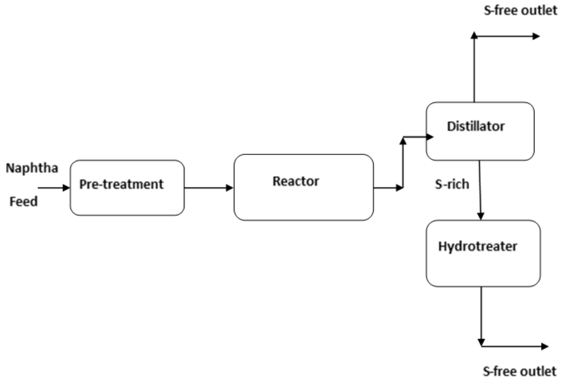

Fig.3 NON-HDS process (OATS reactor)

The mechanism dependent on temperature and catalysts gives rise to side reactions if impurities are present. Hence the pretreatment section is important to remove impurities. Acidic catalysts such as halogenated boron, zinc or aluminum having silica-alumina support are preferred. In many cases, the lighter naphtha is directly sent to gasoline container while the heavy one is sent for hydrotreating. This has the major disadvantage that very severe hydrotreating conditions are required to remove the sulfur further from the heavy components.

OATS reactor followed by distillation and hydrotreating helps in removal of sulfur from the gasoline stream up to 99.5%. But this effectiveness is accompanied by a drawback is that the output of the process has more severe treatment condition requirement than usual. The OATS reactor reduces sulfur from 2 330ppm to 20ppm with only two octane loss [13]. A similar trend was observed using the oxidation of DBT. Using oxygen or any mild oxidizing catalyst the DBT can be converted into DBT sulfone which is poached by H_2O and forms hydroxybiphenyl sulfonate which has a high boiling point. The removal of SO_2 component from the complex results in the formation of hydroxybiphenyl. Analogous to this method, the conversion of thiophene to alkylated thiophenes like 3-hexylthiophenes effects a change in the boiling point to about 85°C [2].

3.2. Desulfurization via extraction

The key reason behind the introduction of this process is that the sulfur constituents present are extensively soluble in various solvents, and their rejection strength for hydrocarbons is notable. The sulfur compounds are transferred from the fuel oil into the mixing tank containing the solvent. These organosulfur compounds are separated from the solvents by the process of distillation [2]. The most vital character of the process is the usage of low pressure and temperature. The mixing can easily occur at ambient temperature and pressure. The solvent must have different boiling temperature than sulfur, and it must be economically feasible. In these processes, if the additional option of the recovery of aromatics is made then a further improvement in the economic efficiency will be the outcome.

Fig. 4 gives a scheme of the setup for general MEROX process. The basic step is the transfer of sulfur from oil to solvents. Further separations can be done using a separator column or fractionators. Several solvents and a varying number of extraction cycles help in removal of sulfur up to 50-90%. The key limitation of the process is the solubility of the sulfur compounds in the solvent. The higher solubility can be easily obtained by the preparation of 'solvent-cocktail.' Acetones, alcohols, and esters are some of the solvents normally used in the preparation of the cocktail. Conversion of sulfur to sulfones also enhances the solubility parameter [13].

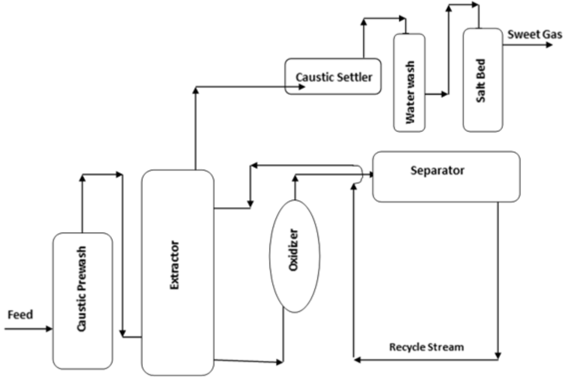

Fig.4 Simplified MEROX as extractive desulfurization

3.3. Desulfurization via conversion and extraction

Petro Starc Inc. first introduced this method in 1996. They presented the combination of conversion and extraction for diesel fuel desulfurization. Before liquid-liquid extraction, the fuel is mixed with an oxidant compound. The process of oxidation was done below 100°C and at atmospheric pressure, thus leading to excellent sulfur removal accompanied by good cetane number. API gravity and aromatics content improvements were achieved. Extensive separation of sulfur and recovery of hydrocarbons to a greater extent were the outcome of the process, then, in turn, enhances the functions of the fuel [12,14]. Proving that the application of the combined processes of oxidation and extraction is very effective. Patented extractive agents that are used in such processes include formamides, sulfoxides, furfurol, and glycols. In case of raw petroleum component and their extraction solvents like glycol derivatives with methyl esters are used to remove the sulfur content up to 94%. Desulfurized yield of lighter oil fractions and straight run gas oil was enhanced using extraction combined with UV radiation catalyzed photochemical reactions.

3.4. SulphCo desulfurization

SulphCo technology uses ultrasound to oxidize sulfur compounds in the water-fuel emulsion, which contains H_2O_2 catalyst. The conditions are maintained at a temperature range of 70-80°C with 1 atmospheric pressure. Bechtel Corp. scientists as a basic estimate put the cost of the process at nearly equal to 50% of one hydrotreater [2,11]. The simple process flow comprises oxidation and extraction phases involving emulsification with ultrasonication. The flow diagram is shown in Fig.5.

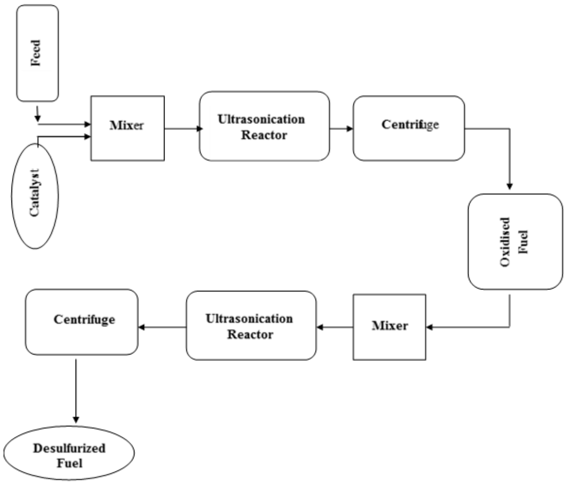

Fig.5. General process-flow of oxidation and extraction involving ultrasound

The basic emulsification process involves a static mixer where suitable pressure and mixing is employed. In this process, the ultrasonication breaks the droplets and produces high hydraulic shear that further divides the constituents into submicron-sized particles. Reduction of droplet diameter influences the reaction kinetics and eliminates the need for phase transfer. Since the contact surface is increased requirement of peroxides is reduced significantly. Ultrasonication process produces intense local heating and enormous pressure. It induces oxidation in the presence of catalysts. The process output confirms the removal of sulfur up to 80-98% thus resulting in sulfur content up to 10ppm.

3.5. Unipure aromatic sulfur reduction

This is based on the oxidation of aromatic sulfur in an aqueous phase before extraction. Mild temperature and pressure conditions are applied to the process. The reduction of sulfur from 270ppm to 2ppm is observed. The basic mechanism is the conversion of sulfide to sulphones with smaller residence time. The analysis of the kinetic study of the reaction suggested a substantial improvement to the process if photons or ultrasound radiations are employed [13].

3.6. Desulfurization by photochemical oxidation and extraction

Desulfurization process combined with photochemical procedures is an advancement to the reported processes. Photodecomposition or photo-oxidation is one of the major discoveries enlisted. Desulfurization involving a combination of photochemical reactions with the extraction of the organosulfur compounds is one of the unconventionality that is specific to this method. Extracted product is further irradiated using UV radiations to form polar compounds; these are then rejected by non-polar hydrocarbons that get concentrated in the solvent. Further removal of the sulfur compounds can be done by using acetonitrile, the best suitable solvent available [15]. Optimization of the combination of solvents and photosensitizer is necessary to increase the rate of the organosulfur compounds by phototransformation. A reduction in the sulfur content almost to 2% in commercial light oil is achieved after 2hrs of irradiations, which has the potential to reduce sulfur content to 1.4% if exposed to 10hrs of radiation. Difficulties in the photosensitizing lead to replacement by H_2O_2, which in turn hinders the energy transfer from DBT to naphthalene. After photo-irradiations solutions are periodically checked for consistency in the amount of carbon present and composition of compounds [15-16].

General oxidative desulfurization (ODS) process achieved under microwave treatment is the most significant application. Microwaves are radiations lying between infrared and radio frequencies. ODS process efficiency is affected by oxidizing agents, catalyst and oil types, microwave power levels, treatment times, temperature and dosage of oxidizing agents [10]. Other essential factors that influence the extent of desulfurization are extraction design and time. The presence of polar molecules like organic sulfides, oxidizing agents, as well as catalysts, significantly help in strengthening and promoting the reactions. Moreover, the sulfur and nitrogen compounds present with a dipole in the crude are also highly sensitive towards microwaves. Operating conditions are less severe, and treatment times are also shorter [16].

Another improvisation in the desulfurization process is the application of ultra-sonication. Various studies suggested that the cavitation phenomenon intervenes in the desulfurization due to the presence of bubbles, which can be made to collapse using ultrasound. Elimination of the usage of the metallic catalysts and maintenance of relatively mild conditions are the other important contributing factors of the method. Comprehensive analysis of the process revealed other parameters that have a positive influence on the outcome include the presence of H_2O_2, glacial acetic acid, number of stages of methanol extraction, temperature control, ultrasound effects, reagents reuse and removal of varied components using mechanical stirring. Increase in sulfur removal requires a higher amount of acetic acid but crossing a certain threshold percentage increase does not affect the sulfur removal. Essentially the ratio of acetic acid and sulfur is maintained at 300:1. Hydrogen peroxide with acetic acid in a proper proportion of approximately 1:5 gives appreciable separation of sulfur, which is accompanied by minimal oil loss. Temperature factor is used to determine the volatile nature of the particles that aid the process efficiency. Ultrasound treatment is applied only for 5mins, which selectively removed up to 90% of the sulfur compound present [11].

3.7. Desulfurization by precipitation

Buildup and subsequent removal of insoluble charge transfer complexes is the basis of this methodology. The sulfur-containing compounds and π-acceptors are charged into batch reactors under agitation at fixed rpm. The reacted components are separated by filtration and further treated for gas oil recovery. Current analysis of the process shows that the efficiency is remarkably low, which can remove only 20% of sulfur. Due to the competitive nature of the reactants, DBTs present have low selectivity towards removal. Excess of TNF provision is required; due to the over stoichiometry, the further removal of the same is necessary [13].

Methylation of DBT using methyl iodide and silver tetrafluoroborate is reported to produce high water-soluble compounds, which lead to the desulfurization. It has also been reported that desulfurization of light gas oils can be catalyzed by adding more alkylation reactors, and it is observed that sulfur content was reduced up to 0.005% w/w basis. Catalytic cracking of naphtha is also a significant process that helps in better desulfurization.

3.8. Selective oxidative desulfurization

As mentioned before, the conversion of sulfur to sulfone form involves oxidation. Acetonitrile was found to be the solvent which helps convert sulfur to the sulfone form. This conversion mainly creates a gradient of temperature among the compounds present by increasing the boiling point, hence a better separation can be achieved [1,13]. The sulfone content is basically dependent upon various factors like nature and consumption of acid catalysts, hydrogen peroxide consumption, temperature, duration of oxidation [17]. Rapid oxidation also helps the refiners in the removal of sulfur selectively from the mixtures, which include heavy aromatics and multi-ring components with DBTs. High activity was obtained for the combination of ammonia tungstate and fluoride complexes [18]. The unique process employs oxidation catalysts in the aqueous phase, where the scope for future development is combining the process with the application of ultrasound or photons [11]. Usage of Cu catalyst in the process has shown enormous separation yields. There are several factors responsible for the desulfurization that include loading, baking temperature, valence state, surface area, pore size, the total pore volume of the catalyst. Based on these observations, the desulfurization breakthrough is deduced and calculated by the following equation:

$$S_t = \frac{q * 10^{-6} * 100\%}{m} \int_0^t (C_0 - C_t)dt$$

where 'S_t' the amount of sulfur adsorbed on the adsorbent (wt percent mg-S/g of adsorbent), 'q' is the flow velocity of the LPG (ml/h), 'C_0' is the inlet concentration of the LPG(mg/m^3) and C_t at any time 't(h)' and the mass of the adsorbent 'g' [19].

The maintenance of the optimum level of the adsorbent is the most crucial factor which is observed in this work. The process must keep 15% of bentonite level at a temperature of 150°C temperature that effects maximum separation of the sulfur. If this level rises to a higher value like 20%, the sulfur removal decreases, as shown in the Fig.6 [19].

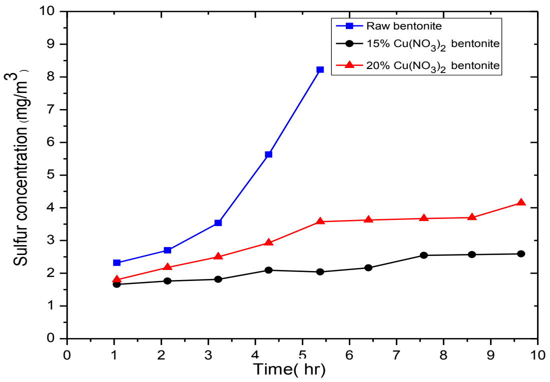

Fig.6. Cu bentonite catalyst effects on sulfur

This process is analogous to the normal distillation of organosulfur compounds. Here, SO_2 is predominantly released, but H_2S molecules may also be formed when the decomposition temperature shoots above 300°C. The observed process efficiency is relatively low, which is up to 40%. Usage of higher catalyst strength is found to increase efficiency, which is a major topic of research currently.

3.9. Desulfurization by adsorption on a solid sorbent

One of the effective ways to remove numerous organosulfur compounds present in the petroleum fraction is by using adsorption technique. Based on mechanisms of sulfur and use of adsorbent, it can be either desulfurization or desulfurization accompanied by adsorptive desulfurization. Regeneration of the sorbent is an essential factor responsible, which is possible by flushing the spent sorbent with a desorbent. Desorption results in the high flow of organosulfur compound in the desorbed stream. It results in the removal of H_2S, S, or any other sulfur oxides present. Simplified process setup is given in Fig.7.

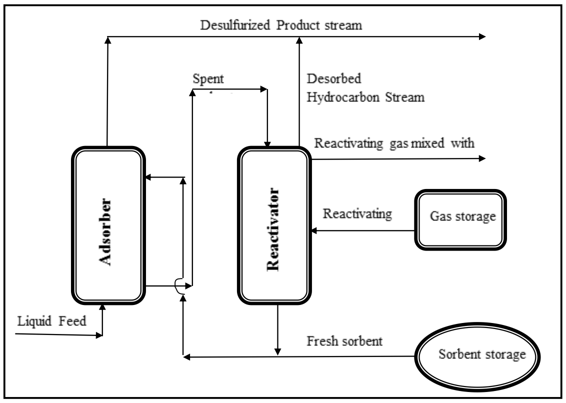

Fig.7. Simplified adsorptive desulfurization process

Salem and Hamid studied adsorptive desulfurization, where two bedded combination of batch reactors were proposed [2], which principally helps in the removal of 4 and 4,6-substituted dibenzothiophenes that are always present in the leftover of the hydrotreatment. In this case, activated carbon, Co-Mo, or silica-alumina like catalysts are employed for the removal of sulfur effectively. Activated carbon is noted for its efficient usage under 100°C [20].

Similarly, IRVAD and Philips S Zorb processes are also widely used. IRVAD is a technology developed by Black and Veatch Pritchard engineering firm, which has a main focus on removing organosulfur compounds. The IRVAD process uses countercurrent moving bed having solid sorbent operating at 240°C, low pressure with a hydrocarbon to the adsorbent ratio of about 1.4 [21]. It further requires additional downstream treatment of the outlet that principally involves high-pressure hydrotreating. The simulations can be done on the sorbent properties to modify the same to gain higher purity [2,14].

Similar flow techniques are applied by IRVAD and S Zorb process, but the nuance of difference is presented in fluidized bed technology. It is mentioned that the process can remove 98% of the sulfur from gasoline, and almost 100% hydrocarbons can be recovered. The key factor of these processes involves octane number maintenance; the loss of the same is observed in the range of 0.5-1.5 of the original [13].

4. Process setups and recent variants

Starting from basic oxidation with/without various ionic or heterogeneous catalysts, the process developments are well documented. Generally, these processes can be divided into two parts; one involves sulfur elimination and another transformation of sulfur into separable compounds. Sulfur elimination majorly includes conventional HDS processes. In the case of sulfur transformation, catalytic distillation, alkylation, extraction, etc. are preferred [2]. Oxidation of sulfur from divalent sulfide to hexavalent sulfone group is one of the major changes that had taken place [3]. In a few models, oil was extracted into the ionic liquid phase and oxidized to their corresponding sulfone by peroxomolybdic compounds.

4.1. Solvent and catalyst engagement

Desulfurization based on adsorptive processes involves solid sorbent which can only absorb or react with the sulfur compounds, which can effectively remove S, SO_2, and H_2S. The efficiency is mostly determined by absorption capacity, reactor area usage, selectivity, removal of aromatics, and durability with regeneration. Selective adsorption is much more effective over HDS. As per the literature, Petro Start Inc. combined conversion and extraction processes in 1996, before extraction fuel mixed with peroxides helps in the advantage of the various factors like cetane number, API gravity and aromatic contents which are accompanied with reduction of sulfur from 4200ppm to 10pmm or even lower [2]. For diesel fuels novel ionic liquids can be used which follow extraction and regeneration simultaneously and helps in removal of sulfur components up to 50ppm. Ionic liquids with the presence of sulfur compounds were able to remove up to 60-70% of the sulfur and aromatic content, which is accepted by industrial standards. Progress of the field is well-known after the application of amorphous silica-alumina (ASA), one of the excellent catalysts used in combination with Pd. This aids in the separation of the aromatics up to 75% also reduces Sulfur to 6ppm. The improvement in the characteristics of catalyst is made by having mainly two types of pore sizes. The catalyst with large pores can adsorb the aromatics and other larger constituents, while the other smaller one which has resistance against the sulfur poisoning can be effectively used for sulfur adsorption and regenerated, so the process efficiency never reduces even if more quantity of sulfur is introduced.

In the case of refinery products, sulfur present in small proportions can be end blended easily for which a lesser quantity of hydrogen is required. Only an integrated approach involving catalyst selection, reactor design, process configuration which will lead to efficient desulfurization, i.e. catalytic desulfurization combined with HDS. Removal of sulfur-containing compounds using H_2O_2 and acetic acid with the presence of sulphuric acid or hydrochloric acid as a supporting catalyst is also one of the core processes. This process is found to remove nearly 90% of the sulfur present, which attracted the attention of the research community. One drawback is the effect on Oxidation efficiency of H_2O_2 by several factors like temperature, pH, and dissolved ions maintained in the process.

4.2. Reactor modules

Reactor modeling and simulation are key factors that bolster the progress of any process setup. Conventional hydrotreating reactors follow co-current streams of oil and hydrogen supply provided one behind another. It leaves traces of these unreacted H_2 and H_2S, that reduces the reactor efficiency [17]. Taking counter current approach is one of the advancements, first invented by Scanraff's Synsat gas treatment process. The process also reported that not only removes sulfur up to 1ppm, but also nitrogen and other aromatic compounds to a very great extent. The major development of the design involves the introduction of co-current and counter-current reactors in a sequential module, which in turn helps in the reduction of the catalyst volume required for desulfurization. Monolithic catalyst preparation and reactor setups involve varied parts including direct extrusion or paste of catalyst, which helps in higher catalyst loading into the reactor. Nowadays monolithic bed reactors are transformed into mobile reactors, which show ideal behaviour and give higher conversion. Monolithic reactors have advantages over normal reactors like larger productivity, better selectivity, and higher efficiency and preclude unsafe conditions. Flow characters of the monolithic reactors are far more superior over the normal reactors that increase its activity. Taking IFP into concern, the process developed by them involves a concept called as T-star catalyst based reactors, characterized by mechanical stability and resistance to attrition. Usage of multi-staged airlift reactors that overcome poor reaction kinetics at low sulfur concentrations with reduction of mixing costs is another development. Mesoporous aluminosilicate molecular sieves are installed in such reactors to direct the space velocity decrease, increase in temperature and Hydrogen pressure, improvement in the vapour liquid contact, scrubbing, and removal of H_2S from the recycle stream. Concerning an article of Oil and Gas Journal wrote in 2001, the Z-sorb process is used for the desulfurization of gasoline as well as diesel. The ultra-deep desulfurization is chosen as the process since it is cost effective and reduces the refinery CO_2, SO_2 emission in comparison to normal processes [13].

The novelty in the alignment of the process catalysts gave rise to multi-bedded catalyst layers separated by gases at lower temperatures. The rise in reactor performance requires an increase in recirculation for heat removal. In the MPCP device process, shown in Fig. 8, liquid, solid mass transfer is majorly involved, that increases the concentration of the hydrogen over the catalyst surface.

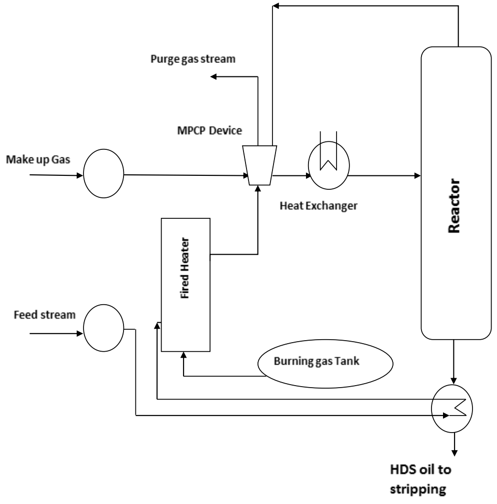

Fig.8. Advanced MPCP unit based process

With decreased catalyst particles size and sudden rise in flow velocity enhancement of the liquid, solid mass transfer is achieved. Lower grade fouling is observed due to the liquid present washes off the corroding constituents present. The most important advantage of the system is the simplification of the heat repercussions, reducing the complications involved in pumping hot oil at 320 - 450°C. In order to array all heat fluxes a common network of recuperates combined with conventional HDS reactor followed by stripper unit increases not only investment costs but also energy expenses for transpiration of a gas-liquid mixture through extremely long pipe-work [22]. Similarly, for natural gas and LPG desulphurization, two methods are employed, first is passive adsorption, and second is catalytic transformation followed by adsorption. Technology developed by Englehard involves a method which combines the fuel with a sub-stoichiometric amount of oxygen and uses a sulfur tolerant monolithic catalyst to oxidize selectively the sulfur compounds to oxides. This is the selective catalytic oxidation. This method is mapped by the author based on catalyst performance as a function of temperature, oxygen-to-carbon ratio, and space velocity. Catalyst deactivation occurs at high temperature, presence of fuel particles in the absence of air, catalyst exposed to fuel-air mixture at ambient temperature [17].

4.3. Novel presence of membranes and nanoparticles

Precursors or solvents are usually immobilized in the membrane pores, hence find critical application in desulfurization. Novel constituent comprises of polymer like, polyoxometalates, that has gained much attention due to their tenability of composition, size, shape and acid-base properties with redox functions. Presence of ionic liquids, which can form π complexes majorly containing chloride ions help to enhance the separation. Desulfurization using metallic compounds over the membrane layers help in the removal of sulfur forming sulfur-metallic bonds or with catalytic decomposition. Various reactions give different products due to the polycrystalline nature of the films with the distribution of surface sites varying from film to film. Hydroxyl-terminated polybutadiene/acrylonitrile(HTBN) polymer material was selected for deep desulphurization of LPG using the solubility parameter method. Interaction between polymer and solvent molecule is used to estimate the separation criteria. Supporting layers like polyacrylonitrile prepared with phase inversion are mainly used below the flat plate composite membranes. Methyl mercaptan is the main substance present inside the LPG, with the sulfur present over which the HTBN membrane proved to be a promising material for separation. The permeability property of methyl mercaptan is also different from other sulfur constituents, which is effectively managed by the membrane [23].

Similar to membranes, the novel field of nanosciences is also applied for the process. Multi-walled CNTs with MnO_x nanocatalyst is used for the desulphurization process where the performance of the same at 25°C and atmospheric pressure indicates the sulfur removal which is up to 99.85% in the first 30 min span [24]. CNTs are chosen for the process because of some unique properties like tube-shaped mesoporous structure, the transmission of reactants and products, resistance towards basic and acidic conditions. They are tested for deep desulfurization for sour naphtha, which is very complicated to remove. In the CNTs, the carbon-carbon double bonds increase their strength at $1560cm^{-1}$which further intensifies the oxidation process preventing the aggregation and precipitation of the multi-walled carbon nanotubes [24]. Peroxidation of sulfur compounds is one of the finest methods that are used, followed by adsorption and extraction.

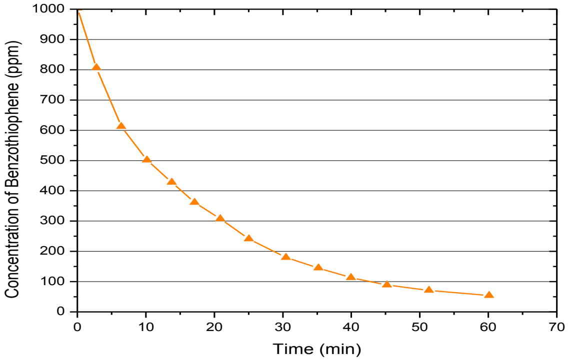

Fig.9. With nanocatalyst presence

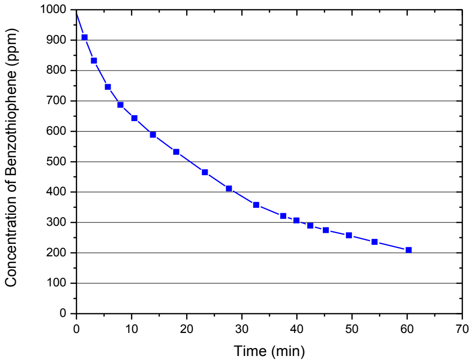

Fig.10. Without catalyst presence

Catalytic properties of the TOB (tungsten oxide bronze) in the nanoparticles size are similar to that of hydrogen peroxide process giving fine desulfurization product. The kinetics of the reaction has directly shown that the concentration dependence of TOB on the oxidation process of benzothiophenes. The chief advantages are high chemical purity, thermal stability even at 800°C. Fig. 9 shows a steep decrease in the concentration of benzothiophene from 242ppm to nearly 12ppm [18]. Similarly, Fig. 10 and Fig. 11 shows the tungsten catalyst based processes where sulfur reduction is observed.

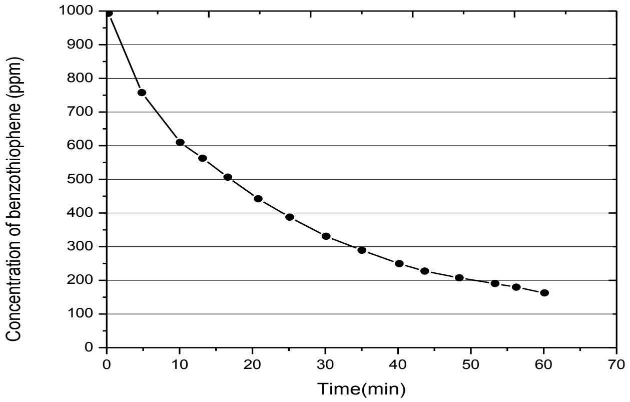

Fig.11. With coarse grade tungsten oxide catalyst

Maintenance of the octane or cetane number is the center of various processes. Philips Petroleum Corporation proposed the pre-aromatization of FCC gasoline that reduces the sulfur content from 300ppm to 10 ppm and augments octane from 89 to 100. Combination of hydrotreating and octane boosting process is known as ISAL process, which basically treats the high naphtha feed and reduces the sulfur from 1450 ppm to 10 ppm without affecting the octane number [2,14]. To avoid octane loss, newer methods follow fractionation before desulfurization for all the components of FCC. It helps in preserving olefins at different selective compound conditions having different boiling points.

4.4. Biocatalyst applications

Nature of sulfur compounds, reaction conditions, the catalyst used are three important factors, and these dominate the reaction pathways of desulfurization. In the near future, the study of polynuclear organic compounds, biocatalysts having complex, abstruse nature are predominantly considered for the deep desulfurization processes. Bio-enzymes are used in the process of desulfurization, and the product resulting from this method is hydroxyphenyl benzene sulphonate which can be commercially used as a feedstock in the surfactant productions. Various research groups have investigated the application of *Nocardia globerula* R-9 for the desulfurization of straight diesel. Its usage graphically follows Michaelis Menten mechanism. It efficiently removes DBT and 4,6-DMDBT at different rates [6]. Desulfurization involves C9-C12 carbon compounds in gasoline and C12-C23 in diesel in diverse ring forms. Pseudomonas and flavin reductase are some initial bio enzymes that are utilized in the process. The basic promoter has been characterized by the presence of sulfur-containing amino acids. Some cases of thermophilic biodesulfurization under high temperature decreases oil viscosity, makes molecular desulfurization easier, improves enzymatic reaction rates, and decreases bacterial contamination.

5. Setbacks of the processes

Initial stages of the process development have problems due to hydrogen deficiencies; especially the HDS process had some difficulties in meeting the demands. Deep HDS problem for diesel stream is exacerbated by the inhibiting effects of co-existing polyaromatics and nitrogen compounds in the feed as well as H_2S in the product. Presence of H_2S usually poisons inorganic catalysts; hence, elimination of the sulfur is highly important. Biocatalysts have fewer disadvantages, but these overweigh disadvantages of all the remaining processes. Cells precipitated at the bottom are an adverse condition for desulfurization. Costly equipment and catalyst preparation methods, skilled labour requirement for supervision are some major pitfalls. Few methods show that desulfurization using old methods precluded the expansion of the reforming unit.

Severe process conditions result in a reduction of the quality of petroleum components and octane number. The temperature required for the process is above 500°C and many causes over cracking of the products. Water is also wasted in the process to clean off the raffinate and remove acetonitrile in case of photo-sensitized processes. Commercial light is also used in the process of removal of sulfur up to the level of 0.05% with 48hrs of rigorous radiations, which is difficult to be used in the industry.

Proper boundary to the application of acidic or basic catalyst must be maintained. The enhancement of reaction becomes less prominent with an increase in phosphotungstic acid.

Sterile Trimethyl Ammonium Bromide (STAB) is a catalyst with high activity and selectivity towards sulfur. The maintenance of STAB at a proper concentration in association with phosphotungstic acid raises the reaction rate.

The increase in mixing speed, interphase mass transfer, and emulsification have a drastic impact on the desulfurization due to larger droplets, presence of high surface area, and high rate of reaction. Formation of stabilized emulsions pose some difficulty in the recovery of oil from water in the BDS, and so one such solution to this problem is the use of destabilizing agents to avoid the formation of the emulsion based bonds. However, a flip side to this method is the higher operating costs and time required.

Grignard reagents are used for separation of thiophenes, benzothiophenes, and DBTs in the presence of nickel/cobalt halide phosphine complexes. Likewise, platinum and molybdenum are the catalysts preferred. However, this is not a cost-effective method. The complex paraffin gets affected by the oxides that need to be suppressed properly. Solvent to oil ratio is the most important bottleneck of the process. Hence proper balance is the major requirement.

The major disadvantage is that they are more expensive than any other reactors. Heavy streams desulfurization is still an enigma in for many scientists where non-reactive sulfur compounds are present. The major problem here is the disposal of the eliminated sulfur and solvent recovery. High chemical purity and thermal stability at 800°C are needed so that the components can thwart the effects of sudden temperature fluctuations. High homogeneity and high reactivity of three-phase reaction system is the most important experimental difficulty in the ionic catalyst process.

The major developments amidst all the processes considered are the design of the reactor – where the introduction of co-current and counter-current reactors in series that in turn helps in the reduction of the catalyst volume required for desulfurization. However, the major disadvantage is that packed bed reactors cannot be used in the process.

6. Concluding remarks

All the above-discussed topics and technologies are revised several times. Such a continuous area of research is present, where numerous permutations and combinations are possible that delivers better and better process setups. To meet the more stringent rules and regulations involved in desulfurization, more and more processes should evolve. New design approaches use enormous chemistry for the production of zero sulfur affordable diesel and gasoline.

Ultra deep desulfurization methods should be challenged now and then, which will focus on the creation of zero sulfur fuels. Liquid hydrocarbon processing, applications of composite membranes are the key sector for future research. Lesser hydrogen requirement, higher efficiency, faster, better, and safer production should be the aim of the processing teams.

Acknowledgments

We thank the management of VIT University and the School of Chemical Department staff for consistent support.

References

[1] Huang D, Wang YJ, Yang LM, and Luo. GS. Chemical oxidation of dibenzothiophene with a directly combined amphiphilic catalyst for deep desulfurization. Industrial & engineering chemistry research, 2006. 45(6): 1880-1885.

[2] Babich I, and Moulijn J. Science and technology of novel processes for deep desulfurization of oil refinery streams: a review. Fuel, 2003; 82(6): 607-631.

[3] Zannikos F, Lois E, and Stournas S. Desulfurization of petroleum fractions by oxidation and solvent extraction. Fuel Processing Technology, 1995; 42(1): 35-45.

[4] Zhang M. et al., Deep oxidative desulfurization of dibenzothiophene with POM-based hybrid materials in ionic liquids. Chemical Engineering Journal, 2013; 220: 328-336.

[5] Guobin S, Jianmin X, Zhang H, and Liu H. Deep desulfurization of hydrodesulfurized diesel oil by *Pseudomonas delafieldii* R-8. Journal of Chemical Technology & Biotechnology, 2005; 80(4): 420-424.

[6] Mingfang L, Guo H, Xing J, Liu H, and Chen J. Microbial desulfurization of model and straight-run diesel oils. Journal of Chemical Technology & Biotechnology, 2003; 78(8): 873-876.

[7] Bhatia S, and Sharma DK. Thermophilic desulfurization of dibenzothiophene and different petroleum oils by *Klebsiella sp*. 13T. Environ Sci Pollut Res Int, 2012; 19(8): 3491-7.

[8] Petrov L, Shishmakov AB, Vakarin SV, and Semerikova OL. Behavior of nanosized tungsten oxide bronzes produced by high-temperature electrolysis in model processes of desulfurization of petroleum products. Russian Journal of Inorganic Chemistry, 2014; 59(1): 7-10.

[9] Zhu W, Li H, Xue J, Yan Y, Lu J, He L, and Xia J. Commercially available molybdic compound-catalyzed ultra-deep desulfurization of fuels in ionic liquids. Green chemistry, 2008; 10(6): 641-646.

[10] Campos-Martin JM, Capel MC, Perez P, and Fierro JLG. Oxidative processes of desulfurization of liquid fuels. Journal of chemical technology and biotechnology, 2010; 85(7): 879-890.

[11] Duarte FA, Paola A, Cezar AB, Matheus AGN, Elizabeth MM, Mauricio SA, Heloisa NM, Valderi LD, and Erico MMF. Sulfur removal from hydrotreated petroleum fractions using ultrasound-assisted oxidative desulfurization process. Fuel, 2011; 90(6): 2158-2164.

[12] Panda SK, Brockmanh KJ, Benter T, and Schrader W. Atmospheric pressure laser ionization (APLI) coupled with Fourier transform ion cyclotron resonance mass spectrometry applied to petroleum samples analysis: comparison with electrospray ionization and atmospheric pressure photoionization methods. Rapid Commun Mass Spectrom, 2011; 25(16): 2317-26.

[13] Pawelec B, Rufino MN, Jose M, and Jose LG. Retracted article: Towards near zero-sulfur liquid fuels: a perspective review. Catalysis Science & Technology, 2011; 1(1): 23-42.

[14] Song C. An overview of new approaches to deep desulfurization for ultra-clean gasoline, diesel fuel, and jet fuel. Catalysis Today, 2003; 86(1-4): 211-263.

[15] Shiraishi Y, Hirai T, and Komasawa I. A Deep Desulfurization Process for Light Oil by Photochemical Reaction in an Organic Two-Phase Liquid−Liquid Extraction System. Industrial & Engineering Chemistry Research, 1998; 37(1): 203-211.

[16] Shang H, Zhang H, Wei Du, and Liu Z. Development of microwave assisted oxidative desulfurization of petroleum oils: A review. Journal of Industrial and Engineering Chemistry, 2013; 19(5): 1426-1432.

[17] Lampert J. Selective catalytic oxidation: a new catalytic approach to the desulfurization of natural gas and liquid petroleum gas for fuel cell reformer applications. Journal of Power Sources, 2004; 131(1-2): 27-34.

[18] Petrov LA, Shishmakov AB, Vakarin SV, Semerikova OL, Melyaeva AA, Yu VM, Zaikov PY, and Chupakhin ON. Behavior of nanosized tungsten oxide bronzes produced by high-temperature electrolysis in model processes of desulfurization of petroleum products. Russian Journal of Inorganic Chemistry, 2014; 59(1): 7-10.

[19] Zhang Q, Shi L, and Meng X. Deep adsorption desulfurization of liquid petroleum gas by copper-modified bentonite. RSC Adv., 2016; 6(12): 9589-9597.

[20] Shen Y, Li P, Xu X, and Liu H. Selective adsorption for removing sulfur: a potential ultra-deep desulfurization approach of jet fuels. RSC Advances, 2012; 2(5): 1700-1711.

[21] Sánchez JM, Ruiz E, and Otero J. Selective removal of hydrogen sulfide from gaseous streams using a zinc-based sorbent. Industrial & engineering chemistry research, 2005; 44(2): 241-249.

[22] Datsevich LB, Zaikov PY, and Chupakhin ON. Deep desulfurization of petroleum streams: Novel technologies and approaches to construction of new plants and upgrading existing facilities. Chemical Engineering Journal, 2009; 154(1-3): 302-306.

[23] Chen J, Chen J, Li J, Han X, Zhan X, and Chen C. Liquefied petroleum gas desulfurization by HTBN/PAN composite membrane. Journal of Applied Polymer Science, 2010; 117(4): 2472-2479.

[24] Mohammadi Meman N, Neda M, and Mahnza P. Synthesis, characterization, and operation of a functionalized multi-walled CNT supported MnOx nanocatalyst for deep oxidative desulfurization of sour petroleum fractions. Journal of Industrial and Engineering Chemistry, 2014; 20(6): 4054-4058.

[25] Zhao Y, Wang R. Deep desulfurization of diesel oil by ultrasound-assisted catalytic ozonation combined with extraction process. Pet Coal, 2013, 55(1): 62-67.

To whom correspondence should be addressed: Dr. M. Aslam Abdullah, Department of chemical engineering, SCHEME, VIT University, Vellore, Tamil Nadu, Republic of India

Petroleum and Coal

Article **Open Access**

NUMERICAL SIMULATION OF ENHANCED OIL RECOVERY USING GUM ARABIC POLYMER

Emmanuel A. Akpan[1], *Oghenerume Ogolo**[1], *Shadrach Ogiriki*[1, 2], *Aminu Y. Kaita*[1], *Daniel Amune*[3]

[1] *Department of Petroleum Engineering, African University of Science and Technology, Abuja, Nigeria*
[2] *Chemical and Petroleum Engineering Department, Afe Babalola University, Ekiti, Nigeria*
[3] *Material Science and Engineering Department, African University of Science and Technology, Abuja*

Received March 12, 2019; Accepted May 21, 2019

Abstract

The era of easy oil is diminishing fast, and companies are looking for oil in remote and hazardous terrains. This, combined with low oil prices, makes drilling for new reserves very expensive and risky. This then considers enhanced oil recovery processes, which increases the amount of oil that can be recovered from a reservoir. This study was aimed at determining the suitability of Gum Arabic as a polymer for EOR operations using numerical simulation. This was done by matching core flooding experiments using Eclipse. The simulation results gave a waterflood oil recovery match of 53% as compared with the experimental recovery of 55% while ASP flooding gave an oil recovery match of 80.53% as compared with the experimental recovery of 82%. Upscaling from core to field simulation, the ASP slug formulated increased field total oil production by increasing recovery from 62.48% at the end of the water flooding to 85.8%. This indeed shows the potential of gum Arabic for EOR operations.

Keywords: *Numerical simulation; Gum Arabic; Enhanced Oil Recovery; Alkaline Surfactant Polymer; Eclipse.*

1. Introduction

The average recovery factor for both primary and secondary conventional recovery technique is about 33%. This shows that over 60% of the original in place oil is still left unrecovery. This amount of oil was either passed by the injected water, or there were too viscous to be displaced by the water injected [1-5]. Kevin and Raymond [6] noted that recovery depends on several factors that include: reservoir properties, existing technology, nature of crude oil, and prevailing economic climate.

Water injection tends to resuscitate the pressure of a depleted reservoir, and it displaces the oil to producers. However, water has high mobility, and it is less viscous. This makes it evade large volumes of oil, and “break-through,” to the producing well before adequately sweeping the reservoir [8] resulting in only part of the reservoir being contacted for a realistic time frame and injection scheme. Also, the reservoir heterogeneity aggravates the injected water’s tendency to only mobilize the oil in regions with high permeability, which leads to an early breakthrough in that region [7].

Chemical flooding methods are usually seen as a special branch of enhanced oil recovery processes to produce the remaining oil after water flooding process has been carried out [5-12]. The performance of the chemicals used, however, varies depending on the particular reservoir rock and fluid properties. Therefore core flood experiments at the laboratory scale are required to evaluate the performance of various chemicals and their impacts on the reservoir rock and crude oil properties [8, 13]. Nowadays, as all field operations are ultimately studied through simulation models of some forms, it is important also that simulation technology is on par with all relevant experimental findings [8].

Over the years, flooding techniques have been done in various forms; surfactant polymer flooding, alkaline polymer flooding, alkaline surfactant flooding, and alkaline surfactant polymer flooding (ASP) [1, 3-4, 10, 14- 21]. ASP has proven from experimental studies to be among one of the chemical flooding processes with the highest recovery factor, and it has been conventionally carried out using polymers like Xanthan gum and partially hydrolyzed polyacrylamide which is not readily available in Nigeria [17, 22- 25]. The polymer used in this study is gum Arabic because it is a polysaccharide and has a similar molecular structure to Xanthan gum, and it is commercially available in Nigeria. There are many experiences on ASP flooding using Xanthan gum and other polymers, but very few on gum Arabic. The aim is this research work is to determine the suitability of gum arabic as a polymer for EOR operations using numerical simulation [5, 14, 26- 28].

2. Literature review

Alkaline-surfactant-polymer (ASP) flooding is an EOR process, in which alkali, surfactant, and polymer are injected at the same time. It has been considered as the most promising chemical methods because it is possible to achieve interfacial tension reduction, wettability alteration, and mobility control effectively [29]. Although the method of surfactants and alkaline solution injection which converts naturally occurring naphthenic acids in crude oils to soaps have long been used to increase oil recovery, key concepts such as the need to achieve ultralow interfacial tensions and the means for doing so using microemulsions were not clarified until a period of intensive research between approximately 1960 and 1985.

Nelson *et al.* [30] recognized that in most cases, the soaps formed by injecting alkali would not be at the "optimal" conditions needed to achieve low tensions. They, therefore, proposed that a relatively small amount of a suitable surfactant be injected with the alkali so that the surfactant/soap mixture would be optimal at reservoir conditions. With polymer added for mobility control, the process would be an alkaline-surfactant-polymer (ASP) flooding.

Hawkins *et al.* [31] reported that the simultaneous injection of alkali and polymer is more effective than the same chemicals injected sequentially with no contact between alkali and polymer. Tong *et al.* [32] reported that the main mechanisms of ASP flooding are interface producing, bridging between inner-pore and outer-pore, and oil-water emulsion. Alkali substances have proven to be an appropriate means to improve the oil recovery from oil-wet reservoirs by reversing the rock wettability to a more favorable condition. Wettability alteration function is predominant at alkali concentration lower than 1% by weight, whereas IFT reduction is oppositely predominant at a higher concentration than 1% by weight [33].

Onuoha and Olafuyi [17] came up with a laboratory study on the use of gum arabic for mobility control. In an ASP flooding they conducted, the displacement efficiencies of two ASP slugs were compared and calculated to be 90.2% for sodium hydroxide (NaOH), lauryl sulphate and gum Arabic slug and 77.9% for sodium hydroxide, Tween 80 and gum Arabic slug. Their work was on light oil in a water-wet unconsolidated glass beads core. Many ASP flood laboratory test and field tests or applications have been done over the years with the use of other polymers such as xanthan, scleroglucan, polyacrylamide, and other cellulose derivatives.

Taiwo *et al.* [25] showed that oil recovery by the imbibition process does not follow a regular pattern. It reveals some complexities in the oil mobilization process and an uneven pattern in the oil recovery due to the simulated reservoir heterogeneity. They showed that it is not only the grain size of the reservoir rock but also the arrangement of the grains in the core affect the oil recovery. They showed that water flooding could recover about 70% while ASP flooding can recover between 16 to 19% of the original oil in place from the synthesized heterogeneous beads pack. Bernheimer core gives the best results for ASP EOR flooding operations. Avwioroko *et al.* [34] showed that oil recovery increases as formation become more strongly water wet. They showed that the displacement efficiency of water floods and ASP flooding is markedly affected by the wettability of the core. The wettability is one of the important factors to determine the oil recovery of water and ASP flooding. Water-wet and oil-wet conditions are favorable to obtain high enhanced oil recovery for ASP flooding.

3. Methodology

3.1. Matching laboratory experiments using numerical simulation

Studies have shown that a better displacement efficiency can be achieved within a range of polymer concentration and that the performance of ASP flood program is dependent on the right slug formulation, the injection rate and the overall project design [25]. Therefore we need to determine the appropriate formulation of this slug and verify its formulation with core flood experiment. The core flood experiment which this work simulated was done by Onuoha and Olafuyi [17] at the EOR lab at the University of Benin, Nigeria and the composition of the Alkaline Surfactant Polymer (ASP) slug used for the experiment are given in Table 1. The properties of the core sample are given in Table 2. While Table 3 gives a summary of the results gotten from the core flooding experiment. The PVT properties of the reservoir fluid used for the core flooding experiment are listed in Table 4. The values of maximum relative permeability (K_{rw_max} and K_{ro_max}) were used in plotting the relative permeability curves using Corey equation.

Table 1. Chemical slug composition [17]

Materials	Names	Concentration
Alkaline	Sodium hydroxide (NaOH) (98%)	1.0wt %
Surfactant	Sodium dodecyl sulfate (SDS)	0.3wt %
Polymer	Gum Arabic	5 000 ppm

Table 2. Core properties [17]

Core properties	Values
Core type	Class IV soda lime glass spheres
Length (cm)	25.6
Bulk volume (cm^3)	112.93
Porosity (%)	0.3367
Pore volume (PV) (cm^3)	38
Permeability (mD)	1540
Oil flow rate (cm^3/h)	60
Waterflood rate (cm^3/h)	60

Table 3. Results gotten from the core flooding experiments [17]

Initial oil saturation	82%
Initial water saturation	18%
Water flood	
Oil recovered	19.5 cm^3
Recovery	55 %
Residual oil	45 %
Asp flood	
Additional oil recovered	11.5 cm^3
Cumulative oil recovered	31 cm^3
Recovery	36.9 %
Residual oil	8.1 %
Residual recovery	82 %

Table 4. Core flooding PVT properties [17]

PVT properties	Values
Initial water saturation	0.18
Residual oil saturation	0.45
K_{rw_max}	0.8
K_{ro_max}	0.4
Water viscosity (cP)	0.32
Water sensity (lb/ft^3)	62.37
Oil density (lb/ft^3)	57.76
Water compressibility (psi^{-1})	3.03E-06
Reference pressure (psia)	118

3.1.1. Coreflooding simulation

A 1D model was developed in Eclipse™ by approximating a cylindrical plug into cuboidal rock sample. Then the cuboid is divided into 100 grid cells, as shown in Figure 1.

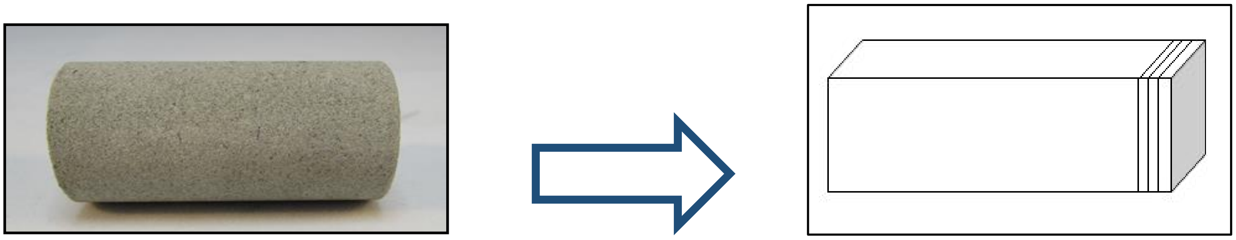

Figure 1. Scheme for approximating a cylindrical plug into cuboidal rock sample

The Eclipse model gave a pore volume of 38 cm^3, which is the same as the experimental pore volume. This model is maintained at a simplistic level to ensure small simulation time, along with ease of modification and debugging. Grid cells of 20, 50, 100, 200, and 500 were used to check for the optimum grid cells to use.

3.1.2. Dynamic simulation constraints

The dynamic model is bounded with the following constraints, as per laboratory experiments:

3.1.2.1. Initial constraints

Constant bottom-hole pressure at producing well = 118 psia = 8.02945 atma. This pressure is lower than the actual reservoir condition. However, due to the absence of any gas in the reservoir, this difference in pressure will not alter the flooding to a large extent. Constant inlet flow rate = 1mL/min = 60cm^3/hr.

3.1.2.2. Assumptions

- The core is completely homogenous,
- Corey law is applicable for relative permeability curves.

Corey law:

$$K_{rw}\,(S_w) = K_{rw,or}\left(\frac{S_w - S_{cw}}{1 - S_{cw} - S_{or}}\right)^{n_w} \quad (1)$$

$$K_{ro}\,(S_w) = K_{ro,cw}\left(\frac{1 - S_w - S_{or}}{1 - S_{cwi} - S_{or}}\right)^{n_w} \quad (2)$$

where: $K_{ro,cw}$ is oil relative permeability at minimum water saturation; S_{cw} is critical water saturation; S_{cwi} is initial water saturation; S_{or} residual oil saturation; N_o & N_w are Corey oil exponent.

Residual oil saturation values are found with terminal values of flooding of water and ASP. In the simulator, all the grid blocks were set at initial saturation. The water flood and ASP process were simulated to generate the oil production curve and oil recovery.

Table 5. Dynamics of flooding

Component	Concentration (ppm)	Approximate Slug Size (PV)
Initial waterflood		7
ASP Flood		
Alkali	10,000	0.3
Polymer	5000	
Surfactant	3000	
Final Water Flood		8

4. Results and discussion

A simple 100 * 1 * 1 model was built (using Eclipse™) with injection in the first cell and production in the last cell. Figs. 2 and 3 shows the saturation map for both the water and oil flooding, respectively in the core as shown by Floviz at the beginning of the flooding simulation. The simulation results show that after injecting 7 PV of water into the core model, the continual injection does not bring about additional recovery as the model is now producing at almost

100% water cut. History Matching is a common reservoir engineering technique to update a geological model. The reservoir model is modified to match the response of the field during the production phase, and further extrapolated to predict the future response of the reservoir. This method is commonly used to fit oil production trend and Bottom Hole Pressure (BHP).

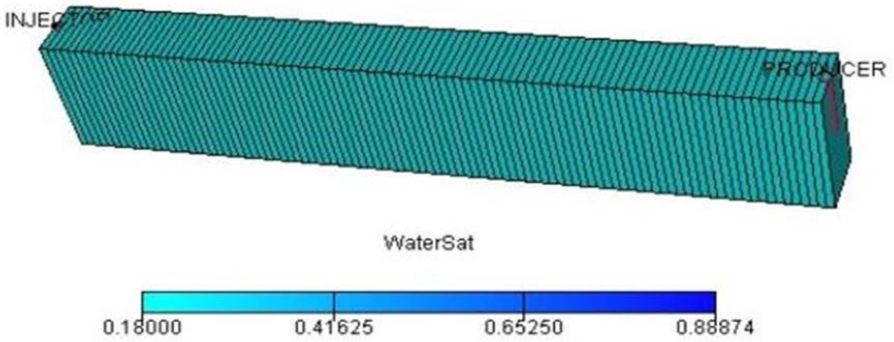

Fig 2. Water saturation map in flooding experiment.

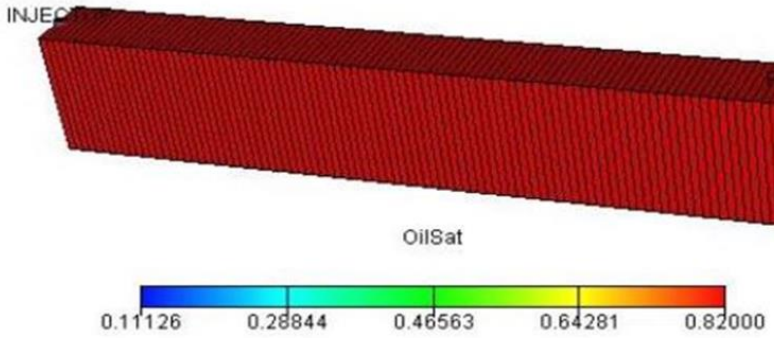

Fig 3. Oil saturation map in flooding experiment.

Figs. 4, 5 and 6 show the plot of oil recovery vs. pore volume of water injected, the plot of water cut vs. pore volume of water injected and total oil produced vs. pore volume of water injected respectively.The simulation model was able to show a total oil production of 19.17cm^3; this gives a waterflood recovery of 53% as compared with a total oil production of 19.5 cm^3 and recovery of 55% from the experimental core flood.

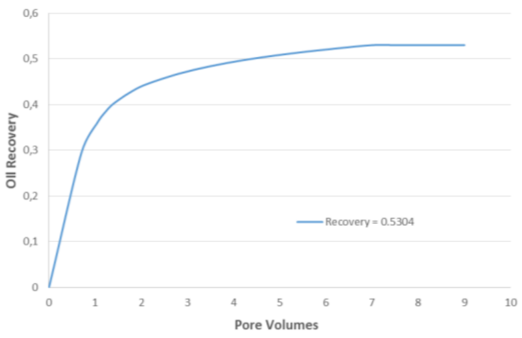

Fig. 4. Oil Recovery match for water flooding

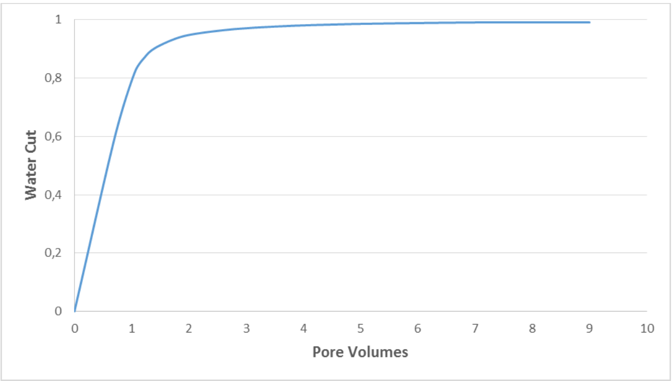

Fig. 5. Water cut match for water flooding

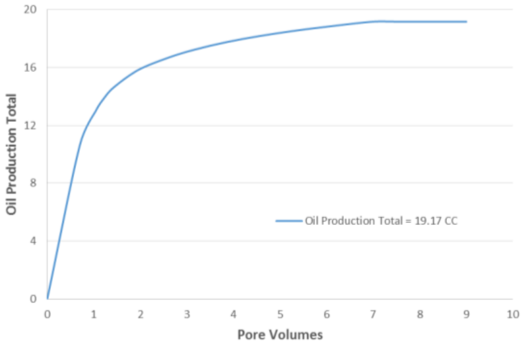

Fig. 6. Oil production total match for water flooding

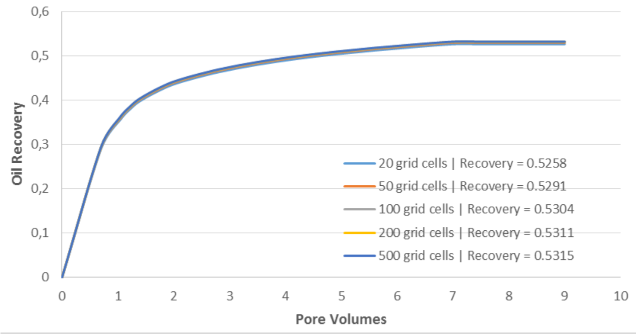

Fig. 7. Oil recovery variation with No of model grid cells

Before beginning the simulation work, a sensitivity analysis was performed to see which number of grid cell would give a result closest to the experimental results. Grid cells of 20, 50, 100, 200, and 500 were used to check for the optimum grid cells to use. From Fig. 7, it was concluded that for this simulation model, grid cell variation has little to no effect on the oil recovery as they gave a recovery ranging from 52% to 53%.

Having matched the water flood, simulation of the alkaline surfactant polymer (ASP) flooding started. Table 6 shows a summary of the flooding results. The simulation model was able to show a total oil production of 29.12 cm^3; this gives the ASP flood recovery of 80.53% as compared with a total oil production of 31.0 cm^3 and recovery of 82% from the experimental core flood. This is seen in Fig. 8.

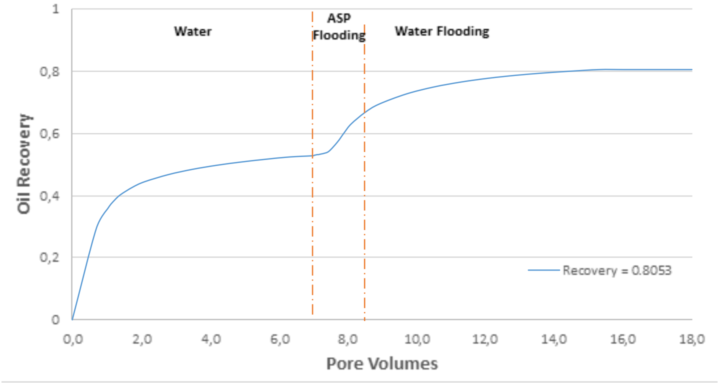

Fig. 8. Oil recovery for ASP flooding

The rise in oil recovery is due to alterations of the contact angle between oil-water-rock equilibrium to mobilize more oil; due to the presence of alkali and surfactant.

Table 6. Flooding results summary

Parameter	Core flooding model	Simulation model
	Waterflood	
Oil recovered	19.5 cm^3	19.17 cm^3
Recovery	55 %	53.04 %
	ASP Flood	
Oil recovered	31 cm^3	29.12 cm^3
Recovery	82 %	80.53 %

4.1. Sensitivity analysis

This involves the study of the effect of alterations in individual parameters of the system on final outputs. Trends of variations of output parameters with the marginal change of an input parameter are plotted. Also, extreme cases are generated to rectify boundary assumptions. Sensitivity analysis plays an important role to understand systems with multiple variable parameters. Core flooding is dependent on different parameters, so sensitivity analysis is often used to explore optimized flooding in reservoirs as well as plugs. The parameters for the sensitivity analysis are shown in Table 7.

Table 7. Sensitivity analysis parameters summary

Parameter	Base case	Sensitivity analysis values/multipliers
Injection Rate	60 cm^3/hr	Keeping injection time constant: cm^3/h Keeping injected PV constant: 30 cm^3/h, 90 cm^3/h and 120 cm3/h
PV of ASP Injected	0.3 PV	PV variation at 0.1, 0.5, 1.0 and 1.5 PV of ASP injected
Viscosity (polymer concentration)	5000 ppm	Viscosity variation with polymer concentration Variation: 0 ppm, 500 ppm, 2500ppm, & 10000 ppm

4.2. Injection rate

Initially, models that were generated for sensitivity analysis of injection rate had equal pore volume injected of each phase, as the base case. This was achieved by adjusting injection time. One model was developed with half of the volume injected at each stage of injection, without altering total injection time. So total pore volume injected became half. Injection rate is one of the important parameters to be adjusted in reservoir engineering because of following pros and cons:

- Injection rates are limited by fracking pressure. Above certain pressure, there is a risk of fracking the reservoir, creating a loss of injection water to some uncertain point of reservoir.
- Higher injection rate will increase production rate; saving money in terms of time
- Higher injection rate have a higher risk of un-swept oil volume (poor volumetric sweep efficiency if not monitored well)

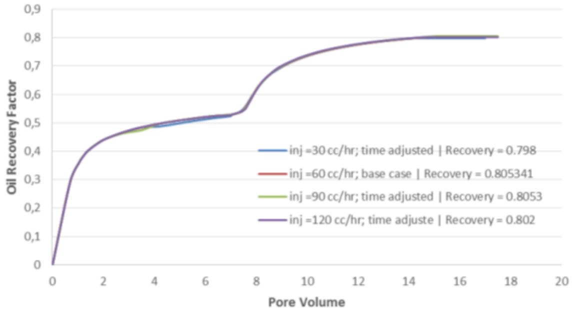

Fig. 8. Injection rate sensitivity with constant volume

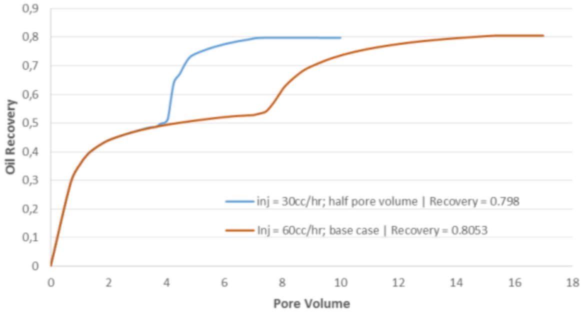

Fig. 9. Injection rate sensitivity with injection time

All injections rates (for constant pore volume injection) show similar production behavior (Fig. 8). Despite injecting lower injection volume, simulation of injection rate of 30cm^3/hr reached almost similar total oil recovery factor (Fig. 9). This can be explained with the long injection of water flooding to achieve a steady state.

4.3. Viscosity (polymer concentration)

Viscosity variation is mainly caused by the polymer concentration. As discussed earlier, polymers give stable waterfront to flooding. This results in higher volumetric sweep efficiency. Followings are the pros and cons of the polymer concentration variation:

- Higher polymer concentration will injection pressure; resulting in increase injection cost
- Lower polymer concentration will not create stable waterfront, might cause fingering effect
- Higher polymer viscosity can cause blockage of small pore size at the injection point, resulting in reduced efficiency of the injector well.

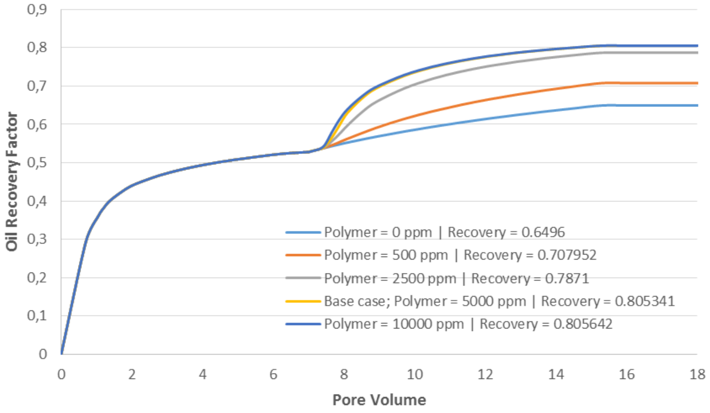

Fig. 10. Results of sensitivity analysis for polymer concentration

With increasing polymer concentration, recovery factor increased (Fig. 10). However, in the lower range of polymer concentration, the marginal increase in recovery factor is higher compared to the marginal increase in a higher concentration of polymer. This can be attributed to the stabilization of the waterfront. Due to stable waterfront above 5000ppm, polymer concentrations above it resulted in almost equal recovery factor but at higher injection cost.

4.4. PV of ASP injected

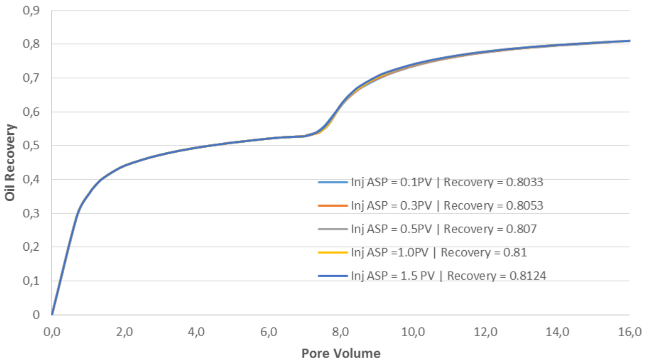

Sensitivity analysis on the pore volume of the ASP injected was carried out to identify the optimum value of ASP slug, which should be injected. With increasing pore volume of ASP slug injected, recovery factor also increased although the increase was very minimal (Fig. 11).

Fig. 11. Results of sensitivity analysis for PV of ASP injected

4.5. Field simulation model

Assuming a synthetic reservoir of three layers with varying permeabilities, a 10x10x3 grid was built in Eclipse with negligible capillary pressure to run a 3D field-scale reservoir simulation. The flow rates of both the injection and production wells are set at 1258 stb/d. All the characteristics of the model have been summarized in Table 8. The reservoir PVT properties is and dynamics for the ASP flooding for the reservoir shown in Table 9 and Table 10, respectively.

Table 8. Eclipse model characteristics

	Layer 1	Layer 2	Layer 3
Blocks	100	100	100
Reservoir pop depth	2600ft	2600ft	2600ft
Layer depth	0.58ft	0.84ft	0.47ft
Porosity	25%	25%	25%
Permeability X and Y	4500md	3300md	2400md
Permeability Z	1050md	1800md	500md

Table 9. Reservoir PVT properties (SI Units)

PVT properties	Values
Initial water saturation	0.2
Residual oil saturation	0.3
K_{rw_max}	0.8
K_{ro_max}	0.5
Water viscosity	0.88
Water density	998
Oil density	850
Water compressibility	4.6 E-06
Reference pressure	270

Table 10. Dynamics of ASP flooding for reservoir

Component	Concentration (ppm)	Approximate flooding duration (days)
Initial waterflood		600
ASP Flood		
Alkali	10,000	50
Polymer	5000	
Surfactant	3000	
Final Water Flood		600

The saturation maps below give the STOIIP of the reservoir during the simulation process. Fig 12 shows the initial oil saturation before the flooding started. On injecting water, we notice how the saturation profile changes as the injected fluid move towards the producer (Fig. 13)

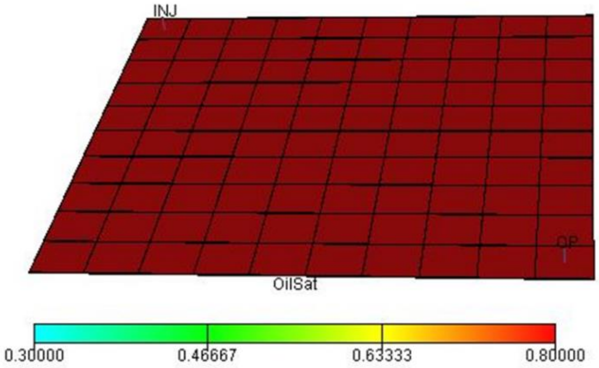

Fig. 12. Oil saturation map in the reservoir at the beginning of the simulation

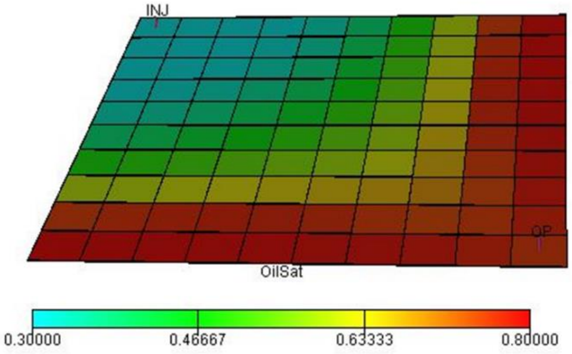

Fig. 13. Oil saturation map in the reservoir during the water flood simulation

After about 400 days of water injection, the oil saturation in the reservoir no longer changes with a continual injection of water (Fig. 14).

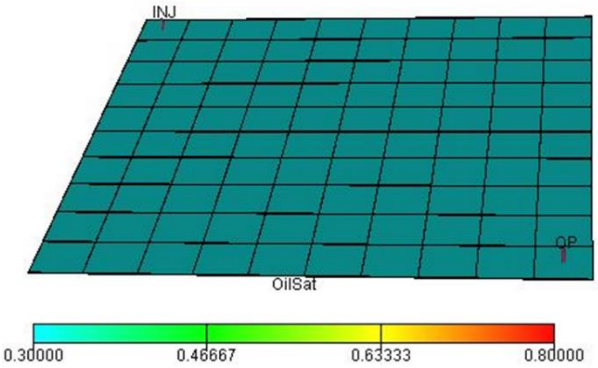

Fig. 14. Oil saturation map at the end of the waterflood simulation

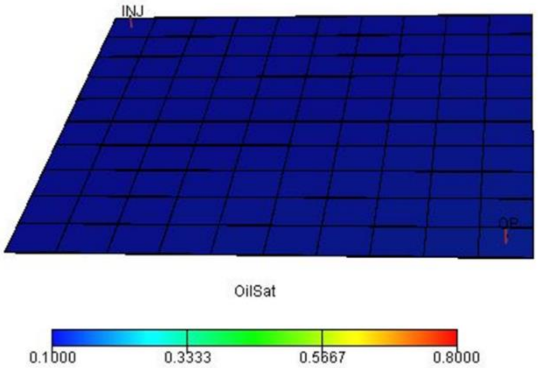

Fig. 15. Oil saturation map at the end of the ASP flood simulation

We then turned to the injection of our ASP slug, followed by water flooding. The field study has proved that the ASP slug formulated is effective has it reduced the oil left the reservoir as shown in the saturation maps (Fig. 15).

The total oil production and oil recovery increased from 10516.51 STB and 62.48 % at the end of the water flooding to 14387.325 STB and 85.8% (Fig. 16) respectively on the addition of an ASP slug. This is an additional recovery of 3870.815 STB.

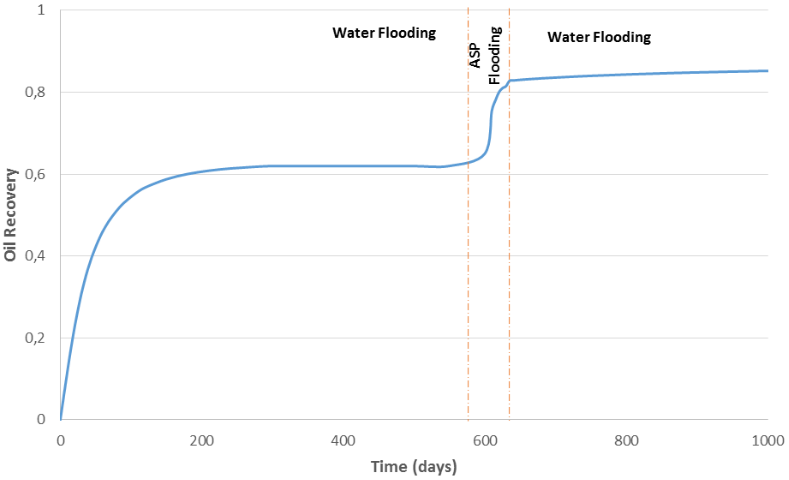

Fig. 16. Oil Recovery profile for ASP flooding of the synthetic reservoir

5. Conclusion

This study showed that the numerical simulation of ASP core flooding using Gum Arabic as a polymer could be done using Eclipse as the simulator. This was done by matching a core flooding experiment using Gum Arabic and formulating an optimal ASP system that reduces residual oil saturation to a minimum to improve oil recovery.

Grid cell variation has little to no effect on the oil recovery on the core as they gave a recovery ranging from 52% to 53% with water flooding. Sensitivity analysis of injection rates (at constant pore volume injected) showed similar production behavior. Despite injecting lower injection volume, (similar injection time), a lower injection rate reached almost similar total oil recovery factor with a long injection of water flooding to achieve a steady state.

Sensitivity analysis of viscosity showed an expected trend of increasing viscosity of injected flooding resulting in increased oil production.Sensitivity analysis on the pore volume of the ASP injected showed recovery factor increased with an increasing pore volume of ASP slug injected, although the increase was very minimal.

Extrapolating from core to field simulation, the ASP slug formulated was able to increase field total oil production by increasing recovery from 62.48 % at the end of the water flooding to 85.8%. Gum Arabic has proven to be an effective polymer for EOR operations based on the numerical simulation results obtained.

References

[1] Dang C, Nghiem L, Nguyen N, Yang C, Chen Z & Bae W. Modeling and optimization of alkaline-surfactant-polymer flooding and hybrid enhanced oil recovery processes. Journal of Petroleum Science and Engineering. 2018. DOI: 10.1016/j.petrol.2018.06.017.

[2] Gabriel A. Economic Value of biopolymers and their use in enhanced oil recovery, Polysaccharides, and Polysaccharases, Academic press, 1979.

[3] Keshtkar S, Sabeti M, & Mohammadi AH. Numerical approach for enhanced oil recovery with surfactant flooding. Petroleum.2016; 2(1): 98–107.

[4] Rai KS, Bera A, Mandal A. Modeling of surfactant and surfactant – polymer flooding for enhanced oil recovery using STARS (CMG) software Modeling of surfactant and surfactant – polymer flooding for enhanced oil recovery using STARS (CMG) software, (October 2015).

Journal of Petroleum Exploration and Production. 2014. https://doi.org/10.1007/s13202-014-0112-3.

[5] Rafael J, Kaczmarczyk. Approximation of Primary , Secondary , and Tertiary Recovery Factors in Viscous Oil Reservoirs Deposited in Ugandan Sands (Masters Thesis). Imperial College London, London, United Kingdom. 2012.

[6] Green DW & Willhite GP. Enhanced Oil Recovery, SPE Textbook Series, Henry L. Doherty Memorial Fund of AIME, Society of Petroleum Engineers, Ricardson, Texas, US. 1998. Vol. 6.

[7] Kevin II & Raymond EA. Potential of Polyacrylamide –Sodium Carboxy-methyl Cellulose Graft Polymer as Flooding Material in Enhanced Oil Recovery. SPE-NAICE 1999.

[8] Sinha KA, Bera A, Raipuria V, Kumar A, Mandal, & Kumar T . Numerical Simulation of Enhanced Oil Recovery by Alkali-surfactant-polymer Floodings,Petroleum Science and Technology. 2015ed. 33:11, 1229-1237.

[9] Dong M, Ma S, & Liu Q. Enhanced heavy oil recovery through interfacial instability: A study of chemical flooding for Brintell heavy oil. Fuel 88, 2009; 1049–1056.

[10] 10.0 Druetta & Picchioni F. Journal of Petroleum Science and Engineering Polymer and nanoparticles flooding as a new method for Enhanced Oil Recovery. Journal of Petroleum Science and Engineering. 2019; 177: 479–495.

[11] Jamaloei BY, Asghari K & Kharrat R. The investigation of suitability of different capillary number definitions for flow behavior characterization of surfactant-based chemical flooding in heavy oil reservoirs. J. Pet. Sci. Eng.2012; 90–91:48–55.

[12] Pei H, Zhang G, Ge J, Tang M & Zheng Y. Comparative effectiveness of alkaline flooding and alkaline–surfactant flooding for improved heavy-oil recovery. Energy Fuels. 2012; 26: 2911–2919.

[13] Ansarizadeh M, Mary P, & Strong J. Alkaline surfactant polymer flooding to revitalize oil production from a mature water flooded field. SPE 155541-MS, SPE EOR Conference at Oil and Gas West Asia, Muscat, Oman, April 16–18, 2012.

[14] Arihara N, Yoneyama T, Akita Y & XiangGuo L. Oil Recovery Mechanisms of Alkali-Surfactant-Polymer Flooding. Society of Petroleum Engineers. 1999.

[15] Druetta P & Picchioni F. Influence of the polymer degradation on enhanced oil recovery processes. Applied Mathematical Modelling. 2019; 69, 142–163.

[16] aiwo, Oluwaseun & Olafuyi, OA. Surfactant and surfactant-polymer flooding for light oil: A gum Arabic approach. Petroleum and Coal. 2015; 57. 205-215.

[17] Onuoha SO & Olafuyi OA. University of Benin. Alkali/Surfactant/Polymer flooding using Gum Arabic; A comparative analysis. Nigeria Annual International Conference and Exhibition, Lagos, Nigeria, 30 July-1 August, 2013.

[18] Thomas S & Ali SMF. Micellar Flooding and ASP-Chemical Methods for Enhanced Oil Recovery. Proceedings. CSPG and Petroleum Society Joint Convention, Digging Deeper, Finding a Better Bottom Line.1999.

[19] Ujuanbi S, SPE, Taiwo OA, Olafuyi OA. Alkaline-Surfactant-Polymer Flooding For Heavy Oil Recovery From Strongly Water Wet Cores Using Sodium Hydroxide, Lauryl Sulphate, Shell Enordet 0242, Gum Arabic And Xanthan Gum, SPE. Presented at the Nigeria Annual International Conference and Exhibition (SPE-NAICE) in Lagos, Nigeria, 4 – 6 August 2015.

[20] Wang Y, Zhao F, Bai B, Zhang J, Xiang W, Li X, Zhou W. Optimized Surfactant IFT and Polymer Viscosity for Surfactant-Polymer Flooding in Heterogeneous Formations. SPE 127391, presented at the 2010 SPE Improved Oil recovery Symposium held in Tulsa, Oklahoma, USA, 24-28 April 2010.

[21] Wang J & Dong M. A Laboratory Study of Polymer Flooding for Improving Heavy Oil Recovery. Proceedings of Canadian International Petroleum Conference. 2007. 1–9.

[22] Hasan AM & Abdel-raouf ME. Applications of guar gum and its derivatives in petroleum industry : A review. Egyptian Journal of Petroleum. 2018; 27(4), 1043–1050.

[23] Orodu OD, Orodu KB, Afolabi RO & Dafe EA. Rheology of Gum Arabic Polymer and Gum Arabic Coated Nanoparticle for enhanced recovery of Nigerian medium crude oil under varying temperatures. 2018. Data in Brief, 19, 1773–1778.

[24] Solomon U, Oluwaseun T, Olalekan O. Alkaline-Surfactant-Polymer Flooding for Heavy Oil Recovery from Strongly Water Wet Cores Using Sodium Hydroxide , Lauryl Sulphate , Shell Enordet 0242 , Gum Arabic and Xanthan Gum. Nigeria Annual International Conference and Exhibition held in Lagos, Nigeria, 4–6 August 2015, SPE-178366-MS.

[25] Taiwo OA, Mamudu A & Olafuyi O. "Comparative Studies of the Performance of ASP Flooding on Core Plugs and Beadspacks" Paper SPE 184291 presented at the Nigeria Annual International Conference and Exhibition held in Lagos, Nigeria, 2 – 4 August 2016.

[26] AlSofi AM, Liu JS & Han M. Numerical simulation of surfactant–polymer core flooding experiments for carbonates. J. Pet. Sci. Eng. 2013; 111:184–196.

[27] Goudarzi A, Delshad M & Sepehrnoori K. A Critical Assessment of Several Reservoir Simulators for Modeling Chemical Enhanced Oil Recovery Processes. Society of Petroleum Engineers. 2013.

[28] Pandey A, Beliveau D, Corbishley D & Kumar MS. Design of an ASP pilot for the Mangala Field: laboratory evaluations and simulation studies. SPE 113131, Indian Oil and Gas Technical Conference and Exhibition, Mumbai, India, March 4–6, 2008.

[29] Mamudu A, Olalekan O & Uyi PG. Analytical Study of Viscosity Effects on Water flooding Performance to Predict Oil Recovery in a Linear System. J Pet Environ Biotechnology. 2018; 6: 221.

[30] Nelson RC, Lawson JB, Thigpen DR & Stegemeier GL. Cosurfactant-Enhanced Alkaline Flooding. Spe/Doe 12672.1984. 413.

[31] Hawkins B, Taylor K, Nasr-El-Din H & Inst PR. Mechanisms of Surfactant and Polymer Enhanced Alkaline Flooding : Application To David Lloydminster and Wainwright Sparky Fields”. Cim Petrol. Soc. & Aostra Tech. Conf. Banff, Can, 4/21-24/91 Preprints, 1(91–28).

[32] Tong Z, Yang C, Wu G, Yuan H, Yu L & Tian G. A Study of Microscopic Flooding Mechanism of Surfactant/Alkali/Polymer. Society of Petroleum Engineers.1998.

[33] Arihara N, Yoneyama T, Akita Y & XiangGuo L. Oil Recovery Mechanisms of Alkali-Surfactant-Polymer Flooding. Society of Petroleum Engineers. 1999.

[34] Avwioroko JE, Taiwo OA, Mohammed IU, Dala JA & Olafuyi OA. A Laboratory Study of ASP Flooding on Mixed Wettability for Heavy Oil Recovery Using Gum Arabic as a Polymer. SPE 172401, Presented at SPE-NAICE, Annual Meeting, Lagos, August 5-7, 2014.

[35] Tarek, Ahmed. Reservoir Engineering Handbook. Burlington, Vermont; Gulf Professional Publishing. 2006.

To whom correspondence should be addressed: Dr. Oghenerume Ogolo, Department of Petroleum Engineering, African University of Science and Technology, Abuja, Nigeria, E-mail: oogolo@aust.edu.ng

Petroleum and Coal

Article **Open Access**

TECHNOLOGY OF MODIFIED BITUMEN PRODUCTION FOR THE ROAD CONSTRUCTION

A. Mardupenko, A. Grigorov, I.Sinkevich, A. Tulskaya

National Technical University «Kharkov Polytechnic Institute», 61002, 2 Kirpichova str., Kharkov, Ukraine

Received March 14, 2019; Accepted May 21, 2019

Abstract

In the current article, there has been proposed technology of production of the modified bitumen that is based on the compounding of petroleum residue with solid domestic wastes at 420–470K. The advantages of technology are compactness of technological scheme, simplicity of technological equipment, and minimal hazardous emission. There have been obtained laboratory samples with the properties that exceed the properties of commodity bitumen PRB-90/130 (petroleum road bitumen). The produced modified bitumen has expanded temperature range of application, which makes the bitumen universal for any climatic exploitation zone.

Keywords: *Modified bitumen; Oil sludge; Polymer wastes; Compounding; Softening point; Fraction; Grinding.*

1. Introduction

Bitumen is the general component of construction and road materials, and its quality defines the exploitation properties of these materials. Bitumen is widely used primarily due to its versatility. Wide range of construction materials may be produced for different purposes using bitumen as a base. However, in some instances, road compositions with bitumen are not available to provide high strength, long operation time, safe exploitation, and durability of road cover. That is why the increase in quality of commodity bitumen is still one of the most important tasks.

2. Aims and scope

The modern production of petroleum bitumen includes the following stages: oxidation and compounding of petroleum residue [1]. The low-quality petroleum bitumen produced in this way can be applied in road construction, but its general drawback is narrow temperature range which does not match the significant annual temperature fluctuations. In this case, we apply modifiers and surfactants to increase the quality of bitumen and the road pavement.

To be applied as a modifier the substance should meet the following requirements: low price; processing ability; easily accessible for industrial scale; ability to form the homogenous structure with a bitumen; not to make a harmful environment affect

It should be mentioned that according to world practice, the most widely used modifiers are polymers that increase the softening temperature of bitumen, its elasticity, and low-temperature properties [2-4].

There are several articles that describe polymer-modified bitumen as a material with inner reinforcement. The polymer frame provides the strength and plastic deformation of material [5-6].

It should also be considered that increase of polymer concentration in bitumen over 12% according to [7] leads to inversion – polymer turns to base (matrix) and bitumen turns to the polymer as a filling agent. Compatibility of bitumen with different polymers is also an important factor. For the practical application of modifying bitumen, we should control the property change of bitumen in the dependence of polymer concentration. Having a significant molecular weight comparing to bitumen, polymers can be applied as an effective thickener. Injection of a small number of polymers into bitumen makes affect the softening temperature of bitumen and decreases penetration [8].

Authors of [9] have presented the research of the new type of material – polyethylene tar astringent of asphalt road pavement with high physical, chemical, and exploitation properties. There is a research of the application of polyethylene for the production of encapsulated bitumen. Addition of polyethylene up to 15 % increase the frost resistance by 30 K and decrease the temperature of bitumen glass-transition to 248 K [10].

Nowadays, the most effective modifiers for bitumen are thermoplastic elastomers that combine high strength and elasticity [11-12].

Bitumen may also be modified by oil polymer tar (OPT) – the specific type of synthetic tar and can be mostly applied in tire and resin production as a softener. Addition of OPT into bitumen makes an affect of its structure – a grid of tar and asphalting bitumen components and high-molecular compounds of tar also there can be observed plasticization of supramolecular tar structure. There has been provided research of bitumen RPB (road petroleum bitumen) 130/200 and B-5 with the addition of OPT that was obtained from heavy pyrolysis tar. Addition of 1-3 % of OPT provides the increase of extensibility, elasticity, the adhesive, and cohesive strength of bitumen composition [13].

Generalizing the given information, it should be mentioned that modifiers are produced through the energy-intensive technological processes and as a result, are very expensive. In this case, the search for relatively cheap and effective modifier should be performed among the domestic wastes, for example, polyethylene, polypropylene, and polystyrene foam.

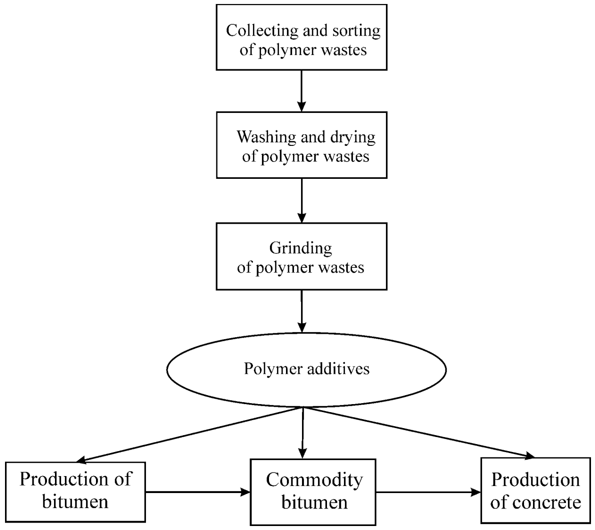

To intensify the technological processing of domestic wastes they should be previously prepared for intensification the general process of modifiers production (Fig. 1)

All technologies of production of bitumen modified with polymers provide the addition of polymers to commodity bitumen (Fig. 1) or while the preparation of asphalt and concrete mixture that increase the energetic expenses. To decrease these expenses, we propose the compounding of warm petroleum waste (oil sludge, in particular) with polymers.

Fig. 1. Structural scheme of modified bitumen production

3. Results and discussion

The proposed technology of modified bitumen production has numerous advantages comparing to the classic technology. Oxidation petroleum residue for production of bitumen provides the heating of raw material up to 530–560 K and force the significant amount of air through the heated raw material. According to the proposed technology heating, the basic petroleum fraction is performed to the polymer melting point, which is 420–470 K depending on the type of polymer. Also, there is no necessary to involve expensive equipment such as oxidizing column, compressor, etc.

Another advantage is that the performing of the proposed technology is not accompanied by thermal destruction of components and as a result – there is possible to avoid harmful emission. Structure of modified bitumen is constant in a wide temperature range, which is connected to the increase of petroleum residue viscosity. Thus the disperse system bitumen-polymer does not get stratified during the storage and transportation.

The proposed technology of modified bitumen production is a part of the system of oil sludge processing and can be performed through the sequence of technological operations (Fig. 2).

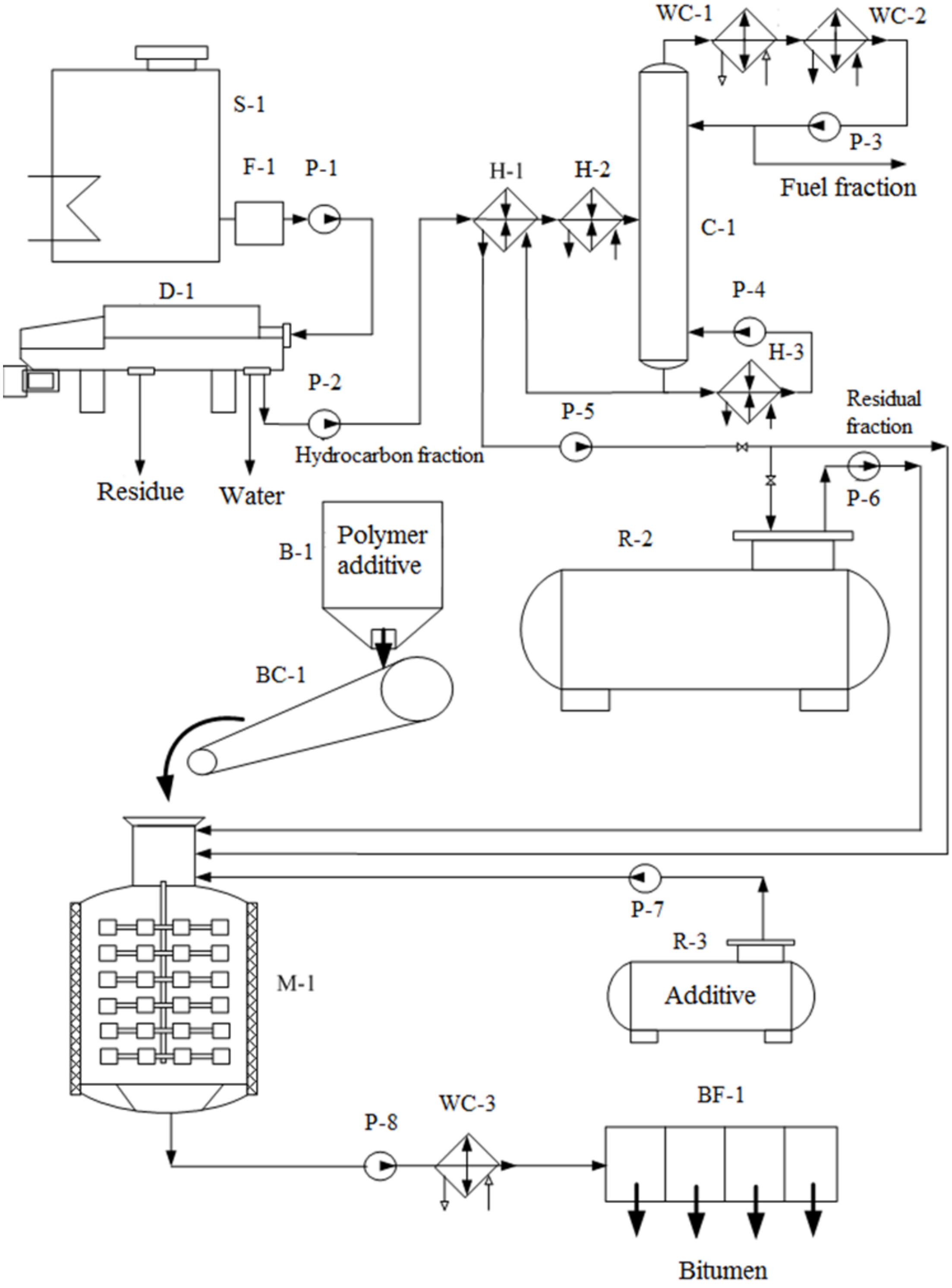

Fig. 2. Technological scheme of modified bitumen production

Oil sludge is a harmful industrial waste and has to be utilized from the feed tank – sump S-1 through the filter F-1 by pump P-1 and goes to decanter D-1. In decanter, D-1 oil sludge is separated into three parts: sludge which is applied as a filler for many construction materials; water which goes to the sump and then to the reverse water cycle and hydrocarbon fraction.

Hydrocarbon fraction goes to distillation column C-1 by pump P-2 through the heat-exchangers H-1 and H-2. In H-1 and H-2 it is heated to the temperature of fraction separation. In C-1 hydrocarbon fraction is separated into fuel fraction (boiling point = 630 K) and residual fraction (boiling point > 630 K). The fuel fraction comes out from the top of column K-1, goes through the air cooler AC-1, water cooler WC-1 then goes to the column K-1 by pump P-3 for irrigation. The excess amount of fuel fraction can be applied as the raw material in primary oil processing or as a boiler or heating fuel. The residue fraction comes out from the bottom of the K-1 and splits into two streams. The stream is pumped by P-4 through the heat-exchanger T-3 and goes back to the column for temperature support. The second stream is pumped by P-5 through the heat-exchanger H-1 and then does to the paddle mixer M-1. The scheme provides the collection of residual fraction in reservoir R-1 from where it can be pumped by P-6 into mixer M-1.

Paddle mixer provides feeding of solid grinded polymer from bunker B-1 through the belt conveyor BC-1. Also, the adhesive additives can be added to M-1 by pump P-7 from the reservoir R-3 if it is necessary.

In M-1 mixture can be heated up to 500 K at the constant mixing at 1000 rpm. Mixer M-1 should also have isolation lining. Parameters of the process, such as the temperature of heating, frequency, and duration, depending on the type of polymer.

After the mixing bitumen goes to the bitumen feeder BF-1 by the pump P-8 through the air-cooler AC-3. In BF-1 it is packed up at 330-340 K and goes to the storage. BF-1 provides the production of four bitumen types, depending on the polymer.

The proposed technological scheme can be performed either at the refineries of as a separate unit. However, for the economic expediency should be applied as a part of the technological scheme at the refinery.

Using the proposed in the laboratory, we produced the bitumen that has been compared to the oxidized bitumen PRB -90/130 that have been chosen according to the annual temperature of the coldest season. The characteristics of this bitumen are presented in Table1.

Table 1. Quality characteristics of bitumen

№	Characteristic	PRB-90/130	Sample №1	Sample №2
1.	Type of polymer	-	PP	PPS
2.	Concentration of polymer, %mass.	-	10	10
3.	Cone penetration depth, mm^{-1} at 298 K	91-130	121	82
4.	The softening point, K	316-325	398	383
5.	Flash point in the open cup, K	230	242	190
6.	Brittleness temperature, K	-15	- 38	-31
7.	Solubility in an organic solvent, no less than, %	99	97,5	96,3
8.	Mass changing after heating, no more than %	1,0	1,0	1,0
9.	Adhesive properties, «active grip with marble and sand of the control sample №1	With stand		

As it has been shown in Table 1, the properties of control samples significantly exceed the properties of bitumen PRB 90/130. This obstacle in its turns expands the temperature range of application, which makes the bitumen universal for any climatic exploitation zone.

4. Conclusion

Modifying of bitumen with polymers is one of the most perspective ways of production high-quality bitumen materials for different fields of industry.

Compounding of petroleum residue with polymers is considered to be the most effective technology for commodity bitumen production. In this case, there is no necessary to involve expensive technological equipment, and it is possible to decrease the duration and temperature of the technological process.

The obtained results have shown that the addition of 5 % of polymers to the petroleum residue allows obtaining the commodity material with exceeding properties comparing to road bitumen produced at the Ukrainian refineries.

References

[1] Himmat S, Jain PK. Bitumen quality and manufacturing processes-Past and present technological status. IJCT, 1997;04(6): 259-276.

[2] Toraldo E, Mariani E. Effects of polymer additives on bituminous mixtures. Construction and Building Materials, 2014; 65: 38-42.

[3] Hudyakova TS, Masyuk AF, Kalinin VV. Osobennosti strukturyi i svoystv bitumov, modifitsirovannyih polimerami. Dorojnaya tehnika, 2003; 7: 174-181.

[4] Zhu J, Birgisson B, Kringos N. Polymer modification of bitumen: Advances and challenges. European Polymer Journal, 2014; 54: 18-38.

[5] Evdokimova NG, Bayguzina YUA, Ivanova AV. O vyibore tehnologii polucheniya ostatochnyih i modifitsirovannyih ostatochnyih dorojnyih bitumov iz sahalinskih neftey. Neftegazovoe Delo, 2017; 4: 55-68.

[6] Andreev AF, Markov SV. Sovremennoe sostoyanie i perspektivyi razvitiya bitumnogo proizvodstva v Rossii. Problemyi ekonomiki i upravleniya neftegazovyim kompleksom, 2009; 7: 31-34.

[7] Gohman LM. O vliyanii kachestva organicheskih vyajuschih materialov na razvitie seti avtomobilnyih dorog v Rossii. Sb. Trudov nauchno-prakticheskoy konferentsii, posvyaschennoy 50-letiyu obrazovaniya bitumnoy laboratorii RGU nefti i gaza imeni I.M. Gubkina. - M.: RGU nefti i gaza im. I.M. Gubkina, 2013; 13-20.

[8] Smirnov NA. Novaya jizn «vyijatyih» bitumov. Dorogi Rossii XXI veka, 2002; 6: 70 – 78.

9\. Gureev AA, Samsonov MV, Overin DI, Zaychenko VA. Polietilengudronovyie vyajuschie – innovatsionnyiy material dlya dorojnogo stroitelstva. Mir nefteproduktov, 2014; 12: 33-35.

[10] Kovalev YAN, Romanyuk VN. Kapsulirovanie bituma himicheski sovmestimoy polimernoy dobavkoy, svoystva modifitsirovannogo vyajuschego i asfaltobetona na ego osnove. Nauka i tehnika v dorojnoy otrasli, 2007; 1: 29 – 31.

[11] Gohman LM. Kompleksnyie organicheskie vyajuschie materialyi na osnove bloksopolimerov tipa SBS. ZAO «EKON-INFORM»,2004. - 585 s.

[12] Kishchynskyi S, Nagaychuk V, Bezuglyi A. Improving Quality and Durability of Bitumen and Asphalt Concrete by Modification Using Recycled Polyethylene Based Polymer Composition. Procedia Engineering, 2016; 143: 119-127

[13] Pozdnyaeva LV. Neftepolimernaya smola v kachestve modifikatora neftyanyih dorojnyih bitu mov. Sb. nauch. tr. GP Rosdornii, 1996;.8: 42 – 55.

To whom correspondence should be addressed: Dr. A. Tulskaya, Ukrainian State Research Institute for Carbochemistry, 61023, 7 Vesnina str., Kharkov, Ukraine, E-mail: fuel.khpi@gmail.com

Petroleum and Coal

Article **Open Access**

TECHNOLOGY OF RECYCLING WASTE LUBRICANT GREASES

Andrey Grigorov[1], Ivan Nahliuk[2], Oleg Zelenskii[1, 3], Natalia Ponomarenko[4]

[1] *National Technical University «Kharkov Polytechnic Institute», 61002, 2 Kirpichova str., Kharkov, Ukraine*
[2] *Kharkiv National Automobile and Highway University, 61002, 25 Yaroslava Mudrogo str, Kharkov, Ukraine*
[3] *Ukrainian State Research Institute for Carbochemistry, 61023, 7 Vesnina str., Kharkov, Ukraine*
[4] *Ukrainian State University of Railway Transport, 61050, 7 Feuerbach square, Kharkov, Ukraine*

Received March 14, 2019; Accepted May 21, 2019

Abstract

A scheme for the production of plastic greases based on high-boiling fractions of oil sludge and used lubricating oils, as well as polymer waste, in the form of HDPE, LDPE, and PP, that is used as a thickener, has been proposed. Based on the used lubricating oils and polymer thickeners, grease lubricants were obtained. They can be used in the temperature range, on average, up to 80–130 °C (depending on the polymer) and speed mode in the bearing up to 4000 rpm. These greases are not worse in their properties to classical ones; analogs obtained based on distillate fractions, thickened with metal soaps, which are widely used in industry today.

Keywords*: Grease; Recycling; Dispersion medium; Thickener; Polymer additives; Waste; Preparation of raw materials.*

1. Introduction

In the recent decade in the technosphere, so-called recycling technologies have been widely developed. They allow expanding the raw material base for many technological processes, in particular in oil refining, through the use of secondary raw materials. These technologies, compared with those that have been around for more than a decade, have been used in the production of marketable petroleum products, and have a number of significant advantages to which include using of industrial and household waste; reducing the cost of production associated with the purchase of raw materials; increasing the production culture and improving the environmental situation.

2. The purpose and objectives of the research

A series of directives [1-2] adopted in the EU and their associate members, in particular in Ukraine, served as an impetus for the development of amendments to the Law of Ukraine "Waste." They governed the behavior of waste based on its sorting by type. Sorting waste by type is the initial stage of any recycling technology, on which its effective implementation largely depends. Also, a lot of important requirements for waste, as the raw material of recycling technology, are its quantity, which is able to provide the necessary production volumes of processing.

Today, the leading place in the world among multi-ton liquid industrial wastes, consisting mainly of hydrocarbons, is oil slime – oil sludge, which is formed when using technological equipment at refineries and used lubricating oils. The peculiarities of their chemical composition make it possible to apply thermo-destructive processing technologies to them, using catalysts, aimed at obtaining different types of fuels. An example is the pyrolysis-reforming technology of oil sludge, which allows you to get up to 35.5 wt% of fuel, its chemical composition (C_7–C_{26}) is similar to diesel fuel and having a value of higher heat of combustion of 46.1 MJ/kg and cetane index 38.51. As a catalyst in this process, it is proposed to use ash, which, due to the content of elements of iron and sulfur, has catalytic properties [3]. A variant of the technology of pyrolysis of oil sludge using a nitrogen carrier gas, in the temperature range of 378–873 K, is proposed. The gaseous products of this technology are 50.88 wt% CO_2; 17.78 wt% H_2O; 6.11 wt% CO and 25.23 wt% of low molecular weight paraffins and olefins (C_1–C_2). The liquid distillate has a calorific value of 45.35 MJ/kg, and its characteristics resemble diesel fuel [4]. Also, it is a very interesting technology of turning oil sludge into pyrogas, which can be used as fuel, by heating it to 1000°C in a plasma arc, without oxygen access [5].

There is a technology for producing fuel, in its characteristics similar to diesel fuel, through pyrolytic distillation, used engine oil. The fuel yield is up to 60 % of the raw materials [6]. In work [7], it was proposed to obtain fuel according to its characteristics (octane number 96 units, flash point 245 K) similar to gasoline, from used engine oil using catalytic pyrolysis technology on an aluminosilicate catalyst. It should be noted that along with the production of fuels, which is important and in demand, is the direction for the production of lubricants, in particular, plastic lubricants. As shown by the analysis of data on the use of recycling technologies, this issue is not given enough attention, and it is precisely the plastic lubricants that are petroleum products that perform their functions in those conditions (high temperatures, loads and rotational speeds) in which no other lubricant is suitable. In this regard, in this paper, we will propose a flow chart for the production of recycling greases; various functional purposes based on oil sludge and used lubricating oils.

3. Results and discussion

As is well known, classic plastic lubricants consist of a base component (dispersion medium), a thickener and additives. As a dispersion medium, you can use waste lubricating oils of any functional purpose: industrial, hydraulic, turbine, engine, and transmission. As for oil sludge, it must be pre-cleaned from water, mechanical impurities, and acidic components that cause corrosion of the equipment. Given its presence in it of light hydrocarbon fractions in the production of greases, it is advisable to use only the fractions obtained during its processing.

The choice as a dispersion medium, oil sludge, and waste oils, which contain a significant amount of high molecular weight resinous asphaltene substances, makes it impossible to use classical thickeners – metal soaps, without prior deep cleaning of raw materials. It should be noted that these substances have high adhesion properties and can act as a natural antiwear additive in the final product, and therefore, their removal from the base component is highly undesirable. In this case, it is necessary to use a thickener, less demanding of the chemical composition of the dispersion medium, which would be distinguished by its availability, cheapness, and of course, a significant amount. Such a thickener can be solid polymeric household waste, represented mainly by-products from high-density polyethylene (HDPE) and low-density polyethylene (LDPE) pressure, as well as polypropylene (PP) [8]. This waste fully meets all the requirements that can be presented to the thickener, alternative to metal soaps. So, along with comparative cheapness and a huge amount, allowing them to be used on an industrial scale, positive physical and chemical properties should also be noted (a melting point not less than 110°C, resistance to water and corrosive media).

It is known that the final properties of the grease will depend not only on the properties of the main components (dispersion medium and thickener) but also on the correct selection of the concentration of the thickener. For used lubricating oils, the range of application of polymeric thickeners is in a rather narrow margin to 10 wt%, the excess of this concentration results in the manifestation of polymer properties in the final product, due to the formation of a polymer matrix in its structure. In this case, talking about the resulting product as grease is no longer has a sense. The concentration of the thickener largely determines the viscosity of the dispersion medium. Thus, a lubricant of a certain consistency (class NLGI) of the base of used hydraulic oil (HLP 46) will contain a higher concentration of polymer thickener than a lubricant of the same consistency based on transmission oil (SAE 85W-90). The viscosity of the dispersion medium and the ability of the thickener to prevent the separation of the dispersion medium from the total amount of grease depend on such an important indicator of greases, which characterizes their storage stability as their colloidal stability. It is established that the lubricant obtained on the bases of used hydraulic oil HLP 46, thickened with 5 % low-pressure polyethylene, has the worst colloidal stability, with the same amount of thickener compared to lubricant based on used SAE90W-140 transmission oil [9]. Typically, to obtain recycling greases, which are analogs of industrial designs, the concentration of polymer thickener should be in the range of 5.0-7.0 wt%. Taking into account the high viscosity of high-boiling fractions of oil sludge, up to 2.0 wt% of polymeric thickener is used for thickening.

However, the total range of concentrations of a polymeric thickener in greases can be significantly expanded when using low viscosity oil fractions or fractions obtained from thermodestructive processing of waste oil as a dispersion medium.

Prediction of the properties of the resulting greases should be carried out while taking into account changes in the composition and properties of raw materials in the process of its technological processing. So, for example, industrial oil I-40 has higher viscosity values compared to hydraulic oil HLP 46, which should determine the higher colloidal stability of the resulting grease. However, an oil I-40 has low thermal stability and in the temperature range of 130–200°C, necessary for obtaining grease, undergoes thermal destruction, which is accompanied by a decrease in the yield of the resulting lubricant and viscosity of the dispersion medium. Therefore, this plastic has the worst colloidal stability in comparison with the lubricant based on oil HLP 46 [9].

Thus, the technology for obtaining recycling greases is a technological process consisting of successive stages, closely related to each other, and is presented in Fig. 1.

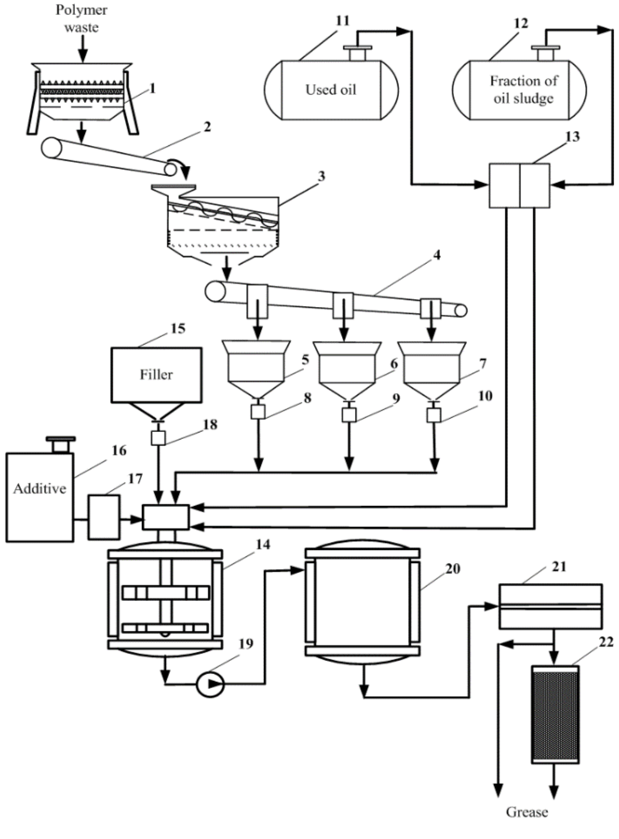

Fig. 1. The scheme for obtaining recycled grease: 1 – chopper; 2, 4 – belt conveyors; 3 – apparatus for washing and drying polymer waste; 5-7, 15 – bunkers; 8-10, 18 – dispensers; 11, 12, 16 – tanks; 13, 17 – dosing pumping devices; 14 – reactor; 19 – pump; 20 – cold-storage space; 21 – homogenizer; 22 – filter

Stage I. At this stage, preparation of the dispersion medium of the grease, thickener, as well as fillers takes place. For used lubricating oil and oil sludge at this stage, water and mechanical impurities are separated by various physicochemical methods described in work [10]. Also, it is necessary to separate the high-boiling fraction from the oil sludge, which will be used as a dispersion medium for the production of plastic lubricants [11]. After these operations, the prepared dispersion medium enters the raw material tanks **11** and **12**.

At this stage, in order to obtain a homogeneous mass with unified properties, in apparatus **1**, the sorted polymeric solid household waste is crushed to particles no larger than 2 × 2 mm. The grinding process can significantly reduce, shorten the duration of the subsequent stages, reduce the size of the apparatus, improve plant performance, due to a full load of raw materials and improve the quality of the lubricants produced due to the homogeneity of the structure. This process is carried out using mainly cutting and impact devices, taking into account the initial characteristics of the polymers. Next, the crushed polymers through the conveyor belt **2** are fed into the apparatus **3**, performing the function of cleaning from contamination with the subsequent removal of moisture from the polymers. First, the crushed polymer waste is fed into a screw washer, where the preliminary soaking of the material is carried out, followed by transportation to the separation bath, where contaminants are separated from the polymer. Next, the waste is fed to the filter press, where the moisture is completely squeezed out, after which the crushed, cleaned and dehydrated polymeric materials are fed to the belt conveyor **4** and then to storage hoppers **5, 6, 7** for different types of polymers (HDPE, LDPE, PP).

To improve the physicochemical and performance properties, greases, along with the main components, may contain various fillers, which can also be chosen from several numerous wastes, for example, used automobile tires or cardboard-paper wastes are suitable for this purpose.

Adding ground tires due to physical interaction with the dispersion medium improves the rheological and adhesive properties of greases, storage stability, and also increases the temperature range of their application. Also, a noticeable improvement in rheological properties and storage stability is observed when paper industry waste is added in the form of cellulose. However, before using them as filler, they must be prepared. So, used car tires are necessary to grind, remove fabric or metal cord (magnetic removal is used), wash and dry, in general, carry out almost the same stages as in the preparation of polymer waste, but using more complex equipment (there is a need for grinding, use more expensive equipment using durable knives and crowns).

The situation is different from paper waste because they contain glue, which must be disposed of to obtain cellulose. In this case, with constant mixing, alkaline washing is carried out with a 10 % solution of NaOH, previously crushed waste. After that, it is necessary to rinse with water and dry the obtained cellulose, followed by its grinding to the required size. The implementation of such preparation, from an environmental point of view, is seen as a complex process, in which it is necessary to provide both the regeneration technology of the spent NaOH solution and the cleaning of the wash water.

At Stage II, the prepared components are fed into the reactor **14** in the strict sequence, they are heated, and the compounding itself by means of a paddle stirrer operating at high speeds. The sequence is such that into the reactor **14**, through a mixer, using a multi-flow dosing pumping device **13**, the prepared dispersion medium from tank **11** or **12** is fed. Here, depending on the desired characteristics of the final product, the crushed polymer is fed through hoppers **5, 6, 7** through dispensers **8, 9, 10.** In the reactor **14**, depending on the melting point of the polymer thickener, the mixture is heated to 130–200°C with constant stirring, for 1.5–3.0 hours.

Moreover, for the quality of the finished product, in particular for its colloidal stability, an important is the degree of dispersion of the polymer thickener and the uniformity of its distribution over the volume of lubricant. The thickener is dispersed by using a mechanical paddle propeller stirrer, which can provide a laminar and turbulent dispersion mode. Along with mechanical dispersion, it is possible to apply ultrasonically, which is carried out by creating a cavitation effect and acoustic flow, in which the structure and properties of the lubricant are changed, that leads to an increase in its homogeneity [12].

Further, from the hopper **15**, a filler is added through the dispenser **18**, and from the tank **16**, an additive is introduced through the dosing pumping device **17**.

Next comes the final *stage III* – this is the cooling of the resulting reaction mixture in the tank-cooler **20**, and the final formation of the structure of the grease in the homogenizer **21**. The cooling process, depending on the desired properties of the final product, can be carried out within 5-24 hours.

Homogenization of plastic grease occurs under mechanical action (punching under pressure through holes 30–50 μm in size) in the valve or rotary-slot homogenizers. In this case, there is an improvement in its appearance and colloidal stability [13]. Further, if necessary, the lubricant may be subjected to filtration in the apparatus **22**.

According to the proposed technology, depending on the properties and degree of preparation of used oils, as well as the selected process parameters, greases can be obtained, whose properties are in the range of values given in Table 1.

Table 1. Properties of recycling greases

Indicator name	Numerical values of indicators		
Dispersion medium	used oils		
Type of thickener	LDPE	HDPE	PP
The concentration of the thickener, wt%	5–7		
Appearance	Homogeneous ointment, black		
Penetration at 25ºC, 0.1·mm	215–325		
Drop point, ºC	95–100	110–115	135–140
Evaporation at 120ºC	0.10–0.75		
Colloid stability, %	3.5–14.0		
Corrosive effects on metals:			
- Steel	Endures		
- Copper	No corrosion traces		
Working speed mode in the bearing, rpm	up to 4000		
Solubility:			
- in water at 100 °C	not dissolve		
- in gasoline at 60 °C	dissolves		

4. Conclusions

The application of recycling technologies in the production of commercial petroleum products allows, not only, to expand the raw material base of the technological process significantly, but also to improve the environmental situation. The studies have shown that industrial waste such as oil sludge and spent oils can be successfully applied in the production of plastic lubricants along with the production of fuels. The production scheme of plastic lubricants based on high-boiling fractions of oil sludge and spent lubricating oils has been proposed; the scheme involves using as a thickener, waste polymer from LDPE, HDPE and PP. The implementation of this scheme will allow obtaining plastic greases that can be used in the temperature range, on average, up to 80–130°C (depending on the polymer) and speed mode in the bearing up to 4000 rpm, and their properties are not worse than ones of classical industrial analogs.

References

[1] Council Directive 1999/31/EC on the landfill of waste. Official Journal L 182, 16 July 1999: 1-19.
[2] Directive 2008/98/EU of the European Parliament and of the council. Official Journal of EU L 312/3, 22 November 2008: 3-30.
[3] Shen Y, Chen X, Wang J, Ge X, Chen M. Oil sludge recycling by ash-catalyzed pyrolysis-reforming processes. Fuel. 2016; 182: 871-878.
[4] Chang CY, Shie JL, Lin JP, Wu CH, Lee DJ, Chang CF. Major products obtained from the pyrolysis of oil sludge. Energy Fuels. 2000; 14(6): 1176-1183.
[5] Diederich R. Advance sludge treatment system by ultrahigh temperature gasification. Proc. in Biomass and Conversion Technologies on Emerging Technology Forum, California, 17-18 April 2006.
[6] Arpa O, Yumrutas R, Demirbas A. Production of diesel-like fuel from waste engine oil by pyrolytic distillation. Applied Energy. 2010; 87(1): 122-127.
[7] Demirbas A. Gasoline-like fuel from waste engine oil via catalytic pyrolysis. Journal Energy Sources. 2008; 30(16): 1433-1441.
[8] Grigorov AB, Zelenskii OI, Sytnik AV. The prospects of obtaining plastic greases from secondary hydrocarbon raw material. Pet Coal. 2018; 60(5): 879-883.
[9] Grigorov A, Zelenskii O, Saienko L, Zhyrnova S. Production of plastic lubricants on the basis of waste lubricated oils. Pet Coal. 2019; 61(2): 319-323.
[10] Khmelev VN, Leonov GV, Barsukov RV, Tsyganok SN, Shalunov AV. Ultrasonic multifunctional and specialized equipment for intensification of technological processes in industry. Barnaul: AltGTU, 2007; 416 p.
[11] Hu G, Li J, Zeng G. Recent development in the treatment of oily sludge from petroleum industry: A review. Journal of Hazardous Materials. 2013; 261: 470-490.
[12] Mardupenko A, Grigorov A, Sinkevich I, Tulskaya A. Oil sludge as source of a valuable carbon raw material. Pet Coal. 2018; 60(3): 353-357.
[13] Fuks IG, Shibryayev SB. Composition, properties and production of greases; Moscow: Gosudarstvennaya akademiya nefti i gaza im. I.M. Gubkina, 1992; p. 153.

To whom correspondence should be addressed: Dr. Oleg Zelenskii, Ukrainian State Research Institute for Carbochemistry, 61023, 7 Vesnina str., Kharkov, Ukraine, zelenskii.ukhin@gmail.com

Petroleum and Coal

Article **Open Access**

FUEL CHARACTERISTICS OF DUDUGURU COAL FROM NASARAWA STATE IN NIGERIA

Bemgba B. Nyakuma[1,2], *Aliyu Jauro*[3], *Olagoke Oladokun*[2,4], *Segun A. Akinyemi*[5], *Mohammed B. Nasirudeen*[6], *Aliyu A. Bello*[4], *Habib Alkali*[2], *Tuan Amran T. Abdullah*[1,2]

[1] *Hydrogen & Fuel Cell Laboratory, Centre of Hydrogen Energy, Universiti Teknologi Malaysia, 81310 Skudai, Johor Bahru, Malaysia*
[2] *School of Chemical & Energy Engineering, Faculty of Engineering, Universiti Teknologi Malaysia, 81310 Skudai, Johor Bahru, Malaysia*
[3] *National Centre for Petroleum Research & Development (NCPRD), Abubakar Tafawa Balewa University, P.M.B 0248, Bauchi State, Nigeria*
[4] *Department of Chemical Engineering, University of Maiduguri, P.M.B 1069, Bama Road, Maiduguri, Borno State, Nigeria*
[5] *Department of Geology, Ekiti State University, P.M.B 5363, Ekiti State, Nigeria*
[6] *Department of Chemistry, Federal University Lafia, P.M.B 146, Lafia, Nasarawa State, Nigeria*

Received March 16, 2019; Accepted May 21, 2019

Abstract

The discovery of vast deposits of various ranks of coal in Nigeria presents significant opportunities to address the nation's persistent energy crises. However, the lack of comprehensive data on the physicochemical, calorific, microstructural, mineralogical, and thermal properties of Nigerian coals remains a significant challenge. Therefore, this paper seeks to investigate the fuel characteristics and energy recovery potential of a newly discovered coal from Duduguru in Obi Local Government Area of Nasarawa State, Nigeria. Results revealed that Duduguru (DDG) coal contains high carbon (59.6%), oxygen (32.9%), volatile matter (76.4%), fixed carbon (16.6%) and higher heating value (HHV = 26.6 MJ/kg), but low nitrogen (1.3%), sulphur (0.6%), moisture (6.5%), and ash (0.5%) content. Based on these properties, DDG is classified as a non-agglomerating, sub-bituminous, grade "A" coal with potentials for electricity generation, cement production, among others. The mineralogical analyses revealed quartz, kaolinite, and aluminosilicates are present in its microstructure. Thermal analysis revealed that DDG is more thermally reactive under flash combustion (FCO) based on its higher mass loss (M_L) and lower residual mass (R_M) compared to flash pyrolysis (FPY) conditions. The temperature profile characteristics of DDG under FCO were considerably lower than the FPY. In conclusion, the findings indicate that combustion is a more practical route for efficient energy recovery from DDG coal in the future.

Keywords: *Fuel characterization; Energy; Duduguru; Coal; Nasarawa; Nigeria.*

1. Introduction

The discovery of vast deposits of various ranks of coal in Nigeria presents significant opportunities to address the nation's persistent energy crises [1]. Despite Nigeria's position as Africa's largest economy and most populous nation, socioeconomic growth and sustainable development remain a significant challenge [2]. Many analysts have attributed the nation's energy crises to numerous socioeconomic, geopolitical, environmental, and technological challenges [3]. Most notably, the lack of comprehensive data on Nigerian coals has hampered progress in the area of power plant development, efficient energy recovery, and resource management [4-5]. Currently, the available data on Nigerian coals is mostly limited to their geological, petrographic, and seismologic properties [6-9]. However, these properties of coal are not crucial for energy recovery, resource management or the design and operation of coal-fired power plants.

Currently, coal accounts for 35 – 40% of global electricity production around the globe [10]. As a result, coal is considered a widely accessible and economically reliable source of cheap electricity for socioeconomic growth and sustainable development, particularly in developing countries with significant resources [11-12]. Numerous studies have reported that Nigeria has over 640 million proven tonnes of coal along with 2.75 billion tonnes of inferred reserves comprising 12% lignite, 49% subbituminous and 39% bituminous [4]. Furthermore, studies have reported that deposits of Nigerian coals are evenly distributed across the six geopolitical zones of Nigeria [13]. Therefore, the exploration, examination, and exploitation of coal for electricity production could potentially address the nation's energy crises, alleviate poverty, and spur long term socio-economic growth and sustainable development.

However, this is expedient on addressing the current challenges posed by poor power generation, transmission, distribution and maintenance. This will be particularly important in coal-fired power plants, which require considerable attention, particularly in the era of global calls for fossil fuel diversification. Furthermore, comprehensive data and knowledge on the fuel properties of various ranks of Nigerian coals will assist in the design, operation, and maintenance of future power plants in the country particularly in the agricultural, mining, and minerals development areas like Nasarawa State, which also has vast deposits of coal in the areas around Atito-Akpuneje, Shankodi-Jangwa and Lafia-Obi [14-16].

Therefore, the primary objective of this paper is to examine the fuel characteristics and energy recovery potential of a newly discovered coal from Duduguru, Obi Local Government Area of Nasarawa State in Nigeria. The paper presents the physicochemical, calorific, microstructural, mineralogical, and thermal properties of Duduguru (DDG) coal. To the best of the author's knowledge, this paper is the first comprehensive examination of the fuel proper-ties, classification, and potential applications of DDG coal from the Middle Benue Trough of Nigeria's sedimentary basin. The findings will provide comprehensive insights on the fuel properties and energy recovery potentials of DDG coal.

2. Materials and methods

2.1. Physicochemical analyses

The physicochemical analysis of the Duduguru (DDG) coal was carried out by ultimate, proximate, and bomb calorimetry methods. The ultimate analysis was carried out to determine the elemental carbon, hydrogen, nitrogen and sulphur (CHNS) composition of the sample using the CHNS analyser (Model: vario MACRO Cube, Germany). Proximate analysis was determined according to the ASTM standards D3173, D3174, and D3175 for moisture, ash and volatile matter contents, respectively. The calorific or higher heating value was determined using the Isoperibol bomb calorimeter (Model: Leco AC350, UK) based on the ASTM standard D240-17. All tests were carried out in duplicate to ensure the reliability and accuracy of the measurements.

2.2. Microstructure and mineralogy analyses

The microstructure (morphological) and mineralogical analyses of Duduguru coal were carried out through scanning electron microscopy (SEM) and energy dispersive x-ray (EDX) spectroscopy. For each test, the Quorum Q150R S apparatus was employed to sputter coat the DDG sample with gold. The sputter coated DDG sample was degassed and subsequently transferred to the SEM/EDX analyser for microstructure and mineralogical examination. The operational settings of the SEM/EDX analyser were set at voltage 20 kV, working distance 5 mm, and ×1000 magnification. On completion, the SEM image was examined using the proprietary AZTEC EDX software from Oxford Instruments (UK). The point ID and mapping feature were subsequently employed to deduce the composition of mineral elements in weight per cent (wt. %).

2.3. Thermal analysis

The thermal properties of Duduguru (DDG) coal were examined by thermogravimetric analysis (TGA) under oxidative and non-oxidative conditions to simulate flash combustion (FCO) and flash pyrolysis (FPY), respectively. For each test, approximately 11 mg of the sample was placed in an alumina crucible and heated under a non-isothermal heating programme from 30°C to 1000°C in a high precision thermogravimetric analyser (TGA Model: Shimadzu TG-50, Japan). For the flash combustion (FCO) and flash pyrolysis (FPY) processes, the TG analyser was flushed with air and ultra-pure nitrogen (purge gas flow rate 20 mL/min), respectively, to purge out the gases evolved during TGA. On completion, the raw data for the mass loss and derivative mass loss were retrieved and analysed to deduce the TG (%) and DTG (%/min) data, respectively. The TG-DTG data was subsequently plotted against temperature to examine the thermal degradation behaviour and characteristics temperature profiles of the sample.

2.4. Temperature profile analyses

The temperature profile characteristics (TPC) of Duduguru (DDG) coal were examined based on the tangent method described in the literature [17]. This is embedded in the data analysis feature of the Shimadzu Thermal analysis software (Version: Workstation TA-60WS). The TPCs deduced for the flash combustion (FCO), and flash pyrolysis (FPY) of DDG coal in this study include; the ignition (T_{ons}), midpoint (T_{mid}), maximum decomposition (T_{max}), and burnout (T_{off}) temperatures along with the mass loss (M_L, %) and residual mass (R_M, %). The detailed description of the temperature profile characteristics (TPC) was presented in our previous study [18].

3. Results and discussion

3.1. Physicochemical properties

Table 1 presents the fuel properties of Duduguru (DDG), reported in as-received (a.r.) basis and compared with other Nigerian coals from Garin Maiganga (GMG) and Shankodi-Jangwa (SKJ) [15].

Table 1. Fuel properties of Duduguru (DDG) coal

Element/ Fuel Property	Symbol/Unit	Duduguru (DDG) (This study)	Garin-Maiganga (GMG) [15]	Shankodi-Jangwa (SKJ) [15]
Carbon	C (wt.%)	59.64	61.96	71.46
Hydrogen	H (wt.%)	5.49	4.42	6.40
Nitrogen	N (wt.%)	1.30	1.07	1.37
Sulphur	S (wt.%)	0.62	0.39	2.03
Oxygen	O (wt.%)	32.95	32.16	18.76
Moisture	M (wt.%)	6.48	5.28	5.14
Volatile matter	VM (wt.%)	76.42	51.16	40.73
Ash	A (wt.%)	0.50	21.05	14.94
Fixed carbon	FC (wt.%)	16.60	22.52	39.18
Higher heating value	HHV (MJ/kg)	26.55	22.95	27.34

As observed, the DDG coal sample contains high contents of carbon ($C > 55\%$), hydrogen ($H > 5\%$), and oxygen ($O > 30\%$) but low values of nitrogen (N) and sulphur (S) all below 5%. Furthermore, the sample contains low moisture (M), and ash (A) contents, which are in good agreement with GMG and SKJ reported in the literature [15]. However, the constituents of volatile matter (VM) and fixed carbon (FC) are significantly higher than reported for similarly ranked coals in literature.

The calorific analysis indicated that DDG coal has a higher heating value of 26.6 MJ/kg. In comparison, the HHV of DDG is somewhat similar to Owukpa (26.51 – 26.67 MJ/kg) [4, 19], but lower than Afuze (30.52 MJ/kg) [20], and Shankodi- Jangwa (27.34 MJ/kg) [21], which are other subbituminous Nigerian coals described in literature. Based on the ASTM D388-12 [22] standard for classification of coals based on HHV, the DDG coal can be classified as a non-agglomerating, sub-bituminous, grade A coal. This indicates that DDG could be potentially utilised for power generation, cement and other industrial applications [23].

3.2. Microstructure and mineralogy properties

The utilisation of coals for various applications, particularly pulverised combustion, requires in-depth knowledge on its mineral composition. This is crucial to the design, operation and maintenance of boilers as well as solid waste and evolved pollutant gas emissions in coal power plants. Therefore, this paper examines the microstructure and mineralogy of DDG coal. The SEM micrograph (magnification ×1000) for DDG is shown in Figure 1(a), whereas the EDX spectrum and chemical data reported are presented in Figure 1(b) and Table 2, respectively.

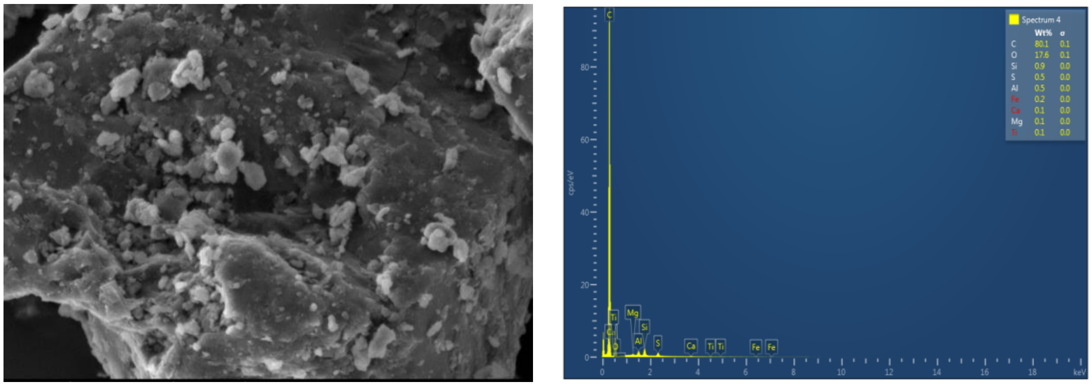

(a) (b)

Figure 1. SEM Micrograph (a) and EDX Spectra (b) for DDG

As observed in the SEM micrograph, the morphology and microstructure of DDG consist of a wide range of medium to large particles that are rough, spherical and crystallite in shape dispersed on its smooth layered surface. Typically, the presence of the white coloured, round, exfoliated or spherical shaped grains is ascribed to quartz [24-25]. This highlights the recycled nature and maturity of the accumulated sediment [25]. However, the coarse particles observed in the micrograph are ascribed to the presence of kaolinite [26]. Kaolin particles are characterised by rolled or rough edges with face to face arrangement. Similarly, the coarse fraction of DDG coal observed in the SEM micrograph may be due to the presence of metallic elements such as Ti and Fe, which typically bear various minerals such as pyrite [25].

The mineralogical composition of the coal sample was subsequently examined, as presented in Table 2, respectively. The characteristic peaks of the elements detected during the EDX analysis are presented in Figure 1(b).

Table 2. Mineral composition of DDG

Mineral element	Symbol of element	Weight % (wt.%)	Atomic (%)
Carbon	C	80.08	85.01
Oxygen	O	17.55	13.99
Magnesium	Mg	0.12	0.07
Aluminum	Al	0.49	0.23
Silicon	Si	0.87	0.39
Sulphur	S	0.53	0.21
Calcium	Ca	0.13	0.04
Titanium	Ti	0.07	0.02
Iron	Fe	0.15	0.03

The results indicate that the elements C, O, Mg, Al, Si, S, Ca, Ti, and Fe were detected in significant and trace quantities during the EDX analysis. The major elements (i.e. with composition > 0.5 wt.%) were; C, O, Si, S, and Al, whereas the minor elements detected were Mg, Ca, Ti, and Fe. The results show that C, Ti, Fe exist in elemental form in the structure of DDG, whereas as O, Mg, Al, Si, S, and Ca exist in combined form as mineral compounds. However, the elements Mg, Al, Si and Ca exist in the form of the oxides MgO, Al_2O_3, SiO_2 and $CaSiO_3$ (wollastonite), respectively.

The elements Al and Si indicate the presence of mixed carbonaceous, aluminosilicate and quartz minerals [27]. The mixed carbonaceous elements may be due to the presence of thin clay minerals or clay minerals with some carbon content, whereas the aluminosilicates indicate the presence of clay minerals and feldspars [28-29]. In addition, the quartz could be due to the presence of crystalline silica materials in the coal structure [30]. Lastly, the high contents of C and O indicate carbonaceous materials with properties similar to coal [27].

3.3. Thermal properties

The thermal properties of Duduguru (DDG) coal were examined by thermogravimetric analysis (TGA) under flash (heating rate, β = 50°C/min) oxidative (combustion) and inert (pyrolysis) conditions. The TG, conversion and DTG plots for the thermal degradation of DDG coal are presented in Figures 2-4, respectively. As observed, the DDG coal sample experienced progressive mass loss under the flash combustion and pyrolysis conditions examined in this study. The TG plots showed that the increase in temperature from RT to 1000°C significantly decomposed the sample during TGA. This is ascribed to increase in thermal energy, which enhanced the thermal degradation of the macerals (organic) fraction in DDG. As a result, there was an increase in the conversion of the sample, as illustrated in Figure 3.

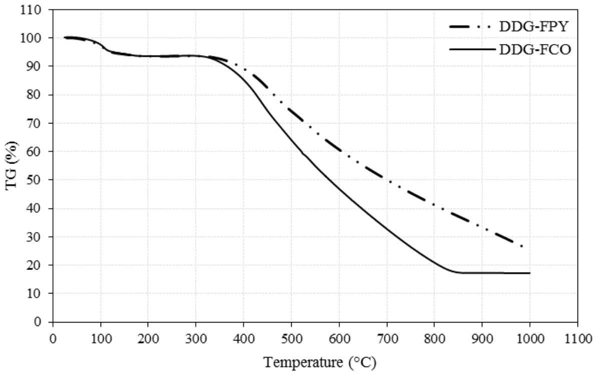

Figure 2. TG plots for flash combustion (FCO) and pyrolysis (FPY) of DDG

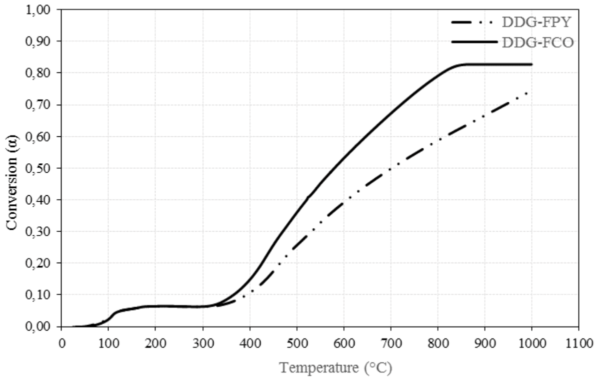

Figure 3. Conversion plots for flash combustion (FCO) and pyrolysis (FPY) of DDG

Therefore, it can be surmised that higher temperatures enhanced the conversion of the coal components due to the increase in the bond breaking reactions of the coal components during TGA. The findings indicate that DDG is thermally reactive and can be effectively degraded into coal products or for efficient thermal energy recovery, either under oxidative or non-oxidative thermal conditions as examined in this study.

Next, the degradation pathway for the thermal degradation of DDG coal was examined through DTG analysis, as presented in Figure 4. The DTG plots of thermally decomposing carbonaceous materials present valuable insights into the mechanism, reaction steps, and temperature profiles of the process [5].

As observed in Figure 4, the thermal decomposition of DDG generated two major endothermic peaks under oxidative (FCO) and inert (FPY) conditions. The first peaks were observed from 30°C to 250°C, which can be ascribed to drying or the loss of moisture. However, the second major peaks occurred in the range 250°C to 850°C for FCO whereas for the FPY process it was from 250°C to 980°C. The mass loss in these ranges could be ascribed to the loss of volatile matter or organic matter content of DDG through devolatilization. Overall, the findings indicate that temperature significantly influenced the thermal degradation of DDG irrespective of whether the reaction occurred under oxidative or inert conditions during TGA. The extent of the degradation of the sample was subsequently examined to determine the temperature profile characteristics (TPCs).

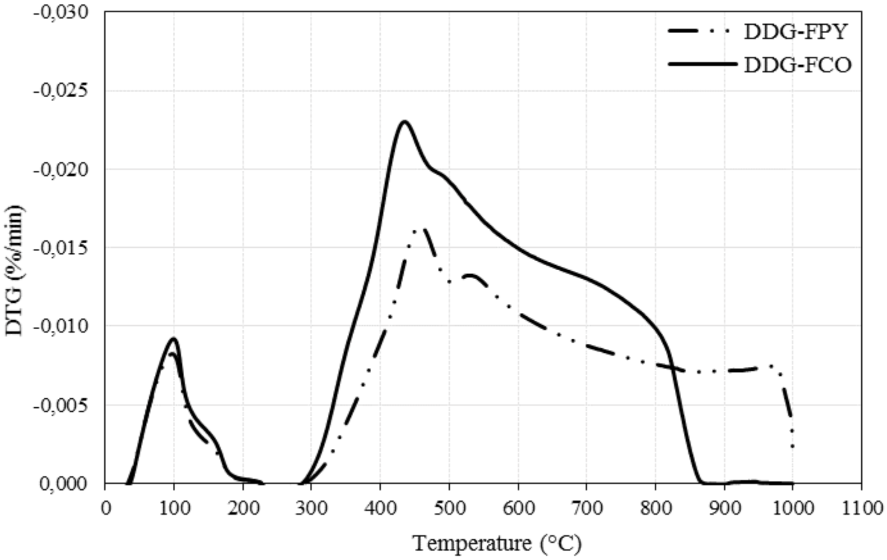

Figure 4. DTG plots for flash combustion (FCO) and pyrolysis (FPY) of DDG

3.4. Temperature profile characteristics

The temperature profile characteristics (TPC) of Duduguru (DDG) coal were examined to deduce the thermal degradation behaviour of the sample under flash oxidative (FCO, combustion) and inert (FPY, pyrolysis) conditions. The TPCs for DDG examined in this study include; ignition (T_{ons}), midpoint (T_{mid}), maximum decomposition (T_{max}), and burnout (T_{off}) temperatures along with mass loss (M_L, %) and residual mass (R_M, %), as presented in Table 3.

Table 3. TPC values for DDG under FCO and FPY conditions

Process	Onset temp. (T_{ons}, °C)	Midpoint temp (T_{mid}, °C)	Burnout temp (T_{off}, °C)	Mass loss (M_L, %)	Residual mass (R_M, %)
FPY	350.73	557.94	732.03	74.22	25.78
FCO	336.75	528.51	688.82	82.90	17.10

The results pyrolysis (FPY) of DDG occurred from 350.73°C to 732.03°C, whereas the flash combustion (FCO) process was between 336.75°C and 688.82°C. This indicates that the ignition and burnout of DDG during FCO occurred at lower temperatures compared to the FPY process. In addition, the midpoint (T_{mid}), and maximum decomposition (T_{max}) temperatures of FCO were lower than the FPY process. This resulting pattern is ascribed to the oxidative nature of the FCO process, which ensured the DDG coal experienced higher thermal energy and hence higher mass loss (M_L = 83.0%) compared to FPY (M_L = 74.2%). Besides, the observation may be due to the exothermic reactions arising from the oxidative nature of the FCO process. As a result, the coal components were more efficiently degraded during FCO, resulting in lower residual mass (R_M ~ 17.1%) compared to the FPY process (R_M ~ 25.8%). Therefore, it can be reasonably inferred that the FCO process is a more thermally reactive and resource efficient process compared to FPY.

4. Conclusion

This study examined the fuel characteristics and energy recovery potential of a newly discovered coal sample from Duduguru in Obi Local Government Area of Nasarawa State, Nigeria. Consequently, the elemental, proximate, calorific, microstructure, mineralogical, and thermal analyses of Duduguru (DDG) coal was examined. The proximate and ultimate analyses revealed that DDG has high carbon (C), volatile matter (VM) and fixed carbon (FC) contents. However, the sample showed low nitrogen (N), sulphur (S), moisture (M), and ash (A) contents. The calorific value showed that DDG has a higher heating value (HHV) of ~26.6 MJ/kg, indicating its potential for efficient energy recovery during thermal conversion. The microstructure and mineralogical analyses revealed medium to large particles with wide-ranging shapes typically ascribed to quartz, kaolinite and other aluminosilicate minerals. The thermal properties of DDG coal studied under flash combustion (FCO) and flash pyrolysis (FPY) conditions showed that FCO is a more thermally reactive and resource efficient process resulting in a higher mass loss (M_L), but lower residual mass (R_M) compared to FPY. Overall, the results indicate that combustion is a potentially practical route for future effective energy recovery from DDG.

Acknowledgements

The authors gratefully acknowledge the National Metallurgical Research and Development Centre (NMDC Jos, Nigeria); National Centre for Petroleum Research and Development (NCPRD) at Abubakar Tafawa Balewa University (ATBU) Nigeria and the Centre of Hydrogen Energy, Universiti Teknologi Malaysia (UTM) Malaysia, for the material and technical support.

References

[1] Ohimain EI. Can Nigeria generate 30% of her electricity from coal? International Journal of Energy and Power Engineering, 2014; 3(1): 28-37.
[2] Oyedepo SO. Towards achieving energy for sustainable development in Nigeria. Renewable and sustainable energy reviews, 2014; 34: 255-272.
[3] Oseni MO. An analysis of the power sector performance in Nigeria. Renewable and Sustainable Energy Reviews, 2011; 15(9): 4765-4774.
[4] Chukwu M, Folayan C, Pam G, and Obada D. Characterization of some Nigerian coals for power generation. Journal of Combustion, 2016; 2016.
[5] Nyakuma BB, Oladokun O, Jauro A, and Nyakuma DD. Evaluating the Energy Recovery Potential of Nigerian Coals under Non-Isothermal Thermogravimetry. IOP Conference Series: Materials Science and Engineering, 2017; 217(1): 012013.
[6] Ogala J. Source rock potential and thermal maturity of the Tertiary lignite series in the Ogwashi-Asaba Formation, Southern Nigeria. Asian Journal of Earth Sciences, 2011; 4(3): 157.
[7] Ogala JE. The geochemistry of lignite from the neogene ogwashi-Asaba formation, niger delta basin, southern Nigeria. Earth Sciences Research Journal, 2012; 16(2): 151-164.
[8] Akande SO, Adeoye MO, and Erdtmann BD. Petroleum Source Rock Potential Assessment of the Oligocene-Miocene Ogwashi Asaba Formation, Southern Anambra Basin, Nigeria. 2015.
[9] Ayinla HA, Abdullah WH, Makeen YM, Abubakar M, Jauro A, Yandoka BMS, and Abidin NSZ. Petrographic and geochemical characterisation of the Upper Cretaceous coal and mudstones of Gombe Formation, Gongola sub-basin, northern Benue trough Nigeria: Implication for organic matter preservation, paleodepositional environment and tectonic settings. International Journal of Coal Geology, 2017; 180: 67-82.
[10] OECD Working Paper, The Global Value of Coal 2012.
[11] Mohammed Y, Mustafa M, Bashi, N, and Mokhtar A. Renewable energy resources for distributed power generation in Nigeria: a review of the potential. Renewable and Sustainable Energy Reviews, 2013; 22: 257-268.
[12] Shahbaz M, Tiwari AK, and Nasi, M. The effects of financial development, economic growth, coal consumption and trade openness on CO_2 emissions in South Africa. Energy Policy, 2013; 61: 1452-1459.
[13] Obaje NG. Geology and mineral resources of Nigeria. 2009; 120.
[14] Ryemshak SA and Jauro A. Proximate analysis, rheological properties and technological applications of some Nigerian coals. International Journal of Industrial Chemistry, 2013; 4(1): 7.
[15] Nyakuma B. Physicochemical Characterization and Thermal Analysis of newly discovered Nigerian coals. Bulgarian Chemical Communications, 2016; 48: 4.
[16] Ocheri C. Revitalization of Coal Development in Nigeria for Industrial Advancement. SFJ Metallurgical Science, 2017; 1(2): 1-9.

[17] Cai J, He Y, Yu X, Bank, SW, Yang Y, Zhang X, Yu Y, Liu R, and Bridgwater AV. Review of physicochemical properties and analytical characterisation of lignocellulosic biomass. Renewable and Sustainable Energy Reviews, 2017; 76: 309-322.
[18] Nyakuma BB, Oladokun O, Ojoko EO, Tanko BL, and Jauro A. Physicochemical and oxidative, thermal analysis of Nigerian lignite coals. Petroleum & Coal, 2018; 60(6): 1207-1215.
[19] Nyakuma BB, Ojoko EO, Oladokun O, Bello AA, Aboje AB, Ivase TJ-P, Al-Shatri AH, and Alkali H. Fuel Characterization and Thermal Degradation Behaviour of Owukpa Coal. Petroleum & Coal, 2018; 60(6).
[20] Nyakuma BB and Jauro A. Chemical and Pyrolytic Thermogravimetric Characterization of Nigerian Bituminous Coals. GeoScience Engineering, 2016; 62(3): 1-5.
[21] Nyakuma B, Jauro A, Oladokun O, Abdullah TAT, and Uthman H. Combustion Kinetics of Shankodi-Jangwa Coal. Journal of Physical Science, 2016; 27(3): 1.
[22] ASTM D388-12. (2012). ASTM Standard D388-12, 2012. Standard classification of coals by rank.
[23] Speight JG. The Chemistry and Technology of Coal. Chemical Industries, 2012: 8.
[24] Garzanti E, Andò S, and Vezzol, G. Settling equivalence of detrital minerals and grain-size dependence of sediment composition. Earth and Planetary Science Letters, 2008; 273(1-2): 138-151.
[25] Sengupta P, Saikia PC, and Borthakur PC. SEM-EDX characterisation of iron-rich kaolinite clay. Journal of Scientific and Research, 2008; 67(1): 812-818.
[26] Bortnikov N, Novikov V, Savko A, Boeva N, Zhegallo E, Bushueva E, Krainov A, and Dmitriev D. Structural-morphological features of kaolinite from clayey rocks subjected to different stages of lithogenesis: Evidence from the Voronezh anteclise. Lithology and Mineral Resources, 2013; 48(5): 384-397.
[27] Sellaro R, Sarver E, and Baxter D. A standard characterisation methodology for respirable coal mine dust using SEM-EDX. Resources, 2015; 4(4): 939-957.
[28] Michalsk, JR, Kraft MD, Sharp TG, Williams LB, and Christensen PR. Emission spectroscopy of clay minerals and evidence for poorly crystalline aluminosilicates on Mars from Thermal Emission Spectrometer data. Journal of Geophysical Research: Planets, 2006; 111(E3).
[29] Reifenstein A, Kahraman H, Coin C, Calos N, Miller G, and Uwins P. Behaviour of selected minerals in an improved ash fusion test: quartz, potassium feldspar, sodium feldspar, kaolinite, illite, calcite, dolomite, siderite, pyrite and apatite. Fuel, 1999; 78(12): 1449-1461.
[30] Hemley R, Jephcoa, A, Mao HK, Ming L, and Manghnani M. Pressure-induced amorphisation of crystalline silica. Nature, 1988; 334(6177): 52.

To whom correspondence should be addressed: Dr. Bemgba B. Nyakuma, Hydrogen & Fuel Cell Laboratory, Centre of Hydrogen Energy, Universiti Teknologi Malaysia, 81310 Skudai, Johor Bahru, Malaysia, Correspondence Email: bbnyax1@gmail.com, bnbevan2@live.utm.my

Petroleum and Coal

Review **Open Access**

IMPROVEMENT PERFORMANCE OF MODIFIED ASPHALT BY ADDING CLAY/NANOCLAY

Eman A. Emam

Department of Petroleum Refining Eng. and Petrochemicals, Faculty of Petroleum and Mining Eng., Suez University, Suez, Egypt

Received March 17, 2019; Accepted May 21, 2019

Abstract

Asphalt is a byproduct of crude oil during petroleum refining process and it is a complex heterogeneous mixture of hydrocarbons. It has many properties, which can be altered due to exposure to heavy loads and unfavorable environmental conditions such as heat, oxygen and ultraviolet light, resulting the reduction of the quality and performance of asphalt. There are many applications of asphalt such as paving and roofing. To maintain of the quality and obtain the best performance of asphalt for a long time, the use of asphalt modifiers may help address various problems of asphalt applications. Clays are cheap and abundant in nature, mostly consist of aluminosilicates. Clays can use as a asphalt modifier in macro and nanoscale. The present paper reviews the using of clay as a modifier to improve the performance of asphalt. This review summarizes the studies of the modification of asphalt by using clay, nanoclay, clay/nanoclay as a second modifier with polymer, clay/nanoclay with other materials. Results proved that, the overall performance of clay/nanoclay modified asphalt improved the different properties of asphalt such as increased softening point and viscosity, decreased penetration, improved rutting and fatigue cracking resistance, etc. Furthermore, many other modifiers can combine with clay/nanoclay in the manufacture of asphalt to lower bitumen viscosity, reduce carbon emissions, lower energy consumption, enhance the aging resistance and improve bitumen workability.

Keywords*: Asphalt, Modified asphalt, Clay, Nanoclay, Montmorillonite, Polymer, Nanocomposite.*

1. Introduction

Asphalt (or bitumen) is a byproduct found from crude oil during petroleum refining process. Asphalt composes of a complex heterogeneous mixture of hydrocarbons [1]. It is a dark brown to black, cement-like semisolid or solid or viscous liquid. It has good adhesive and viscoelastic properties, for example, at high temperatures it flows, at room temperature it is flexible, and at lower temperatures it is rigid and brittle [1-2]. There are several applications of asphalt such as construction of roads, paving of airfield, waterproofing agent, thermal and acoustic insulation, corrosion protection of metals by coating, etc. while, the main division of applications are about 90% for paving and the remaining 10% for roofing material [1,3].

During the applications, asphalt exposes to different loads and environmental conditions such as heat, oxygen and ultraviolet light, etc., for a period of time, its chemical and physical properties can change, resulting the reduction of the quality and performance of asphalt [3-5]. Different and repeated loads can decrease strength because of fatigue [6]. Oxidation causes pavement degradation and consequent moisture damage to binder, which influences the aging of asphalt and leads to cracking [5,7]. Rainwater can affect the adhesion between asphalt and the aggregate, while the brittleness of asphalt at low temperatures often causes thermal cracking [2,8]. Asphalt becomes soft with a low stiffness and susceptible to permanent deformation at high temperatures [8]. All these factors can lower the performance of asphalt [1-2]. Furthermore, asphalt cost continuously increases due to the reduction of petroleum reserves [9]. As a result, modification and reinforcement of asphalt are essential. In the asphalt industry many modifiers can be used with the goal of improving asphalt performance, reducing carbon emissions, save energy consumption, and cost, improving the durability of asphalt and decrease maintenance requirements [1-4,8-10].

Many modifiers can be used in the manufacture of asphalt such as polymers, clay, nanoparticles [1-4,8-9]. Clays include montmorillonite (MMT), vermiculite, rectorite and kaolinite, they are cheap and abundant in nature, mostly consist of aluminosilicates. The separation of the clay layers produces a nanoclay with a special active specific surface area (700-800 m^2 g^{-1}) [1,11]. The addition of nanoparticles like nanoclay in asphalts increases the viscosity and enhances the rutting and fatigue resistance of asphalt [6-7]. Nanoclay can also be used as the second modifier in polymer modified asphalts either as an agent to enhance the polymer physical and mechanical properties or as a filler to decrease the used amount of polymer [8,12-15]. Other properties could be improved such as thermal and storage stability, the aging resistance, high gas barrier and flame retardation [3,10-11]. The aim of this review is to summarize the results of studies to improve the performance of the modified asphalt by adding clay, nanoclay, clay/nanoclay as a second modifier with polymer, clay/nanoclay with other materials.

2. Experimental procedures

2.1. Materials

Asphalt conventional penetration grades were used in the most studies. Several types of clays are used to modify asphalt such as kaolin [16], sodium bentonite [6] and vermiculite [12]. Montmorillonite (MMT) is the most important clay of bentonite. MMT is abundantly available in nature and with some modifications it can be used to generate different forms of nanoclays such as Cloisite-15A [1,5,17,18], Cloisite 20-A [19], Cloisite-30B [10], Nanofil-15 [1], and Nanofil-116 [5]. Cloisite and Nanofil are the common types of nanoclays which are most applicable as the modifiers of asphalt [1,5,10,17-19]. Several types of polymers can be used to modify asphalt and produce nanocomposites with the nanoclay, such as styrene-butadiene-styrene (SBS) [8,14-20], styrene-ethylene-butylene-styrene (SEBS) [21], styrene-butadiene-rubber (SBR) [22], ethylene-vinyl-acetate (EVA) [13], and polyethylene [23].

2.2. Preparation of modified asphalt

Generally, some nanoparticles are known to aggregate during mix with the asphalt [24]. Some researchers showed that the properties of asphalt such as stiffness and hardness could be improved depending on the mixing procedure, temperature and clay concentration [4,18,19,24-26]. In order to obtain a homogenous mixture of the asphalt and modifier, it is essential to select the appropriate mixing process [24].

To prepare the clay/nanoclay modified asphalt, the base asphalt is firstly heated to about 140°C and stirred for about 5 min [4]. Then, the temperature is raised for a wide range from 150 to 180°C according to the nature of the research [4,18,19,26], for about 2 or 3 hrs to reach a fluid state. The heated base asphalt is then stirred with a high speeds and heated during the slowly addition of the different percentages of clay/nanoclay. The temperature and mixing speed and time are adjusted to control the quality of the modified asphalt. Common types of mixers are mechanical, high shear, and ultrasonic. The prepared asphalt is left to cool at room temperature.

To prepare the modified asphalt with clay/nanoclay and polymer, in general, there are two mixing procedures refer to the different mixing sequences. The first one is the physical mixing by adding the first modifier (polymer or clay) to the asphalt, then adding the second modifier (clay or polymer) to the mix. While in the second one the polymer is primarily mixed with clay, thereby forming a polymer nanocomposite, then the nanocomposite is added to the base asphalt [12,19,27].

2.3. Asphalt tests

There are many numbers of tests to evaluate the different properties of modified asphalt, the most common tests are listed as the following:

- Physical properties, can be measured by: penetration, softening point, ductility, viscosity [17-18];
- Rheological properties, can be measured by: dynamic rheological parameters, dynamic shear rheometer (DSR) [1,14,17-18,28];
- The ageing index, can be measured by: Fourier Transform Infrared Spectroscopy (FTIR) [14,28];
- Mechanical properties, can be measured by: Marshall stability test [1,16-17,29];
- Storage stability test, can be measured by the difference between softening point of the top and the bottom sections of the sample, could be regarded as storage stable blend [1,3,27,30];
- Microscope methodology, can be measured by: Atomic Force Microscopy (AFM), X-ray diffraction (XRD), Transform Infrared Spectroscopy (FTIR) [26];
- Moisture resistance [29].

3. Results and discussion

3.1. Clay modified asphalt

Many types of clays can be used as asphalt modifiers [6,12,16,31-32]. Bentonite clay is a natural material with high ductility. The low cost of bentonite makes it logically, economically and industrially attractive for wider applications [33]. Shahabadi [6] studied to modify AC 60-70 asphalt binder with sodium bentonite clay (BT) and organically modified sodium bentonite (OBT) (in the concentrations range from 0 to 6 wt%) by melt processing under sonication and shearing stresses. The suggested structures of BT and OBT modified asphalt were an intercalated and exfoliated, respectively. The result proved that BT and OBT modified asphalts increased softening point and viscosity, while ductility reduced more by BT as compared to OBT. Adding BT and OBT significantly improved the dynamic rheological properties through higher complex modulus, lower phase angle and higher rutting parameter [6]. Asphalt cement tests were investigated the characteristics of modified bitumen using about 10 to 30% content of BT [34]. Results showed that the addition of BT improved the mechanical properties and Marshall parameters of bitumen. At adding 20% BT (wt% of bitumen), it is considered as optimum BT content and leaded to increase softening point and decrease penetration, and ductility [34]. In another study, addition of BT can increase the rutting resistance and the shear strength of hot mix asphalt (HMA). Moreover, the fatigue life of modified asphalt mixtures was longer than that of the conventional HMAs [33]. Furthermore, the dissipated energy of the bitumen containing 10% and 15% of BT is higher than the control bitumen. However the increasing trend declined at higher percentages of BT [35].

The most important clay mineral of bentonite is montmorillonite (MMT). Yu *et al.*, [36] modified asphalt using MMT and organically modified montmorillonite (OMMT). X-Ray diffraction analyses showed that MMT and OMMT modified bitumen had an intercalated and exfoliated structures, respectively. Results demonstrated that both MMT and OMMT increased viscosity, softening point, improved the rheological properties of the bitumen and increased the resistance at high temperature. At adding less than 3% of both MMT and OMMT, stable results were obtained for storage stability [36]. Whereas, the addition of OMMT decreased the effect of UV ageing and after short and long term ageing ductility retention rate increased [37].

Kaolin is an another type of clay. Kaolin can influence the physical and rheological properties of asphalt and its effect on the performance of porous asphalt mixture was investigated [16]. Results showed that the addition of kaolin macro-clay reduced temperature susceptibility and hardened the bitumen. It also improved strength and durabili 4% of macro-clay [16]. Also, the addition effect of kaolin clay on the hot-mix asphalt (HMA) was studied using a Marshall stability and flow testes, including stiffness, density, voids in total mix, and voids in filled with asphalt. Results showed that adding 2% of kaolin clay enhanced HMA properties such as good stability and stiffness by using it as filler [38].

The effects of Batu Pahat soft clay (BPSC) on the performance of HMA mixture was evaluated. The 4% of BPSC modified bitumen increased the strength of asphalt mixes, decreased the susceptibility to moisture damage and gave a better resistance to deformation than the controlled asphalt mixture [31]. In addition, BPSC modified asphalt binder can improve the rheological and physical properties, which means, BPSC could be considered as an appropriate modifier to improve the properties of asphalt binder [31-32].

3.2. Nanoclay modified asphalt

Nanoparticles definite as materials with at least one dimension in the range between 1 and 100 nm. According to the small size and high surface area, the property of nanoparticles is much different from normal size particles. The performance enhancement of asphalt modification using nanoparticles can be expected, according to the high surface-to-volume ratio of nanoparticles, and the modification required much lower concentrations to achieve equivalent properties, compared to conventional, normal size particles [4].

In general, the addition of nanoclay to asphalt decreased the mixture susceptibility to moisture damage, improved tensile strength and reduced susceptibility to water and deicers [39-40]. Van de Ven *et al.* [41] found that the addition of nanoclay in asphalt mixture increased the viscosity of the binder and thus ageing resistance was high since only less contact with air and in particular oxygen. Yang and Tighe [42] reported that an increase of the viscosity, rutting and fatigue resistance of the asphalt mixture was achieved by adding nanoclay. Many advantages of asphalt modified with nanoparticles in low temperatures as well as in high temperatures were observed, despite the disadvantage of having a low resistance to fatigue [6].

Montmorillonite (MMT) nanoclay was selected to modify bitumen with different weight percent as the 2:1 type layer structure makes it more compatible with others material. MMT and organic montmorillonite (OMMT) nanoclays have been studied to modify asphalt. The sodium montmorillonite (Na-MMT) and OMMT nanoclays can promise potential to reduce the permanent deformation or rutting of asphalt [43]. The improvement in aging properties of the OMMT nanoclay modified bitumen was obtained [44]. Yu *et al.* [45] reported that the improvement degree of the adding three different organic modifiers of OMMT nanoclay to bitumen depends on the type of the organic modifier. Also, the results showed an enhancement in rutting resistance of the aged modified binder, resulting better resistance to permanent deformation at high and intermediate temperatures [45]. The excellent fatigue resistance of modified asphalt containing OMMT was concluded [46]. Mahdi *et al.* [28] concluded that the adding about 9% OMMT nanoclay in bitumen resulted less penetration, while softening point and viscosity increased comparing to 3% and 5% nanoclay in bitumen. In general, the organic clay modified asphalts has the best properties which may be according to: (i) a better dispersion of the exfoliated structure of the organic clay platelets modified asphalts, (ii) the compatibility of organic clay nanoparticles with the organic molecules of the asphalt matrix is better [6,34].

There are several researches conducted to use and compare Cloisite and Nanofil nanoclays to modify asphalt. Cloisite-15A particles are larger in size as compared to the Nanofil-15 particles [5]. Both Cloisite-15A and Nanofil can improve stiffness, rutting resistance, indirect tensile strength, resilient modulus, and Marshall stability [47]. Ghile [48] evaluated the mechanical properties of an asphalt binder by adding Nanofil and Cloisite nanoclays. The results showed that both nanoclays were greatly significant the influence the rheology of bitumen and performance of bituminous mixes. Stiffness along with resistance against rutting and indirect tensile strength improved by adding 3% of Cloisite-15A. At 6% Nanofil, an improvement of both short and long term ageing-resistance was obtained [48]. The fatigue cracking resistance of the binder reduced and viscosity increased with Nanofil and Cloisite nanoclays [26], which will save money for maintenance and repairs, and also made the bitumen easy to work with in hot places. However, at low temperatures, the fatigue resistance of nanoclay modified bitumen was lower than the unmodified bitumen [48].

Jahromi *et al.* [49] studied to modify PEN 60/70 asphalt by adding Nanofil-15 and Cloisite-15A nanoclays. Results showed that the modified asphalt by nanoclay increased the stiffness and enhanced resistance to aging. Additionally, a low percent of nanoclay in asphalt could be modify in rheological parameter, decreasing penetration and ductility as well as increasing softening point and ageing resistance. At low temperatures, fatigue cracking performance decreased [49]. The research by Nazzal *et al.* [26] showed that Cloisite-20A nanoclay significantly increased the dynamic shear complex modulus values of the tested asphalt when prepared at high temperature (at 160°C) and rotation (2500 rpm) for 3 hrs in order to get desired exfoliation. Results of the direct tension test showed that the strain failure rate reduced by adding nanclay in asphalt, while the secant or direct tension moduli increased [26].

Kumar and Suman [17] investigated the influence of the blending 1% to 9% of Cloisite-15A nanoclay on the physical and mechanical properties of bitumen binder. The results showed an improvement of rutting resistances, an increase in softening point, dynamic viscosity and complex modulus, while a decrease in binder penetration, phase angle. Results also showed a significant improvement in Marshall stability and insignificant enhancement in flow value. 5% Cloisite-15A nanoclay gave the best improvement in the modified binder [17]. While, Blom *et al.* [18] concluded that in a hard bitumen, nanoclay addition has no effect on the penetration value, because the bitumen is already so hard. But, a slight increase of stiffness and elasticity obtained through the addition of 5% nanoclay in bitumen at low frequencies. Cloisite-15 has good storage stability in the bitumen [18]. Varun and Gehlot [1] reported about the improvement of the physical properties such as penetration, softening point, penetration index and ductility of modified asphalt binder by using common types of nanoclay, organoclay (OMMT), Cloisite-15A, Nanofil-15, through the wet-modified nanoclay in combination with the coupling agent then dispersed in the asphalt.

Bagshaw *et al.* [2] prepared nanoclay (Nanomer 1.44P)/bitumen nanocomposites to decide whether expensive and time-consuming blending was essential to reach important changes in the properties of the bitumen composites. Blending for longer times and/or higher shearing speeds resulted an increase of the dispersion and exfoliation of the nanomer clay, but, no significant effect on the physico-chemical and rheological properties of the modified bitumen. Simple paddle mixing was sufficient to disperse the nanomer to improve the physical properties of the modified bitumen. Nanomer dispersion into the softer bitumen grade caused larger apparent changes than blending into the stiffer grade. As a result, the use of simple, low-cost blending methods could be possible to manufacture effective clay-bitumen nanocomposites [2].

The effect of clay sizes such as macro- and nano-size on the performance of bitumen was studied [4,17]. El-Shafie *et al.* [4] compared between the effect of unmodified clay (macroscale) and organically modified nanoclay on the physical and mechanical properties of asphalt binders. The results showed an increase in softening point; kinematics viscosity and decrease in penetration. The tensile strength of modified asphalt enhanced at all percentages by a comparison with both macroclay and unmodified asphalt. 6% nanoclay obtained the best improvements in the modified asphalt [4]. The physical and mechanical properties of asphalt were significantly improved compared to the control asphalt as follows: (i) an increase of softening temperature was 12°C, kinematic viscosity values increased by about 222% and 179% at 135 and 150°C, respectively, the stress values increased by about 179% and 370% at -7°C and 25°C, respectively, (ii) a decrease of about 25% was in the penetration value, the strain values decreased by about 41% and 35% at -7°C and 25°C, respectively [4].

3.3. Clay/nanoclay and polymer modified asphalt

Polymer modified asphalt has increasingly used to improve the flexibility, deformation stability, durability and other properties of asphalt [23]. The most common polymers used in asphalt modification are styrene-butadiene-styrene (SBS), styrene-butadiene-rubber (SBR), ethylene-vinyl-acetate (EVA), and polyethylene. A significant improvement of properties are achieved by using the clay as a second modifier in polymer modified asphalt [8,13-23]. For example, a small amount of nanoclay reinforcement can enhance the compressive and shear strength of thermoplastic polymers [4]. The gallery spacing increased and the resulting morphology was an intercalated structure, when the polymer dispersed between the layers of the nanoclay [50]. Another morphology is an exfoliated, produces when the clay layers are extensively delaminated and completely separated thorough polymer penetration using different dispersion methods [27,43,50]. The silicate layers also can be prevent the diffusion of oxygen through polymer modified asphalt, enhancing the aging resistance [12]. This enhancement realized at the addition of the clay either separately or premixed with the polymer in the asphalt [27,43,50].

Many studies were investigated the clay/nanoclay with polymers modified asphalt. Khodary [15] evaluated the properties of SBS-clay nanocomposite modified bitumen and mixtures. Results showed that both penetration and softening point of all modified bitumen improved by adding SBS-clay nanocomposite. Tensile strength of modified mixtures was higher than unmodified mixtures by about three times with 5% SBS and 6% nanoclay. Fatigue life of SBS-clay modified mixtures was about 3.4 times higher than unmodified bitumen [15]. Ouyang *et al.* [21] added kaolinite (KC) to styrene-ethylene-butylene-styrene (SEBS) to modify asphalt. Results showed that the ratio of SEBS/KC in the mix has a significant effect on the storage behavior at high-temperature. At the SEBS/KC ratio of about 2, the modified asphalt was stable. The compatibility of asphalt/polymer was changed by adding clay with direct implications on storage stability, mechanical and thermal properties [21].

MMT nanoclay and organic modification of nanoclay layered silicates has been successfully used in the modification of polymer to significantly improve the thermal stability, mechanical and barrier properties of asphalt [14,23]. Jasso *et al.* [51] examined the addition effects of MMT to SBS modified bitumen binders. Results demonstrated that MMT addition to SBS modified bitumen enhanced rheological benefits. Furthermore, it was concluded that the addition of the nanoclays increased the viscosity, improved the complex modulus, and decreased the phase angle of the SBS-modified asphalt, by the formation of an intercalated and exfoliated structures in the SBS modified asphalt binder using the Na-MMT and OMMT nanoclays, respectively [45]. On the other hand, Zhang *et al.* [20] found that OMMT could enhance the UV ageing resistance of asphalt by modifying SBS-asphalt with OMMT. Baochang *et al.* [22] found that SBR/MMT modified asphalt was very stable in a different content range of SBR/MMT and formed an ideal fine network structure. Additionally, SBR/MMT improved viscoelastic properties and resistance to rutting in modified asphalts at high temperature with higher complex modulus and lower damping factor exhibited [22]. Yao *et al.* [52] studied the rheological properties effects by using only MMT nanoclay and combined with polymers in bitumen binder. Results showed a significantly increase of viscosity and complex shear modulus values by adding nanoclay to bitumen, but, nanoclay combined polymer decreased these values slightly. However, better results for fatigue crack and rutting by using nanoclay combined polymer modified bitumen was achieved [52].

Yasmin *et al.* [53] obtained that the produced materials had higher elastic modulus than that of the pure epoxy when Nanomer I.28E and Cloisite-30B added into epoxy polymers. Furthermore, the physical and rheological properties of bitumen and polymer modified bitumen could be significantly enhanced by the addition of OMMT [4]. Sureshkumar *et al.* [13] also concluded that organomodified Cloisite or dellite clay had a high compatibilizing effect on asphalt and EVA copolymer can lead to the better dispersion of the polymer in the asphalt. In another study, the ternary blends of MMT clay and triblock copolymer (SBS, SIS, or SEBS) to the asphalt showed a relatively higher complex modulus and enhanced viscoelastic properties, which improved its resistance to rutting at high temperatures [27]. The optical microscopy of morphology exhibited the significant compatibility between triblock asphalt/polymer/MMT, thus influencing the final rheological properties of asphalt [27]. Pamplona *et al.* [12] observed an improvement on the physical and rheological properties, probably due to the intercalation of the asphalt in the nanoclay layers. A similar behavior of the asphalt modified by 2.5% and 4% of SBS with 2.5% of OMMT clays and organically modified vermiculite (OVMT). The addition of OMMT and OVMT in the binder leaded to save the required polymer. The black diagrams also showed the similar effect of nanoclays (OVMT and OMMT) as Cloisite®20A. The addition of OVMT enhanced the storage stability of SBS modified asphalt [12].

Polacco [43] investigated the addition procedures effect of Cloisite-20A as a third component in SBS polymer modified asphalts. The X-ray analysis showed that the mixing procedure had no significant effect on the formation of an intercalation between the interlayer distance of clay. The mixing procedure also seemed not to be affected the low-temperature glass transitions. Moreover, the final rheological properties were significantly affected by the mixing procedure [43]. Merusia *et al.* [19] studied asphalt modification produced from binary and ternary preparation procedures using linear SBS copolymer and Cloisite-20A clay. Ternary blends produced strong mechanical response of the system and significantly influenced by the nanocomposite modification. In case of bitumen was initially blended with clay and then with the polymer, the mechanical properties significantly improved but the general rheological properties remained as the same that of the bitumen/SBS binary blend [19].

The modified effect of Cloisite-15A and Cloisite-11B nanoclays on the moisture susceptibility and the cost analysis of PG 64-22 bitumen was studied and compared with polymer modified bitumen [54]. Results showed that the nanoclay addition gave a reverse influence on moisture resistance of plain binder, which enhanced the performance of bitumen in respect of stiffness and saved the money. At 2 and 4% nanoclay could save 22-33% of the cost when compared to polymer modified bitumen [54].

3.4. Clay/nanoclay and others modifiers

Every year, much amount of waste polymers are produced. Hence the waste polymers could be used as a good alternative to the new polymers for asphalt modification, as it will economical and might solve the problem of waste disposal to some extent [23]. The significant improvement in the Marshall stability of the modified bitumen by using MMT nanoclay and waste low density polyethylene (LDPE) and polypropylene (PP) obtained from waste carry bag, crumb rubber found from waste tire (CR). The highest stability value is obtained at 1% MMT and 4% of LDPE/PP [23]. Yu *et al.* [55] reported that asphalt rubber (AR) was prepared by blending crumb rubber and bitumen, gave various advantages such as superior rutting resistance, lower road-tire noise and longer service life, but it had poor storage stability, which in turn limits its wider application. Hence, they dispersed three types of nanoclays into hot AR binder by high shear blending. Results showed that the selected nanoclays had insignificant influences on workability, rutting and fatigue properties, but providing superior storage stability. The best storage stability of AR obtained by using pure MMT nanoclay with Na^+ inorganic group, which has an intermediate hydrophilic property and middle layer gap [55]. Mahalakshmi *et al.* [56] studied the modification of bitumen using both plastic waste (LDPE) and nanoclay individually and as a composite. Results showed that LDPE modified bitumen is preferred if the high temperature is reached on roads. But nanoclay is preferred in cold climatic regions, because it has much resistance for temperature susceptibility. For mixed climatic regions, composites of LDPE and nanoclay enhanced the properties of mix like strength and durability [56].

For environmental concerns, the asphalt industry interests to the promotion of green asphalt technologies [5]. Several researchers studied the application of bio-based asphalt binder to use as a modifier or alternative for bituminous asphalt [5,10,25]. The study results by Hosseinnezhad *et al.* [5] showed a significant reduction in the aging rate of modified asphalt binder with bio-binder (derived from swine manure) and Nanofil-116 nanoclay. The highest increase in gallery spacing was obtained at the equal ratio of bio-binder and clay, resulted from the interactions between amide functional groups of bio-binder and the silicate layer of nanoclay [5]. Walters *et al.* [10] studied the modified effect of Cloisite-30B nanoclay and bio-char grinded to nano-scales on asphalt rheological properties. Results showed that the addition of nanoclay and bio-char to modify asphalt binder improved the high temperature performance and aging resistance of asphalt. These results were mainly attributed to the modify of layer spacing in nanoclay as observed by XRD [10]. The authors also concluded that Cloisite-11 nanoclay leaded to a higher increase in viscosity compared to Cloisite-15A nanoclay of asphalt binder and enhancement of asphalt aging resistance. Further enhancement of asphalt properties when bio-char added to nanoclay modifiers to assist silicate platelets dispersion by decreasing electrostatic forces between the nanoparticles. Moreover, 3% Cloisite-11 found to be as effective as 6% Cloisite-11 combined with 3% bio-char to enhance aging resistance of base asphalt [25].

Modification of asphalt using other different types of modifiers and clay/nanoclay was studied. The addition of nanoclay and two different warm asphalt additives (WAA), Rediset® and

Cecabase® increased the softening point and viscosity, and improved the temperature susceptibility and physical properties of the asphalt [3]. The addition of nanoclay or synthesized nanosilica improved the performance of the asphalt binder by decreasing penetration, increasing softening point and viscosity. By increasing nanosilica percentage increased brookfield rotational viscosity (RV) at temperature of 135°C and up to 150°C, but, at small percentages of nanoclay increased the RV, while at higher temperature up to 165°C, RV values did not change significantly by using both nanomodifiers [24].

Yalçın *et al.* [9] reported that the conventional properties of asphalt binder improved with the addition of MMT nanoclay contains 35-45 wt% dimethyl dialkyl amine (DANC). Results of dynamic shear rheometer showed that the temperature and the frequency had a significant effect on the complex modulus of MMT and DANC modified asphalt. Results also indicated that the DANC has promising potential to decrease the permanent deformation or rutting of asphalt pavements [9].

Yao *et al.* [7] studied to improve the rutting and fatigue cracking resistance of asphalt binders by the addition of micro- and nanomaterials (Nanomer I.44P, carbon microfiber, non-modified nanoclay and polymer modified nanoclay). The addition of nano or micro modifiers to asphalt binders increased the complex shear modulus and improved the performance of resistance to rutting. Whereas, the addition of polymer modified nanoclay increased the resistance to fatigue crack and decreased complex shear modulus. Moreover, the aging and oxidation effect can be delay and weaken by adding of four modifiers to the asphalt binder [7]. They also concluded that the dynamic modulus of micro- and nanomodified asphalt mixtures enhanced significantly and the rutting susceptibility reduced [57].

Bonati *et al.* [58] and Pei *et al.* [59] studied to limit the fire reaction of asphalt. Results of nano calorimeter test showed that aluminum hydroxide gave the best results for heat and smoke released and nanocomposite use provided benefits [58]. The addition of 1% OMMT and 3% alumina-trihydrate gave the best results for fire reaction. According to the results, the use of both additives together gave less gas emissions during fire and sustained better thermal stability compared to pure bitumen [59].

The interlayer space of MMT and OMMT increased from 1.41 nm to 1.95 nm and 2.08 nm to 2.42 nm through the fictionalization the clays by isophorone diisocyanate (IPDI) and hydrogenated diphenylmethane diisocyanate (HMDI), respectively. The modified asphalt with fictionalized clays by IPDI and HMDI gave a maximum softening point of about 57°C and 62°C, initial decomposition temperature of about 360°C and 370°C, respectively and possessed good storage stability [30].

One of the commonly occurring distresses in asphalt pavements is a moisture damage. The addition of nanoclay and carbon microfiber enhanced the performance of the mixture's moisture susceptibility or decreased the moisture damage potential [40]. The effects of nanoclay and nanohydrated lime on moisture susceptibility of a continuously graded asphalt mix were investigated. Results demonstrated that the addition of 5 wt% nanohydrated lime and 2 wt% of nanoclay increased tensile strength ratio of asphalt mixes by 52 and 49%, respectively [29]. On the other hand, the modifications of the asphalt with layered double hydroxides (LDHs), OMMT and carbon black (CB) improved the anti-UV ageing asphalt. LDHs decreased the ageing rate of asphalt most effectively, followed by OMMT then CB [14].

Zhang *et al.* [8] selected kaolin, carbon white, sulfur (S), tetramethylthiuram disulfide (TMTD), zinc oxide (ZnO), and butylated hydroxytoluene (BHT) to improve the performance of the SBS-modified bitumen stabilizer powder. The presence of S, TMTD, ZnO, and BHT significantly improved the storage stability and aging resistance of SBS-modified bitumen. These components also improved the softening point and viscosity and decreased the penetration. Furthermore, kaolin, carbon white significantly improved the storage stability of SBS-modified bitumen [8].

4. Conclusions

Using clays as modifiers considered to be very important, efficient and economical in asphalt industry. Different types of clays such as bentonite, kaolin and vermiculite are obtainable and used as asphalt modifier in different sizes. The addition of clay/nanoclay in asphalt improved several properties. The BT and OBT modified asphalts increased softening point and viscosity and significantly improved the dynamic rheological properties through higher complex modulus, lower phase angle and higher rutting parameter. OMMT modified asphalt decreased the effect of UV ageing. Nanoclay modified asphalt decreased the mixture susceptibility to moisture damage. Both Cloisite and Nanofil nanoclays can improve stiffness, rutting resistance, indirect tensile strength, resilient modulus, and Marshall stability of asphalt. A significant improvement of properties are obtained by adding clay/nanoclay as a second modifier in polymer modified asphalt. Clay/nanoclay can combine with many different types of materials used as modifiers of asphalt such as waste polymers, bio-char, different types nanomaterials, etc.

References

[1] Varun, Gehlot T. IOSR J. of Mechanical and Civ. Eng., 2018; 15(1): Ver. III, 25-30.
[2] Bagshaw SA, Kemmitt T, Waterland M, Brooke S. Road Materials and Pavement Design, May 2018; 1-22.
[3] Abdullah ME, Zamhari KA, Nayan N, Hainin MR, Hermadi M. World J. Eng., 2012; 9(2): 155-160.
[4] El-Shafie M, Ibrahim IM, Rahman AMM, Abd EI. Egyptian J. Pet., 2012; 21(2): 149-154.
[5] Hosseinnezhad S, Fini EH, Abu-Lebdeh TM. American J. Eng. Appl. Sci., 2018; 11(2): 433-443.
[6] Shahabadi ZA, Shokuhfar A, Ebrahimi-Nejad S. Constr. Build. Mater., 2010; 24: 1239-1244.
[7] Yao H, You Z, Li L, Shi X, Goh SW, Lee CH, Yap YK, Shi X. Constr. Build. Mater., 2013; 38: 327-337.
[8] Zhang W, Ding L, Jia Z. Appl. Sci., 2018; 8, 457, 1-16.
[9] Yalçın E, Yılmaz M, Kök BV, Çeloğlu ME. E&E Congress, 6th Eurasphalt & Eurobitume Congress, Prague, Czech Republic, 2016.
[10] Walters RC, Fini EH, Abu-Lebdeh T. American J. Eng. and Appl. Sci., 2014; 7(1): 66-76.
[11] Jahromi SG, Andalibizade B, Vossough S. Arab. J. Sci. Eng., 2010; 35(1B): 89-103.
[12] Pamplona TF, Amoni B de C, de Alencar AEV, Lima APD, Ricardo NMPS, Soaresa JB, Soares S. deA. J. Braz. Chem. Soc., 2012; 23 (40):, 639-647.
[13] Sureshkumar MS, Filippi S, Polacco G, Kazatchkov I, Stastna J, Zanzotto L. European Polymer J., 2010; 46: 621-633.
[14] Hu J, Wu S, Liu Q, Hernández MIG, Zeng W, Xie W. Advances in Mater. Sci. and Eng., Sep. 2017; 9 pages.
[15] Khodary F. International J. of Current Eng. and Technol., 2015; 5(2): 949-954.
[16] Nurulain CM, Ramadhansyah PJ, Haryati Y, Norhidayah AH, Abdullah ME, Wan Ibrahim MH. Mater. Sci. Eng., 2017; 271: 1-5.
[17] Kumar A, Suman SK. International J. of Civil and Environ. Eng., 2017; 11(2): 172-177.
[18] Blom J, De Kinder B, Meeusen J, van den Bergh W. Mater. Sci. Eng., 2017; 236; 1-8.
[19] Merusia F, Giuliania F, Polaccob G. Procedia-Social and Behavioral Sci., 2012; 53: 335-345.
[20] Zhang H, Yu J, Wu S. Constr. Build. Mater., 2012; 27(1): 553-559.
[21] Ouyang C, Wang S, Zhang Y, Zhang Y. European Polymer J., 2006; 42: 446-457.
[22] Baochang Z, Man X, Dewen Z, Huixuan Z, Baoyan Z. Constr. Build. Mater., 2009; 23: 3112-3117.
[23] Sadeque M, Patil KA. Architecture and Civ. Eng., 2014; 12(1): 1-9.
[24] Ezzat H, El-Badawy S, Gabr A, Zaki E-SI, Breakah T. Procedia Eng., 2016; 143: 1260-1267.
[25] Walters R, Fini EH, Abu-Lebdeh T. International J. of Pavement Research and Techno., 2014; 7(6): 451-455.
[26] Nazzal MD, Asce M, Kaya S, Gunay T, Ahmedzade P. J. Nanomech. Micromech., 2013; 3(1): 1-8.
[27] Vargas-Hernández MA, Vázquez-Torres H. Revista Mexicana de Ingeniería Química, 2015; 14(2): 503-515.
[28] Mahdi LMJ, Muniandy R, Yunus RBt, Hasham S, Aburkaba E. Indian J. Sci. and Technol., 2013; 6(11): 5434-5442.
[29] Kavussi A, Barghabani P. Study of Civ. Eng. and Architecture, 2014; 3: 36-40.
[30] Zhang D, Xiao X, Cui Y. Polymers & Polymer Composites, 2017; 25(5): 405-417.
[31] Al Allam AM, Masirin MIM, Abdullah ME, Kamaruddin NHM. ARPN J. Eng. and Appl. Sci., 2016; 11(4): 2380-2386.
[32] Masirin MIM, Al Allam AM, Bader Ali AS, Pertanika J. Sci. & Technol., 2017; 25(S): 101-108.

[33] Ziari H, Babagoli Z, Akbari A. Road Materials and Pavement Design, Nov. 2014; 101-118.
[34] Ziari H, Divandari H, Babagoli R, Akbari A. International J. Civ. and Environ. Eng., 6(8): 629-634, 2012.
[35] Ziari H, Babagoli R. Ameri M, Akbari A. Constr. Build. Mater., 2014; 68: 685-691.
[36] Yu J, Zeng X., Wu S., Wang L., Liu G., Mater. Sci. Eng., 2007; 447: 233-238.
[37] Yu J, Feng P, Zhang H, Wu S. Constr. Build. Mater., 2009; 23: 2636-2640.
[38] Mohd Satar MKI, Jaya RP, Rafsanjani MH., Che`Mat N., Hainin MR, Aziz MdM.A., Abdullah ME, Jayanti DS. J. of Physics: Conf. Series, 2017; 1049: 1-8.
[39] You Z, Mills-Beale J, Foley JM, Roy S, Odegard GM, Dai Q, Goh SW. Constr. Build. Mater., 2011; 25: 1072-1078.
[40] Goh SW, Akin M, You Z, Shi X. Constr. Build. Mater., 2011; 25: 195-200.
[41] van de Ven MFC, Molenaar AAA, Besamusca J. Nanoclay for binder modification of asphalt mixtures. Advanced Testing and Characterization of Bituminous Materials, Loizos Part II, Scarpas & Al-Qadi (eds) Taylor & Francis Group, London, 2009; 133-142.
[42] Yang J, Tighe S. 13th COTA International Conference of Transportation Professional Procedia - Social and Behavioral Sciences 96, 2013; 1269-1276.
[43] Polacco G, Kríž P, Filippi S, Stastna J, Biondi D, Zanzotto L. European Polymer J., 2008; 44: 3512-3521.
[44] Liu G, Wu S, van de Ven M, Molenaar A, Besamusca J. AES-ATEMA, 3rd International Conference on Advances and Trends in Eng. Materials and their Applications/Montreal, Canada, 2009.
[45] Yu J, Wang X, Hu L, Tao Y. J. Mater. Civ. Eng., 2010; 22(8): 788-793.
[46] Wu S, Wang J, Jiesheng L. Mechanic Automation and Control Eng. (MACE), IEEE, 2010; 1595-1598.
[47] Ahmadi NA, Mortazavi SM, Vossough S, Jahromi SG. Int. J. Sci. Technol. Trans. Civ. Eng., 2011; 35(C2): 277-281.
[48] Ghile DB. Delft University of Technol., 2005; 1-151.
[49] Jahromi SG, Ahmadi NA, Mortazvi SM, Vosough S. Int. J. Sci. Technol. Trans. Civ. Eng., 2011; 35(C2): 277-281.
[50] Ke YC, Stroeve P. Polymer-layered Silicate and Silica Nanocomposites, Elsevier, The Netherlands, 2005.
[51] Jasso M, Bakos D, MacLeod D, Zanzotto L. Constr. Build. Mater., 2013; 38: 759-765.
[52] Yao H, You Z, Li L, Shi X, Goh SW, Mills-Beale J, Wingard D. Constr. Build. Mater., 2012; 35: 159-170.
[53] Yasmin A, Abot JL, Daniel IM. Scr. Mater., 2003; 49: 81-86.
[54] Husain Z, Zaman M, Hawa T, Saha MC. J. Mater. Civ. Eng., 2014; 27(10): 1-9.
[55] Yu J, Ren Z, Yu H, Wang D, Shekhovtsova S, Korolev E, Gao Z, Guo F. Materials, 2018; 11, 2093: 1-15.
[56] Mahalakshmi M, Prakash KE, Suresh Babu S. International J. of Advance Eng. and Research Development, 2017; 4: 516-522.
[57] Yao H, You Z. J. of Nanomaterials, 2016; 14 pages.
[58] Bonati A, Merusi F, Bochicchio G, Tessadri B, Polacco G, Filippi S, Giuliani F. Constr. Build. Mater., 2013; 47: 990-1000.
[59] Pei J, Wen Y, Li Y, Shi X, Zhang J, Li R, Du Q. Constr. Build. Mater., 2014; 72: 41-47.

To whom correspondence should be addressed: Dr. Eman A. Emam, Department of Petroleum Refining Eng. and Petrochemicals, Faculty of Petroleum and Mining Eng., Suez University, Suez, Egypt, E-mail: emamtah@yahoo.com

Petroleum and Coal

Article **Open Access**

OLIGOMERIZATION OF LIGHT OLEFINS OVER HZSM-5 ZEOLITE CATALYST WITH DIFFERENT SI/AL RATIOS

Laleh Shirazi

Gas Division, Research Institute of Petroleum Industry (RIPI), Tehran, Iran

Received March 27, 2019; Accepted June 13, 2019

Abstract

Na-ZSM-5 zeolite with Si/Al molar ratios in the range of 10-50 was synthesized and then transformed into HZSM-5 using ion-exchange method. Techniques such as XRD, FT-IR, SEM, EDX, TG-DTA, BET and NH_3-TPD were used to characterize the zeolite. Light olefins oligomerization reaction was studied over HZSM-5 zeolite catalyst with Si/Al molar ratios in the range of 10-50. The reaction was carried-out at atmospheric pressure, temperature in the range of 250 - 400°C and GHSV = 195-1170 h^{-1}. The study showed that by increasing the temperature from 250 to 300°C, the C_7^+ hydrocarbons in the product increased, whereas above this temperature, they decreased. Similarly increase in GHSV caused the C_7^+ hydrocarbons in the product to decrease. The highest C_7^+ hydrocarbons were obtained with HZSM-5 of Si/Al molar ratio = 25, at temperature 300°C and GHSV = 195 h^{-1}.

Keywords: *HZSM-5; Zeolite; Light olefins oligomerization; Liquid fuels; Si/Al ratio.*

1. Introduction

Oligomerization of light olefins is an intermediate stage in the production of gasoline and distillate fuels from natural gas. It has long been known that oligomerization of light olefins to higher molecular weight hydrocarbon occur on acid-type catalyst. The products of reaction on acid-type catalyst, includes; primarily olefins from straight oligomerization or mixture of olefins, paraffins, cyclo-alkanes and aromatics from what has been termed "conjunct" polymerization [1]. Among the acid-type catalysts, phosphoric acid on Kieselguhr and ZSM-5 zeolite are able to catalyze such a reaction [2]. The technology via phosphoric acid on Kieselguhr, goes back to 1935 to convert propene and butene to C_6-C_{10} isoolefins. The use of ZSM-5 zeolite for oligomerization of light olefins was proposed in 1970's by Mobil. The process is known as Mobil Olefins to Gasoline and Distillate (MOGD) [3].

Due to shape selectivity and acid catalyzed properties of ZSM-5 zeolite, this catalyst then replaced the phosphoric acid catalyst for oligomerization [4]. Apart from its high selectivity and activity due to its structure and Si/Al ratio, which reflects the number and strength of the acid sites, its low deactivation rate compared with other type of zeolites, is also another important factor for its catalytic behavior [5-6]. Light olefins oligomerization over ZSM-5 zeolite with different Si/Al ratio was investigated at different temperature and GHSV [7-12]. The hydrocarbon produced at 277°C and above, was predominantly gasoline rather than distillate and as temperature was reduced, the product was much heavier hydrocarbons (C_{11}-C_{20}) [13]. 1-butene oligomerization over H-ZSM-5 zeolite has been investigated in a differential reactor operating at ambient pressure. Optimum conditions for selectivity for C_8^+ hydrocarbons (86 wt.%) was obtained with H-ZSM-5, at 200°C and 0.5 bar [14].

The effect of Si/Al ratio of ZSM-5 in the range of 20-500 on propene oligomerization at 220-300°C was investigated and showed that as Si/Al ratio decreased, hydrocarbon products of up to C_{12} were increased. This is in agreement with the work done by Gnep *et al.* [15], where it was found that in propene oligomerization over ZSM-5 with Si/Al ratio of 30 at 300°C, hydrocarbon products of up to C_{13} were produced.

In this work HZSM-5 zeolite with Si/Al molar ratio in the range of 10-50 with different crystal size and morphology was synthesized. Their performance as catalyst for light olefins oligomerization at atmospheric pressure, temperature in the range of 250 - 400°C and GHSV = 195-1170 h^{-1} was investigated.

2. Experimental

2.1. Reagents

The reagents used in the present study were aluminum sulfate ($Al_2(SO_4)_3.18H_2O$, laboratory grade, Merck), sulphuric acid solution (H_2SO_4, 98%, Aldrich), silicagel powder (grade 923, 100-200 mesh, Aldrich), sodium hydroxide (NaOH, flake, Merck), Tetrapropylammonium bromide (TPA-Br, $C_{12}H_{28}BrN$, Merck), ammonium nitrate (NH_4NO_3, laboratory grade, BDH) and propene and butene (99.5 % purity, Linde)

2.2. HZSM-5 preparation

ZSM-5 zeolite was first synthesized from a hydrogel mixture prepared by combining two solutions as follows:

Specified amount of aluminum sulfate was dissolved in de-ionized water and after complete digestion, the required amount of sulphuric acid solution was added to the solution and it was named as solution A. Sodium silicate solution with the composition of 29.50 wt% SiO_2 and 10.50 wt% Na_2O was prepared by dissolving silica gel powder in an alkaline solution and it was named as solution B. Solutions A and B were mixed together under vigorous agitation until a homogenous gel mixture was obtained. Tetrapropylammonium bromide solution was then added to the gel mixture and stirring was continued for about 2 h. The final gel mixture had a pH = 10.5.

The gel mixture was put into a 500 cc high-pressure stainless steel autoclave reactor (manufactured by Autoclave Engineers INC. (BURTON CORBLIN, 60101 NOGENT OISE), France) and synthesis was carried out under agitation speed of 700 rpm at 180 °C for 24 h. At the end of the synthesis, the solid product was filtered and washed several times with warm de-ionized water. The solid product was dried at 120°C and then calcined at 550°C for 3 h under airflow in order to remove the organic template trapped inside the zeolite pores and the final product was Na-ZSM-5. The zeolite was then ion-exchanged with 2 M solution of ammonium nitrate with the ratio of 1 g zeolite/10 cc solution for 24 h under stirring at 80°C to transform Na-ZSM-5 to NH_4^+-ZSM-5. Afterwards, the NH_4^+-ZSM-5 was filtered and washed with de-ionized water. The sample was calcined at 550°C for 3 h under airflow to decompose the ammonium ions to produce HZSM-5.

The gel molar compositions and synthesis conditions used in this work to synthesis ZSM-5 with different Si/Al molar ratios are given in Table 1.

Table 1. Gel molar compositions and synthesis conditions* for ZSM-5 with different Si/Al molar ratios

TPA-Br	Na_2O	Al_2O_3	SiO_2	H_2O
9.15	8.0	1.0	60	2 137.5
9.95	8.0	1.0	100	3 562.5
10.6	8.0	1.0	115	4 096.9
10.5	8.0	1.0	125	4 453.1

** Temperature and synthesis time were 180°C and 24 h*

2.3. Characterization

The synthesized samples were analyzed by X-ray diffraction (XRD) for phase identification using a Philips PW 1840 equipped with a Cu Kα radiation, λ = 1.54060 Å at 40 kV and 25 mA with a nickel filter in the range of 2θ = 5 - 90º.

The FT-IR spectra of the zeolite were recorded using BRUKER Model IFS 88 in the range 1300-400 cm^{-1} on thin wafers of KBr in which 1 wt. % of zeolite was dispersed.

The morphology and crystal size of the zeolite were examined using a Philips scanning electron microscope (SEM) model XL30. The samples were coated with gold. Coating was performed by physical vapor deposition (P.V.D.) method for 400 s at 10-3 Torr in a BAL-TEC sputter coater model SCDOOS. The aluminum and silicon content of the zeolite were analyzed using Energy Dispersive X-ray (EDX) microanalysis coupled with SEM. The sodium content of the sample was analyzed using a Perkin-Elmer Atomic Absorption Spectrometer Model AAnalyst 200.

Thermal analyses to determine the removal rate of water and template trapped insides the zeolite pore, were carried out using a Simultaneous Thermal Analyzer Model STA 1640. The temperature of the sample was raised at a rate of 10ºC min^{-1} from ambient to 700°C in an air flow of 50 cm^3 min^{-1}. In the thermograms, the weight loss, the differential temperature and the temperature of the sample were plotted simultaneously.

The surface area of the zeolites was determined using a BET method on QUANTA CHROME physical adsorption series using nitrogen as adsorbate at −196°C. The samples were preheated at 200°C for 2 h to remove moisture and degassed at 300°C under vacuum. The sample was allowed to cool, nitrogen was fed into the system and adsorption of the gas took place and surface area of the zeolite was then evaluated.

The acidity of the zeolite was measured by NH_3-TPD using a chemical adsorption instrument of AMERICAN Micrometrics 2900. The samples were first heated up to 500°C with a helium flow of 20 cm^3 min^{-1} for 1 h in order to desorb all traces of adsorbed water and then cooled to 100°C. The adsorption of NH_3 was then started and continued until saturation. Desorption was achieved by increasing the temperature from 100 to 700°C at a rate of 10ºC min^{-1}.

2.4. Light olefins oligomerization

2.4.1. Set-up

The set-up used to study light olefins oligomerization is shown in Figure 1. The set up was consisted of a tubular stainless steel reactor with 0.9 cm i.d. and 40 cm long housed in a three-zone heating jacket, a temperature controller to maintain the heating rate and the temperature of the jacket, mass flow controller (Brooks Model 5850), a separator and a GC to analyze the product.

2.4.2. Procedure

The prepared zeolite powder was made into disk-shaped pellet with 2 mm thickness and 10 mm diameter. The pellet was then grounded and sieved to particles with approximately 1 mm in size needed for the reaction and 2 g of the particles were placed in the reactor (Figure 1).

Prior to each experiment the reactor was heated up to 550°C under a flow of N_2 at atmospheric pressure and kept at this temperature for 2 h. The reactor was then allowed to cool down to the reaction temperature under the flow of N_2. After reaching the desired temperature, it was maintained for 1 h at that temperature, and after that the flow of nitrogen was stopped and light olefins was fed to the reactor through mass flow-controller (MFC). A thermocouple was placed at the center of the catalyst bed to observe the temperature change during the reaction. The liquid products were collected in the separator and analyzed using a CP 3800 gas chromatograph equipped with a flame ionization detector on a Petrocol TM DH capillary column. For each experiment, fresh catalyst was used. Reaction conditions used in this work for light olefins oligomerization are given in Table 2.

Table 2. Reaction conditions for propene oligomerization*

Propene flow rate (cc min^{-1})	10, 37 and 60
GHSV (h^{-1})	195, 731 and 1170
Reaction temperature (°C)	250, 300, 350 and 400

* *All reactions were carried out at atmospheric pressure*

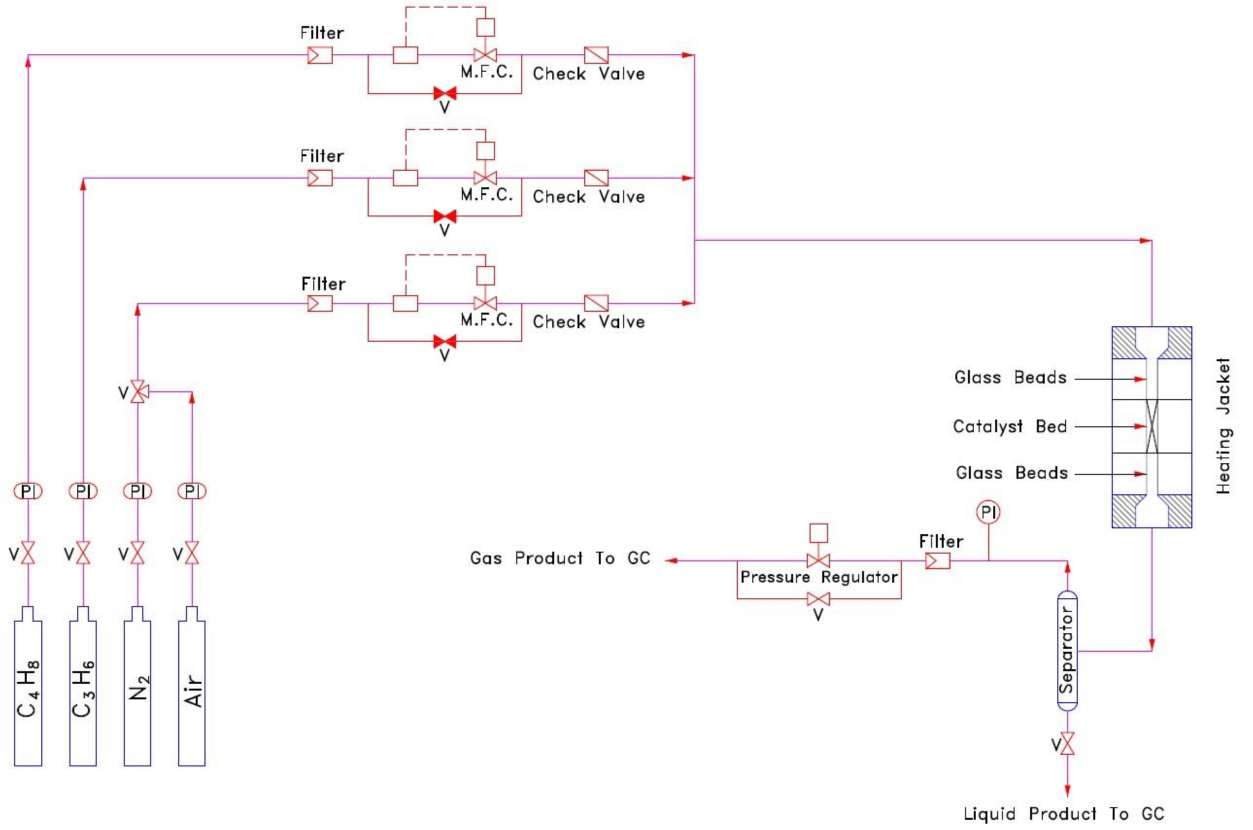

Figure 1. Set-up used for propene oligomerization

3. Results and discussion

The gel compositions in Table 1 produced ZSM-5 zeolite with different Si/Al molar ratios, morphology and crystal size. In this work they are referred to as ZSM-5 (X), where X refers to 10, 25, 40 and 50 molar ratio of Si/Al.

The X-ray diffraction (XRD) patterns of the as-synthesized ZSM-5 zeolite with different Si/Al molar ratios are shown in Figure 2. All samples gave similar XRD patterns, and agreed well for ZSM-5 reported in the reference [16].

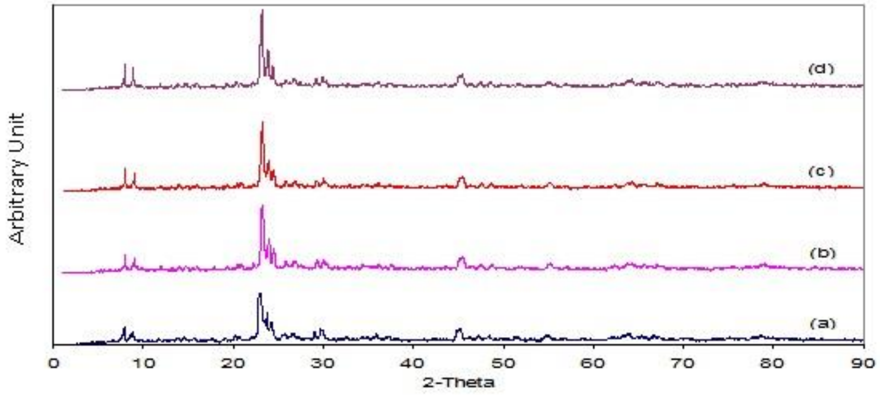

Figure 2. XRD patterns of the synthesized ZSM-5 zeolite with different molar ratios of Si/Al: (a) 10, (b) 25, (c) 40 and (d) 50

To further examine the purity of the as-synthesized ZSM-5 zeolite, the infrared absorption spectra of the sample were also taken. Figure 3 shows the infrared absorption spectra of the as-synthesized zeolite with different molar ratios of Si/Al in the region of 1300-400 cm^{-1}. The absorption bands near 788, 1084 and 1218 cm^{-1} are characteristic of SiO4 tetrahedron units. The strong absorption band in the region 1000-1200 cm^{-1} has been assigned to the internal vibration of SiO_4, AlO_4 tetrahedral for ZSM-5, and also for silica and quartz. The graph shows that the asymmetric stretching vibration frequencies at 1218 and 1084 cm^{-1} generally shift to higher wavenumbers with an increase in the Si/Al ratio. The bands near 1218 and 543 cm^{-1} provide information on the differences between these zeolites (ZSM-5) and other zeolite types. The external asymmetric stretching vibration near 1218 cm^{-1} was assigned to the presence of structures containing four chains of 5-membered rings arranged around a two-fold screw axis, as in the case ZSM-5 structure [17]. The band around 1084 cm^{-1} is attributed to the internal asymmetric stretching vibration of Si-O-T linkage and is observed to shift towards higher wavenumbers with increasing Si/Al ratio of the zeolite. This shift is due to the slightly lower mass of aluminum as compared to that of silicon [18]. The band near 788 cm-1 is assigned to the symmetric stretching of the external linkages, and the strong band near 543 cm^{-1} is attributed to the double five-ring lattice vibration of the external linkages [19]. The absorbance at around 450 cm^{-1} is due to the T-O bending vibrations of the SiO_4 and AlO_4 internal tetrahedral. The absorption bands around 543 and 450 cm^{-1} are characteristic of the ZSM-5 crystalline structure and the ratio of the intensities of these two peaks provides an approximate estimate of the degree of crystallinity of a given zeolite sample [20]. The ratio of the absorbance of these two bands falls between 0.74-0.85 for as-synthesized forms of zeolites. These value compare to a literature value of 0.8, suggested for pure ZSM-5 zeolites. The FT-IR spectra confirmed that, the synthesized zeolites exhibit good crystallinity. This is in agreement with the results of XRD.

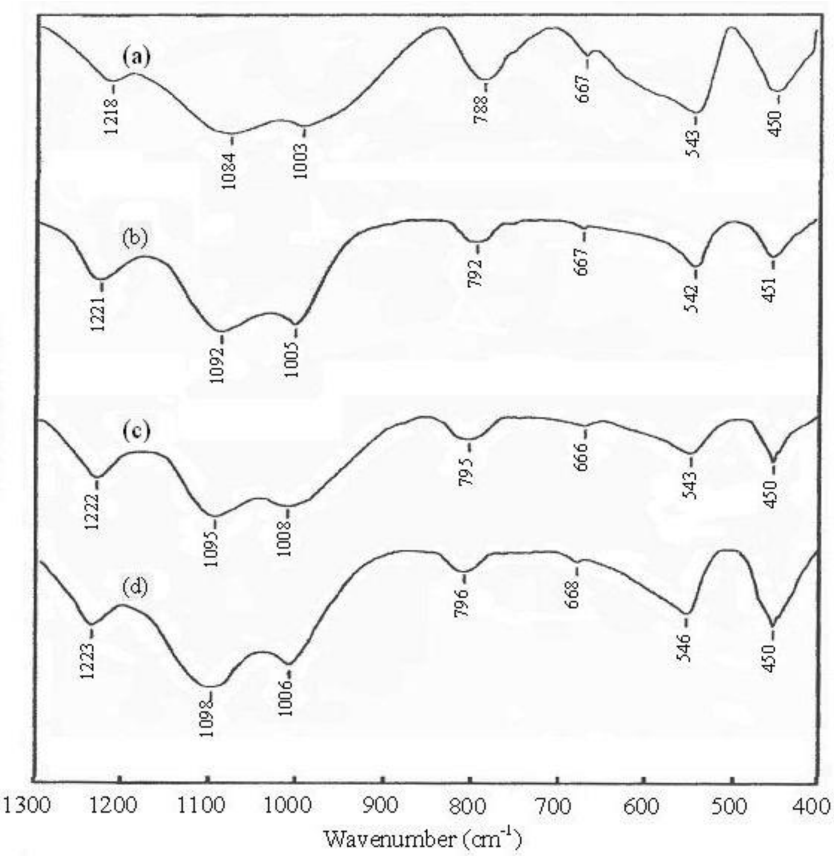

Figure 3. FT-IR spectra of the synthesized ZSM-5 zeolite with different molar ratios of Si/Al: (a) 10, (b) 25, (c) 40 and (d) 50

The morphology and crystal size of the synthesized ZSM-5 zeolite examined using SEM are shown in Figure 4. The samples had different crystal morphologies, from ellipsoidal to cuboidal and also aggregate of highly intergrowth crystals with uniform size distribution. The results show that increase in the aluminium content of the zeolite, decrease its crystal size and change its morphology.

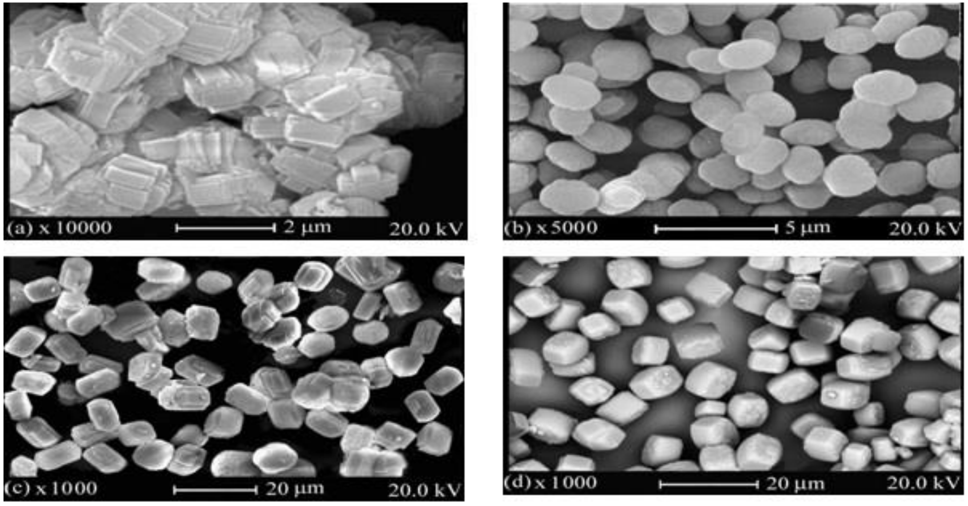

Figure 4. Scanning electron micrographs of the synthesized ZSM-5 zeolites with different molar ratios of Si/Al: (a) 10, (b) 25, (c) 40 and (d) 50

Surface area of the samples determined by BET method showed that, the surface area of the samples increased with increase in molar ratios of Si/Al (Table 3).

Table 3. Properties of HZSM-5 zeolite with different Si/Al molar ratios

Sample	BET surface area (m^2 g^{-1})	Crystal size µm	Total acidity mmole NH_3/g catalyst
HZSM-5(10)	355	aggregates	27.02
HZSM-5(25)	371	2	21.38
HZSM-5(40)	386	7	19.93
HZSM-5(50)	392	9	19.93

Thermogravimetric analysis of the synthesized ZSM-5 zeolite was carried out to determine the removal rate of water and template from zeolite. TGA and DTA curves of the samples are shown in Figure 5. The total percent weight losses in the temperature range 20-600°C represent water loss as well as loss of template. These two losses are overlapped in the thermogram and thus provide an approximate estimation. Dehydration occurred below 300°C. The weight loss in the temperature up to 300°C represented by a broad region in the thermogram is believed to be due to water loss. The water loss decreased with increasing Si/Al ratio of the zeolites (Figure 6). This is because the acidity of the zeolite decreases with increasing Si/Al ratio in zeolite; thus increases its hydrophobic nature. Therefore, less water is present in the zeolites with low aluminum content. The weight loss in temperature range of 300-600 °C can be attributed to template removal increases with increasing Si/Al molar ratio of the zeolites.

The acidity of the HZSM-5 zeolite with different Si/Al molar ratios determined by NH_3-TPD, are shown in Figure 7. All samples exhibit two well resolved desorption peaks: the low-temperature peak (LTP) at 210-255°C and the high-temperature peak (HTP) at 420-465°C. LTP and HTP generally correspond to weak and strong acid sites, respectively. As shown in Figure 7, the peak intensity at 420-465°C increased as the Si/Al ratio decreased. This is primarily due to the increase in extra-framework aluminum content as well as the in the framework. Figure 7 also shows that the desorption temperature of ammonia from the strong acid sites shifted to higher temperature as the Si/Al ratio decreased, strongly suggesting the existence of aluminum in extra-framework positions.

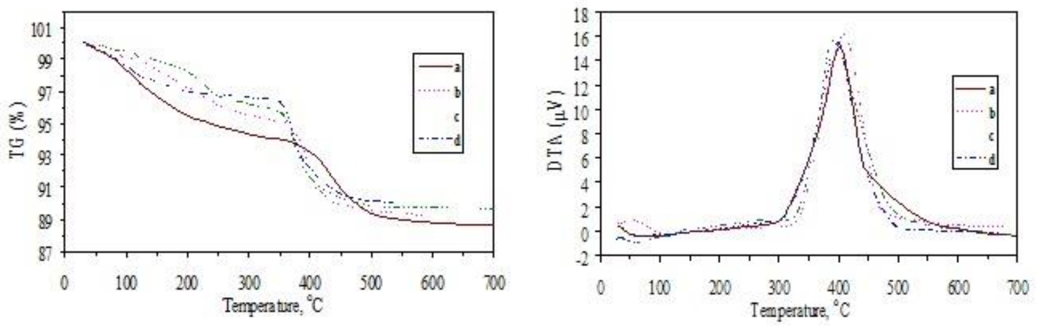

Figure 5. TGA and DTA curve of the synthesized ZSM-5 zeolites with different molar ratios of Si/Al: (a) 10, (b) 25, (c) 40 and (d) 50

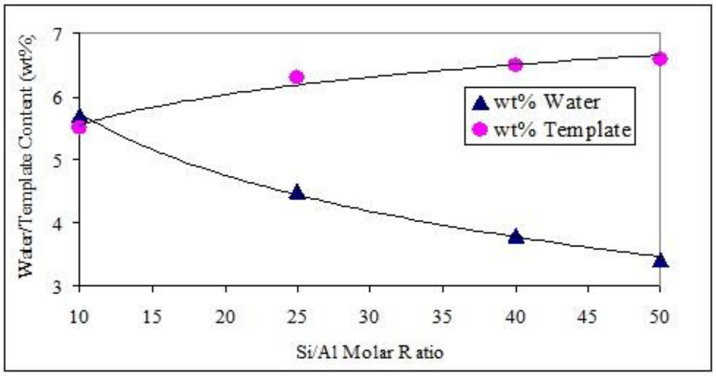

Figure 6. Water and template contents as a function of Si/Al molar ratio of the as-synthesized zeolites

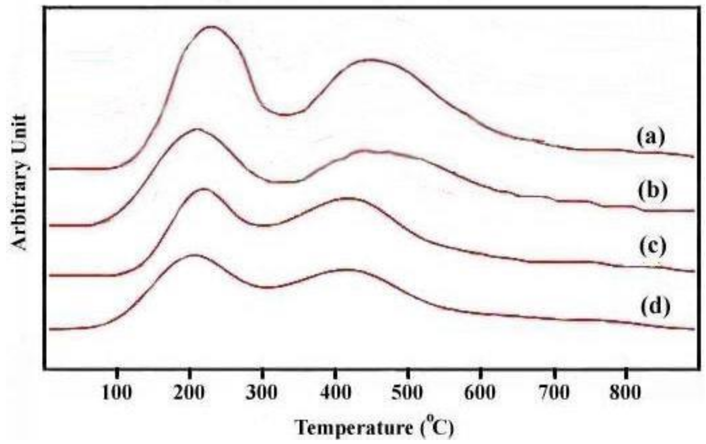

Figure 7. NH_3-TPD profile of HZSM-5 with different molar ratios of Si/Al: (a) 10, (b) 25, (c) 40 and (d) 50

The total acidity for HZSM-5 with different molar ratio of Si/Al is shown in Table 3. This table shows that the total acidity of HZSM-5 decrease with increasing of Si/Al molar ratio, which agrees well with those, reported in the literature [21-22]. Other properties of HZSM-5 zeolite with different Si/Al molar ratios are also listed in this table.

3.1. Oligomerization of light olefins over HZSM-5 zeolite

The hydrocarbon product distribution during light olefins oligomerization reaction over HZSM-5 with different Si/Al molar ratio at different temperatures and GHSV are shown in Figure 8.

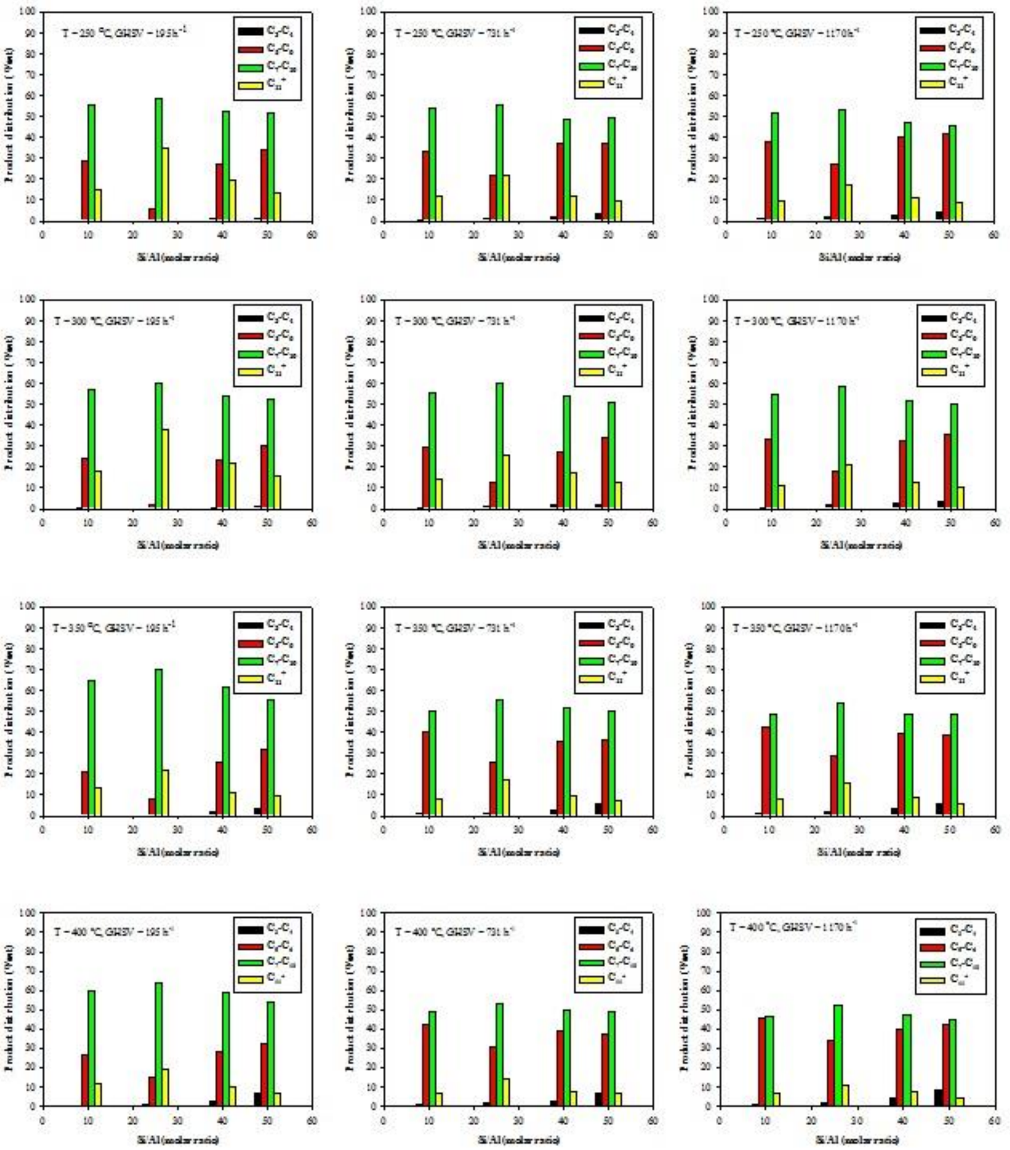

Figure 8. Product distribution obtained for light olefins oligomerization at atm. pressure, various temperatures and GHSV on HZSM-5 with different Si/Al molar ratios

The results showed that the product selectivity changed with aluminum content of the zeolite and since the aluminum content attributes to the acidity of the zeolite, therefore for a desirable acidity for oligomerization reaction, the aluminum content of zeolite plays an important role. As it is shown in Table 3, the change in Si/Al molar ratio not only changed the acidity of the zeolite but also the crystal size was affected. It can be concluded that, the acidity and crystal size of zeolite simultaneously affect the hydrocarbon product distribution.

Results for hydrocarbon product distribution at different Si/Al molar ratio showed that for all Si/Al molar ratios other than 10, the selectivity for C_7^+ hydrocarbon decreased with the increase in Si/Al ratio. At Si/Al ratio of 10, a complex effect of all reactions due to their interaction with each other occur on different acid sites, make this zeolite to behave differently which can not only be correlated by its Si/Al molar ratio and acidity. These effects may be due to that in which oligomerization reaction is a structural sensitive reaction, where all the catalyst parameters such as crystal size, morphology and Si/Al ratio can affect the product distribution.

Taking into account that the production of heavier olefins or oligomers (i.e., C_7^+) is the target to reach in oligomerization reaction. It can be seen from the results that at Si/Al =25 the C_7^+ hydrocarbons is at its most and therefore it can be concluded that for light olefins oligomerization the optimum ratio of Si/Al is 25. This shows that Si/Al ratio of zeolite has a pronounced effect on product distribution for oligomerization reaction.

The increase in GHSV can always change the product distribution during a catalytic reaction. This effect was also noted in this work. As it can be seen from Figure 8, the highest amount of C_7^+ hydrocarbon produced at different temperatures was obtained at GHSV = 195 h^{-1}, whereas at higher GHSV, the amount of C_7^+ hydrocarbon decreased.

Figure 8 shows that temperature rise had two distinct effect, increase in temperature from 250 to 300°C, increased the oligomerization (i.e., production of C_7^+ hydrocarbons) but above 300°C, the lighter olefins (i.e., < C_7 hydrocarbons) production increased. This is an indication that the cracking of heavier olefin to lighter olefin increases with increase in temperature. This effect can be seen clearly in Figure 9. As it can be seen, parameters such as temperature and GHSV affected simultaneously the production of different hydrocarbon product.

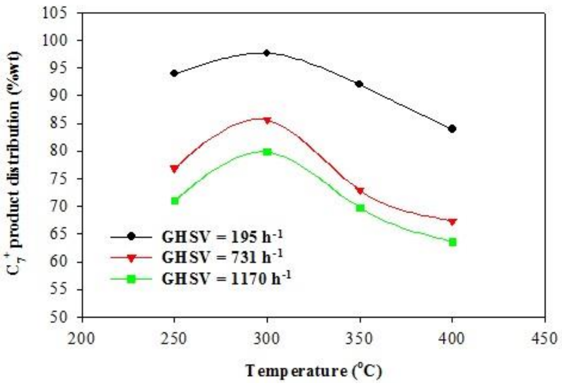

Figure 9. Liquid product distribution obtained for light olefins oligomerization at atm. pressure, different temperatures and GHSV on HZSM-5 with Si/Al molar ratio of 25

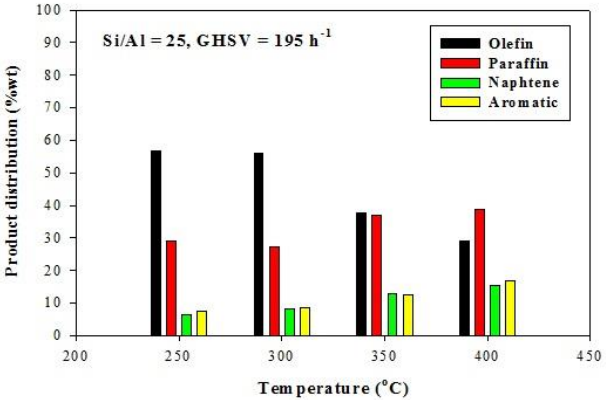

Figure 10. Effect of temperature on C_7^+ product distribution for light olefins oligomerization at various GHSV on HZSM-5 with Si/Al molar ratio of 25

It is postulated [23], that in oligomerization reaction, propene will oligomerize to C_6, C_9, C_{12}, etc., oligomers. These then isomerizes and recrack, forming a range of light olefins. Lastly, these then reoligomerize to an equilibrium distribution of heavier iso-olefin. As a result of having both forward (oligomerization) and reverse (cracking) reactions, a continuous carbon number distribution occurs in the product.

The effect of temperature on hydrocarbons produced during light olefins oligomerization reaction over HZSM-5 with Si/Al molar ratio of 25 and GHSV = 195 h^{-1} at different temperatures is shown in Figure 10. As it can be seen, at 250°C, the amount of olefin & aromatic produced is 56.85 and 7.58 wt%, respectively, whereas at 400°C, these amounts have been changed to 28.99 and 16.74 wt%. It can then be concluded that, at lower temperature, oligomerization of olefins is the dominant reaction. A significant quantity of paraffins presumably as a result of hydrogen transfer processes is also produced. Increase in temperature, increased the formation of aromatics, naphtenes (cycloalkanes) and paraffins.

It can be seen from the results that the amount of C_7^+ hydrocarbons produced over zeolite with Si/Al=25 at 300°C and GHSV = 195 h^{-1} is the highest (97.68 wt %) and is the lowest (63.6 wt %) at 400°C with GHSV = 1170 h^{-1} (Figure 9).

4. Conclusions

NaZSM-5 zeolites with different molar ratios of Si/Al in the range of 10-50 were first synthesized. They were then calcined under the airflow at 550 °C to remove the template. Afterwards, the zeolites were ion-exchanged with a 2.0 M aqueous solution of ammonium nitrate at 80°C for 24 h and transformed into HZSM-5. All synthesized samples as confirmed by their X-ray diffraction and IR patterns, were pure ZSM-5.

SEM images showed that the morphology of the synthesized zeolites was cubical, hexagonal and ellipsoidal in shape. In zeolite with Si/Al molar ratio of 10, intergrowth and twinning of crystal with high aggregation were observed, whereas for other Si/Al ratio, crystals with well-defined morphology were observed. The BET surface areas of the prepared HZSM-5 zeolites increased with increasing Si/Al molar ratio. The crystal size of the zeolite also increased with the increase in Si/Al molar ratios. Analysis by TGA showed that water content of the synthesized zeolite decreased, while the template content increased with increasing Si/Al molar ratios. NH_3-TPD profiles showed that zeolite with different Si/Al molar ratios had different acidity and total acidity decreased with increasing the Si/Al molar ratio.

The catalytic performance of the prepared zeolites with different Si/Al molar ratios for light olefins oligomerization at different temperatures and GHSV was studied in a fixed-bed reactor. The results showed that the hydrocarbon product distribution during oligomerization reaction highly depends on molar ratios of Si/Al, temperature and GHSV. A simultaneous effect of the acidity and crystal size of zeolite is also thought to change the product distribution. For all Si/Al molar ratios other than 10, the C_7^+ selectivity decreased with the increase in Si/Al ratio, this can be postulated as follow; at Si/Al ratio of 10 a complex effect of acid sites and morphology of the zeolite on all reaction taking place on the zeolite, make this zeolite to behave differently which cannot be correlated only by its Si/Al molar ratio and acidity. It can be concluded that, the crystal size, morphology and Si/Al ratio of the zeolite have a conjugative effect on light olefins oligomerization.

The results showed that the amount of C_7^+ increased with increasing temperature from 250 to 300°C. Above 300°C, due to cracking, the product distribution changed to lighter hydrocarbons. The results also showed that at low temperature (i.e., 250°C), oligomerization of olefins is the dominant reaction while at higher temperature, the formation of aromatics, naphtenes (cycloalkanes) and paraffins increased.

The results showed that the optimum condition for light olefins oligomerization reaction to produce C_7^+ hydrocarbons, was using a HZSM-5 zeolite with Si/Al molar ratio of 25, at 300°C and GHSV = 195 h^{-1}.

Acknowledgements

The author is grateful to the Research Institute of Petroleum Industry (RIPI) for financial support, which enabled this work to be undertaken.

References

[1] Knifton JF, Saderson JR. Olefin oligomerization via zeolite catalysis, Catalysis Letters, 1994; 28: 223-230.
[2] Peratello S, Molinari M, Bellussi G, Perego C. Olefins oligomerization: thermodynamics and kinetics over a mesoporous silica–alumina, Catalysis Today, 1999; 52: 271-277.
[3] van Grieken R, Escola JM, Moreno J, Rodriguez R. Liquid phase oligomerization of 1-hexene over different mesoporous aluminosilicates (Al-MTS, Al-MCM-41 and Al-SBA-15) and micrometer/nanometer HZSM-5 zeolites,Applied Catalysis A: General, 2006; 305: 176-188.
[4] Sanati M, Hornell Ch, Jaras SG. Oligomerization of alkene by heterogen. Catalyst, Catalysis, 1999; 14: 236-287.
[5] Schonlinner J, Kohler E, Burgfels G, Schmidt F, Wernicke HJ, de Pontes M, Roberts HL. Conversion of olefins to diesel, Conf. Industrial Applications of Zeolites, Brugge-Belgium, October 2000.
[6] Benito PL, Gayubo AG, Aguayo AT, Olazar M, Bilbao J. J. Chem. Tech. Biotechnol., 1996; 66: 183-191.
[7] Olefin oligomerization process, US patent 9580525, 2017.
[8] Dzikh IP, Lopes JM, Lemos F, Ribeiro FR. Transformation of light alkenes over templated and non-templated ZSM-5 zeolites,Applied Catalysis A: General, 1999; 177: 245-255.
[9] Popov AG, Fedosov DA, Ivanova II, Vedernikov OS, Kleimenov AV, Kondrashev DO, Miroshkina VD, Abrashenkov PA, Kuznetsov SE. A ZSM-5 zeolite-based catalyst for oligomerization of the butane–butylene fraction, Petroleum Chemistry,March 2016; 56(3): 237–243.

[10] Verrelst WH, Martens LRM. WIPO Patent 9,522,516 A1, 1995.

[11] Borges P, Ramos Pinto R, Lemos MANDA, Lemos F, Védrine JC, Derouane EG, Ramôa Ribeiro F, Light olefin transformation over ZSM-5 zeolites: A kinetic model for olefin consumption, Applied Catalysis A: General, 2007; 324(1): 20-29

[12] Borges P, Pinto RR, Lemos MANDA, Lemos F, Vedrine JC, Derouane EG, Ribeiro FR. Light olefin transformation over ZSM-5 zeolites: A kinetic model for olefin consumption, Applied Catalysis A: General, 2007; 324: 20-29.

[13] Oliveira P, Borges P, Ramos Pinto R, Lemos MANDA, Lemos F, Védrine JC, Ramôa Ribeiro F. Light olefin transformation over ZSM-5 zeolites with different acid strengths – A kinetic model, Applied Catalysis A: General, 2010; 384(1–2): 177-185.

[14] Coelho A, Caeiro G, Lemos MANDA, Lemos F, Ramôa Ribeiro F. 1-Butene oligomerization over ZSM-5 zeolite: Part 1 – Effect of reaction conditions, Fuel, 2013; 111: 449-460.

[15] Gnep NS, Bouchet F, Guisnet MR. Comparative study of the oligomerization of C_2-C_5, olefins on HZSM-5, Symposium on alkylation, aromatization, oligomerization and isomerization of short chain hydrocarbons over heterogeneous catalysts, New York City Meeting, August 1991; 620-626.

[16] Treacy MMJ, Higgins JB, Von Ballmoos R. Collection of simulated XRD powder patterns for zeolites, Elsevier, New York 1996; 523.

[17] Wang F, Fang K, Hu J, Ren J, Sun Y. Propene oligomerization over ZSM-5 zeolites with varying crystal size, State Key Laboratory of Coal Conversion, Institute of Coal Chemistry, Chinese Academy of Sciences, 2010; Taiyuan, 030001, P. R. China.

[18] Li X-B, Hu J-X, Wang F, Ren J. Propene oligomerization over zirconium containing ZSM-5 zeolites, Journal of Fuel Chemistry and Technology, 2004; 32(4): 498-503.

[19] Fan W, Li R, Ma J, Fan B, Cao J. Synthesis, characterization and catalytic properties of MFI-type zeolites prepared in the system Na_2O SiO_2 Al_2O_3 $H_2N(CH_2)6NH_2$ NH_4F, Microporous Materials, 1995; 4: 301-307.

[20] Saidina Amin NA, Anggoro DD. Dealuminated ZSM-5 zeolite catalyst for ethylene oligomerization to liquid fuels, J. Natural Gas Chemistry, 2002; 11: 79-86.

[21] Ali MA, Brisdon B, Thomas WJ. Synthesis, characterization and catalytic activity of ZSM-5 zeolites having variable silicon-to-aluminum ratios, Applied Catalysis A: General, 2003; 252: 149-162.

[22] Costa C, Dzikh IP, Lopes JM, Lemos F, Ribeiro FR. Activity–acidity relationship in zeolite ZSM-5. Application of Brönsted-type equations, J. Mol. Catal. A: Chem., 2000; 154: 193-201.

[23] Kriván E, Tomasek S, Hancsók J. Application Possibilities of Zeolite Catalysts in Oligomerization of Light Olefins, Periodica Polytechnica Chemical Engineering, 2014; 58(2): 149-156.

To whom correspondence should be addressed: Dr. Laleh Shirazi, Gas Division, Research Institute of Petroleum Industry (RIPI), Tehran, Iran, E-mail shirazil@ripi.ir

Petroleum and Coal

Article **Open Access**

PERFORMING THE CALCULATIONS ON LAB SULFONATION PARAMETERS USING THE MATHEMATICAL MODEL

Anastasiya A. Solopova, Maria A. Pasyukova, Ajur A. Bunaev, Irena O. Dolganova*

Engineering School of Natural Resources, Tomsk Polytechnic University, Russia

Received March 29, 2019; Accepted June 13, 2019

Abstract

The continuous growth of demand on synthetic detergents worldwide, which include such components as surfactants causes increasing of research and optimization interests towards the process of obtaining linear alkylbenzenes or the problem of linear alkylbenzenes sulfonation. The method of mathematical modelling used in this paper was chosen as the best concerning the optimization of the process. It allows monitoring the influence of main parameters without interfering in the process. As the result mathematical model of linear alkylbenzenes (LAB) sulfonation process was obtained. Adequacy of which is supported by the correspondence of calculated and experimental dependencies of the main parameters (such as yields of target and some side products, which are alkylbenzene sulfonic acid (ASA) and, for example, highly viscous component respectively). Also, information about the dependency of highly viscous component accumulation and ASA from temperature and film thickness in the reactor is obtained.

Keywords*: Sulfonation; Linear alkyl benzene; Alkylbenzene sulfonic acid; Highly viscous component; Multi-tubular film reactor; Mathematical modeling.*

1. Introduction

Linear alkylbenzene sulfonates (LAS) are among the most used component in the production of synthetic detergents and surfactants. LAS are alkyl aromatic chemical compounds which include saturated hydrocarbon side-chain of 10-13 carbon atoms and one or several sulfonic groups [1].

According to "BusinessStat," the demand for the detergents market in Russia in 2015 was 1.64 million tons. Until 2020, the market size will overpass 1.75 million tones so that the increase will be 6.7%. In 2017 the global market of liquid detergents was valued at $27,405 million, up to 2025 it is projected to reach $40,482 million, increasing by 5.2% from 2018 to 2025 according to "Allied Market Research" [2-3].

The continuous growth of world synthetic detergents production challenges the science with research and optimization of related production processes having an increase of economic efficiency as the main purpose.

The process of alkylbenzene sulfonic acid (ASA) production consists of following stages [1,4], introduced on Fig.1:

1. Unbranched (C_9–C_{14} mainly) alkanes dehydration: polyalkanes are the products in this stage;
2. Hydration of polyalkanes from the previous stage, in reverse, to monomers;
3. Benzene alkylation using liquid catalyst – hydrofluoric acid. In this stage linear alkylbenzenes are the products flowing further downstream while HF-catalyst treated in regenerator column;
4. Linear alkylbenzene sulfonation with sulfur trioxide in multitube film reactor. The final stage – alkylbenzene sulfonic acid is the main product of the whole process.

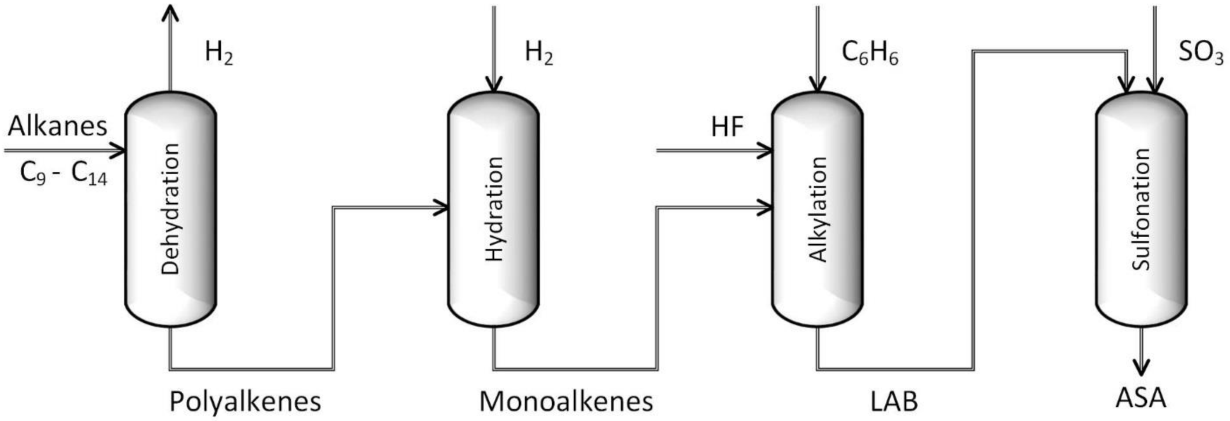

Figure 1. Stages of ASA production

2. Experimental

2.1. Study object

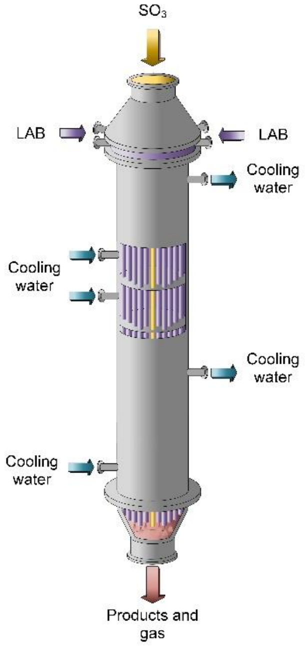

In this research, a multi-tubular film reactor for linear alkylbenzenes sulfonation installed in one of the real petrochemical productions was considered as the study object. The reactor itself is depicted in Fig. 2.

The sulfonation reaction takes place in the tube side consisting of 120 vertical tubes. Linear alkylbenzenes flow into the upper part of the reactor, where they are distributed uniformly by distribution device. Inside the tubes, linear alkylbenzenes run off in the form of thin film forced by gravitation and gaseous sulfur trioxide flow [5-7].

The optimal ratio of alkylbenzenes and gas is maintained inside each of the tubes. Thus, reaction gas includes 5-5.5% vol. of trioxide.

Heat reduction from the reaction volume is performed with cooling water circulation outside of tubes.

Figure 2. LAB sulfonation reactor

2.2. Sulfonation process chemistry

2.2.1. Gas mixture production

Sulfur anhydride obtaining occurs in stages:

1. Liquid sulfur burning in excess of treated air obtaining sulfur dioxide:

$$\mathbf{S + O_2 \rightarrow SO_2}$$

2. Catalytic oxidation of the dioxide in excess of drain air with sulfur trioxide as the product:

$$\mathbf{2SO_2 + O_2 \rightarrow 2SO_3}$$

2.2.2. Sulfonation

The formation of sulfonic acid due to the interaction of linear alkyl benzene with a linear saturated hydrocarbon chain, consisting of 10 to 13 carbon atoms, with sulfuric anhydride:

$$\mathbf{R\text{-}C_6H_5 + SO_3 \rightarrow R - C_6H_4 - SO_3H}$$

Possible side reactions with the formation of sulfonic anhydride or one of the types of sulfonic acid:

$$\mathbf{2\ R{-}C_6H_4{-}SO_3H + 3SO_3 \rightarrow R{-}C_6H_4{-}SO_2{-}O{-}SO_2{-}C_6H_4{-}R + H_2SO_4}$$

$$\mathbf{R{-}C_6H_5 + 2SO_3 \rightarrow R{-}C_6H_4{-}SO_2{-}O{-}SO_3H}$$

The concentration of sulfones, the part of unsulfonated matter, does not overpass 1 %wt. It does not depend from technological parameters unless SO_3/LAB ratio is more than 1.08 – in this case, a rapid increase of formation rate takes place.

Structure formula of sulfones is following:

$$\mathbf{R - C_6H_4 - SO_2 - C_6H_4 - R'}$$

Sulfonic acid may resolve, interact with remaining LAB or hydrolyze by water as well:

$$\mathbf{R{-}C_6H_4{-}SO_2{-}O{-}SO_3H + R{-}C_6H_5 \rightarrow 2\ R - C_6H_4 - SO_3H}$$

$$\mathbf{R - C_6H_4 - SO_2 - O - SO_2 - C_6H_4 - R + H_2O \rightarrow 2\ R - C_6H_4 - SO_3H}$$

2.2.3. Highly viscous component

Highly viscous component accumulation occurs during sulfonation. It is caused by aromatics contained in the stock. As those components accumulate, the uniform flow of the film in tubes of the reactor interrupts. Thus, trioxide diffusion into organic phase decreases, which leads to the low-quality product as an output – mass concentration of unsulfotated matter increases as well as the color index lowers [8-12].

When highly viscous component concentration in tube hits its critical point, the reactor is washed with water to eliminate products which interfere normal reaction course. Thus, monitoring of highly viscous component accumulation is essential to maintain the required quality of the product.

At present, the need for washing the reactor is determined by the pressure in it, which depends on the amount of highly viscous component. In practice, this method does not allow to achieve maximum efficiency of the process and is associated with the risk of formation of a substandard product.

2.2.4. Methodology

The model proposed involves energy and mass and balances. Finally, some additional assumptions were made for the mathematical model:

- No entrainments of liquid droplets into gas or of gas bubbles into the liquid film occur;
- Fully developed film (entrance and exit effects to the reactor are neglected);
- The liquid film is symmetric with respect to the reactor axis;
- There are no radial gradients, of neither temperature nor con-centration;
- The deactivation of reacting mixture stems from viscous component formation and affects the reaction rate constants inverse exponentially.
- The astronomic time is abandoned in favor of the volume of raw materials processed during the time between reactor washings.

In line with the assumptions above, the sulfonation reactor model can be described as follows:

$$G\frac{\partial C_i}{\partial Z} + G\frac{\partial C_i}{\partial V} = \sum_j W_j \cdot a_j \qquad (1)$$

$$G\frac{\partial T}{\partial Z} + G\frac{\partial T}{\partial V} = \frac{1}{C_p}\sum_j W_j \cdot (-\Delta H_j) \cdot a_j \qquad \begin{array}{l} Z=0,\ C_i=C_i^{in},\ T=T^{in}\ ; \\ V=0,\ C_i=C_i^{in},\ T=T^{in}\ . \end{array}$$

where the activity of reaction mixture is defined as:

$$a_j = e^{\delta C_{v.c.}} \qquad \text{If } Z=0\ C_{v.c.}=0,\ \delta=1 \qquad (2)$$

where: a_j – activity, rel. units; C_i – concentration of the i-th component (mol m^{-3}); C_i^0 – initial concentration of the i-th component (mol m^{-3}); $C_{v.c.}$ – concentration of highly viscous components (mol·m^{-3}); G – flow rate (kg h^{-1}); T – temperature (K); T_0 – initial temperature (K); W_j – reaction rate (mol m^{-3} hour^{-1}); Z – the total volume of the recycled raw materials (m^3); $-\Delta H_j$ – heat of the j-th reaction (J mol^{-1}); δ – a change in the j-th reaction rate due to viscous component or coke accumulation.

3. Results and discussions

During the modeling of the process of sulfonation in a multi-tubular film reactor, a dynamic model of the reactor was used under the assumption concerning the mode of plug flow. The chemical reactions rate constants were determined by solving the inverse kinetic problem on the basis of experimental data – Table 1.

Table 1. Base reactions of the sulfonation process

Reaction	Ea	k
LAB + SO_3 →ASA	$3{,}80\cdot10^4$	6,25
LAB + ASA →Unsulf. matter + H_2O	$3{,}50\cdot10^4$	$9{,}38\cdot10^{-2}$
2ABSK + SO_3 →ASA anhydride + H_2SO_4	$4{,}00\cdot10^4$	$4\cdot10^{-4}$
ASA anhydride + H2O →2ASA	$2{,}50\cdot10^4$	$9{,}89\cdot10^{-1}$
Unsulf. matter →VK	$4{,}00\cdot10^4$	$8{,}39\cdot10^{-5}$

3.1. Prediction of the period between reactor washings duration

Calculations concerning reactions taking place inside the sulfonation reactor were made using developed modelling system. As the result dynamics of the mass concentration of the key components such as ASA, unsulfonated matter, or sulfuric acid were obtained. Those results are presented for two periods between reactor washing: 16.02.2018 – 05.03.2018 and 15.09.2018 – 10.10.2018 on Fig. 3 and 4.

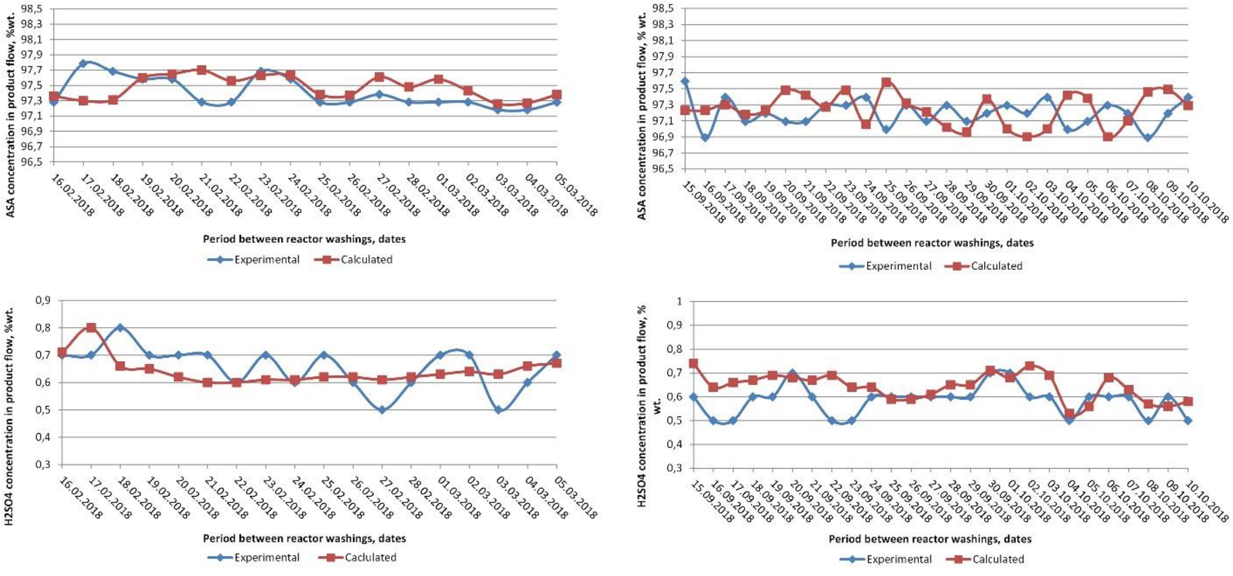

Figure 3. Dynamic of ASA and H_2SO_4 concentration during the period between reactor washing

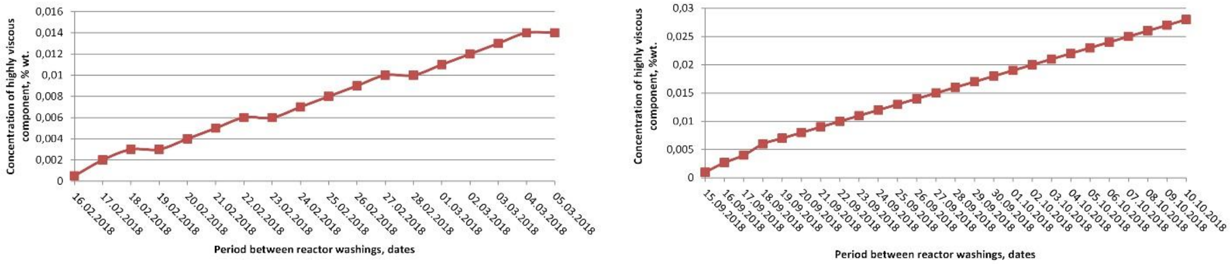

Figure 4. Dynamic of highly viscous component accumulation

Thus, the average deviation of the calculated data from the experimental data during the period between reactor washings was less than one percent, which suggests that the calculated dependencies correspond to the experimental data. This means that the model is adequate and may be used to study the main parameters of the process.

The usage of this computer simulation system allows making predictions about the duration of the period between reactor washings on the basis of the concentration of highly viscous components. The critical concentration was found by calculations based on the prescribed viscosity of the product and is 0.034 %wt.

Also, as a result of calculations, the dynamics of accumulation of a highly viscous component during the period between reactor washings were obtained. Fig. 4 show the results of calculations of the accumulation of a highly viscous component for two cycles.

Thus period between reactor washings from 16.02.2018 to 05.03.2018 ended up with highly viscous component concentration reaching 0.014 %wt., making the duration of the period itself 14 days long.

The duration of the second period made up 26 days; reactor washing was performed when highly viscous component concentration reached 0.028 %wt.

Then calculations were made until highly viscous component reach 0.034 %wt. With this, the duration of the first period extended on 22 days, while the second – 4.

3.2. Study of temperature influence in the reactor on the highly viscous component accumulation

The process of sulfonation can take place in the temperature range from 30 to 55°C. Thus, calculations were also made to study the effect of the temperature regime of the process on the concentration of the highly viscous component.

As can be seen in Fig. 5, the temperature of the sulfonation process affects the concentration of the highly viscous component. As the temperature in the reactor rises, the concentration of the highly viscous component formed over 1 day increases. Thus, at a temperature of 10 °C, 0.000321%wt. of a highly viscous component is formed per day, at 30°C - 0.000992 %wt., and at 50°C - 0.00263 %wt.

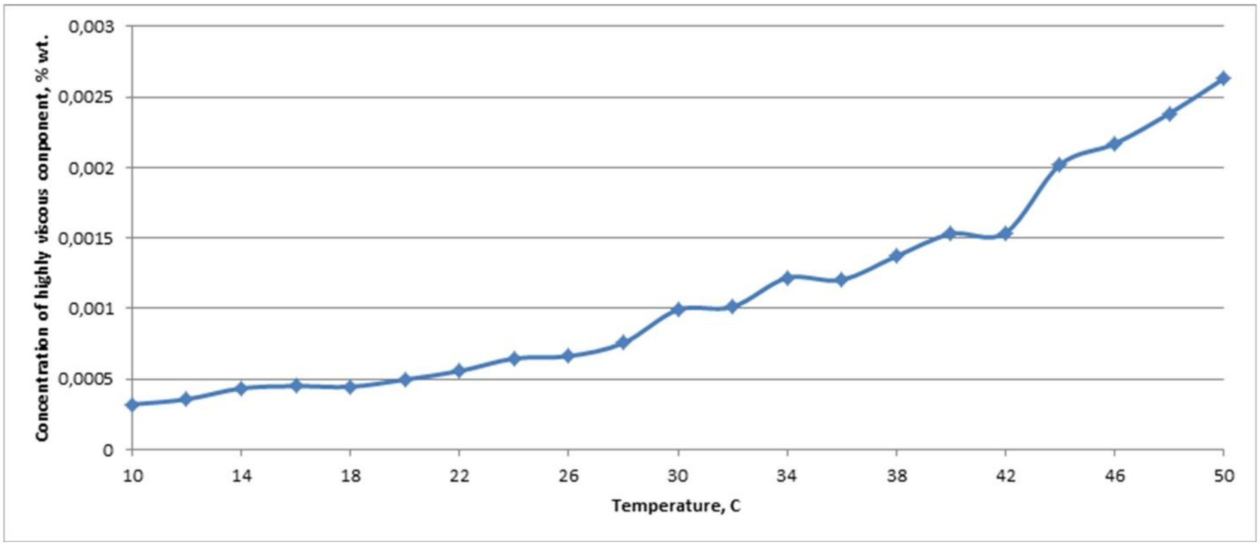

Figure 5. Concentration of highly viscous component on the first day of period between reactor washings at different temperature

Then calculations were carried out at different temperatures during two periods between reactor washings, the results of which are shown in Fig. 6.

At a temperature of 30°C, the concentration of the highly viscous component on the last day of the period was 0.024 %wt, at 40°C - 0.040 %wt., at 50°C - 0.065 %wt. Accordingly, with an increase in the temperature of the process, the rate of accumulation of the highly viscous component increases, the duration of the period between reactor washings is reduced.

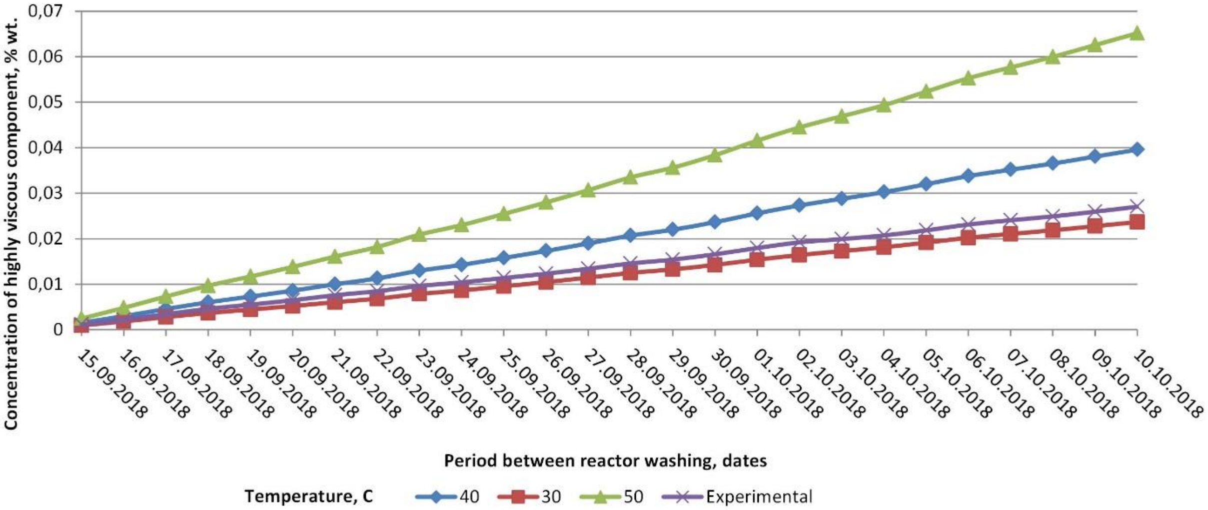

Figure 6. Dynamic of highly viscous component accumulation at different temperature.

3.3. Study of film thickness influence in the reactor on main parameters

A period between reactor washings with a duration of 20 days was chosen for analysis. Fig.7 shows the dynamics of accumulation of a highly viscous component when varying the film thickness in the reactor from 0.3 mm to 3 mm.

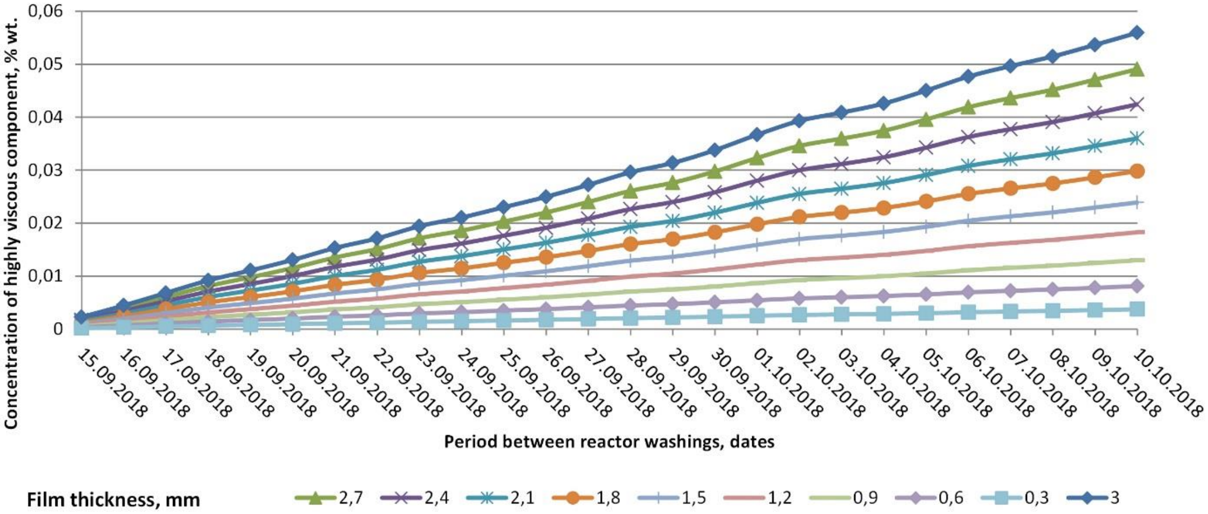

Figure 7. Dynamic of highly viscous component accumulation at a different film thickness

As can be seen from the graph, as the film thickness in the reactor increases, the concentration of the highly viscous component increases. This is because as the film thickness increases, diffusion of SO_3 molecules through the film thickness becomes difficult, and the reaction occurs only on its surface.

Thus, at a film thickness of 0.3 mm, the concentration of the highly viscous component on the last day of the period between reactor washings is 0.004 %wt., at 1.5 mm – 0,024 %wt., and at 3 mm – 0.056 %wt.

With increasing film thickness, the formation of H2SO4 increases. With film thickness in the reactor of 0.3 mm, the concentration of sulfuric acid on the last day is 0.16 %wt., while with

1.5 mm it was 0.68 %wt. and with 3 mm – 1.17 %wt. At the same time, the experimental value is 0.6%wt.

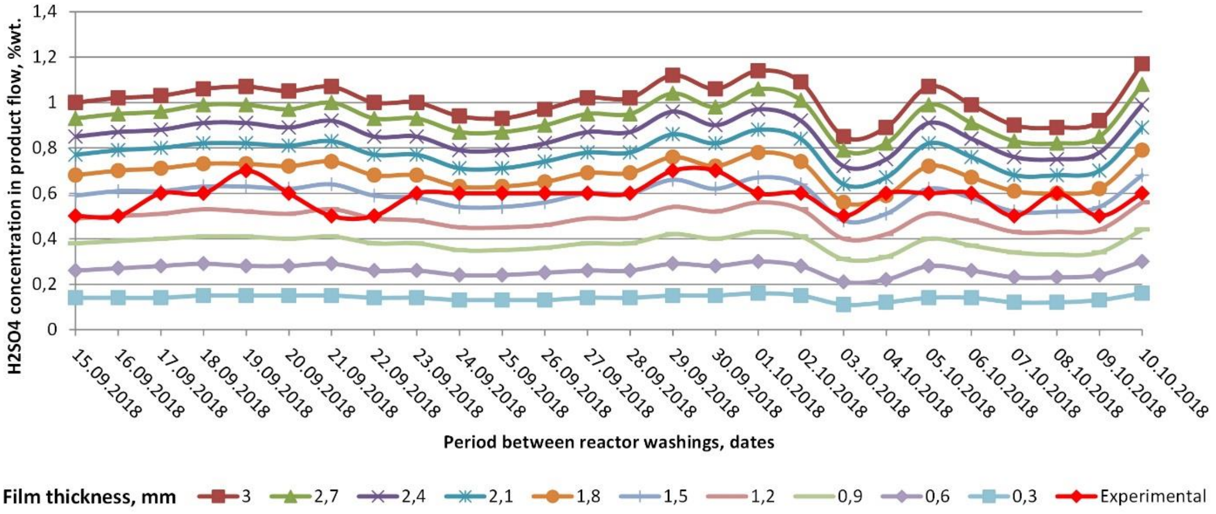

Figure 8. Dynamic of H_2SO_4 concentration at a different film thickness

With an increase in film thickness, the concentration of ASA decreases due to the formation of a larger amount of unsulfonated matter, which negatively affects the quality of the product flow, as shown in Fig. 9. With film thickness in the reactor of 0.3 mm, the concentration of alkylbenzene sulfuric acid on the last day is 97.94% mass., while with 1.5 mm it was 96.99 %wt. and with 3 mm – 97.59 %wt. At the same time, the experimental value is 97.59 %wt.

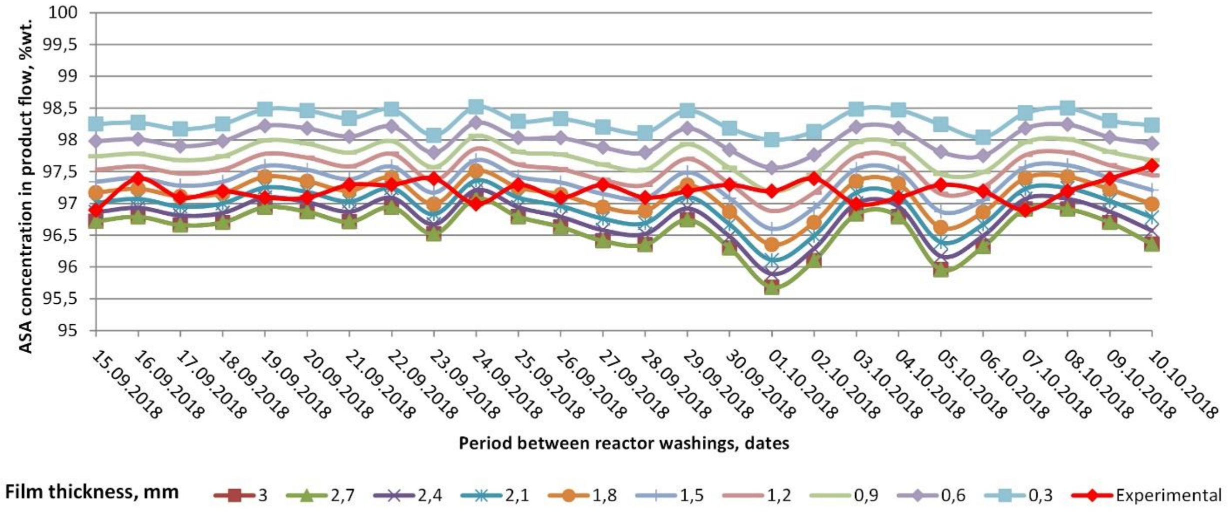

Figure 9. Dynamic of ASA concentration at a different film thickness

4. Conclusions

Thus, during the test calculations on the modeling system, it was noted that the dynamics of the experimental and calculated mass fractions of the necessary products of the sulfonation process, as well as their dependence on the film thickness inside the reactor tubes, are in good correlation, which indicates the adequacy of the model.

Also, the developed model makes it possible to predict the duration of the period between reactor washings, thus increasing its duration without harming the quality of the target product - increasing the economic efficiency of the LAB sulfonation process.

It was found that increasing the film thickness in the reactor has a negative effect on the duration of the period between reactor washings and the formation of the target component, ASA, since with increasing film thickness, the formation and accumulation of the highly viscous component is accelerated, which, accordingly, reduces the proportion of ASA. Also, as the film thickness increases, the proportion of unsulfonated matter in the product flow increases. This is because the reaction takes place only on the surface of the LAB film in the reactor.

Acknowledgements

The experimental calculations were carried out at Tomsk Polytechnic University within the framework of Tomsk Polytechnic University Competitiveness Enhancement Program grant.

References

[1] Bannov PG. Processy pererabotki nefti. P.G. Bannov. M.: CNIITEHneftekhim. – 2001. – 625 p. [in Russian].
[2] Liquid Detergent Market by Nature (Organic and Conventional), Application (Laundry and Dishwashing), Distribution Channel (Online Sales Channels, Supermarket & Hypermarket, Departmental & Convenience Stores, and Independent Grocery Stores), and End User (Residential and Commercial): Global Opportunity Analysis and Industry Forecast, 2018 – 2025 [Internet] Available from: https://www.alliedmarketresearch.com/liquid-detergent-market
[3] BusinesStat Analyze of detergents market in Russia in 2011-2015, forecast on 2016-2020.[In Russian]
[4] Roberts D. Optimisation of the Linear Alkyl Benzene Sulfonation Process for Surfactant Manufacture. Organic Process Research & Development, 2003; 7: 172−184.
[5] Zaid TA, Benmaza K, Chitour CE. Sulfonation of linear alkyl benzene (LAB) in a corrugated wall falling film reactor. Chemical Engineering Journal, 2000; 76: 99-102.
[6] Ward RS, Diaper RL, Roberts DW. Relative Rates of Sulfonation of Linear and Branched Long-Chain Alkylbenzenes. Journal of Surfactants and Detergents, 2001; 4(3): 263–270.
[7] Roberts DW, Ward RS, Hughes PJ. Correlations of Relative Rate Constants for Sulfonation of Alkylbenzenes with Molecular Structure. Journal of Surfactants and Detergents, 1998; 1(2): 161–165.
[8] Moreno A, Bengoechea C, Bravo J, Berna JL. A contribution to understanding secondary reactions in linear alkylbenzene sulfonation. Journal of surfactants and detergents, 2003; 6(2): 137-142.
[9] Dolganova IO, Dolganov IM, Bunaev AA, Pasyukova MA. Nature of highly viscous component in the alkylbenze sulfonic acid technology and its influence on the process efficiency. Petroleum and Coal, 2019; 61(1): 25-31.
[10] Dolganova IO, Dolganov IM, Ivanchina ED, Ivashkina EN. Alkylaromatics in Detergents Manufacture: Modeling and Optimizing Linear Alkylbenzene Sulfonation. Journal of Surfactants and Detergents, 2018; 21(1): 175-184.
[11] Molever K. Monitoring the Linear Alkylbenzene Sulfonation Process Using High-Temperature Gas Chromatography. Journal of Surfactants and Detergents, 2015; 8(2): 199-202.
[12] Ahmadi AN, Mehdizadeh A, Jalili AH. Determination of Sulfonation Conditions of HAB as a By-product of Linear Alkylbenzene Production. Journal of Petroleum Science and Technology, 2015; 5(2): 45-50.

To whom correspondence should be addressed: Dr. Maria A. Pasyukova, Polytechnic University, 30, Lenin Avenue, Tomsk, 634050, Russia, E-mail: maria.pasyukova11@gmail.com

Petroleum and Coal

Article **Open Access**

IMPROVING THE EFFICIENCY OF MULTISTAGE PRODUCTION OF ALKYLBENZENE SULFONIC ACID

Irena O. Dolganova[1], Anatoli Borissov[2]*

[1] Chemical Engineering Department, Tomsk Polytechnic University, Russia
[2] General Vortex Energy Inc., Missouri City, United States

Received March 29, 2019; Accepted June 13, 2019

Abstract

The object of the research is multi-stage integrated production of linear alkylbenzenes and linear alkylbenzene sulfonic acid. The established thermodynamic and kinetic laws of the transformations of C_9–C_{14} hydrocarbons and the activity of catalysts used in the synthesis of linear alkylbenzenes provided the creation of mathematical models suitable for optimizing the main stages of the synthesis. the assessment of the full range of nonstationarity factors caused by the deactivation of catalysts was made on the basis of a computational and industrial experiment simulation. the model calculations allowed improving the efficiency of multistage production of alkylbenzene sulfonic acid and to increase the desired product yield from 170 –172 to 174–176 tones/day.

Keywords*: Mathematical modeling; Dehydrogenation; Alkylation; Sulphonation; Catalyst activity.*

1. Introduction

The technology of multi-stage integrated production at oil refinery should ensure the maintenance of high yield of target products with required quality and minimum waste (substandard lots of products with a high content of by-products).

The creation of such a technology is possible only if the efficiency of each of the associated processes and devices at all stages is increased, considering their interconnection by the method of mathematical modeling. With large volumes of commodity production, economic indicators can reach a significant value.

Long-term studies of the Tomsk Polytechnic University [1–3] of the processes of production of alkylbenzene sulfonic acid (ASA) and linear alkylbenzene sulfonates determined the creation of an integrated mathematical model of the ASA technology describing the processes proceeding as at separate stages of hydrogenation, alkylation, sulfonation, and the relationship between the structural units of the entire chemical-technological system.

The application of the developed model at one of the Russian refineries ensured the fulfillment of forecast and optimization calculations and made it possible to establish the mutual influence of the processes and phenomena occurring in the LAB-ASA technology apparatuses.

A method has been developed for controlling the catalyst activity of the alkanes dehydrogenation process, which consists in controlling the catalyst activity by increasing the water supply to the dehydrogenation reactor to reduce the intensity of coke formation [4-5].

Conducted numerical and pilot-scale studies in industrial conditions allowed developing a new method to control the catalyst activity of the dehydrogenation process, increasing the yield of the target product and preserving the service life of the catalyst.

The development of work in this direction should consider studies of the HF-catalyst in the benzene with higher olefins alkylation process. Their main task is to theoretically substantiate the existence of optimal operating conditions for the HF catalyst and to develop recommendations for maintaining the optimal consumption of HF-acid supplied for regeneration to ensure stable operation of the chemical-technological system for LAB production using a toxic catalyst.

The introduction of the developed model to predict the dynamics of the formation of high-molecular organofluorine aromatic hydrocarbons in the alkylation process o made it possible to increase the duration of stable operation of the column from one to three months to one year. At the same time, increasing the production efficiency of ASA production depends on the final stage of LAB sulfonation in a decisive way [6-9].

2. Experimental

When modeling multicomponent hydrocarbon synthesis processes, a large amount of experimental research is required. To reduce them when comparing various chemical synthesis schemes, the laws of chemical thermodynamics are widely used.

For the thermodynamic calculation of the dehydrogenation process of higher C9–C14 paraffins, the method of quantum chemical modeling was used. For reactions of all types, the Gibbs energies ΔGr, the enthalpies of the reactions ΔHr and the entropy ΔS were calculated at an average process temperature of 753 K and a pressure of 0.2 MPa.

Thermodynamic analysis of reactions proceeding in the alkylation process was carried out at an average process temperature of 328 K and a pressure of 0.5 MPa.

The established thermodynamic laws formed the basis of a formalized scheme for the conversion of hydrocarbons, which takes into account the reactions of the alkylation process, which is presented in Fig. 1.

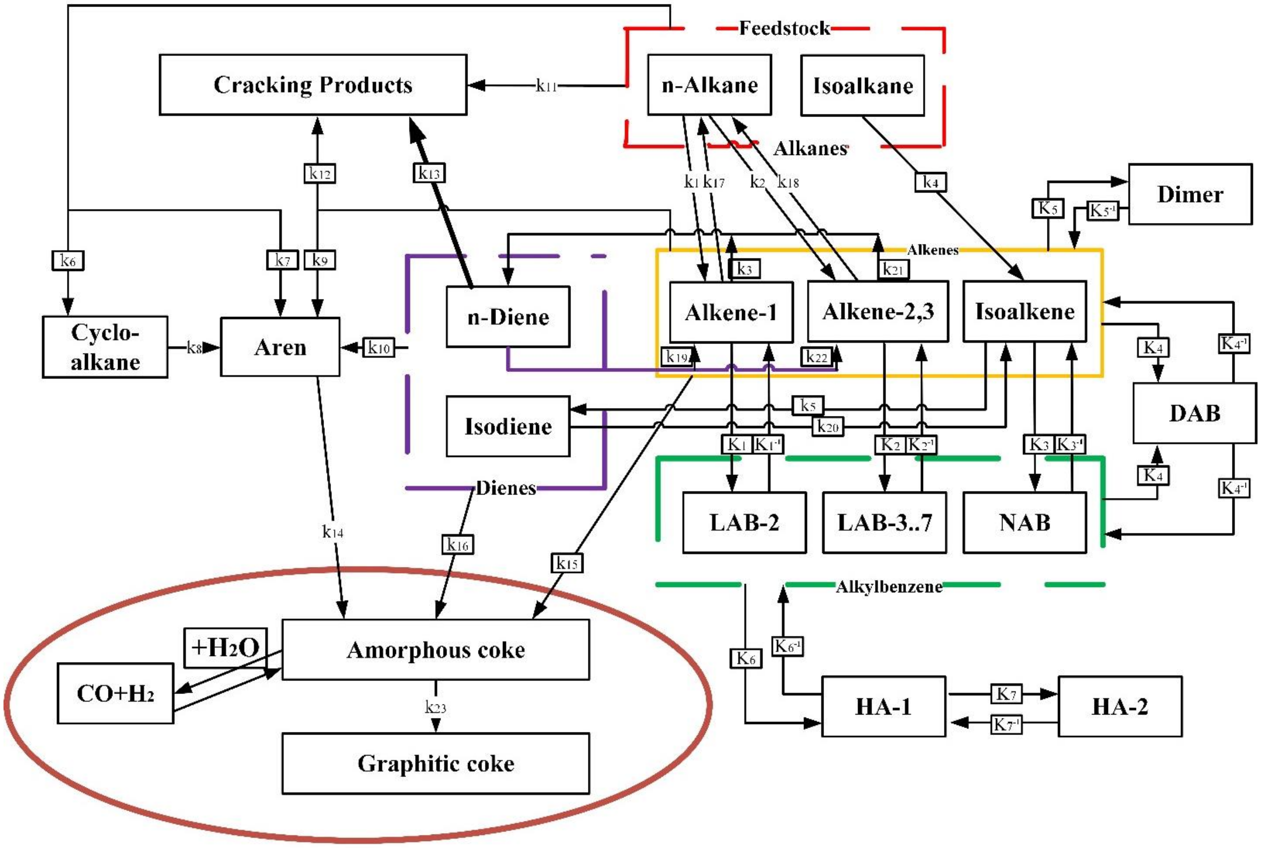

Fig. 1. Generalized reaction network of dehydrogenation and alkylation processes

Here LAB-2 - 2-phenylalkane; LAB-3 ... 7 - linear alkyl benzenes with a substituent in advising position; DAB - dialkylbenzenes; NAB - nonlinear alkylbenzenes; HAR-1, HAR-2 - "heavy" alkylaromatic compounds that have the following structure (Fig. 2):

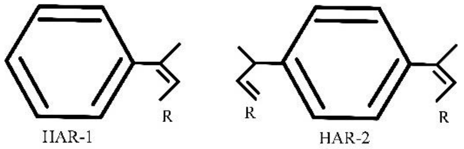

Fig. 2. Structure of HAR molecules

When developing a mathematical model, the components were combined into groups: the group of olefins includes the components α, β, γ-olefins, and isoolefins; the LAB group includes the LAB-2, LAB-3..7, NAB components; the HAR group includes the HAR-1 and HAR-2 components.

As can be seen from the reaction network, linear alkyl benzenes are intermediate substances in the formation of high molecular weight aromatic and alkylaromatic compounds. In this case, both the target and side reactions are catalyzed by HF-acid.

On the basis of the proposed reaction network, mathematical models were developed for the main stages of the synthesis of LAB, represented by a system of equations of material and heat balance. Thus, the model of the dehydrogenation process is made up of the assumption that the model of the ideal displacement reactor is applicable as a hydrodynamic model of the reactor.

Along with material and heat balances of the dehydrogenation reactor, the developed mathematical model includes a description of the Pt catalyst deactivation by coxogenic compounds (CGC). The coke concentration on the catalyst is calculated based on a formalized reaction network, as the product of coke-formation reactions from aromatic and diene hydrocarbons.

Considering the change in catalyst activity during coke accumulation provided its predictive ability with respect to the service life of the catalyst when changing the composition and consumption of raw materials, the process temperature, the circulation ratio of the hydrogen-containing gas.

The mathematical model of the alkylation reactor (1) contains the parameter for changing the activity of the HF catalyst, which is determined by the content of HAR-1 and HAR-2 and depends on the consumption of acid for regeneration.

$$\begin{cases} \dfrac{dC_i}{d\tau} = k_j \cdot a \cdot C_i \\ \rho\ C_P \dfrac{dT}{d\tau} = \sum\limits_{j=1}^{N} (-\Delta H_j) W_j \end{cases} \quad (1)$$

where: Initial conditions: t=t0 Ci=Ci0; T=T0.
τ – contact time, s; *Ci* – concentration of the i-th component (benzene, olefins, diolefins, LAB, heavy alkylate, HAR, dimers), mole/l; *kj* – the rate constant of the *j*-th reaction, l/(mol·s); Δ*Hj* – heat of chemical reaction, J/mole; *Wj* – the rate of the *j*-th chemical reaction, mol/(m^3·s); *Cp*– mass heat capacity of the reaction mixture, J/(kg·K); *ρ* – density of the reaction mixture, kg/m^3; *T* – temperature, K; *a* – catalyst activity (relative units).

3. Results and discussion

3.1. Increasing the selectivity of the dehydrogenation process by reducing coke formation in oxidation and hydrogenation reactions

A literature review has shown that techniques such as diluting raw materials with hydrogen or supplying water to the reactor can increase the selectivity of industrial synthesis of LAB at the dehydrogenation stage. At the same time, excessive moisture leads to an increase in cracking reactions, with a lack of water, coke formation reactions are intensified, which also results in a lack of hydrogen in the system. At the same time, an increase in the rate of circulation of hydrogen-containing gas leads to a decrease in the yield of the target products - alkenes. Therefore, it is important to choose the optimal conditions for the industrial process, ensuring a long term stable operation of the catalyst with the desired yield of the target product and the minimum concentration of secondary components.

The next stage of research was to consider the possibility of the reaction of the oxidation of amorphous coke with water.

The numerical and experimental-industrial studies at the oil refining enterprise allowed us to perform thermodynamic analysis of the coke formation process and using a mathematical model of the dehydrogenation process to develop an optimal flow calculation method water. This technique is based on the need to maintain the conversion of an amorphous coke-forming structure with water over the entire temperature range of the process being constant.

But in the case of operation of the dehydrogenation catalyst under conditions of a lower hydrogen/hydrocarbon molar ratio, it is necessary to adjust the schedule of water flow to the reactor due to the increased intensity of coke formation reactions. To assess the performance of the dehydrogenation process when operating the unit at a lower hydrogen/hydrocarbons molar ratio, an industrial experiment was conducted at the plant for the production of alkenes-precursors.

Fig. 3 shows the temperature of the dehydrogenation process before and during the industrial experiment, as well as in the raw material cycle of the platinum-containing dehydrogenation catalyst of the same brand and batch in 2013–2014.

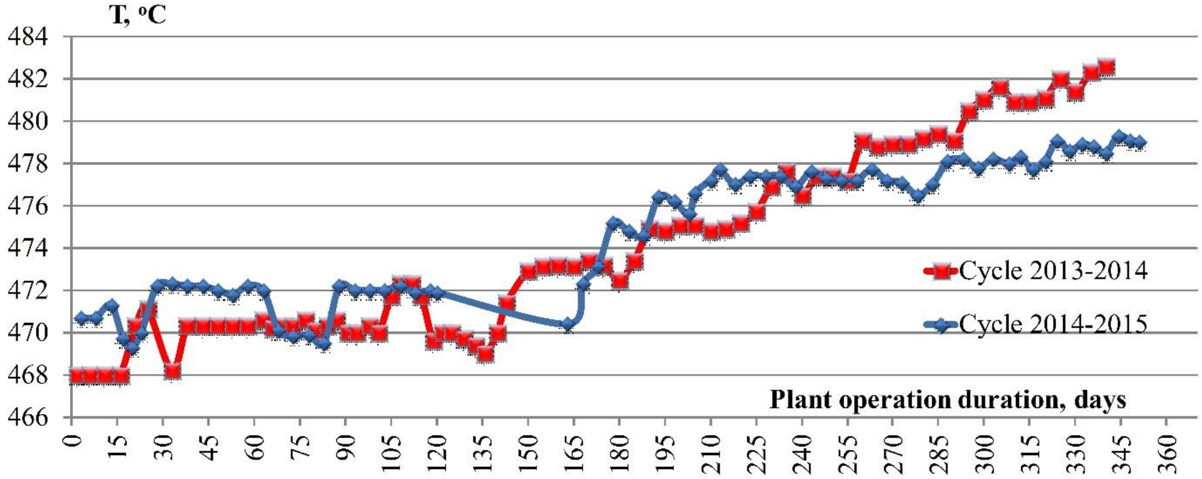

Fig. 3. Temperature mode of operation of the dehydrogenation reactor in two raw cycles of the catalyst

As can be seen, since the start-up of the reactor after the installation was repaired, the process temperature was increased to 475 °C, and over the next 4.5 months, it was increased by 3°C to 478°C, while not changing significantly during the experiment.

In the raw material cycle of the catalyst in 2013–2014, the temperature of the process on average was 1.5–2.5ºC higher than in the 2014–2015 cycle in the period of the industrial experiment.

The decrease in the hydrogen/feedstock molar ratio from 7/1 to 6/1 made it possible to increase the yield of alkenes due to a shift in the equilibrium of the target dehydrogenation reaction towards the formation of products to 8.8–9.4 wt % instead of 7.8–9.1 wt. % at a molar ratio of hydrogen / raw materials, equal to 7/1.

Thus, the experiment allowed us to establish the positive effect of reducing the hydrogen / feedstock molar ratio. At the same time, quantitative patterns of changes in water consumption were established using a mathematical model in the face of changes in the hydrocarbon composition of the processed raw materials.

3.2. Increasing the selectivity of the alkylation process by reducing the HF consumption

Alkanes are a source of education and such by-products as dienes, entering into chemical interaction with LAB at the stage of alkylation with the formation of heavy aromatic compounds - HAR. This reaction is catalyzed by HF, and the activity of the HF catalyst is defined as the ratio of the amount of acid, not deactivated by HAR, to its total amount.

Thus, HF activity depends on the current HAR concentration in the alkylation reactor, that is, on the concentration of dienes formed at the dehydrogenation stage and the amount of HAR discharged to the regenerator in the acid flow.

The results of the predictive calculations of the parameters of the joint operation of the alkylation reactor and the acid regenerator, depending on the number of dienes in the feedstock, is presented in Table 1.

Table 1. Predicting the optimal consumption of HF-acid, depending on the consumption of dienes in the alkylation reactor

Consumption of dienes in the alkylation, kg/hour	Amount of TAP accumulating in the alkylation reactor, kg/hour	Optimum HF flow rate to regeneration column, m^3/hour	ΔLAB, tones/day
56.25	20.27	3.64	2.10
58.78	21.18	3.80	2.1
61.31	22.10	3.97	2.3
63.83	23.00	4.13	2.0
66.36	23.91	4.29	2.2
68.89	24.82	4.46	2.5
71.42	25.74	4.62	1.9
73.94	26.64	4.78	2.2

It follows from the above data that in order to maintain maximum LAB production, it is required to increase HF flow rate regeneration column from 3.64 to 4.78 m^3/hour as the diene consumption in the alkylation reactor increases from 56.25 kg/hour to kg/hour. At the same time, the amount of HAR formed in the alkylation reactor increases from 20.73 to 26.64 kg/hour. The positive effect of maintaining the consumption of HF-acid at an optimal level is to increase the average daily production of the target product by an average of 2.0-2.5 tones/day.

4. Conclusion

The recommended hydrogen/feedstock molar ratio of 6/1, which increases the selectivity of the dehydrogenation stage in the synthesis of LAB, requires adjusting the flow rate of water supplied to the dehydrogenation reactor to 13–14 L/hour instead of 9–10 L/hour by the end of the feed cycle.

The introduction of recommendations for changing the consumption of HF-acid in the regenerator, ensuring the maintenance of catalyst activity at an optimal level, has increased the yield of LAB rom 170 –172 to 174–176 tones/day.

Acknowledgements

The research was supported by Tomsk Polytechnic University within the framework of the Tomsk Polytechnic University Competitiveness Enhancement Program.

References

[1] Roberts D. Optimisation of the Linear Alkyl Benzene Sulfonation Process for Surfactant Manufacture. Organic Process Research & Development, 2003; 7: 172−184.
[2] Dolganova IO, Dolganov IM, Ivanchina ED, Ivashkina EN. Alkylaromatics in Detergents Manufacture: Modeling and Optimizing Linear Alkylbenzene Sulfonation. Journal of Surfactants and Detergents, 2018; 21(1): 175-184.
[3] Kafarov V. Mathematical modeling of the basic chemical production processes: a tutorial. Kafarov V.V., Glebov M.B. - M.: High School, 1991. - 399 p. (in Russian)

[4] Kravtsov AV, Fetisov VA, Frantsina EV. Technology and modeling of reactive processing of higher paraffins to linear alkylbenzenes: a tutorial. - Tomsk: Publishing house of Tomsk Polytechnic University, 2010. - 297 p. (in Russian)

[5] Frantsina E, Ivashkina E, Ivanchina E, Romanovskiy R. Decreasing the hydrogen-rich gas circulation ratio and service life extension of the C9–C14 alkanes dehydrogenation catalyst. Chemical Engineering Journal, 2015; 282: 224–232.

[6] Corma A, Martínez-Soria V, Schnoeveld E. Alkylation of Benzene with Short-Chain Olefins over MCM-22 Zeolite: Catalytic Behaviour and Kinetic Mechanism. J Catal., 2000; 192(1):163–73.

[7] Odedairo T, Al-Khattaf S. Comparative study of zeolite catalyzed alkylation of benzene with alcohols of different chain length: H-ZSM-5 versus mordenite. Catal Today, 2013; 204:73–84.

[8] Zaid TA, Benmaza K, Chitour CE. Sulfonation of linear alkylbenzene (LAB) in a corrugated wall falling film reactor. Chem Eng J., 2000; 76(2):99-102.

[9] Molever K. Monitoring the linear alkylbenzene sulfonation process using high-temperature gas chromatography. J Surfactants Deterg., 2005; 8(2):199-202.

To whom correspondence should be addressed: Dr. Irena O. Dolganova, Chemical Engineering Department, Tomsk Polytechnic University, 30, Lenin Avenue, Tomsk, 634050, Russia; E-mail: dolganovaio@sibmail.ru

Petroleum and Coal

Article **Open Access**

APPLICATION OF CONVENTIONAL GEOPHYSICAL METHOD IN INVESTIGATING AND CHARACTERIZING LANDFILLS

Lawal L. Adebayo, Fatai A. Wahaab, Sulaiman K. Lawal*

Department of Physics and Material Science, Kwara State University, Malete, Nigeria

Received April 1, 2019; Accepted June 13, 2019

Abstract

The geophysical investigation was conducted using integrated Wenner-Schlumberger Array to determine the extent of waste on soil and groundwater around Madi area of Ilorin West L.G.A of Kwara State, Nigeria. 2-D resistivity meter with a digital read out resistivity meter (ABEM SAS 1000) was used to acquire data on the study area. Contaminant leachate plume was delineated with both electrical sounding curve 1-D and 2-D resistivity sections as low resistivity zones. The results are presented in terms of resistivity, thickness, and depth (1-D). The 2-D sections are identified as bluish zones of lower resistivity (less than 17Ωm−36Ωm) with the depth ranging from 5 m to 40 m. The result of the electrical resistivity survey also showed three layers of geo-electric sections and an H type sounding curve. Groundwater at 5 m and above will pose a major threat to the health of the inhabitants of the study area due to contaminant leaching.

***Keywords**: Landfill gas; Geo-electric; Wenner-Schlumberger array; Resistivity; Contaminant plume.*

1. Introduction

Water is one of the most valuable natural resources vital to the existence of any form of life. Groundwater is widely distributed under the ground, and it is replenished resource unlike other resources of the Earth. Groundwater has become immensely important for human water supply in urban and rural areas in developed and developing nations alike [3]. Groundwater contamination can occur in many ways and from many sources, both natural and humanly induced. Groundwater commonly contains one or more naturally occurring chemicals, leached from soil or rocks by percolating water, in concentrations that impair its uses. Water can be contaminated from the smallest activities, throwing plastics into the body of water, throwing the trash into a river, dumping oil into streams, improper disposal of wastes all this leads to water contamination.

Much geophysical technique has subsequently been used for groundwater characterization, but the greatest success has been shown with the electrical and electromagnetic method [4]. In the electrical resistivity method, direct current or low-frequency alternating current is applied at the ground surface, and the potential difference is measured between two points. Variations in resistance to current flow at depth cause distinctive variations in the potential difference measurements, which provide information on subsurface structure and materials [5]. Ohm's law ratio given by equation (1) is the governing principle of the electrical resistivity method.

$$\rho_a = 2\pi k \frac{V}{\mathrm{I}} \qquad (1)$$

where ρ_a is the apparent resistivity (Ωm) which is equivalent to the resistivity of an electrically homogenous and isotropic half-space earth; I the applied current (A); V the measured potential gradient and k is the geometric factor in (Ωm) which depends on the electrode array configuration. For the Wenner-Schlumberger array employed in this research, the apparent resistivity equation becomes equation (2) [6], which corresponds to the arrangement in Figure 1.

$$\rho_a = \pi a n(\mathrm{n}+1)\frac{V}{\mathrm{I}} \qquad (2)$$

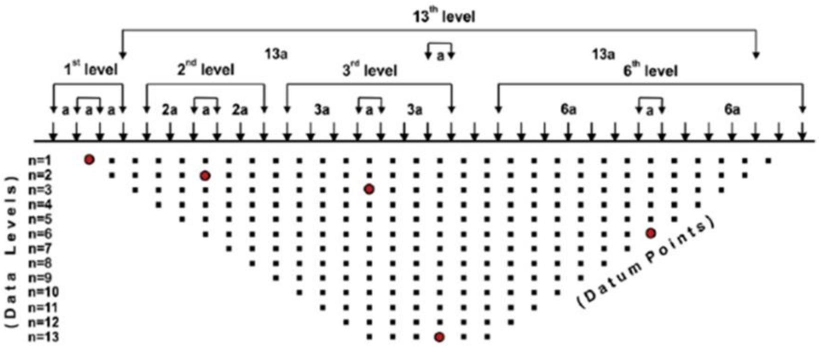

Figure 1. Schematic of Wenner-Schlumberger electrode array configuration [1]

Numerous geophysical investigations have been carried out in different parts of the world for groundwater investigation. Etu-Efeotor *et al.* [7], Amadi *et al.* [8], and Ugwu & Nwosu [9] carried out studies in various parts of Rivers State. Ehrim *et al.* [10] carried out a geophysical and hydro-physiochemical study of the contaminant impact of a solid waste landfill (SWL) in Port Harcourt municipality, Nigeria and concluded that the contamination of ground water and soil is dominantly by landfill gases, while the excessive amounts of microorganisms is an indication of leachate contamination. Previous research work at a public dumpsite in Ita-amo Ilorin, Kwara State has indicated the direction of groundwater flow through the aid of surface topography. The presence of leachate and their pattern of migration using electrical resistivity method in the study area have also been previously outlined. Several other studies have investigated [11-14] have investigated the possibility of producing gas from old municipal landfill as an alternative form of energy.

The study area (Abandoned Ita-Amo waste disposal site, Ilorin) is located within latitude $8^0$25′N and $8^0$30′N, and longitude $4^0$20′E and $4^0$30′E as outlined in Figure 2. The approximate area extent of the dumpsite is $3.63 \times 10^6 m^2$ with average dump thickness of 7–9 m. Geologically, the area lies in the Precambrian basement complex of southwestern Nigeria and is underlain by the rock of metamorphic and igneous type [15]. However, weathered lateritic soils are predominant in the study area. Also, intrusive and extrusive conglomerate lateritic rocks are present in Figure 3(b).

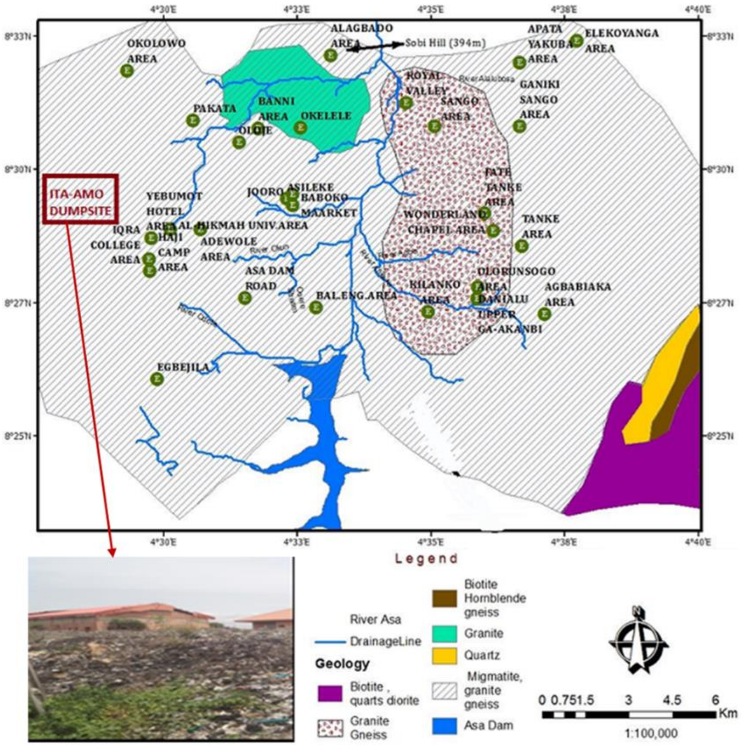

Fig. 2. Location map of the study area (*modified after reference [2]*)

Figure 2. Pictures from the study area. (a) Data acquisition process at the study area, showing cable reel, electrode and resistivity meter (ABEM SAS 1000) (b) Rock formation in the study area

2. Experimental

The geo-electric resistivity field survey was carried out to obtain the apparent resistivity data around the Ita-Amo dumpsite. Wenner-Schlumberger electrode array was employed because of its moderate sensitivity to both horizontal and vertical variations in the apparent resistivity of the subsurface. This was used to characterize the various lithological units and, to determine the depth to the water table, the extent of percolation (depth) of contaminants, and migration path of contaminants. The two outer electrodes are the current electrode, and two inner ones are the potential electrode, but unlike other configurations, equal spacing does not exist between the four electrodes as illustrated by

Wenner-Schlumberger configuration with maximum current electrode separation (AB/2) of 90m was employed. This method consists of four electrodes like all other types of Wenner configurations. However, there exist equal spacing between the first two electrodes and the last two electrodes.

A total of four profile were selected, each consisting of ten sounding points. Two of these traverses were chosen at the northward axis of the dumpsite. The first of the northern axis traverse was 3m away from the dumpsite and the second was 13m away from the dumpsite with profile lines oriented in the east-west direction. The profile lines covered a length of 200m with inter stations of 20m. The third and fourth profile were oriented in the north-south and west-east directions, respectively with a sounding point interval of 30m as depicted by Figure 4: Profile line of the sounding points.

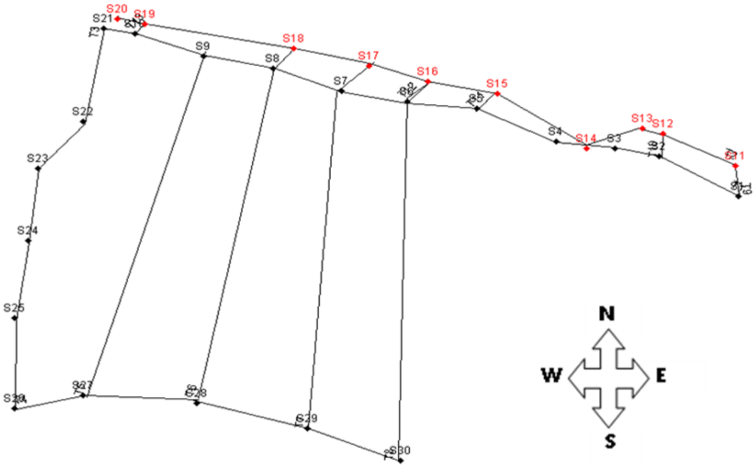

Figure 3. Profile line of the sounding points

3. Results and discussion

The topographic map of the area was obtained by analyzing the coordinates data obtained through the Global Positioning System (GPS). The obtained data were processed using Surfer 8. The result from the software revealed that the dumpsite area is fairly-undulated and sloped towards the north-western axis of the neighboring environment with elevation ranging from 308–330 m illustrated by the topography (Figure 4) and contour map (Figure 5).

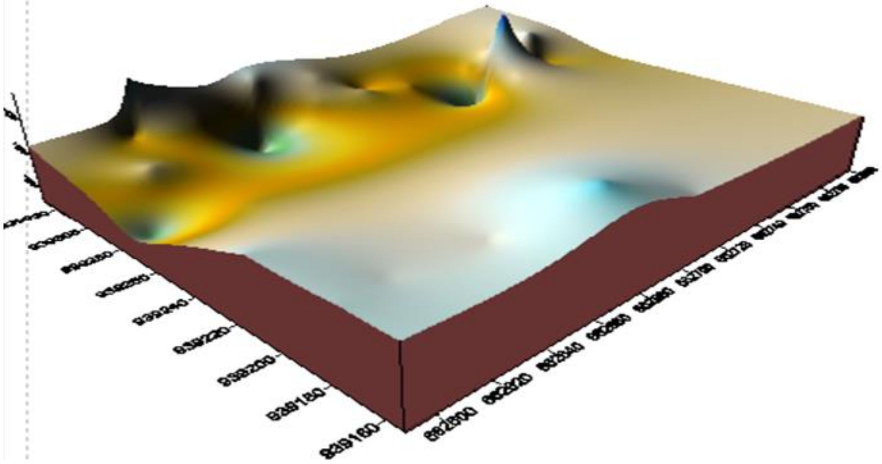

Figure 4. Topography of the study area

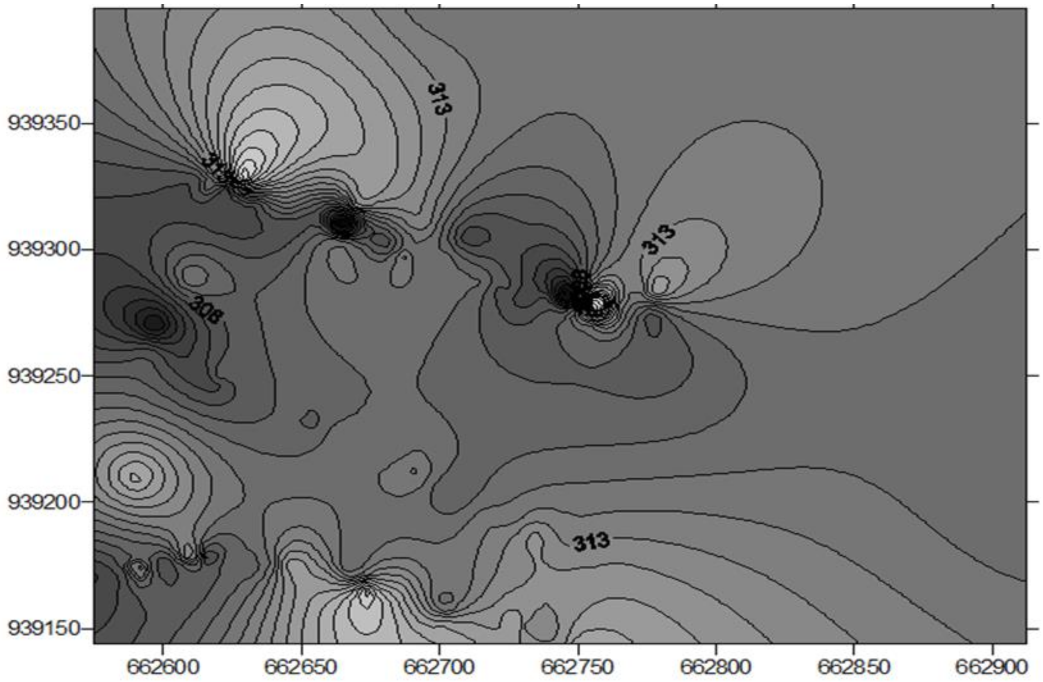

Figure 5. Contour map of the study area

The field curves and the interpreted 1D models are presented in. The curves show a characteristic type H curve across the dumpsite (Figure 6). The 2-D pseudosections map out zones of high and low resistivity. Comparing the pseudosections along with each profile, we could identify the drift pattern of the contaminant plume, the depth of the plume and other characteristics across each profile.

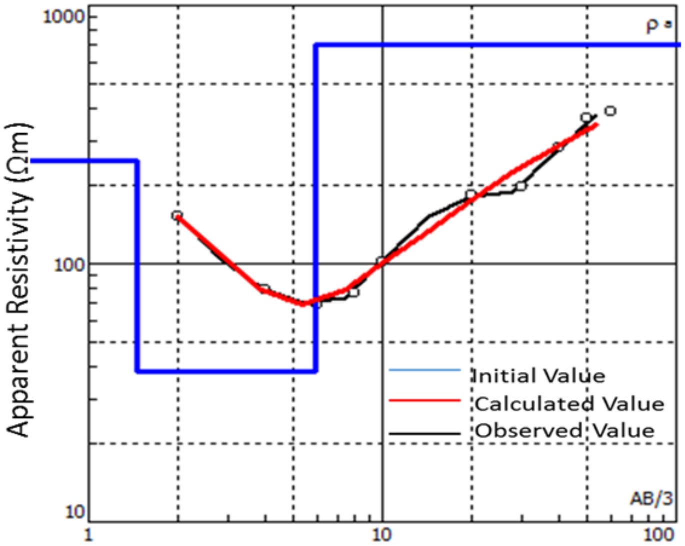

Figure 6. Observed and calculated apparent resistivity value in 1D at a VES point

Profile 1 is located 3m away from the dumpsite, and it is 16m away from community settlement near the dumpsite. The average elevation along this profile is 307.3m. The contaminant is highly concentrated along with this domain of the dumpsite.2D shows that the contaminant plume is drifting from the southern to the northern axis. This shows that the contaminant is drifting toward the settlements enveloping the dumpsite. The apparent resistivity value ranges from 30–606 Ωm. Zones of high resistivity value ranging from 134–606 Ωm existed near the surface. Underlying the zone of a high resistive chemical compound is the zone of low resistivity (less dense zone) with resistivity value ranging from 36–121 Ωm with the depth ranging from 1.5–30 m.

Profile 2 is located 13m away from the dumpsite and 6m away from a settlement near the dumpsite. It was parallel to profile 1 and has a separation distance of 10m. The average elevation along this profile is 314.94m. The contaminant is highly concentrated along this axis of the dumpsite. 2D Pseudosection maintains the pattern of contaminant drift as depicted in profile 1. The apparent resistivity value is ranging from 13–4014 Ωm. Zones of high resistivity values range from 148Ωm–4014Ωm exists near the surface. Underlying the zone of a high resistive chemical compound is the zone of low resistivity (less dense zone) with resistivity value ranging from (14Ωm-148Ωm) with the depth ranging from 1.5–32 m (Figure 7).

The average elevation along profile 3 is 311.45m. The apparent resistivity value is ranging from 64–712 Ωm. Zone of highly resistivity value ranges from 124 – 712 Ωm existed near the surface. Underlying the zone of a high resistive chemical compound is the zone of low resistivity (less dense zone) with resistivity value ranging from 64 – 124 Ωm with the depth ranging from 1.5 - 38 m (Figure 8).

Profile 4 is along the entrance of the dumpsite. The average elevation along this profile is 317.64m.2-D Pseudosection shows that the contaminant plume is not concentrated along this axis; therefore, we may assume this profile to be the true resistivity of the surroundings. The apparent resistivity value is ranging from 27 -1200 Ωm. Zone of high resistivity value ranges from 114 – 1200 Ωm existed near the surface. Underlying the zone of the high resistive structure is the zone of low resistivity (less dense zone) with resistivity value ranging from 27 – 77 Ωm with the depth ranging from 1.5 – 23 m. between the high resistive chemical compound and the low resistive zone are sands of varying sizes and thickness. The bluish portion shows zone of low resistivity (contaminant leachate plume), red to brownish portion shows zone of high resistivity (solid waste and maybe lateritic soil or rock) and the yellow portion shows zone of water bearing (sands). The migration of the leachate to the bottom is an indication that it is denser.

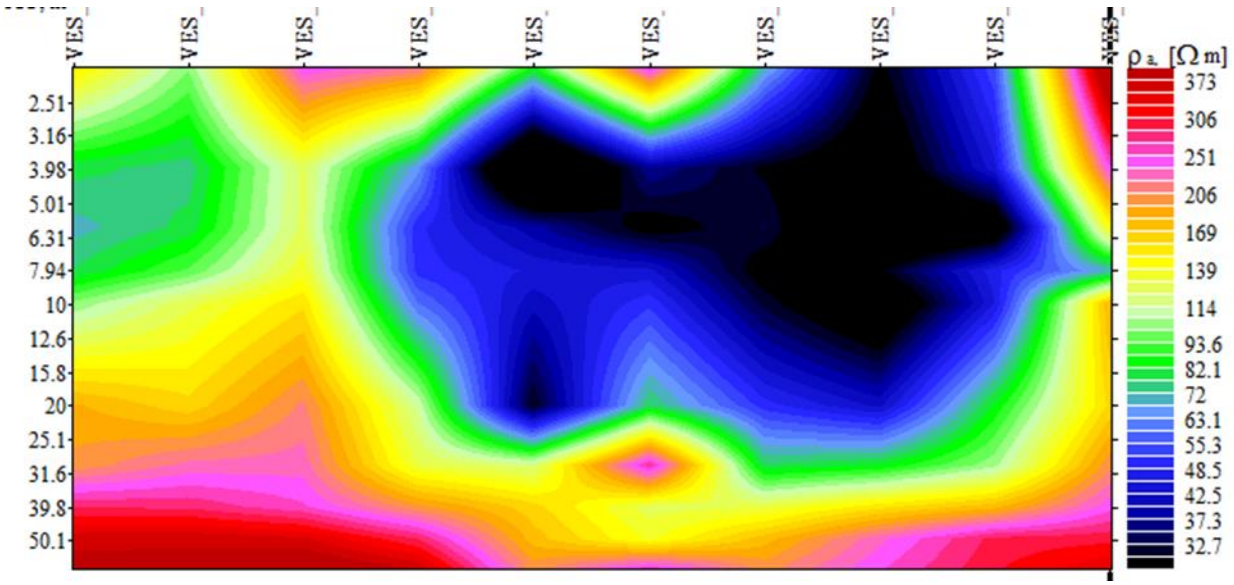

Figure 7. 2D Pseudosection showing profile 2

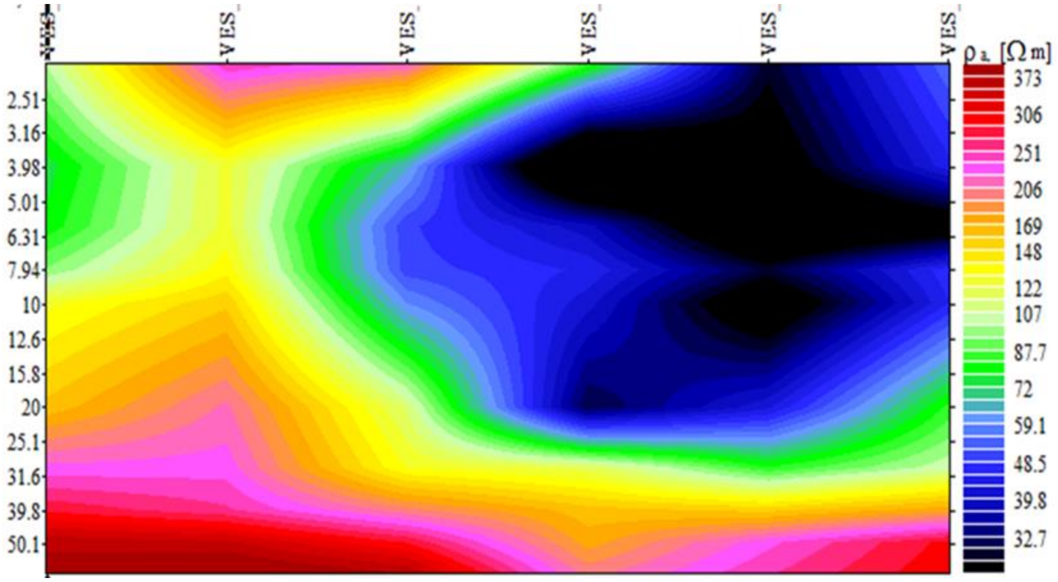

Figure 8. 2D Pseudosection showing profile 3

4. Conclusion

High and low resistive zones were identified in the study area (Ita-Amo dumpsite). The high resistive areas may indicate gravel, sand and rock fragments lying on top of elevated solid rock, while the low resistive areas indicate areas where the host rock has been hampered by faulting, void, and fracture. The very low resistive with high conductivity contains contaminant plume due to percolation of leachate (heavy metals, toxic chemical and carcinogenic), making the area less resistive to electrical current. Contaminants occur at depths between 0–30 m, and the migration path of the plume is toward the north-west direction. The more detailed geochemical and biological investigation should be conducted for water obtained at this site for precise characterization of the contaminant. Borehole exceeding 30 m depth should be dug in this settlement if there is no alternative water source.

Acknowledgement

The authors would like to appreciate the entire staff of Physics and Material Science department of Kwara State University for their support during the cause of this project.

References

[1] Ekinci YL, Türkeş M, Demirci A, and Erginal AE. Shallow and deep-seated regolith slides on deforested slopes in Çanakkale, NW Turkey. Geomorphology, 2013; 201: 70-79.

[2] Ifabiyi I, Ashaolu E, and Omotosho O. Hydrogeological Characteristics of Groundwater Yield in Shallow Wells of the Regolith Aquifer: a Study from Ilorin, Nigeria. Momona Ethiopian Journal of Science, 2016; 8(1): 23-36.

[3] Omosuyi G. Geoelectric assessment of groundwater prospect and vulnerability of overburden aquifers at Idanre, southwestern Nigeria. Ozean Journal Of Applied Sciences, 2010; 3(1): 19-28.

[4] Eke K, and Igboekwe M. Geoelectric investigation of groundwater in some villages in Ohafia Locality, Abia State, Nigeria. British Journal of Applied Science & Technology, 2011; 1(4): 190.

[5] Burger HR, Sheehan AF, and Jones CH. Introduction to applied geophysics: Exploring the shallow subsurface. WW Norton, 2006, ISBN-13: 978-0393926378.

[6] Wightman W, Jalinoos F, Sirles P, and Hanna K. Application of geophysical methods to highway related problems. Blackhawk GeoSciences, A Division Of Blackhawk GeoServices 2004. http://www.ce.memphis.edu/7137/PDFs/Geophysical/geotechPdf.pdf

[7] Etu-Efeotor J, and Odigi M. Water supply problems in the eastern Niger Delta. Journal of Mining and Geology, 1983; 20(1-2): 183-193.

[8] Amadi U, and Amadi P. Salt water migration in the coastal aquifers of southern Nigeria. J Min Geol, 1990; 26: 35-44.

[9] Ugwu S, and Nwosu J. Effect of waste dumps on groundwater in Choba using geophysical method. Journal of Applied Sciences and Environmental Management, 2009; 13(1): 85-89.

[10] Ehirim C, Ebeniro J, and Olanegan O. A geophysical investigation of solid waste landfill using 2-D resistivity imaging and vertical electrical sounding methods in Port Harcourt municipality, Rivers State, Nigeria. The Pacific Journal of Science and Technology, 2009; 10(2): 604-613.

[11] Hayati A, Emalya N, Munawar E, Schwarzböck T, Lederer J, and Fellner J. Analysis the potential gas production of old municipal solid waste landfill as an alternative energy source: Preliminary results. in IOP Conference Series: Materials Science and Engineering, 2018; 334(1): 012031.

[12] Njoku PO, Odiyo JO, Durowoju OS, and Edokpay JN. A Review of Landfill Gas Generation and Utilisation in Africa. Open Environmental Sciences, 2018; 10(1): 1-15.

[13] Siddiqui FZ, Zaidi S, Pandey S, and Khan ME. Review of past research and proposed action plan for landfill gas-to-energy applications in India. Waste Management & Research, 2013; 31(1): 3-22.

[14] Idehai IM, and Akujieze CN. Estimation of landfill gas and its renewable energy potential in Lagos, Nigeria. International Journal of Energy and Environmental Engineering, 2015; 6(3): 329-343.

[15] Zonge K, Wynn J, and Urquhart S. Resistivity, induced polarization, and complex resistivity. in Near-surface geophysics: Society of Exploration Geophysicists, 2005; pp. 265-300.

To whom correspondence should be addressed: Dr. Lawal L. Adebayo, Department of Physics and Material Science, Kwara State University, Malete, Nigeria, E-mail: adebayolawallanre@yahoo.com

Petroleum and Coal

Article **Open Access**

RESERVOIR CHARACTERIZATION OF ILLAM FORMATION IN KUPAL OIL FIELD, SW OF IRAN

*Yosra Mohammadkhani, Hossein Tabatabaei**

Department of Petroleum Engineering, Gachsaran Branch, Islamic Azad University, Gachsaran, Iran

Received April 7, 2019; Accepted June 13, 2019

Abstract

Porosity, shale volume, and fluid saturation are the most important parameters used to determine the characteristics of oil reservoirs. The kupal oil field has located in Dezful embayment. Illam formation introduced as a fractured reservoir at the southwest of Iran. In this study, wells No.48 and 54 investigated. Based on this study and using well logging diagrams, the main lithology determined Limestone. It is worth mentioning that substrates of shale, dolomite and in some cases anhydrite can see. As well as based on the performed study, this formation divided into three zones, including two permeable zones and one non-permeable zone. In the non-permeable section, main minerals have determined as clay, being types of Montmorillonite, Mix layers, and Illite. Base on Gr log, the average volume of shale in wells No. 48 and 54 was 8% to 17% respectively, that overall shows Low percent volume of shale. In this field, the amount of porosity increased from SE to NW. Accordingly, the well log plot, there are appropriate porosity and water saturation in this horizon. To enhance the accuracy of formation of water saturation calculations, we calculate it by software using Indonesian and Simandoux methods. Such that the average effective porosity and water saturation are 7.9 and 43.4 %, respectively. Finally, it can be stated this formation has poor to mean reservoir characteristic, but it can achieve reservoir capacity from some wells and adjacent fields.

Keywords*: Petrophysical evaluation, Porosity, Water Saturation, Illam formation, Kupal oil field, Geolog Ver 6.7.1.*

1. Introduction

Achieve the information related to porosity and permeability of formations is one of the major problems of oil engineers [1]. These parameters are among the most important information in designing and controlling discovery operation [2]. The most significant application of wire line logs is an evaluation of petrophysical characteristics of the formations in order to survey the reservoir quality of different sections of reservoir formation and find the most appropriate zones for efficient exploitation of the reservoir and for a more assured development of oil fields [3]. Porosity, shale volume, and fluid saturation are the most important parameters that were used to determine the characteristics of oil and gas reservoirs [4]. For the first time, Illam formation was studied by James and Wynd [5].

Since Illam formation was considered one of the most prominent oil reservoir rocks in southwest of Iran, a comprehensive and precise revision of this formation and surveying petrophysical and petrofabric characteristics of this formation is of great importance in the oil industry.

2. Geological setting

The Kupal oil field located in the middle of Dezful Embayment. This anticline is an asymmetrical structure with NE-SW trend, and southern flank dip is higher than northern flank and causes to change the axis to follow the west trend in the northern part and southern trend in the west. The thickness of the Asmari reservoir in this field is 347m and divided into 8 zones based on petrophysical data. The most important character of the Asmari presence of extended natural fracture systems, which causes high productivity of wells not withstanding low matrix porosity (Figure 1).

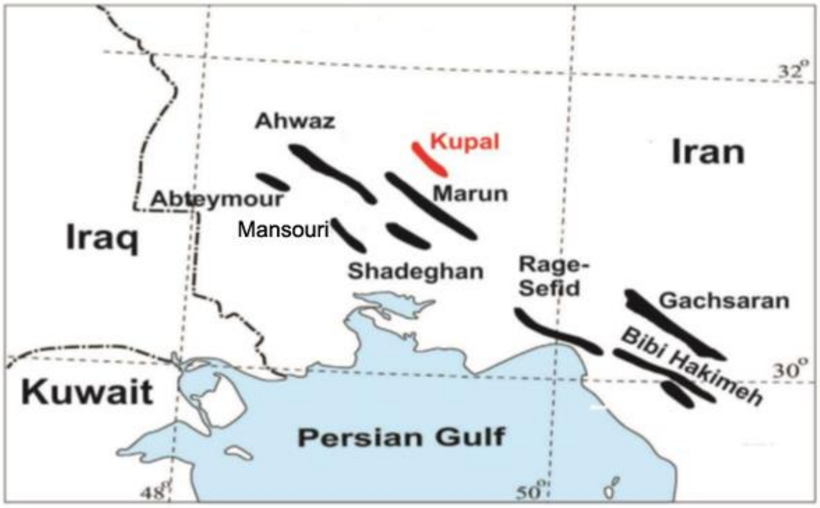

Figure 1. Located of Kupal oil field in Dezful embayment, near the other oil fields, Southwest of Iran

3. Methodology

In this study, 2 wells (Wells No. 48 and 54) in Kupal oilfield have considered for petrophysical studies. These wells have almost complete information and logging data. In this study, the raw data from two wells with Geolog ver. 6.7.1 software has been using to determine reservoir parameters affecting the reservation quality of Illam formation.

Recognition of lithology, calculation of shale volume (Vsh), total porosity (PHIT), effective porosity (PHIE) and water saturation (Sw), are the most important parameters in the petro physical evaluation, and these are necessary to find the quality of the formation [6].

4. Result and discussions

In this study, 2 wells (Wells No. 48 and 54) in Kupal oilfield have considered for petrophysical studies. These wells have almost complete information and logging data. In this study, the raw data from two wells with Geolog ver. 6.7.1 software has used to determine reservoir parameters affecting the reservation quality of Illam formation.

4.1. Shale volume calculation

There are various methods for calculating shale volume. In some cases, only a log can be calculated, and in some cases, a combination of two or more logs can be used to calculate shale volume. Here, for more accuracy and removal of the effect of uranium, we use the available CGR results to calculate. Among of Shale volume has calculated for this Formation (Table.1).

$$V_{sh} = \frac{CGR - CGR_{min}}{CGR_{max} - CGR_{min}} \tag{1}$$

Table 1. Shale volume (V_{sh}) in Kupal wells (Well No. 48 and 54).

Well No.	Min Shale volume	Average Shale volume	Max Shale volume
48	0	0.1741	1.000
54	0	0.0808	1.000

4.2. Type of clay mineral

Shale does not have fixed mineralogy. Among clay minerals, Illite is found more often than other minerals, and chlorite is abundant, while kaolinite is relatively rare [7]. We need a CGR logs to determine the type of clay minerals in different wells, and thorium-potassium cross-plots (Th vs. K) have used [8]. As shown in Figures 2 and 3, clay minerals are dominant in both wells.

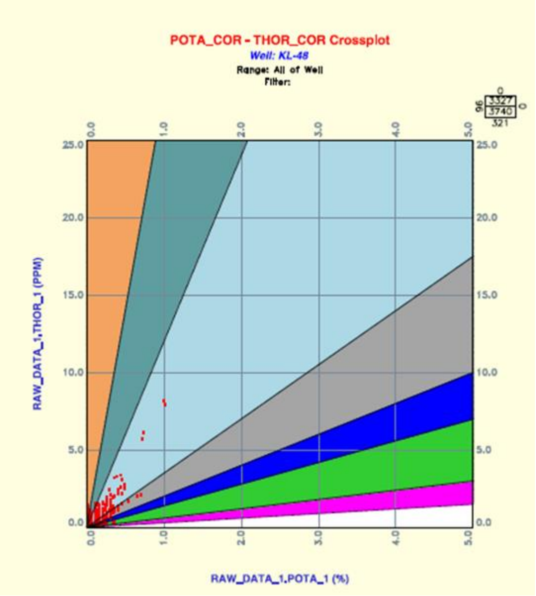

Figure 2. Type of clay minerals determination in well 48, Kupal oil field

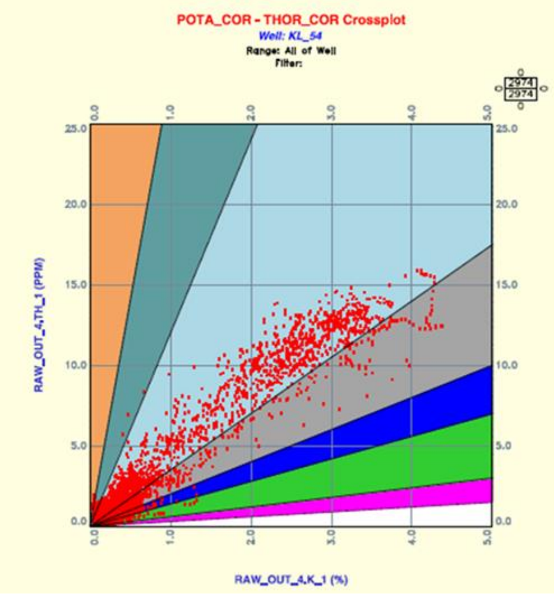

Figure 3. Type of clay minerals determination in well 54, Kupal oil field.

4.3. Porosity calculation

There are several methods for calculating porosity, depending on the type of logs available in each well. Porosity logs, i.e., neutron-density logs and sonic logs, used to calculate porosity. Porosity can be obtained from a log or a combination of different logs [9]. In this study, the porosity calculation (Table.2) was performed using the Sonic logs (Equation 2) and the neutron-density logs (Equation 3).

$$\emptyset_{Sonic} = \frac{DT-DT_{ma}}{DT_{fl}-DT_{ma}} \qquad (2)$$

$$\emptyset_{ND} = \sqrt{\frac{{\emptyset_N}^2+{\emptyset_D}^2}{2}} \qquad (3)$$

Table 2. Calculation of sonic, neutron-density, effective, and total porosity

Well No.	$\emptyset_{Sonic}\ (v/v)$	$\emptyset_{ND}\ (v/v)$	$\emptyset_T\ (v/v)$	$\emptyset_E\ (v/v)$
48	0.059	0.130	0.0963	0.074
54	0.070	0.064	0.079	0.084

4.4. Detection of porosity types based on velocity log

The velocity deviation log will be computed from the composition of the sonic logs with the neutron or density log (Table.3), and it can be used to get information on the types of porosity (Table.4) in carbonates, the tracing of distribution of empty digenetic spaces and prediction of permeability. In order to construct this log, in the first step, porosity log data will be converted to artificial velocity using the mean time-Willey equation, and its difference plotted with the actual velocity derived from the sonic log as the velocity deviation log [10].

In the well No.48, by examining the velocity deviation log, because most of the positive and zero deviations shown, we conclude that the porosity types in this well are moldic and intra porosity due to positive zones and intergranular and intercrystalline porosity due to zero zones. In two depths of 4146 and 4163 meters, with negative deviation in the velocity log, according to the Caliper logs, we conclude that the negative zone is due to casting.

In the well No.54, by examining the velocity deviation log, because of most positive deviations, we conclude that the porosity types in this well are moldic and intra, and in small amounts of zero deviation, we expect intergranular and intercrystalline porosity.

Table 3. Maximum, minimum and mean velocity deviations calculation

Well No.	VDL(m/s) min	VDL(m/s) mean	VDL(m/s) max
48	-2511.773	-85.3341	23152.0078
54	-267.778	149.6735	2842.0579

4.5. Secondary porosity

Given availability of neutron-density porosity logs to calculate total porosity and sonic logs to calculate initial porosity (this log ignores vuggy porosity), it is possible to calculate the secondary porosity which introduced as a secondary porosity index (SPI) [11].

The most common method for determining the secondary porosity (Table.4), is to deduct porosity of the sonic logs (φ_{sonic}) from porosity of FDC or CNL [8]. In this study, the following formula used to calculate the secondary porosity:

Table 4. Secondary porosity calculation

Well No.	SPI
48	0.0496
54	0.0271

$$\emptyset_{secondary} = \emptyset_{ND} - \emptyset_{SONIC} \qquad (4)$$

4.6. Lithology

One of the main uses of well logs is Lithologic detection. There are several methods for determining the lithology that their application is dependent on the availability and type of Lithologic-sensitive logs [12]. There are various cross-plots that combine two or three charts, suggest two or three different mineralogy; one of the most suitable are M-N plots. Considering the complex lithology of Asmari reservoir in the studied field, a combination of different logs can useful for lithology detection, the best way to use M-N plot. This cross-plot obtained by combining three neutron, density, and sonic porosity logs. In this graph, the parameter M is the integration of the sonic-density measurement, and the N is cross plot slope of the neutron-density. M and N obtained according to the following equations (5 and 6) and drawn against each other [13].

$$M = \left[\frac{\Delta t_f - \Delta t}{\rho_b - \rho_f}\right] \times 0.01 \qquad (5)$$

$$N = \frac{\emptyset_{Nf} - \emptyset_N}{\rho_b - \rho_f} \qquad (6)$$

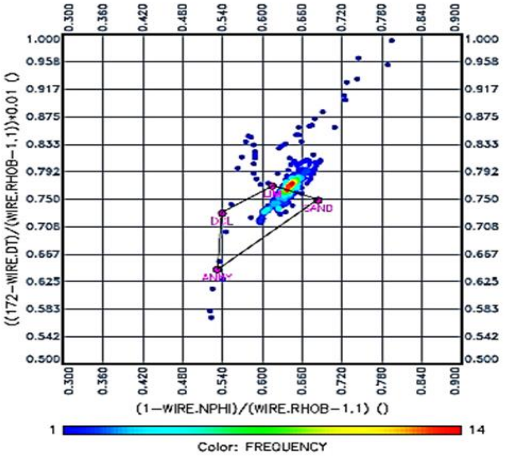

Figure 4. M-N Plot in Well No.48, Kupal oil field and lithological detection

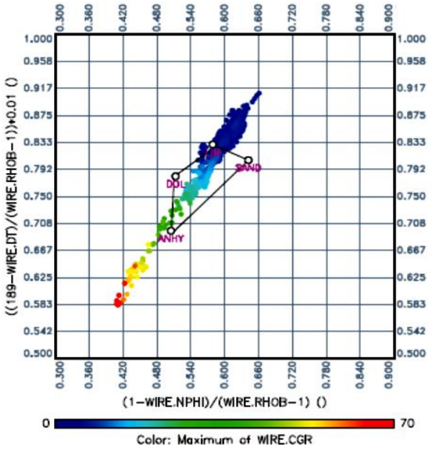

Figure 5. M-N Plot in Well No.54, Kupal oil field and lithological detection

Based on cross-plots drawn from the two wells, and according to the color range of CGR chart, the dominant lithology of carbonate detected (In well No.48, calcite is more than dolomite and in well No.54 is almost lime shale). Also, well No.54 shows shale's more (Figure 4 and 5).

In well logging with consideration to the well situation, some appropriate physical parameters chosen for surveying the geological layers. Among them, the ratio of pressure wave to cutting (Vp/Vs) can use as a key factor in diagnosing some important characteristics of the reservoir such as lithology [14]. In order to distinguish lithology, this ratio calculated in wells (Well No. 48) (Fig. 6).

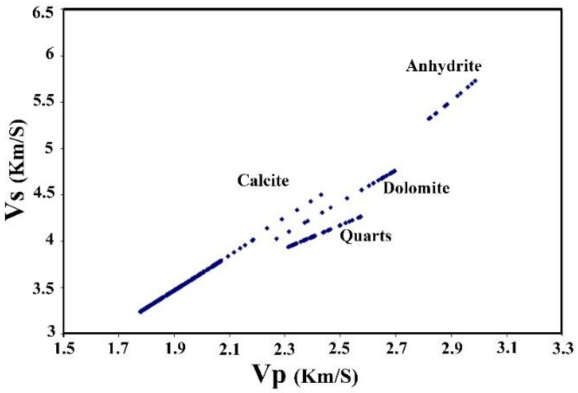

Figure 6. Dispersion diagram of the ratio of Vp/Vs. in well logging data of Kupal oil field (Well No. 48)

4.7. Calculation of water saturation

There are different methods to calculate water saturation [15]. Among these methods, the Indonesian equation is more efficient in carbonate rocks. In this study, the Indonesian equation used as follows [8,16]:

$$\frac{1}{R_t}=\left[\frac{\o^{m}}{a\times R_w}^{0.5}+\frac{V_{sh}^{(1-0.5\times V_{sh})}}{R_{sh}{}^{0.5}}\right]^2\times S_w^n \qquad (7)$$

To enhance the accuracy of formation of water saturation calculations, we calculate it by software using Indonesian and Simandoux methods. The volume of water in each well can be obtained in this way as a result of these calculations, as shown in Table 5.

Table 5. Calculation of water saturation in well No. 48 and 54, Kupal oil field

Well No.	S_{W-E}	S_{W-SIM}	S_{W-INDO}	V_UW$_{at}$
48	0.427	0.441	0.448	0.018
54	0.473	0.419	0.420	0.023

Considering that in the previous calculations, the effective porosity and effective water saturation values calculated in each well, equation (8) can be used to calculate the volume of oil.

$$VOL-UOIL=(1-SW_E)PHIE \qquad (8)$$

5. Conclusion

Based on the analysis of well logs and calculation of petrophysical reservoir parameters, the results are as follows:

Illam Formation in this field has a low average shale volume, and the upper part of this formation is important in production, the reservoir made of clean lithology and the amount of shale in the lower parts of the formation is slightly higher. The low amount of shale is probably due to sedimentation of the formation in an energetic environment. Well logs analysis shows that this reservoir has good porosity, especially in the upper part of the formation. Porosity variations are not high at the surface of the field, but due to the low amount of shale, we conclude that most of this porosity is effective. Proper porosity in this field can be affected by sedimentation. For determining the porosity types, artificial velocity deviation logs have used. The tendency of these logs to the positive side indicates porosity of the mold, vuggy, and intra. The lithology of Illam Formation has estimated using various methods including two logs, three logs, and a variety of cross-plots. All of these methods indicate the predominance of carbonate lithology (calcite, dolomite). In this study, Indonesian and Simandoux equations have used to calculate water saturation. Due to the low amount of shale, the values obtained from these equations are very close. Based on the thresholds defined for separation of gross and net sections, the thickness of these segments has calculated. Due to the amount of low shale and good porosity, almost all of the formation is a good reservoir, but due to the amount of water saturation, the thickness of the produced zone varies in wells. According to the lithological and petrophysical characteristics of Illam reservoir in the studied wells, this formation classified into different zones. Based on thorium-potassium cross-plot, in both wells the dominant clay minerals have identified as Illite.

References

[1] Pickett GR. Acoustic character logs and their applications in formation evaluation. JPT, 1963; 15: 650-667.

[2] Bhatt A, Hell HB. Committee neural networks for porosity and permeability prediction from well logs. Geophysical Prospecting, 2002; 50: 645-660.

[3] Tiab D, and Donaldson CE. Petrophysics, theory and practice of measuring reservoir rock and fluid transport properties. Gulf Professional Publishing, Elsevier, Second edition, 926 pages, 2004.

[5] James G A, Wynd JG. Stratigraphic nomenclature of Iranian oil consortium, agreement area. American Association of Petroleum Geologists Bulletin, 1965; 49(12): 2182 – 2245.

[6] Poupon A, Leveaux J. Evaluation of water saturation in shaly formations. SPWLA 12th Annual logging symposium, 1971.

[7] Patchett G. An Investigation of Shale Conductivity. The Log Analyst, 1975; 16(6):.25.

[8] Rezaee MR. Application of Well Log Analysis. A short Course for N.I.O.C, 1997.

[9] Shazly TF, Ramadan MA. Well logs application in determining the impact of mineral types and proportions on the reservoir performance of Bahariya formation of Bassel-1x well, western desert, Egypt. Journal of American Science, 2011; 7(1): 498-505.

[10] Anselmetti FS, Eberli GP. The Velocity Deviation Log; A Tool to Predict Pore Type Permeability Trends in Carbonate Drill Holes From Sonics And Porosity or Density Logs. AAPG Bulletin, 1999; 83(3): 450-466.

[11] Farzadi P, and Hesthammer J. Diagnosis of the Upper Cretaceous Paleokarst and Turbidite Systems from the Iranian Persian Gulf using Volume-based Multiple Seismic Attribute Analysis and Pattern Recognition. Petroleum Geoscience Journal, 2007; 13(3):227-240.

[12] Clavier C, Rust DH. Mid-plot, a new lithology technique. The Log Analyst, 1976; 17(6): 16-31.

[13] Burke JA, Schmidt AW, Campbell RL. The Litho/Porosity Cross Plot. The Log Analyst, 1969; 10(6): 1969.

[14] Rezaee MR, Kadkhodaie A, and Barabadi A. Prediction of shear wave velocity from petrophysical data utilizing intelligent systems: An example from a sandstone reservoir of Carnarvon Basin, Australia. Journal of Petroleum Science and Engineering, 2007; 55: 201–212.

[15] Archie GE. The electrical resistivity log as an aid in determining some reservoir characteristics. Petroleum Transactions of AIME, 1942; 146: 54–62.

[16] Simandoux P. Mesure électriques en milieu poreux, application a mesure des saturations en eau. Etude du Comportment des massifs Argileux, Supplementary Issue, Revue de I'Institut Francais du Petrol, 1963.

To whom correspondence should be addressed: Dr. Hossein Tabatabaei, Department of Petroleum Engineering, Gachsaran Branch, Islamic Azad University, Gachsaran, Iran, E-mail Tabatabaei.h@gmail.com

Petroleum and Coal

Article **Open Access**

A COMPREHENSIVE ELECTRICAL MODEL FOR THE ELECTROSTATIC DESALTING PROCESS OF CRUDE OIL

Farzad Mohammadi[1], *Mehdi Mohammadi*[2], *Behrouz Nonahal*[2]

[1] *Department of Electrical Engineering, University of Tehran, Tehran, Iran.*
[2] *Electrocoalescers Research Laboratory, Petroleum Refining, and Processing Technology Development Division, Research Institute of Petroleum Industry, P.O. Box 14665-137, Tehran, Iran*

Received July 10, 2018; Accepted October 19, 2018

Abstract

An electrical model is presented consisting of two interconnected parts of the power unit and the electrical load within the electrostatic AC/DC desalter of crude oil. This model can be used to design the power unit and the internal electric field of electrostatic desalters. Also, the effects of parameters such as vessel dimensions, the geometry of electrode plates, oil conductivity, and relative permittivity of oil can be investigated on the electrical performance of the desalting process. The effect of the oil conductivity and simultaneous use of two parallel power units on the desalting plant have been studied. The simulation results show that the positive and negative plates in the electrostatic desalter act as a resistance-capacitance electrical load for a high-voltage electric power source that charged and discharged in each cycle. On the one hand, an increase in conductivity of the crude oil causes a faster discharge of the plates, resulting in a voltage drop in the electric field between the plates and thus reducing the efficiency of the water separation process. On the other hand, it will increase the power consumption of the desalting unit, significantly. Also, the results of the model show that the simultaneous use of two parallel power units with different phase angles can increase the effective voltage between the plates, which will result in a significant increase in the efficiency of the water separation process from oil.

Keywords: *Electrostatic Desalter; Electrical Model; Dual Polarity; Oil Conductivity.*

1. Introduction

The process of separating water droplets from crude oil under the effect of an electric field is referred to as the term electrostatic desalting. Crude oil is initially in the form of an emulsion of saline droplets in oil so that the water phase is saturated with various salts. The removal of water from crude oil is important for various reasons in the oil industry, such as the presence of various water-soluble salts causing corrosion and sedimentation in oil installations. Also, water separation before transportation reduces transportation costs. The simultaneous removal of some other impurities such as fine particles, clay, iron oxide, and iron sulfide is another advantage of the desalting process of crude oil [1].

Considering the importance of the desalting process, several types of research have been carried out modeling this process. Shahi *et al.* introduced a model for water droplet stability using double variable population equilibrium equations [2]. Ariyafard et al. proposed a mathematical model to predict the efficiency of water and salt removal [3]. Otabaye *et al.* introduced a model using neural network method to investigate the effect of process parameters such as the concentration of demulsifiers, temperature, wash water, mixing time and residence time on the efficiency of the desalting process [4]. Pronda et al. proposed an econo-mathematical model to obtain the optimum temperature for the desalting process [5]. However, no research has ever been carried out to model the electrical performance of the desalting process. This model needs to consider important parameters such as electrical characteristics of the high voltage power unit, conductivity and relative permittivity of crude oil, dimensions, and spacing of the plates.

In this research, a comprehensive electrical model has been introduced for a dual polarity (AC/DC) desalter of crude oil. In this type of desalters, first, crude oil passes through a weak AC field where a large portion of water is removed from the oil. Then, in order to remove the droplets of residual water, it passes through a strong DC field between the electrode plates (Fig. 1). Since the DC field exists only between the plates where the amount of salty water is very low, electrical corrosion will be reduced, significantly [1].

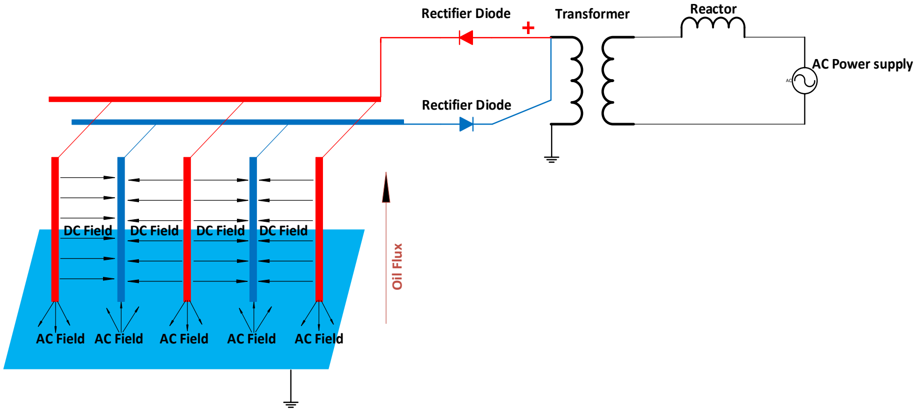

Fig. 1. Schematic AC/DC desalter

Fig. 1 displays the structure of the AC/DC desalter. As can be seen, the electrical supply section includes a reactor, transformer, and rectifier diodes. The role of the primary reactor in a transformer is described in section (2.1). The electrical load part consists of a desalter vessel and built in parallel plates which are connected one among to positive and negative bus bars.

Later on, the electrical model of the process will be described along with the method of calculating its parameters. First, the power unit model and the use of the series reactor will be described to achieve 100% reactance, and then the electrical load model and its parameters will be expressed. This two-part model is implemented for a desalter to study the effect of the oil conductivity and the effect of simultaneous using of two parallel power units.

2. Electrical model

A two-part model for the power unit and electrical load (desalter vessel) is introduced, and the method of calculating the relevant parameters is described. The elements of this electrical model include a resistor, capacitor, inductor, and ideal transformer. Also, the method of calculating reactance for a series reactor with a transformer, with a target of 100% reactance, is considered as one of the most important factors in the design of this special power unit.

2.1. Electrical power unit model

Fig. 2 displays the equivalent circuit of the power unit, and Table 1 introduces the elements of the circuit. The parameters of the model based on the design methodology are presented by the transformer manufacturers [6-8] and can also be specified through electrical tests [9].

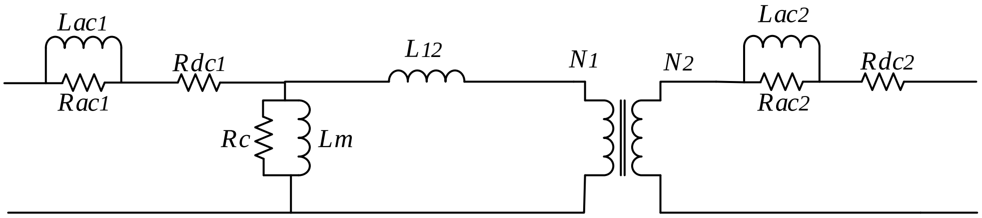

Fig. 2. The equivalent electrical circuit of the electrostatic field in desalter vessel

Table 1. Parameters of the power unit model

Parameter	Description
Rac_1 and Lac_1	Primary winding AC resistance modeling
Rac_2 and Lac_2	Secondary winding AC resistance modeling
Rdc_1 DC	Primary winding resistor
Rdc_2 DC	Secondary winding resistor
R_c	Core losses modeling
L_m	Magnetization inductance
N_1	Number of primary winding wires
N_2	Number of secondary winding wires
L_{12}	Mutual inductance

With respect to the possibility of changing the water-oil emulsion based on the type of crude oil, the temperature and the water content in the crude oil and the possibility of rising the level of accumulated water at the bottom of the vessel, the electrical power source of desalter must be designed in such way that in the case of secondary short-circuit (excessive increase in charge conductivity), the transformer current to be limited to the nominal current. For this purpose, by adding a series inductor (reactor) to the transformer, the design of the power source is achieved with a 100% reactance. By disregarding the transformer inductance, the inductance of the series inductor is calculated through Equation (1) and Equation (2) [9]:

$$X_R = Z_{BL} = \frac{(V_{BL})^2}{S} \tag{1}$$

$$L_R = \frac{X_R}{2\pi f} \tag{2}$$

where V_{BL} is the nominal voltage of the low voltage side; S is the nominal transformer power; Z_{BL} is the transformer impedance; X_R is the series inductor impedance; L_R is the inductance of the series inductor, and f is the voltage frequency.

Electrical power consumption of transformer is one of the important factors in the design of a desalting unit that depends on the conductivity of crude oil, dimensions of the vessel, distance between the electrode plates and the number of the plates. The electrical power of the transformer, P, can be calculated by Equation (3), where V_{rms} and I_{rms} are effective voltage and current, respectively.

$$P = V_{rms} \times I_{rms} \tag{3}$$

2.2. Electrical load model

In this section, based on the geometry of the vessel, the dimensions and distances of the electrodes (plates) inside the vessel and the electrical properties of the fluids (w/o emulsions) in different parts of the vessel, an electrical model is developed for the consumer (internal electric field). The important parameters in calculating the electrical model are the dimensions of the vessel, the dimensions and the distance between the plates, as well as the electrical properties such as crude oil conductivity and the relative permittivity in different parts of the vessel.

The electrodes are connected as a plate to the positive and negative bus bars inside the vessel. There are capacitance and electrical current between the opposite plates that are modeled using a capacitor and electrical resistor. Regarding the water phase accumulated at the bottom of the desalter vessel, due to the high water conductivity, it is possible to consider the water layer and the body of the reservoir as an integrated part. Between all plates and reservoir surface and water, electrical conductivity and capacitance are modeled using resistors and capacitors.

Table 2 presents the dimensions of the vessel and the internal plates. Fig. 3 shows the cross section of the vessel, together with the fluid distribution profile in different regions. At the lowest level of the vessel, the water layer is located at the highest conductivity (4 S/m) and at the top of the water layer there is a water-filled emulsion with a conductivity of 500 nS/m. At the bottom of the plates, because of the reduction of water due to droplet sedimentation, the crude oil conductivity decreases to 100 nS/m. The highest layers, related to the dehydrated crude oil between the plates and the top of the plates near the outlet, have a minimum conductivity of about 10 nS/m [9]. The relative permittivity of the crude oil is $\varepsilon_r = 2.5$.

Table 2. The geometry of the desalter vessel and internal electrodes

Vessel length	21 m
Vessel diameter	4.2 m
Number of electrode plates	140
Height of electrode plates	15 cm
Length of electrode plates	3.2 m
Distance between electrode plates	15 cm

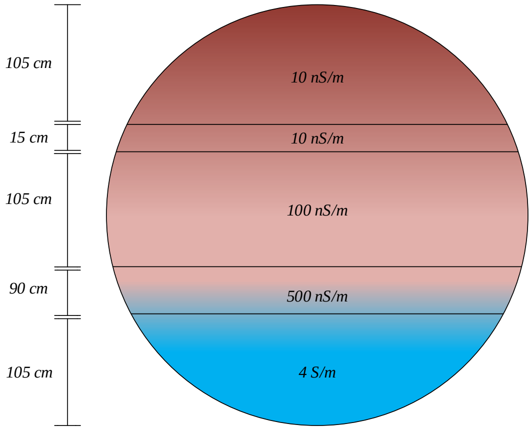

Fig. 3. Fluid conductivity profile in different areas within the vessel

In order to calculate the capacitive property between the electrode plates and to reduce the computational time, only a part of the vessel containing 8 electrode plates is considered. The layout of the desired plates and the geometry of the problem are depicted in Fig. 4. The capacitance of the plates (P_1 to P_8) with the vessel body (V_0) in terms of picofarad is as the following matrix. The first line of the matrix is related to the capacitance between the vessel and the plates, and the next lines of the matrix are related to the capacitance between the plates with each other. As you can see, the capacitance between a plate and its adjacent plates is much larger than the capacitive property between that plate and its non-adjacent plates. For example, the capacitance between plates 3 and 4 is 75.236pf, while the capacitance between plates 3 and 5 is 9.16pf. Therefore, the capacitance between the non-adjacent plates can be ignored.

$$\left[\begin{array}{cccccccccc}
\backslash & V_0 & P_1 & P_2 & P_3 & P_4 & P_5 & P_6 & P_7 & P_8 \\
V_0 & 341.12 & -68.41 & -37.276 & -33.333 & -32.075 & -32.12 & -36.876 & -36.876 & -36.876 \\
P_1 & -68.41 & 170.73 & -81.503 & -11.596 & -4.4988 & -2.1954 & -1.1926 & -0.7071 & -0.6233 \\
P_2 & -37.276 & -81.503 & 210.15 & -75.53 & -9.267 & -3.865 & -1.5951 & -0.8692 & -0.7199 \\
P_3 & -33.333 & -11.596 & -75.53 & 210.99 & -75.236 & -9.1601 & -3.3237 & -1.5957 & -1.2143 \\
P_4 & -32.075 & -4.4988 & -9.267 & -75.236 & 211.03 & -75.222 & -9.1264 & -3.3765 & -2.2264 \\
P_5 & -32.12 & -2.1954 & -3.865 & -9.1601 & -75.222 & 211.23 & -75.298 & -9.2761 & -4.5733 \\
P_6 & -33.206 & -1.1926 & -1.5951 & -3.3237 & -9.1264 & -75.298 & 210.91 & -75.434 & -11.739 \\
P_7 & -36.876 & -0.7071 & -0.8692 & -1.5957 & -3.3765 & -9.2761 & -75.434 & 209.95 & -81.817 \\
P_8 & -67.82 & -0.6233 & -0.7199 & -1.2143 & -2.2264 & -4.5733 & -11.739 & -81.817 & 170.73
\end{array}\right]$$

The finite element method is used to calculate the current flow between the plates and vessel and water surfaces. Fig. 5 displays a plate with the part of the vessel. The length of the vessel is along the Z axis. Color layers are characterized by water, high water emulsion, low water emulsion, and dry crude oil, each of which has different conductivity according to Fig. 3. The electrode plate is placed inside a yellow rectangular cube. Using the finite element method, the surface density of the current is calculated, and then, by integrating the surface density of the current on the yellow packet surface, the amount of electric current is calculated. By dividing the voltage assigned to the plate into the output current of the electrode plate, the resistance between the electrode plate and the vessel can be calculated.

With respect to the fact that the distance between the plates relative to their area is small, the resistance between the plates can be calculated with a good approximation of the Equation (4):

$$R = \frac{\rho l}{A} \tag{4}$$

where ρ is the resistivity of the crude oil between the electrode plates; l is the distance between the plates and A is the area of the plate.

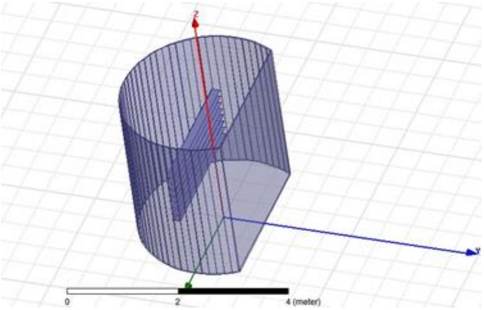

Fig. 4. The electrode plates and vessel body used to calculate the capacitive property (The surface of the water and the vessel's body are considered unified due to the equal voltage of earth connection)

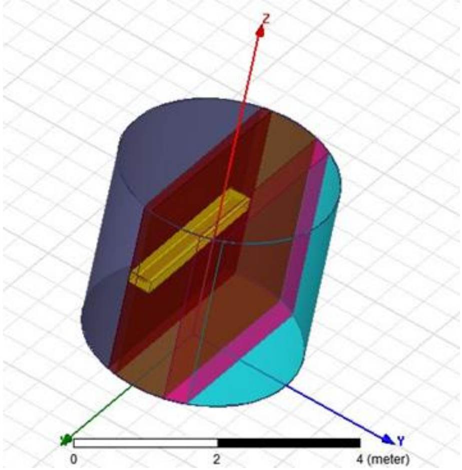

Fig. 5. The geometry used to calculate the output current from one electrode plate according to the fluid conductivity profile

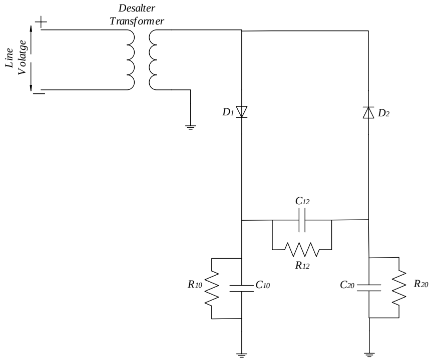

Fig. 6. The equivalent electrical circuit of the vessel

Since the resistors and capacitors between the electrode plates, the resistors and capacitors between the positive plates and the vessel's surface, and the resistors and capacitors between the negative plates and the vessel's surface are parallel; the equivalent electrical circuit of the vessel can be shown as Fig. 6.

In Fig.6, R_{12} and C_{12} are the resistor and capacitor between the plates, R_{10} and C_{10} are the equivalent resistor and capacitor between the positive plates and the vessel, R_{20}, and C_{20}, are the equivalent resistor and capacitor between the negative plates and the vessel. D_1 and D_2 are rectifier diodes at the transformer's output voltage.

3. Implementation of the electrical model for a desalting system

In section (2), an electrical model of the equivalent circuit of the power source and an electrical model of electrical load (inside the vessel) are introduced. The method of calculating the parameters of the two parts of the model are described separately. In this section, the model derived from the previous section, including the power unit and the desalter's vessel (electrical load), is implemented to simulate the electrical components of the process.

The electric power is considered to be 15 KVA, the primary/secondary voltage is 380V/22KV, and the frequency is 50 Hz. Other information regarding this power unit is provided in Table 3.

The values for the source electrical model according to Fig. 2 are as follows:
L_{ac1}=365.2 uH, L_{ac2}=1.75 H ;R_{ac1}=105.6 mΩ, R_{ac2}=257.2 Ω ; R_{dc1}=56.72 mΩ, R_{dc2}= 210.6 Ω; R_C=1.219 KΩ; L_m=1.64 H; L_{12}=1.105 mH; N_1=109, N_2= 6311;$L_R = \frac{X_R}{2\pi\times 50} = 30.6\ \text{mH}$

Fig. 7 shows the variation of the secondary voltage with the voltage of the positive plates. As can be seen, due to the capacitance between the plates, the voltage of the plates is reduced at a lower speed than the transformer secondary voltage. This phenomenon maintains a DC voltage difference between the positive and negative plates (the electrodes inside the vessel). Therefore, a DC electric field generates between the positive and the negative plates.

Table 3. Information on the section on increasing transformation

Core manufacture	THOM & SKIN
The geometric structure of the core	1.125 × 5 (3) MH
Core type	EI Lamination 18.5 mil
The core weight	105 kg
Total core weight + winding	321.5 Kg
Iron losses	118.4 W
Copper losses	187.2 W
Increased transformer temperature	39.14 °C
Number of primary winding wire	109
Number of secondary winding wire	6311
The size of the primary wire	AWG 20
The size of the secondary wire	AWG 11

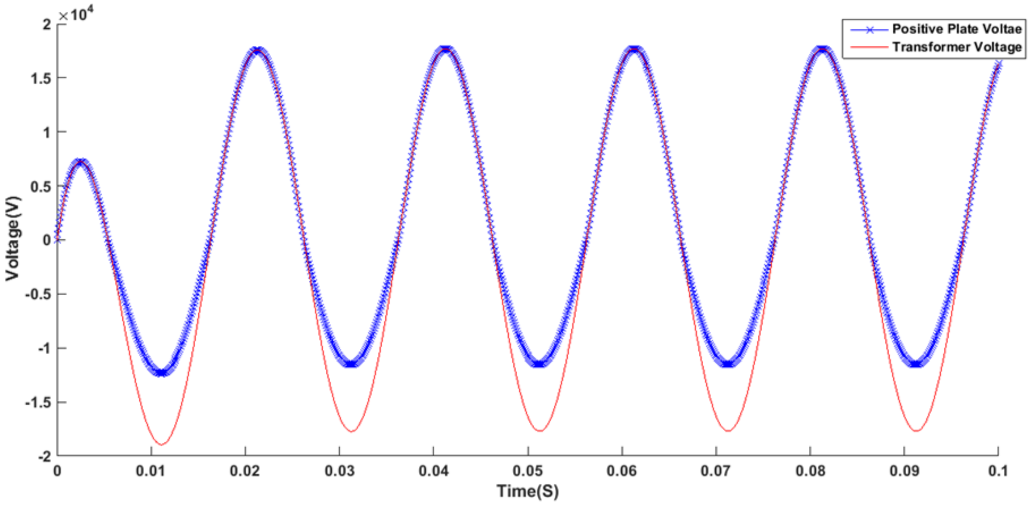

Fig. 7. Transformer secondary voltage with positive plates voltage

Fig. 8 displays the DC voltage difference between the vessel plates, which is the result of the difference between the negative and positive plates voltage. Fig. 9 shows the average DC voltage between the plates, which determines the electric field between the plates. The intensity of the electric field is one of the important factors in the efficiency of the process of desalting of crude oil.

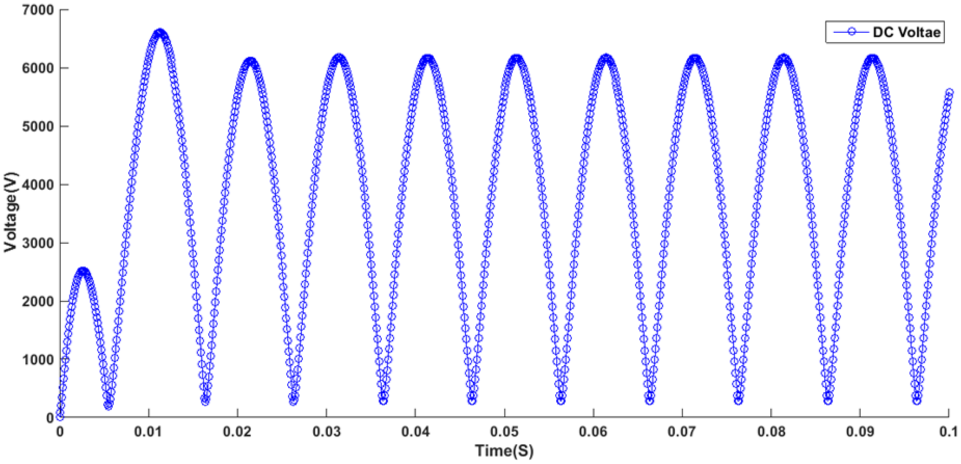

Fig. 8. DC voltage between the plates

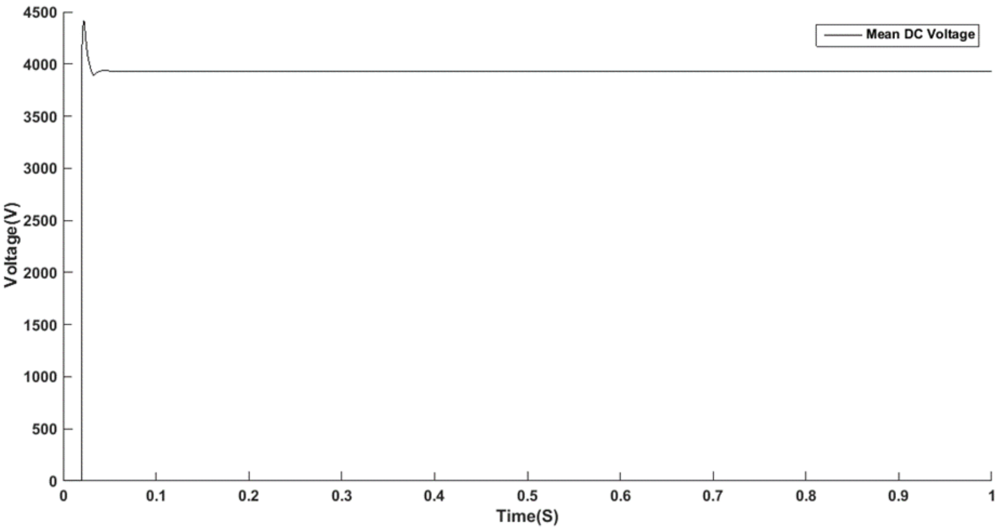

Fig. 9. The average DC voltage between the plates

In the case where the amount of crude oil conductivity in all the layers inside the vessel is affected by the type of crude oil, the increase in water percent and operating temperature, becomes 10 times of the stated values in Fig. 3, the simulation is repeated, and the result for the DC voltage between the plates is shown in Fig. 10. As can be seen, this change will reduce DC voltage to 1/8 of the previous value, and as a result, the efficiency of the desalting process will be reduced, significantly. This confirms the problems of processing high-conductivity crude oils.

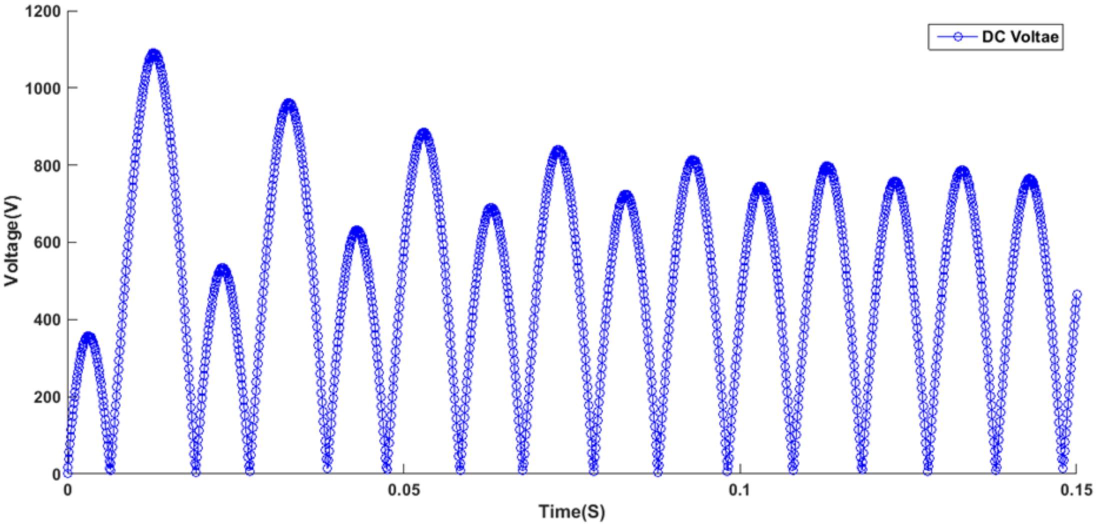

Fig. 10. The DC voltage between the plates in the case of conductivity 10 times the values of Fig. 3

One of the most commonly used methods in industrial desalting plants is applying of two or three power units connected to isolated industrial power phases on a desalting vessel. Fig. 11 shows the positive and negative plate voltages for the case of two parallel transformers with different power supplies (phase difference of 120°). It should be noted that in this case, the transformers outputs after passing the rectifier diodes are connected in parallel. Due to the 120 degrees phase difference of secondary voltage of the transformers, the positive and negative plate voltages have less time for discharging, and this increases the electrical field between the plates and as a result, improves the desalting process of crude oil.

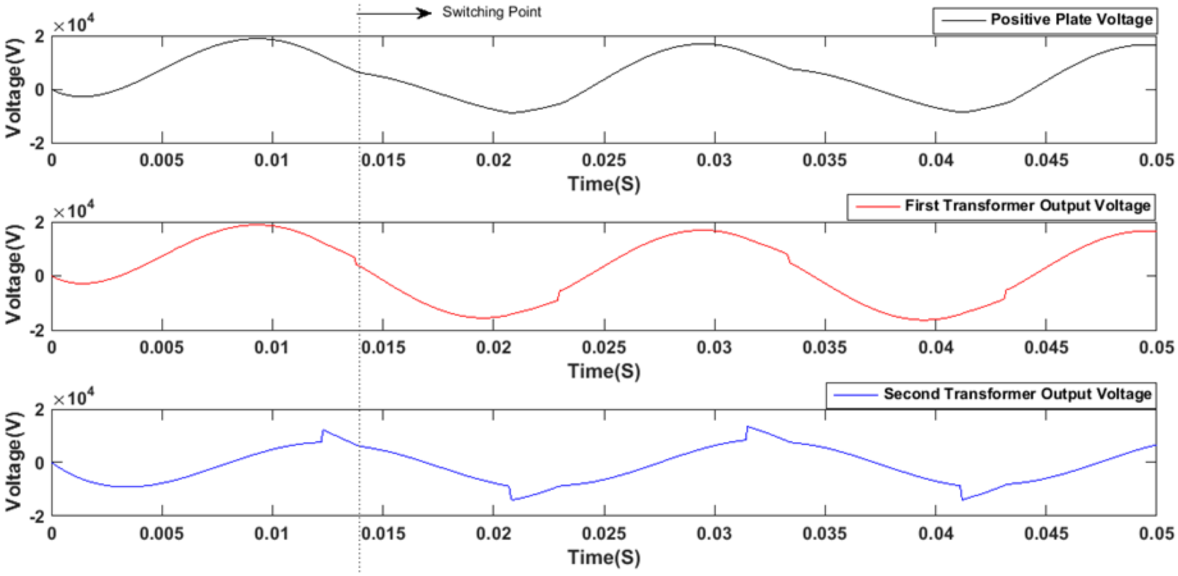

Fig. 11. Positive voltages with the secondary voltage of each transformer

In Fig. 12, and Fig. 13, the DC voltage between the plates and the average voltage difference between the plates are shown in the case of two parallel transformers. As can be seen, the difference between the effective DC voltages is more than twice that of a single source (compared to Fig. 8). This result shows that the use of two power units simultaneously will have a significant effect on the improvement of the desalting process.

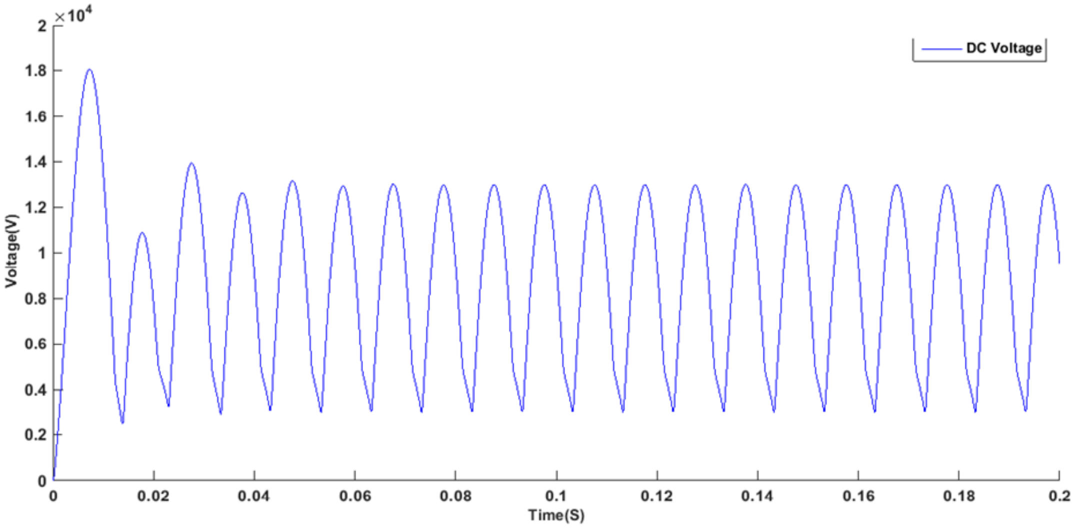

Fig. 12. DC voltage between the electrode plates in the case of two parallel transformers

4. Discussion

As shown in section (3), the electrode plates in the desalter vessel act as an RC load for a high voltage electric power unit. Due to the capacitive property, in positive half-cycle of sinusoidal voltage, positive plates are charged, and negative plates are discharged, and this is done in the negative half-cycle vice versa. We know that the time constant for capacitor discharge is defined as follows:

$$\tau = RC \tag{5}$$

where R is the resistance, and C is the capacitance of the load.

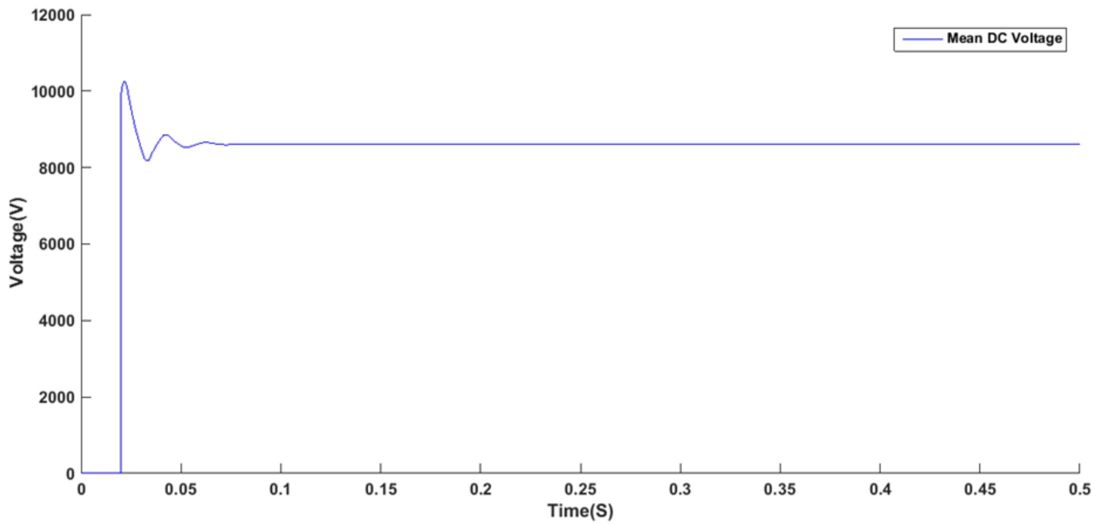

Fig. 13. The average DC voltage between the plates in the case of two parallel transformers

With regards to the above relationship, increasing the conductivity of the crude oil causes a decrease in time constant and, as a result, a faster discharge of the plates. This is considered undesirable in the process of desalting because with the discharge of the plates, the effective voltage difference between them and the intensity of the electric field will decrease, which will lead to a reduction in the efficiency of the separation process in the desalter. However, in accordance with this relationship, an increase in relative permittivity increases the time constant and resulting in an increase in discharge time of the plates, but the relative permittivity for different types of crude oil is almost the same and does not change significantly.

Fig. 14 displays the DC voltage between the plates in terms of the conductivity of the crude oil for both cases using one 15 KVA transformer and two parallel 15 KVA transformers. As expected, the increase in conductivity has a significant effect on the effective voltage between the plates and, consequently, the performance of separation in the desalting process. Important factors in determining the conductivity of water-in-oil emulsion are the type of components of crude oil, process temperature, and water content [10]. With respect to Fig. 14, this interval of variations in the conductivity of the crude oil has a great influence on the DC effective voltage between internal electrodes of the vessel. Another important point in this figure is the DC voltage difference for two cases of using a single transformer and double parallel transformers, which is large in small conductivity and reduces with increasing conductivity. For example, for the conductivity of 10 ns/m, the voltage is in the case of a single transformer is 6720 V and in a two parallel transformer case is of 35000 V, and for the conductivity of 2000 nS/m, the DC voltage between the plates is 248 V and 496 V respectively.

An important feature in the design of a desalting unit is electrical power consumption. Fig. 15 shows the power consumption in terms of the conductivity of the crude oil using Equation (3) for two different cases: 1st for the base case of Table (2); and 2nd for the case of twice diameter vessel and halved number of plates. As can be seen, the increase in the conductivity of crude oil has a significant effect on the increase of power consumption of the unit and consequently, an increase in unit costs. For example, in the base case (1st), an increase in the conductivity of the crude oil from the normal values of about 50 nS/m to relatively high values such as 1000 nS/m, rises the power consumption to more than twice.

The increase in the conductivity of crude oil reduces the R_{10}, R_{20}, and R_{12} resistances shown in Fig. 6. On the other hand, reducing the vessel size, reducing the distance between the plates and increasing number of plates are other factors that reduce these resistances. Regarding Fig. 15, inappropriate selection the above geometries can lead to excessive consumption of power, even in low levels of crude oil conductivity.

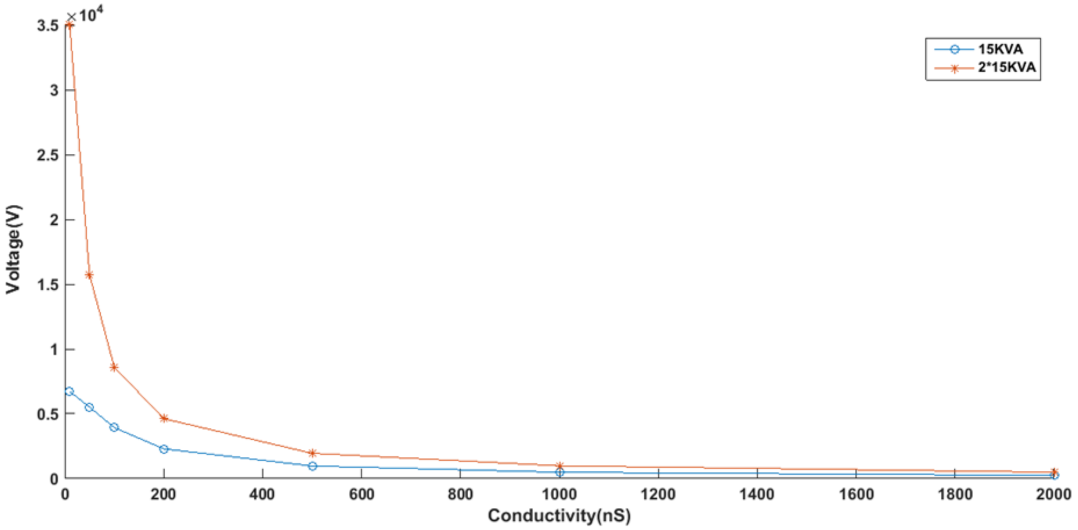

Fig. 14. The Effect of crude oil conductivity on the effective DC voltage between the plates for single and double power unit application

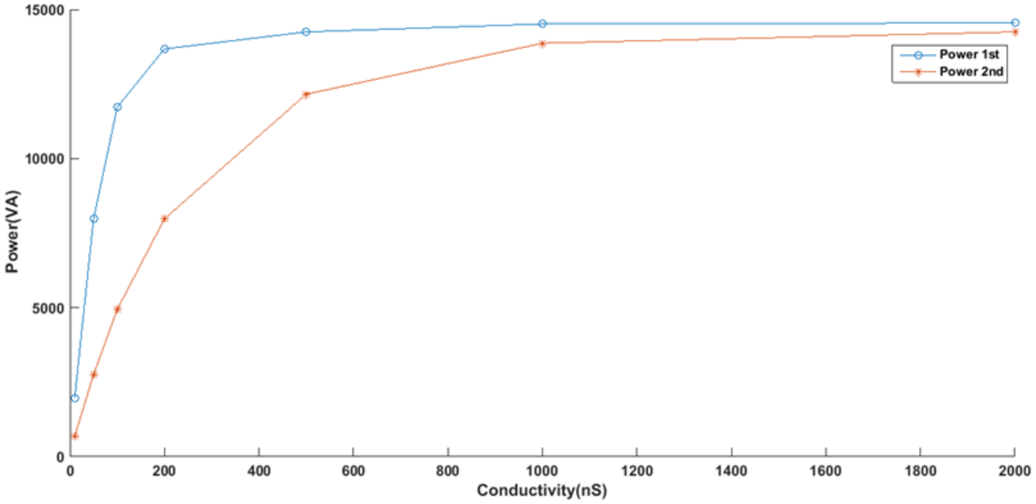

Fig. 15. The effect of crude oil conductivity on electric power consumption for 1st: the base case of Table (2); and 2nd: the case of doubled diameter vessel and halved number of plates

The 2nd diagram of Fig. 15 relates to a case state in which the diameter of the vessel is doubled, and the number of plates is halved. As can be seen, in this case, power consumption is less for the usual values of conductivity than the 1st case. For example, in the conductivity of 100 nS/m, the power consumption in the 1st case is 11.7 KVA, and in the 2nd case, it is 5 KVA. Thus, the conductivity of the crude oil, the dimensions of the vessel, the distance between the plates and the number of plates are the key factors in the process of electrostatic desalting that affect both the quality of the desalting process and the electrical power consumption of the unit.

Conclusions

An electrical model was presented for the dual polarity (AC/DC) desalting unit. The model consisted of two parts: the high-voltage power unit and desalter vessel (electrical load). This model can be used to design an external power unit and an internal electric field. Also, using this model, the effects of different geometric parameters such as vessel dimensions, electrode plates, and electrical properties such as crude oil conductivity on the performance of the desalting process were investigated.

Using the model, the effect of crude oil conductivity on the desalting process was studied. It was found that the increase in conductivity could reduce the electric field between the plates and, as a result, reduce the performance of separation in the desalting process. For example, the DC voltage between the plates in the case of the crude oil conductivity of 100 nS/m was equal to 4 KV, but at a conductivity of 1000 nS/m, this value was reduced to 500 V. Furthermore, the effect of the oil conductivity, desalter vessel dimension, and plates geometry on the power consumption of the process was investigated. It was determined that increasing crude oil conductivity and inappropriate selection of geometric parameters could increase the electrical power consumption, noticeably.

Also, the effect of simultaneous use of two parallel electrical sources on a desalter vessel was investigated through simulations. It was determined that the use of two parallel transformers could increase the DC voltage between the plates, which is more effective in low levels of crude oil conductivity. For an oil conductivity of 10 nS/m, in the state of using one transformer the DC voltage between the plates is 6720 V and in the case of using two parallel transformers is 35000 V; and in oil conductivity of 1000 nS/m, the DC voltage is 493 V for single source and 990 V for double source.

In addition to the items examined in this study, the proposed model can be used to explore, develop, and design equipment used in newer technologies for crude oil desalting, such as dual frequency technology.

References

[1] Sellman EL, Sams G, Mandewalkar P. Benefits of using advanced electrostatic fields in crude Oil dehydrators and desalters. SPE International production and operations conference & exhibition, Doha, Qatar. 2012.
[2] Meidanshahi V, Jahanmiri AH, Rahimpour MR. Modeling and optimization of two stage AC electrostatic desalter. Sep. Science Tech. 2012; 47(1): 30-42.
[3] Aryafard E, Farsi M, Rahimpour MR. Modeling and simulation of crude oil desalting in an industrial plant considering mixing valve and electrostatic drum. Chem. Eng. Process. Process Intensif. 2015; 95: 383-389.
[4] Al-Otaibi MB, Elkamel A, Nassehi V, Abdul-WahabSA. A computational intelligence based approach for the analysis and optimization of a crude oil desalting and dehydration process. Energy Fuels 2005; 19(6): 2526–2534.
[5] Pruneda EF, Escobedo E, Vazquez F. Optimum temperature in the electrostatic desalting of maya crude oil. J. Mex. Chem. Soc. 2005; 49: 14-19.
[6] Winders JJ. Power transformers: principles and applications. CRC Press; 2002.
[7] Del-Vecchio RM, Poulin B, Feghali PT, Shah DM, Ahuja R. Transformer design principles: with applications to core-form power transformers. 2nd ed., CRC Press; 2010.
[8] López-Fernández XM, Ertan H, Turowski J. Transformers: analysis, design, and measurement. Boca Raton: CRC Press; 2013.
[9] Sen PC. Principles of electric machines and power electronics. John Wiley&Sons; 1989.
[10] Mohammadi M, Mohammadi F. Parametric study on electrical conductivity of crude oils; basis experimental data. Petroleum & Coal. 2016; 58(6): 629-634.
[11] Boschee P. Advances in electrostatic treatment of crude oil. Oil gas facilities 2012; 10: 17-21.

To whom correspondence should be addressed: Mehdi Mohammadi; Electrocoalescers Research Laboratory, Petroleum Refining and Processing Technology Development Division, Research Institute of Petroleum Industry, P.O. Box 14665-137, Tehran, Iran

Petroleum and Coal

Article **Open Access**

A SENSITIVITY ANALYSIS FOR THE EFFECTIVE PARAMETERS DISPARITY ON PRESSURE AND PRESSURE DERIVATIVE OF WELL-TESTING IN A HORIZONTAL WELL

Arash Pourabdol Shahrekordi[1, 2], Mohammad Behnood[1], Armin Hosseinian[3], Sajjad Mozaffari[1, 2], Seyed Jamal Sheikhzakariaee[1]*

[1] *Department of Petroleum and Chemical Engineering, Science and Research Branch, Islamic Azad University, Tehran, Iran*
[2] *Young Researchers and Elite Club, Science and Research Branch, Islamic Azad University, Tehran, Iran*
[3] *Department of Earth, Ocean and Atmospheric Sciences, University of British Columbia, Vancouver, Canada*

Received May 2, 2019; Accepted June 13, 2019

Abstract

In this study, the pressure and pressure derivative of a drawdown test for a horizontal well was investigated. The examined well, it is located in the middle of a homogeneous oil reservoir and the calculation has been obtained using an industry standard PTA software known as Saphir software. Afterward, from the pressure derivative curve, initial radial, linear and final radial flow periods were observed, respectively. Then, the variation of the effective three parameters was inspected using the sensitivity analysis tool provided in Saphir software. The considered parameters are the ratio of the vertical to horizontal permeability (K_z/K_r), skin factor (S) and the horizontal length of the well (L_w). that the results reveals that by increasing the ratio of K_z/K_r and L_w the pressure curve is lowered, and it shifts upward with growing the S parameter. Meanwhile, by increasing the value of parameter K_z/K_r ratio, the initial radial flow becomes shorter in the pressure derivative curve and the linear flow starts earlier. In the other hand, within a pressure derivative diagram, as the value of S parameter rises, the hump becomes larger resulting a delay in the start of the first radial flow. Besides, the other consequences will be shifting downward the curves of the first radial flow and linear flow periods, increasing the duration of the linear flow, and also the final radial flow starts later. The analysis outcomes of this study were in conjunction of what it will be expected in well-testing procedure.

Keywords: *Horizontal Well; Skin Factor; Permeability; Well-Testing; Saphir well-testing Software; Sensitivity Analysis.*

1. Introduction

Horizontal drilling is one of the most advanced technologies which has been used in the last thirty years in oil and gas industry. In fact, the horizontal wells are type of directional wells and they have many different practical applications. Those can be categorized in different aspects. The horizontal wells are being employed to reach the reservoirs located below the sea, lake, river, residential areas and mountainous terrain, where vertical access to these reservoirs is not possible [1]. In oil reservoirs with a high ratio of vertical to horizontal permeability, oil has a much tendency to move in a vertical direction. Therefore, horizontal wells cause an increase in oil production from this type of reservoirs [2]. These kinds of wells reduces the pressure drop due to production in the area around the well, slows down and delays water and gas coning phenomena, which is the main application of horizontal wells [1]. In reservoirs with thin pay zone, horizontal wells cause a greater degree of the well to reservoir contact, thus the production from this type of reservoirs increases, significantly [2]. Moreover, in the naturally fractured oil reservoirs, drilling horizontal wells leads to the division of existing vertical fractures, resulting in a considerable improvement in oil production [2]. Figure 1 shows a schematic representation of a horizontal production well.

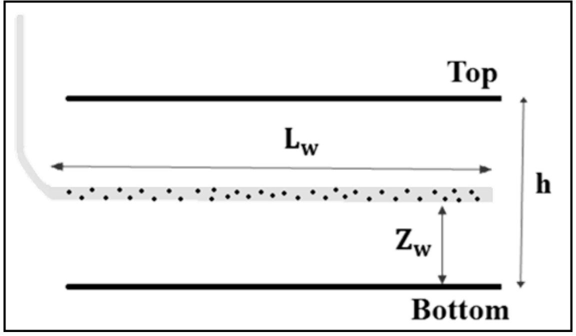

Figure 1.Schematic representation of a horizontal production well [3]

As shown in Figure 1, a well with the horizontal length of L_w is drilled in a reservoir with thickness h in a way that the distance from the lower horizontal line of the reservoir is Z_w.

Above the benefits of using horizontal wells, there are several applications of such a wells which they cause the interpretation of their pressure and the pressure derivative curves. Accordingly, there are some important and effective parameters [3]. In this study, we did a sensitivity analysis on the effect of changes in three different parameters of K_z/K_r ratio, Skin factor (S), and the horizontal length of the well (L_w) on the pressure and its derivative of a horizontal well. Since inside the horizontal wells, the motion of oil or gas is exist it is important to introduce briefly different type of fluids.

2. Different types of flow around a horizontal production well

It is assumed that the storage effect has not affected any flow period near the horizontal well. Therefore, during the analysis of pressure behavior of a horizontal production well which is drilled close to one of the upper or lower reservoir boundaries (Top or bottom), four unsteady state flow regimes can be observed in the middle time region [5]. The mentioned flow regimes are characteristics of the reservoir that are listed as follows:

2.1. Initial radial flow

As the oil production starts from the reservoir, a radial flow in the vertical direction is formed around the horizontal production well (Fig. 2). This regime is indicated with the existence of a straight line with zero slopes in the pressure derivative diagram (Fig. 6).

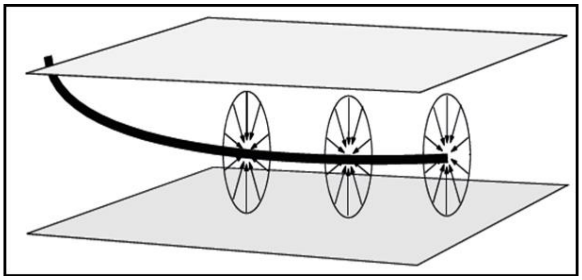

Figure 2. Initial radial flow (normal radial flow) [4]

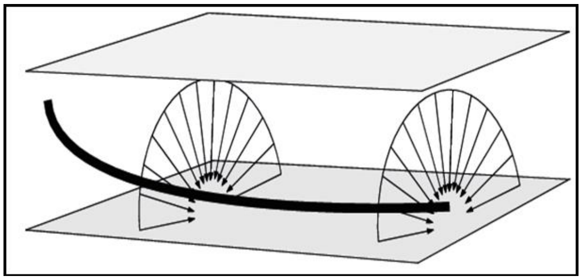

Figure 3. Semi-radial flow [4]

2.2. Semi-radial flow

In the case that the horizontal production well is drilled near one of the upper or lower reservoir boundaries (Top or bottom), the radial flow is terminated when the pressure pulse reaches the nearest boundary and the semi-radial flow starts (Fig. 3). Observing a horizontal straight line on the pressure derivative with more value than the radial flow indicates the semi-radial flow period (Fig. 6).

2.3. Linear flow

After the semi-radial flow reaches to the farthest vertical boundary of the reservoir, the linear flow is formed (Fig. 4). In this state, the behavior of the horizontal well is similar to the behavior of a vertical well with infinite conductivity fractures. The existence of the straight line with slope + 0.5 in the pressure derivative curve is the sign of this flow regime (Fig. 6).

2.4. Final radial flow

Since a radial flow in the horizontal direction causes the conduction of oil towards the production well, the final radial flow is called the horizontal radial flow (Fig. 5). The existence of the straight line with zero slopes in the pressure derivative diagram indicates this flow regime (Fig. 6).

It should be mentioned that all four regimes cannot be observed in real well- testing because the wellbore storage effects cover the first radial and semi-radial flow regimes [4]. More details of using the flow regimes resulted in this study will provide in following sections.

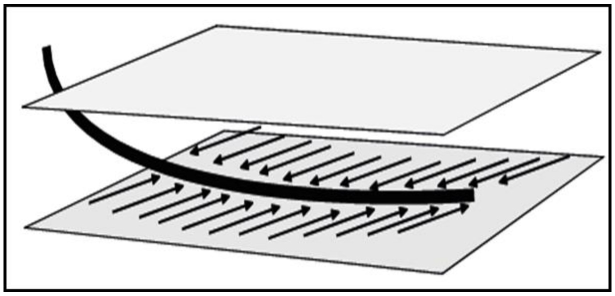

Figure 4. Linear flow [4]

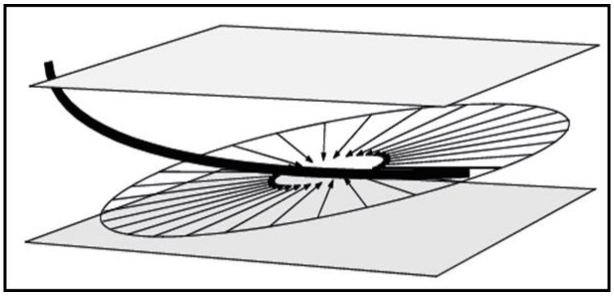

Figure 5. Final radial flow (horizontal radial flow) [4]

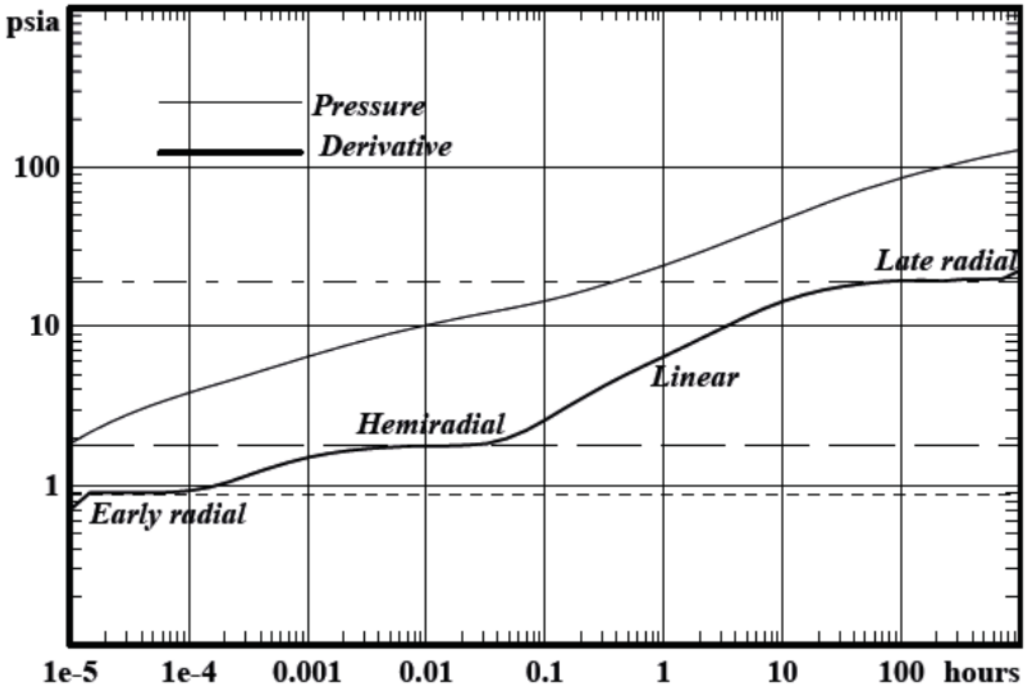

Figure 6. Pressure and pressure derivative curves in a horizontal well [4]

3. Research method

A drawdown test was performed on a horizontal production well which is located in the middle of a homogeneous oil reservoir. In this test, a horizontal well produced with a constant rate of 500 STB/day during a flow period of 78498.3 hours. The data of flowing pressure change (P_{wf}) is obtained with time (t) shown in Table 1, as presented in previous literature [3]. The other primary properties of the horizontal well as well as the indicated reservoir are listed in Table 2.

Table 1. Data of flowing pressure change (P_{wf}) is obtained with time (t) in a drawdown test

t (hr)	P_{wf} (psia)	t (hr)	P_{wf} (psia)	t (hr)	P_{wf} (psia)
0.00078	4985.61	0.63672	4849.689	516.4664	4509.059
0.00095	4983.088	0.76694	4846.231	622.0856	4483.915
0.00114	4980.402	0.92378	4842.784	749.3043	4457.79
0.00137	4977.49	1.11269	4839.348	902.5397	4430.767
0.00165	4974.351	1.34024	4835.921	1087.112	4402.932
0.00199	4970.968	1.61433	4832.503	1309.431	4374.371
0.0024	4967.354	1.94446	4829.091	1577.214	4345.168
0.00289	4963.524	2.34211	4825.676	1899.76	4315.403
0.00348	4959.497	2.82108	4822.24	2288.267	4285.151
0.00419	4955.311	3.398	4818.75	2756.226	4254.478
0.00505	4950.996	4.09291	4815.157	3319.884	4223.443
0.00608	4946.595	4.92992	4811.401	3998.812	4192.102
0.00732	4942.146	5.93811	4807.415	4816.583	4160.499
0.00882	4937.684	7.15247	4803.129	5801.591	4128.675
0.01062	4933.242	8.61518	4798.484	6988.037	4096.665
0.01279	4928.844	10.37701	4793.428	8417.115	4064.498
0.01541	4924.508	12.49915	4787.914	10138.45	4032.199
0.01856	4920.249	15.05527	4781.899	12211.79	3999.79
0.02236	4916.07	18.13412	4775.341	14709.15	3967.289
0.02693	4911.973	21.84262	4768.196	17717.22	3934.711
0.03244	4907.953	26.30951	4760.416	21340.46	3902.068
0.03907	4904.006	31.6899	4751.952	25704.65	3869.373
0.04706	4900.126	38.1706	4742.751	30961.35	3836.632
0.05668	4896.305	45.97662	4732.763	37293.05	3803.854
0.06827	4892.537	55.379	4721.93	44919.61	3771.045
0.08224	4888.814	66.7042	4710.197	54105.83	3738.211
0.09905	4885.132	80.34544	4697.509	65170.67	3705.354
0.11931	4881.486	96.77637	4683.812	78498.3	3672.48
0.14371	4877.87	116.5675	4669.051		
0.1731	4874.281	140.4059	4653.18		
0.2085	4870.716	169.1195	4636.158		
0.25114	4867.171	203.705	4617.953		
0.3025	4863.645	245.3634	4598.545		
0.36436	4860.135	295.541	4577.931		
0.43887	4856.64	355.9803	4556.122		
0.52862	4853.159	428.7795	4533.148		

Table 2. Primary Properties of the horizontal well and reservoir

Parameters	Unit	Value
h	ft	100
r_w	ft	0.3
B_o	rbbl/STB	1.53951
μ_o	cP	0.342268
ϕ	----	0.23
C_t	Psia^{-1}	$1.06044*10^{-5}$
P_i	psia	5 000

Considering the provided data, pressure and flow rate diagrams were plotted with time by entering data from Tables 1 and 2 as well as production flow rate of well into Saphir software. The results are shown in Figure 7. Later, by using the icons for separating the pressure and pressure derivative (i.e. dp and dp$'$ respectively), the pressure and pressure derivative of the horizontal well were plotted and matching procedure was implemented in Figure 8. Consequently, the final properties of the horizontal well and reservoir were determined and the results are shown in Table 3. Other results would achieved and three types of flow were observed around the horizontal well and shown in the pressure derivative diagram of Fig. 8. Those flow types were initial radial flow, linear flow, and final radial flow, respectively.

Table 3. The final properties of the horizontal well and reservoir

Parameters	Unit	Value
S	-	0.00756612
C	rbbl/psi	0.00114098
Z_w	ft	50.4052
L_w	ft	1097.39
K_h	md.ft	104.282
K	md	1.04282
K_z/K_r	-	0.886349

In the final stage of this study, the effect of variation of different parameters on pressure and the pressure derivative of the horizontal well was investigated using the sensitivity analysis icon in Saphir software. In this study, sensitivity analysis is performed on three different parameters as the ratio of the vertical to horizontal permeability (K_z/K_r), the skin factor (S) and the horizontal length of the well (L_w). The results of such study are described in following sections.

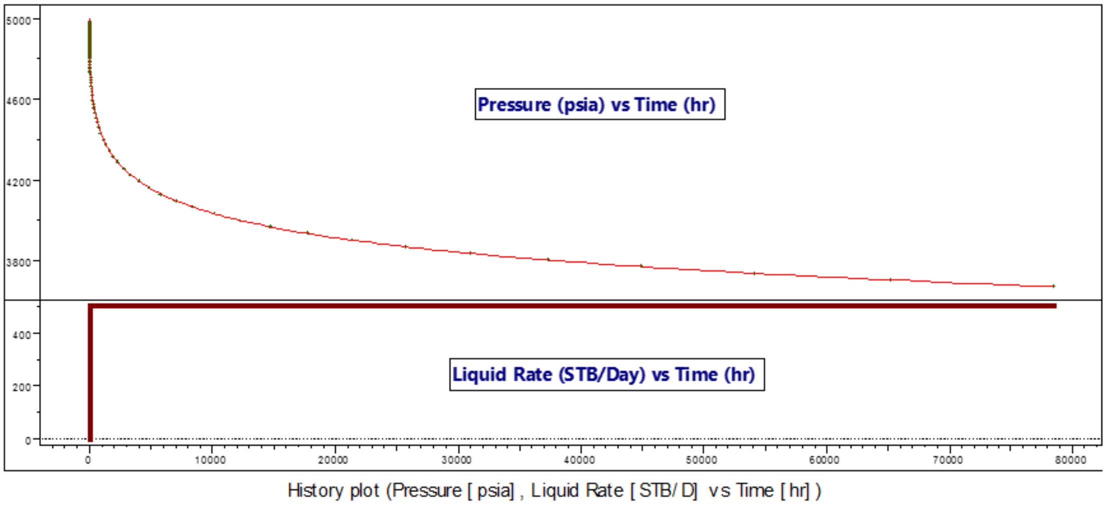

Figure 7. Pressure change and flow rate diagram

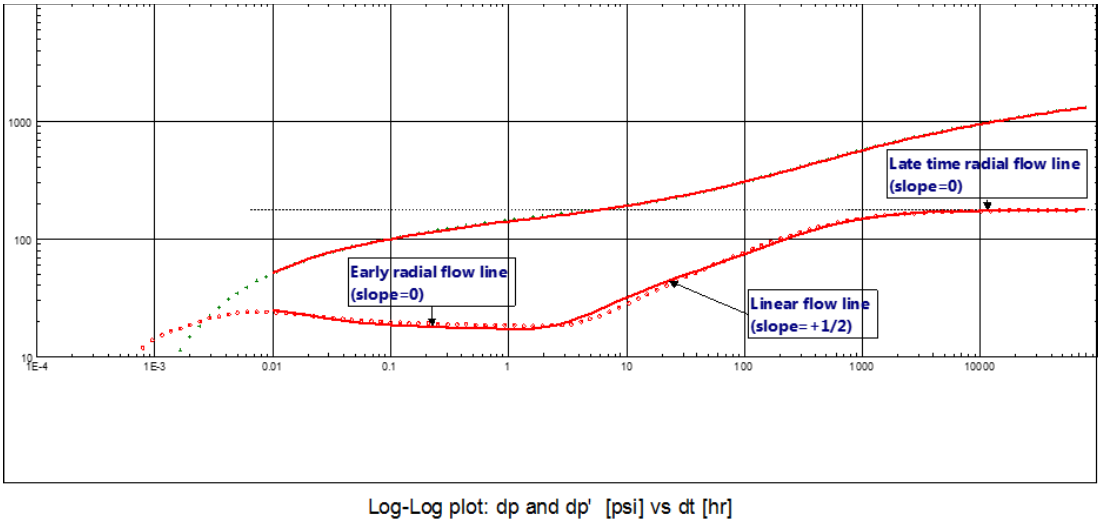

Figure 8. Pressure and pressure derivative diagram of the horizontal well after performing matching procedure

4. Results and discussions

In this section the effect of three critical parameters on pressure and pressure derivative diagrams in a nominated horizontal well are being discussed respectively as follow:

4.1. Effect of variation of vertical to horizontal permeability (K_z/K_r)

Counting on pressure curves in Figure 9, it reveals that the more the value of parameter K_z/K_r, the pressure diagram will be lower. Besides, as shown in the pressure derivative in Fig. 9, as the value of parameter K_z/K_r goes higher, the propagation speed of initial radial flow in the vertical direction will be more. Consequently, the initial radial flow reaches the upper and lower boundaries, sooner. This causes the initial radial flow to be shorter leading to the earlier start of a linear flow and its shorter duration.

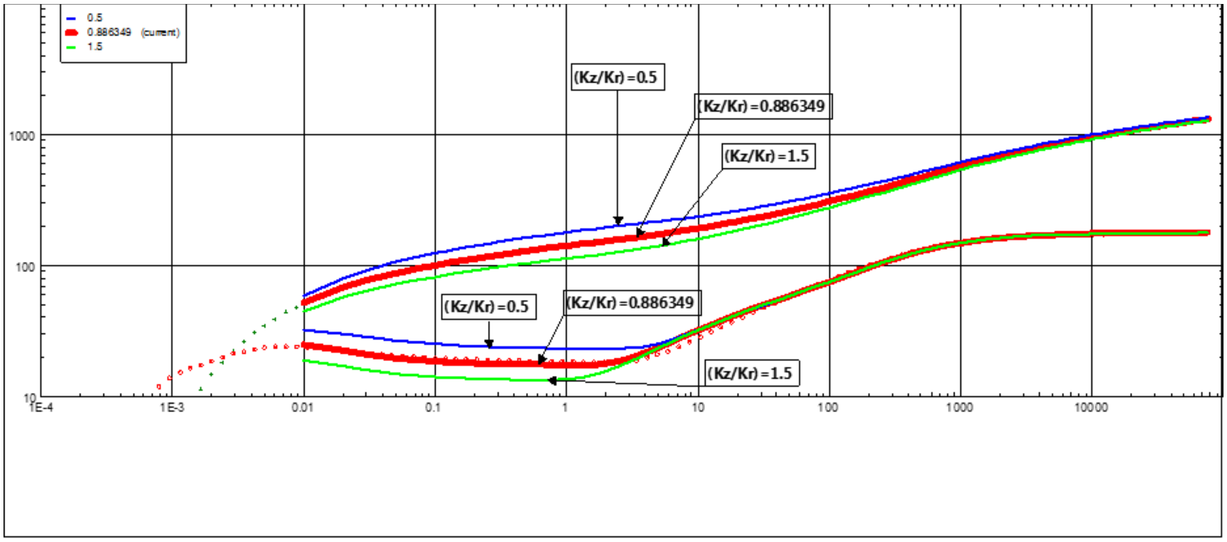

Sensitivity to kz/kr: dp and dp' [psi] vs dt [hr]

Figure 9. The effect of variation of the vertical to horizontal reservoir permeability (K_z/K_r) on the pressure and pressure derivative diagrams in a horizontal well

4.2. Effect of skin factor (S) variations

As shown in pressure diagrams in Fig. 10, the more the *S* parameter, the pressure diagram will be higher. Moreover, as observed in the pressure derivative diagrams in Figure 10, the higher the *S* parameter value, the height of hump will be larger. Following the mentioned trend, initial radial flow delays and its duration decreases, too. Additionally, as shown in Figure 10, when the *S* parameter goes to higher values, the distance between the two pressure and the pressure derivative graphs will be also higher.

4.3. Effect of variation of the horizontal length of the well (L_w)

In Figure 11 the pressure graphs is plotted for the sensitivity analysis on L_w parameter. From this figure, it can be seen that as the L_w parameter goes higher, the pressure diagram will be lower the pressure diagram.

Meanwhile, as in the pressure derivative diagrams in Figure 11, it is indicated that as long as the value of L_w parameter reach higher, the level of initial radial and linear flow periods will be lower, and the period of linear flow will be longer. Those illustrations can be a reason that the final radial flow begins later in compare to other flow regimes.

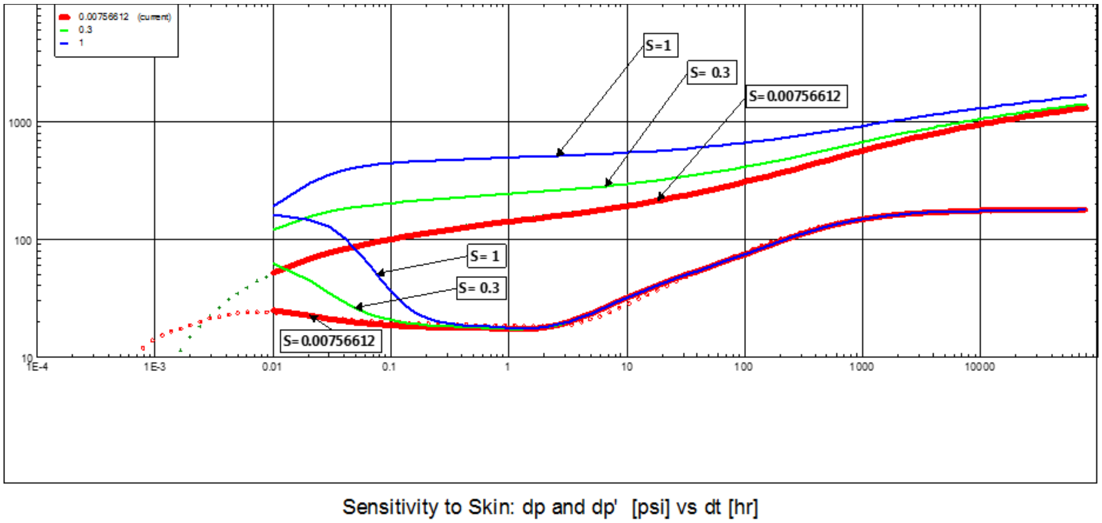

Figure 10. Effect of the skin factor parameters (S) on the pressure and the pressure derivative diagrams of a horizontal well

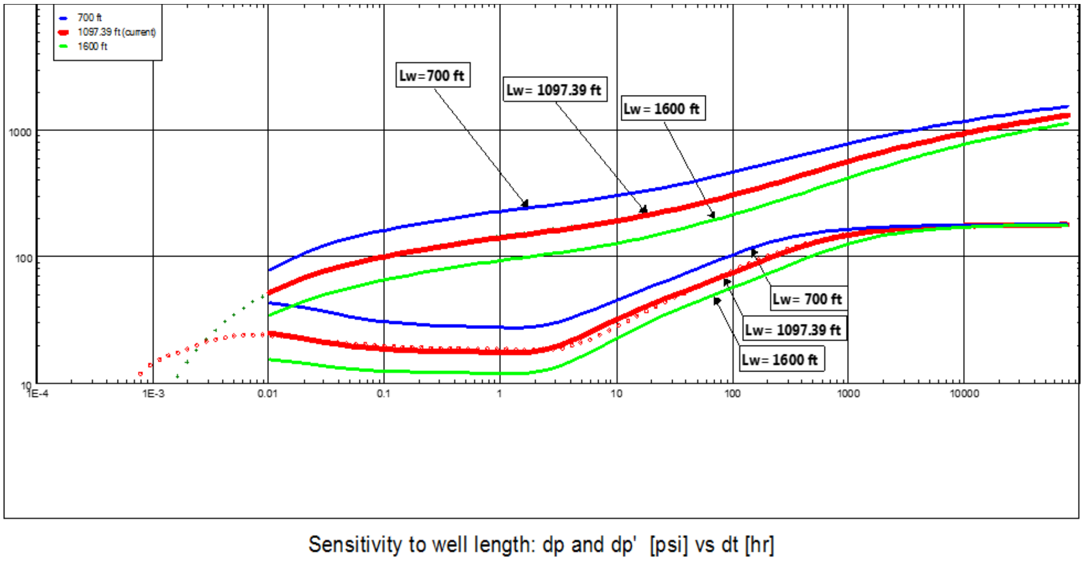

Figure 11. Effect of variation of the horizontal length of the well (L_w) on pressure and the pressure derivative diagrams of a horizontal well

5. Conclusions

Three parameters which affecting the pressure and pressure derivative diagrams (known as (K_z/K_r), (S) and the L_w), were subjected for sensitivity analysis in this study and some results were achieved. The results indicated that by increasing the parameter K_z/K_r increases, the pressure diagram is lowered. Also, considering the pressure derivative diagram, the higher the parameter K_z/K_r, the sooner the initial radial flow is over so that the linear flow starts earlier and its duration is longer. In contrast, as the value of the parameter S increases, the pressure graph shifts upward. In the pressure derivative diagram it indicated that, the larger S parameter values, the higher the hump height. Additionally, the initial radial flow begins later, and its time period is shorter. The higher values of S parameter it is shows the same trend for the distance between the two pressure and the pressure derivative graphs which will be higher too. In contrast, the pressure diagram shifts downward with an increase in parameter L_w. Furthermore, the higher the parameter L_w, the lines of the pressure derivatives of the initial radial and linear flow periods will be lower. Besides, the duration of the linear flow becomes longer, resulting in the later start of the final radial flow.

References

[1] Joshi SD. Horizontal and Multi-Lateral Wells: Performance Analysis-An Art or a Science. Journal of Canadian Petroleum Technology, 2000; 39(10): 19-23.

[2] Joshi SD. Horizontal Wells: Successes and Failures. Journal of Canadian Petroleum Technology, 1994; 33(3): 15-18.

[3] Kuchuk FJ. Well Testing and Interpretation for Horizontal Wells. Journal of Petroleum Technology, 1995; 47(1): 36-41.

[4] Horne RN. Modern Well Test Analysis: A Computer-Aided Approach, 2nd ed.; Petroway Inc.: Palo Alto, 1995; Chapter 7; p. 142.

[5] Kuchuk FJ, Goode PA, Brice BW, Sherrard DW and Thambynayagam M. Pressure Transient Analysis for Horizontal Wells. Journal of Petroleum Technology, 1990; 42(8): 974-984.

To whom correspondence should be addressed: Dr. Arash Pourabdol Shahrekordi, Department of Petroleum and Chemical Engineering, Science and Research Branch, Islamic Azad University, Tehran, Iran, E-mail-Poorabdol66@yahoo.co.uk

Petroleum and Coal

Article **Open Access**

STATIC BIOLEACHING OF PC BOARDS BY *ACIDITHIOBACILLUS FERROOXIDANS*

Milan Semerád[1]*, Hana Vojtková*[2]*, Alžbeta Takáčová*[1,3]*, Slavomír Čerňanský*[1]*, Ladislav Danč*[3]*, Tomáš Mackuľak*[4]

[1] *Department of Environmental Ecology, Faculty of Natural Sciences, Comenius University in Bratislava, Ilkovičová 6, 842 15 Bratislava, Slovakia*
[2] *Institute of Environmental Engineering, Faculty of Mining and Geology, Technical University of Ostrava, 17. listopadu 2172/15, 708 00 Ostrava, Czech Republic*
[3] *VÚRUP, a.s., Vlčie Hrdlo, 820 01 Bratislava, Slovakia*
[4] *Department of Environmental Engineering, Faculty of Chemical and Food Technology, Slovak University of Technology in Bratislava, Radlinského 9, 812 37 Bratislava, Slovakia*

Received March 29, 2019; Accepted June 12, 2019

Abstract

Printed circuit boards (PC board) incorporated in most electrical and electronic equipment comprise metals, polymers, ceramics and toxic substances, and herein we used stationary bioleaching by *Acidithiobacillus ferrooxidans* to mobilise economically valuable metals and toxic elements from PC boards. The bioleaching experiments were performed in 250 mL Erlenmeyer flasks with 95 mL 9K medium, 5 mL inoculum and 1 g of non-sterile PC board fine powder. All flasks were cultivated stationary at 25°C for 10 or 20 days. The highest leaching efficiencies of 29 % Al, 36 % Cu, 25 % Ni, 3 % As, 45 % Cd, 17 %, Pb and 6 % Sb were recovered after 20 days bioleaching. However, these percentages obtained after 20 days bioleaching were only 4–5 % higher than the recoveries after 10 days, and precipitation of jarosite caused immobilisation of soluble metals in the medium. Our results ultimately established that static PC board bioleaching by *A. ferrooxidans* at laboratory temperature is relatively ineffective in extracting these elements.

Keywords*: Printed circuit boards, Bioleaching, Acidithiobacillus ferrooxidans, Metals, Toxic elements.*

1. Introduction

Electronic waste (e-waste) proceeds from discarded devices that use electricity; and these devices include computers, televisions, washing machines, refrigerators and cell phones [1]. Moreover, the rapid technological development in recent decades has led to a significant increase in the diversity and public consumption of these electronic and electrical devices, [2] and their reduced lifetime and high assembly costs have produced increased e-waste. This has, therefore, made e-waste the fastest growing waste stream with an estimated worldwide annual production of 50 million tonnes [3].

The basic component of most electronic and electrical devices is a printed circuit board (PC board) which forms a platform for assembling components and provides connections between the internal components [4]. Although over 68 % of the PC board weight consists of non-metallic components such as plastics, glass and ceramics, they also contain approximately 28–32 % of economically valuable metals including Al, Cu, Fe and Ni. Their main environmental hazard, however, comprises the content of toxic substances such as chlorinated and brominated flame retardants, epoxy resins and heavy metals [5]. PC board recycling is therefore imperative from both economic and environmental aspects.

The PC boards are currently recycled by pyrometallurgical, mechanical or hydrometallurgical processes. While hydrometallurgical processes mainly obtain metals from PC boards by leaching with concentrated inorganic acids, pyrometallurgical processes use PC board heat treatment and the resultant roasting, smelting and mechanical processes involve grinding and subsequent separation of metals from the non-metallic materials [6-8]. All these processes are energy intensive with high cost and the pyrometallurgical PC board processing releases dust and toxic gases such as dioxins and furans into the atmosphere [8-9].

In addition, the use of bioleaching to obtain metals from ores and wastes has attracted great interest in recent decades. These are essentially hydrometallurgical processes using microorganisms such as bacteria, archaea and fungi, which can increase the solubility of metals in substrates. The natural ability of microorganisms to oxidise or utilise organic and inorganic substrates in these processes produces a metal dissolving agent [10], and this metal recovery method is very promising because of the low operating costs, the creation of smaller volumes of less toxic wastewater and zero air contamination [11-13].

The acidophilic *Acidithiobacillus ferrooxidans* has proven one of the most important agents in industrial bioleaching of copper from low-concentrated sulphide ores [14]. This chemoautotrophic species acquire energy by oxidising Fe^{2+} ions, elemental sulphur and reduced sulphur forms to produce Fe^{3+} and sulfuric ions [15.16]. The strong acidification present in bioleaching by these bacteria combines with the strong Fe^{3+} oxidising agent to dissolve most metals from the substrates [17].

Moreover, several studies investigating PC board bioleaching by *A. ferrooxidans* have demonstrated high metal recovery efficiency. However, the bioleaching experiments were performed by continuous agitation on shakers at high temperatures [18-25], and both the high energy and operating costs involved have restricted PC board used in industrial metal extraction.

This study aims to provide an energy saving method which can be used in industrial metal recovery, and we, therefore, performed stationary bioleaching of non-sterile PC boards at laboratory temperature for 10 and 20 days. The recovery efficiency of economically valuable metals (Al, Cu and Ni) and toxic elements (As, Cd, Pb, and Sb) was then compared with the studies bioleaching PC boards on shakers at high temperatures.

2. Experimental

2.1. Materials and methods

2.1.1. Printed circuit board

The PC boards used in this study were demounted from personal computers. Initially, the capacitors, resistors, chips, fans and heatsinks were removed, and the PC boards were then ground in a laboratory vibrating mill WM4 (Czech Republic). The obtained PC board powder was sieved through a <200 µm mesh, and the resultant fine powder was used in all bioleaching experiments. Table 1 lists the content of the selected elements in this powder.

Table 1. Chemical composition of PC board fine powder used in this study

Element	Content (%)	Element	Content (%)
Al	0.821 ± 0.057	Ni	0.567 ± 0.039
As	0.215 ± 0.015	Pb	2.108 ± 0.169
Cd	0.015 ± 0.001	Sb	0.084 ± 0.051
Cu	7.368 ± 0.663		

All values are in mean (n = 3) ± S.D.

2.1.2. Microorganism and culture condition

The pure culture of *A. ferrooxidans* was obtained from the Institute of Environmental Engineering at the VŠB - Technical University of Ostrava. The standard used to grow *A. ferrooxidans* was 9K medium containing: 3 g L^{-1} $(NH_4)_2SO_4$, 0.5 g L^{-1} K_2HPO_4, 0.5 g L^{-1} $MgSO_4·7H_2O$, 0.1 g L^{-1} KCl, Ca $(NO_3)_2$ 0.01 g L^{-1} and 44.22 g L^{-1} $FeSO_4·7H_2O$, and the medium pH of was adjusted to 2 with H_2SO_4.

2.1.3. Bioleaching experiments

The bioleaching experiments were conducted in 250 mL Erlenmeyer flasks containing 95 mL of 9K medium and 1 g of non-sterile PC boards fine powder. The flasks were inoculated with 5 mL of pure *A. ferrooxidans* inoculum and cultivated stationary at 25°C for 10 and 20 days. The pH was measured periodically, and each bioleaching experiment was performed in triplicate.

2.1.4. Analytic methods

PC board fine powder was dissolved in aqua regia for element analysis: 1 g PC board sample and 40 mL of aqua regia were combined in 250 mL Erlenmeyer flasks, and the mixture was left to stand for 24 hours before centrifugation at 500 rpm for 15 minutes. The supernatant was stored at 4°C for element concentration analysis, and after bioleaching, the PC board, the samples were passed through 0.22 µm nitrocellulose membrane filters to remove cells and precipitates. The filtrate was then stored at 4°C until elements concentration analysis. The concentrations in the supernatant and filtrate were determined by inductively coupled plasma optical emission spectrometry (ICP-OES, ThermoFisher iCap 7600, USA) at the following wavelengths (nm): A1 (396.153), As (193.696), Cd (228.802), Cu (327.393), Ni (231.604), Pb (220.353) Sb (206.836). The pH was measured by digital pH metre (WTW pH 3210 Germany), and element recovery was calculated by the following equation; C_F/C_E*100; where C_F is the concentration of leached elements in the solution after bioleaching experiments (mg L^{-1}), and C_E is the concentration of elements in the PC board before the bioleaching experiments (mg kg^{-1}).

3. Results and discussion

3.1. Variation in pH during PC board bioleaching

Figure 1 shows variations in solution pH during PC board bioleaching by *A. ferrooxidans*. Here, the pH increased throughout the experiment from initial pH 2 to pH 3 on the 10th day and pH 4 on the 20th day. The factors causing pH increase were proton consumption by both the alkaline substances present in the PC board [6,21] and during bacterial oxidation of Fe^{2+} ions to Fe $^{3+}$ (1) [2,13].

$$2Fe^{2+} + 0,5O_2 + 2H^+ \xrightarrow{A.\ ferrooxidans} 2Fe^{3+} + H_2O \qquad (1)$$

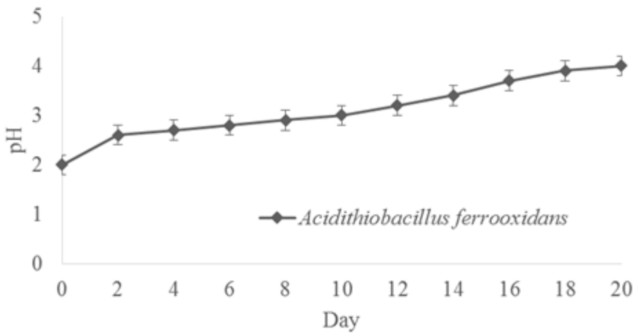

Fig. 1. Variation in pH during PC boards bioleaching by *Acidithiobacillus ferrooxidans*. All values are in mean (n = 3) ± S.D.

3.2. Recovery of economically valuable metals

The Al, Cu and Ni metals accounted for approximately 9 % of the PC boards used in the bioleaching experiments (Tab. 1). Most of these are present in elemental form, and oxidative leaching is therefore effective for their extraction. The Fe^{3+} ions produced by bacterial oxidation are strong oxidizing agents. These generate a redox potential of 0.77 V in aqueous solution [12,16,19] and can oxidise the elemental metals present in PC boards to their soluble cations while concurrently being reduced to Fe $^{2+}$ ions (2) [6,18,26].

$$M^0 + Fe^{3+} \rightarrow M^{2+} + Fe^{2+} \qquad (2)$$

Although the produced Fe^{2+} ions are re-oxidised by the bacteria and continuously dissolve the metals from PC boards [18,19], the increasing Fe^{3+} ion concentration, higher pH values and progressive bioleaching time led to hydrolysis of the accumulated Fe^{3+} ions and formation of the red-brown $KFe_3(SO_4)(OH)_6$ jarosite precipitate (3, 4). This jarosite then reduced the concentration of iron in the medium which is required for the oxidation of metals from PC boards and acts as a source of bacterial energy [12,18].

$$Fe^{3+} + H_2O \rightarrow Fe(OH)_3 + H^+ \tag{3}$$

$$Fe(OH)_3 + SO_4^{2-} + Fe^{3+} + H_2O + K^+ \rightarrow KFe_3(SO_4)(OH)_6 + H^+ \tag{4}$$

The metal dissolution during PC boards bioleaching occurs by direct oxidation with atmospheric oxygen in an acidic environment, and this mechanism was confirmed by leaching PC boards with sulfuric acid and pure 9K medium. However, the amount of leached metals was minimal at less than 2 % (5) [12,19].

$$M^0 + 4H^+ + O_2 \rightarrow Me^{2+} + 2H_2O \tag{5}$$

The experiment results reveal higher metal leaching efficiency after longer bioleaching by *A. ferrooxidans*. While 25 % Al, 27 % Cu and 20 % Ni were leached into solution after 10 days bioleaching, the recovery increased to 29 % Al, 36 % Cu and 25 % Ni after 20 days (Fig. 2).

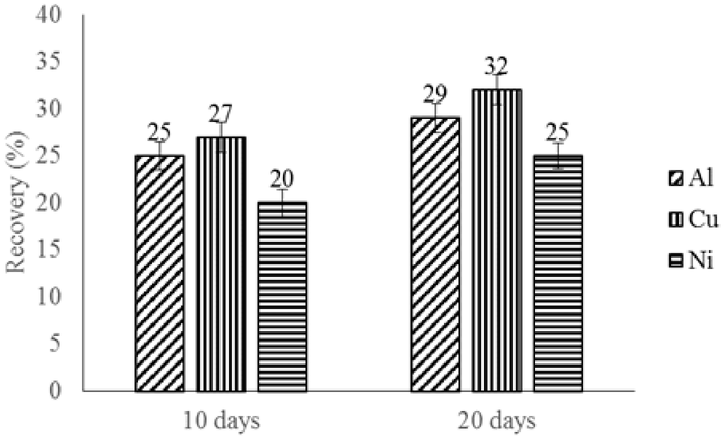

Fig. 2. Recovery of Al, Cu and Fe from printed circuit boards (PC boards) after 10 and 20 days bioleaching by *Acidithiobacillus ferrooxidans*. All values are in mean (n = 3) ± S.D.

However, this was only a slight increase in metal recovery after prolonged bioleaching, and most likely due to the precipitation of jarosite, which immobilises metals dissolved in solution [12,18,21]. In support, Choi *et al.* reported higher copper concentration in jarosite precipitates than in solutions after bioleaching of PC boards by *A. ferrooxidans* [27] and Zhu *et al.* observed jarosite coating on PC board particles which prevented leaching agent penetration to the PC board metals [12].

In addition, stationary PC board bioleaching at 25°C temperature by *A. ferrooxidans* has been shown to be inefficient in metal extraction compared to shaker experiments at high temperatures; where PC boards bioleaching experiments by *A. ferrooxidans* on shakers at 130–200 rpm and higher 28–30°C temperatures provided recovery of 75.4–90 % Al, 80–100 % Cu and 73–100 % Ni (Tab. 2).

A. ferrooxidans species optimal temperature ranges from 25–40°C, and the higher temperatures accelerate bacterial metabolic activity and chemical reaction rates [28]. Moreover, shaker bioleaching results in continuous media mixing which increases gas exchange and medium oxygenation [29], and *A. ferrooxidans* uses dissolved oxygen as an electron acceptor to obtain energy by oxidising Fe^{2+} ions, elemental sulphur and reduced sulphur compounds [15-16]. The bacterial concentration and oxidation rate then increase with increasing dissolved oxygen in the medium [30].

Table 2. PC board bioleaching experiments by *Acidithiobacillus ferroxidans* with their experimental conditions and highest recoveries

Bioleaching (days)	Temperature (°C)	Shaker (rpm)	Recovery (%)	Literature
18	30	170	94 Cu, 81 Ni, 64 Pb	[18]
9	28	150	99 Cu, 74 Pb	[19]
20	30	170	100 Cu, 100 Ni	[20]
10	30	150	90 Al, 90 Cu, 90 Ni, 0 Pb	[21]
7.25	30	160	85.24 Al, 96,75 Cu	[22]
3	30	170	75.4 Al, 96,8 Cu	[23]
10	32	200	80 Cu, 73 Ni, 72 Pb	[24]
20	30	170	100 Cu, 100 Ni	[25]

Although abiotic oxidation of Fe^{2+} to Fe^{3+} ions can occur during bioleaching due to high dissolved oxygen concentrations (6), this is almost negligible at pH below 4 [31].

$$M^0 + 4H^+ + O_2 \rightarrow Me^{2+} + 2H_2O \tag{6}$$

3.3. Recovery of toxic elements

The toxic elements As, Cd, Pb and Sb which account for more than 2 % of PC board are most commonly present as alloys (Tab. I). The *A. ferrooxidans* bioleaching recovery results revealed 2 % As, 32 % Cd, 13 % Pb and 4 % Sb recovery after 10 days bioleaching and this increased to.3 % As, 45 % Cd, 17 % Pb and 6 % Sb after 20 days bioleaching (Fig. 3). Cd was, therefore, most efficiently recovered from PC boards by *A. ferrooxidans* bioleaching.

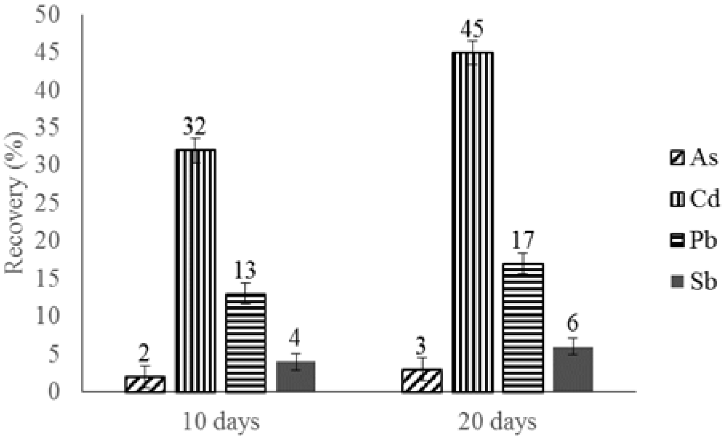

Fig. 3. Recovery of As, Cd, Pb and Sb from printed circuit boards (PC boards) after 10 and 20 days bioleaching by *Acidithiobacillus ferrooxidans*. All values are in mean (n = 3) ± S.D

Similar results were recorded by Karwowska *et al.* who reported over 93% Cd extracted by a mixed acidophilic sulphur-oxidizing bacterial culture after 2 days PC board bioleaching on a 100 rpm shaker at laboratory temperature [32]. Liang *et al.* found 72 % Pb recovery from PC board bioleaching by *A. ferrooxidans* at 32°C and 200 rpm shaking [24]. In contrast, Brandl *et al.* experienced different results with no PC board Pb bioleaching by *A. ferrooxidans* using 150 rpm shaking at 30°C, and the Pb dissolved in the solution precipitated as $PbSO_4$ [21].

The latest literature reviews reveal no research has concentrated on the mobilisation of As and Sb toxic semimetals by microbial leaching of PC boards. Previously, only low concentrations of these metals were recovered even after 20 days bioleaching, thus indicating their poor solubility from PC boards alloys. Moreover, Savvilotide *et al.* obtained similar results from leaching PC boards with a mixture of concentrated inorganic acids at different temperatures. These authors found that 0.16 % was their highest As recovery following one-hour leaching of PC boards at 80°C with a mixture of concentrated acids and water in the 5:1:4 ratio of HCl: HNO_3:

H_2O. In addition, the highest Sb recovery they observed was 0.5 % after one-hour leaching PC boards with a mixture of hydrochloric acids and water HCl: H_2O (3:2) at 80°C [33].

4. Conclusions

The stationary PC boards bioleaching by *A. ferrooxidans* at laboratory temperature proved inefficient for element extraction. The lower than expected element recovery was most likely due to the low dissolved oxygen concentration in the medium, which is so important for bacterial metabolism, and also the lower bioleaching temperature, which slowed bacterial metabolic activity.

In conclusion, the highest recovery of economically valuable metals of 29 % Al, 36 % Cu, 25 % Ni and toxic elements 3 % As, 45 % Cd, 17 % Pb and 6 % Sb occurred after 20 days bioleaching, and although this was an improvement on the recovery rate after the shorter 10 day bioleaching, the increased recovery percentages measured only 4-5 %. Finally and most importantly, the jarosite precipitation emanating from higher pH values and longer bioleaching period retarded recovery rates by immobilising the metals dissolved in solution.

References

[1] Robinson BH. Sci. Total Environ,. 2009; 408(2): 183-191.
[2] Baldé CP, Wang F, Kuehr R, Huisman J. The Global E-waste Monitor 2017: Quantities, Flows and Resources; United Nations University: Tokyo, 2015; chapter 1; p. 13.
[3] Baldé CP, Forti V, Gray V, Kuehr R, Stegmann P. The Global E-waste Monitor 2017: Quantities, Flows and Resources; United Nations University: Bonn, 2017; Chapter 3; p. 49.
[4] Duan H. Hou K, Li J, Zhu X. J. Environ. Manage., 2011; 92(3): 392-399.
[5] Sohali J, Muniyandi SK, Mohamad SS. J. Emerging Trends Eng. Appl. Sci. 2012 ; 3(1): 12-18.
[6] Yang T, Xu Z, Wen J, Yang L. Hydrometallurgy, 2009; 97(1-2): 29-32.
[7] Tuncuk A, Stazi V, Akcil A, Yazici EY, Deveci H. Miner. Eng., 2012; 25(1): 28-37.
[8] Cui J, Zhang L. J. Hazard. Mater., 2008; 158(2-3): 228-256.
[9] Wang H, Zhang S, Li B, Pan D, Wu Y, Zuo T. Resour., Conserv. Recycl., 2017; 126: 209-218.
[10] Deveci H. Ball T. Miner. Process. Extr. Metall. Rev., 2010; 31(3): 176-190.
[11] Olson GJ, Brierley JA, Brierley CL. Appl. Microbiol. Biotechnol., 2003; 63(3): 249-257.
[12] Zhu N, Xiang Y, Zhang T, Wu P, Dang Z, Li P, Wu J. J. Hazard. Mater., 2011; 192(2): 614-619.
[13] Shah MB, Tipre DR, Purohit MS, Dave SR. J. Biosci. Bioeng., 2015; 120(2): 167-173.
[14] Johnson DB. Curr. Opin. Biotechnol., 2014; 30: 24-31.
[15] Johnson DB, Hallberg KB. Adv. Microb. Physiol., 2008; 54: 201-255.
[16] Nemati M., Harrison STL, Hansford GS, Webb C. Biochem. Eng. J., 1998; 1(3): 171-190.
[17] Wu A, Yin S, Wang H, Qin W, Qiu G. Bioresour. Technol., 2009; 100(6): 1931-1936.
[18] Priya A, Hait S. Hydrometallurgy, 2018; 177: 132-139.
[19] Wang J, Bai J, Xu J, Liang B. J. Hazard. Mater., 2009; 172(2-3): 1100-1105.
[20] Arshadi M, Mousavi SM. Sep. Purif. Technol., 2015; 147: 210-219.
[21] Brandl H, Bosshard R, Wegmann M. Hydrometallurgy, 2001; 59(2-3): 319-326.
[22] Yang C, Zhu N, Shen W, Zhang T, Wu P. J. Mater. Cycles Waste Manage., 2017; 19(1): 247-255.
[23] Yang Y, Chen S, Li S, Chen M, Chen H, Liu B. J. Biotechnol., 2014; 173(10): 24-30.
[24] Liang G, Mo Y, Zhou Q. Enzyme Microb. Technol., 2010; 47(7): 322-326.
[25] Arshadi M, Mouusavi SM. Bioresour. Technol., 2014; 174: 233-242.
[26] Bosecker K. FEMS Microbiol. Rev., 1997; 20(3-4): 591-604.
[27] Choi M-S, Cho K-S, Kim D-S, Kim D-J. J. Environ. Sci. Health, Part A: Toxic/Hazard. Subst. Environ. Eng., 2004; 39(11-12): 2973-2982.
[28] Daoud J, Karamanev D. Miner. Eng., 2006; 19(9): 960-967.
[29] Rao DV, Shivannavar CT, Gaddad SM. Indian J. Exp. Biol., 2002; 40: 319-324.
[30] Gleisner M, Herbert RB, Kockum PCF. Chem. Geol., 2006; 225(1-2): 16-29.
[31] Johnson DB, Hallberg KB. Sci. Total Environ., 2005; 338(1-2): 3-14.
[32] Karwowska E, Andrzejewska-Morzuch D, Lebkowska M, Tabernacka A, Wojtkowska M, Telepko A, Konarzewska A. J. Hazard. Mater., 2014; 264: 203-210.
[33] Savvilotidou V, Hahladakis JN, Gidarakos E. Waste Manag., 2015; 45: 314-324.

To whom correspondence should be addressed: Dr. Milan Semerád, Department of Environmental Ecology, Faculty of Natural Sciences, Comenius University in Bratislava, Ilkovičová 6, 842 15 Bratislava, Slovakia

Article **Open Access**

INVESTIGATION OF RELATIONS OF PROPERTIES OF STRAIGHT RUN AND H-OIL UNCONVERTED VACUUM RESIDUAL OILS

Dicho Stratiev[1], Ivelina Shishkova[1], Ekaterina Nikolaychuk[1], Vassia Atanassova[2], Krassimir Atanassov[2]

[1] *LUKOIL Neftohim Burgas, Bulgaria*
[2] *Dept. of Bioinformatics and Mathematical Modelling, Institute of Biophysics and Biomedical Engineering, Bulgarian Academy of Sciences, 105 Acad. G. Bonchev Str., Sofia 1113, Bulgaria*

Received April 8, 2019; Accepted June 13, 2019

Abstract

24 straight run vacuum residual oils (SRVROs) and 28 H-Oil vacuum tower bottom products (VTBs) obtained during processing different blends of the 24 SRVROs in the LUKOIL Neftohim Burgas (LNB) ebullated bed vacuum residue (EBVR) H-Oil hydrocracking unit were analyzed for their physical and chemical properties. It was found that in both primary and secondary vacuum residual oils (VROs), the density and the Conradson carbon content strongly correlate. The properties of H-Oil VTB Conradson carbon content and density correlate with the VTB hydrogen content and H/C atomic ratio in the same manner as the SRVROs. It was also confirmed that the VRO saturate content can be predicted from data of VRO density and the use of the second order polynomial fits for both SRVROs and H-Oil VTBs. It was established that the lower density VROs have a lower density, a higher hydrogen content of asphaltenes, resins and of aromatics than those of the higher density VROs. The H-Oil VTBs have higher density asphaltenes and lower density maltenes than the SRVROs, which can explain the lower colloidal stability of the H-Oil VTBs. Dissimilar to the SRVROs the H-Oil VTB viscosity does not correlate with the asphaltene content. Instead, it correlates with the saturated content. While the SRVRO softening point strongly correlates with its viscosity, such a relation does not exist for the H-Oil VTBs, which suggests different rheological properties of the H-Oil VTBs in contrast to these of the SRVROs.

***Keywords**: Vacuum residue; Vacuum residue hydrocracking; SARA; Asphaltenes; correlations.*

1. Introduction

The International Maritime Organisation (a branch of the UN) has stated that as of the 1 January 2020 all ships must reduce their sulphur emissions from 3.5% thresholds to 0.5%. The regulation has already been passed, and any attempt to change the regulation would potentially take another 22 months (i.e. the regulation will go through on the stated date). The aim of this regulation is to reduce the emission of sulphur dioxide (which results in acid rain and environmental damage) [1].

This new regulation presents a big challenge for the petroleum refining industry since the available technologies for the time being are not capable of providing solutions for the production of residual oil bunker fuel whose sulphur content must be less than 0.5%. Therefore new ways for utilization of the unconverted residual oils from the residue conversion processes have to be searched. In order to find a new application of the unconverted residual oils, one needs to know more about their properties and the relations between them.

This study is a continuation of our recent work [1] in which the effect of vacuum residual feedstock properties on the ebullated bed vacuum residue H-Oil hydrocracking (EBVRHC) conversion at approximately the same level of sediments of 0.4% in the atmospheric tower bottom (ATB) product was investigated. A relation of vacuum residual feedstock properties to the conversion that is achievable in the EBVRHC at sediments of about 0.4% in the H-Oil ATB product was found. However, the properties of the obtained vacuum tower bottom (VTB) products were not discussed there. The current study aims at investigating the relations between properties of 28 H-Oil VTB products obtained in the LUKOIL Neftohim Burgas (LNB) ebullated bed vacuum residue (EBVR) H-Oil hydrocracking unit and juxtaposes these H-Oil VTB properties relations to those of the vacuum residual oils extracted from 15 crude oils and 3 imported atmospheric residues, whose blends were processed in the LNB EBVR H-Oil hydrocracking unit.

The aim of this work is to investigate the relations of properties of the straight run vacuum residual oils and those of the obtained thereof unconverted vacuum residual oils in the LNB EBVR H-Oil hydrocracking unit and define the similarity and the dissimilarity between them in terms of their further usage.

2. Experimental

The studied straight run vacuum residual oils (SRVROs) were obtained by TBP distillation of crude oils and atmospheric residual oils (AROs) which have been processed in the LNB refinery. The atmospheric part of the TBP distillation was performed in accordance with ASTM D-2892, while the vacuum part of the TBP distillation was carried out in accordance with ASTM D-5236. The SRVROs were the fractions of the crudes or atmospheric residual oils which boil above 540°C.

The secondary H-Oil vacuum residual oils were obtained at the LNB H-Oil vacuum residue hydrocracking during processing SRVROs which were produced from blends of crudes and AROs under study. The methods used to measure the vacuum residue properties are explained in our recent work [2]. The density of the vacuum residual oils and their C_5- and C_7-asphaltenes were measured indirectly from the densities of a series of solutions of asphaltenes and vacuum residues in toluene at different concentrations as described in [2]. Solutions of asphaltene in toluene at concentrations up to an asphaltene mass fraction of 3% were prepared. Solutions of vacuum residues in toluene at concentrations up to a vacuum residue mass fraction of 6% were prepared.

The density of the SRVROs was also measured by pycnometer according to ASTM D 941. Properties of crudes and AROs and the obtained thereof SRVROs are presented in Table 1. Table 1 includes more than one set of data for some crude oils. They are related to different cargoes of the same crude and are indicators for some variability in some properties of the same crude. Table 2 summarizes the properties of the 28 H-Oil vacuum tower bottom products under study. The data about vacuum residue densities reported in Tables 1 and 2 are obtained by dilution with toluene.

3. Results and discussion

In order to find a statistically meaningful correlations between the different studying properties, an intercriteria analysis (ICrA) was performed. More about the application of ICrA for crude and oil fractions is discussed in [3]. The correlations between the studied properties are called: 'positive consonance', 'negative consonance' or 'dissonance' [3]. The values of positive consonance with μ = 0.75÷1.00 means a statistically meaningful positive relation, where the strong positive consonance exhibits values of μ = 0.95÷1.00, and the weak positive consonance exhibits values of μ = 0.75÷0.85. Respectively, the values of negative consonance with μ = 0.00÷0.25 means a statistically meaningful negative relation, where the strong negative consonance exhibits values of μ = 0.00÷0.05, and the weak negative consonance exhibits values of μ = 0.15÷0.25. Table 3 presents data of ICrA matrix of the statistically meaningful relations of properties of the studied crudes and derived thereof vacuum residual oils.

It is evident from the data in Table 3 that the crude density strongly correlates with the vacuum residual oil content (μ = 0.98), weakly correlates with the vacuum residue viscosity (μ = 0.80), and moderately correlates with vacuum residue penetration (μ = 0.90). The crude sulphur content moderately correlates with the vacuum residual oil properties: density (μ = 0.93); Conradson carbon content (CCR) (μ = 0.92); saturates content (μ = 0.10); C_7-asphaltene content (μ = 0.90); C_5-asphaltene content (μ = 0.88); density of C_5-deasphalted oil (DAO C_5 d_{15}) (μ = 0.92); density of C_7-deasphalted oil (DAO C_5 d_{15}) (μ = 0.88); density of C_5-

asphaltenes (d_{15} C_5 asp.) (μ = 0.85); viscosity (μ = 0.87); softening point (SP) (μ = 0.89); and penetration (μ = 0.06). The crude sulphur content strongly correlates with the vacuum residue sulphur content (μ = 0.98). These findings are in line with the conclusions of Swafford, and McCarthy [4] according to which the sulphur content correlates with the aromaticity. The higher the crude sulphur content the higher the vacuum residue density, and Conradson carbon content (which are known to correlate with the aromaticity [5]), and the lower the saturate content. It is interesting to note here that the vacuum gas oil (VGO) property density moderately correlates with the vacuum residual (VR) oil properties density (μ = 0.93); CCR (μ = 0.86); sulphur (μ = 0.94); saturate content (μ = 0.12); DAO C_5 d_{15} (μ = 0.91); DAO C_7 d_{15}) (μ = 0.87); d_{15} C_5 asp. (μ = 0.89); d_{15} C_7 asp. (μ = 0.80); SP (μ = 0.86); and penetration (μ = 0.07). These correlations of the VGO density with the vacuum residue properties density and Conradson carbon content suggest a feasible similarity of the aromatic structures in the VGO with those of the VR. Having in mind that the VGO is easier to characterize than the VR one may suppose that the conclusions of analyzing the VGO from a crude oil might be transferred to those of the VR from the same crude.

The VR density strongly correlates with the VR CCR (μ = 0.97) that supports the conclusion, that the correlation between these two properties can be used to verify the correctness of their measurements, stated in our recent work [5]. It should be noted here that densities of the SRVROs were measured not only by dilution with toluene but also by the use of pycnometer (ASTM D 941). The measured by pycnometer densities were found to not correlate with many of the VR properties that correlate with the density measured by dilution with toluene, and the reason is that the SRVRO density measured by dilution with toluene does not statistically meaningful correlate with the SRVRO density measured by pycnometer as depicted in Figure 1 (R<0.75).

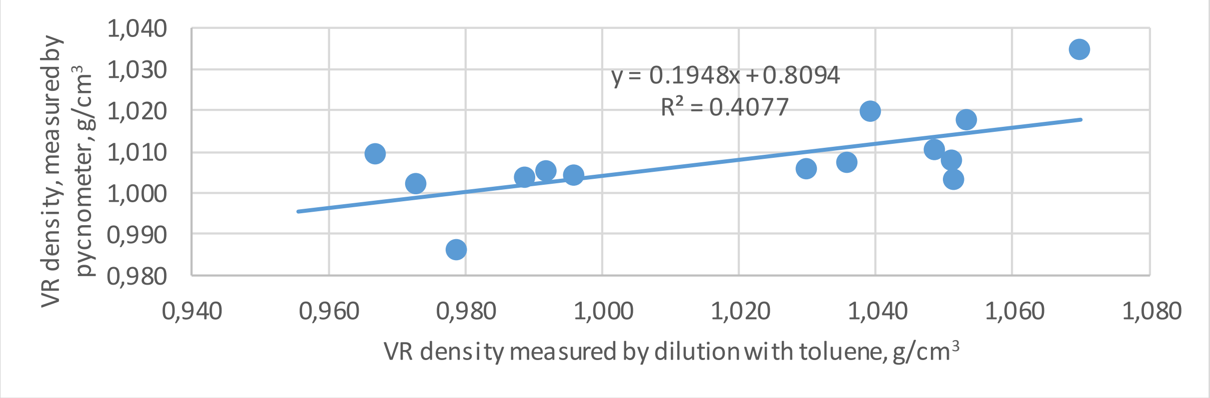

Figure 1. Relation of vacuum residue density measured by pycnometer to that measured by dilution with toluene

The SRVRO density measured by dilution with toluene strongly correlates with the SRVRO properties DAO C_7 d_{15} (μ = 0.95) and d_{15} C_5 asp. (μ = 0.95). It moderately correlates with the SRVRO properties sulphur (μ = 0.93); saturate content (μ = 0.06); DAO C_5 d_{15} (μ = 0.91); softening point (μ = 0.87); and penetration (μ = 0.07). The density weakly correlates with the content of C_7-asphaltenes (μ = 0.81); content of C_5-asphaltenes (μ = 0.84); d_{15} C_7 asp. (μ = 0.77); viscosity (μ = 0.79).

The SRVRO Conradson carbon content moderately correlates with the SRVRO properties sulphur content (μ = 0.90); saturate content (μ = 0.07); the content of C_7-asphaltenes (μ = 0.87); the content of C_5-asphaltenes (μ = 0.88); DAO C_7 d_{15} (μ = 0.90); d_{15} C_5 asp. (μ = 0.91); DAO C_7 d_{15} (μ = 0.90); viscosity (μ = 0.93); softening point (μ = 0.93); and penetration (μ = 0.07). It weakly correlates with DAO C_7 d_{15} (μ = 0.84).

Considering that the VR sulphur content strongly correlates with the crude oil sulphur content (μ = 0.98) the properties of VR that correlate with the sulphur content have been already discussed above.

Table 1. Physical and chemical properties of the crude oils and derived thereof vacuum residual oils (SRVROs)

	Urals1	Urals2	AM	AH	AH2	VD	BL	BL2	BH	KK	IH	KEB	EB	KH	NAR	IRB	KH2	KH3	CPC1	CPC2	LSCO1	LSCO2	VAR	TAR
d_{15} °C, g/cm^3	0.877	0.875	0.8721	0.889	0.892	0.8321	0.878		0.905	0.873	0.882	0.876	0.891	0.858		0.9794	0.8754	0.878	0.795	0.805	0.854	0.8469		0.959
Sulphur, %	1.53	1.39	2.48	2.91	2.97	1.97	2.85		3.86	2.65	2.27	2.64	1.76	0.81		2.71	0.65	0.40	0.55	0.63	0.57	0.59	0.91	2.16
IBP- 110 °C , wt.%	6.5	6.2	8.9	6.9	6.9	14.8	8.4		6.7	9.4	8.5	8.5	5.7	16.3			5.3	5.8	17.8	16.5	8.6	9.9		
110-180 °C , wt.%	8.6	8.7	10.8	9.1	8.9	15.7	10.5		9.0	11.8	10.1	10.3	9.1	10.9			7.6	6.0	19.5	16.8	11.4	10.7		
180-240°C, wt.%	8.7	9.4	9.1	7.5	8.1	11.0	7.7		7.8	8.5	7.9	8.8	8.9	2.3			7.7	5.8	12.7	13.1	9.1	10.2		
240-360°C, wt.%	21.0	20.8	20.4	18.7	19.9	21.4	18.9		17.7	20.2	19.6	19.9	19.0	11.8	3.4	14.5	20.6	19.0	24.1	23.2	23.1	24.6		
360-540°C, wt.%	29.0	29.0	24.6	24.8	24.5	21.6	25.2		24.0	24.4	24.8	23.9	30.2	34.2	46.7	25.5	30.8	39.1	18.1	20.0	28.1	25.6		
> 540 °C, wt.%	25.2	24.9	25.2	32.0	30.5	14.6	28.3		33.8	24.6	28.1	27.7	26.2	23.7	50.0	60.0	27.1	23.4	6.8	9.3	18.7	17.4		
VGO d_{15}, g/cm^3	0.910		0.923	0.926		0.934	0.927		0.944	0.925	0.927	0.924	0.913	0.895			0.897	0.900	0.890	0.897	0.904	0.913		0.916
VR d_{15} °C, g /cm^3	0.996	0.995	1.030	1.040	1.047	1.052	1.051	1.045	1.070	1.053	1.049	1.036	1.049	0.989	1.001	1.0421	0.9730	0.967	0.956	0.981	0.992	0.993	0.979	1.007
VR CCR, wt.%	17.5		20.7	23.6		21.4	23.8		28.9	25.2	23.9	23.3	25.5	17.1		23.5	13.6	10.9	9.2	16.0	14.0	14.9	13.5	18.8
VR sulphur, %	3.0	2.9	5.4	5.8		6.0	5.9		7.1	5.9	5.2	5.7	3.3	1.7	2.9		1.48	0.94	1.32	2.10	1.58	1.59	1.2	
Saturates, wt.%	25.6	22.4	11.8	12.4	12.0	11.7	12.3	15.0	12.3	15.2	17.0	15.0	12.0	33.0	28.7	16.9	36.9	44.5	44.4				30.4	22.4
Aromatics, wt.%	52.5	66.5	68.3	61.9	62.2	73.5	64.8	65.0	54.1	55.4	52.6	64.2	57.9	50.2	50.9	57.6	44.9	42.7	46.2	40.8		42.9	53.2	55.5
Resins, wt.%	7.8	4.9	5.3	4.4	6.1	6.4	4.9	6.2	5.8	5.0	5.0	4.2	12.6	5.7	6.7	5.9	5.8	9.8	3.8	10.3		4.5	8.1	10.0
C_7-asph., wt.%	14.1	6.3	14.6	21.3	19.9	8.5	18.0	13.8	27.7	24.3	25.4	16.6	17.5	11.1	13.7	19.6	12.3	3.0	5.6	3.4	7.8	5.6	8.3	12.1
C_5-asph., wt.%	17.6	13.9	25.5	32.9	29.5	19.5	27.7	22.5	37.0	33.1	36.2	25.7	27.3	17.8	21.3	30.2	24.5	8.7	11.9	11.0	15.5	13.1	16.3	22.1
DAO C_5 d_{15}, g/cm^3	0.969		0.991	0.983		1.024	1.005		1.014	0.997	0.981	0.997		0.965		0.992			0.942		0.970		0.957	0.975
DAO C_7 d_{15}, g/cm^3	0.977	0.985	1.007	1.011	1.031	1.037	1.023		1.027	1.013	1.004	1.008	1.024	0.979		1.010			0.949		0.978		0.965	0.987
C_5-asph. d_{15}, g/cm^3	1.147		1.166	1.177		1.182	1.195		1.180	1.191	1.194	1.168		1.116		1.179			1.070		1.135		1.111	1.135
C_7-asph. d_{15}, g/cm^3	1.132	1.172	1.191	1.158	1.204	1.244	1.204		1.201	1.204	1.209	1.207	1.193	1.075		1.200			1.074		1.199		1.161	1.174
Kin. vis.at 80°C, mm^2/s of the blend 70%VR/ 30 %FCC HCO	220.9		338.3	374.6		219.3	368.9		731.9	514.1	528.6	392.3		117.1							116.9			
Softening point,°C	40.1	42.4	44.7	51.2		43.7	50.3		68.6	58.1	61.9	47.8		27.8		54.0	31.5							
Penetration	182.0		104.0			79.0					20.0	67.0		300.0										
V, ppm	255		143.0	115		21	42	77	187	139	202	81	80.0		226	127		105	120		116	79	40	115
Ni, ppm	79		40.0	48		17	12	21	48	49	63	24	74.0		27	63		12	35		46	32	8	20

Table 2. Physical and chemical properties of the H-Oil VTBs under study

Nr.	1	2	3	4	5	6	7	8	9	10	11	12	13	14	15	16	17	18	19	20	21	22	23	24	25	26	27	28
Conversion,wt.%	75	69	70.4	74.9	64.6	64.2	58.5	67.5	73.0	67.3	61.3	62.0	55.3	72.3	67.4	65.8	64.9	72.5	75.3	81.2	70.7	74.3	72.7	75.7	67.0	68.9	64.7	67.3
ATB HFT, wt.%	0.23	0.41	0.38	0.36	0.44	0.38	0.46	0.42	0.16	0.53	0.42	0.65	0.32	0.38	0.42	0.50	0.49	0.30	0.10	0.36	0.39	0.20	0.370	0.290	0.410	0.640	2.290	0.440
d_{15},g/cm^3	1.005	1.010	1.020	1.020	1.024	1.014	1.001	1.025	1.035	1.028	1.008	1.015	0.985	1.026	1.019	1.012	1.017	1.033	1.041	1.055	1.029	1.058	1.036	1.049	1.008	1.022	0.995	1.009
CCR,wt.%	21.8	22.6	23.4	24.1	23.6	22.1	19.1	23.6	24.0	23.1	22.5	22.5	17.9	24.7	23.3	22.4	23.3	25.5	25.5	28.2	24.4	28.8	25.7	27.6	22.2	22.4		
VIS (70%VTB/30% HCO) at 80°C, mm^2/s	90.7	106.7	112.8	103.1	103.7	117.2	89.2	116.4	114.7	103.3	89.6	106.6	78.4	89.6	96.5	90.2	74.2	107	111.7	113.9								
Soft. point, °C	37.8	38.4	37.5	38.1	41.3	37.9	27.6	41.0	36.0		40.7	37.4	26.7	39.4	33.5	33.5	28.0	40.85	44.6	50.9	55.8	56.3	44.7	51.1				
H, wt.%	10.8	10.7	10.6	10.4	10.5	10.9	11.2	10.4	10.6	10.2	10.6	10.7	11.7					10.4	10.6			9.6					11.21	
C, wt.%	88.2	88.0	88.2	88.4	88.7	87.2	87.2	87.8	87.7	87.2	87.3	88.0	87.4					87.7	88.2			87.7					88.13	
N, wt.%	0.4	0.4	0.5	0.5	0.5	0.6	0.5	0.5	0.6	0.7	0.5	0.5	0.5					0.66	0.6			0.7					0.48	
S, wt.%	1.22	1.44	1.66	1.40	1.42	1.39	1.50	1.58	1.52	1.61	1.62	1.49	1.07	1.56	1.53	1.55	1.53	1.61	1.40	1.61	1.38	1.69	1.78	1.59	1.47	1.58	1.17	1.30
H/C	1.46	1.46	1.44	1.41	1.42	1.49	1.53	1.43	1.45	1.41	1.45	1.46	1.60					1.42	1.44			1.31						
S/N	3.4	3.3	3.7	2.9	2.9	2.5	3.1	3.4	2.6	2.3	3.4	3.3	2.1															
Saturates, wt.%	29.1	29.5		26.0		23.1		23.2		20.0		21.7	34.5					23.5	22.6		19.4		23.1	21.4			26.1	25.6
Aromatics, wt.%	50.1	49.9		53.1		55.6		53.2		40.9		48.7	44.2					51.3	51.4		53.5		47.4	50.3			51.6	56.4
Resins, wt.%	10.7	13.8		6.5		5.9		7.2		24.4		18.9	5.6					6.7	7.5		5.7		5.4	10.0			10.3	5.8
C_7- asphaltenes, wt.%	10.1	6.8	15.4	14.5	16.1	15.3	10.8	16.4	14.5	14.7	18.2	10.7	15.7	17.7	16.4	10.2	15.4	17.2	18.5	20.0	21.3	22.8	21.4	18.3	14.6	16.4	12.0	12.2
C_5-asphaltenes,wt.%	21.0	26.4	26.0	27.0	23.6	24.9	25.5	26.0	28.5	28.6	28.9	27.7	24.5	27.4	25.4	26.3	24.4	25.8	28.5	23.1	26.0	27.5	24.2	29.8	21.9	24.0		
C_7-asph.d_{15}, g/cm^3	1.262	1.219	1.272	1.249	1.231	1.273	1.222	1.266	1.272	1.304	1.198	1.198	1.157	1.249	1.208	1.258	1.249	1.240	1.289		1.265	1.327	1.249	1.240	1.268	1.267	1.266	1.216
C_5-asph. d_{15}, g/cm^3	1.198	1.209	1.214	1.268	1.222	1.185	1.162	1.177	1.203	1.191	1.189	1.165	1.138	1.197	1.202	1.185	1.209	1.224	1.242	1.250	1.226	1.283	1.238	1.230	1.217	1.221		
DAO C_7 d_{15}, g/cm^3	0.983	0.997	0.985	0.989	0.992	0.978	0.979	0.988	1.004	0.992	0.974	0.997	0.959	0.988	0.989	0.990	0.983	0.998	0.997		0.979	0.998	0.989	1.014	0.974	0.984	0.967	0.986
DAO C_5 d_{15}, g/cm^3	0.964	0.954	0.966	0.951	0.975	0.968	0.955	0.980	0.981	0.974	0.949	0.967	0.944	0.973	0.969	0.962	0.967	0.980	0.978	1.008	0.974	0.992	0.984	0.988	0.962	0.971		
<540°C	13.33	13.21	13.21	13.67	10.77	11.43	12.14	12.33	13.44	13.75	13.00	13.00	13.33	15.59	16.56	17.06	19.00											

Table 3. Intercriteria matrix of properties of crude oils and derived thereof vacuum residual oils (the figures in bold mean statistically meaningful correlation)

	Crude d 15	*Crude Sul*	*VGO d15*	*VR d 15*	*VR CCR*	*VR Sul*	*Sat*	*C7-asp*	*C5-asp*	*DAO C5 d15*	*DAO C7 d15*	*d15-C5 asp*	*d15-C7asp*	*C5 ins.-C7 sol*	*VIS*	*SP*	*Pen.*
Crude d_{15}	1																
> 540 °C	**0.98**	0.63															
VR d_{15}	0.62	**0.93**	**0.93**	1.00													
VR CCR	0.61	**0.92**	**0.86**	**0.97**	1.00												
VR Sul	0.58	**0.98**	**0.94**	**0.93**	**0.90**	1.00											
Sat.	0.47	**0.10**	**0.12**	**0.06**	**0.07**	**0.11**	1.00										
Aro	0.49	0.71	0.70	0.67	0.62	0.70	-0.80										
C_7-asp	0.60	**0.90**	0.73	**0.81**	**0.87**	**0.78**	-0.69	1.00									
C_5-asp	0.62	0.88	0.75	**0.84**	**0.88**	**0.81**	-0.73	**0.98**	1.00								
DAO C_5 d_{15}	0.64	**0.92**	**0.91**	**0.91**	**0.84**	**0.90**	**-0.89**	0.52	0.61	1.00							
DAO C_7 d_{15}	0.64	**0.88**	**0.87**	**0.95**	**0.90**	**0.87**	**-0.93**	0.63	0.72	**0.97**	1.00						
d_{15}-C_5 asp	0.68	**0.85**	**0.89**	**0.95**	**0.91**	**0.89**	**-0.94**	**0.76**	**0.82**	**0.85**	**0.91**	1.00					
d_{15}-C_7asp	0.57	0.64	**0.80**	**0.77**	0.65	0.67	**-0.87**	0.41	0.52	**0.81**	0.77	**0.81**	1.00				
VIS	**0.80**	**0.87**	**0.75**	**0.79**	**0.93**	0.73	-0.55	**0.92**	**0.92**	0.41	0.47	0.65	0.51	0.25	1.00		
SP	0.40	**0.89**	**0.86**	**0.87**	**0.93**	0.83	-0.73	**0.84**	**0.82**	0.47	0.59	**0.80**	0.64	0.15	**0.97**	1.00	
Pen.	**0.10**	**0.06**	**0.07**	**0.07**	**0.93**	**0.08**	**0.87**	0.45	-0.74	0.39	0.31	**0.02**	**0.07**	**0.13**	**-0.85**	**-0.92**	1.00

**Note:* *The marked in bold figures concern statistically meaningful correlation*

The VR saturate content moderately correlates with the VR properties: DAO C_5 d_{15} (μ = 0.89); DAO C_7 d_{15} (μ = 0.93); d_{15} C_5 asp. (μ = 0.94); d_{15} C_7 asp. (μ = 0.87); and penetration (μ = 0.87). It weakly correlates with the VR aromatics content (μ = 0.80). It is interesting to note here the correlation of the VR saturate content with the VR C_5 asphaltene density, which suggests that the higher the VR saturate content, the lower the asphaltene aromaticity is. One could also suppose that the lower density higher saturates content SRVROs may have aromatic and resin fractions which are richer in hydrogen and has lower aromaticity similar to their asphaltene fractions than the lower density, the lower saturate content SRVROs. In order to verify this assumption, two SRVROs not included in the data of Table 1 were separated in SARA fractions and their element compositions were determined. The data for these two SRVROs are summarized in Table 4.

Table 4. SARA analysis data and element composition of SARA fractions of a lower and a higher density SRVRO

SARA, wt.%		*C, %m/m*	*H, %m/m*	*N, %m/m*	*S, %m/m*	d_{15}
A higher density (d_{15}=1.0511) SRVRO						
Sat.	15.0	84.9	13.9	0.1	3.7	0.895
Aro.	65.0	83.1	9.9	0.3	8.3	1.059
Res.	6.2	81.0	9.75	1.11	6.9	1.068
Asp. (C_7)	13.8	81.5	7.4	0.87	10.4	1.202
Whole VR			10.1	0.36	7.2	1.051
A lower density (d_{15}=0.9580) SRVRO						
Sat.	48.5	86.3	13.9	< 0.01	0.1	0.895
Aro.	39.3	86.7	10.8	0.59	1.4	1.017
Res.	9.5	83.6	10.5	1.26	1.6	1.031
Asp. (C_7)	2.7	85.1	8.2	1.13	2.9	1.153
Whole VR			12.2	0.38	0.82	0.958

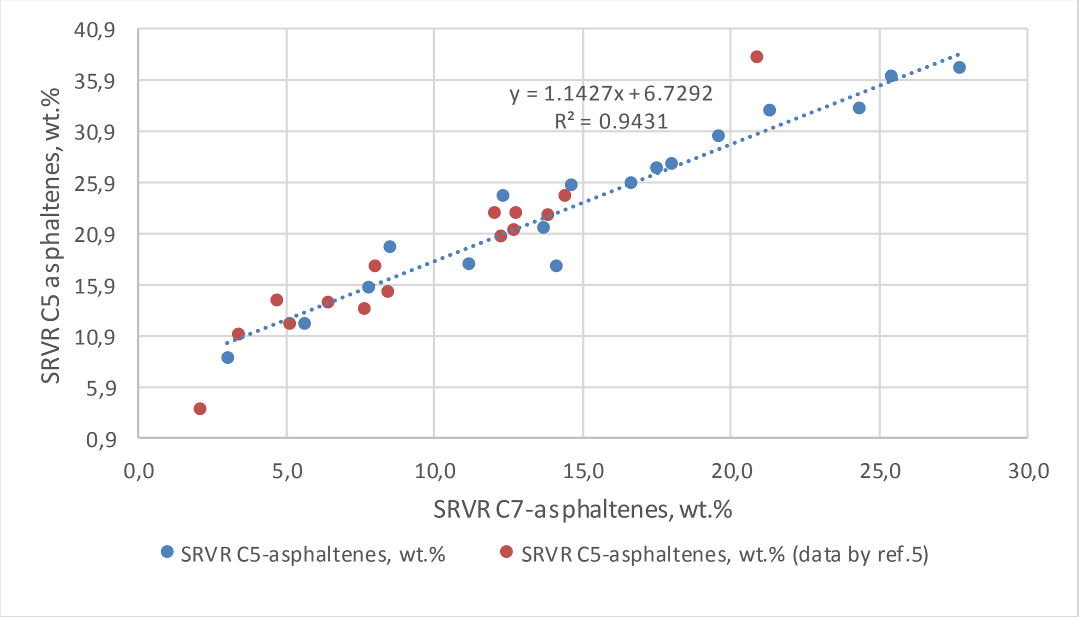

Figure 2. Relation of C_7 to C_5 asphaltenes in SRVROs originating from different crudes

It is evident from the data in Table 4 that indeed the lower density, the lower saturate content SRVRO has aromatic, resin and C_7 asphaltene fractions which have a lower hydrogen content and lower density than the same SARA fractions of the higher density, lower saturate content SRVRO.

The VR C_7 asphaltene content strongly correlates with the C_5 asphaltene content ($\mu = 0.98$), moderately correlates with the VR viscosity ($\mu = 0.92$) and weakly correlates with the VR softening point ($\mu = 0.84$) and the C_5 asphaltene density ($\mu = 0.76$). Figure 2 exemplifies the relation of C_7 to C_5 asphaltenes in SRVROs originating from different crudes. The data in blue squares are from this work, while that in red diamonds are taken from ref. 5. This data indicates that when information of C_5 or C_7 asphaltene content for an SRVR is available, the content of the other asphaltenes can be predicted by the equation shown in Figure 2.

Table 5 presents data of ICrA matrix of the statistically meaningful relations of properties of the studied 28 H-Oil VTB products.

Table 5. Intercriteria matrix of properties of VTBs (the figures in bold mean statistically meaningful correlation)

	Conv	*VTB D15*	*VTB CCR*	*VTB VIS*	*SP*	*H*	*H/C*	*Sat*
Conv	1.00							
d_{15}	**0.78**	1.00						
CCR	**0.82**	**0.96**	1.00					
SP	0.66	**0.80**	**0.82**	0.68	1.00			
H	0.34	**0.10**	**0.07**	0.37	**0.08**	1.00		
Sul	0.35	0.64	0.59	0.32	0.37	**0.23**		
H/C	0.30	**0.12**	**0.06**	0.38	**0.08**	**0.99**	1.00	
Sat	0.38	**0.23**	0.30	**0.23**	**0.19**	**0.75**	0.74	1.00
C_7-asp d_{15}	0.59	0.59	0.56	0.49	0.55	0.32	0.26	0.38
C_5-asp d_{15}	**0.79**	**0.75**	**0.81**	0.38	0.70	**0.22**	**0.19**	0.64
DAO C_7 d_{15}	0.65	**0.79**	**0.73**	0.58	0.46	0.27	0.28	0.47
DAO C_5 d_{15}	0.69	**0.91**	**0.84**	0.55	0.69	0.28	0.29	**0.22**

**Note: The marked in bold figures concern statistically meaningful correlation*

The data in Table 5 indicates that the SRVRO conversion in the EBVRHC weakly correlates with the VTB properties density ($\mu = 0.78$); Conradson carbon content ($\mu = 0.82$); and the density of C_5 asphaltenes ($\mu = 0.79$). Therefore with increasing of VR conversion in the EBVRHC aromaticity of the VTB product increases most probably as a result of denuding of the alkyl chains attached to the aromatic cores of the VR aromatic molecules.

Similar to the SRVROs, the properties density and CCR content strongly correlate ($\mu = 0.96$). However, as evident from Figure 3, the relation of CCR to density in H-Oil VTBs is a bit different than that of the SRVROs. Figure 3 also includes data from ref.5 with red diamonds which are based on SRVROs (77% of the data), H-Oil VTBs (17% of the data) and visbreaker vacuum residual oils (6% of the data). From this data, one may conclude that the relation established in ref. 5 is very close to that for the SRVROs since the data in ref.5 is mainly based on SRVROs (77% of the data) and that the relation of the properties VR CCR and density may vary for the straight run VROs and the secondary VROs. However, this relation is always strong.

The H-Oil VTB properties density and CCR as evident from Table 5 moderately correlate with hydrogen content ($\mu = 0.10$; and $\mu = 0.07$ respectively) and H/C atomic ratio ($\mu = 0.12$; and $\mu = 0.06$ respectively). As shown in Figures 4 and 5 the relation of the H-Oil VTB properties density and CCR lie on the curve established in ref.5 and therefore can be calculated from the relations for these properties determined in ref.5.

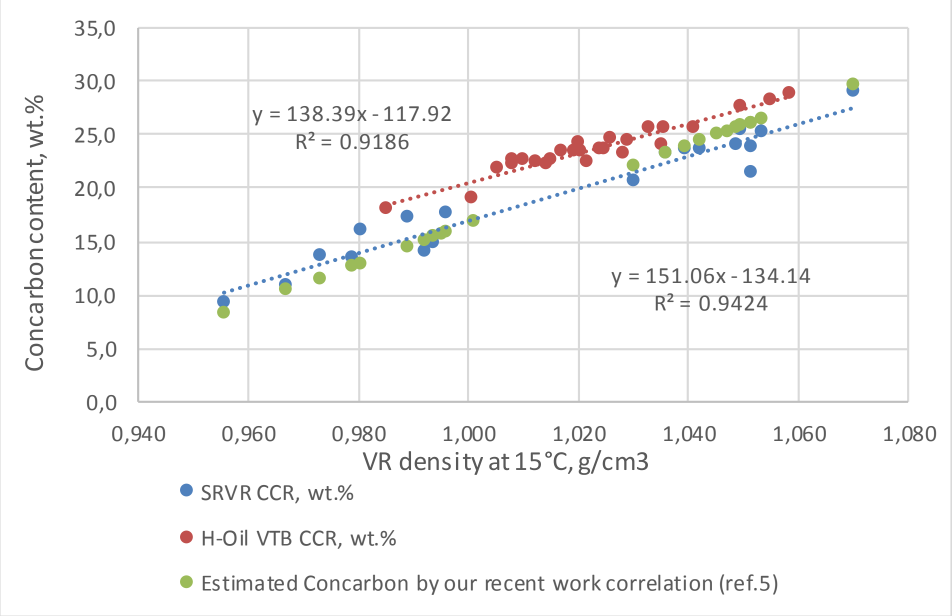

Figure 3. Relation of density to Conradson carbon content for SRVROs and H-Oil VTB products

Similar to the SRVROs, the H-Oil VTB density correlates with the density of C_5-asphaltenes and with the C_5-deasphalted oil (DAO). Figures 6 and 7 illustrate the relations of VR density to the C_5-asphalene density and the C_5-DAO density for SRVROs and H-Oil VTBs. This data shows that the increase of VR density is associated with an increase of C_5-asphalene density and the C_5-DAO density. However, the curve of H-Oil VTB C_5-asphalene density lies above that of the SRVOs, while the curve of the C_5-DAO density of H-Oil VTB lies below that of the SRVOs. These findings are in line with the lower colloidal stability of the secondary H-Oil VTB in which a higher aromatic, higher density asphaltenes are surrounded by a lower aromatic, lower density DAO.

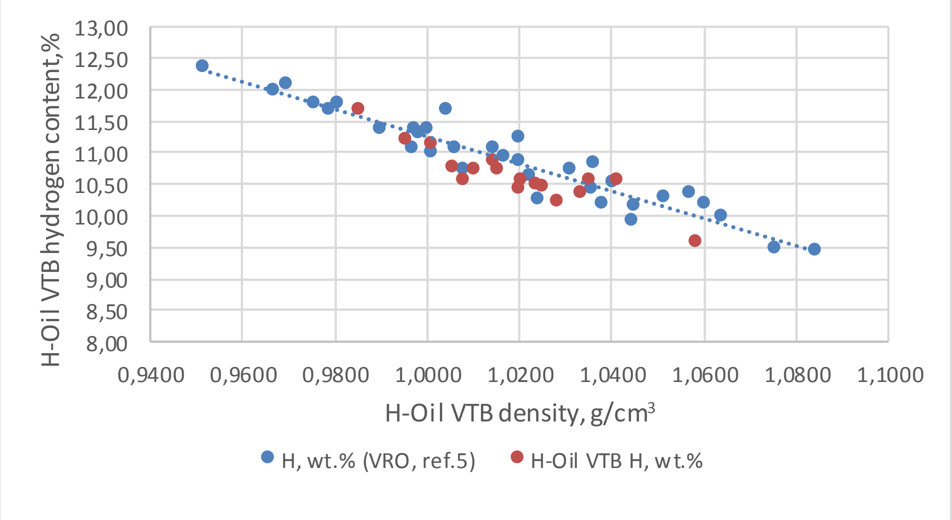

Figure 4. Relation of H-Oil VTB density to H-Oil VTB hydrogen content

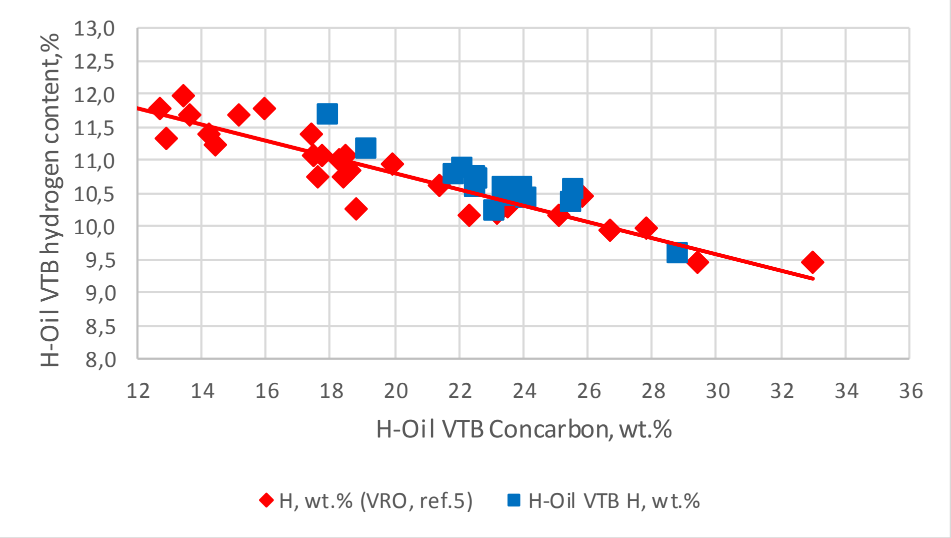

Figure 5. Relation of H-Oil VTB Conradson carbon content to H-Oil VTB hydrogen content

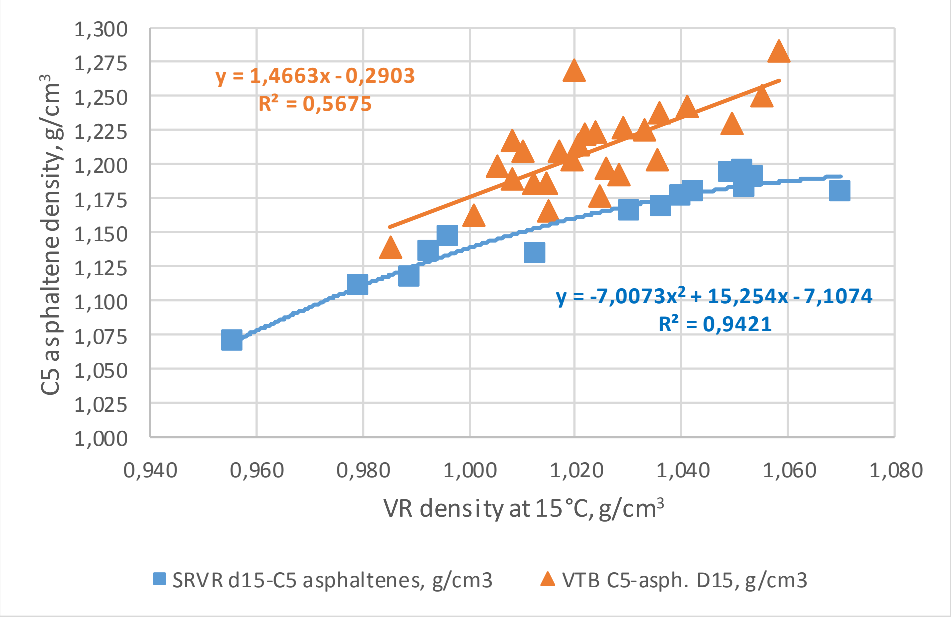

Figure 6. Relation of VR density to C5-asphaltene density for SRVROs and for H-Oil VTBs

Figure 8 shows the relation of VR density to saturate content of SRVROs and H-Oil VTBs. This data indicates that the VR saturate content in both primary and secondary VROs can be estimated from a second order polynomial of the VR density. However, the H-Oil VTBs have a higher saturate content at the same value of the density of the VRO. The relations shown in Figure 8 can be used as a tool for verifying the correctness of the SARA analysis. If the measured saturate content deviates from the established dependence on density, it would mean or incorrect measurement of SARA or density, or appearance of a new phenomenon not accounted for in this relation. It must be pointed out that this second order polynomial dependence of VR saturates on density has been tested on 97 SRVROs measured in different laboratories and proved its validity [6]. This study shows that the second order polynomial also fits the dependence of the H-Oil VTB saturates on density.

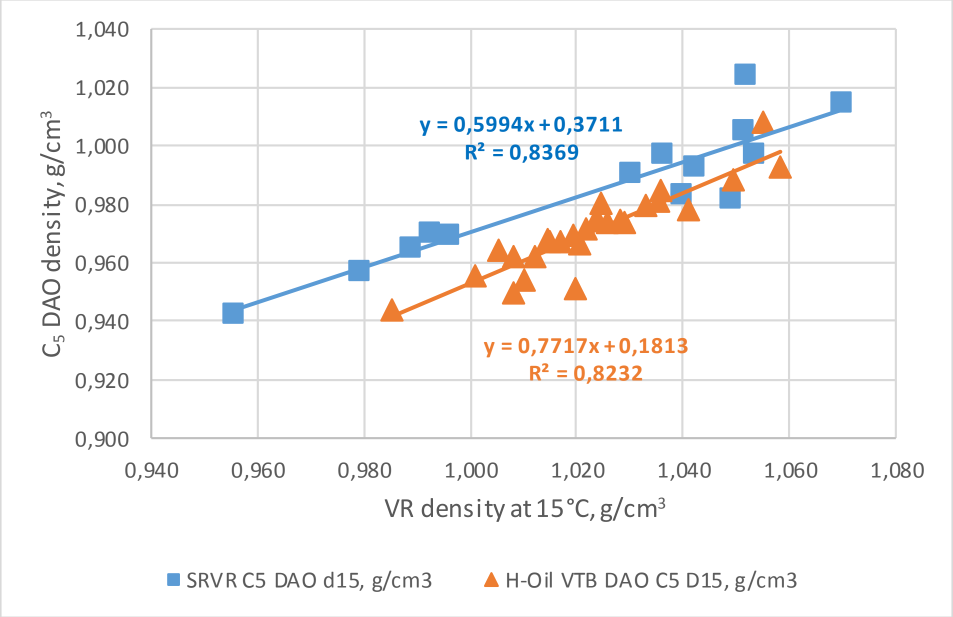

Figure 7. Relation of VR density to C_5-DAO density for SRVROs and for H-Oil VTBs

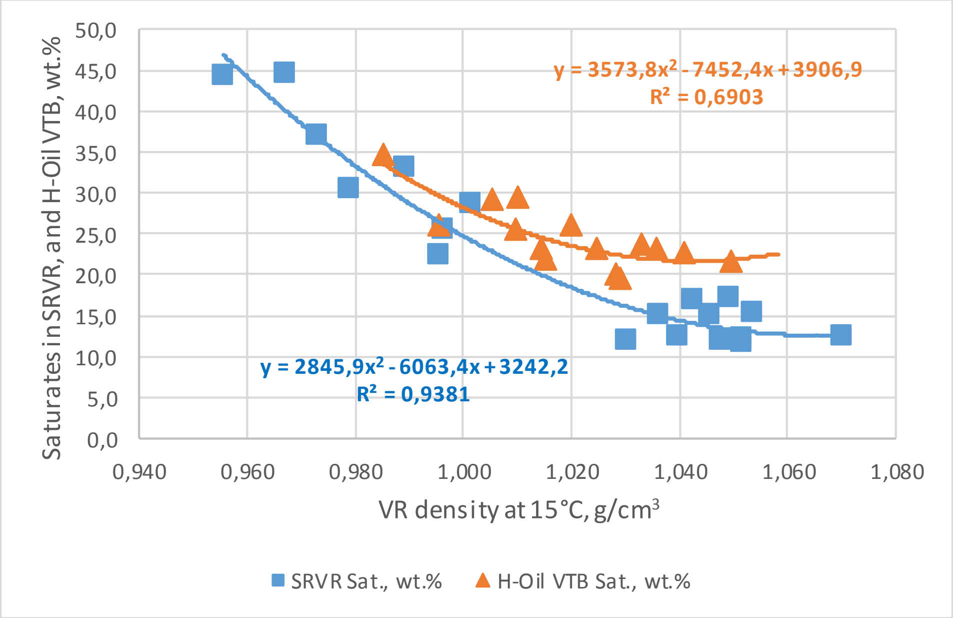

Figure 8. Relation of VR density to saturate content of SRVROs and of H-Oil VTBs

Similar to the SRVROs the VR Conradson carbon content of the H-Oil VTBs correlates with the property softening point. Figure 9 shows this dependence and indicates that at the same CCR, the H-Oil VTBs are harder and have a lower softening point.

Dissimilar to the SRVROs, the H-Oil VTB viscosity does not correlate with the asphaltene content, as shown in Figure 10. Instead, the H-Oil VTB viscosity correlates with the saturate content as presented in Figure 11. This data suggests that the H-Oil VTB viscosity depends on the hydrogenation activity of the catalyst, and it is not influenced by the number of asphaltenes in it in contradiction to the SRVROs. The lower viscosity of the H-Oil VTBs at the same asphaltene content supposes a different size and shape of the asphaltenes in comparison to the SRVRO asphaltenes. It also suggests higher mobility of the asphaltenes in the H-

Oil VTBs which along with the lower aromaticity of the DAO contributes to the easier asphaltene aggregation observed in the H-Oil VTBs.

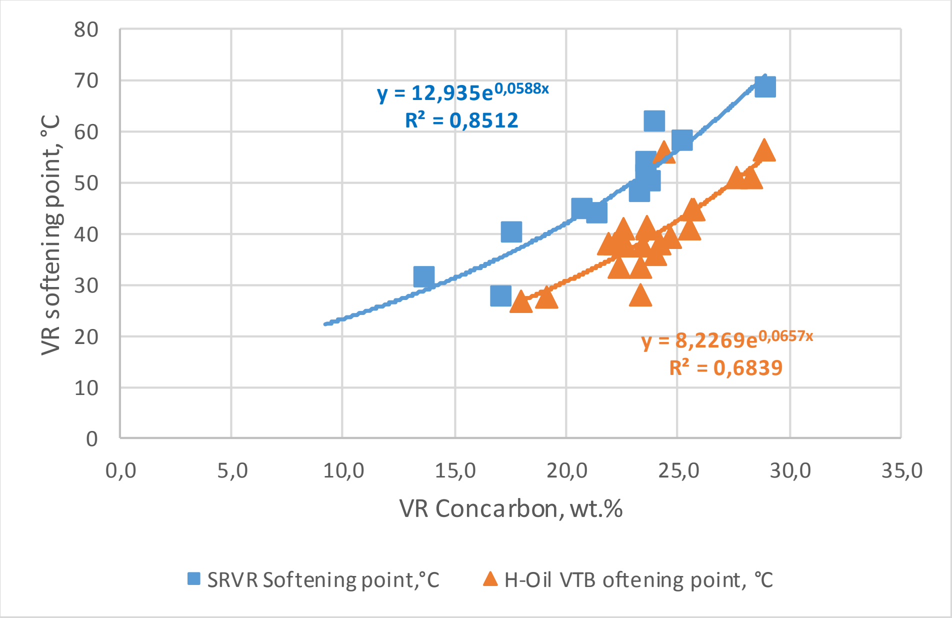

Figure 9. Relation of VR Conradson carbon content to softening point for SRVROs and for H-Oil VTB s

By regression the data for VTB density and 540°C- fraction content in H-Oil VTB and the kinematic viscosity of the blend 70% H-Oil VTB/30% FCC HCO the following equation was developed:

$Kin.Vis = 685.3D15 - 3.866(540°C -) - 543.5$ R=0.84

where: Kin. Vis = kinematic viscosity of the blend 70% H-Oil VTB/30% FCC HCO at 80°C mm^2/s; (properties of the diluent FCC HCO are given in ref.7); D15 = density of H-Oil VTB at 15°C, g/cm$^{3;}$ 540°C = fraction content of the material boiling below 540°C according to high temperature simulation distillation, ASTM D 7169.

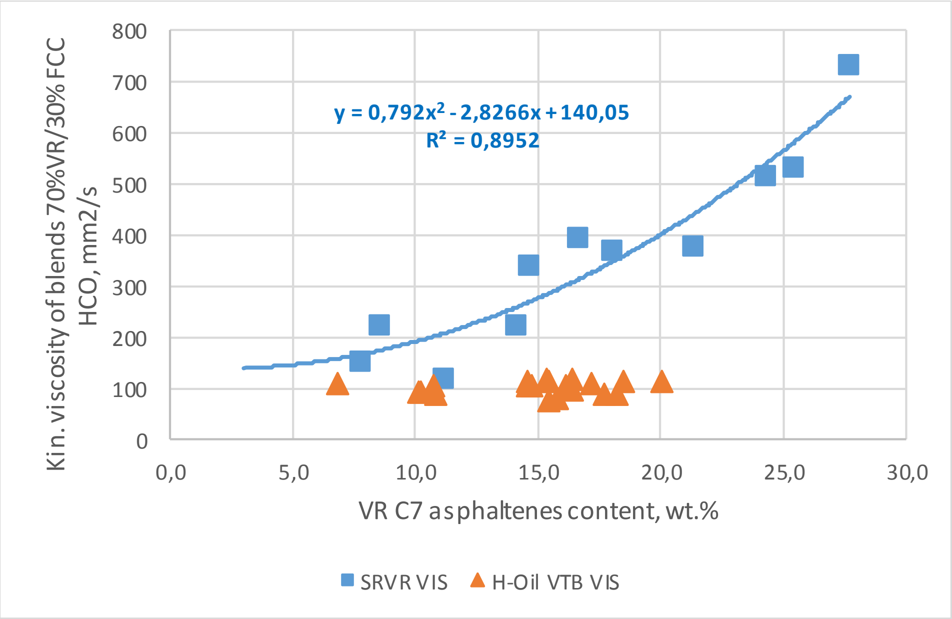

Figure 10. Relation of VR asphaltene content to viscosity for SRVROs and for H-Oil VTBs

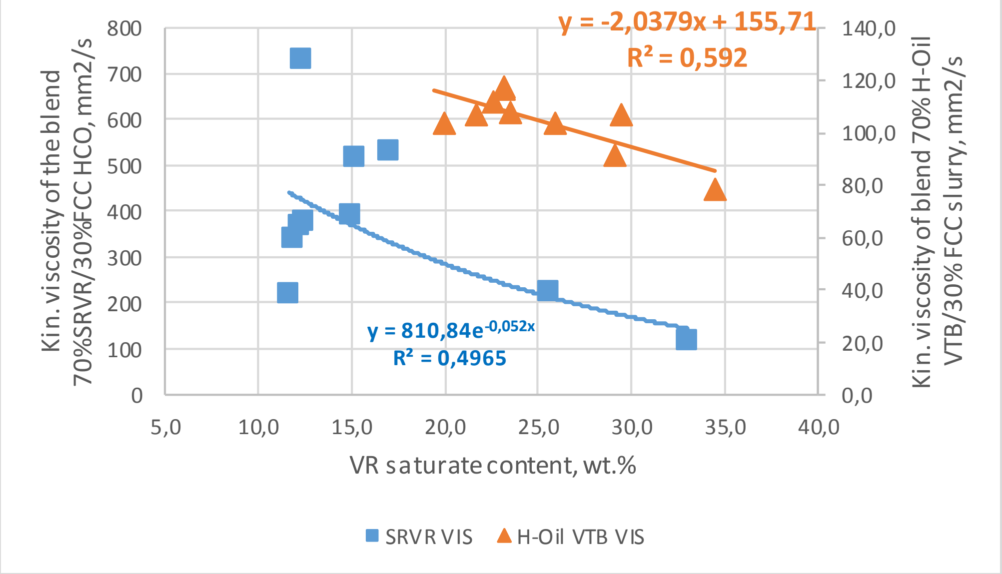

Figure 11. VR saturate content versus VR viscosity for SRVROs and for H-Oil VTBs

The sediment content in the H-Oil residual oils is the main limiting factor that constraints severity and consequently, conversion increase [2]. From the data in Tables 2 and 5, no relation of ATB sediment to any of the VTB properties can be seen. It should be pointed out here that the ATB and VTB sediments correlate (sediments of H-Oil VTB = 1.6 H-Oil ATB) as shown in [7]. In LNB H-Oil hydrocracker ATB sediments are controlled due to the higher reliability of the measurement of the lower viscosity ATB product. That is why ATB sediment content is given in Table 2, where properties of the H-Oil VTBs are presented. It seems that none of the measured properties of the VTBs in this work can explain the phenomenon of sediment formation in the H-Oil vacuum residue hydrocracking. Additional work is needed to puzzle out which properties of the H-Oil residual oils govern the process of sedimentation.

4. Conclusions

24 straight run vacuum residual oils and 28 H-Oil VTBs obtained during processing different blends of the 24 SRVROs in the LNB EBVR H-Oil hydrocracking unit were analyzed for their physical and chemical properties. It was found that in both primary and secondary VROs, the density and the Conradson carbon content strongly correlate. This dependence can be used as a tool to verify the correctness of the measurement of these properties. It was confirmed again that the measurement of the density of the VROs by pycnometer gives unreliable data and dilution with toluene is proposed to correctly measure the VRO density. It was also confirmed that the VRO saturate content can be predicted from data of VRO density and the use of second order polynomial fits for both SRVROs and H-Oil VTBs. However, the H-Oil VTBs have a higher saturate content than the SRVROs at the same density. It was established that the lower density, the higher saturate content VROs have a lower density, a higher hydrogen content of asphaltenes, resins and of aromatics than those of the higher density lower saturate content VROs. The H-Oil VTBs have higher density asphaltenes and lower density maltenes than the SRVROs, which can explain the lower colloidal stability of the H-Oil VTBs. The properties of H-Oil VTB Conradson carbon content and density correlate with the VTB hydrogen content and H/C atomic ratio and these correlations coincide with those already established on the base of data of SRVROs (77% of the data), of H-Oil VTBs (17% of the data) and of visbreaker vacuum residual oils (6% of the data) as shown in ref.5. Therefore the data of density and CCR can be reliably used to correctly estimate hydrogen content and H/C atomic ratio in both SRVROs and H-Oil VTBs.

Dissimilar to the SRVROs the H-Oil VTB viscosity does not correlate with the asphaltene content. Instead, it correlates with the saturate content. Therefore the H-Oil VTB viscosity depends on the hydrogenation activity of the catalyst, and it is not influenced by the number of asphaltenes in it in contradiction to the SRVROs. The viscosity of the H-Oil VTBs is lower than that of the SRVROs, but the softening point of the H-Oil VTBs is higher than that of the SRVROs. While the SRVRO softening point strongly correlates with its viscosity, such a relation does not exist for the H-Oil VTBs, which suggests different rheological properties of the H-Oil VTBs in contrast to these of the SRVROs

References

[1] Odey F, Lacey M. IMO 2020 – Short-term implications for the oil market, August 2018, https://www.schroders.com/getfunddocument/?oid=1.9.3060731.

[2] Stratiev D, Shishkova I, Nikolaychuk E, Ijlstra W, Holmes B, Caillot M. Feed Properties Effect on the Performance of Vacuum Residue Ebullated Bed H-Oil Hydrocracking. Accepted for publication in Oil Gas European Magazine.

[3] Stratiev DS, Sotirov S, Shishkova I, Nedelchev A, Sharafutdinov I, Veli A, Mitkova M, Yordanov D, Sotirova E, Atanassova V, Atanassov K, Stratiev DD, Rudnev N, Ribagin S. Investigation of relationships between bulk properties and fraction properties of crude oils by application of the Intercriteria Analysis. Petroleum Science and Technology, 2016; 34(13): 1113-1120.

[4] Swafford P, McCarthy R. Improving crude oil selection, PTQ Q3, 2008; 125-129.

[5] Stratiev D, Shishkova I, Tsaneva T, Mitkova M, Yordanov D. Investigation of relations between properties of vacuum residual oils from different origin, and of their deasphalted and asphaltene fractions. Fuel 2016; 170, 115–29.

[6] Mitkova M, Stratiev D., Shishkova I, Dobrev D. Thermal and thermo-catalytic processes for heavy oil conversion. Professor Marin Drinov Publishing House of Bulgarian Academy of Sciences. 2017.

[7] Stratiev D, Dinkov R, Shishkova I, Sharafutdinov I, Ivanova N, Mitkova M, Yordanov D, Rudnev N, Stanulov K, Artemiev A, Barova I, Chushkov B. What is behind the high values of hot filtration test of the ebullated bed residue H-Oil hydrocracker residual oils?, Energy & Fuels, 2016; 30(9): 7037–7054.

To whom correspondence should be addressed: professor Dr. Dicho Stratiev, Lukoil Neftochim Bourgas, Bulgaria

Petroleum and Coal

Article **Open Access**

RESERVOIR SIMULATION AND PREDICTION: A CASE STUDY OF AN OIL-RIM RESERVOIR IN A NIGER DELTA OILFIELD

Uwaezuoke Nnaemeka and Igwilo K. Chinwuba*

Department of Petroleum Engineering, Federal University of Technology, P.M.B 1526, Owerri, Nigeria

Received April 24, 2019; Accepted July 1, 2019

Abstract

The water-injection-only option was started when simultaneous water and gas injection were stopped in an oil-rim reservoir. With geologic and pressure-volume-temperature dataset and production history of the oil-rim reservoir, an estimate of the oil-in-place, a forecast of production performance and other important parameters such as aquifer size and drive mechanisms were determined. The Material balance and Monte Carlo tools of MBAL reservoir engineering toolkit were employed, and the workflow was followed. An estimate of the original oil in place from material balance simulation of 93.4839 MMSTB, higher than the Monte Carlo simulation, with the P50 estimate of the Oil in Place as 82.9607 MMSTB were determined. Water Injection and Gas Cap Expansion were shown to be the major drive mechanisms in the years ahead till 2025, with increasing contribution from Fluid Expansion. A large aquifer exists, and reservoir pressure is expected to be high in the year 2025. The water-injection-only option has been shown to be capable of maintaining production efficiency in the oil-rim reservoir, based on the study of the oil reservoir in the Niger Delta.

Keywords: *History matching; Material balance equation; Production forecast; Reservoir simulation.*

1. Introduction

Beneath the earth's surface where hydrocarbon is found, reservoir engineers use parameters such as rock and fluid properties to estimate hydrocarbon in place and make predictions. The behavior of gas and liquid phases of hydrocarbon is affected by factors that assist in the estimation of hydrocarbon in places such as basic physics, chemistry, mathematics, and subsurface geology [1]. Production forecast is important because, In addition to inputs to the economics models and well timing requirements and design of facilities, they are used to schedule workover frequencies and optimize production.

In this work, simultaneous water and gas injection was started after about eleven months of production in the field. Due to the available market for the gas produced, the gas injection was stopped in 2017, and water injection alone was continued for pressure maintenance, improved recovery, and efficiency. The decision to use a single technique of water injection instead of combining two techniques of simultaneous water and gas injection was also justifiably expected to maintain production efficiency in accordance with research findings [2]. As a result of the strategy, material balance (MBAL) reservoir simulation software, used in reservoir engineering studies was used to estimate the hydrocarbon in place, determine aquifer size, reservoir drive mechanism, to make forecast of expected production and reservoir pressure up to 2025 for water-injection-only option since gas injection was stopped earlier in the life of the well. An estimate was made with the Monte Carlo simulation as a validator to compare with the MBAL simulation output of the oil in place.

2. Literature review

Oil reservoirs sandwiched between bottom water and gas cap have been termed oil rim reservoirs [3]. In the work, it was pointed out that most oil reservoirs in the Niger Delta basin are less than 80ft of thickness, and water/gas coning are common problems. Reservoir porosity and permeability values of 6-28% and 1-6208md are common [4].

However, a lot has been presented on oil rim reservoirs. Work on the assessment of oil rim reservoirs to highlight the strengths and weaknesses of existing models have been presented [5]. It was pointed out that inconsistency, the limited scope of application, and non-robustness are due to their inability to capture the physics of oil rim reservoirs.

Other recent works that have presented strategies for production in oil rim reservoirs exist. Simultaneous water and gas injection (with the maintenance of voidage replacement) has been shown as a technique to improve recovery in oil rim reservoirs [6]. In the work, reservoir simulation with sensitivity analyses of well placement, aquifer strength, permeability anisotropy, oil column thickness, and gas oil ratio relaxation policy on oil rim development was carried out. They suggested that simultaneous water and gas injection could increase the recovery factor of recovery by up to 15% of the stock tank oil initially in place. This is in contrast with another finding that simultaneous water and gas injection does not appreciably increase production efficiency [2]. In the work, they revealed that combining two techniques do not significantly increase recovery efficiency over a single technique to justify the cost of implementation. However, integrated approach and innovation in the form of state of the art engineering, technical initiatives, and application of new technologies have been suggested as tools to make significant changes in oil rim reservoir development [7]. The data used in their simulations may differ. In other words, no two reservoirs are expected to have exactly the same features.

Similarly, estimation of stock tank oil initially in place, and aquifer properties have been key reservoir engineering challenges, and reservoir material balance analyses provide solutions. From its initial development to advances in the material balance equation for both single and multi-tank models, lots of works have been presented for reserves estimation and other purposes [8- 12]. They highlighted that early stage use of production data is inapplicable, and that self-adaptive nonlinear regression could be adopted to advance material balance analysis. Also, analysis of distinct reservoir geologic units and features were shown to be possible by the use of MBAL multi tank option, and a tool for reservoir performance analysis that saves time and cost was presented. In summary, reserves estimation remained an essential task, and currently, there is no standardized reserves estimation procedure.

In particular, the generalized material balance equation (MBE) is given as [13],

$$N = (N_p\left[B_o + \left(R_p - R_s\right)B_g\right] - \left(W_e - W_p B_w\right) - G_{inj}B_{ginj} - W_{inj}B_{wi}) \div ((B_o - B_{oi}) + (R_{si} - R_s)B_g + mB_{oi}\left[\left({}^{B_g}\!/_{B_{gi}}\right) - 1\right] + B_{oi}(1+m)x\left[\frac{S_{wi}C_w + C_f}{1 - S_{wi}}\right]\Delta p) \tag{1}$$

This is expressed for an oil reservoir as;

$$F = NE_t + W_e \tag{2}$$

The underground withdrawal, F, equals the surface production of oil, gas, and water with under reservoir conditions:

$$F = N_p * \left(B_o - B_g * R_s\right) + B_g * \left(G_p - G_i\right) + (W_p - W_i) * B_w \tag{3}$$

$$E_t = (B_o - B_{oi}) + (R_{si} - R_s)B_g + mB_{oi}\left({}^{B_g}\!/_{B_{gi}} - 1\right) + (1+m)B_{oi}\left[\frac{S_{wc}c_w + c_f}{1 - S_{wc}}\right](P_i - P) \tag{4}$$

When there is no aquifer influx, $W_e = 0$, hence;

$$F = NE_t \tag{5}$$

$${}^{F}\!/_{E_t} = N \tag{6}$$

A plot of F/Et will yield a horizontal straight line, and the intercept is N. Similarly, from equation (2);

$$F - W_e = NE_t \tag{7}$$

A plot of $F - W_e$ against E_t will give a straight line with slope N, and;

$${}^{F}\!/_{E_t} = N + {}^{W_e}\!/_{E_t} \tag{8}$$

Also, if the aquifer model is accurate, a plot of F/E_t against W_e/E_t will give a straight line with an intercept at N and a unit slope.

Reservoir simulation using MBAL software is fundamental based on Equation (1) to Equation (8). Reservoir simulation has been in use by reservoir engineers [14] and has been used for single and multi-tank analyses [10], due to demonstrable repeatability and consistency criteria that usually lack in computational methods [15]. Decline curve analysis [16] and Monte Carlo simulation [17] are also used for estimation of recoverable oil in the reservoir. Though numerous questions have been asked on the reliability of Monte Carlo, lack of enough data will remain a problem [17].

Reservoir performance predictions are also carried out when history data are available, basically by the use of relative permeability. Nonetheless, errors and uncertainties occur in predictions. It could be due to the generalization of data gathered from only a small portion of the reservoir. It has been shown that additional data can and always reduce uncertainty [18].

Work has also been presented on a field in the Niger Delta basin [16]. In addition to presentations of the material balance workflow for the estimation of the oil initially, in place and decline curve analysis, it compared the estimate of the original oil in place derived by the use of material balance method and decline curve analysis. They reported that the value derived from material balance simulation was higher compared with the decline curve method. Though the results compared quite fine, they recommended the use of Monte Carlo analysis as another validator.

3. Materials and method

The geologic, pressure-volume-temperature, production and pressure history data used are associated with previous work in an oil-rim reservoir [3]. The material balance equation outlined earlier was applied for reserves estimation and production forecast. Also, the aquifer size and drive mechanisms were determined when the MBAL workflow was followed [16].

Table 1. Geologic data

Thickness	88.9865ft
Porosity	0.28
Saturation	0.25

Table 2. PVT Data

Formation GOR	998 scf/stb	Water Salinity	120000ppm
Oil Gravity	38 API	Oil Viscosity	0.27cP
Gas Gravity	0.75 sp.g	Oil Formation Volume Factor	1.69 rb/stb

Table 3. Relative permeability data

	Residual saturation	End point (fraction)	Exponent
Krw	0.25	0.75	2
Kro	0.20	0.8	2
Krg	0.20	0.85	2

4. Results and discussion

From the possible sources of energy in the reservoir and aquifer systems, the energy plot (Figure 1) is used to show the relative contributions of the main sources of energy. Whereas at the beginning of the production history, gas injection and water injection did not contribute to the drive mechanisms, the parameters contributed towards the end of the history. Particularly, water injection became the dominant drive mechanism in the year 2025, since gas injection was stopped some years earlier. Therefore, when determining the OOIP, initial production points were considered.

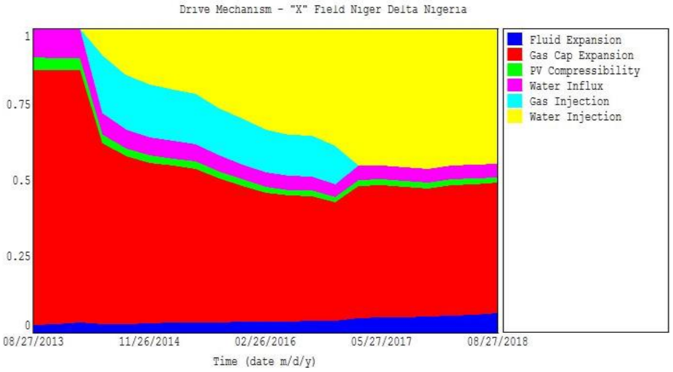

Figure 1. Energy plot showing the drive mechanisms

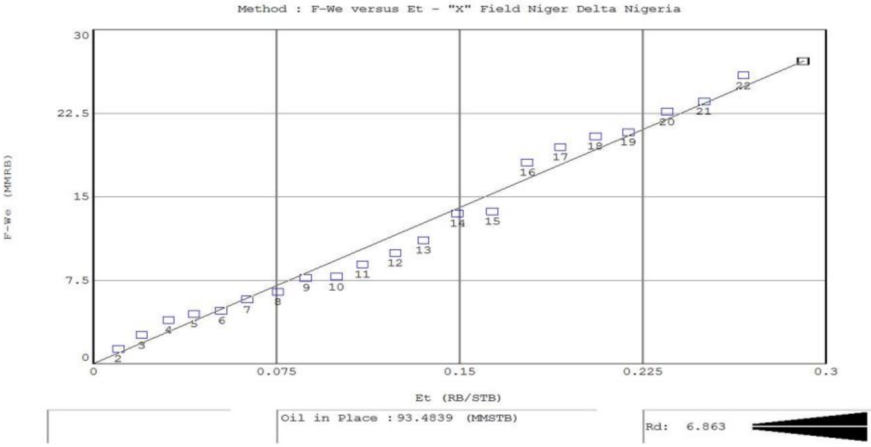

```
Oil in Place : 93.4839  (MMSTB)
Rd:   6.863
```

Figure 2. The graphical plot used to determine the Oil in Place (N)

The graphical plot (Figure 2) was derived from the material balance equations. The model was adjusted until the best line fit was obtained. The oil-in-place (N) was determined by the slope of the straight line.

Also, the analytical plot (Figure 3) provided non-linear regression to determine unknown aquifer and reservoir parameters. The outputs include oil production and water influx. The red line (without aquifer influx) underestimates the production compared with the blue line (with aquifer influx) since it serves as a check. At a reservoir pressure of 3560 psi, the oil production with aquifer influx is 21 MMSTB compared to 19.5 MMSTB without aquifer influx.

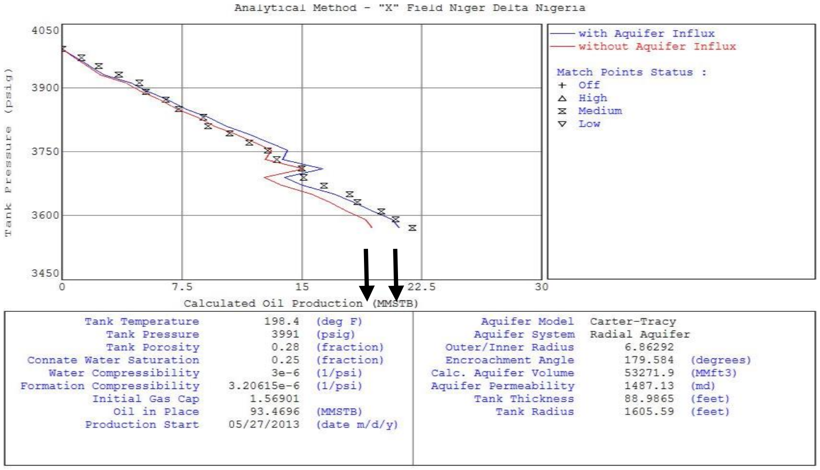

```
              Tank Temperature        198.4   (deg F)             Aquifer Model   Carter-Tracy
                 Tank Pressure         3991   (psig)             Aquifer System   Radial Aquifer
                 Tank Porosity         0.28   (fraction)    Outer/Inner Radius        6.86292
      Connate Water Saturation         0.25   (fraction)    Encroachment Angle        179.584   (degrees)
        Water Compressibility          3e-6   (1/psi)      Calc. Aquifer Volume       53271.9   (MMft3)
  Formation Compressibility     3.20615e-6   (1/psi)     Aquifer Permeability       1487.13   (md)
              Initial Gas Cap       1.56901                        Tank Thickness       88.9865   (feet)
                 Oil in Place       93.4696   (MMSTB)                 Tank Radius       1605.59   (feet)
             Production Start    05/27/2013   (date m/d/y)
```

Figure 3. Regression output depicted by the analytical plot

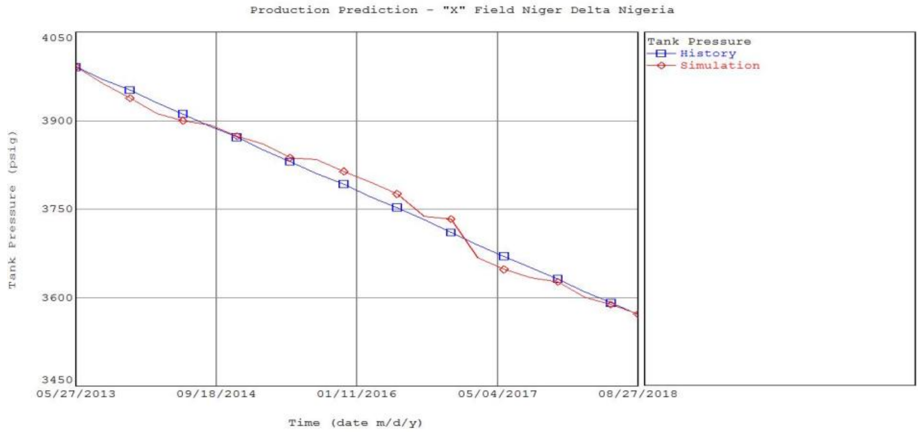

Figure 4. Historical production data compared with production simulation

To perform predictive analyses, a production simulation plot was generated and shown with the historical data (Figure 4). Similarly, Figure 5 and Figure 6 are the production predictions of reservoir pressure and oil production from start to end of production, respectively. The prediction makes use of well performance definitions and production constraints.

Moreso, reservoir pressure prediction (Figure 7) and oil production prediction (Figure 8) from start to the year 2025 were made with the water injection the only option of fluid injection. The reservoir pressure will be about 2960 psi by 2015, while the prediction for oil production is in the range 50-51 MMSTB.

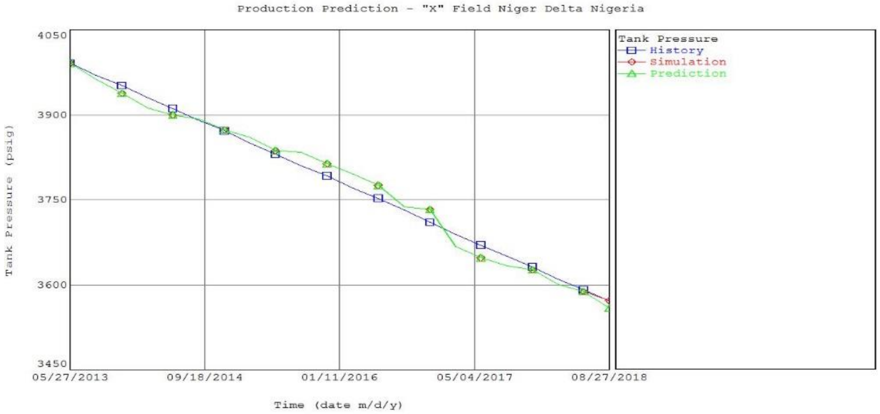

Figure 5. Production prediction of reservoir pressure from start to end of production

Figure 6. Production prediction of oil production from start to end of production

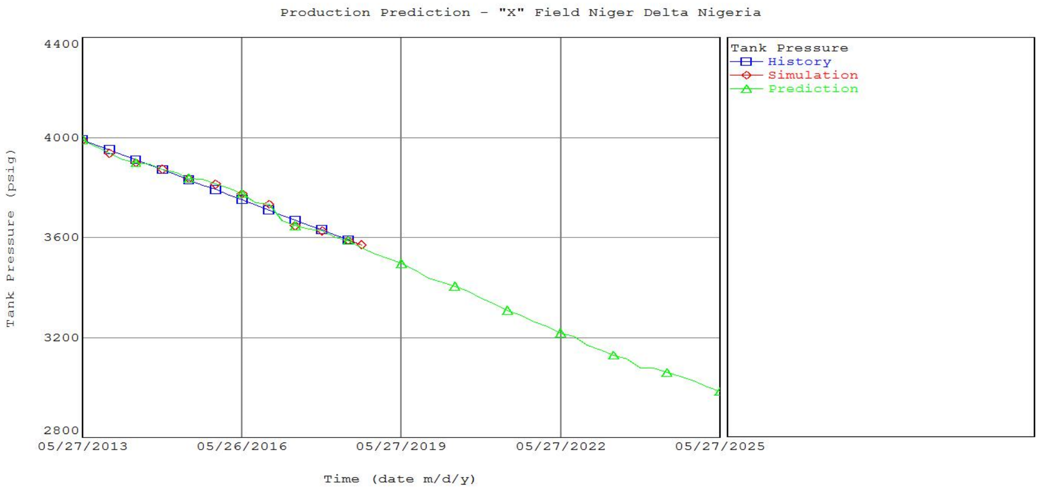

Figure 7. Production prediction of oil reservoir pressure from start to the year 2025

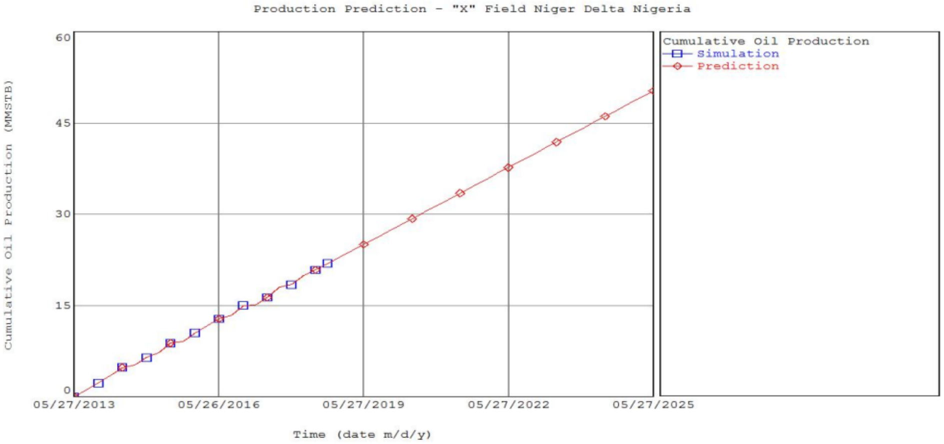

Figure 8. Production prediction of oil production from start to the year 2025

Table 4. Summary of results as output from the analytical plot

S/N	Parameter	MBAL Estimate
1	STOIIP (MMSTB)	93.4696
2	Initial Gas Cap (MMSCF	1.56901
3	Outer/Inner Radius Ratio	6.86292
4	Reservoir Radius (ft)	1605.59
5	Encroachment Angle (degree)	179.584
6	Porosity	0.28
7	Aquifer Volume (MMft^3)	53271.9

The result of the Monte Carlo simulation (Figure 9) at 50 percent probability is 82.9607 MMSTB with a standard deviation of 30.7929 MMSTB and mean reward of 80.6793 MMSTB. Also, the STOIIP from MBAL estimate is 93.4696 MMSTB (Table 4).

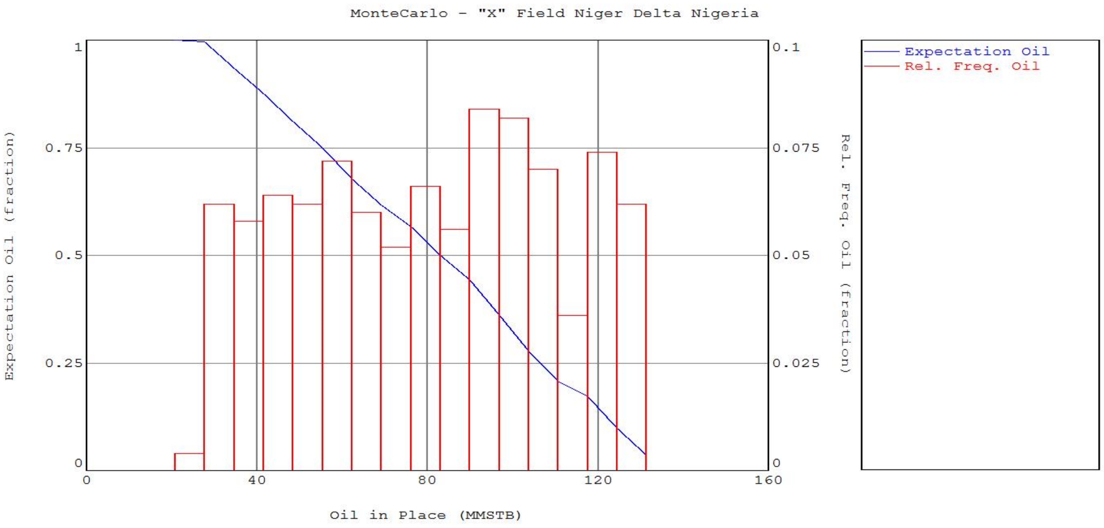

Figure 9. Plot of Monte Carlo simulation

5. Conclusion

The Original Oil in Place estimate from material balance simulation of 93.4839 MMSTB is higher than the Monte Carlo simulation, with the P50 estimate of the Oil in Place as 82.9607 MMSTB. Accuracy of the Monte Carlo simulation would be improved with more data. Water Injection and Gas Cap Expansion are the major drive mechanisms, with increasing contribution from Fluid Expansion. The reservoir has strong aquifer support that may have contributed to the performance at the end of the prediction period in addition to the high permeability.

Nomenclature

B_g	*gas formation volume factor, bbl/scf*
B_{gi}	*gas formation volume factor at pi, bbl/scf*
B_{ginj}	*gas formation volume factor of the injected gas, bbl/scf*
B_o	*oil formation volume factor at reservoir pressure p, bbl/STB*
B_{oi}	*oil formation volume factor at initial reservoir pressure p_i, bbl/STB*
B_w	*water formation volume factor, bbl/STB*
B_{wi}	*water formation volume factor at initial pressure, bbl/STB*
C_f	*formation (rock) compressibility, psi^{-1}*
C_w	*water compressibility coefficient, psi^{-1}*
G_{inj}	*cumulative gas injected, scf*
G_p	*cumulative gas produced, scf*
M	*ratio of gas cap gas volume to oil volume, bbl/bbl*
N	*initial oil-in-place, STB*
N_p	*cumulative oil produced, STB*
R_p	*cumulative produced gas-oil ratio, scf/STB*
R_s	*current gas solubility factor, scf/STB*
R_{si}	*gas solubility at initial pressure, scf/STB*
S_{wi}	*initial water saturation*
Δp	*change in the volumetric average reservoir pressure, psi*
W_e	*cumulative water influx, bbl*
W_{inj}	*cumulative water injected, STB*
W_p	*cumulative water produced, STB*
MBAL software	*Material balance software*

References

[1] Dake LP. The practice of reservoir engineering (revised edition). Amsterdam - London- New york- Oxford- Paris- Shannon-Tokyo: Elsevier 2001.
[2] Ogolo NA, Molokwu VC, and Onyekonwu MO. Techniques for effective oil production from thin oil rim reservoirs. Society of Petroleum Engineers (2018); SPE-193382-MS: https://doi.org/10.2118/193382-MS
[3] Onwukwe SI, Obah B and Uwaezuoke N. A model approach of controlling coning in oil rim reservoirs. Journal of Petroleum Engineering and Technology (2012); 2(1): 1-10.
[4] Ologe O. Reservoir evaluation of "T-X" field (Onshore, Niger Delta) from well log petrophysical analysis. Bayero Journal of Pure and Applied Sciences (2016) 9(2): 132-140.
[5] Kazeem AL, Inewari AW and Ademola OA. Preliminary assessment of oil-rim reservoirs: a review of current practices and formulation of new concepts. Society of Petroleum Engineers (2010); SPE-136955-MS: https://doi.org/10.2118/136955-MS
[6] Onyeukwu IH, Peacock A, and Matemilola SA. Improving recovery from oil rim reservoirs by simultaneous gas and water injection. Society of Petroleum Engineers (2012); SPE-162956-MS: https://doi.org/10.2118/162956-MS
[7] Rahim M, Hooman K, and Mohamad BO. How to get the most out of your oil rim reservoir? Society of Petroleum Engineers (2013); IPTC-16740-MS: https://doi.org/10.2523/IPTC-16740-MS
[8] Hurst W. The material balance equation. Society of Petroleum Engineers (1974); SPE-4920-MS
[9] Kanu AU, Onyekonwu MO. Advancement in material balance analysis. Society of Petroleum Engineers (2014); SPE-172415-MS: https://doi.org/10.2188/172415-MS
[10] Mogbolu E, Okereke O, Okporiri C, Ukauku I, Esharegharan O, Taiwo I and Sukubo I. Using Material balance (MBAL) multi tank model to evaluate future well performance in reservoirs with distinct geological units. Society of Petroleum Engineers (2015); SPE-178484-MS: https://doi.org/10.2118/178484-MS
[11] Nwaokorie C and Ukauku I. Well predictive material balance evaluations: a quick tool for reservoir performance analysis. Society of Petroleum Engineers (2012); SPE-162988-MS: https://doi.org/10.2118/162988-MS
[12] Demirmen F. Reserves estimation: the challenge for the industry. Journal of Petroleum Technology (2014); 59(05); 80-89.
[13] Tarek A. Advanced reservoir engineering. Amsterdam – London – New York – Oxford – Paris – Shannon – Tokyo : Elsevier (2005)
[14] Odeh AS. Reservoir simulation…what is it? Society of Petroleum Engineers (1969); SPE-2790-PA: https://doi.org/10.2118/2790-PA
[15] Lee WJ, Sidle R, and McVay D. Reservoir simulation: a reliable technology? Society of Petroleum Engineers (2011); SPE-146524-MS: https://doi.org/10.2118/146524-MS
[16] Diaso ER, Enaworu E, Seteyeobot I and Onuh CY. Reservoir simulation and decline curve analysis: a case study of "der" field, Niger delta basin, Pet Coal (2018); 60(5): 933-942.
[17] Murtha JA. Monte Carlo simulation: its status and future. Society of Petroleum Engineers (1997); SPE-37932-JPT: https://doi.org/10.2118/37932-JPT
[18] Bu T and Damsleth E. Errors and uncertainties in reservoir performance predictions. SPE Formation Evaluation (1996); SPE-30604-PA: https://doi.org/10.2118/30604-PA

To whom correspondence should be addressed: Dr. Uwaezuoke Nnaemeka, Department of Petroleum Engineering, Federal University of Technology, P.M.B 1526, Owerri, Nigeria

Petroleum and Coal

Article **Open Access**

A NEW APPROACH IN THE SIMULATION AND CALIBRATION OF THE AMINE REGENERATOR COLUMNS

Hamid Reza Mahdipoor

Gas Transportation and Processing Technology Development Divisio, Research Institute of Petroleum Industry, Tehran, Iran

Received April 28, 2019; Accepted July 1, 2019

Abstract

The sour gases coming from gas reservoir or oil refinery units contain acidic non-hydrocarbon components, such as hydrogen sulfide and carbon dioxide which can increase the problems caused by corrosion, hydrate formation, SO_2 emission and environmental pollution in the oil and gas refineries to reduce the amounts of CO_2 and H_2S below the technical and environmental standards. Amine process is considered as the most common process in the oil and gas refineries. Performing a reliable simulation of the regenerator column is a key point for improving the design and optimization of amine sweetening units. In this paper, the regenerator column of an industrial Amine sweetening unit is simulated by ProMax software. Then, the accuracy of the results is checked by industrial data, and a new method is presented to calibrate the simulation. The achieved results reveal the capability of this method for accurate simulation of the amine sweetening units.

***Keywords**: Amine sweetening unit, Regenerator column, Simulation, Calibration, Hydrogen sulfid.*

1. Introduction

Natural gas is considered as the most important and attractive fossil fuel in terms of lower emission compared to the other fossil fuels and ease of use. However, the sour gas coming from the well usually contains some non-hydrocarbon components, such as hydrogen sulfide and carbon dioxide which can arise several problems, e.g. corrosion, hydrate formation, and environmental pollution [1-2]. Moreover, the sour gases in the oil refineries usually contain considerable amounts of hydrogen sulfide which burning such gas as fuel will increase the emission of SO_2 to the atmosphere and rise environmental problems. Therefore, the gas treatment for removing impurities, such as CO_2 and H_2S, is one of the main parts of gas and oil refineries [3]. The concentration of H_2S and CO_2 in the natural gas stream must be kept below 4 ppm and 2 mol%, respectively [4-5]. There are several processes to remove acid gases from sour gases, for instance, solid bed process, and chemical solvent process. Among them, Amine process is considered as the most common process in the oil and gas refineries. Alkanamines such as monoethanolamine (MEA) and diethanolamine (DEA) and methyl-diethanolamine (MDEA) possess a high affinity to chemically absorb acid gases [6].

In a conventional amine sweetening unit, firstly CO_2 and H_2S of sour gas coming from the gas reservoir or oil refinery units are absorbed by amine solution in the absorber column (see Figure 1). The rich amine leaves the bottom of the absorber column and sent to the flash drum to release trapped hydrocarbons in lower pressure. Then, the rich amine after passing through the lean/rich heat exchanger enters the regenerator column in which the absorbed CO_2 and H_2S gases are released and leave the top of the regenerator column. The lean amine leaves the bottom of the regenerator column and then cooled in the lean/rich heat exchanger and Amine cooler and pumped and recycled to the top of the absorber column. The sweet gas leaves the top of the absorber column and sent to downstream units for more treatment if needed [7].

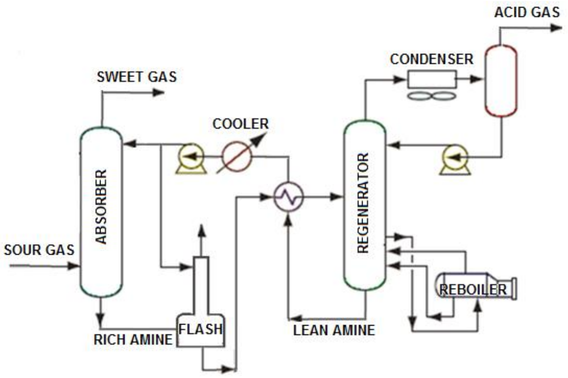

Figure 1. Schematic diagram of a typical amine sweetening unit

Since as described above, the absorber and regenerator columns are the most important equipment in the amine sweetening unit, the simulation, and modeling of amine absorption/desorption columns for natural gas sweetening process have been studied for decades [8]. As a result, two main methods, i.e., equilibrium and mass transfer, are developed to simulate the amine sweetening columns which identified by their accuracy and fast calculations, respectively [9]. These models are applied in the commercial simulation software such as Aspen, ProMax, etc. and used for design and optimization of the amine units. However, the results achieved from the commercial software usually include some deviations from actual data and need to be tuned and calibrated [10-15]. In the next section, a regenerator column of a typical Amine sweetening unit is simulated by ProMax software, and the accuracy of the results is checked by industrial data. Then, the achieved results are corrected by means of a new approach for calibration of the amine regenerator column.

2. Regenerator column simulation and calibration

In order to investigate the ability of the ProMax software for simulation of the regenerator column, a typical regenerator column in an industrial amine sweetening unit is considered. The specifications of the rich amine, which is considered as the regenerator column feed, are given in table 1. Moreover, Table 1 shows the specifications of acid gas leaves the top of the column, and lean amine leaves the bottom of the column. The considered regenerator column has 23 valve trays, and the duty of reboiler is equal to 22.12 MW. By means of this duty, the amounts of residual CO_2 and H_2S in the lean Amine are decreased to 0.01 mole% (188.6 mg/L) and 0.03 mole% (141.6 mg/L), respectively.

Table 1. Specifications of the input and output streams of regenerator column

	Rich amine	Acid gas	Lean amine
Temperature, °C	377	328	406
Pressure, kPa	340	210	260
Molar flow, kmole/h	11 000	471	10 529
Composition			
CO_2	2.34	54.49	0.01
H_2S	1.63	37.42	0.03
H_2O	85.27	7.63	88.74
MDEA	10.74	0.00	11.22
CH_4	0.02	0.47	0.00

The simulation of the amine regenerator column has been performed by ProMax software developed by BR&E company, which is a proper software for simulation of the Amine sweetening units [16]. In the simulation of a separation column, a solution is reached when all equations used to describe the steady state condition of that column, i.e., MESH equations, are solved and converged. These equations involve [17]: Material balance equations; Equilibrium equations; Summation equations; Heat balance equations.

The rigorous computational methods presented to solve these equations can be divided into four major groups:

1. The bubble-point methods (BP)
2. The sum-rates methods (SR)
3. The 2N Newton methods
4. The global Newton or simultaneous correction (SC) methods

Further classifications include:

5. Inside-out methods
6. Relaxation methods
7. Homotopy-continuation methods
8. Non-equilibrium models

Among them, items 5, 6, and 7 are modified forms of the first four methods in order to solve difficult systems. The non-equilibrium models are rate-based methods that instead of efficiencies, applying mass transfer correlations [17].

In the BP methods, the stage temperatures are found directly from solving the bubble-point equation. While, in the SR methods, the energy balances are used to adjust the stage temperatures. In the 2N Newton's methods, the temperatures and total flow rates are solved with each other, but compositions are calculated separately. Contrary to these three methods, in the SC method, the MESH equations and variables are solved simultaneously. Ishii and Otto method is considered as SC methods and has been used by ProMax software to solve the tower equations [17].

There are two general approaches for design and simulation of separation columns [15-19], (1) Applying overall efficiency to convert the theoretical stage numbers to real required tray numbers. The following relation can be considered:

$$\mathit{Teoritical\ Stage\ Numbers} = \mathit{Overal\ Efficiency} \times \mathit{Real\ Tray\ Numbers} \tag{1}$$

(2) Using real required tray numbers and applying component efficiencies for each tray. The Murphree efficiency of the tray j is defined as below:

$$E_i = \frac{y_{i,j}-y_{i,j-1}}{y^*_{i,j}-y_{i,j-1}} \tag{2}$$

wherein, $y_{i,j}$ is the mole fraction of component i in the vapor leaving the tray j. The star sign indicates the equilibrium condition.

Some commercial softwares such as Aspen-Hysys suppose component efficiencies for CO_2 and H_2S, while the others such as ProMax suppose component efficiencies equal to 100% and suggest using overall efficiency for simulation of separation columns. The conventional overall efficiency for Amine regenerator column is supposed to be equal to 50 percent [15-17].

Since this study is performed using the ProMax software, the simulation of the considered Amine regenerator column is performed firstly by considering an overall efficiency equal to 50 percent for this column. Therefore, the number of theoretical stages set equal to 12 ($23\times0.5 \approx 12$). "TSWEET Alternate Stripper" model is used as a distillation calculation procedure which does not take column hydraulic into consideration. The degree of freedom for running the regenerator column is equal to 2. As mentioned above, by setting the condenser temperature equal to 50°C and reboiler duty equal to 22.12 MW, the simulation can be executed. The achieved results presented in Table 2 shows that there is not a significant error in the predicted values for compositions of CO_2 and H_2S in the acid gas stream. On the other hand, the calculated values of the residual CO_2 and H_2S in the lean Amine have considerable errors.

Table 2. The composition of acid gas and lean amine streams in the first simulation

Stream		CO_2	H_2S
Acid gas composition, %mol	Actual	54.04	37.51
	Simulation	54.49	37.42
	Error %	0.52	0.66
Lean amine composition (mg/L)	Actual	183.96	143.61
	Simulation	111.28	326.07
	Error %	39.51	127.05

Since the amounts of residual CO_2 and H_2S in the lean amine can affect on the performance of the amine absorbers, a good prediction of them will be an important factor in the simulation of amine sweetening units [20]. Therefore, in the next step, a mixed approach is used by applying both mentioned efficiencies, i.e., overall efficiency together with component tray efficiency. According to the information presented in Table 2, the predicted value for the residual CO_2 gas in the lean amine is less than its actual value (111.28 compared to 183.96). Conversely, the predicted value for the residual H_2S gas in the lean amine is more than its actual value (326.07 compared to 143.61). More release of H_2S from amine solution and therefore, a decrease of the residual H_2S in the lean amine stream can be expected by increasing the efficiency of CO_2 in the regenerator column. For this purpose, a case study is performed in which the influence of decreasing the CO_2 efficiency on the concentration of the CO_2 and H_2S in the acid gas and lean amine streams leaving the regenerator column was studied. The results of this case study are summarized in Table 3. Moreover, the changes in residual H_2S and CO_2 in the lean amine vs. CO_2 efficiency is presented in Figure 2. As is shown in this figure, the decrease of the CO_2 efficiency decreases the residual H_2S and increases residual CO_2, simultaneously. In accordance with the information presented in Table 3, when the efficiency of CO_2 is equal to 70%, the amount of residual H_2S reaches to 144.07 mg/L which is near to its actual value, i.e., 143.61 mg/L.

Table 3. The influence of decreasing the CO_2 efficiency on the concentration of the CO_2 and H_2S

Efficiency (%)		Acid gas (mol %)		Lean amine (mg/L)	
CO_2	H_2S	CO_2	H_2S	CO_2	H_2S
100	100	54.49	37.42	111.28	326.07
85	100	54.32	37.58	194.12	233.35
70	100	54.14	37.77	318.22	144.07
55	100	53.94	37.96	487.73	71.34
40	100	53.75	38.15	704.02	26.35

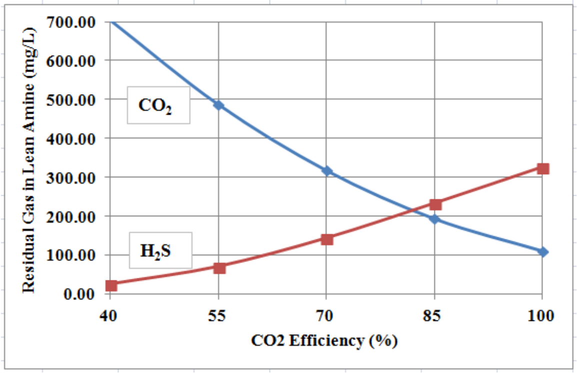

Figure 2. The changes of residual H_2S and CO_2 in the lean amine vs. CO_2 efficiency

The results of the second simulation in which the CO_2 efficiency is supposed to be equal to 70%, are presented in Table 4. As indicated in this table, the absolute error of CO_2 composition in the acid gas stream is decreased from 0.52% in the first simulation to 0.12% in the second simulation. Furthermore, the error of H_2S is decreased from 0.66% to 0.26%. On the other hand, although the absolute error of H_2S composition in the lean amine stream is decreased considerably from 127% in the first simulation to 0.32% in the second simulation, the difference between calculated and actual values of residual CO_2 in the lean amine stream is increased in the second simulation rather than the first run. This increase is due to the assumption of an efficiency lower than 100% for CO_2 in the regenerator column, which causes less CO_2 to be released.

Table 4. The composition of acid gas and lean amine streams in the second simulation

Stream		CO_2	H_2S
Acid gas composition, %mol	Actual	54.04	37.51
	Simulation	54.14	37.77
	Error %	0.12	0.26
Lean amine composition (mg/L)	Actual	183.96	143.61
	Simulation	318.22	144.07
	Error %	72.98	0.32

By increasing the number of stages in the regenerator column, disengaging of the CO_2 will be enhanced. Therefore, the effect of changing tray numbers or overall efficiency on residual CO_2 in the lean Amine is investigated in the next step of this work. The results of this case study are presented in table 5. Moreover, the changes of residual H_2S and CO_2 in the lean amine vs. tray numbers (overall efficiency) has been shown in Figure 3.

Figure 3 reveals that desorption of H_2S occurs mostly thermodynamically and has not affected by adding the number of trays. On the other hand, desorption of CO_2 occurs kinetically and is increased by adding the number of trays in the regenerator column (the residual CO_2 is decreased by increasing the number of trays). According to the information presented in table 5, when regenerator column has 16 trays in the simulation (i.e., overall efficiency is equal to 16/23 ≈ 70%), the amount of residual CO_2 reaches to 180.04 mg/L which is near to its actual value, i.e., 183.96 mg/L.

Table 5. The influence of changes in overall efficiency on the concentration of the CO_2 and H_2S

Overall efficiency	Equilibrium tray No	Acid gas (mol%)		Lean amine (mg/L)	
		CO_2	H_2S	CO_2	H_2S
43	10	54.09	37.81	420.42	160.84
52	12	54.14	37.77	318.22	144.07
61	14	45.19	37.72	239.25	140.69
70	16	54.22	37.68	180.04	141.36
78	18	54.25	37.65	136.32	142.79

The results of the third simulation in which both of the CO_2 efficiency and overall efficiency are supposed to be equal to 70%, are presented in table 6. As indicated in this table, the absolute errors of CO_2 and H_2S composition in the acid gas stream have more improvement in the third simulation rather than the second one. The absolute error of CO_2 composition in the lean amine stream is decreased from 39% in the first simulation and 73% in the second simulation to 2% in the third simulation which is in good agreement with industrial data can be considered as a satisfactory result. Although the error of calculated H_2S has a bit increase in the third simulation rather than the second simulation, since the total errors of the simulation are significantly decreased, it can be ignored.

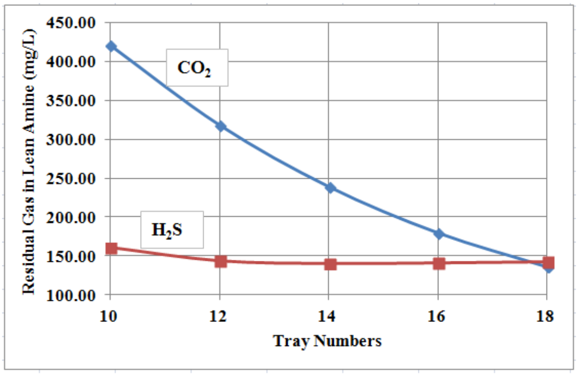

Figure 3. The changes of residual H_2S and CO_2 in the lean amine vs. tray numbers

Table 6. The composition of acid gas and lean amine streams in the third simulation

Stream		CO_2	H_2S
Acid gas composition, %mol	Actual	54.04	37.51
	Simulation	54.22	04
	Error %	0.03	0.26
Lean amine composition (mg/L)	Actual	183.96	143.61
	Simulation	180.04	141.36
	Error %	2.13	1.56

3. Conclusions

Amine process is considered as a common process in the oil and gas refineries to reduce the amounts of the acid gases from natural and fuel gases to overcome operational as well as environmental problems. Performing a reliable simulation of the regenerator column is a key point for improving the design and optimization of Amine sweetening units. Therefore, an industrial regenerator column was considered and simulated by ProMax software. Checking the simulation results with industrial data shows significant errors in the residual CO_2 and H_2S of lean Amine stream. A new approach was presented to adjust and calibrate the achieved results by means of applying overall efficiency and component efficiency concepts simultaneously. By considering the overall efficiency of the regenerator column equal to 70% and also, component efficiency of CO_2 equal to 70%, the total error of simulation was minimized, and the satisfactory results were achieved.

References

[1] Mohamadbigy Kh, Bazmi M, Behradi R, Binesh R. Amine absorption column design using mass transfer rate simulation. Petroleum & Coal, 2005; 47(2): 39-46.

[2] Hafizi A, Koolivand-Salooki M, Janghorbani A, Ahmadpour A, and Moradi MH. An Investigation of Artificial Intelligence Methodologies in the Prediction of the Dirty Amine Flow Rate of a Gas Sweetening Absorption Column. Petroleum Science and Technology, 2014; 32: 527-534.

[3] Mandal BP, and Bandyopadhyay SS. Simultaneous absorption of carbon dioxide and hydrogen sulfide into aqueous blends of 2-amino-2-methyl-1-propanol and diethanolamine. Chemical Engineering Science, 2005; 60(22): 6438-6451.

[4] Stewart M, and Arnold K. Gas Sweetening and Processing Field Manual, Gulf Professional Publishing, Waltham, 2011.

[5] Nourmohamadi Taemeh A, Shariati A, and Khosravi Nikou MR. Analysis of energy demand for natural gas sweetening process using a new energy balance technique, Petroleum Science and Technology, 2018; 36(12): 827-834.

[6] Saghatoleslami S, Salooki M K, and Mohamad N., Auto-Design of Neural Network–Based GAs for Manipulating the Khangiran Gas Rfinery Sweetening Absorption Column Outputs. Petroleum Science and Technology, 2011; 29: 1437-1448.

[7] Anonymous. Gas Processors Suppliers Association (GPSA). Engineering Data Book, GPSA, Tulsa, Chapter 22, 1987.

[8] Kohl AL, and Nielsen RB. Gas purification. 5th. Ed. Gulf Publishing Company, Houston, 1997.

[9] Danckwerts PV. Gas absorption accompanied by chemical reaction. AIChE Journal, 1995; 1(4): 456–463.

[10] Øi LE, and Kvam SHP. Comparison of energy consumption for different CO_2 absorption configurations using different simulation tools. Energy Procedia, 2014; 63: 1186-1195.

[11] Øi LE. Comparison of Aspen HYSYS and Aspen Plus simulation of CO_2 absorption into MEA from atmospheric gas. Energy Procedia, 2012; 23: 360-369.

[12] Garciaa M, Knuutilab HK, Gu K. ASPEN PLUS simulation model for CO_2 removal with MEA: Validation of desorption model with experimental data. Journal of Environmental Chemical Engineering, 2017; 5: 4693-4701.

[13] Gervasi J, Dubois L, Thomas D. Simulation of the post-combustion CO_2 capture with Aspen HysysTM software: study of different configurations of an absorption regeneration process for the application to cement flue gases. Energy Procedia, 2014; 63: 1018-1028.

[14] Alkatheri M, Grandas R, Betancourt-Torcat A, Almansoori A. Tapping Singular Middle Eastern Ultrasour Gas Resources Combining Membrane and Absorption Systems: Potential for Energy Intensity Reduction. Ind. Eng. Chem. Res., 2018; 57(17::5748-5763

[15] Mahdipoor HR, Dehghani A. Feasibility study of a sulfur recovery unit containing mercaptans in lean acid gas feed. Journal of Natural Gas Science and Engineering, 2016; 31: 585e588.

[16] Mahdipoor HR, Ghorbani A, Hamidnia M Kh. Technical Investigation of Integrated Gas Sweetening and Enrichment Process. Petroleum Research, under publication, 2018.

[17] Kister HZ. Distillation Design, McGraw-Hill, New York, 1992.

[18] Mahdipoor HR, Shirvani M, Jafari Nasr MR, Shakiba S. Rigorous dynamic simulation of an industrial tray column, considered liquid flow regime and efficiency of trays. Chemical Engineering Research and Design, 2007; 85(8): 1101–1111.

[19] Manning FS, Thompson RE. Oil field processing of petroleum, Volume One: Natural gas, Pennwell Publishing Company, Tulsa, Oklahoma, 1991.

[20] Mahdipoor HR. The influence of acid gas loading on the performance of acid gas enrichment (AGE) absorber column. IJCPS, 2015; 4(1): 1-7.

To whom correspondence should be addressed: Dr. Hamid Reza Mahdipoor, Gas Transportation and Processing Technology Development Divisio, Research Institute of Petroleum Industry, Tehran, Iran E-mail mahdipoorhr@ripi.ir

Petroleum and Coal

Article **Open Access**

EXPERIMENTAL RESEARCH AND FIELD IMPLEMENTATION OF CARBONATED WATER INJECTION TO ENHANCE OIL RECOVERY

Chang Hong Gao

American University of Ras Al Khaimah, United Arab Emirates

Received May 2, 2019; Accepted July 1, 2019

Abstract

Carbon dioxide is a major greenhouse gas that leads to global warming. Injection of CO_2 into oil reservoirs not only improves oil recovery but also stores large quantities of CO_2 in the reservoir. However,the limited supply of carbon dioxide often restricts the implementation of CO_2 flooding projects. Carbonated water injection (CWI) can be a good alternative when carbon dioxide is inadequate. Laboratory tests revealed that CO_2 effectively improved oil recovery by increasing oil volume and reducing oil viscosity. Several field cases in the USA demonstrated that CWI not only improved oil production but also enhanced water injection.

Keywords: *Carbon dioxide; Oil recovery; Carbonated water; Literature review.*

1. Introduction

After primary recovery and secondary recovery processes, usually more than 50% OOIP (original oil in place) still remains in reservoirs. Various methods have been developed to improve oil recovery. The most widely-adopted enhanced oil recovery (EOR) methods include steam injection, polymer flooding, and carbon dioxide injection.

Carbon dioxide generated by the consumption of fossil fuel is regarded as a major greenhouse gas that contributes to global warming. On the other hand, carbon dioxide can be injected into oil reservoirs to enhance oil production [1]. Moreover, large quantities of carbon dioxide can be stored underground, which reduces carbon dioxide emission to the atmosphere [2].

Large-scale carbon dioxide EOR projects are underway in the USA and Canada. Kinder Morgan Company injects 1.2 Bcf (billion cubic feet) of carbon dioxide per day in Texas and New Mexico oil fields [3], including SACROC unit, Yates field, Katz unit, and Tall Cotton unit in Texas, as shown in Fig. 1. The Weyburn field in Canada aims to store 30 million tons of carbon dioxide over 30 years [4]. Moreover, these projects proved to be financial successes because the additional oil production pays for the cost of carbon dioxide.

However, carbon dioxide EOR projects face several challenges. Projects are often restricted by the supply of carbon dioxide. Most of the carbon dioxide EOR projects are conducted in North America, where carbon dioxide supply is adequate [5]. However, the success in the USA and Canada cannot be easily duplicated in other regions, because of the shortage of carbon dioxide supply elsewhere. Secondly, carbon dioxide is much less viscous than reservoir oil. The injected carbon dioxide thus channels through the high-permeability strata without sweeping oil effectively. As a result, the carbon dioxide EOR projects in USA and Turkey reported early gas breakthrough [6].

When the supply of carbon dioxide is limited, carbonated water injection (CWI) may be a good alternative to carbon dioxide injection. The CWI process is to inject water saturated with carbon dioxide into reservoirs. Carbon dioxide in the carbonated water diffuses into oil and mobilizes the residual oil. Compared with carbon dioxide injection, CWI requires much less supply of carbon dioxide [7].

Besides, carbonated water has a much higher viscosity than pure carbon dioxide gas. As a result, the tendencies of gas channeling and early breakthrough are reduced. Moreover, CWI can be applied to reservoirs with high temperature and high salinity. For such harsh reservoirs, polymer injection has a slim chance to succeed [8-9].

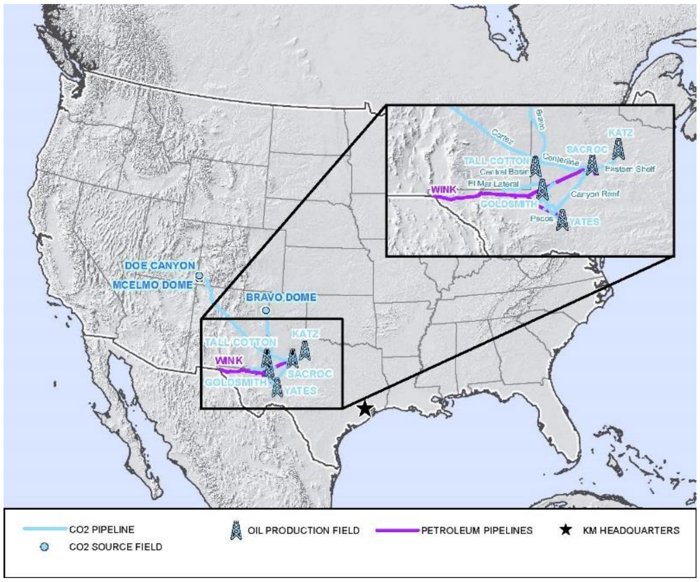

Fig. 1. Carbon dioxide EOR projects in Texas

2. Influences of carbon dioxide on oil and rock properties

After carbonated water is injected into the reservoir, carbon dioxide diffuses into oil because of the higher solubility of carbon dioxide in oil than in water. Experiments were conducted to study the solubility of carbon dioxide in hexadecane and heavy oil [10]. The properties of oil samples are presented in Table 1. The solubility test results are presented in Fig. 2. It can be concluded a significant amount of carbon dioxide can dissolve in oil, especially at high pressure. Besides, dissolution of carbon dioxide led to a reduction in oil viscosity, as shown in Fig. 3. Heavy oil viscosity reduced from 172 to 120 cP after 8 hours of contact with carbon dioxide at 50°C.

Table 1. Properties of oil samples

Oil sample	Specific gravity	API gravity	Viscosity at 50°C (cP)
Hexadecane	0.77	55.6	2.8
Heavy Oil	0.97	13	172

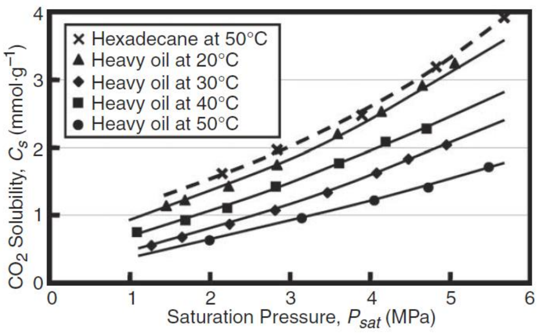

Fig. 2. Solubility of carbon dioxide in oil samples

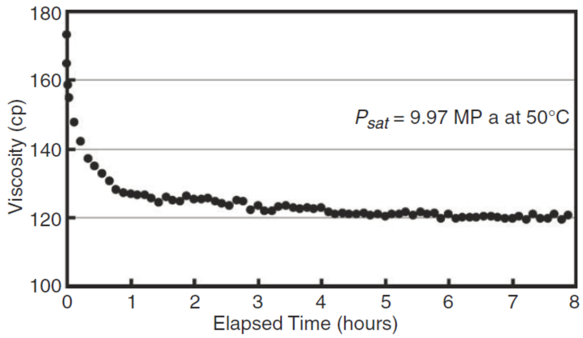

Fig. 3. Effect of carbon dioxide on oil viscosity

Another experimental study was conducted to measure the swelling of oil due to CO_2 dissolution [11]. The test oil sample was a heavy oil with a specific gravity of 0.97 and viscosity of 4,510 cP at 25°C. Test results in Fig. 4 show that oil volume increased by more than 6% due to carbon dioxide dissolution. Besides, the viscosity of the heavy oil significantly reduced, as shown in Fig. 5.

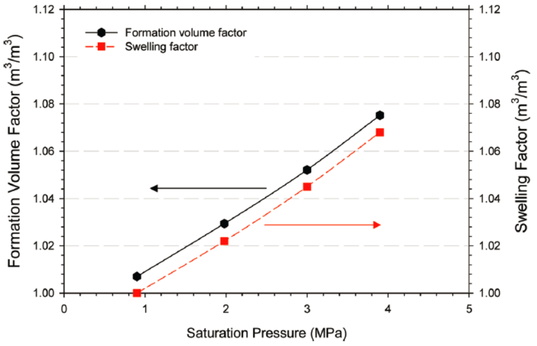

Fig. 4. Effect of carbon dioxide on oil swelling

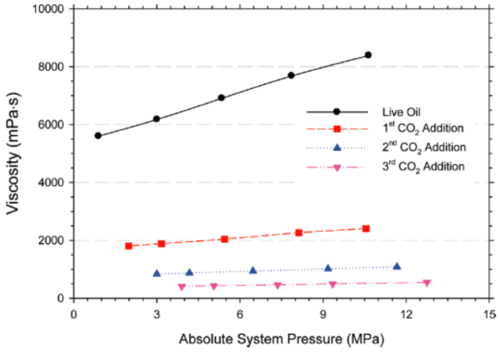

Fig. 5. Effect of carbon dioxide on the viscosity of extra heavy oil

After carbon dioxide is mixed with water, the pH of water decreases due to the production of carbonic acid, even though the majority of carbon dioxide stays in the aqueous phase as carbon dioxide molecules. While carbonated water migrates in the reservoir, carbonic acid, even though being weak, reacts with rock matrix and results in an increase in rock permeability [12]. It was reported that permeability of limestone cores improved by more than 10% after carbonated water injection [13].

3. Oil recovery tests with CWI

At Shell Oil Company, the research on CWI began in the 1960s. A number of sand pack tests were conducted at 120ºF and various pressures. The sand packs were either 3 ft long or 8 ft long. The viscosity of two oil samples was 10.7 and 57.4 cP. It was reported that CWI improved oil recovery by 4.5% for the 10.7 cP oil, and 13% for 57.4 cP oil.

In 1986, Shell conducted CWI tests with cores from Denver unit and crude oil from south Texas. The tests were conducted at 2,500 psi and 120ºF. It was revealed that CWI improved oil recovery by 18%. Oil swelling was recognized as the EOR mechanism, with swelling factor reaching 1.3.

In 2011, Shell Oil Company reported new test results on CWI. Carbonated water was injected into eight sand packs at varied injection velocities. The sand packs were 1.35 inch in diameter and 1 ft in length. The porosity of the sand packs were around 30%, and the permeability ranged from 2 to 4 Darcy. The crude oil samples had a specific gravity of 0.937 and viscosity of 70.7 cP under test conditions. The tests were carried out at 600 psi and 104ºF, and the injection rates were controlled at 1, 2, 4, and 15 pore volume/day. The CO_2 solubility was reaching 100 scf/stb under experimental conditions. The recovery was very high (80%) at a high injection rate, but the authors claimed that displacement became unstable at very high injection rate. Under injection velocity similar to field conditions, oil recovery improved by 9% [14].

At Herriot Watt University, carbonated water was injected in a rock sample obtained from North Sea field. The porosity and permeability or the cores were 0.35 and 4.58 Darcy, respectively. The core was injected with brine and subsequently carbonated brine. The brine composition was similar to the brine being injected in the North Sea field. Core flood tests were carried out at 2,500 psi and 100ºF. The tests revealed CWI improved oil recovery by 9% [15]. The authors also estimated that 11 million tonnes of carbon dioxide per year could be stored in the North Sea offshore fields.

4. Field cases of CWI

Oil Recovery Corporation carried out 6 CWI projects in the 1960s, with four being in Oklahoma, one in Kansas and one in Texas [16]. The field data is given in Table 2. The injection involved four steps. Firstly, liquefied butane was injected into wells to trigger a flood. Secondly, carbonated water containing a low concentration of surfactants was injected. Thirdly, CWI continued without surfactants. Finally, plain water was injected in the final phase.

Table 2. Field information for CWI projects

Field Name	Location	Reservoir depth (ft)	Average reservoir permeability (md)	Average reservoir porosity	Oil gravity (API)
K&S	Oklahoma	1,300	56	0.18	33
Wirt	Oklahoma	Not reported	44	0.16	33
Post Oak	Oklahoma	Not reported	43	0.17	35
White and Baker	Texas	1,750	24	0.21	31
Dome	Oklahoma	1,850	22	0.15	32

4.1. K&S Field

The K&S project was the first commercial CWI project. The 240 acre pilot was located near Bartlesville, Oklahoma. The field began production in 1905. The producing formation was sandstone at a depth of 1,300 ft. The detailed reservoir parameters are presented in Table 2. Before the CWI project started, the field had produced 512 thousand barrels of crude oil, and the oil production was only 30 BPD (barrels per day). The CWI project started in April 1958, involving 35 injection wells and 24 production wells. By late 1959, oil production rose from 30 to 2,300 BPD. Until early 1962, the oil rate was still above 600 BPD, as shown in Fig. 6.

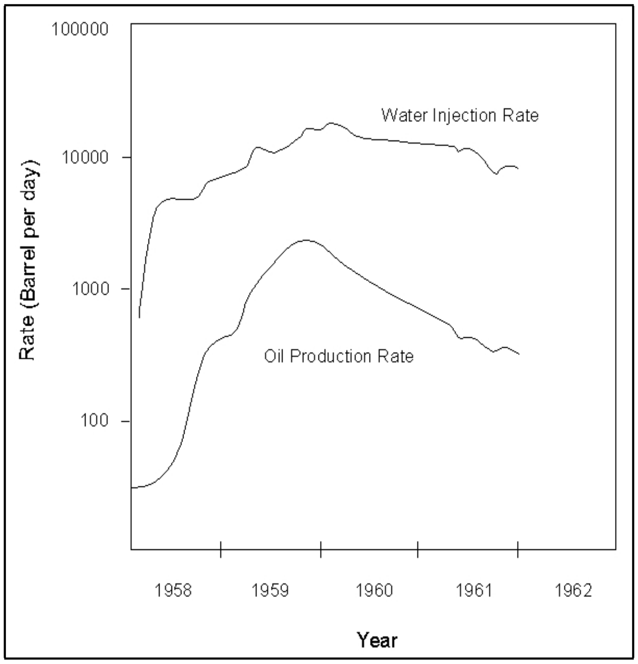

Fig. 6. Production history of K&S field

Water injection also improved. The water injection was initially 10 BPD per well. After CWI, the water injection rate rose to 700 BPD per well, and this improvement in injectivity lasted more than two years. It was observed that CWI not only improved rock permeability but also reduced bacteria that caused slime in the reservoir.

4.2. Wirt Field

The Wirt field is located north to the K&S project. CWI was initiated in March 1959. Within one year, the field oil production from four production wells increased continuously from 15 BPD to a peak of 420 BPD. Improved injectivity was also observed. The water injection rate climbed from 700 BPD to 1,500 BPD.

4.3. Post Oak Field

The post oak pilot lies to the south of the K&S pilot. Carbonated water was injected into 5 wells that control an area of 240 acres [17]. The CWI operation was started in April 1960, when the field was producing oil at 300 BPD. Within one year, the oil rate climbed to 870 BPD. Meanwhile, the water injection rate steadily increased from 2,500 BPD to 10,000 BPD.

4.4. White and Baker field

The 1,170-acre White and Baker pilot was located in Pecos County in Texas. The pilot involved 31 production wells and 16 injection wells. The field suffered from low injectivity. Before CWI, each injection well was receiving 100 BPD of water on average, and the oil production rate was only 150 BPD of oil. After CWI started in November 1960, water injection rate and oil production rate started to increase immediately. Unfortunately, very limited data was reported for this project.

For the K&S project, Wirt field and post oak project, carbon dioxide was supplied by on-site generating plants. Natural gas was burnt in boilers to produce flue gas containing 10% carbon dioxide. Carbon dioxide was extracted by the absorption process, then compressed, dried, and transported to wells through the pipeline.

While for the White and Baker project, carbon dioxide was purchased from a gas liquefaction plant, where carbon dioxide was removed from the natural gas produced from the Pecos County in Texas. The liquid carbon dioxide was then transported in insulated tanks to the storage facilities onsite.

4.5. Dome Field

The dome unit is located near Bartlesville in Oklahoma. The field started producing in 1910. Till 1961, it was estimated that 1.255 million barrels of oil had been produced. The daily oil production before CWI was 7-10 BPD.

CWI started in October 1961. Before initiation of CWI, each well was treated with 500 gallons of propane and 25 gallons of detergent. Water was injected through 2–inch tubing run to the bottom of the well. Liquid carbon dioxide was injected through half-inch tubing concentric to the 2-cinch tubing. Water and carbon dioxide mixed at the bottom of the well before entering the rock formations. About 5,000 tons of carbon dioxide was injected [18].

Production rate responded quickly to injection of carbonated water. In November 1961, oil production climbed to 448 BPD. In January 1962, oil production peaked at 740 BPD. Despite the good responses in production rates, the oil recovery was lower than expectation. Well, tests indicated that some wells had been fractured. It was believed that the injected carbonated water channeled through fractures, without effectively sweeping the oil in place.

4.6. Reservoir treatments with CWI

In the 1950s and 1960s, more than 300 wells in Oklahoma, Kansas, and Texas received carbonated water treatments to improve injectivity. Among these well, 225 wells received high-concentration carbonated water, while 70 wells were treated with low-concentration carbonated water [19].

For example, wells G-2 and G-3 in Kansas were treated with CWI. The production sandstone was 12.7 ft in thickness located at a depth of 790 ft. The reservoir porosity and permeability were 20% and 32 md, respectively. Before CWI, water injection rates declined to 22 BPD for well G-2 and 4 BPD for well G-3 due to scale problems. CWI started in October 1962. Both wells responded quickly. In November 1962, water injection climbed to 105 BPD and 57 BPD for well G-2 and G-3, respectively.

5. Conclusions

Carbonate water injection can be a good alternative to CO_2 flooding if the supply of CO_2 is limited. CWI improves oil recovery by swelling oil volume and reducing oil viscosity. Laboratory studies demonstrated CO_2 could significantly reduce the viscosity of heavy oil. Several CWI projects were carried out in USA. CWI improved both oil production and water injection. In conclusion, CWI has good potential for industrial application as an effective EOR method.

References

[1] Holm LW. CO_2 flooding: its time has come. Journal of Petroleum Technology, 1982; 34 (12) 2739-2745.

[2] Gao C, Guo L, Li X. Heavy oil production by carbon dioxide injection. Greenhouse Gases Science and Technology, 2013; 3 (3) 185-195.

[3] Xiao C, Harris M, Wang F. Field testing of CO2 EOR in Sacroc field. SPE 147544 Presented at Unconventional Resources Conference, 15-17 November 2011, Calgary Canada.

[4] Condor J, Suebsiri J, Wilson M. Carbon footprint in CO_2 EOR projects the Weyburn case. SPE 138885 Presented at Latin America Petroleum Conference, December 2010, Lima Peru.

[5] Koottungal L. Worldwide EOR survey. Oil and Gas Journal, 2012, 101 (4) 55-70.

[6] Larkin R. To remediate inter-well communication problems in Sacroc project. SPE113305 Presented at EOR Symposium, 19–23 April 2008, Tulsa Oklahoma.

[7] Sohrabi M, Kechut N, Riazi M, Jamiolahmady M, Ireland S, Robertson G. Core flooding studies to investigate the potential of carbonated water injection as an injection strategy for improved oil recovery and CO_2 storage. Transport in Porous Media, 2012 (1) 101-121.

[8] Gao C. Scientific research and field applications of polymer flooding in heavy oil recovery. Journal of Petroleum Exploration and Production Technology, 2011, 1 (2) 65–70.

[9] Gao C, Shi J, Zhao F. Successful polymer flooding and surfactant-polymer flooding projects at Shengli oil field from 1992 to 2012. Journal of Petroleum Exploration and Production Technology, 2013, 4 (1) 1-8.

[10] Or C, Sasaki K, Sugai Y, Swelling and viscosity reduction of heavy oil by CO_2 gas foaming in immiscible condition. May 2016 SPE Reservoir Evaluation and Engineering.

[11] Luo P, Zheng Y, Wang X, Huang S, Propane-Enriched CO_2 Immiscible Flooding For Improved Heavy Oil Recovery. Energy and Fuels 2012, 26 (4) 2124-2135.

[12] Perez J, Poston S, Sharif Q. Carbonated water imbibition flooding: an enhanced oil recovery process for fractured reservoir. SPE 24164 Presented at the EOR Symposium, 22–24 April 1992, Tulsa Oklahoma.

[13] Mohamed I, He J, Nasereldin H. Permeability change during CO_2 injection in carbonate rock. SPE 140943 Presented at Production Operation Symposium, 27–29 March 2011, Oklahoma City.

[14] Dong Y, Dindoruk B, Ishizawa C. An experimental investigation of carbonated water flooding. SPE 145380 Presented at SPE Annual Conference, 30 October-2 November 2011, Denver Colorado.

[15] Kechut N, Riazi M, Sohrabi M, Jamiolahmady M. Tertiary oil recovery and CO_2 sequestration by carbonated water injection. SPE 139667 Presented at SPE International Conference on CO_2 Capture Storage and Utilization, 10-12 November 2010, New Orleans

[16] Christensen R. Carbonated water flood results – Texas and Oklahoma. SPE 66 Presented at the Seventh Annual Meeting of AIME, 25-26 May 1961, Farmington New Mexico

[17] Hicock C, Ramsay H. Case history of carbonated water flood in Dewey Bartlesville field. SPE 333 Presented at SPE Secondary Recovery Symposium, 7–8 May 1962, Wichita Falls, Texas.

[18] Scott J, Forrester C. Performance of domes unit carbonated water flood first stage. SPE 1126 Presented at SPE Production Research Conference, 3-4 May 1965, Tulsa Oklahoma.

[19] Ramsay H, Small F. Use of carbon dioxide for water injectivity improvement. Journal of Petroleum Technology, 1964, 16 (1) 25-31.

To whom correspondence should be addressed: Dr. Chang Hong Gao, American University of Ras Al Khaimah, United Arab Emirates

Petroleum and Coal

Article **Open Access**

IMPROVING OIL RECOVERY USING Fe_2O_3 NANOPARTICLES FLOODING

A.N. El-hoshoudy[1,2], S. Gomaa[2], and M. Taha[2]*

[1] *Production Department, Egyptian Petroleum Research Institute, Naser City, Cairo, Egypt*
[2] *Petroleum Engineering Department, Faculty of Engineering, British University in Egypt, Elshorouk City, Cairo, Egypt*

Received May 4, 2019; Accepted July 1, 2019

Abstract

Both primary and conventional secondary recovery methods can approximately produce 35% of the original oil in place (OOIP). Application of nanotechnology in the petroleum industry has already drawn attention for its great potential of enhancing oil recovery. In the last few years, some publications have already addressed this topic, but its mechanism to enhance oil recovery has not been released very clearly. The main objective of this paper is to investigate the effect of Fe_2O_3 nanoparticles to improve oil recovery. This paper also aims to investigate the reason behind this improvement in oil recovery. A series of sandpack flooding runs were conducted to study the effect of Fe_2O_3 nanoparticles concentration in the displacing brine on wettability alteration, oil viscosity, interfacial tension, and finally the ultimate recovery factor. Fe_2O_3 nanoparticles were prepared in four different concentrations (0.005, 0.01, 0.1 and 1 wt. %) using sonication method. Then Fe_2O_3 nanoparticles used for flooding in a sand pack model after saturation of brine and crude oil respectively. The crude oil supplied from the western desert in Egypt with API= 30.749º. All nanoparticles have the same size of 5.0 nm. The base run was performed using conventional water flooding. The ultimate recovery factor by water flooding was 50.4 % of the OOIP. Results have proved an enormous improvement in the recovery factor that reaches 70 % of the OOIP by using Fe_2O_3 nanoparticles at a concentration of 0.01 wt%. Moreover, the effect of Fe_2O_3 nanoparticles on oil viscosity, interfacial tension, and wettability alteration was investigated. Finally, an economic study was conducted through a comparison between Fe_2O_3 nanoparticles flooding and conventional water flooding.

***Keywords**: Fe_2O_3 nanoparticles; Improved oil recovery; Wettability alteration; Oil viscosity; Interfacial tension.*

1. Introduction

Currently, enhanced oil recovery through chemical flooding acquires incremental attention on both laboratory and field scale [1-7]. The remaining oil in place after applying primary and secondary oil recovery methods reaches in most oil fields, 65% of the original oil in place [8]. In the few past years, some changes were noticed in the way which crude oil is extracted all over the global market. As in Latin America, the production of crude oil was increased by approximately 4.4 MMbbl/day. About 1.0 MMbbl/day out of this production growth, was produced by the upgrading of crude oil properties from Venezuela [9]. Nanotechnology deals with various structures of materials having dimensions of what is called a nanoscale level, perhaps from 1 to l00 nm [10]]. One nanometer (nm) is one billionth of a meter, and it is 10,000 times smaller than the diameter of a human hair. A nanoelement compares to a basketball, like a basketball to the size of the earth. The promise and essence of the nanoscale science and technology are based on the demonstrated fact that materials at the nanoscale have distinct chemical, electrical, magnetic, mechanical and optical properties rather than the bulk materials [11]. Many researchers investigated the effect of some nanoparticles on improving oil recovery. They stated that the nanoparticles have the ability to penetrate the edge of the discontinuous phase and form a film between the oil and the rock, thus improves the oil recovery, as illustrated in figure 1. This mechanism is known as a joint mechanism [12-14].

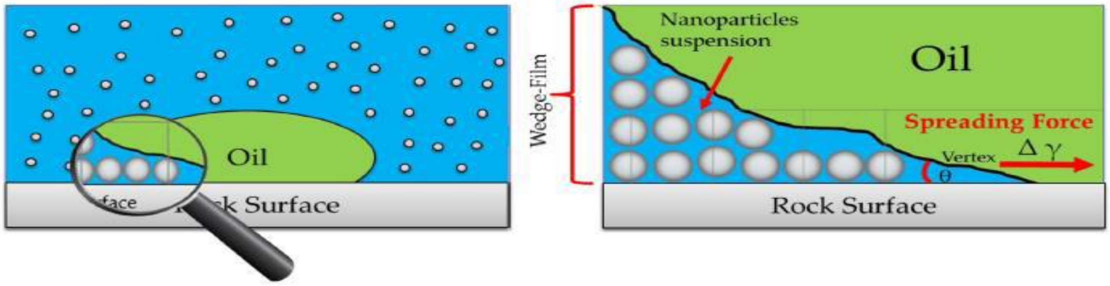

Fig. 1. Clarifying the joint mechanism due to the presence of nanoparticles in the injection fluid

Alomair *et al.* [15] and Alomair and Alajmi [16] have stated that there is a noticeable effect on interfacial tension of crude oil/ brine and oil viscosity through flooding of nano-SiO_2, NiO and tungsten trioxide. The nanoscale of any particle type has shown their ability in the change of its chemical and physical properties; due to the difference between the particles at their naturally occurring size, to the nanoscale size. In other words, nanoparticles of a certain material exhibit different behavior than the material in its original size [17]. Lower production from heavy oil reservoir can be a result of the high crude oil viscosity. Therefore, decreasing the viscosity of crude oil is the best way to deal with these reservoirs. When the oil viscosity decreases, the oil mobility increases, and then an increase in the oil recovery occurs. The main reason for increasing the viscosity of crude oil is the reactions between the clusters. These micelles like clusters are the product of the asphaltene molecules agglomeration inside the crude oil.

Reduction of crude oil viscosity can occur when the clusters reactions stop by breaking the agglomeration between asphaltene molecules. One of the recommended solutions is reducing the crude oil viscosity by adding kerosene to crude oil. By the way, it was widely assumed that kerosene does not break the asphaltene molecules agglomeration. However, kerosene has shown its role as an effective diluent [18]. Nano-sized particles have shown their ability to change the physical and chemical properties compared to the particles in their natural size. These nanoparticles have also proved the ability to break down the agglomeration between the asphaltene molecules, so the interactions between clusters stop and the oil viscosity decreases [19]. Clark *et al.* [20] concluded that increasing the reservoir temperature is not the only way that decreases the oil viscosity. A series of chemical reactions have shown also a noticeable performance for decreasing the crude oil viscosity. The addition of nanometals to the process of thermal hydrocarbon recovery can guarantee a more reduction in the oil viscosity when it is compared with steam injection only. However, there is not a possible way to combine these nanoparticles with the steam injection until now [21]. Accordingly, this research suggests that the best applicable method to investigate the effect of nanoparticles on the crude oil viscosity through measuring the oil viscosity after being exposed to nanofluid flooding. In addition, another method was used to study the effect of adding nanoparticles at different concentrations on crude oil at 200 °F that represents the actual reservoir temperature.

Wettability alteration or the change of the formation surface from oil wet to water wet has approved its ability to show a great enhancement to the oil recovery. Wettability alteration affects the relative permeability, fluid distribution, and fluid flow behavior [22]. Some nanoparticles have proved their ability to change the surface from hydrophobic to hydrophilic. In other words, some of the nanoparticles can change the surface properties from repelling water, to attract water and repelling oil instead. Accordingly, the electrostatic repulsion between oil and formation is noticed to be much higher during the existence of some nanoparticles. Then, a higher oil recovery occurs [22]. The probability of exploring new huge hydrocarbon fields is not that high as the way it was before. On the other hand, exploring small oil fields is not economical because of its highly expensive costs [23]. Therefore, the most economical solution is to produce trapped oil inside the previously developed field. Surfactant flooding and nano flooding displacement are the two common methods that are used from enhanced hydrocarbon methods, to produce this trapped oil and to increase the oil recovery [24]. The use of nanotechnology was commonly needed in the downstream industry [25]. However, there are researches that have proved the great impact of using nanoparticles inside the reservoirs, where an enhancement of viscosity, interfacial tension, and wettability alteration occur [26].

For the optimum nanofluid displacement, the concentration of nanoparticles has to exceed the critical micelle concentration, to decrease the interfacial tension and to increase the oil recovery [27]. Giraldo *et al.* [28] used SiO_2 nanoparticles-based nanofluid and NiO/SiO_2 nanoparticles-based nanofluid at a concentration of 100 mg/L and size of 116.5 nm. The researchers stated that the IFT in the absence of nanoparticles has a value of 26.2 mN/m. When nanoparticles are added to the system, the IFT decreases with both nanoparticles and is lower for the NiO/SiO_2 nanoparticles regarding the SiO_2 nanoparticles for the whole range of concentration evaluated. A minimum of the interfacial tension is observed at 100 mg/L for both SiO_2 and NiO/SiO_2 nanoparticles with values of 20.5 mN/m and 17 mN/m, respectively. However, they stated that SiO_2 did not show an increase in oil recovery regarding the one obtained in the water flooding step. Meanwhile, the NiO/SiO_2 nanoparticles at the same concentration showed an increase in oil recovery up to 50%. Sayed and Mohamed [29] investigated the effect of silica nanoparticles on enhanced oil recovery. They found that the ultimate recovery factor has been increased at a certain size and concentration. They indicated that the enhanced oil recovery in this situation results from the wettability alteration. Sayed, Adel, and Mohamed [29-30] investigated the effect of alumina (Al_2O_3) nanoparticles on enhanced oil recovery. They found that the ultimate recovery factor of 81.13% is achieved at 10 g/L. of Al_2O_3. They indicated that the enhanced oil recovery in this situation results from the wettability alteration. Moreover, they have addressed the importance of some nanoparticles in reducing crude oil viscosity and enhanced oil recovery.

This research serves to investigate the effect of Fe_2O_3 nanoparticles flooding on oil recovery. Four different concentrations of (0.005, 0.01, 0.1 & 1 wt.%) with size of <50 nm will be used. Conventional water flooding case was considered as the base run. Then the Fe_2O_3 nanoparticles will be sonicated in brine and used as a secondary recovery method. The crude oil viscosity and interfacial tension are measured before and after adding Fe_2O_3 nanoparticles. The effect of Fe_2O_3 nanoparticles on wettability alteration and improving oil recovery were investigated.

2. Experimental work

2.1. Materials and chemicals

Fe_2O_3 nanoparticles are iron(III) oxide, CAS no. 1309-37-1, with a size of less than 50nm, purchased from Sigma Aldrich.

2.2. Preparation of brine

Sodium chloride (NaCl) was used for preparing brine with a concentration of 35,000 ppm. This brine was then used for saturating sand pack, then soaked by crude oil to retrieve the initial reservoir conditions. Moreover, brine was used for preparing the nanofluid solution, which is then undergoing a sonication process.

2.3. Determining fluid properties

Pycnometer was used to measure the density of the fluids. While Chandler rolling ball viscometer was used to measure the fluid's viscosity. Finally, Tensiometer was used to measure the interfacial tension. The density of crude oil was measured to be 0.87 g/cc (API= 30.7º). The interfacial tension between crude oil and brine was 37.9 dyne/cm. While the measured crude oil viscosity = 9 cp.

2.4. Sandpack model

Average porosity is 28%, and the average absolute permeability is 832 mD. Sand pack inner diameter was 6 cm, and the length is 15 cm. Bulk volume is equal to 425 cc. Figure 2 illustrates a schematic representation of the flooding apparatus.

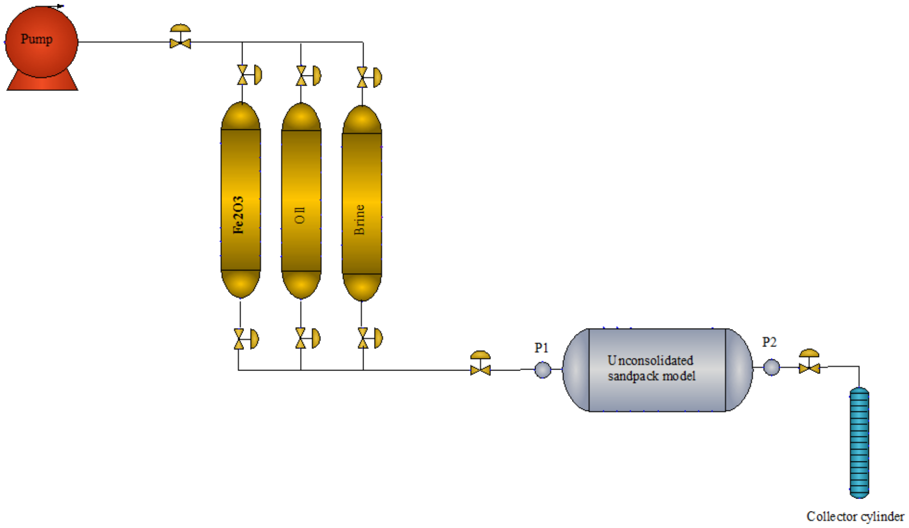

Figure 2. Schematic representation of displacement apparatus.

2.5. Sand pack initiation

Nanoparticles were prepared by the required concentrations in the previously prepared brine. Then this solution undergoes the sonication process inside a sonicator for 2-3 hours to make all nanoparticles suspended inside the solution or nanofluid.

2.6. Flooding operation

First, the sand pack is filled with sand while considering packing the sand well. Then brine is injected to the sandpack till the sandpack is fully saturated with brine. Then, inject oil to displace the existing brine. Not all the brine is displaced by the oil. Accordingly, the amount of displaced brine is the same amount of the initial oil in place for this case, and by subtracting the amount of brine displaced by oil from the total amount of brine that was initially injected to saturate the sand pack, now the calculated amount of un-displaced brine can represent the connate water saturation. Thus, it is possible to have the sand pack conditions like initial reservoir conditions.

2.7. Water flooding

In the base run case, brine was injected to displace the oil, and this case represents the conventional water flooding scenario. The amount of oil displaced by brine was measured to determine the oil recovery factor. Then, viscosity and interfacial tension of the displaced oil was measured. Relative permeability curve was constructed to determine if the sand pack is oil wet or water wet. This case was considered as a reference case for each following case, where the results of each nanofluid case were compared to this case of the conventional water flooding.

2.8. Injection of nanofluids

After constructing the conventional water flooding as a reference case, Fe_2O_3 nanofluid was injected in four different concentrations (0.005, 0.01, 0.1, 1.0 wt%). The oil recovery of each case was determined, along with measuring viscosity, interfacial tension, and wettability alteration. Accordingly, the reason behind the change (whether enhancement or reduction) in oil recovery for each case, was identified (due to change in oil viscosity, interfacial tension, and wettability). The experimental procedure was performed as follow:

1. Fill the sand pack with sand and consider packing the sand well. Then, determination of its dry weight.
2. Inject brine until the sand pack is fully saturated; calculate absolute permeability from Darcy equation. Then, measuring the sand pack weight at its saturated condition.
3. Subtract dry weight from saturated weight and then divide the result by brine density to calculate the pore volume.
4. Inject oil to displace the existing brine, where the amount of displaced brine is the same amount of the initial oil in place for this case. By subtracting the amount of brine displaced by oil from the total amount of brine that was initially injected to saturate the sand pack, now the calculated amount of un-displaced brine can represent the connate water saturation. The sand pack then simulates the reservoir having original oil in place and connate water.
5. Inject brine to displace the oil. For each fraction of the pore volume injected, the amount of injected brine is measured and the time is determined to calculate flow rate, then by substituting in Darcy equation, effective permeability is easily calculated.
6. Measure the amount of oil extracted to determine the oil recovery percentage.
7. Construct a relative permeability curve using absolute and effective permeability to determine the change in wettability.
8. Measure the viscosity of the extracted crude oil.
9. Measure the interfacial tension between the extracted crude oil with the injected solution.

To construct other cases than the conventional one, in step five, inject the prepared nanofluid instead of brine. Then, compare the results to the conventional water-flooding scenario.

3. Results and discussion

3.1. Wettability alteration

3.1.1. Base run: Conventional water flooding

Relative permeability curve, as shown in Figure 3 for conventional water-flooding, depicts that the intersection of both curves occurs at water saturation of 0.36. Accordingly, the formation is strong oil wet. Then, any noticeable alteration in the wettability will decrease the residual oil saturation and increases oil recovery. The ultimate recovery factor reaches up to 50% of the original oil in place, as shown in Figure 4.

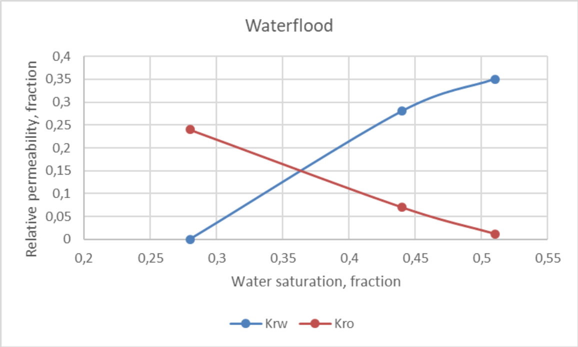

Fig. 3. Relative permeability curve for conventional water flooding

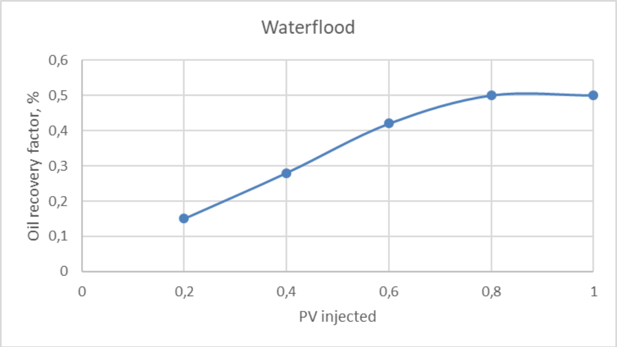

Fig. 4: Effect of conventional water flooding on oil recovery

3.1.2. Fe_2O_3 flooding (Case 1)

The Fe_2O_3 is added to brine in concentrations of 0.005 wt %. After sonication, the nanofluids were injected to the core sample to displace the oil. Relative permeability curve, as shown in figure 5. The intersection of both curves occurs at water saturation of 0.38, that means that formation is now slightly more water wet than the conventional water-flooding case. The oil recovery factor is 48 % of the original oil in place, as shown in figure 6.

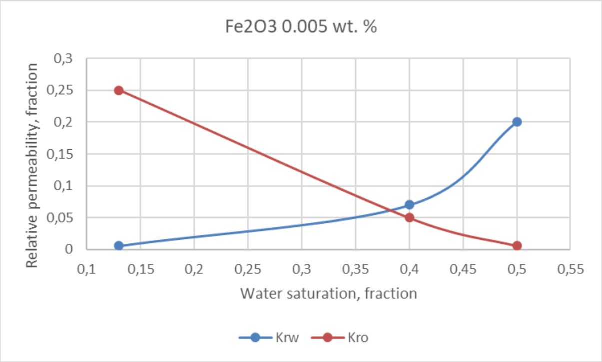

Fig. 5. Relative permeability curve at 0.005 wt % Fe_2O_3

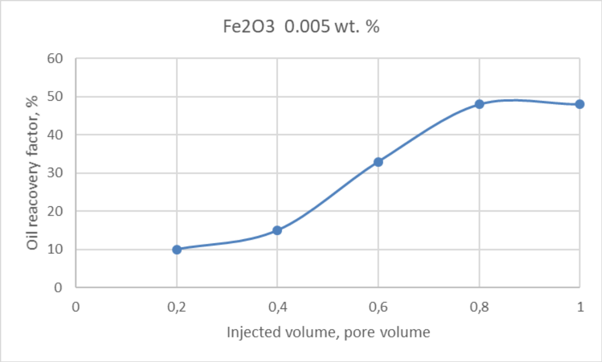

Fig. 6. Effect of 0.005 wt. % Fe_2O_3 on oil recovery

3.1.3. Fe_2O_3 flooding (Case 2)

The Fe_2O_3 is added to brine in concentrations of 0.01 wt. %. After sonication, the nanofluids were injected to the core sample to displace the oil. Relative permeability curve, as shown in Figure 7. The intersection of both curves occurs at water saturation of 0.42, that means that formation is more water wet than the conventional water-flooding case. The oil recovery factor is 80 % of the original oil in place, as shown in Figure 8.

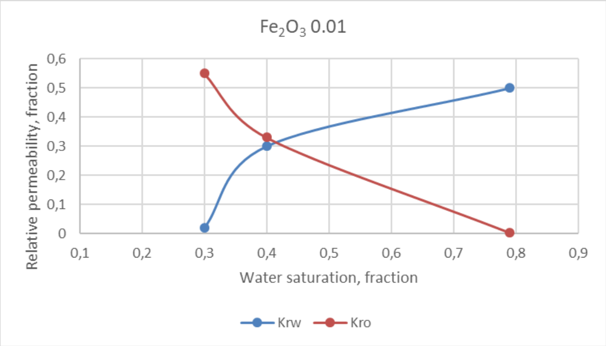

Fig. 7. Relative permeability curve at 0.01 wt % Fe_2O_3

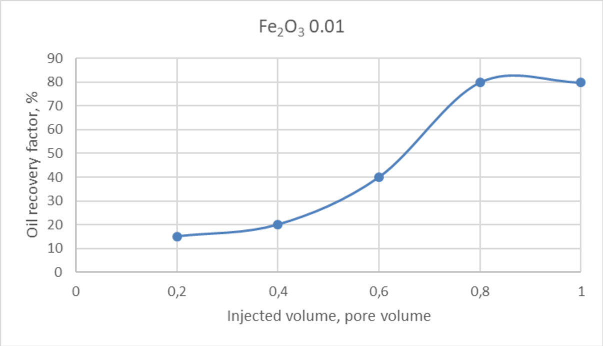

Fig. 8. Effect of 0.01 wt % Fe_2O_3 on oil recovery

3.1.4. Fe_2O_3 flooding (Case 3)

The Fe_2O_3 is added to brine in concentrations of 0.1 wt %. After sonication, the nanofluids were injected to the core sample to displace the oil. Relative permeability curve, as shown in Figure 9. The intersection of both curves occurs at water saturation of 0.43 that means that formation is more water wet than the conventional water-flooding case but less than a case of 0.01. The oil recovery factor is 50 % of the original oil in place, as shown in Figure 10.

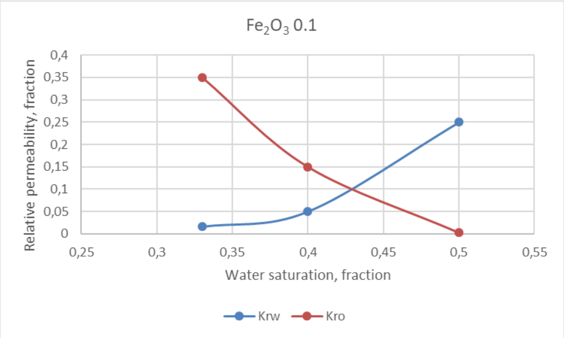

Fig. 9. Relative permeability curve at 0.1 wt. % Fe_2O_3

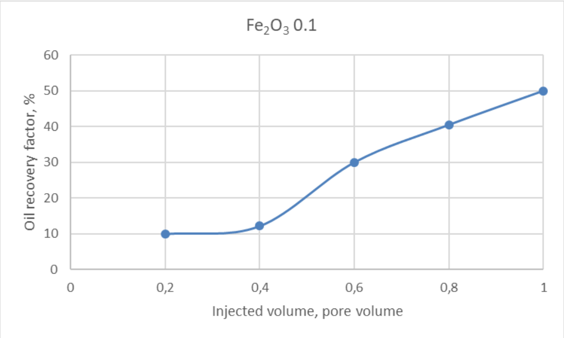

Fig. 10. Effect of 0.1 wt. % Fe_2O_3 on oil recovery

3.1.5. Fe_2O_3 flooding (Case 4)

The Fe_2O_3 is added to brine in concentrations of 1 wt. %. After sonication, the nanofluids were injected to the core sample to displace the oil. Relative permeability curve, as shown in Figure 11. The intersection of both curves occurs at water saturation of 0.46, that means that formation is now slightly more water wet than the conventional water-flooding case. The oil recovery factor is 45 % of the original oil in place, as shown in Figure 12.

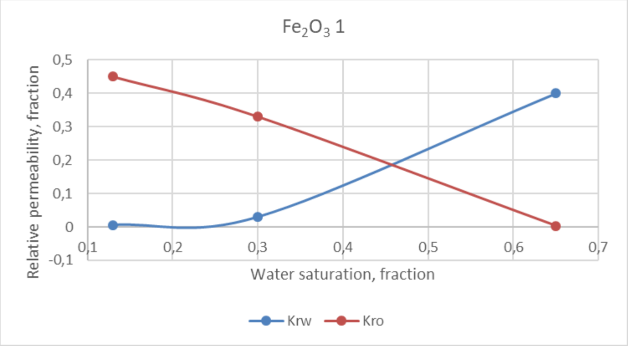

Fig. 11. Relative permeability curve at 1 wt. % Fe2O3

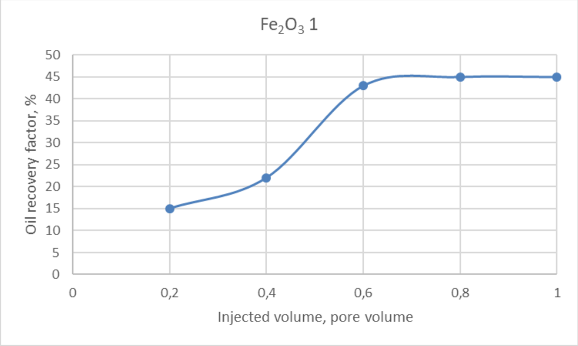

Fig. 12. Effect of 1 wt. % Fe2O3 on oil recovery

4. Reduction of crude oil viscosity

Fe_2O_3 nanoparticles with four concentrations (0.005, 0.01, 0.1 and 1 wt. %) are added to the crude oil. The mixture is sonicated. Then, the crude oil viscosity is measured using rolling ball viscometer at 200 ºF that represents the actual reservoir temperature. Figure 13 shows the effect of each concentration of Fe_2O_3 nanoparticles on crude oil viscosity. When the concentration of Fe_2O_3 nanoparticles increases the crude oil viscosity decreases.

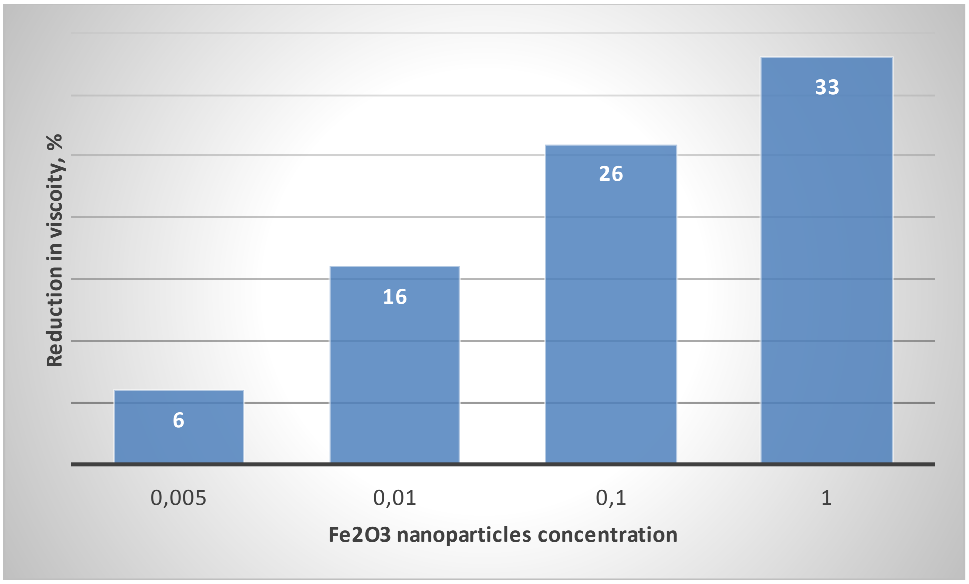

Figure 14. Effect of Fe2O3 nanoparticle on crude oil viscosity

5. Reducing interfacial tension between crude oil & flooding fluid

Fe_2O_3 nanoparticles with four concentrations (0.005, 0.01, 0.1 and 1 wt. %) are added to the crude oil. The mixture is sonicated. Then, the interfacial tension is measured by using Tensiometer. Figure 15 shows the effect of each concentration of Fe_2O_3 nanoparticles on interfacial tension. When the concentration of Fe_2O_3 nanoparticles increases the interfacial tension decreases.

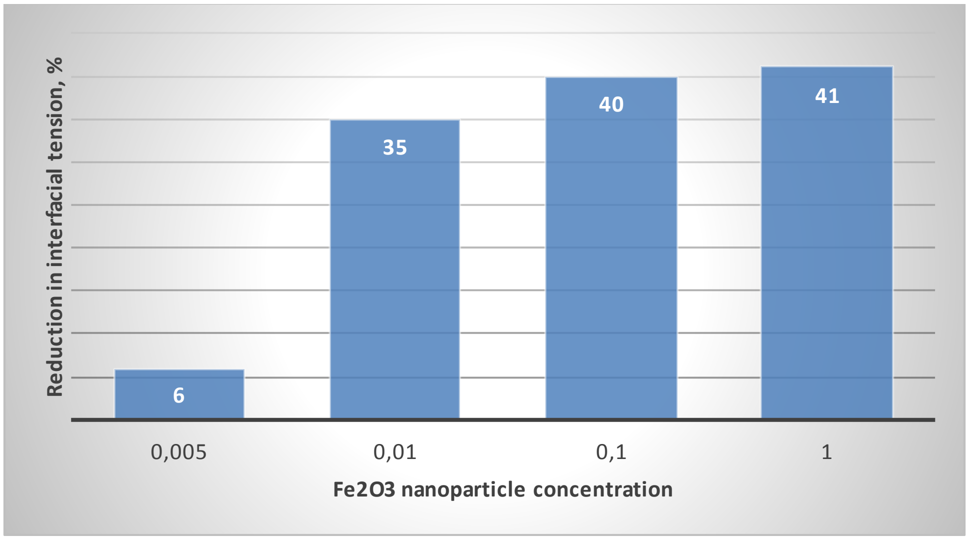

Figure 15. Effect of Fe_2O_3 nanoparticle on interfacial tension

6. Economic profile

To find whether the need for this recovery mechanism is applicable or not. The net present value for the total project has been estimated. Firstly, the initial oil in place for a field is assumed to be 100 MM STB, and the field comprises four production wells with the same decline rate. Also, the number of years for production is assumed to be 10 years. Moreover, drilling and production operational cost is assumed to be 25 million dollars considering the cost of flooding operations. More and more, a discount factor of 10% is also assumed. All the previous assumptions were applied to all the cases. However, the only variable now is the nano cost. The net present value for the water flood case is shown in Figure 16, and the net present value for the Fe_2O_3 nanoparticles flooding of concentration 0.01 wt. % is shown in Figure 17. It is clear from the figures that the net present value in case of using the Fe_2O_3 nanoparticles is more than that of the conventional water-flooding case.

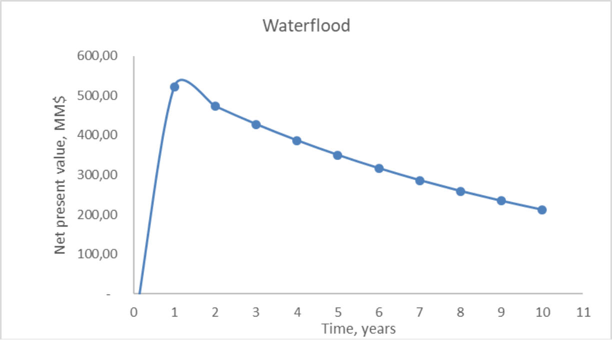

Fig. 16. Net present value for waterflood scenario

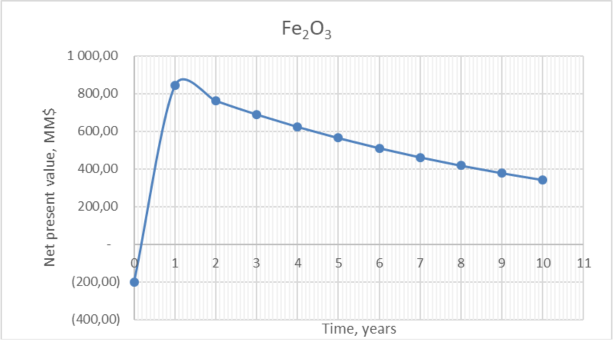

Fig. 17. Net present value for Fe_2O_3 nanoparticles 0.01 wt. % scenario

7. Conclusion

The effect of Fe_2O_3 nanoparticles with four different concentrations (0.005, 0.01, 0.1, 1 wt.%) on crude oil viscosity, interfacial tension, wettability alteration, and oil recovery factor was investigated. Flooding of Fe_2O_3 nanoparticles as a secondary recovery has proved its ability to reduce interfacial tension, crude oil viscosity, alter formation wettability, thus increase oil recovery. The oil recovery factor is 50 % of the original oil in place by conventional water flooding and increased to 80 % by using Fe_2O_3 nanoparticles with a concentration of 0.01 wt.

%. This work proved the ability of Fe_2O_3 nanoparticles to alter the formation to more water wet. Moreover, Fe_2O_3 nanoparticles can reduce oil viscosity and interfacial tension.

Acknowledgment

We are extremely thankful to the British University in Egypt and the Egyptian Petroleum Research Institute for allowing us to use their labs.

References

[1] El-hoshoudy, AN Mohammedy MMM, Desouky SM, Ramzi M, Attia AM. Experimental, modeling and simulation investigations of a novel surfmer-co-poly acrylates crosslinked hydrogels for water shut-off and improved oil recovery. Journal of Molecular Liquids 2019; 277:142-56.

[2] El-hoshoudy AN, Desouky SMD. Synthesis and evaluation of acryloylated starch-g-poly (Acrylamide/ Vinylmethacrylate/1-Vinyl-2-pyrrolidone) crosslinked terpolymer functionalized by dimethylphenylvinylsilane derivative as a novel polymer-flooding agent. International Journal of Biological Macromolecules 2018; 116:434-42.

[3] El-hoshoudy AN, Desouky SMD, Attia AM. Synthesis of starch functionalized sulfonic acid co-imidazolium/silica composite for improving oil recovery through chemical flooding technologies. International Journal of Biological Macromolecules 2018.

[4] El-Hoshoudy A, Desouky S, Elkady M, Alsabagh A, Betiha M, Mahmoud S. Investigation of optimum polymerization conditions for synthesis of cross-linked polyacrylamide-amphoteric surfmer nanocomposites for polymer flooding in sandstone reservoirs. International Journal of Polymer Science 2015;2015.

[5] El-hoshoudy A, Desouky S, Elkady M, Alsabagh A, Betiha M, Mahmoud S. Hydrophobically associated polymers for wettability alteration and enhanced oil recovery–Article review. Egyptian Journal of Petroleum 2017.

[6] El-hoshoudy AN. Quaternary ammonium based surfmer-co-acrylamide polymers for altering carbonate rock wettability during water flooding. Journal of Molecular Liquids 2018; 250: 35-43.

[7] El-hoshoudy AN. Synthesis of acryloylated starch-g-poly acrylates crosslinked polymer functionalized by emulsified vinyltrimethylsilane derivative as a novel EOR agent for severe polymer flooding strategy. International Journal of Biological Macromolecules 2019; 123: 124-32.

[8] Wei B, Qinzhi L, Wang Y, Gao K, Pu W, Sun L. An Experimental Study of Enhanced Oil Recovery EOR Using a Green Nano-Suspension. SPE Improved Oil Recovery Conference. Society of Petroleum Engineers; 2018.

[9] Shah RD. Application of nanoparticle saturated injectant gases for EOR of heavy oils. *SPE annual technical conference and exhibition.* Society of Petroleum Engineers; 2009.

[10] Poole Jr CP, Owens FJ. Introduction to nanotechnology. John Wiley & Sons; 2003.

[11] Mansoori GA. Principles of nanotechnology: molecular-based study of condensed matter in small systems. World Scientific; 2005.

[12] Wasan D, Nikolov A, Kondiparty K. The wetting and spreading of nanofluids on solids: Role of the structural disjoining pressure. Current Opinion in Colloid & Interface Science 2011;16(4):344-9.

[13] Chengara A, Nikolov AD, Wasan DT, Trokhymchuk A, Henderson D. Spreading of nanofluids driven by the structural disjoining pressure gradient. Journal of colloid and interface science 2004;280(1):192-201.

[14] Mcelfresh PM, Wood M, Ector D. Stabilizing nano particle dispersions in high salinity, high temperature downhole environments. *SPE International Oilfield Nanotechnology Conference and Exhibition.* Society of Petroleum Engineers; 2012.

[15] Alomair OA, Matar KM, Alsaeed YH. Nanofluids application for heavy oil recovery. *SPE Asia Pacific Oil & Gas Conference and Exhibition.* Society of Petroleum Engineers; 2014.

[16] Alomair O, Alajmi A. Experimental Study for Enhancing Heavy Oil Recovery by Nanofluid Followed by Steam Flooding NFSF. *SPE Heavy Oil Conference and Exhibition.* Society of Petroleum Engineers; 2016.

[17] Temperley H, Trevena D, Raveché HJ. Liquids and their Properties: A Molecular and Macroscopic Treatise with Applications. Physics Today 1980; 33: 53.

[18] Heinze J. Cyclic voltammetry—"electrochemical spectroscopy". New analytical methods (25). Angewandte Chemie International Edition in English 1984;23(11):831-47.

[19] Wei L, Zhu J-H, Qi J-H. Application of nano-nickel catalyst in the viscosity reduction of Liaohe extra-heavy oil by aqua-thermolysis. Journal of Fuel Chemistry and Technology 2007;35(2):176-80.

[20] Clark PD, Clarke RA, Hyne JB, Lesage KL. Studies on the effect of metal species on oil sands undergoing steam treatments. Aostra J Res 1990;6(1):53-64.

[21] Hamedi Shokrlu Y, Babadagli T. Effects of nano-sized metals on viscosity reduction of heavy oil/bitumen during thermal applications. Canadian Unconventional Resources and International Petroleum Conference. Society of Petroleum Engineers; 2010.

[22] Hendraningrat L, Li S, Torsæter O. A coreflood investigation of nanofluid enhanced oil recovery. Journal of Petroleum Science and Engineering 2013; 111: 128-38.

[23] Zargartalebi M, Barati N, Kharrat R. Influences of hydrophilic and hydrophobic silica nanoparticles on anionic surfactant properties: Interfacial and adsorption behaviors. Journal of Petroleum Science and Engineering 2014; 119: 36-43.

[24] Sharma T, Kumar GS, Chon BH, Sangwai JS. Thermal stability of oil-in-water Pickering emulsion in the presence of nanoparticle, surfactant, and polymer. Journal of Industrial and Engineering Chemistry 2015; 22: 324-34.

[25] Esmaeilzadeh P, Hosseinpour N, Bahramian A, Fakhroueian Z, Arya S. Effect of ZrO2 nanoparticles on the interfacial behavior of surfactant solutions at air–water and n-heptane–water interfaces. Fluid Phase Equilibria 2014; 361:289-95.

[26] Arashiro EY, Demarquette NR. Use of the pendant drop method to measure interfacial tension between molten polymers. Materials Research 1999;2(1):23-32.

[27] Hezave AZ, Dorostkar S, Ayatollahi S, Nabipour M, Hemmateenejad B. Investigating the effect of ionic liquid (1-dodecyl-3-methylimidazolium chloride ([C12mim][Cl])) on the water/oil interfacial tension as a novel surfactant. Colloids and Surfaces A: Physicochemical and Engineering Aspects 2013; 421: 63-71.

[28] Giraldo LJ, Gallego J, Villegas JP, Franco CA, Cortés FB. Enhanced waterflooding with NiO/SiO2 0-D Janus nanoparticles at low concentration. Journal of Petroleum Science and Engineering 2019; 174: 40-8.

[29] Gomaa S, Salem A, Hassan M. Relative Permeability Curves and Wettability Alterations by Alumina Nano Particles Flooding. Journal of Al Azhar University Engineering Sector 2017;12(42):103-19.

[30] Gomaa S, Salem A, Hassan M. Nanofluids hold EOR potential in Egypt's Western Desert. Oil & Gas Journal 2018;116(4):52-5.

To whom correspondence should be addressed: Dr. A.N. El-hoshoudy, Production Department, Egyptian Petroleum Research Institute, Naser City, Cairo, Egypt, E-mail Abdelaziz.Nasr@bue.edu.eg

Petroleum and Coal

Article **Open Access**

NATURAL FRACTURES ANALYSIS OF RESERVOIR ROCK VIA FMI IMAGE LOGS IN BIBI- HAKIMEH OIL FIELD, SW OF IRAN

*Javid Abbasi, Hossein Tabatabaei**

Department of Petroleum Engineering, Gachsaran Branch, Islamic Azad University, Gachsaran, Iran

Received May 21, 2019; Accepted July 1, 2019

Abstract

Fracture system in carbonate reservoirs is very complex. Understanding the features of fractures such as dip, strike and the other parameters can help to distinguish the behavior of reservoir in any exploration and production plan. Evaluation of fractures and their parameters, such as aperture and density, is necessary in the optimization of oil production and field development. Image log is the best way to investigate feature planes like fracture and bedding. This enables the petroleum geoscientists to describe in detail the structural fracture networks very essential for structural analysis and improved reservoir characterization. Their aperture may be open, tight (closed) or filled with some minerals such as calcite, anhydrite, clays and pyrite. The main objective of FMI log was to determine structural dip and characterize probable fractures intersected by the well. Discussion on various fracture attributes is given in the following: Based on observations and interpretation of the images logs from Asmari formation, the closed fracture, has N27°E-S27°W strike and 73 degrees inclination to S55°E and the open fractures in directions N83°E, S83°E and N7°W with dips of 14° to 90° (43°). Fracturing is observed strongly in the studied interval. The brittle nature of the formation could be the reason for development of fractures in the drilled section of Asmari formation. Thus permeability of reservoir rock is much and result production of hydrocarbon is high.

***Keywords**: Fracture analysis, Image logs, Asmari formation, Bibi- Hakimeh oil field.*

1. Introduction

To identify small natural fractures around the well, most of the methods, such as geophysical logs, wells and drilling mud data, are not sufficiently precise due to their low resolution [1]. The FMS / FMI imaging logs provide high resolution images of well wall at millimeter scale, which are based on the physical properties of wells like electric resistances [2]. Imaging logs for reservoir geologists allow for the identification of small-scale phenomena within well wall boundaries. The most important application of imaging logs is to identify the types of fractures and their characteristics (type, orientation, and spacing) in oil and gas wells [3].

Natural fractures are caused by tectonic stresses. Zones that have natural fractures are important and are explored in reservoir rocks because of dramatic drainage and significant increases in permeability. Although fractures can have a major impact on the total permeability of the formation, they have very little effect on porosity, fluid saturation and other petrophysical properties of the rock. The features of the natural fractures are in [4].

Natural fractures are usually perpendicular to the slope of the layer. The extent and development of horizontal fractures is much less than that of vertical fractures. Their predominant direction is usually aligned with the orientation of regional faults. Natural fractures cause small amount of wellbore wall to fracture and collapse by drilling bit during drilling operation [5]. Fractures are usually seen in dense and tight rocks, which, in the absence of fracture during drilling, cause the diameters of drilling bit and wellbore to be the same. From the point of view of production, only open fractures are useful.

In the case of artificial fractures, the wellbore wall is always affected by horizontal tensions and damage caused by drilling. There are two types of artificial fractures which are as following: borehole breakout due to shear stresses and induced hydraulic fractures caused by damages during drilling [6], which is not discussed in this study.

2. Geological setting

Well No.91 of Bibi-Hakimeh oil field is located 25Km South-East of Gachsaran city in SW of Iran (Fig.1). This well was drilled in the Eastern part of the Bibi-Hakimeh oil field near the crest of anticline. Asmari formation was the target formation of the well, which was drilled with a 6.125 inch bit. The FMI and FMS logging with open well logs (neutron, density, gamma ray and electrical resistance) was carried out by National Iranian Oil Company to better understand the structural features. Dimensions of the Asmari reservoir at the water-oil interface are about 70 km in length and 7 km in width [7].

Figure 1. Located of Bibi- Hakimeh oil field in Dezful embayment, near the other oil fields, Southwest of Iran.

3. Methodology (FMI and FMS imaging logs)

In this study, the FMS and FMI image logs were used to identify the types of natural fractures of wellbore wall of well No.91 in Bibi-Hakimeh oil field and the results were compared with the studies of open well logs. Finally, the density, orientation and impact of fractures in the permeability of Asmari formation were investigated.

Imaging logs are cylindrical and virtual images of a high-resolution wellbore wall that can display the delicate phenomena of the wellbore wall. Each plate-shaped construction, such as stratification and fracturing that interrupts the wells vertically and horizontally, can be seen in the ellipsoidal in wellbore cylinder. If the cylinder is cut and opened along its axis, the same shape as shown in the imaging log, will illustrate the fracturing or stratification as a sine wave. Also in the imaging log, the vertical fracture (parallel to the well axis) is represented by vertical straight lines and horizontal fractures (perpendicular to the well axis) will appear as horizontal straight lines.

The FMI tool is a new generation of electrical imaging devices that has double wall coverage as compared to FMS. The FMI is equipped with four vertical caliper arms. At the end of each arm, a pad and flap are attached. Pads and flaps contain a number of electrical resistive sensors (usually 24 sensors for each pad and flap), which results in a high resolution level of about 0.3 inches. The data from sensors are used to process and create an image that is based on the difference in electrical resistance of the wellbore wall [8]. In this study, the FMS log has 4 pads as well as 16 sensors on each pad.

The FMS and FMI tools collect information about wells cross-section and geometry as well as electrical resistive image information. In general, imagers are used to determine natural fractures and artificial fractures, and can be used to calculate gradient and fracture length and stratification levels.

The crude data extracted from the oil wells is interpreted after processing and correction on them. The processing of image graphs involves processes that eliminate some of the errors and increase the quality. The processes performed on the images are divided into two categories: a) fundamental corrections that are necessary for electrical imaging diagrams, including depth correction, speed correction, correction of broken and disabled pads, etc.; b) Process of image quality improvement which includes equalization and normalization of the correction [9].

In image diagrams, sometimes, image strips have different brightness and darkness due to the curvature of the pad. Normalization is used to correct the buttons response. Similarly, in order to highlight geological elements and structures in graphic diagrams, the correction equalization option is used. At the end of this step, two static and dynamic images are created; the static image is often used to identify stratification and lithology changes, and the dynamic image is usually used to identify natural and artificial fractures [9].

4. Analysis of fractures via Image logs

FMI logs are used to interpret the geometry of natural fractures. Natural fractures are observed on the logs as sinusoidal regions, which may have electrical resistance or electrical conductivity [10]. Based on the appearance of the fractures, two types of fractures on the FMI log are identified: Open fractures that easily allow the fluid to pass and closed fractures that inhibit fluid to pass quickly.

The opening of the fractures may be open, closed or filled with minerals such as clays, calcite, anhydrite, pyrite, and the like. On FMI / FMS images, fractures tend to occur linearly, which generally has a steeper slope than the stratification slope. Open fractures in a clean clay-free clay structure have a conductive look on the images. This is due to the penetration of the conductive drilling mud into the opening of the fractures. If the fractures are closed or filled with calcite and anhydrite minerals, it will have an electrical resistive appearance. However, fractures filled with clay and pyrite will have conductive responses [11]. Sedimentation and stratigraphic data of the study area are essential to distinguish the electrical conductivity resulted from filling by mud and filling by clay and pyrite. Of course well logs can be used in some cases to detect such differences [12].

FMS and FMI images showed any fractures in Asmari formation. The fractures did not have the same appearance, some were resistant and some were conductive. There was a tight fracture with resistive presentation that was grouped as a closed fracture (Fig.2 and 3), and all fractures with continuous or discontinuous conduction effects were considered as open fractures. The reason for the conduction of these fractures is due to the infiltration of the drilling mud into the open regions. In the next stage, open fractures were divided into further groups based on the appearance and lateral continuity in the wellbore (Fig.2 and 3). The characteristics of open and closed fractures and subgroups are presented in Table.1 and the spatial position of the types of fractures, both closed and open, in terms of slope, tensile angle and slope angle are given in Table.1.

Table 1. Classification of fractures

Main types of fracture	Subgroups of fracture	Number of fractures	Dominant Strike	Dominant Dip Azimuth	Dominant Dip Inclination (deg.)
Closed fractures	Discontinues closed	34	N27E-S27W	S55E	73
Open fractures	Discontinues Continues	37 54	N83E-S83W	N7W	43 (Range 14-90)

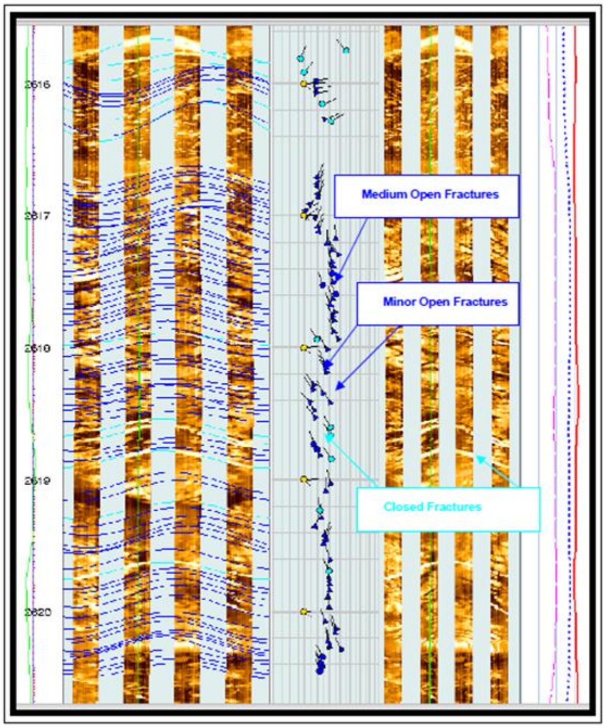

Figure 2. Minor open fractures (blue triangle dips), Medium open fractures (blue circular dips) and Closed fractures (Cyan circular dips) shown by FMI image in Asmari Formation

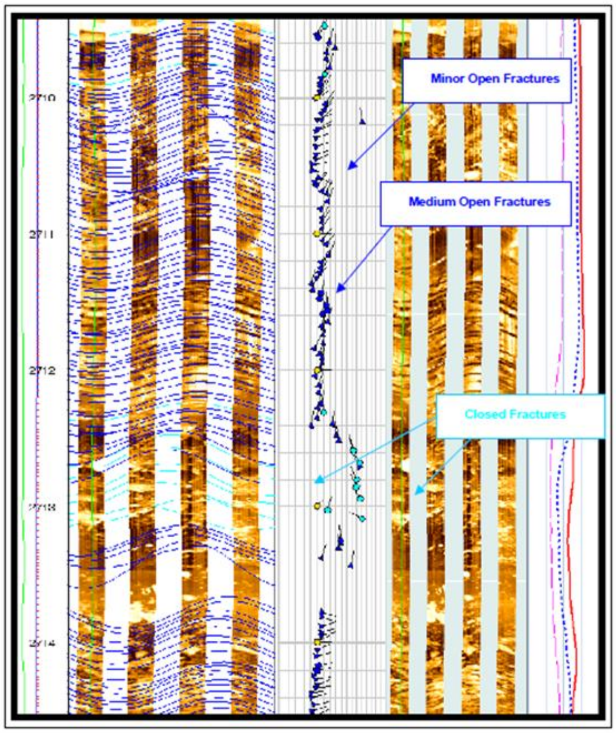

Figure 3. Minor open fractures (blue triangle dips), Medium open fractures (blue circular dips) and Closed fractures (Cyan circular dips) shown by FMI image in Asmari Formation

Open-well log data showed that the main lithology of the reservoir is limestone or marl. The drilled region of the Asmari formation has the most developed fracture, due to the brittle nature of this formation against tectonic stresses. Therefore, fractures in this region are significant and even they are considered as fractured.

5. Conclusions

Based on observation and interpretation of images log from Asmari formation, the following important conclusions are as follows:

Open-well log data indicates that the main lithology of the reservoir rock is limestone or marl. In the study region, fracture is strongly seen. 34 Number of closed fracture, 37 discontinues open fractures and 54 continues open fracture were detected from FMI image logs. Closed fracture was identified with slope direction of S55°E slope and slope angle of 73°. Open fractures were detected with slope directions N83E-S83W and slope angle ranging from 14° to 90°. The statistical survey of this region from Asmari formation shows that fractures are high developed and this is probably due to the brittle nature of the reservoir rock, so the evaluation shows that the reservoir has a good permeability and will have a positive effect on the production of hydrocarbon from the well.

References

[1] Aghli G, Soleimani B, Charchi A, Zahmatkesh I. Detection of fracture using petrophysical logs by new method and it's correlation with image logs. Petroleum Research, 2016; 25: 120–134.

[2] Abdideh M, Bahadori Birgani N, Amanipour H. Estimating the Reservoir Permeability and Fracture Density Using Petrophysical Logs in Marun Oil Field (SW Iran), Petroleum Science and Technology, 2013; 31(10): 1048-1056.

[3] Shahinpour A. Borehole image log analysis for sedimentary environment and clay volume interpretation. M.Sc. dissertation, Norwegian University of Science and Technology 2013.

[4] Alizadeh B, Telmadarreie A, Shadizadeh SR, Tezhe F. Investigating Geochemical Characterization of Asmari and Bangestan Reservoir Oils and the Source of H_2S in the Marun Oilfield, Petroleum Science and Technology, 2013; 30(10): 967-975.
[5] Zahmatkesh I, Aghli G, Mohamadian R. Systematic fractures analysis using image logs and complementary methods in the Marun Oilfield, SW Iran. Geopersia,2015; 5: 139–150
[6] Movahed Z. Fractures study in Asmari Formation. Schlumberger Well Services, 2007: 5.
[7] Motiei H. Geology of Iran; Zagros Stratigraphy. Geological Survey of Iran Publications (in Persian), 1994, 1994536P.
[8] Ekstrom MP, Dahan CA, Chen MY, Lloyd PM, and Rossi DJ. Formation imaging with micro electrical scanning arrays. Log Anal., 1987; 28: 294–306.
[9] Serra O. 1989, Formation micro scanner image interpretation, 2nd ed., Schlumberger Educational Services, 1989, 117p.
[10] Barton CA, Zoback MD, and Moos D. Fluid flow along potentially active faults in crystalline rock. Geology, 1995; 23(8): 683–686.
[11] Schlumberger Well Services, 1999, Oil Field Services, Schlumberger Well Services Well Services, 21.
[12] Schlumberger Well Services, 2002, Schlumberger Method, Schlumberger Well Services, 14.

To whom correspondence should be addressed: Dr. Hossein Tabatabaei, Department of Petroleum Engineering, Gachsaran Branch, Islamic Azad University, Gachsaran, Iran, E-mail tabatabaei.h@gmail.com

Petroleum and Coal

Article **Open Access**

DESIGN, CONSTRUCTION AND PERFORMANCE RELIABILITY VERIFICATION EVALUATION OF A HIGH PRESSURE VOLUMETRIC SORPTION SYSTEM FOR CO_2 SORPTION IN SOUTH AFRICAN COALS

K. Premlall[1], M. M. Mabuza[2], and J. H. Potgieter[3]

[1] *Department of Chemical, Metallurgical and Materials Engineering, Tshwane University of Technology, Pretoria, South Africa*
[2] *Department of Chemical Engineering, Vaal University of Technology, Secunda, South Africa*
[3] *School of Chemical and Metallurgical Engineering, University of Witwatersrand, Johannesburg, South Africa*

Received May 5, 2019; Accepted July 15, 2019

Abstract

High pressure sorption equipment are based on the gravimetric or volumetric principle method of gas sorption onto a specific sorbent. This paper discusses the design, construction and performance consistency testing that was conducted on a recently constructed in-house high pressure volumetric sorption system (HPVSS) in South Africa (SA) which was used for the evaluation of supercritical carbon dioxide (CO_2) sorption on SA coals. A detailed description of the equipment, the commissioning phase, leak testing evaluation, estimation of sample, reference and void volume, as well as the method of conducting the measurements of the sorption isotherms are explained.

Six (6) South African (SA) coals were selected based on their myriad of properties i.e. coal rank, coal type, and petrographic and proximate analyses. The samples were used as the sorbing material for pure CO_2 in supercritical phase to conduct the isothermal sorption investigations. In order to evaluate the system, multiple reliability experimental runs were conducted and the isotherms were evaluated and the sorption data was verified using the one-way analysis of variance method (ANOVA) to ensure the equipment performance was statistically reliable. Both the, system temperature and pressures, were varied to determine the potential risks of leaks in order to validate the consistency of the system at varying conditions of supercritical gas injection.

For the total number of experimental test runs that were conducted, was observed that very good repeatability of the sorption data was reproduced under all conditions. The data exhibited good homogenous variance in all data sets compared, thus demonstrating overall confidence in the repeatability of these CO_2 results, and that the reliability of the HPVSS has been confirmed in the test sorption experiments. A comparison to both national and international published data sets also confirmed good fit of the findings.

Keywords*: Sorption of super-critical CO_2; Volumetric system; High pressure; Coal, Design validation; Repeatability investigations.*

1. Introduction

The awareness of, and the issues relating to climate change has become more evident in recent decades. These are reflected by increases in global temperature leading to severe droughts, hurricanes, typhoons, etc. and an increase in global sea mean level (GSML) [1]. The increase in greenhouse gases (GHG's) over the last few decades, especially for anthropogenic carbon dioxide (CO_2), from the burning of fossil fuels for energy, is reportedly responsible for climate change. The latest atmospheric CO_2 measurement recorded for August 2018 stands at 409 parts per million (ppm) compared to the recording from 2005 which was at 378 ppm [2]. According to the stipulated 2°C increase limit as outlined as at the COP 21 (December 2015) Paris Agreement held by the United Nations Framework Convention on Climate Change (UN-FCCC) at which a 195 countries, including South Africa (SA) agreed upon, it was declared that urgent reform in mitigating CO_2 emissions must be implemented with immediate effect. Thereafter, following COP 22 held in Marrakesh (November 2016), it was finalized that further decisions relating to the "global stocktake" process looking at long term goals, market mechanisms and implementation relating to timelines, duration and output for individual country compliance to GHG emissions will be reviewed at the next COP 24 to be held in Poland in November 2018 [3].

Despite being a developing country, SA has been ranked as one of the top 15 emitters of CO_2 in the world [4]. Due to the South African economy's high carbon intensity and hence high CO2 emissions, it must be assumed that pressures on SA to reduce emissions can only increase. The country has committed itself to a low carbon emission future and in doing so launched SA's White paper on Climate Change [5] confirming to engage in all aspects to reduce and to mitigate CO_2 emissions. Three key elements have been identified: is a long term goal in the form of national emissions trajectory range to 2050: 2), is a medium term goal which will be within the range of 398 – 614 Mt of CO_2 equivalent in the years from 2025 and 2030; and 3), to provide periodic reviews in the medium/longer term to try and align to meet the 2°C target [5].

Carbon capture and storage (CCS) technologies are one of the integral aspects of the Intergovernmental Panel on Global Climate Change [6]. With the need to reduce the current SA emissions in line with the mandatory requirements, as outlined, that motivated the current research into evaluating the potential for the sorption capacity of $CO_{2,}$ for emission reduction purposes, in unmineable SA coals. This will have the additional benefit of potentially enhancing methane (CH_4) recovery for use as an energy alternative, whilst also sequestering CO_2 emissions from large industrial point sources to establish a low carbon emission economy is anticipated. The research work seeks to develop key knowledge understanding of the sorption potential of SA coals. This work follows on from investigations and findings from the Carbon Capture Centre for Capture and Storage (SACCCS). After investigations and the subsequent publication of the SA Atlas [7], it was established that an overall storage capacity of 150 gigatons (Gt) (on-shore) was readily available relating to CO_2 storage capacity of approximately 1 271.9 million tonnes (Mt) [7-8].

In order to conduct such work relating to establishing sorption capacity at high injection pressures of CO_2 into SA coal, our research investigation required the need of a high pressure sorption system to undertake the necessary CO_2 sorption evaluations for capacity estimation of a myriad of SA coal types. This led to the need to design and construct a system that could be effective in generating research data to validate the SA coals sorption capacity and assess the potential for sequestration.

2. Design of the high pressure volumetric sorption equipment

In order to achieve the required high pressures of CO_2 needed for in-situ (underground) storage conditions during injection (supercritical gas state), a high-pressure volumetric sorption system was designed in order to conduct experiments to produce CO_2 sorption isotherms in order to estimate the maximum sorption capacities of the six (6) different SA coal types under investigation. There are many factors that influence the choice of sorption system (volumetric or gravimetric) to use for high-pressure sorption experiments. These include, but are not limited to: cost time of construction, accuracy, availability of material, and maintenance. In literature it has been extensively documented that the volumetric sorption method has been proven to be the most widely used and effective technique for determining gas sorption capacities on coal by numerous researchers [9–28]. The setups are generally either custom made, or designed in-house, and consist typically of calibrated reference and sample reactor cells.

The current volumetric system (HPVSS) designed for use of these SA coals sorption capacity trial estimations was modelled and designed as per designs found in literature was constructed in-house at Tshwane University of Technology (TUT), SA. Chemvak cc (Applied Chemical and Vacuum Systems), Pretoria, South Africa, constructed and refined the design with TUT over a period of two and a half years. Equipment commissioning took three (3) months.

Since the HPVSS final modification and inception, there have been four (4) peer-reviewed journal publications [29–32] as well as five (5) peer-reviewed international and local conference [33–37] contributions based on the sorption experiments conducted using this equipment to verify the reliability of its operation and data generated from it. A summary of details to consolidate the equipment design, construction, commissioning and verification is provide in detail in this paper.

2.1. Equipment description

A simple schematic diagram of the in-house designed and constructed High-Pressure Volumetric Sorption System (HPVSS) is shown in Figure 1.

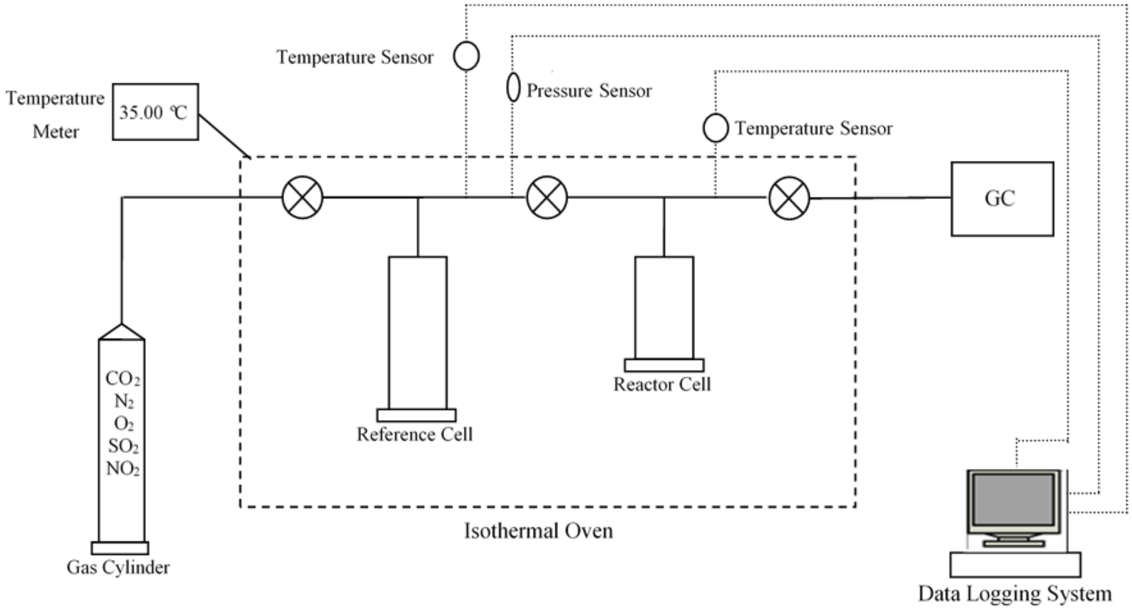

Figure 1. Simple schematic presentation of the high-pressure volumetric sorption system

The experimental setup consists of a reservoir cell (reference cell), a sorption / reactor cell (sample cell), and a digital control system for temperature and pressure control. The reservoir and sorption cells were manufactured of stainless steel and have volumes of 467.20 and 43.79 cm^3, respectively (after final modification). Maximum pressures of 15.0 MPa can be attained. The pressure in the reservoir and sorption cells was controlled and monitored by a digital control system connected to a WIKA pressure transducer (model A-10). A data logging system connected to the temperature and pressure transducers was used to collect the temperature and pressure data every second.

The interconnecting manifolds were made of stainless steel tubes and the valves were designed to withstand high pressures. However, these valves needed to be regularly replaced, depending on the frequency of use of the equipment, to prevent any gas leakages. Metallic (stainless steel) seals were used to join the various manifolds. They were selected based on the fluid used (either gas or super-critical) and the operational temperature (30–60ºC) and pressure (0–15.0 MPa).

A gas chromatograph (GC) (Model 8610), supplied by Chromspec chromatography is connected to the HPVSS experimental setup by a 1/8 in. stainless steel tube (Figure 1). Most importantly, proper calibration of the GC was essential; if not done frequently and correctly, the resulting sorption results will not be reliable. During the GC commissioning, the GC was calibrated by the supplier (Afrox Pty Ltd) using pure gases. This procedure was repeated performed on a quarterly basis.

The comprehensive HPVSS diagram is presented Figure 2 in which details of each component in the equipment are described. The supplier equipment details are outlined in Table 1.

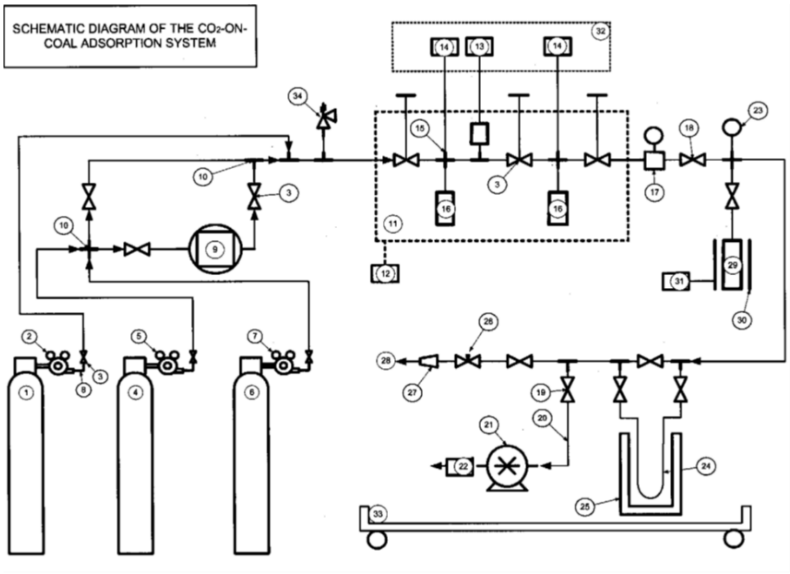

Figure 2. Detailed schematic diagram of high-pressure volumetric sorption system

Table 1. Components descriptions of the HPVSS

No.	Component	Supplier	No.	Component	Supplier
1	N2 gas cylinder	Afrox	18	SS ¼" shut-off valves	Chemvak
2	N2 pressure regulator	Afrox	19	NW 16 vacuum valve	Chemvak
3	¼" SS bellows seal valves	Chemvak	20	NW 16 vacuum line + couplings + O-rings + clamps	Chemvak
4	CO2 cylinder	Afrox	21	2 m3/h sliding vane fore-vacuum pump	Chemvak
5	CO2 pressure regulator	Afrox	22	Outlet oil mist trap	Chemvak
6	Flue gas cylinder	Afrox	23	Mechanical vacuum gauge	Chemvak
7	Flue gas pressure regulator	Afrox	24	U-tube volatiles trap	Chemvak
8	¼" SS tubing	Chemvak	25	Liquid N2 dewar (small)	Chemvak
9	Compressor	Chemvak	26	SS ¼" Needle valve	Chemvak
10	Swagelok ¼" SS unions	Chemvak	27	SS reducer to GC	Chemvak
11	Used GC oven	Chemvak	28	Gas chromatograph	Chromspec
12	Temperature control and Power Supply	Chemvak	29	Clamp-on heater	Chemvak
13	0-200 bar pressure transducer + digital readout + PS (Model A-10)	WIKA	30	Clamp-on heater	Chemvak
14	Thermocouple (2) + digital readout + switch	Chemvak	31	Temperature controller (basic) + Thermocouple + PS	Chemvak
15	Thermocouple SS couplings	Chemvak	32	Instrument panel	Chemvak
16	Reference and Sample Cells	Chemvak	33	Trolley	Chemvak
17	Single-stage, in-line pressure regulator + couplings	Chemvak	34	Pressure release valve	Chemvak

Figure 3 shows the actual HPVSS that was constructed and tested using the six (6) SA coals in –house at TUT, SA. Figure 3(a) shows a picture of the total designed equipment, while Figure 3(b) shows a picture the internals of the HPVSS.

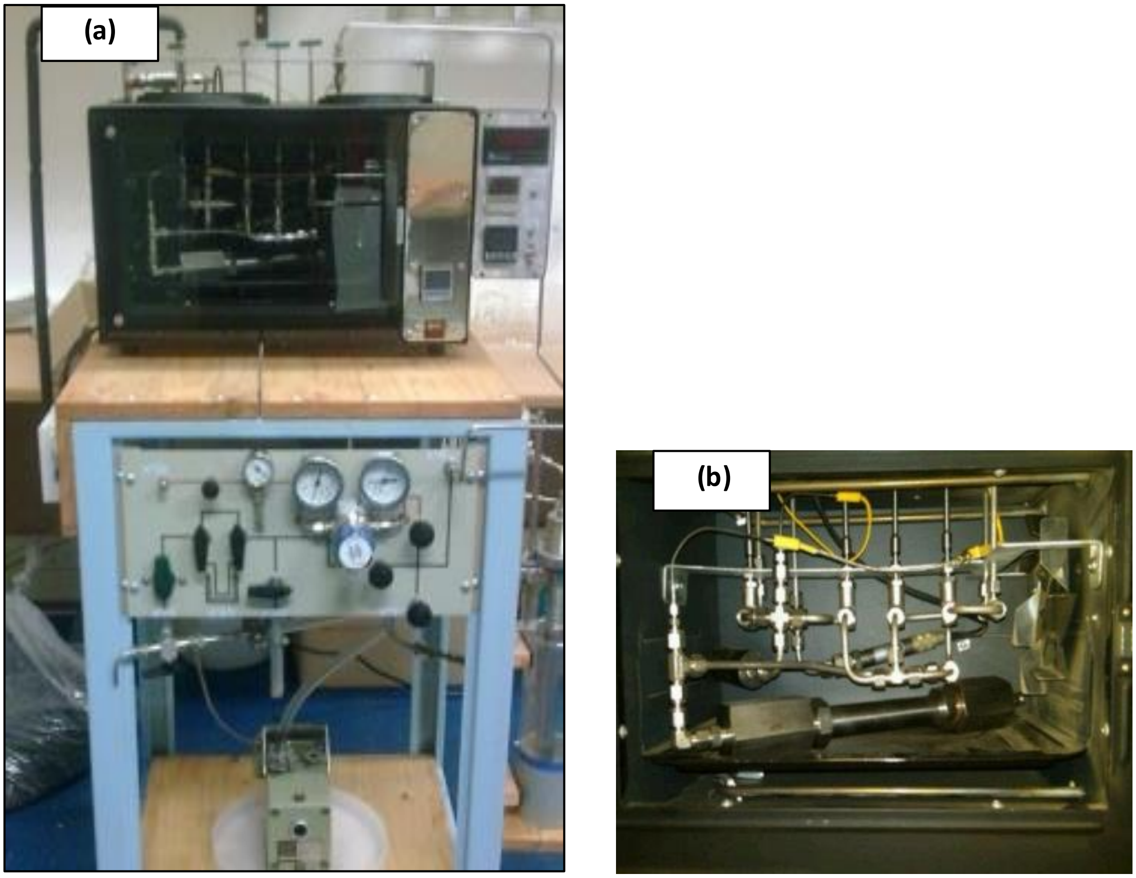

Figure 3. (a). Picture detailing the High-Pressure Volumetric Sorption System; 3(b). System internals

2.2. Equipment commissioning

2.2.1. Leak test

Due to the small volumes and high-pressures associated with the experimental setup, a leakage test was necessary to certify a hermetic seal of the entire equipment. This test was performed by introducing helium to the system at a pressure of 0.9 MPa with using incremental temperature from 35 to 60ºC. These temperatures and final pressure were selected based on the desired maximum sorption conditions. The pressure was monitored and recorded continuously at constant temperatures for 48 hours. Any leakage occurrences were detected by a decline in the system pressure with time. An Afrox Safetest Leak Detection Solution was applied to the pressurized connections. Formation of bubbles suggested a leakage, and, thus, the connections were tightened and fixed accordingly. In case the Swagelok connections were worn due to cross-threading or any other possible reasons, they were immediately replaced before any tests were conducted.

2.3. Determination of the reference and sample cells volumes

The use of a volumetric system requires accurate measurements of the reference and sample cells volumes. Hence, this procedure was central during the commissioning of this HPVSS equipment [14-15, 20, 22, 38-39]. Initially, the empty volumes were evacuated using a vacuum pump. The volumes were determined by a series of helium expansions from the reference cell to the sample cell. The expansions were carried out at low helium pressures (0.1, 0.2, 0.3 and 0.4 MPa) and at a room temperature of 25ºC. The assumption was that helium acts as an ideal gas under these conditions; thus, the ideal gas law equation was used for calculations. Furthermore, an additional cell of known volume was required to aid in determining these cells' volumes. After this procedure, the additional cell was disconnected from the system since it was not necessary during to sorption experiments. The detailed procedure and equations governing the estimation of these volumes are described in detail by Mabuza [40].

3. Measurement of sorption isotherms

3.1. Sample degassing and moisture equilibrating

The sorption capacity and other properties such as the coal density, pore size, surface area, and porosity of the coals could be affected by the presence of moisture within the coal sample [41-42], other elucidations cannot be precluded entirely; however, residual moisture seems to play the most dominant role in affecting the sorption capacity on coals [42-43]. Each coal sample was degassed and dried before the sorption measurements were conducted. A sample mass in excess of 10 g (to account for the mass reduction after degassing) was weighed and placed in the HPVSS sample preparation cell and clamped on the heating element (component 29 in Figure 2). The sample was evacuated (- 0.7 bar) at a temperature of 120ºC for a maximum period of 2 hours. Thereafter, the samples were moisture equilibrated to 4% using distilled water prior the sorption experiments. The moisture content of 4% was chosen based on the average moisture content of the coals under investigation. A UniBloc Moisture Analyzer (Mode MOC63u) was used to accurately measure the coal moisture content.

3.2. Placement of the coal sample in the sample cell

After degassing and moisture equilibrating the sample, the sample was pre-weighed to get a prescribed amount of 10 g and was placed inside the sample cell. The sample cell was thoroughly tightened secured in its place. The sample was placed under vacuum for 60 s; thereafter, the system was leak tested using helium [45].

3.3. Measurement of sorption isotherms

3.3.1. Estimation of the void volume in the sample ell

Before sorption isotherms measurements, by the introduction of the sorbate gas (CO_2 or flue gas) into the sample cell could commence, the void volume (V_{void}) was estimated using the helium expansion approach. This approach is similar to the one applied in section 2.2. According to Ozdemir [39] the V_{void} is the available volume in gas-phase in the sample cell, Krooss *et al*. [14] simplified the description of V_{void} by referring to it as the volume not occupied by the solid sample as shown in Figure 4. It should be noted that V_{void} is dependent on the sample volume; thus, one can obtain a different value for the same material unless the mass consistently remains unchanged.

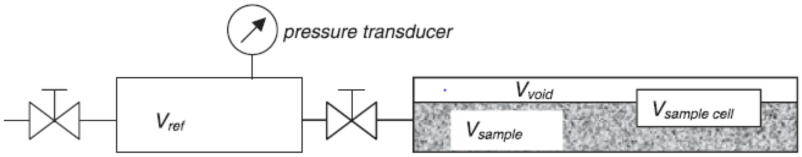

Figure 4. Focused area of the HPVSS showing the definitions for the volumetric method [15-16]

The detailed procedure and equations governing the estimation of the void volume are described and discussed as follows using Figure 5 which shows a simplified diagram of the HPVSS.

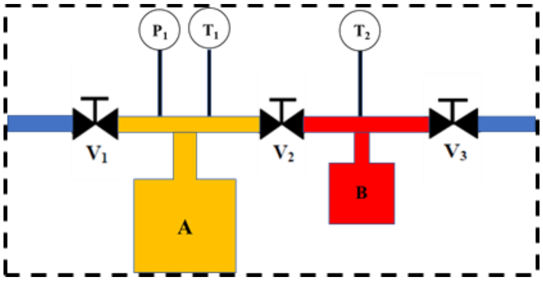

Figure 5. Simplified HPVSS diagram with the reference and sample cells volumes (without the standard cell)

The experimental procedure was as follows:

1. The system was evacuated using a vacuum pump with valves V_2 and V_3 open, and valves V_1 closed.
2. All valves were closed after 60 seconds of evacuation.
3. Helium was introduced into the reference cell, V_A, with valve V_1 open. The displayed pressure P was recorded as P_i.
4. Valve V_1 was closed and helium was allowed to expand to the sample cell, V_B, by opening valve V_2. The displayed pressure was recorded as P_f. Following the approach by Sudibandriyo [45] and the expressions that govern the approach, the recorded data was used as follows:

$$V_{void} = n_{He}\left(\frac{z_{He}RT}{P}\right) \qquad (1)$$

where number of moles of helium introduced into the cell is:

$$n_{He} = \frac{V}{RT}\left(\frac{P_i}{z_{He,i}} - \frac{P_f}{z_{He,f}}\right) \qquad (2)$$

where: V is the volume of the dozing cylinder; P_f and P_i represent final and initial pressure of that cylinder respectively; R is universal gas constant and *z* is the compressibility factor.

The helium compressibility factor was evaluated using the Peng-Robinson equation of state. The helium compressibility factor is given by:

$$z_{He} = 1 + \frac{\left(1.471\times10^{-3} - 4.779\times10^{-6}T + 4.92\times10^{-9}T^2\right)}{P} \qquad (3)$$

where P is in atmosphere and T is in Kelvins.

This expression is based on the experimental data from National Bureau of Standards Technical Note 631 for helium [46]. The same procedure was repeated for pressures up to 0.9 MPa.

3.3.1. Estimation of sample volume

The sample volume determination is essential for calculation purposes in the measurement of sorption isotherms. The following expression has been successfully applied by Busch *et al.* [16] to determine the sample volume and had since been adopted in the current research:

$$V_{sample.Cell} = V_{sample} + V_{void} \qquad (4)$$

Knowing $V_{sample.Cell}$ obtained from section 2.2 and V_{void} obtained from section 3.3.1 allows the, V_{sample} to be determined as follows:

$$V_{sample} = V_{sample.Cell} - V_{void} \qquad (5)$$

The gas phase specific density is significantly lower than that of the adsorbed phase and the volume of the latter can be neglected. In this case, the evaluation scheme results in the so called "excess sorption" or Gibbs sorption [13, 17].

3.1.2. Estimation of sample density

According to Hidnert and Peffer [47], the density of a solid having a fixed geometrical form may be reasonably estimated by a volumetric approach with an error of about 1 percent. This estimation can be performed using the following expression:

$$\rho_s = \frac{m_s}{V_s} \qquad (6)$$

where ρ_s is the sample density; m_s is the sample mass, and V_s is the volume of the sample inside the sample cell.

The sample mass may be conveniently obtained using a balance, accurate to 3 decimal figures, prior to placing the sample inside the sample cell. Thus, knowing V_s from Equation 5 and m_s from Section 3.2, the estimated value of the coal sample density may, then, be computed. The density value acquired through the use of Equation 6 was validated using a helium Stereopycnometer. Details of coal densities for these SA coals are summarized in Table 3. Details of the use of a helium Stereopycnometer, as well as the equations that govern its use, are presented and described fully by Mabuza [40].

Table 2. Experimental conditions for pure CO$_2$ sorption isotherm measurements

	Coal samples					
Experimental conditions	AN	IN	SF	GS	EM	SM
Temperature (ºC)	35	35	35	35	35; 50; 60	50, 60
Average sample mass (g)	5.04	5.05	5.04	5.01	5.05; 9.96; 10.0	9.68; 10.01
Average sample density (g/cm^3)	1.59	1.47	1.59	1.64	1.84	2.02
Average void volume (cm^3)	61.75	61.46	61.75	61.48	61.81; 38.33; 38.38	38.75; 38.82
System Pressure (MPa)	<……………………..1.0 – 9.0 --………………………… …>					
Incremental pressure steps	9	9	9	9	9	9
Gas composition (mol%)	99.999 CO$_2$	99.999 CO$_2$	99.999 CO$_2$	99.999 CO$_2$	99.999 CO$_2$	99.999 CO$_2$
Fluid state	Gaseous to supercritical					

Table 3. Proximate, ultimate and petrographic data of SA coals tested

Sample ID:	***AN***		***SM***		***SF***		***GS***		***IN***		***EM***	
	db	*daf*	*db*	*daf*	*db*	*daf*	*db*	*daf*	*db*	*daf*	*db*	*daf*
PROXIMATE												
Moisture %	1.4		1.1		5.0		3.4		2.0		4.5	
Vol. matter %	5.2	5.7	7.7	9.9	24.3	30.1	32.3	36.0	23.3	28.6	39.0	47.5
Ash %	8.8	9.6	18.2	22.2	19.3	23.9	10.3	11.5	18.4	22.5	17.9	21.9
Fixed C %	84.6	92.8	72.9	89.1	51.4	63.7	53.9	60.1	56.3	69.0	27.8	33.9
ULTIMATE												
Sample ID:	***AN***		***SM***		***SF***		***GN***		***IN***		***EM***	
C %	82.0	89.9	73.7	90.1	59.5	73.7	69.8	77.8	66.8	81.9	60.3	73.5
H %	3.1	3.4	3.3	4.1	3.7	4.6	4.9	5.5	4.0	4.9	3.7	4.5
N %	1.9	2.1	1.6	2.0	1.5	1.9	1.8	2.0	1.6	1.9	1.5	1.9
O%	3.3	3.7	2.5	3.1	14.5	18.0	12.7	14.2	8.3	10.2	15.9	19.4
S %	0.9	1.0	0.6	0.8	1.4	1.8	0.5	0.5	0.9	1.1	0.5	0.6
Total	100.0		100.0		100.0		100.0		100.0		100.0	
PETROGRAPHIC DATA												
Sample ID:	***AN***		***SM***		***SF***		***GN***		***IN***		***EM***	
Vitrinite vol%^{a}	33.4		88		20.8		51.4		50.2		13.9	
Inertinite vol%^{a}	66.6		12		76.7		43.9		47.3		82.2	
Liptinite vol%^{a}	0		0		2.5		4.7		2.5		3.6	
Mineral Mat. vol%	4.6		4.5		12.4		11.2		10.4		9.8	
R$_o$V$_{mr}$ vol%^{b}	2.91		2.24		0.65		0.7		0.81		0.64	
Coal Rank	***HRC***		***HRC***		***MRC***		***MRC***		***MRC***		***MRC***	
Density (g/cm^3)	1.59		1.8		1.59		1.48		1.47		1.64	

3.3.4. Construction of sorption isotherms

3.3.4.1. Pure gas (CO$_2$) sorption isotherms

Sorption isotherms and sorption capacities for pure CO$_2$ on the selected six (6) South African coal samples were measured under simulated in-seam conditions. This included pressures up to 9.0 MPa and isothermal temperatures ranging from 35°C for five of the different coals and up to 50 and 60ºC for two other coal types. The experimental conditions are presented in Table 2. Table 3 details the proximate, ultimate and petrographic data of the selected coals that were tested during this investigation.

Three repeatability CO_2 sorption tests were conducted on the first coal type, AN at 35°C. Thereafter two repeats per rest for the four coal types were done to ensure reproducibility. Judgements were based on visual observations of the sorption isotherms. After this, a small modification was done to the system to reduce the reactor cell volume which lead to a reduction in void volumes. It was thereafter, that the temperatures for tests on the two selected coal types, EM and SM were changed and test runs were done for temperatures of 50 and 60°C. Three (3) sorption trials were performed due to the nature of deviations that could occur for higher temperatures, as outlined by Oldenburg, Charriére *et al.*, and Qing-Ling *et al.* [48-50].

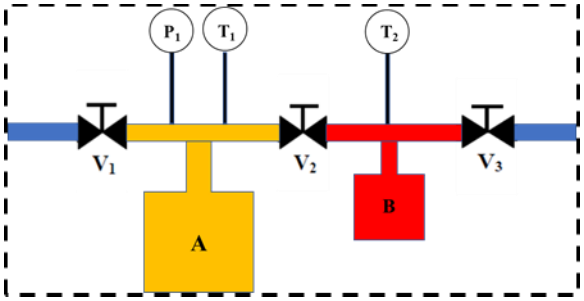

Figure 6: Simplified HPVSS Diagram for Determining the Reference and Sample Cells Volumes (without the standard cell)

To generate isotherms, the following procedure, with reference to 3 and Figure 6, was followed:

- The system oven was switched on and set to a desired temperature, as per the experimental conditions in Table 2. To achieve thermal equilibrium, at least 15 minutes were allowed in the system oven. However, during the initial thermal stability tests of up to 30 minutes it was confirmed that 10 minutes was sufficient to reach thermal equilibrium for these specific mass of coal samples used.
- The system was then evacuated using a vacuum pump with valves V_2 and V_3 open. The reference cell was charged with CO_2 gas to desired pressure by opening valve V_1, with valves V_2 and V_3 closed. Valve V_1 was closed to separate the reference cell from the CO_2 gas cylinder. Up to 5 minutes were allowed for the pressure in the reference cell to stabilize; in some instances, this pressure stability was achieved in much lesser time.
- The computer data logger was initialized to start recording the pressure and temperature of the sorption experimental run.
- The gas in the reference cell was, then, expanded to the sample cell by opening valve V_2. The pressure of the system was closely monitored until equilibrium was reached. In the initial (trial) tests run up to 24 hours. However, it was found that, 90 minutes was adequate for the equilibrium point to be reached.
- The same procedure was repeated for eight more pressure steps up to the final pressure of 9.0 MPa as shown in Figure 7.

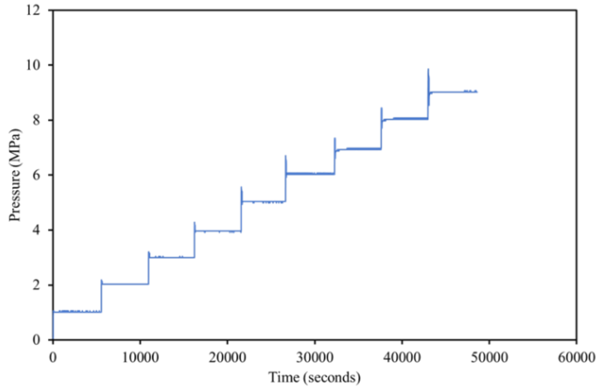

Figure 7. Sorption experimental pressure steps

The most fundamental operational procedure to quantify gas sorption on solid surfaces is the Gibbs approach. With this approach, the amount of gas sorbed (n_{sorbed}) is defined as the difference between the total amount gas (n_{total}) present in the system and the amount occupying the void volume (V_{void}), i.e. the volume unoccupied by the solid sample. According to Krooss *et al.* [14] the Gibbs approach as mathematically described in Equation 7, assumes a constant ratio of condensed phase volume and void volume throughout the sorption experiments and requires no further assumptions. The initial and equilibrium pressure molar densities of the gas phase were determined using data acquired from the National Institute of Standards and Technology WebBook (NIST) database [51]. The NIST Chemistry WebBook uses the Span and Wagner [5] equation of state for CO_2 covering the fluid region from the triple-point temperature to 826.85ºC at pressures up to 800 MPa. Details of the equations applied in the calculation of the CO_2 fluid sorbed on the coal surface are described in Mabuza [40].

The Gibbs approach was used to calculate the amount of CO_2 sorbed. This approach is based on the mass balance between the sample cell and the reference cell for each pressure expansion step. The Gibbs approach is based on the following expression:

$$n_{sorbed}^{excess} = \frac{n_{total} - \rho_{eq} V_{void}}{m_s} \tag{7}$$

Furthermore, the amount of gas adsorbed was expressed in the absolute form in Equation 8.

$$n_{sorbed}^{absolute} = \frac{n_{sorbed}^{excess}}{1 - \rho_{gas}/\rho_{ad}} \tag{8}$$

where n_{sorbed}^{excess} is the absolute adsorbed amount of CO_2 (mmol/g); ρ_{adsorbed} is the gas adsorbed phase density (in this case CO_2) (mmol/cm^3).

The adsorbed phase density is usually assumed to be constant across the experimental range [52]. In this study the value of 22.6 mmol/cm^3 for CO_2 was adopted since it has been found to be a reasonable estimation and was previously successfully applied by numerous other authors [43-44, 48, 53]. The adsorbed-phase density estimates do, however, affect the calculated absolute adsorption isotherm [45].

3.3.5. Data analysis methods

3.3.5.1. Analysis of variance (ANOVA)

The experimental CO_2 sorption data generated using the HPVSS for all repeat tests runs for the different SA coal types and at the different temperatures (35, 50 and 60°C) was analysed for variance (determination of repeatability) using a one way ANOVA method available in the data tool pack (add-in) in Microsoft Excel. It is a non-parametric method that is most recommended to be used in comparing two or more groups of sorption sample data in order to determine inequality in the data sets and is a hypothesis test with the F statistic (ratio of two quantities) which was used to test the null and alternative hypotheses. Specifically, it tests the null hypothesis:

$$H_o: \mu_1 = \mu_2 = \mu_3 = \cdots = \mu_k \tag{9}$$

where μ = group mean and k = number of groups.

This means that "There is *not* a significant difference between the groups; any observed differences may be due to chance and sampling error". This is realised from the computed data key criteria, i.e the F statistic value must be less than the calculated F critical value. Furthermore, the P value computed must be greater than 0.05 which is the smallest level of significance [54].

4. Results and discussions

4.1. Leakage tests

Due to the nature of high pressure work and the reliability of results needed for the sorption by pressure difference calculations, the system was subjected to a number of leak tests. Five (5) South African bituminous coal (same coal) samples were subjected to pressure for a number of days (Figure 8). Some of the tests were stopped at different intervals (for some of the trial tests) due to testing, modification requirements, and installation of a new automated data logging system. This was also necessary due to the long adsorption test times noted. Results below are indicative of manual pressure and time recordings.

As seen in Figure 9, a good comparison for trial runs for tests 2, 3, and 5 showed evidence of good repeatability for a specific SA bituminous coal type. This was considered to be an acceptable starting point for further test work, and eliminated concerns regarding system leaks at CO_2 super-critical conditions.

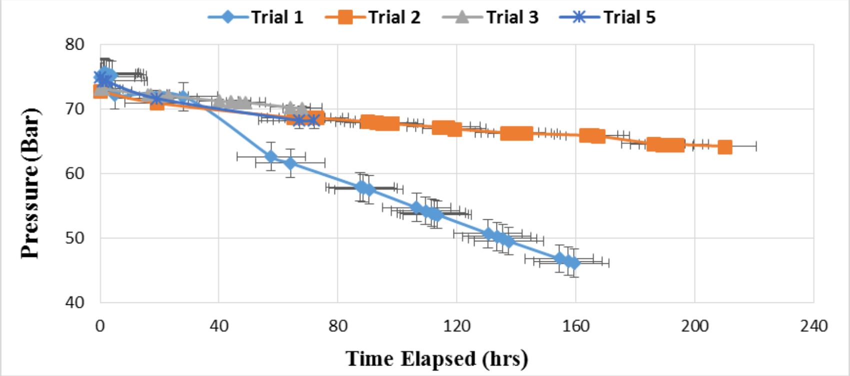

Figure 8. CO_2 injection pressure leakage tests

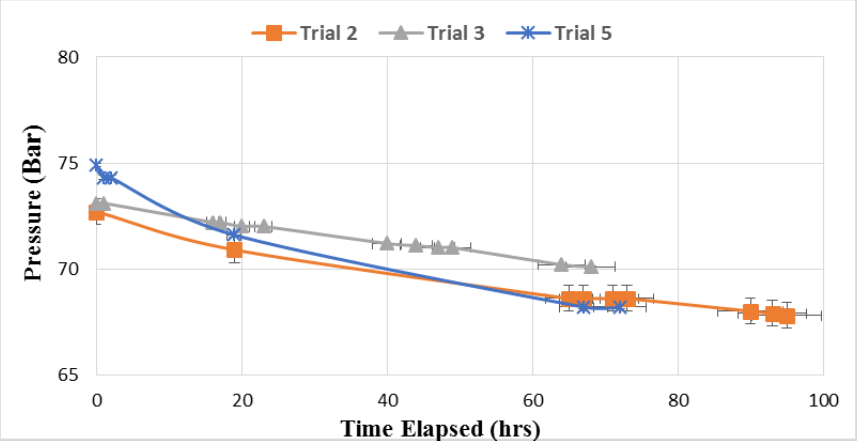

Figure 9. Three repeatability trial tests
Trial 2 run for 67.8 hrs ~ 3 days; Trial 3 run for 68 hrs = ~ 3 days; Trial 5 run for 72hrs = ~ 3 days

After inclusion of the data logging system, further leak tests were conducted. The adsorption system was again also checked for leaks to ensure that there were no pressure drops inside the reactor as this would influence the CO_2 adsorption results.

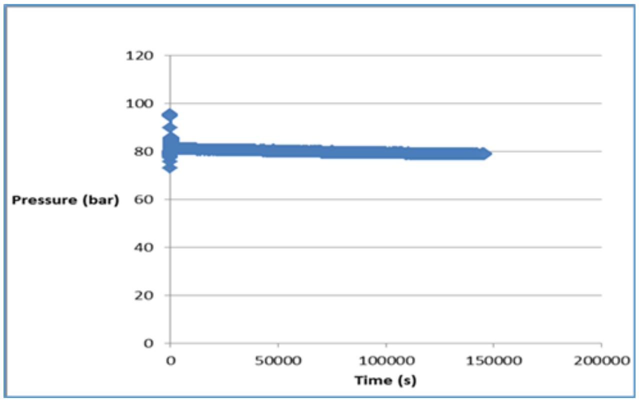

Figure 10. Leak test results on adsorption data logging system

The leak test was done by conducting a blank experiment where the pressure in the empty reactor was raised to approximately 98 bars, then the equipment was left overnight (12 hours or longer). It was expected that due to the temperature drops at night a slight pressure drop of small magnitude would take place. A significantly large pressure drop would indicate leakages in the system, possibly around the pipe fittings and valves. The final results of the leak test on the HPVSS are presented in Figure 10.

From the data logged results of leak tests undertaken, an insignificant pressure drop was experienced (Figure 9). This confirmed that the CO_2 sorption data acquired gave confident results presented hence forth. Individual coals were then repeatedly tested to obtain the individual coal CO_2 sorption isotherms shown in section 4.2.

4.2. Sorption isotherms conducted at 35°C

To evaluate the repeatability of the HPVSS, five (5) different SA coal types were tested using the incremental pressure step to a maximum of approximately 9 Mbar. Figures 11, 12 and 13 illustrate the individual repeat test sorption isotherms for these coals. Coal AN's CO_2 sorption capacity was tested using three trial runs, thereafter the other four coals; EM, GS, IN and SF, were repeat tested twice. For each sorption test a fresh coal sample was prepared and used under the same experimental conditions of temperature (35°C) and pressure up to 9 Mbar. The mean ($\bar{x}$) total sorption capacity of each individual coal sample was then computed from the repeat data. The mean value, as well as the standard deviation (SD), is shown in Figure 13 and summarized in Table 4.

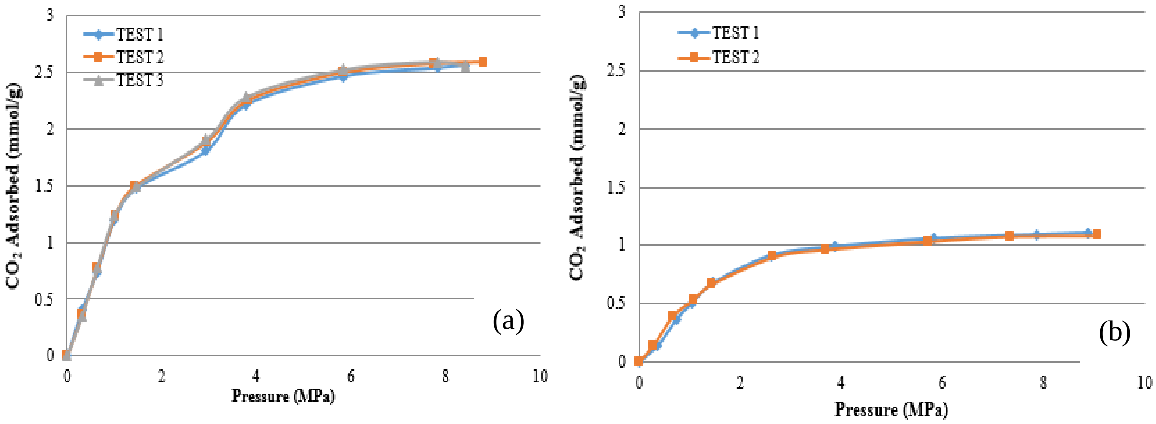

Figure 11. Adsorption Isotherms @ 35°C – (a) coal AN and (b) Coal EM

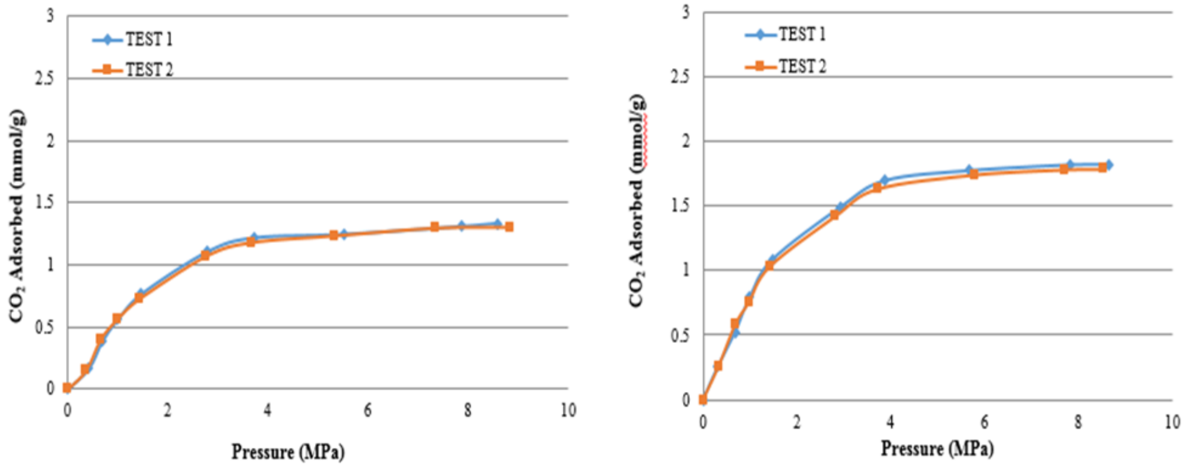

Figure 12. Adsorption Isotherms @ 35°C – (a) coal GS and (b) Coal IN

Sorption capacity isotherms for all coal types and the repeat tests increased monotonously from low to sub-critical pressures and exhibits an asymptotic behavior at high pressures (~ 6 MPa). From visual observations, it is quite obvious that a very good reproducibility of sorption results has been obtained for the repeat tests in all five of the coals tested. The differences in the measures (amounts) of CO_2 sorption capacities (mmol/g), as is clearly seen in Figure 14, is due to the nature of coal type and the details thereof informing this behavior will not be discussed in this paper. Only the validity of the specifically designed and constructed high pressure volumetric sorption systems' ability to produce reliably repeatable results with homogenous variance will be focused on.

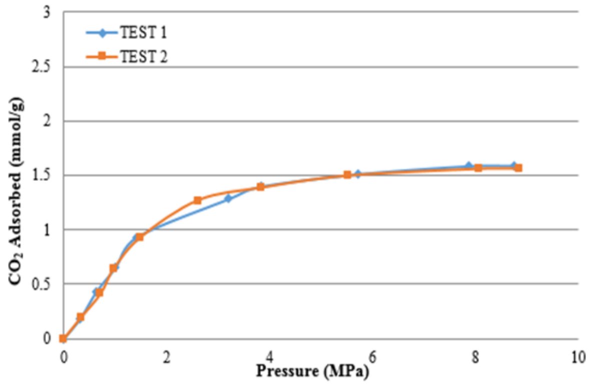

Figure 13. Adsorption Isotherms @ 35 °C – Coal SF

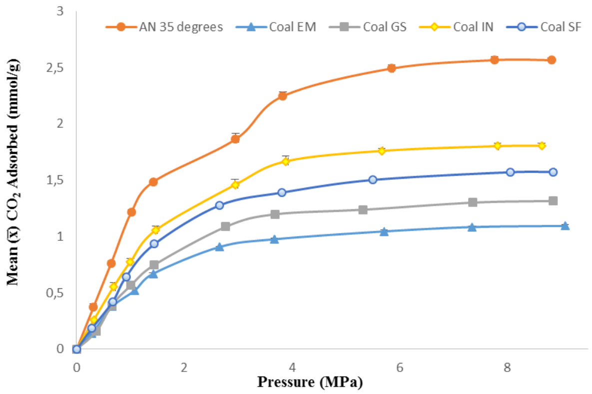

Figure 14: Average of repeat adsorption isotherms @ 35°C

Table 4. Summary of CO_2 sorption capacity data at 35°C

Sample ID and Test		Total sorption capacity (mmol/g)	Reference graph figure	Mean total sorption capacity $(\bar{x})$	Sample Final Standard Deviation (SD)
Coal AN	TEST 1	2.56	Figure 10 (a)	2.56	0.02
	TEST 2	2.58			
	TEST 3	2.55			
Coal EM	TEST 1	1.10	Figure 10 (b)	1.09	0.014
	TEST 2	1.08			
Coal GS	TEST 1	1.33	Figure 11 (a)	1.32	0.02
	TEST 2	1.30			
Coal IN	TEST 1	1.82	Figure 11 (b)	1.81	0.02
	TEST 2	1.79			
Coal SF	TEST 1	1.59	Figure 12	1.57	0.02
	TEST 2	1.56			

4.3. Sorption isotherms conducted at 50°C and 60°C

To evaluate the equipment repeatability and sorption capacity reliability with respect to *increased experimental temperatures*, two (2) different SA coal types were tested using the same incremental pressure step to a maximum of approximately 9 Mbar at two temperatures, namely: 50°C and then 60°C [49-51]. Three (3) freshly prepared samples for each coal type for each sorption test were used. Figures 15 and 16 illustrates the experimental sorption isotherms for both these coal samples.

As was also noted in Section 4.2, sorption capacity isotherms for all coal types and the repeat tests can be seen to have increased monotonously from low to sub-critical pressures and exhibited an asymptotic behaviour at high pressures (~ 6 MPa). Visual inspection of the sorption isotherms, clearly imply that a good reproducibility of sorption data has been achieved. The mean $(\bar{x})$ total sorption capacity (mmol/g) of each samples was computed from the experimental repeat data, as well as the standard deviation (SD) and is summarized in Table 5.

Standard deviations computed for the coals tested at 50°C range from 0.061 – 0.068 and for temperature 60°C range from 0.021 – 0.027. The differences in these values are significantly small and show good repeatability was obtained for these test runs overall. The computed mean $(\bar{x})$ sorption isotherms depicting the average CO_2 sorption capacities (mmol/g) for both temperatures for the two tested coals, EM and SM, are illustrated in Figure 17 (a) and (b) respectively.

Table 5. Summary of CO_2 sorption capacity data at 50 and 60ºC

Sample ID and test at 50ºC		Total sorption capacity (mmol/g)	Reference graph figure	Mean total sorption capacity ($\bar{x}$)	Sample final standard deviation (SD)
Coal EM	TEST 1	2.77	Figure 14 (a)	2.84	0.07
	TEST 2	2.83			
	TEST 3	2.90			
Coal SM	TEST 1	2.92	Figure 14 (b)	2.93	0.06
	TEST 2	2.88			
	TEST 3	2.99			
Sample ID and test at 60ºC		Total sorption capacity (mmol/g)	Reference graph figure	Mean total sorption capacity ($\bar{x}$)	Sample final standard deviation (SD)
Coal EM	TEST 1	2.25	Figure 15(a)	2.22	0.03
	TEST 2	2.22			
	TEST 3	2.19			
Coal SM	TEST 1	2.54	Figure 15 (b)	2.55	0.02
	TEST 2	2.57			
	TEST 3	2.53			

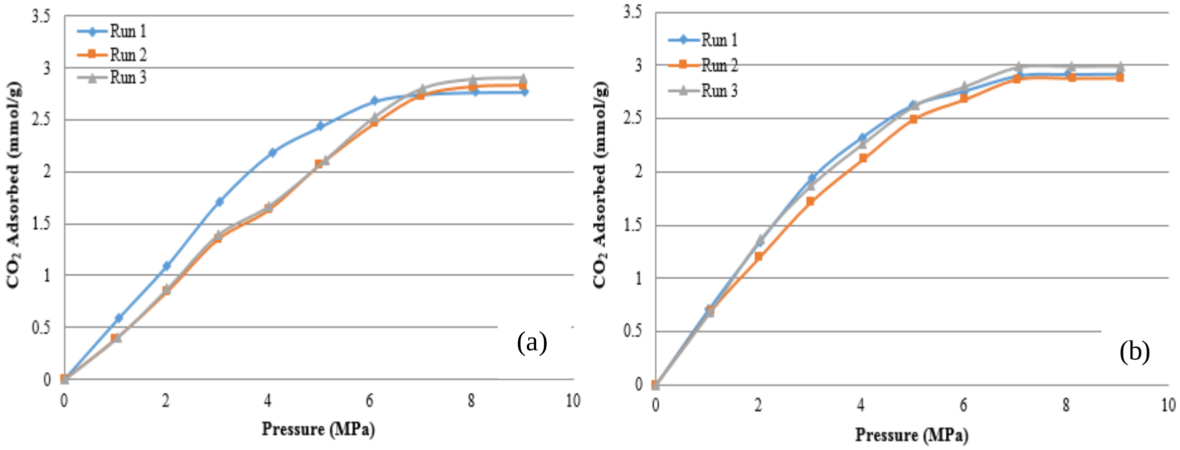

Figure 15. Adsorption Isotherms @ 50ºC – (a) coal EM and (b) Coal SM

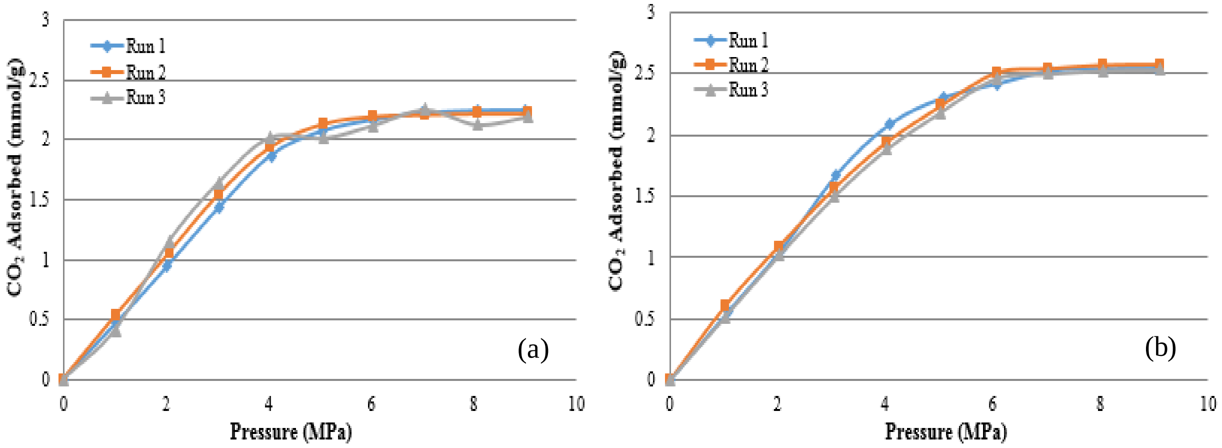

Figure 16. Adsorption Isotherms @ 60ºC – (a) coal EM and (b) Coal SM

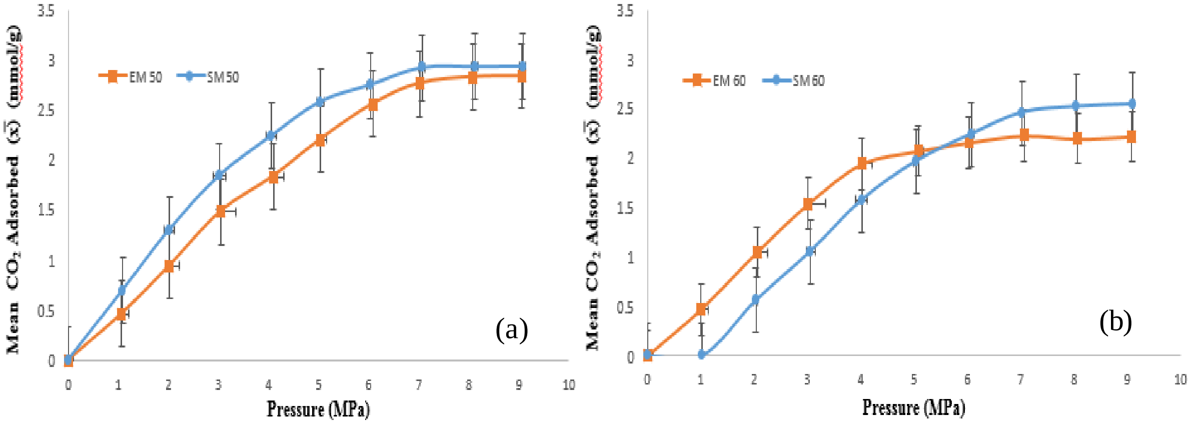

Figure 17. Average of Adsorption Isotherms @ 50 and 60°C

4.4. Analysis of Variance (ANOVA) results

The ANOVA statistical data was computed using Microsoft excel data tool pack, as detailed in Section 3.3.5.1 and was used to evaluate the potential of any variation of the experimental CO_2 sorption data set results. Results for the SA coals tested at experimental temperatures of 35°C, 50°C and 60°C are discussed in sections 4.4.1, 4.4.2 and 4.4.3 respectively. Tables 5, 6 and 7 summarize the statistical data showing results calculated for the sample sum (Σ), mean ($\bar{x}$), sample variance (s^2), standard deviation (SD), sum of squares (SS), degrees of freedom (d*f*), mean squared values (MS), F statistic (F), P-value and F critical values for each sample group, i.e. coal tested and repeat tested.

4.4.1 Coals tested at 35°C

Figure 18 illustrates the comparison of the five (5) SA coals tested at 35°C (coals AN, EM, GS, IN and SF) versus the computed mean sorption ($\bar{x}$) results in mmol/g per experimental coal sample. Error bars which represent the calculated standard deviation (SD) show that good repeatability can be observed for each coal type and test run conducted.

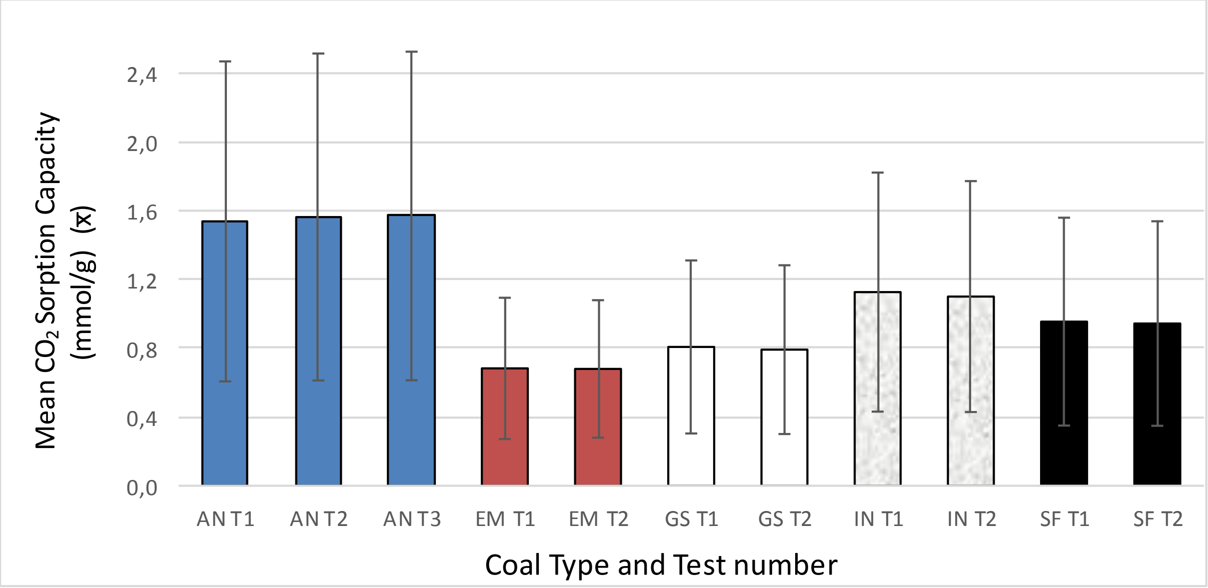

Figure 18. CO_2 sorption capacity comparison at 35°C using ANOVA results

Table 6 summarizes the statistical data computed. For all coals the F statistic values range in the region of 0.0 – 0.01, which is less than the computed F critical value range (3.35 –

4.41). This indicates an acceptable confidence level for repeat results obtained in this study. The p-values computed, range from 0.93 – 0.99, showing very good acceptable reproducibility of CO_2 sorption results from all these five SA coals tested. Therefore, the null hypothesis for these experiments is valid, i.e. there is *not* a significant difference between the groups or data sets.

Table 6. Data summary and ANOVA results of coals tested at 35°C

Summary data	*Test number*	*Count (n)*	*Sum (Σ)*	*Mean ($\bar{x}$)*	*Variance (s^2)*	*Standard deviation (SD)*
Coal AN	TEST 1	10	15.4	1.54	0.87	0.9
	TEST 2	10	15.6	1.56	0.90	1.0
	TEST 3	10	15.7	1.57	0.91	1.0
Coal EM	TEST 1	10	6.8	0.68	0.17	0.9
	TEST 2	10	6.8	0.68	0.16	0.4
Coal GS	TEST 1	10	8.1	0.81	0.25	0.5
	TEST 2	10	7.9	0.79	0.24	0.5
Coal IN	TEST 1	10	11.3	1.13	0.48	0.7
	TEST 2	10	11.0	1.10	0.45	0.7
Coal SF	TEST 1	10	9.6	0.96	0.37	0.6
	TEST 2	10	9.4	0.94	0.35	0.6

ANOVA results	*Source of variation*	*SS*	*df*	*MS*	*F*	*P-value*	*F critical*
Coal AN	B/G	0.07	2.00	0.003	0.003	0.99	3.35
	W/G	24.16	27.00	0.895			
Coal EM	B/G	0.00	1.00	0.00	0.00	0.97	4.41
	W/G	2.96	18.00	0.16			
Coal GS	B/G	0.001	1.00	0.001	0.01	0.95	4.41
	W/G	4.45	18.00	0.25			
Coal IN	B/G	0.003	1.00	0.003	0.01	0.93	4.41
	W/G	8.41	18.00	0.47			
Coal SF	B/G	0.00	1.00	0.001	0.002	0.97	4.41
	W/G	6.78	18.00	0.36			

B/G - Between groups; W/G - Within groups

4.4.2. Coals tested at 50°C

Figure 19 illustrates the comparison of the two (2) SA coals tested at 50°C versus the computed mean sorption ($\bar{x}$) (results in mmol/g per coal sample.

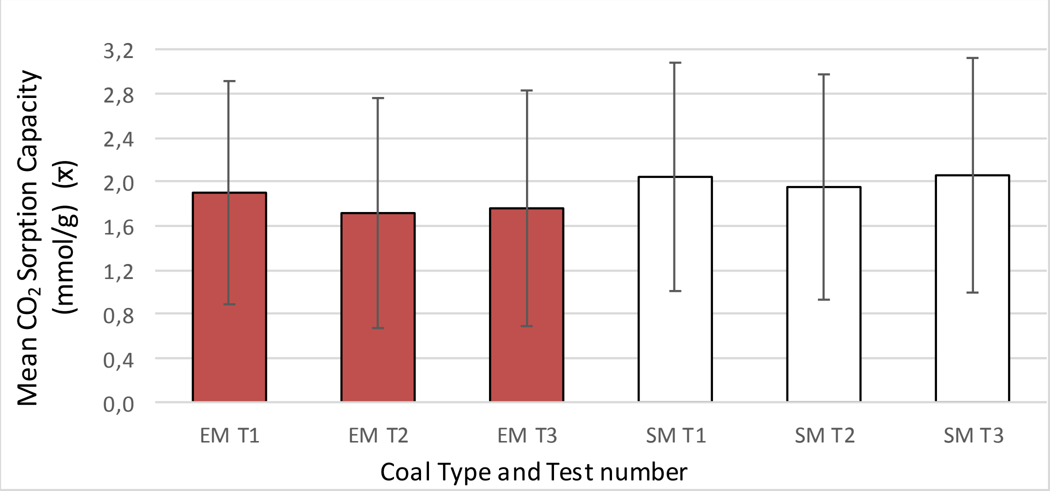

Figure 19. CO_2 sorption capacity comparison at 50°C using ANOVA results

Error bars which represent the calculated standard deviation (SD) show good repeatability was achieve for each coal type and test run done conducted. Table 7 summarizes the ANOVA statistical data. For both coals tested the F statistic values range in the region of 0.03 – 0.09, which is less than the computed F critical value (3.35). This indicates that a good confidence level for repeat results, proving that the null hypothesis for these experiments is valid i.e. there is *not* a significant difference between the groups or data sets. The p-values computed, range from 0.92 – 0.97, showing excellent reproducibility of CO$_2$ sorption results for both these SA coals tested.

Table 7. Data summary and ANOVA results of coals tested at 50°C

Summary data			*Count (n)*	*Sum (Σ)*	*Mean ($\bar{x}$)*	*Variance (s^2)*	*Standard deviation (SD)*
Coal EM	TEST 1		10	19.0	1.90	1.02	1.0
	TEST 2		10	17.2	1.72	1.09	1.0
	TEST3		10	17.6	1.76	1.14	1.1
Coal SM	TEST 1		10	20.4	2.04	1.07	1.0
	TEST 2		10	19.5	1.95	1.04	1.0
	TEST3		10	20.6	2.06	1.13	1.1
ANOVA results	*Source of variation*	*SS*	*df*	*MS*	*F*	*P-value-*	*F critical*
Coal EM	B/G	0.19	2.00	0.09	0.09	0.92	3.35
	W/G	29.23	27.00	1.08			
Coal SM	B/G	0.07	2.00	0.03	0.03	0.97	3.35
	W/G	29.22	27.00	1.08			

B/G - Between groups; W/G - Within Groups

4.4.3. Coals tested at 60°C

Figure 20 illustrates the comparison of the two (2) SA coals tested at 60°C versus the computed mean sorption ($\bar{x}$) results in mmol/g per coal sample.

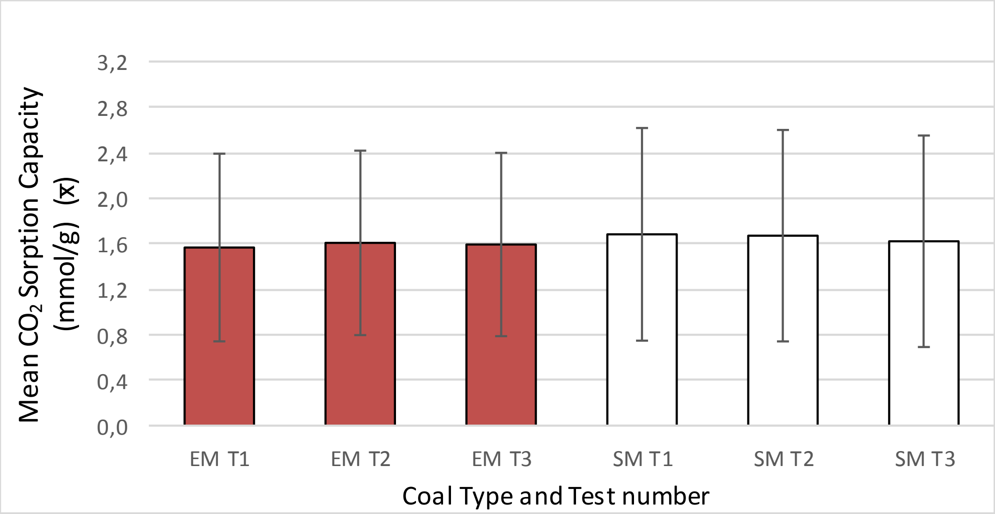

Figure 20. CO$_2$ sorption capacity comparison at 60°C using ANOVA results

Error bars which represent the calculated standard deviation (SD) show good repeatability was obtained for each coal type and test run conducted. Table 8 summarizes the ANOVA statistical data. For both coals tested the F statistic values are 0.01, which is less than the computed F critical value in the range of 3.35 -3.40. This indicates a good confidence level for these repeat results obtained in this study, proving that the null hypothesis for these experiments is valid i.e. there is *not* a significant difference between the groups or data sets. The p-values computed, are at 0.99, showing very good and acceptable reproducibility of the CO$_2$ sorption data set comparison of the repeat test results for both these SA coals, even at elevated temperatures.

Table 8. Data summary and ANOVA results of coals tested at 60°C

Summary data			*Count (n)*	*Sum (Σ)*	*Mean $(\bar{x})$*	*Variance (s^2)*	*Standard deviation (SD)*
Coal EM	TEST 1		10	15.6	1.56	0.68	0.8
	TEST 2		10	16.1	1.60	0.66	0.8
	TEST3		10	16.0	1.59	0.65	0.8
Coal SM	TEST 1		10	15.1	1.68	0.87	0.9
	TEST 2		10	15.0	1.67	0.86	0.9
	TEST3		10	14.6	1.62	0.86	0.9
ANOVA results	*Source of variation*	*SS*	*df*	*MS*	*F*	*P-value-*	*F critical*
Coal EM	B/G	0.01	2.00	0.004	0.01	0.99	3.35
	W/G	17.87	27.00	0.66			
Coal SM	B/G	0.01	2.00	0.004	0.01	0.99	3.40
	W/G	17.87	27.00	0.66			

B/G - Between groups; W/G - Within roups

4.4.4. Summary of international published CO_2 sorption data comparison

Table 9 summarises some of the internationally published CO_2 sorption data. Reported here are only data that has been published in the units of milli mole per gram (mmol/gram) of adsorbed CO_2 as was the findings in this investigation. Other published data could not be compared as conversion to units of mmol/g cannot be undertaken due to unknown sample masses (g) used from the tests published.

Table 9. Summary of published data on CO_2 adsorption in coal (low and high pressure)

Publication	Coal type	Coal rank	Ash/ Mineral	Particle type	Test conditions	CO_2 adsorption capacity (mmol/g)
Shimada *et al.* [54]	Japanese (Akabira)	Bituminous rank B		powder	60 bar, 35°C	1.65
Busch *et al.* [15].	US (Argonne Premium)**	High & medium volatile C bituminous	Low – Medium	powder	73.8 bar, 22 °C	1.05 – 2.31
Ceglarska-Stefanska & Zarebska [55].	Polish	Hard coal B	Medium	powder	40 bar, 25°C,	22
		Hard coal M	Low			26
Bae & Bhatia [56]	Australian (Bowen Basin)	High vol. bit.	Medium	powder	200 bar 313K	0.033-0.06
					323K	0.034.-039
					333K	0.019-0.026
Soares *et al.* [57]	Brazilian	High volatile C bituminous	High	powder	<1 bar, 30°C 30°C	0.089-0.186
Goodman *et al.* [43]	US (Argonne Premium coals)	Low vol. bit.	Low	powder	150 bar, 55°C	0.44 – 9.07
		High vol. bit.	Medium			0.733-0.909
		Lignite	Low			0.68-1.476
Yu *et al.* [59]	Chinese (Qinshui Basin)		Low	powder	~60 bar, 28°C	0.97 – 1.3
Dutta *et al.* [24]	USA (Illinois)	High Volatile bituminous A	Medium	powder	50 bar, 28.6°C	0.929
		High Volatile bituminous B				0.998-1.198
Gruszkiewicz *et al.* [60]	US (Lower Pennsylvania)	Lack Warrior	Low – medium	powder	22-34 bar, 35 – 40°C	0.7-0.82
Gertenbach [61]	South Africa (Highveld, Waterberg)	Low Rank A-Medium Rank C	Low-medium	powder	50 bar, 35°C	0.3-1.5
Charriére *et al.* [62]	France	High Volatile Bituminous B	Low	powder	10 – 50 bar, 10 – 60 °C	0.34 – 1.55

Publication	Coal type	Coal rank	Ash/ Mineral	Particle type	Test conditions	CO_2 adsorption capacity (mmol/g)
Pone *et al.* [63]	USA (Kentucky)	Bituminous	Low	powder	69 bar,	1.17
Ozdemir & Schroeder [64]	Argonne Premium coals	Low Volatile B	Low	powder	30 bar, 22°C	1.25
		Med Volatile B	Medium			1.07
		High Volatile B	Low-high			1.17-1.65
		Sub bituminous	Low			1.97
		Lignite	Low			1.72
Li *et al.* [65]	Chinese	Anthracite	Low, Medium	powder	250 bar, 35°C	3.03
		Medium Volatile Bituminous				2.02
		Sub-bituminous				4.36
He *et al.* [66]	Korean	Anthracite	Medium –high	crushed	152 bar, 25 – 45°C	1.4 – 1.5
Zhang *et al.* [67]	Chinese	Bituminous	Low, Medium	powder	60 bar, 35°C	2.2, 1.0
			Low, Medium		120 bar, 50°C	1.6, 1.23
Pini *et al.* [68]	Swedish	Medium Volatile Bituminous	Low, medium	powder	190 bar, 45°C	0.75 – 1.31
Weniger *et al.* [69]	Silesia	Medium Volatile Bituminous	Low, medium	powder	55 bar, 20°C	1.07 – 1.36
Mabuza [40]	South Africa	High & medium volatile C bituminous	Medium – High	crushed	90 bar, 35°C	1.08 – 2.58
Ramasamy *et al.* [70]	Australian	Low, med, high volatile bituminous &, sub-bituminous	Medium	crushed	65 bar, 45.5°C	~1.0
Premlall K. current paper	South Africa	Anthracite, and Low, med, high volatile bituminous	Low - high	Crushed	~88 bar, 35°C	1.09 – 2.56
					~88 bar, 50°C	2.84 – 2.13
					~88 bar, 60°C	2.22 – 2.55

A good comparison in terms of calculated CO_2 sorption data can be seen from the previous reported sorption data acquired from other researchers using the same volumetric sorption method [15,43, 56-70], as compared to the CO_2 sorption data findings from the SA coals finding discussed in this paper using the volumetric sorption research equipment. It must be noted that most results presented are for powdered coals tested.

The comparison of CO_2 sorption results (mmol/g) from other researchers' studies, as presented in Table 9, shows good comparison and sits well for crushed SA samples and most certainly show a good assimilation and comparison thereof. Crushed samples used in this study give a very good indication that the compiled results can be well fitted using this experimental volumetric set up. It must be noted that crushed samples and powdered samples will show small discrepancies in absolute CO_2 sorption amounts (mmol/g), but this is acceptable as a given range per coal type and pressure injection is slightly varied in terms of the sorption test variables of test. Also to note that variation in sample mass, size and temperature and pressure variations are all to be taken into account when doing comparative review of all results.

5. Conclusions

In light of the construction of the only CO_2 sorption pressurized system in SA, the following conclusions regarding the validity of the system, can be drawn from this investigation and the testing of the constructed sorption volumetric system from the varied CO_2 isothermal sorption isotherms, as well as from the analyzed ANOVA statistical assessment, demonstrated that the repeat test runs conducted at 35°C, 50°C and 60°C illustrated that exceptional equipment reliability and reproducibility of sorption data was achieved.

1. The overall sorption results for the five (5) South African coals tested at 35 and the two (2) evaluated at 50°C and 60°C, shows highly acceptable confidence levels for repeat results. The calculated p-values in all cases provide that the null hypothesis for these experiments is valid, i.e. there is *not* a significant difference between the groups or data sets that were re-produced. This is indicative of great reproducibility and consistency of the HPVSS during the test sorption experiments.
2. According to the set of sorption data that has been rigorously acquired and compared with the performance from other equipment reported in literature, it can be concluded that the data generated with this HPVSS are reliable and reproducible, thus affirming confidence in the designed and constructed high pressure volumetric sorption system.

References

[1] Blakemore E. 2017. Six irrefutable pieces of evidence that prove climate change is real. Popular Science. Online: https://www.popsci.com/evidence-climate-change-is-real. Accessed: May 2017.

[2] National aeronautics and space administration (NASA), 2018. Global Climate Change: Carbon dioxide latest measurements, [Online]: https://climate.nasa.gov/vital-signs/carbon-dioxide/; Accessed: August 2018.

[3] Centre for climate and energy solutions, Outcomes of the U.N. Climate Change Conference in Paris: 21st Session of the Conference of Parties to the United Nations Framework Convention on Climate Change (COP 21), December, 2016.

[4] van der Merwe, C. 2010. Energy and Climate change-policy and progress, ZEROCO_2.

[5] National climate change policy, 2018. South Africa's Greenhouse Gas Emission Reduction System; [Online]: http://pmg-assets.s3-website-eu-west-1.amazonaws.com/180213enviro.pdf. Accessed: August 2018.

[6] IPCC, 2014: Summary for Policymakers. In: Climate Change 2014: Mitigation Climate Change Contribution of working group III to the Fifth Assessment Report of the Intergovernmental panel on Climate Change (eds Edenhofer, O., et al.), Cambridge, UK and New York, USA.

[7] Cloete M. 2010. Atlas on geological storage of carbon dioxide in South Africa (No. ISBN: 978-1-920226-24-4). Silverton, Pretoria, South Africa: Council for Geoscience VILJOEN, J., H, A,

[8] Stapelberg FDJ, Cloete M. 2010. Technical Report on the Geological Storage of Carbon Dioxide in South Africa. Silverton: Pretoria: Council for Geoscience.

[9] Jouber, JI, Grein CT, Bienstock D. Sorption of Methane in Moist Coal, Fuel, 1973; 52:181-185.

[10] Clarkson CR, Bustin RM. The effect of methane gas concentration, coal composition and pore structure upon gas transport in Canadian coals: implications for reservoir characterisation, International Coalbed Methane Symposium, Tuscaloosa, Al, Tulsa, May 1997, 12-16.

[11] Clarkson CR, Bustin RM. The effect of pore structure and gas pressure upon the transport properties of coal: a laboratory and modeling study. 1. Isotherms and pore volume distributions. Fuel, 1999; 78(11):1333-1344.

[12] Nodzenski A. Sorption and desorption of gases (CH_4, CO_2) on hard coal and active carbon at elevated pressures. Fuel, 1998; 77: 1243-1246.

[13] Laxminarayana C, Crosdale PJ. Role of coal type and rank on methane sorption characteristics of Bowen basin, Australia coals, International Journal of Coal Geology, 1999; 40: 309-325.

[14] Krooss BM, van Bergen F, Gensterblum Y, Siemons N, Pagnier HJM, David P. High-pressure methane and carbon dioxide adsorption on dry and moisture-equilibrated Pennsylvanian coals. International Journal of Coal Geology, 2002; 51, 69-92.

[15] Busch A, Gensterblum Y, Krooss BM. Methane and CO_2 sorption and desorption measurements on dry Argonne premium coals: pure components and mixtures. International Journal of Coal Geology, 2003; 55, 205-224.

[16] Busch A, Gensterblum Y, Krooss BM. 2004. Methane and CO_2 sorption and desorption measurements on dry Argonne premium coals: pure components and mixtures. International Journal of Coal Geology, 2004; 45: 5.

[17] Busch A, Gensterblum Y, Krooss BM, Littke R. Methane and Carbon dioxide adsorption-diffusion experiments on coal: upscaling and modelling, International Journal of Coal Geology, 2004; 60: 151-168.

[18] Busch A, Gensterblum Y, Krooss BM, Siemons N. 2006. Investigation of high-pressure selective adsorption/desorption behaviour of CO_2 and CH_4 on coals: An experimental study, International Journal of Coal Geology, 2006; 66: 53-68.

[19] Busch A, Krooss BM. Molecular concept and experimental evidence of competitive adsorption of H_2O, CO_2 and CH_4 on organic material, Fuel, 2014; 115: 581–588.

[20] Belmabkhout Y, Frère M, de Weireld G. High-Pressure adsorption measurement. A comparative study of the volumetric and gravimetric methods. Measurement Science and Technology, 2004; 15: 848-858.

[21] Harpalani S, Prusty BK, Dutta P. Methane/CO_2 sorption modeling for coalbed methane production and CO_2 sequestration. Energy & Fuel; 2006; 20: 1591-1599.

[22] Siemons N, Busch A. Measurement and interpretation of supercritical CO_2 sorption on various coals, International Journal of Coal Geology, 2007; 69: 229-242.

[23] Zarębska K, Ceglarska-Stefańska G. The change in effective stress associated with swelling during carbon dioxide sequestration on natural gas recovery, International Journal of Coal Geology, 2008; 74: 167-174.

[24] Dutta P, Harpalani S, Prusty B., Modeling of CO_2 sorption in coal. Fuel, 2008; 87: 2023-2036.

[25] Dutta P, Bhowmik S, Das S. Methane and carbon dioxide sorption on a set of coals from India, International Journal of Coal Geology, 2011; 85: 289-299.

[26] Masterlez M, Gluskoter H, Rupp J. Carbon dioxide and methane sorption in high volatile bituminous coals from Indiana, USA, International Journal Coal of Geology, 2012; 60: 43-56.

[27] Merkel A, Gensterblum Y, Krooss BM, Amann A. Competitive sorption of CH_4, CO_2 and H_2O on natural coals of different rank, International Journal of Coal Geology, 2015; 150-151: 181-192.

[28] Li Z, Liu D, Cai Y, Shi Y. Investigation of methane diffusion in low-rank coals by a multiporous diffusion model, Journal of Gas Science and Engineering, 2016; 33: 97-107.

[29] Premlall K, Mabuza M, Wagner N. Evaluating CO_2 Sorption Capacity of a Number of South African (SA) Coal Types: Comparative Study of the Different Coal Properties at Incremental Pressures up to Supercritical Pressures. Energy Procedia, 2014; 51**,** 299-307.

[30] Mabuza M, Premlall K. Assessing Impure CO_2 Adsorption Capacity on Selected South African Coals: Comparative Study Using Low and High Concentrated Simulated Flue Gases. Energy Procedia, 2014; 51**,** 308-315.

[31] Lukhele KD, Premlall K, Shongwe M, Mabuza M, Daramola M. O. Effect of SO_2 co-feeding on CO_2 adsorption capacity of South African coals during CO_2 sequestration. Pet Coal, 2017; 59**,** 177-186.

[32] Mabuza M, Premlall K, Onyango MS, Daramola MO. 2018. Low-high temperature flue gas direct injection in south African bituminous and anthracite coals: sorption capacity assessment, Current Science, 2018; 115(4): 682-691.

[33] Premlall K, Wagner NJ. Evaluating Sorption capacity of a myriad of South African Coal types: Comparative Study of Sub-critical to Supercritical pressures, ICCS&T: International Conference on Clean Coal Technology, 29th September – 3rd October 2013, Penn Stater Hotel, Pennsylvania State University, USA.

[34] Premlall K, Wagner NJ. Laboratory experiments to determine best potential for cyclic supercritical CO_2 injections in SA coals to evaluate CH_4 desorption for ECBM potential, ICCS&T (International Conference on Coal Science & Technology), Hosted by: Engineers Australia and IChemE, 27th September – 2nd October 2015, Melbourne, Australia.

[35] Shongwe MG,Premlall K. Adsorption of flue gas on in-situ temperature profile of coal seam depth, ICCS&T (International Conference on Coal Science & Technology), Hosted by: Engineers Australia and IChemE, 27th September – 2nd October 2015, Melbourne, Australia.

[36] Mabuza M, Premlall K. Sorption of industrial flue gases on South African coals for CO_2 storage: experimental study on laboraotory scale, APOEEC 2015 – 3rd African Public Officials Energy and Environment Conference and Workshop, 3 – 5 June 2015, St. Georges Hotel and Convention Centre, Hosted by CEEP (Centre for Electric Energy and Power), Tshwane University of Technology Pretoria, South Africa. Proceedings ISBN: 978-0-620-65945-1.

[37] Premlall K, Wagner NJ. Feasibility of continued cyclic supercritical CO_2 injection in SA coals to evaluate CH_4 desorption for ECBM potential, APOEEC 2015 – 3rd African Public Officials Energy

and Environment Conference and Workshop, 3 – 5 June 2015, St. Georges Hotel and Convention Centre, Hosted by CEEP (Centre for Electric Energy and Power), Tshwane University of Technology Pretoria, South Africa. Proceedings ISBN: 978-0-620-65945-1.
[38] He J, Shi Y, Ahn S, Kang JW, Lee C-H. Adsorption and Desorption of CO_2 on Korean Coal under Subcritical to Supercritical Conditions. The Journal of Physical Chemistry B, 2010; 114**,** 4854-4861.
[39] Ozdemir E. Chemistry of the adsorption of carbon dioxide by Argonne Premium coals and a model to simulate CO_2 sequestration in coal. PhD, University of Pittsburgh 2004.
[40] Mabuza MM. 2013. Evaluating the adsorption capacity of supercritical carbon dioxide on South African coals using a simulated flue gas, Magister Technologiae, Tshwane University of Technology, Pretoria, South Africa.
[41] Day S, Sakurovs R, Weir S. Supercritical gas sorption on moist coals, International Journal of Coal Geology, 2008; 74(3-4): 203-214.
[42] Goodman AL, Busch A, Duffy GJ, Fitzgerald JE, Gasem KAM, Gensterblum Y, Krooss BM, Levy, J, Ozdemir E, Pan Z, Robinson RL, Schroeder K, Sudibandriyo M, White CM. 2004. An Interlaboratory Comparison of CO_2 Isotherms Measured on Argonne Premium Coal Samples. Energy & Fuels, 2004; 18: 1175-1182.
[43] Goodman AL, Busch M, Bustin L, Chikatamarla S, Day GJ, Duffy JE, Fitzgerald JE, Gasem KAM, Gensterblum Y, Hartman C, Jing C, Krooss BM, Mohammed ST, Pratt T, Robinson RL, Romankov V, Sakurovs R, Schroeder K, White CM. Inter-laboratory comparison II: CO_2 isotherms measured on moisture-equilibrated Argonne premium coals at 55 ^{0}C and up to 15 MPa, International Journal of Coal Geology, 2007; 72(3-4): 153 – 164.
[44] Gumma S, Talu O. Gibbs Dividing Surface and Helium Adsorption. Adsorption, 2003; 9:17-28.
[45] Sudibandriyo M. A Simple Technique for Surface Area Determination Through Supercritical CO_2 Adsorption. Makara of Technology Series, 2010; 14(1):1-6.
[46] McCarty RD Thermophysical properties of helium-4 from 2 to 1500 K with pressures to 1000 atmosphere. NBS Technical note 631. US Department of Commerce 1972.
[47] Hidnert P, Peffer EL. Density of Solids and Liquids. USA: Washington: United States Department of Commerce 1950.
[48] Charriére D, Pokryszka Z, Behra P. Effect of pressure and temperature on diffusion of CO_2 and CH_4 into coal from the Lorraine basin (France). International Journal of Coal Geology. 2010; 81: 373-380.
[49] Qing-Ling Z. Adsorption mechanism of different coal ranks under variable temperature and pressure conditions. Journal of China University of Mining and Technology, 2008; 18(3):395-400.
[50] Oldenburg C. Joule-Thomson Cooling Due to CO_2 Injection into Natural Gas Reservoirs, Energy Conversion and Management, 2007; 48: 1808-1815.
[51] NIST. 2016. National Institute of Standards and Technology-NIST Chemistry WebBook [Online]. Available: https://webbook.nist.gov/chemistry/#Search [Accessed]: 23 May 2018.
[52] Span R, Wagner W. 1996. A new equation of state for carbon dioxide covering the fluid region from the triple-point temperature to 1100 K at pressures up to 800 MPa. Journal of Physical and Chemical Reference Data, 25**,** 1509-1596.
[53] Kim HJ, Sh, Y, He J, Lee H-H, Lee C-H. Adsorption characteristics of CO_2 and CH_4 on dry and wet coal from subcritical to supercritical conditions. Chemical Engineering Journal, 2011; 171**,** 45-53.
[54] Corder GW, Foreman DI. 2009. Nonparametric Statistics for Non-Statisticians. Hoboken: John Wiley & Sons. pp. 99–105. ISBN 9780470454619.
[55] Shimada S, Li H, Oshima Y, Adachi K. Displacement behaviour of CH_4 adsorbed on coals by injecting pure CO_2, N_2 and CO_2-N_2 mixture, Environmental Geology, 2005; 49: 44-52.
[56] Ceglarska-Stefańska G, Zarębska K. Sorption of carbon dioxide-methane mixtures, International Journal of Coal Geology, 2008; 62: 211-222.
[57] Bae JS, Bhatia SK, Rudolph V, Massarotto P. 2009. Pore Accessibility of Methane and Carbon Dioxide in Coals, Energy & Fuels, 2009; 23-3319-3327.
[58] Soares JL, Oberziner ALB, José HJ, Rodrigues AE, Moreira RFPM. Carbon dioxide adsorption in Brazilian coals, Fuels, 2007 ; 21: 209-215.
[59] Jessen K, Tang G-Q, Kovscek AR. Laboratory and Simulation investigation of enhanced coalbed methane Recovery by gas injection, Transport in Porous Media, 2008; 73(2): 141-159.

[60] Gruszkiewicz MS, Naney MT, Blencoe JG, Cole DR, Pashin JC, Carroll RE. Adsorption kinetics of CO_2, CH_4, and their equimolar mixture on coal from the Black Warrior, West-Central Alabama, International Journal of Coal Geology, 2009; 77: 23-33.

[61] Gertenbach RM. Methane and Carbon Dioxide sorption studies on South African coals, MSc Dissertation, University of Stellenbosch 2009.

[62] Charriére D, Pokryszka Z, Behra P. Effect of pressure and temperature on diffusion of CO_2 and CH_4 into coal from the Lorraine basin (France). International Journal of Coal Geology.2009; 81:373-380.

[63] Pone JDN, Halleck PM, Mathews JP. Sorption capacity and sorption kinetic measurements of CO_2 and CH_4 in confined and unconfined bituminous coal. Energy & Fuels, 2009; 23: 4688-4695.

[64] Ozdemir E, Schroeder K. Effect of Moisture on Adsorption Isotherms and Capacities of CO_2 on coals, Energy & Fuels, 2009; 23: 2821-2831.

[65] Li K. Carbon Capture by Adsorption. Cooperative Research Centre for Greenhouse Gas Technology (CO_2CRC): Monash University 2011.

[66] He J, Shi Y, Ahn S, Kang JW. Adsorption and Desorption of CO_2 on Korean Coal under Subcritical to Supercritical Conditions. The Journal of Physical Chemistry B, 2010; 114(14):4854-4861.

[67] Zhang D, Cui YJ, Li SG. Adsorption and diffusion behaviours of methane and carbon dioxide on various rank coals. Journal of Chinese Coal Society, 2011; 10:1693–8.

[68] Pini R, Ottiger S, Burlini L, Storti G, Mazzotti M. Sorption of carbon dioxide, methane and nitrogen in dry coals at high pressure and moderate temperature. International Journal of Greenhouse Gas Control, 2012; 4(1):90–101.

[69] Weniger P, Franců J, Hemza P, Krooss BM. Investigations on the methane and carbon dioxide sorption capacity of coals from the SW Upper Silesian Coal Basin, Czech Republic. International Journal of Coal Geology, 2012; 93(0):23-39.

[70] Ramasamy S, Sripada PP, Khan MM, Tian S, Trivedi J, Gupta R. Adsorption behaviour of CO_2 in Coal and Coal Char, Energy & Fuels, 2014; 28, 5241-5251.

To whom correspondence should be addressed: Dr. K. Premlall, Department of Chemical, Metallurgical and Materials Engineering, Tshwane University of Technology, Pretoria, South Africa, 0001; Premlallk@tut.ac.za

Petroleum and Coal

Article **Open Access**

EPOXIDE OF RAPESEED OIL-MODIFIER FOR BITUMEN AND ASPHALT CONCRETE

Yurii Hrynchuk[1], *Iurii Sidun*[2], *Volodymyr Gunka*[1], *Yurii Prysiazhnyi*[1], *Volodymyr Reutskyy*[1], *Mykola Mosiuk*[3]

[1] *Institute of Chemistry and Chemical Technology, Lviv Polytechnic National University, 12 Bandera street, Lviv, Ukraine*
[2] *Institute of Building and Environmental Engineering, Lviv Polytechnic National University, 12 Bandera street, Lviv, Ukraine*
[3] *Institute of Tourism and Geosciences Ivano-Frankivsk National Technical University of Oil and Gas, 15 Karpatska Street Ivano-Frankivsk Ukraine,*

Received May 8, 2019; Accepted July 1, 2019

Abstract

We managed increasing properties of road bitumen and asphalt concrete based on it with help of modification of road bitumen by epoxy compounds based on renewable raw materials, namely by epoxide of rapeseed oil (ERO). Physical-mechanical properties of initial and ERO modified bitumens and asphalts were researched and analyzed. Also was made a comparison of obtained results with similar indexes for trade additives for road bitumen, namely with wax and polymer modifier of SBS type.

Keywords*: Bitumen; Epoxide of rapeseed oil; Modification; Asphalt concrete.*

1. Introduction

Oil bitumen have a wide use including applying as binding component in the production of asphalt concrete for building and maintenance of the roads. Unsatisfactory heat resistance, elasticity and adhesion, low temperature behavior of bitumen are among main reasons of early destruction of asphalt concrete coatings on their basis.

As the world practice shows, modifiers of different nature are used to solve this problem and to improve the operational properties of bitumen. Modification reduces the sensitivity of bitumen to changes in temperature and long-term load, increases their cohesive strength, provides elasticity and improves low-temperature properties [1-2]. As a result, the strength, displacement and cracking strength of road surfaces and their resistance to fracture due to fatigue increases.

Epoxy asphalt is also used for road construction, it is a special kind of asphalt concrete as containing epoxy constituents for increasing the strength and deformation properties of asphalt concrete [3-4].

It should be noted that the main reason that hinders the increase in the use of asphalt concrete on the basis of modified bitumen is the high cost of modifiers. Their adding in bitumen raises the cost of binder in 1.5-2.5 times. The use of cheaper additives does not reduce costs due to the required higher content in the mixture (from 5 to 7%). In addition, cheap additives do not provide bitumen with the necessary properties, such as: elasticity, high heat resistance, increased plasticity and deformability at low temperatures, etc. Commodity modifiers are mostly expensive and not manufactured by the Ukrainian industry. Researches that are going in this direction are described in [5-9].

Our research group developed an additive which, at significantly lower cost, would not yield by efficiency to foreign analogues. Conducted search showed that the most suitable basis for modifier is renewable plant raw material, namely rapeseed oil – cheap product that is produced in Ukraine in large quantities. Previously was found that modification of road bitumen by epoxy compounds based on renewable raw material increases properties of bitumen, and due to content of the additive and method of its addition we can receive bitumen with different properties [10]. Based on this previous research we can state that ERO is a perspective and relatively cheap material for modification [11]. In order to simplify process of production and to exclude use of solvent [12] we received ERO by modified method of epoxidation [13]. This allowed us to decrease duration of the process and provided a high quality product without changing such important physical and chemical parameters as epoxy number, iodine and bromine number.

The main goal of this work was to develop a technology for the modification of road oil bitumen by ERO and to obtain improved properties of bitumen and asphalt concrete mixtures on their basis.

2. Experimental

2.1. Initial materials

As initial bitumen for modification we used oxidized bitumen 70/100 (BND 70/100) produced by PJSC "Transnational financial and industrial oil company Ukrtatnafta" (Kremenchuk, Ukraine). Also for comparison experiments we used trade additives for road bitumens: Licomont.BS 100 (Clariant, Switzerland) and SBS type polymer Kraton D1192 (Kraton Polymers, USA). Main physical-mechanical properties of initial bitumen are presented in the Table 1.

Table 1. Main physical and mechanical parameters of bitumen BND 70/100

Index and values	BND 70/100
Penetration at 25°C, м$\cdot 10^{-4}$ (0,1 мм)	95
Softening point, °C	45
Ductility at 25°C, м$\cdot 10^{-2}$ (см)	>100

Properties of the Licomont.BS 100 and Kraton D1192 are presented in the Table 2 and Table 3. «Licomont BS 100» is a product of reaction of mixtures of the long chain fatty acids with aliphatic diamines. There are two types of this additive –Licomont.BS 100 (used in this work) and Licomont BS 100 MB. Kraton D1192 polymer is a clear linear block copolymer based on styrene and butadiene with bound styrene of 30% mass. There are following types of Kraton D1192: AT - supplied as porous pellets dusted with talc, AS - supplied as porous pellets dusted with amorphous silica, ASM - supplied as powder dusted with amorphous silica, ATM - supplied as powder dusted with talc for the North American market. For this research we used Kraton D1192 AT.

Table 2. Properties of the Licomont BS 100

Characteristics	Unit	Target value	Test method
Acid value	mg KOH/g	max. 8	ISO 2114
Drop point	°C	139 - 144	ISO 2176
Density (23°C)	g/cm^3	~ 1,00	ISO 1183
Bulk density	g/l	450 - 700	ISO 60

Table 3. Properties of the Kraton D1192

Characteristics	Unit	Typical Value	Test Method
Hardness, Shore A (15 sec)	-	70	ASTM D 2240
Bulk Density	kg/dm^3	0,4	ASTM D 1895 method B
Specific gravity	-	0,94	ISO 2781
Melt flow rate, 200C/5kg	g/10min.	<1	ISO 1133
300% modulus	MPa	4,8	ISO 37
Elongation at break	%	1000	ISO 37
Tensile strength	MPa	33	ISO 37

2.2. Experimental procedure

2.2.1. Obtaining of ERO

Epoxidation of rapeseed oil (RO) was conducted by method created for epoxidation of soy oil [13]. For synthesis we used trade samples of RO without additional purification. Influence of solvent and time of reaction on conversion of C=C – bonds during epoxidation of RO T=70ºC is shown in the Table 4.

Table 4. Influence of solvent at time of reaction on conversion of the C=C – bonds during epoxidation of RO at T=70°C

№	Solvent	Reactants			General time of re-action, hr	Conversion C=C -bonds, %	EN ERO, %	Mass ERO, g
		RO, g/mol C=C	H_2O_2, g/mol	HCOOH, g/mol				
1	Toluene	372/1.82	225/3.97	46/1	3.5	59.3	5.10	408
2	Toluene	372/1.82	225/3.97	46/1	4.5	76.0	5.63	405
3	Cyclohexane	372/1.82	225/3.97	46/1	4.5	75.0	5.58	406
4	No solvent	372/1.82	225/3.97	46/1	4.0	90.5	6.12	461
5	No solvent	372/1.82	225/3.97	46/1	4.0	92.0	6.72	401

The relatively low epoxy number of the obtained product and the high residual value of the bromine number indicate incomplete conversion of double bonds (~ 60%). With an increase in the time of adhering the mixture to 2 hours and the time to withstand of the reaction mass to 2.5 hours, the conversion of C = C-bonds increases to almost 76% (Table 1). The epoxy number of the resulting epoxy increases to 5.63%. The use of cyclohexane as a solvent practically does not affect the performance of the process.

The value of the epoxy number was determined according to the standard methodology described in the work [13]. It was established that the use a of RO with an epoxy number of ~ 0,3% as raw material allows its epoxidation without solvent and without the additional addition of epoxidized oil into the system. In this case, the conversion of C = C-bonds over 90%is achieved, and the obtained epoxidized oil has an epoxy number equal to 6.7%, with a theoretically possible 7.2- 7.4%, depending on the content of C = C-bonds in raw materials.

Thus, the proposed improvement makes it possible to abandon the preliminary treatment of RO and the use of solvent, and hence the additional energy costs associated with solvent distillation and to improve the environmental aspects of production.

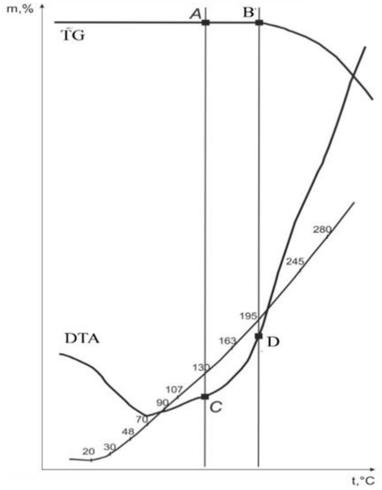

Figure 1. Curves of thermogravimetric and differential thermal analysis to epoxide of rapeseed oil

In order to determine the temperature range in which ERO can be used to modify road bitumen, its thermal stability was studied by the method of complex thermogravimetric and differential-thermal analysis (Figure. 1).

The nature of the curves of thermogravimetric and differential-thermal analysis shows that before temperature is 130°C (point C) the epoxide is stable, on the DTA curve there is an endeavor associated with the heating of the ERO sample. In the region of temperatures 130-195°C (points C and D), according to the differential thermal analysis, there are processes that are accompanied by the release of heat, which may be due to the disclosure of the epoxy cycle and the partial crosslinking of the chains to the oligomers, which corresponds to the appearance on the DTA curve of the exothermic effect. This process is not accompanied by the release of volatile scheduled products and the loss of mass on the TG curve (points A and B). At a temperature above 195°C on the curve of TG (point B) there is an intense mass loss that corresponds to the process of thermal destruction of the sample and is accompanied by the appearance of a pronounced exothermic effect on the DTA curve.

In order to confirm the obtained results an IR spectral analysis of samples of RO and its epoxy at different temperatures was made.

The data of the IR spectral analysis of samples confirm the fact of the disclosure of the epoxy cycle at temperatures above 130°C, since the intensity of the band corresponding to the fluctuation of epoxy groups decreases. According to the results of complex thermo-gravimetric and differential-term analysis and infrared spectra, it can be argued that the rapeseed oil epoxy is thermally stable in the temperature range up to 130°C.

2.2.2. Obtaining of modified binders

The bitumen modification process was performed by adding an additive when stirred in a thermostatically controlled reactor with a shaker blender. The temperature of the process of modification of the ERO was 190°C, the content of the additive-2, 3, 5, 7% by weight, the agitation time with stirring was 1-5 hr. [14]. Technological parameters of modification by commodity additives were following: modification of BND 70/100 by synthetic wax Licomont BS 100, modification temperature 160°C, time 3 hr, modification by polymer Kraton D1192 made at temperature 180°C during 5 hr.

2.3. Analysis of raw material and products

Temperature of softening was defined by [15], penetration at temperature 25 °C [16], ductility at temperature 25°C [17], elasticity at 25 °C [18].

The strength limit at compression at 20°C and 50°C of asphalt concrete was determined on mechanical presses at the speed of the press plate (3.0± 0.1) mm/min. Before testing, the specimens are thermostated in a container with water for (60±5) min at the temperature: (50±1)°C, (2± 1)°C. For tests of a compression strength of 50°C before being thermostated at a given temperature, samples are placed in dense polyethylene bags to prevent their contact with water. The average density of asphalt concrete was determined by hydrostatic weighing. Water saturation was determined by the amount of water absorbed by the sample at a given saturation regime in a vacuum installation. The coefficient of long-term water resistance was established by reducing the strength of compression at a temperature of (20 ± 1)°, samples of asphalt concrete under the action of water for 15 days in comparison with the samples sustained in the air at a temperature (20±1)°C.

3. Results and discussion

3.1. Modification of bitumen by ERO

As it was determined [14] the optimum temperature of the modification of bitumen by ERO is 190°C, the addition of the additive and bitumen was carried out exactly at that temperature. Changing the penetration and softening temperature depending on the content of the additive (over the bitumen mass) and the modification time at a given temperature is given in Fig. 2 and 3 respectively.

Analyzing the Fig. 2-3 with an increase in the concentration of ERO in bitumen, initially the softening temperature decreases at the initial stages of modification, but when stirred for 3 hours, the content of the additive 2 and 3% by weight softening temperature begins to grow. A similar effect of the modifier is observed on penetration of bitumen. That is so, because the ERO first provides bitumen plasticity, and then certain transformations in the structure of the binder (which need to be further investigated) occur, which leads to an increase in its hardness. We establish that variants of the content of the modifier 2 and 3% by weight and the modification time of 5 hours at 190°C may be modifications in the effective variants. Bitumen modification was also made by Licomont BS 100-3% by weight, and Kraton D1192 AT-3% by weight over a mass of bitumen.

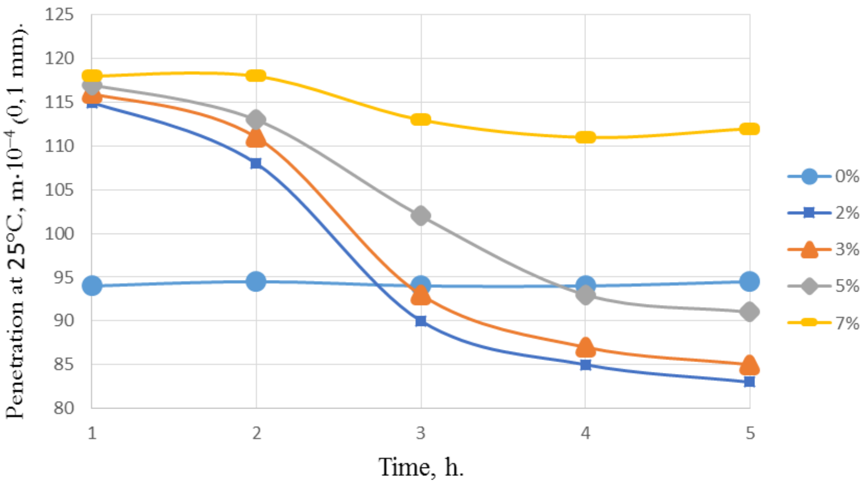

Figure 2. Dependence of penetration from ERO content and time of modification

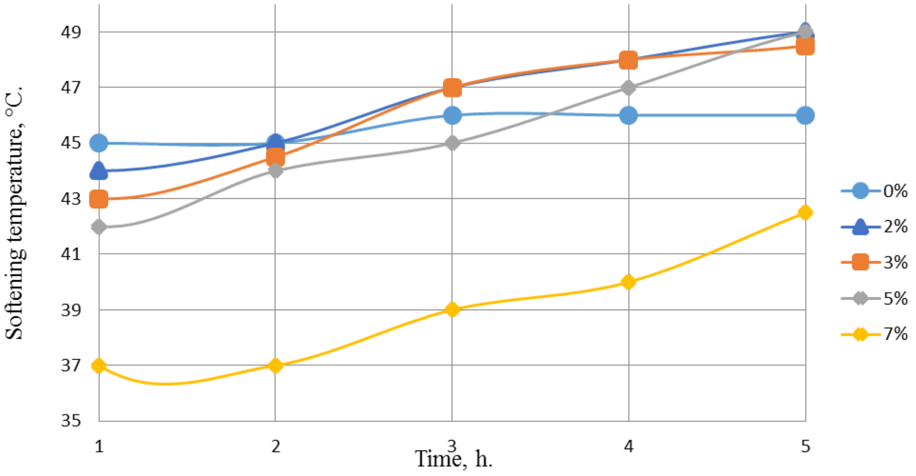

Figure 3. Dependence of softening temperature from ERO content and time of modification

A comparison of the properties of modified bitumen for the same dosage (3% by weight over the weight of bitumen) is shown in Table. 5. BND 70/100+ERO did not significantly change the properties of bitumen, but created the hypothesis that asphalt concrete using such a binder would be characterized by increased physical and mechanical performance.

Table 5. Physical-mechanical properties of initial and modified bitumen

Index	BND 70/100	BND 70/100 + ERO	BND 70/100 + Licomont.BS 100	BND 70/100 + Kraton D1192
Homogeneity			homogeneous	
Penetration at 25°C, м·10^{-4} (0,1 мм)	95	85	62	51
Softening point, °C	45	49	77	57
Ductility at 25°C, м·10^{-2} (см)	>100	>100	59	38
Elasticity за 25 °C, %	-	-	-	84

3.2. Influence of ERO on quality of asphalt concrete

To study the effectiveness of the modifiers, the granulometric composition of the mineral part of the asphalt concrete mixture (hot fine-grained dense with residual porosity from 2% to 5%, with a grain size of more than 5 mm-45-55% and a maximum grain size of up to 20 mm) was selected on the basis of granite gravel and non-activated limestone mineral powder

(Table 6) respectively. Bituminous content in asphalt concrete mixtures on unmodified and modified astringents was 6.2 wt. % over the weight of mineral constituents. Physical and mechanical properties of preformed models of asphalt concrete are given in Table. 7

Table 6. Composition of asphalt concrete

Material	Content of material in asphalt concrete, %	Material	Content of material in asphalt concrete, %
Rubble fr. 20-15 mm	5.0	Rubble waste fr. 0,63-0,071 mm	18.0
Rubble fr. 15-10 mm	15.0	Mineral powder	10.0
Rubble fr. 10-5 mm	20.0	**Total, %**	100.0
Rubble waste fr. 5-0,63 mm	32.0	Bitumen	6.2

Table 7. Physical and mechanical characteristics of fine-grained asphalt concrete

Index	Asphalt concrete with bitumen:			
	BND 70/100	BND 70/100+ERO	BND 70/100+ Licomont BS 100	BND 70/100 + Kraton D1192
Average density, g/sm^3	2.40	2.40	2.40	2.40
Water saturation, % for volume	0.50	0.45	0.49	0.40
Compressive strength. MPa, at a temperature:				
20°C	4,1	6,7	4,9	6,5
50°C	1,4	2,6	1,6	2,5
Coefficient of long-term water resistance	0.92	0.98	0.95	0.97

Analyzing Table 6, we note that the strength of asphalt concrete with BND 70/100+ERO at a temperature of 20°C increases 1.6 times, and 1.8 times at 50°C, compared with asphalt concrete on unmodified bitumen. That may indicate that this asphalt concrete is characterized by a higher heat resistance, and the coating, arranged with its use, will have greater resistance to corrosion under operating conditions. The obtained water saturation and the coefficient of long-term water resistance of asphalt concrete on BND 70/100+ERO indicate a better water resistance of this material. In general, the impact of ERO on asphalt concrete is similar to the effect of polymer modification.

4. Conclusion

1. The basis of the technology of high-quality road bitumens modified by rapeseed oil epoxy was developed.
2. We improved the method of obtaining rapeseed oil epoxide, which was first used as a modifier of road bitumen, improves the properties of modified bitumen and road pavements on their basis.
3. The thermal stability of rapeseed oil epoxide was studied, the temperature limits of its stability were established and it was shown that the ERO is thermally stable in the temperature range up to 130°C.
4. It is shown how the properties of modified by ERO road bitumen depend on its content, temperature and time of modification.
5. There are no special changes in the physico-mechanical parameters of bitumen for the modification of its ERO, but it is unambiguous to increase the quality characteristics of the made samples of asphalt concrete. Additional research is needed to understand this interesting fact.

References

[1] Zolotarev V, Pyrig Y, Galkin A. Cohesion of bitumen: its opportunities and prospects. Road Materials and Pavement Design, 2018; 1-14.

[2] Vinogradov V, Isayev G & I, Zolotarev A & A., Verebskaya V & A. E. Rheological properties of road bitumens. Rheologica Acta, 1977; 16: 266-281.

[3] Vyrozhemskyi V, Kopynets I, Kischynskyi S, and Bidnenko N. Epoxy asphalt concrete is a perspective material for the construction of roads. IOP Conference Series: Materials Science and Engineering, 2017; 236:.

[4] Zhong K, Yang X, Wei X. Investigation on surface characteristics of epoxy asphalt concrete pavement. International Journal of Pavement Research and Technology, 2017; 10(6): 545-552.

[5] Nykypanchuk M, Hrynchuk Y, Olchovyk M. Effect of Modified Bitumen on Physico-Mechanical Properties of Asphalt Concrete. Chemistry & Chemical Technology, 2013; 7: 467-470.

[6] Pyshyev S, Grytsenko Y, Solodkyy S, Sidun I, Vollis O. Using bitumen emulsions based on oxidated, distillation and modified oxidated bitumens for slurry seal production. Chemistry and Chemical Technology, 2015; 9 (3): 359-366.

[7] Demchuk Y, Gunka V, Pyshyev S, Bratychak M. Obtaining of the modifiers of road bitumen from phenol fraction of coal tar. Coal Chemistry Journal, 2017; 5: 23-28.

[8] Demchuk Y, Sidun I, Gunka V., Pyshyev S, Solodkyy S. Effect of phenol-cresol-formaldehyde resin on adhesive and physico-mechanical properties of road bitumen. Chemistry and Chemical Technology, 2018; 12 (4): 456.

[9] Solomentsev A, Zhdanyuk V, Malyar V, Krut V. Effect of surfactants on the kinetics of oxidation of vacuum resid and the quality of asphalt. Chemistry and Technology of Fuels and Oils - Chem technol fuels oils-engl, 1999; 35: 285-287.

[10] Hrynchuk Y, Nykypanchuk M. Epoxy compounds based on rapeseed oil as modifiers for road bitumen. The Bulletin of the Lviv Polytechnic National University. Chemistry, technology of substances and their application, 2011; 700: 474-477.

[11] Hrynchuk Y., Nykypanchuk M. Modification road asphalt epoxide olefins higher based on renewable raw materials. 15th International Symposium of Students and Young Mechanical Engineers Advances in Chemical and Mechanical Engineering. Poland, Gdansk, 2012.

[12] Hrynchuk Y, Nykypanchuk M. Improving the method of epoxidation of rapeseed oil. Materials of the 10th open scientific conference of the professor-teaching staff of the IPMFN, National University "Lviv Polytechnic", 2011.

[13] Kopach GE. Improvement of the technology of obtaining epoxy plasticizers. Dis. Cand. tech Sciences: 05.17.04 / State University "Lviv Polytechnic", 1996, 124.

[14] Hrynchuk Y, Nykypanchuk M. Influence of conditions and method of modification of road bitumen with rapeseed oil epoxide on their physicochemical properties. Bulletin of the National University "Lviv Polytechnic". Chemistry, technology of substances and their application, 2013; № 761, 465-469.

[15] EN 1427. European Standard. Bitumen and bituminous binders. Determination of the softening point. Ring and Ball method.

[16] EN 1426. European Standard. Bitumen and bituminous binders. Methods of tests for petroleum and its products. Determination of needle penetration.

[17] EN 13587. Bitumen and bituminous binders. Determination of the tensile properties of bituminous binders by the tensile test method.

[18] EN 13398 Bitumen and bituminous binders - Determination of the elasticity.

To whom correspondence should be addressed: Dr. Volodymyr Gunka, [1]Institute of Chemistry and Chemical Technology, Lviv Polytechnic National University, 12 Bandera Street, Lviv, Ukraine, 79013

Petroleum and Coal

Article **Open Access**

CALCULATION OF HEAT FLUX DENSITY AT A LARGE OIL TANK FIRE AFFECTING NEIGHBORING TANKS

Ján Horváth[1], *Jaroslava Štefková*[2]

[1] *Technical University in Zvolen, Faculty of Wood Science and Technology, Slovakia*
[2] *Technical University in Zvolen, Institute of Foreign Languages, Slovakia*

Received May 9, 2019; Accepted July 15, 2019

Abstract

In general, the storage volume of the bulk tanks is five up to ten times bigger compared to the storage tanks built several decades ago. The potential risk of such a fire cannot be eliminated even by the most strict regulations or precautions. When there is an oil storage tank fire, radiant heat is formed which spreads further into an environment often containing other storage tanks. The paper presents the calculation of the heat flux density in a specified distance from the burning tank. The resulting value of the heat flux density in the surrounding of the tank depends simultaneously on several factors. The construction of bulk oil tanks is recommended to have, in the future, legislation regulations also considering the value oil radiant heat at a fire. Based on the calculation of the radiant heat values in a specific area, the minimum separation distance between storage tanks shall be stated.

Keywords*: Oil fire; Fire scenario; Bulk storage tank; Heat flux density.*

1. Introduction

In case oil catches on fire, the rapid spread of fire and intense burning can be assumed. The fire shall spread across the entire surface of the flammable liquid. Oil has high calorific value and the flame temperature achieves 1000 to 1300°C [1]. If a big fire or explosion occurs at an oil hub or a storage center it is rather likely that the fire shall strike also other tanks and adjacent facilities and that it shall spread farther. This situation is called a domino effect. The risk analysis of domino effect fires in storage areas was investigated by [2]. They claim that domino accidents account for the largest proportion (44%) in the causes of pool fires at storage areas and therefore it needs further thorough investigations. The example is presented by the fire in Čechovice (Poland) in 1971. The fire risk forms especially at pumping stations where there are more storage tanks within the proximity. The individual storage tanks are placed in the distance close to their diameter, rarely closer. At fires of large storage tanks, the heat flux density achieves in the order of 10^5 W.m^{-2}. The decrease in the density of the heat flux is rather moderate and the space considered safe is in the distance of hundreds of meters from the fire spot. The heat impact is constantly changing at crude oil fires as there are influences by the fire development, climatic conditions, and human interference during the fire suppression [3].

2. Objectives

The main objectives of the paper are to introduce the calculation of the heat flux at the selected distance of a large storage tank. This calculation shall then be applied on selected large capacity tanks and at various fire scenarios considering other neighboring tanks. The necessary parameters related to a fire and separation distances are described next.

2.1. The fire parameters calculation

Energy release rate:
It is energy released per unit of time (kJ s^{-1}); it changes with time, whereas:

- At a natural fire of tanks, the rate becomes the constant,
- depends on the tank diameter *D,*
- at the diameter over 0.2 m the burning rate per unit area increases until a certain diameter then it becomes constant m''_{∞},
- it depends on the constant *k.β* – the product of radiation flux characteristic for fuel which is set for liquids and thermoplastic.

When a large storage tank is burning, it is assumed that it is a fuel limited fire as there should not be access of air into the fire limited by any means. Energy release rate at the fire is calculated from the equation (1):

$$Q^{\bullet} = A_f \cdot m''_{\infty} \cdot (1 - e^{-k \cdot \beta \cdot D}) \cdot \chi \cdot \Delta H_C \qquad (1)$$

where: A_f -horizontal burning area (m^2); m''_∞ – burning rate per unit area (kg m^{-2} · s^{-1}); *k.β*– the product of flame heat flux constants against flammable liquid surface; *D*– tank diameter (m); *χ*–fuel efficiency (%); ΔH_c – total heat of combustion (kJ.kg^{-1}) [4].

The values of energy release at the fire are necessary to calculate the mean length of the flame at a fire.

2.1.1. Mean flame length

Averaging of the visible flame in time, *y* (flame appearance) 1.0 permanent visible flame length; 0.5 half of the flame in time; on the *x* axes distance from the flame *L* (m). It is stated experimentally based on the video records in harmony with subjective optical perception. The correlation of flame length is caused by the turbulent nature and relation to the area of combustion *D* and *Q*.

At real fires the fuel geometry must be also taken into account-vertical or horizontal layout of the fuel), the impact of shells, ceiling, openings [5].

The mean flame length L_f (m) is calculated from the equation (2):

$$L_f = 0{,}235 \cdot \sqrt[5]{Q^{\cdot 2}} - 1{,}02 \cdot D \qquad (2)$$

The mean flame length for large storage tanks can be calculated by substituting the energy release rate calculated from equation (1) into the equation (2). The mean flame length values are essential to calculate the heat flux density.

2.1.2. Calculation of flame heat flux density

Heat flux density *q* (kW · m^{-2}) (equation 3) is determined from the equivalent time of fire duration τ_e or τ_{em} (it is hypothetical time of fire duration during which a fire would last in the fire compartment according to the stated temperature curve and would pose equivalent impacts in the construction as a real fully developed fire), or possibly from the calculated fire load p_v or p_{vm} and gas temperature which is expressed by a standardized temperature curve T_N (°C), (STN 92 0201-4, 2000) for the equivalent time of fire duration (equation 4).

$$q = (T_N + 273)^4 \cdot 5{,}67 \cdot 10^{-11} \qquad (3)$$

$$T_N = 20 + 345\, log(8t + 1) \qquad (4)$$

where: *q*–heat flux density (kW·m^{-2}); T_N–standardized gas temperature in a burning compartment (°C); *t*–the equivalent time of fire duration (τ_e or τ_{em} in minutes, p_v, or p_{vm} in *kg m^{-2}*,from Table No.2, STN 92 0201-4, max. value 180).

The flame heat flux density for crude oil fires is calculated from equation (3), where *t* = 180 min.

T_N = 20 + 345 log(8 180 + 1) = 1 110°C

q = (1110 + 273)^4 5.67 10^{-11} = **207.4 kW.m^{-2}**

The calculated value of 207.4 kW.m^{-2} shall be considered in further calculations.

The flame heat flux densities depending on its temperature are given in Table 1. The values of flame heat flux temperatures for specific flame temperatures are compared to those of stated by *Michejev* [6]; *Olšanský* [7] ranging from 1 000° to 1 300 °C, at crude oil boiling (stated by *Olšanský* [7]) up to 1 500°C.

Tab. 1 Flame heat flux densities for given flame temperatures

T (°C)	1 000	1 110	1 200	1 300	1 500
q (kW m^{-2})	148.9	207.4	266.9	347.1	560.3

2.1.3. Heat flux density at the specific distance

The heat flux density at a specific distance can be calculated via a distance factor - coefficient φ (-). The distance factor affects the total radiant heat being emitted by a radiant surface which lands on the receiving surface. Its value depends on the size of the emitting surface, the distance of the receiving surface from the emitting surface and on their mutual orientation. The parallel position presents the simplest arrangement. A partial distance factor is expressed in equation (5). In Figure 1 the basic area presents the receiving area at the vector towards the *S* area, which presents the emitting area.

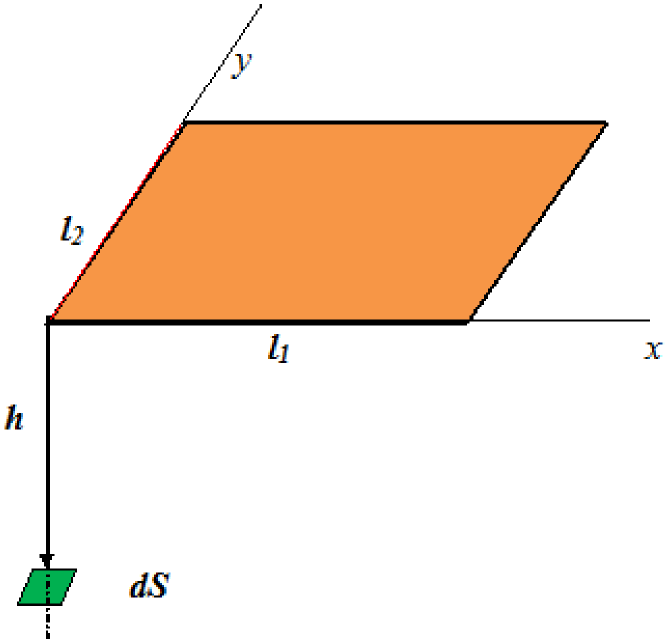

Fig.1. Basic area (dS) towards the top of the *S* area

To calculate the heat flux density in the specific area, the relation (5) according to Kadlec [8] was used. The relation was modified by inserting relevant tank parameters and the mean length of flames.

$$\varphi dS,S = \frac{1}{2\cdot\pi}\left(\frac{l_1}{\sqrt{h^2+l_1^2}}\cdot arctg\frac{l_2}{\sqrt{h^2+l_1^2}} + \frac{l_2}{\sqrt{h^2+l_2^2}}\cdot arctg\frac{l_1}{\sqrt{h^2+l_2^2}}\right) \qquad (5)$$

The final value of the heat flux density (having calculated the position factor) can be achieved via a modified relation (7) out of the relation (6),

$$\varphi_{cr} = \frac{q_{cr}}{q} \qquad (6)$$

where: q_{cr} – the specific value of critical flux (kW m^{-2}); q–the density of the radiation flux (kW m^{-2}).

$$q_L = \varphi \cdot q \qquad (7)$$

where: q_L–heat flux density in the specified distance (kW m^{-2}); φ– position factor (coefficient) (-); q–flame heat flux density (kW m^{-2}).

The final value of the position factor in the chosen distance and the calculated flame heat flux density of 207.4 kW.m^{-2} from (8) are inserted in the modified – derived relation (7) and the product of these parameters is the heat flux density in the given distance from the outer shell of the affected tank.

2.2. The energy release rate and mean flame length

In the world, there are several variants of the large storage tanks for crude oil. The comparison of the fire safety of the storage tanks and possibilities to extinguish the fires of such large storage tanks is devoted a minimal attention in the scientific community in European countries.

The calculations of the parameters are conducted for selected volumes of the large storage tanks. The tanks of two sizes–30 000 m^3 and 70 000 m^3 are currently in operation in Slovakia. The crude oil pump station in Tupá (Slovak Republic) comes as the fourth one in order from the east border from Ukraine. There are six tanks of the 30 000 m^3 volume and two of 70 000 m^3

volume in operation. The tank of 125 000 m^3 volume is used to store crude oil in the Central Crude Oil Tank Farm Nelahozeves of Mero Company (Czech Republic), where 16 crude oil tanks with the total storage capacity of 1 550 000 m^3 are located. The calculations of the energy release rate and mean flame length tanks of the mentioned capacities are described individually further.

The chosen tanks are of similar construction and make, however, they have different dimensions which shall be used in the investigation. When considering double layer aboveground storage tanks where there is free space between the storage tank layer and the outer safety shell, several fire scenarios should be taken into account. To simplify the issue, the horizontal area of the outer tank diameter, which is, in fact, the sum of the storage tank area and the ring towards the outer safety shell, is being used for calculations.

The fire scenarios which might occur:

1. A fire in the space between the tank roof and tank shell- **S1 scenario.**
2. A fire of the outer safety tank and the space between the roof and tank shell–**S2 scenario.**
3. A fire of the storage tank - full-area fire (the floating roof is immersed)–S3 scenario.
4. A simultaneous fire of the storage tank and safety tank (the floating roof of the storage tank is immersed and the outer shall of the safety tank is damaged)–**S4 scenario.**
5. A fire in the outer safety tank (a fire in the ring)–**S5 scenario**.

The S3 and S4 scenarios seem to be the most complicated. Therefore, they are used in the further study.

3. Calculations

3.1. Storage tank of 30.000 m^3 volume – energy release rate

D–tank diameter (42.8 m); D_h–diameter of the safety tank (53.6 m); *Af*–horizontal burning surface area (1 439 m^2); $A_{f\,h}$ – horizontal burning surface area of the safety tank (2 256 m^2); m''_∞– planar burning rate (0.02833 kg m^{-2} ·s^{-1}); *k.β* – the product of flame radiation flux constants against flammable liquid surface (2.8 m^{-1}); *χ* – fuel efficiency (70 % i.e. 0.7); ΔH_c – total crude oil combustion heat (42.5 MJ. kg^{-1} = 42 500 kJ. kg^{-1})

$$Q^{\cdot} = 1\,439 * 0.02833\,(1 - e^{-2.8.\,42.8})\;0.7\;42\,500 = 1\,212\,814.4 \text{ kJ s}^{-1} = 1\,212.8144 \text{ MW}$$

During a fire of a large storage tank of 30,000 m^3 volume, the energy release rate shall be approximately **1 213 MW**.

3.1.1. Storage tank of 30.000 m^3 volume - the mean flame length L_f (m)

$$L_f = 0.235 \cdot \sqrt[5]{Q^{\cdot 2}} - 1.02 \cdot D$$

$$L_f = 0.235 \cdot \sqrt[5]{1\,212\,814.4^2} - 1.02 \cdot 42.8 = 20.1\ m$$

The mean flame length shall be approximately **20.1 m**.

3.2. The storage tank of 70,000 m^3 volume - energy release rate

D–tank diameter (66 m); D_h –diameter of the safety tank (80 m); A_f – horizontal burning surface area of the tank (3421 m^2); $A_{f\,h}$–horizontal burning surface area of the safety tank (5027 m^2); m''_∞ – planar burning rate (0.02833 kg m^{-2} · s^{-1}); *k.β* –the product of flame radiation flux constants against the flammable liquid surface (2.8 m^{-1}); *χ* – fuel of crude oil (70 % i.e. 0.7); ΔH_c – total crude oil combustion heat (42.5 MJ · kg^{-1} = 42 500 kJ ·kg^{-1})

$$Q = 3\,421\;0.02833\,(1 - e^{-2.8.\,66})\;0.7\;42\,500 = 2\,883\,278.7 \text{ kJ s}^{-1} = 2\,883.2787 \text{ MW}$$

During the fire of a large storage tank of 70 000 m^3, the energy release rate shall be approximately **2 883 MW**.

3.2.1. The storage tank of 70,000 m³ volume-the mean flame length

$L_f = 0.235 \cdot \sqrt[5]{2\,883\,278.7^{\,2}} - 1.02 \cdot 66 = 22.84\ m$. The mean flame length shall be **22.84 m**.

3.3. The large storage tank of 125 000m³ – energy release rate

D tank diameter (84.47 m); D_h–diameter of the safety tank (90.47 m); A_f –horizontal burning surface area of the tank (5 604 m²); $A_{f\,h}$–horizontal burning surface area of the safety tank (6 428 m²); m''_∞ – planar burning rate (0.02833 kg m^{-2} s^{-1}); $k.\beta$–the product of flame radiation flux constants against the flammable liquid surface (2.8 m^{-1}); χ – fuel of crude oil (70 % i.e. 0.7); ΔH_c – total crude oil combustion heat 42.5 MJ kg^{-1} = 42 500 kJ kg^{-1})

$\dot{Q} = 5\,604 \cdot 0.02833\,(1 - e^{-2.8\,\cdot\,84.47})\;0.7 \cdot 42\,500 = 4\,723\,149.3$ kJ s^{-1} = 4 723.1493 MW

During a fire of a large storage tank of 125 00m³, the energy release rate shall be approximately **4 723 MW.**

3.3.1 The large storage tank of 125 000 m³ - the mean flame length

$L_f = 0.235 \cdot \sqrt[5]{4\,723\,149.3^{\,2}} - 1.02 \cdot 84.47 = 23.68\ m$

The mean flame length at the fire shall be approximately **23.68 m**.

The parameters of energy release rate at a fire and the mean flame length are stated in Table 2. These parameters are compared for large storage tanks in the most complicated scenarios. The comparison of the values of the energy release rate shows the direct proportionality in increasing the energy release rate with the increasing size of the fire area.

Tab. 2 Comparison of calculated parameters for the chosen fire scenarios

Tank calculated volume	30 000 m³ 29 062 m³		70 000 m³ 72 803 m³		125 000 m³ 124 968 m³	
Scenario	S3	S4	S3	S4	S3	S4
Diameter(m)	42.8	53.6	66	80	84.47	90.47
Area (m²)	1 439	2 256	3 421	5 027	5 604	6 428
$\dot{Q}$ (MW)	1 213	1 901	2 883	4 237	4 723	5 418
L_f (m)	20.10	21.65	22.84	23.57	23.68	23.76

3.4. Calculation of the heat flux density affecting the neighboring tanks

To calculate the heat flux density in a specific distance there was used the relation 8 modified from the relation 5 [8], which was modified by inserting selected parameters of the tank and the mean flame length.

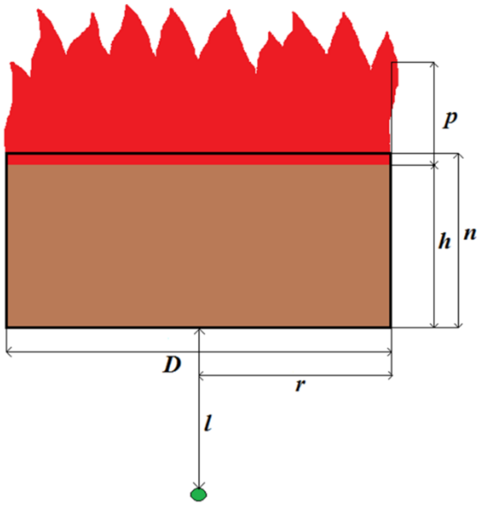

Figure 2 shows the basic parameters of the large crude oil storage tank, where: *h*–crude oil level height in the tank (maximum height considered); ℓ–the distance from the burning tank shell; *D* – tank diameter; *r* – radius of the tank; *n* – tank shell height; *p* – flame length (calculated mean flame length L_f), which were used to calculate the heat flux at a specific distance from the burning large oil storage tank.

Figure 2. The scheme of a burning tank and relevant parameters

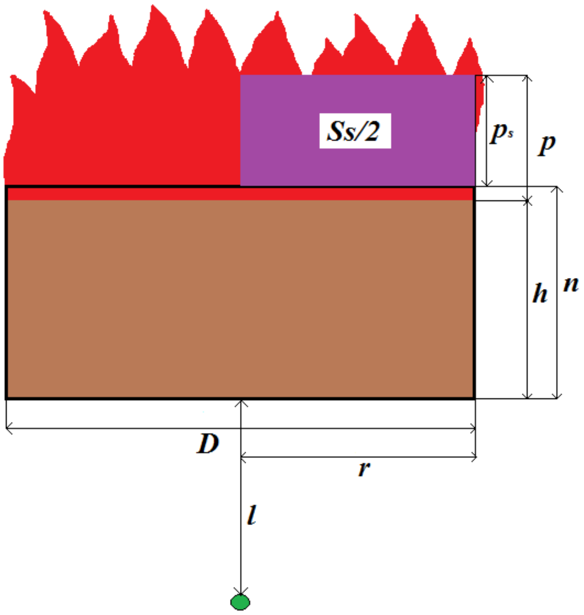

Figure 3 shows the half of the emitting flame surface (referred to as *Ss/2*) in purple color. This area of emitting flame is the basis for the calculation of the distance factor considering the effect of heat flux on the neighboring container. Referring to S3 scenario the calculations shall be projected for radiation on the neighboring tank of the same dimensions as the burning tank at the level of the upper edge of the neighboring tank shell. In case of the fire of the safety tank (S4 scenario) the final values of heat flux density projected at the height of the safety tank on the outer shell of the neighboring tank.

Fig. 3 Half of the cross section area of the ratiating flame Ss/2 ; *Ss/2* (radians) – half of the area of the radiating flame p_s

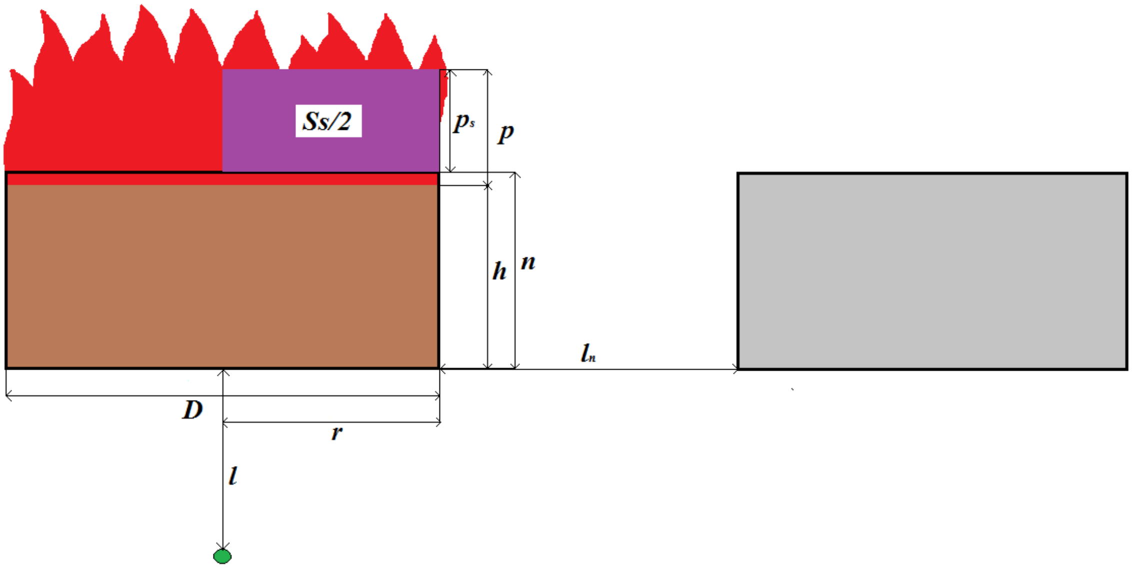

Fig. 4 Scheme of the heat flux effect on the neighboring tank with marked parameters

Figure 4 shows the distance between the tanks l_n.

$$\varphi dS,Ss/2 = \frac{1}{2\cdot\pi}\left(\frac{r}{\sqrt{l_n^2+r^2}}\cdot arctg\frac{p_s}{\sqrt{l_n^2+r^2}} + \frac{p_s}{\sqrt{l_n^2+p_s^2}}.\,arctg\frac{r}{\sqrt{l_n^2+p_s^2}}\right) \tag{8}$$

$$\varphi dS,Ss = 2\cdot Ss/2 \tag{9}$$

where: p_s – the length of the radiating flame – the length of the flame lowered by the difference between the height of the tank shell and height of the oil level in the tank; $p_s = p - (n - h) = (p - n + h)$; l_n – the distance of the neighboring tank shell from the shell of the burning tank.

4. Results

4.1. The large storage tank of 30 000 m^3 volume

To calculate the heat flux density against the neighboring tanks the distance of 35 m to 70 m was used. Table 3 states the calculated values of the heat flux effect on the neighboring tanks in specified distances. The first column of Table 3 specifies the distance (marked as l_n) in meters for the heat flux density calculation q_L (kW m^{-2}) in the second column of S3 scenario in the second column and for S4 in the third column.

The basic data for further heat flux density calculations in specified distances between the storage tanks of 30 000 m^3 are:
for S3 scenario: $D = 42{,}8$ m, $r = 21{,}4$ m, $n = 22{,}6$ m, $h = 20{,}2$ m, $p = 20{,}1$ m;
for S4 scenario: $D_h = 53{,}6$ m, $r_h = 26{,}8$ m, $n_h = 14{,}5$ m, $h_h = 12{,}9$ m, $p_h = 21{,}65$ m.

The length of the radiating flame p_s is calculated out of the basic data, whereas the data for the safety tank are indexed with $_h$.
For S3 scenario–in equation (8) there is used: $p_s = p-(n-h) = (p-n+h) = (20.1-22.6+20.2) = 17.7$ m.
For S4 scenario–in equation (8) there is used: $p_s = p_h-(n_h-h_h) = (p_h-n_h+h_h) = (21.65-14.5+12.9) = 20.05$ m.

Fig. 3 The heat flux of the 30 000 m^3 tank against the neighboring tanks – S3 and S4 tanks

l_n (m)	q_L (kW.m^{-2}) S3 scenario	q_L (kW.m^{-2}) S4 scenario	l_n (m)	q_L (kW.m^{-2}) S3 scenario	q_L (kW.m^{-2}) S4 scenario
35	28.91	36.38	55	14.15	18.87
40	23.74	30.46	60	12.17	16.36
45	19.75	25.74	65	10.56	14.29
50	16.62	21.94	70	9.24	12.58

The calculated values in Table 3 illustrate that the heat flux density is higher in the safety tank fire in all specified distances. The graph in Figure 5 presents the calculated values of heat flux densities from Table 3 for 30 000 m^3 tank and compares both scenarios for the particular tank.

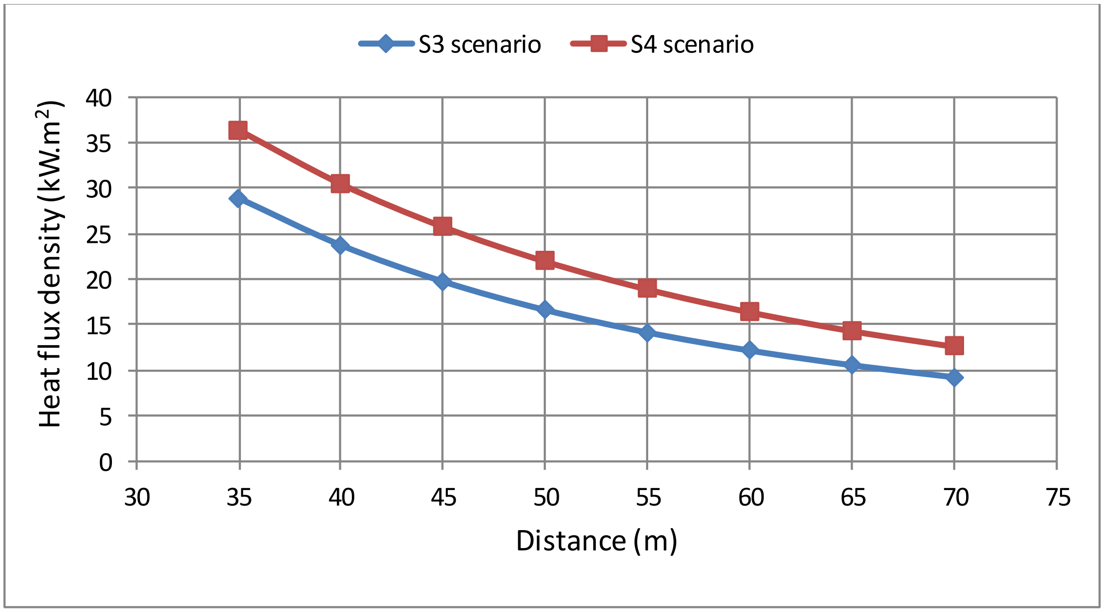

Fig. 5 Heat flux density effects on the neighboring tank at a fire of the large storage tank of 30 000 m^3 volume–S3 and S4 scenarios

4.2. The large storage tank of 70 000 m^3 volume

The basic data for the calculation of the heat flux in specified distances between large storage tanks of 70 000m^3 volume are:

For S3 scenario: D = 66 m, r = 33 m, n = 236 m, h = 21.28 m, p = 22.84 m.

For S4 scenario: D_h = 80 m, r_h = 40 m, n_h = 15.3 m, h_h = 14.5 m, p_h = 23,57 m.

Consequently, the length of the flame p_s is calculated:

S3 scenario – in the equation (8) the following values are used: $p_s = p - (n - h) = (p - n + h)$ = (22.84 – 23.6 + 21.28) = **20.52 m**

S4 scenario – in the equation (8) the following values are used: $p_s = p_h - (n_h - h_h) = (p_h - n_h + h_h)$ = (23.57 – 15.3 + 14.5) = **22.77 m**

Table 4 states the calculated levels of heat flux density in specified distances for a large storage tank of 70 000 m^3. Figure 6 shows the graph illustration of the calculated values for both fire scenarios.

Tab. 4 Heat flux of 70 000 m^3 tank against neighboring tanks – S3 and S4 scenarios

l_n (m)	q_L (kW m^{-2}) S3 scenario	q_L (kW m^{-2}) S4 scenario	l_n (m)	q_L (kW m^{-2}) S3 scenario	q_L (kW m^{-2}) S4 scenario
35	41.06	47.61	55	22.33	27.49
40	34.91	41.23	60	19.51	24.26
45	29.87	35.84	65	17.16	21.52
50	25.74	31.31	70	15.18	19.18

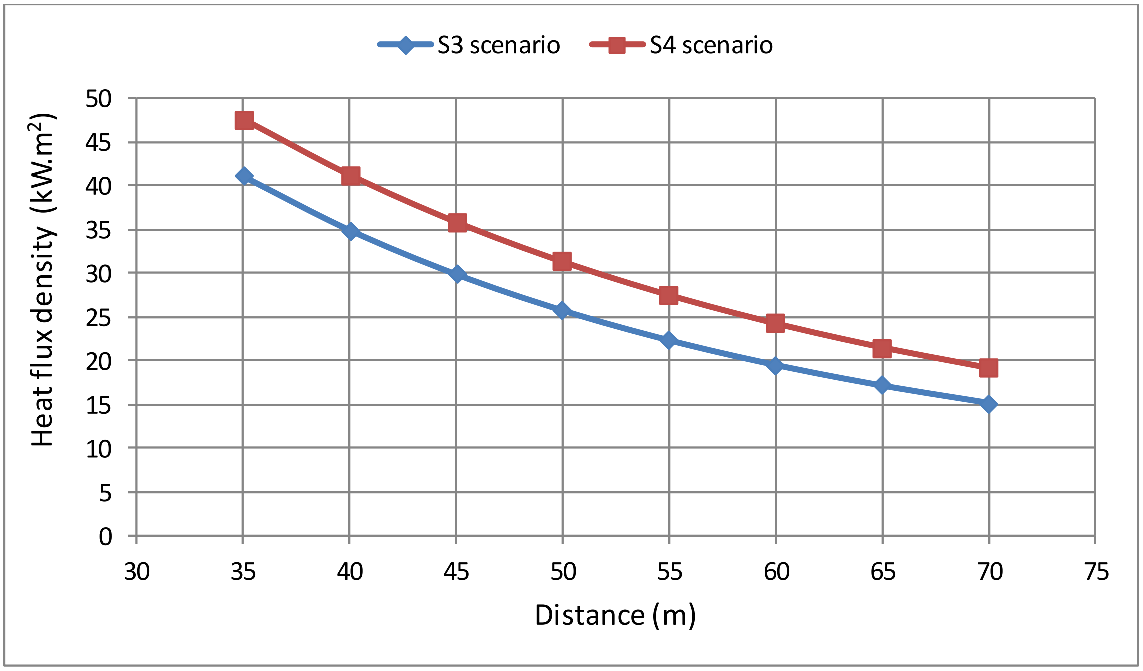

Fig. 6 Heat flux density effects of 70 000 m^3 storage tank on the neighboring tanks–S3 and S4 scenarios

4.3. The large storage tank of 125 000 m^3 volume

The values for heat flux density for the tank of 125 000m^3 volume were calculated for distances l_n ranging from 35 m to 75 m, which correspond to the real distances between the shells of safety tanks.

Table 5 states the calculated values for the storage tank of 125 000 m^3 volume. Basic data for further calculations of heat flux density in specified distances between the large storage tanks of 125 000 m^3 volume are:

- for S3 scenario: D = 84,47 m, r = 42,235 m, n = 24,1 m, h = 22,3 m, p = 23.68 m,
- for S4 scenario: D_h = 90,47 m, r_h = 45,235 m, n_h = 19,75 m, h_h = 19,44 m, p_h = 23,76 m.

The flame length p_s for particular scenarios is then calculated:

S3 scenario – in the equation (8) is inserted the value: $p_s = p - (n - h) = (p - n + h)$= (23.68 – 24.1 + 22.3) = **21.88 m**.

S4 scenario – in the equation (8) is inserted the value $p_s = p_h - (n_h - h_h) = (p_h - n_h + h_h)$ = (23.76 – 19.75 + 19.44) = **23.45 m**.

Tab. 5 Heat flux of 125 000 m^3 storage tank against neighboring tanks – S3 and S4 scenarios

l_n (m)	q_L (kW m^{-2}) S3 scenario	q_L (kW m^{-2}) S4 scenario	l_n (m)	q_L (kW m^{-2}) S3 scenario	q_L (kW m^{-2}) S4 scenario
35	47.18	50.48	60	24.23	26.73
40	40.92	44.13	65	21.52	23.84
45	35.63	38.70	70	19.21	21.36
50	31.17	34.06	75	17.23	19.21
55	27.41	30.11			

The graph in Fig. 7 illustrates the calculated values for S3 and S4 scenarios for the 125 000 m^3 tank previously stated in Table 5.

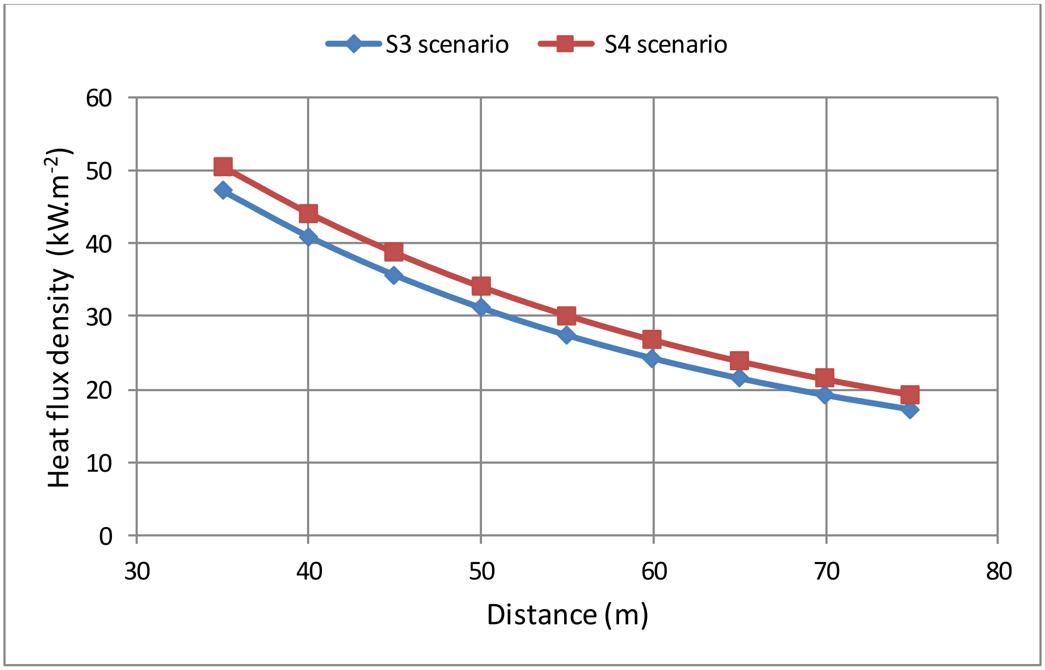

Fig. 7. Heat flux density affecting the neighboring tanks at a fire of 125 000 m^3 tank–S3 and S4 scenarios

The graph in Fig. 8 shows the curves of heat fluxes for the particular tanks for S3 scenario when heat flux affects a neighboring tank.

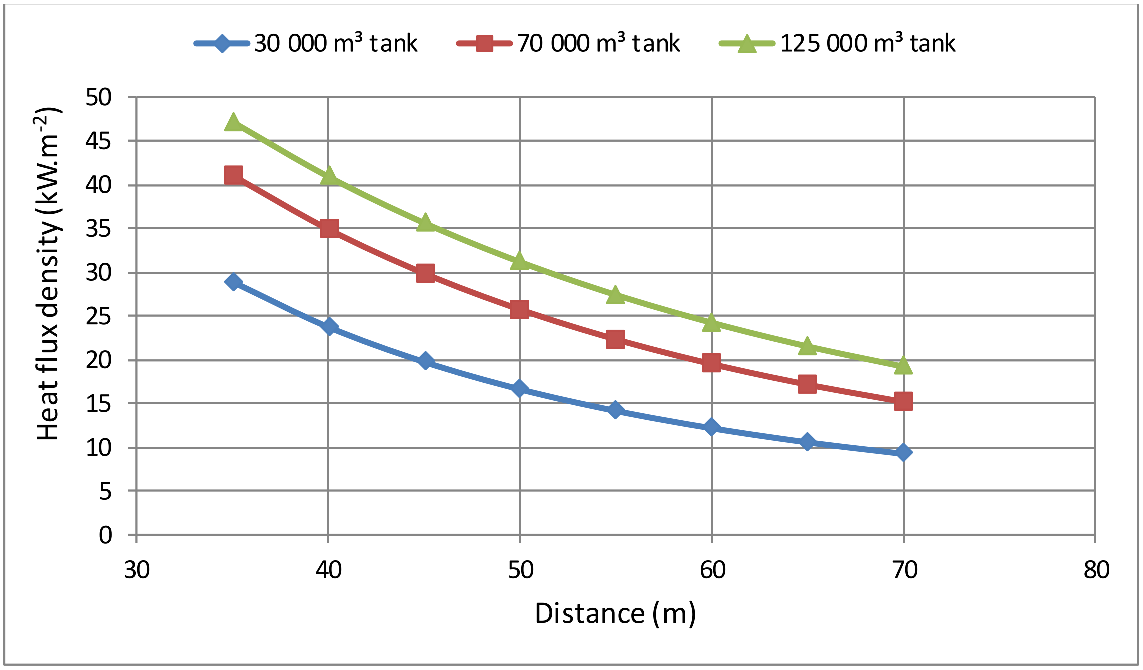

Fig. 8. Comparison of heat flux density against neighboring tanks – S3 scenario

The graph in Fig.8 clearly shows that the size of the heat flux density grows with the size of the storage tank at the same distance and at the same height of the storage tank shell. The graph in Fig.9 shows heat flux densities calculated for S4 scenario, the highest values appear for 125 000 m^3 tank.

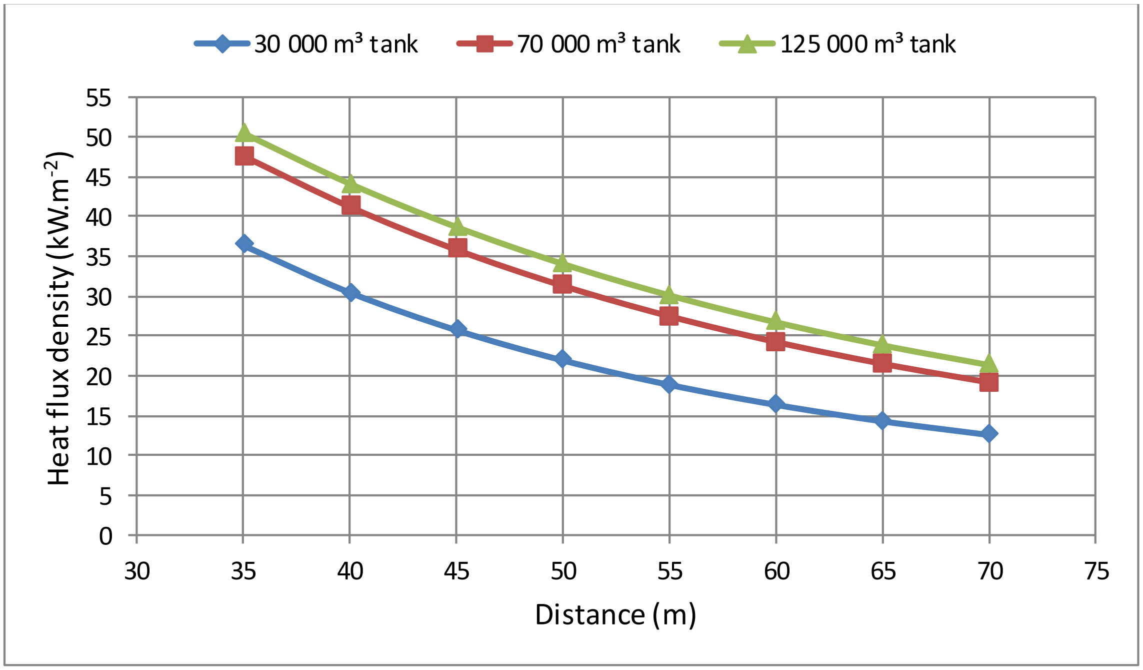

Fig. 9. Comparison heat flux density against neighboring tank – S4 scenario

We found out that the compared calculated rates of energy release at a fire are proportional to the area of a fire. In case of the fire of large storage tanks, the size of the area of the fire calculated is total horizontal area of stored crude oil.

There were four scenarios suggested, however, the calculations were conducted for two of them considered the most severe. Three different sizes were chosen and constant rate of energy release was calculated per time unit and per area unit i.e. areal energy release rate $q_f^{''}$= 842.8 kJ s^{-1} m^{-2} (0.8428 MW m^{-2}) for crude oil based on the earlier described circumstances. Baum a McGrattan [9] claim that energy release rate for a large crude oil storage tank of 84 m diameter and 27 m height, was 4.7 GW; after recalculating this value into areal energy release rate, this presents approximately $q_f^{''}$= 848 kW m^{-2} (0.848 MW m^{-2}). The conditions of the surroundings include wind 6 m s^{-1} at 27 meters above the terrain and outside temperature of 20°C. After deducting smoke absorbing radiation (10% referred smoke absorption), the areal energy release rate appears to be $q_f^{''}$=900 kW m^{-2} (0.9 MW m^{-2}). The paper does not mention the crude oil characteristic.

The same authors [10] state the energy release rate for crude oil as $q_f^{''}$= 1 900 kW m^{-2}, planar burning rate as m''_∞ = 0.045 kg m^{-2} s^{-1} and total combustion heat as ΔH_c=42 600 kJ kg^{-1} and fuel efficiency as χ = 1 (100 %).

The calculations in this paper employ planar burning rate of m''_∞ = 0.028 kg m^{-2} s^{-1}, total combustion heat of ΔH_c=42 500 kJ kg^{-1} and fuel efficiency of χ=0.7 (70 %). Considering that the burning rate used in this paper is substantially lower, the resulting planar energy release rate was 55% lower than the value referred to by the earlier mentioned authors [10].

5. Conclusions

Generally, it would be sufficient for large storage tanks from a certain diameter to substitute a constant energy release rate per unit of time and unit of area (areal energy release rate) and the area of stored crude oil with the same characteristic. Even for a different flammable liquid, the constant of energy release per a time unit and area unit would be proportional to the total combustion heat, areal burning rate, fuel efficiency and the product of the constants of flame radiation against the flammable liquid surface.

Considering the ratios of diameters and volumes of the selected tanks, there were recorded the differences only from a few centimeters to tens of decimeters among the calculated values of the mean flame length. The mean flame length was more than 20 m for every tank. These values apply only in case of a calm. However, wind or other unexpected situations such as blow, boilover explosion, tank deformation, floating roof failure, may expand the flame length several times.

In conclusion, it can be claimed that the heat flux density in the surrounding of a burning tank depends simultaneously on a few parameters. If the weather conditions are not the case, it concerns especially: tank diameter; tank shell height; crude oil level in the tank; distance from the tank; position against the tank; a level above the terrain; mean flame length; flame temperature; emission rate and smoke shadowing of the flame.

Acknowledgements

The paper was written within the scope of the project KEGA 030UMB-4/2017 supported by the granting agency KEGA (Cultural and Educational Agency) of the Ministry of Education, Research and Sport of the Slovak Republic.

References

[1] Michel Z. Základy protipožární techniky ve výrobních závodech a skladech minerálnych olejů. *(transl. The Principles of Fire Protection Systems in Manufacturing Operations and Mineral Oils Storage Areas)* ČSVTS. Práce. Praha. 1960.

[2] Chen F, Zhang M, Song J, Zheng F. Risk Analysis on Domino Effect Caused by Pool Fire in Petroliferous Tank Farm. In *Procedia Engineering* [online] 2018; 211: 46-54.

[3] Balog K, Kvarčák M. Dynamika požáru. (*transl. Fire Dynamics*) Ostrava: SPBI, 1999. 118 s. ISBN 80-86111-44-X.

[4] Karlsson B. Enclosure Fire Dynamics. Boca Raton: CRC Press 2000.

[5] Kačíková D. Vybrané kapitoly z dynamiky rozvoja požiaru: Študijné texty pre voľný ročník inžinierskeho študijného programu Hasičské a záchranné služby.(*transl. Selected Chapters of*

Fire Development Dynamics: the Studying Materials for Master's Degree of the Fire And Rescue Services Programme). Zvolen: Technická univerzita vo Zvolene, 2006. 51 s.
[6] Michejev MA. Základy sdílení tepla. 1.*(transl. The Principles of Heat Transfer*) Vydanie. Praha: Průmyslové vydavatelství 1952. 384 s.
[7] Olšanský J. Metodika hasenia ropy a ropných produktov v nádržiach. *(transl. Methodology of extinguishing of crude oil and crude oil products in tanks)* Bratislava: 1976, 43 s.
[8] Kadlec Z. Průvodce sdílením tepla pro požární specialisty. *(transl. Heat Transfer Guide for Fire Protection Engineers)* Ostrava: SPBI Spektrum 1. vyd., 2009. 100s. ISBN: 978-80-7385-061-6.
[9] Baum HR, McGrattan K B. Simulation of large industrial outdoor fires. National Institute of Standards and Technology Building and Fire Research Laboratory Gaithersburg, MD 20899. 1998. 30 s.
[10] McGrattan KB, Baum HR, Hamins AP. Thermal Radiation from Large Pool Fires, National Institute of Standards and Technology 6546, https://doi.org/10.6028/NIST.IR.6546.
[11] STN 92 0102-4. 2000: Požiarna bezpečnosť stavieb. Spoločné ustanovenia, Časť 4: Odstupové vzdialenosti. *(transl. Standard STN 92 0102-4. 2000: Structural Fire Protection. General Provisions. Part 4: Separation distances)*

To whom correspondence should be addressed: Dr. Ján Horváth, Technical University in Zvolen, Faculty of Wood Science and Technology, T.G. Masaryka 24, 960 53 Zvolen, Slovakia E-mail: xhorvathj@tuzvo.sk

Petroleum and Coal

Article **Open Access**

INVESTIGATING OF PETROPHYSICAL AND LITHOLOGICAL PARAMETERS OF ASMARI FORMATION IN BIBI-HAKIMEH OIL FIELD, SW OF IRAN

*Javid Abbasi, Hossein Tabatabaei**

Department of Petroleum Engineering, Gachsaran Branch, Islamic Azad University, Gachsaran, Iran

Received May 21, 2019; Accepted July 1, 2019

Abstract

Carbonate rocks, along with sandstone, constitute the main reservoirs of oil and gas in the world. Examination of petrophysical properties includes parameters such as porosity, permeability and fluid saturation, lithological variations according to depth and hydrocarbon properties including effective and ineffective thickness and effective hydrocarbons column. Asmari reservoir of Bibi- Hakimeh oilfield is one of the tertiary carbonate reservoirs in Iran located 210 km southeast of Ahwaz. The reservoir is divided into 8 zones, each zone having its own petrological characteristics and lithology. Considering the fact that all three major lithologies of reservoirs (limestone, dolomite and Shale) exist in the Asmari reservoir of Bibi- Hakimeh oilfield, lithological study and its impact on petrophysical parameters of reservoirs are very important. Based on the assessments, zone 1 with more than 85% limestone has the most effective hydrocarbon column, the highest net thickness and the highest net to total thickness ratio, and due to its low water saturation (about 20% for effective zones), it has the best reservoir quality among the other zones. Following zone 1, zones 2 and 3 take the second and the third places, respectively. Zones 4 to 8 are below the water-oil interface, hence they are not included in productive zones and have lower reservoir quality. Zone 1 is considered as the best oil producing layer with respect to petrophysical parameters.

***Keywords**: Petrophysical parameters, Water saturation, Porosity, Bibi- Hakimeh oil field.*

1. Introduction

The main objective of studying reservoir characteristics is to reconstruct petrophysical properties such as porosity, permeability and fluid saturation. The porosity distribution can be a common relationship between these characteristics. In this regard, well logging charts are a good tool [1]. The relationship between petrophysics and geology (lithology) has been a subject of great study since 1955. The porosity and permeability of the carbonate layer are due to the reaction between the various types of precipitated primary materials and a variety of diagenetic processes. Well logging diagrams provide continuous recording of constructive parameters relative to depth, which is very useful for geological applications [2]. The composition of formations can be expressed as mineral or chemical elements using well logging diagrams (such as density, neutron and gamma), and therefore there is a relationship between petrophysical parameters and rock composition. The resulting information could lead to a better interpretation of the exploration and production, and hence the advanced characteristics of the reservoir [3].

Carbonate rocks, along with sandstone, constitute the main reservoirs of oil and gas in the world. The hydrocarbon deposits in these rocks are essentially associated with dolomite [4-5]. Dolomite accounts for about 30% of the world's carbonate reservoirs, accounting for roughly 80% of North American carbonate rocks. Two-thirds of Middle Eastern oil is located in carbonates, and Asmari reservoirs of Iran with the age of Oligo-Miocene (tertiary) are also listed as dolomite reservoirs [6]. These types of reservoirs are very heterogeneous to the plastic (e.g. sandstone) reservoirs [5]. For example, with increasing depth, dolomite creates better reservoirs than calcareous stones. Considering that all three major lithologies of reservoirs

(Limestone, Dolomite and Shale) are presented in the Asmari reservoir of Bibi- Hakimeh oilfield, the study of lithologies and their impact on petrophysical parameters of reservoirs is very important.

This issue is essentially related to the sedimentary environments of numerous facies, tectonic and diagenetic processes (cementation, dolomitization, recrystallization, fracturing, etc.) that accompany carbonate rocks [7-8]. In addition, the fracture also plays an important role in the reservoirs, and the generated porosity and permeability cause major anisotropy in the reservoir [5,9]. Therefore, studying different lithologies and their effect on petrophysical parameters of reservoirs is very important [10].

2. Bibi- Hakimeh oil field

Bibi- Hakimeh oilfield is located in 210Km southeast of Ahwaz (Fig. 1) and lacks any surface structure and is essentially determined by seismology. This field was discovered in 1928 and has several reservoir formations (Asmari, Sarvak and Khami formation). This field was exploited since 1962, and by June 2017, about 120 wells were drilled. Based on maps drawn from seismic studies and underground structure mapping, the Bibi- Hakimeh oilfield can be considered as an anticline from the northwest to the southeast. The slope of the northern lamb is slightly higher than that of the southern lamb which is around 11-13 degree and 6-9 degree, respectively. The slope of eastern and western capes is about 2-2.5 degree.

The Asmari reservoir contain oil with 30 ^{o}API and 2% sulfur [11]. Dimensions of the Asmari reservoir at the water-oil interface are about 70 km in length and 7 km in width. The water-oil contact in this reservoir is determined at a depth of 1979 meters below sea level. Given that the reservoir crest on the structural map is about 1729m below the sea level, and considering the last closed curve of the reservoir (2014m), the vertical closure is calculated to be about 285m, the height of the oil column in the central regions of the reservoir is about 250 meters, which decreases with moving to the reservoirs crest.

Figure 1. Located of Bibi- Hakimeh oil field in Dezful embayment, near the other oil fields, Southwest of Iran.

3. Lithology

Petrographical investigations of thin sections and study of the graphs indicated that the Asmari reservoir in this field are periodic consists of limestone, dolo limestone, dolomite, shale limestone and shale. Asmari reservoir is divided into 8 zones (layers) and each zone has its own petrophysical lithology properties. Zone 1 is mostly shaly carbonate (shaly limestone and shaly dolomite), zones 2, 3, 4 and 5 are mainly limestone (with some dolomite), zone 6 is a combination of limestone, dolomite and shale, and zones 7 and 8 are calcareous. Fig. 2 and Fig. 3 show the percentage of limestone, calcareous dolomite and clay in various zones of wells 39 and 116 in this field.

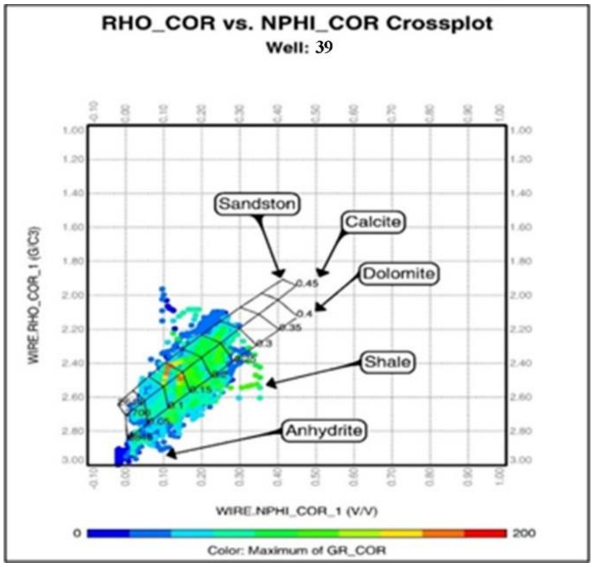

Figure 2. Cross plot of Neutron-Density-GR, Well No.39 in Bibi- Hakimeh oil field

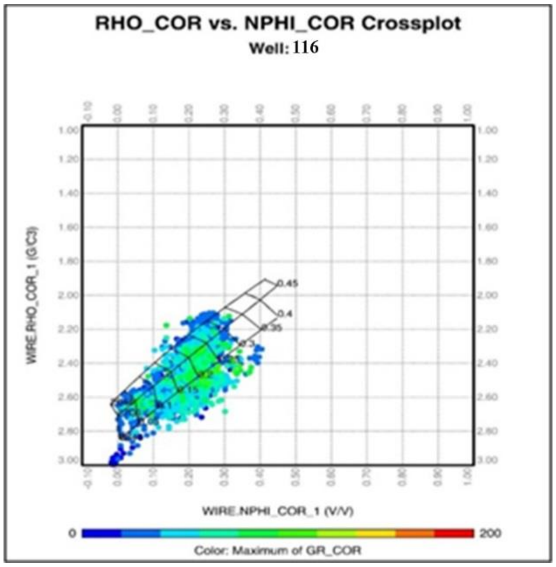

Figure 3. Cross plot of Neutron-Density-GR, Well No.116 in Bibi- Hakimeh oil field

4. Petrophysical parameters

Asmari reservoir in Bibi- Hakimeh oil field is divided into 8 zones (Table 1 and 2). Zones 1, 2 and 3 contain hydrocarbons, and the each zones are saturated with water. Zone 1 in this reservoir has a remarkable reservoir capacity over the rest of the zones. In Fig.4 and 5 shows a number of petrophysical parameters log of the reservoir for Bibi- Hakimeh in wells No. 39 and 116. The petrophysical assessment of these zones is as follows:

Zone 1:

This layer is composed mainly of limestone and calcareous dolomite and a layer of shale lime, and has a good to very good porosity. The net thickness in this zone ranges from less than 1 meter to 25 meters. The net thickness in the central regions of the anticline is more than that of the edges and the crest of the anticline. The net to total thickness ratio varies as well and it is higher in central parts anticline, especially around the wells 29, 39, 51, 116 and 18 which is higher than 0.6. This ratio is the highest (0.95) around well No.116. The average water saturation of net thicknesses is between 17.8% and 47.8% and it is not lower than 17% in any well. The level of the effective column of hydrocarbons in this zone reaches a maximum of 6.4 meters (Well No. 39).

Zone 2:

This layer is composed mainly of Limestone shale lime and calcareous, and is characterized by the development of good and very good, and sometimes moderate porosity, and it contains hydrocarbon. According to the estimates, this zone has better reservoir quality than other zones. The net thickness and net to total thickness ratio as well as the effective column of hydrocarbons in this zone were high, so that the net thickness and hydrocarbon column in some wells are more than 24m and 7.2m, respectively. Basically, zones 2, 3, 4 and 5 in Bibi-Hakimeh oil field are composed mainly of Limestone with high density of fracture, the reservoir quality of these horizons is very high.

Zone 3:

This layer is composed mainly of Limestone, Shaly Limestone and Dolomite Limestone, and has a periodic transition from very good to low porosity, and in the middle part it has thick veins of hydrocarbon. The major part of this carbonate zone plays an important role in increasing the quality of the reservoir. According to this studies, generally, in this field, the net to gross ratio is lower than that of zone 2, although sometimes it exceeds 0.73 (Well No.51), this layer has a good hydrocarbon column. This layer is productive and has a relatively good reservoir quality.

Zones 4 to 8:

Since the oil-water contact for the entire field is located at a depth of 1979 meters below the sea level, the lower part of zone 3 and zones 4, 5, 6, 7, and 8 of Asmari reservoir is located below the water-oil interface, and the net thickness, the effective column of hydrocarbon and the net to gross ratio in these zones are zero or very small.

Table.1 Average porosity foe each zone of Asmari formation, Bibi- Hakimeh oil field

Zone	1	2	3	4	5	6	7	8
Well No39	17	13	14	6.7	1.5	5.3	2	4.6
Well No 116	16	15	16	3.5	3	5.9	0	5

Table.2 Average water saturation for each zone of Asmari formation oil field

Formation	Zone	Well No39	Well No 116
Asmari	Z.1	17.7	22.2
	Z.2	21.8	23.4
	Z.3	23.6	22.1
	Z.4	41.6	38
	Z.5	42	47.8
	Z.6	42.5	31.7
	Z.7	43.9	46.7
	Z.8	38.7	47.4

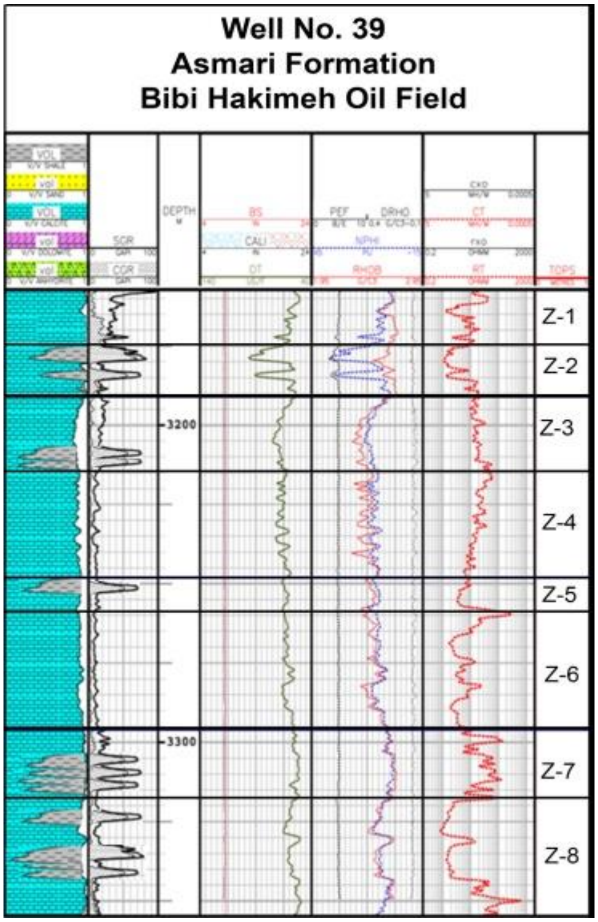

Figure 4. Petrophysical and lithological logs in well No.39, Bibi- Hakimeh oil field

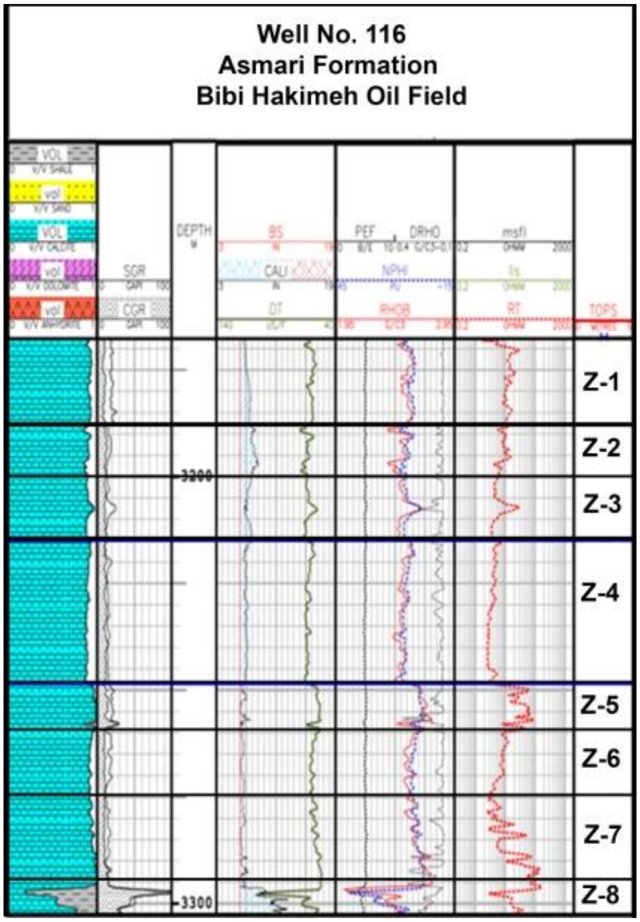

Figure 4. Petrophysical and lithological logs in well No.116, Bibi- Hakimeh oil field

5. Conclusions

The Asmari reservoir is divided into 8 zones (layers), each zone having its own petrophysical lithology and characteristics. Zone 1 is mainly carbonate (limestone and dolomite) with some Shale, zones 2, 3, 4 and 5, mostly limestone, zone 6 is a combination of limestone, dolomite and shale, and zones 7 and 8 are calcareous and shale.

Comparison of different reservoir zones in Wells No. 39 and 116 shows that with increasing depth, the amount of shale and limestone is increased relatively. The amount of dolomite is reduced by increasing depth and its highest amount is observed in zone 1.

The saturation percentage of oil in Wells No. 39 and 116 in zones 2 and 3 decreases, indicating that the concentration of oil is more in the limestone layer. In zone 1, which is a calcareous-dolomite zone, the changes of these two parameters are significant, the percentage of oil saturation is more than that of zone 2 and 3.

Based on the evaluations, zone 1 with more than 85% limestone has the highest value of effective hydrocarbon column, net thickness and the net to gross ratio, and due to its low water saturation (20% for the effective zones), it has the best reservoir quality among other zones. Following zone 1, zones 2 and 3 are ranked as the second and the third, respectively. Since the zones 4 to 8 are below the water-oil contact, they are not productive and have a low reservoir quality.

References

[1] Lucia FJ. Carbonate reservoir rocks, Springer-Verlog Berlin Heidelberg New York 1999, 226 P.
[2] Schlumberger. Log interpretation/ Application, 2nd edition, Schlumberger Well Services 1989.
[3] Durrast H, and Siegesmund S. Correlation between rock fabrics and physical properties of carbonate reservoir rocks, Int. J. Earth Sci., 1999; 88: 392-408.
[4] Jardine D, Wilshart JW. 1987, Carbonate reservoir description. Soc. Econ. Paleont. Min., Spec. Public: 1987; 4: 152-129.
[5] Sun SQ. Dolomite reservoirs: Porosity evolution and reservoir characterization, AAPG Bull., 1995; 79: 186-204.
[6] Warren J. Dolomite: occurrence, evolution and economically important associations, Earth Science Reviews, 2000; 52: 1-81.
[7] Murray RC, and Pray LC. 1965, Dolomitization and limestone digenesis, an introduction, Soc. Econ. Paleont .Min, Spec. Public, 1965; 13: 1-2.
[8] Wardlaw NC. 1965, Pore geometry of carbonate rocks, as revealed by pore casts and capillary pressure, AAPG Bull., 1965; 60: 245-257.
[9] Nelson RA. Geological analysis of naturally fractured reservoirs. Gulf Publishing, Houston, 1985, pp.1-320.
[10] Luo P, Machel HG. 1995, Pore size and pore throat types in a heterogeneous dolostone reservoir, Devonian Grosmont Formation, Western Canada sedimentary basin. Am. Assoc. Petr. Geol. Bull., 1995; 79: 1698-1720.
[11] Motiei H. Geology of Iran. The stratigraphy of Zagros. 5st ed. Geological Survey of Iran 1993.
[12] Zenger DH, Dunham JB, and Ethington RL. 1980, Concepts and models of Dolomitization, Soc. Econ. Paleont. Min., Spec. Public, 1980; 320-1: 28.

To whom correspondence should be addressed: Dr. Hossein Tabatabaei, Department of Petroleum Engineering, Gachsaran Branch, Islamic Azad University, Gachsaran, Iran, E-mail tabatabaei.h@gmail.com

Petroleum and Coal

Article **Open Access**

Sequence Stratigraphic Signatures from XEN-1 Well: Key for Understanding Cretaceous–Tertiary Transitional Events in the Northwestern Niger Delta Basin, Nigeria

*Jerry Osokpor and Ovie B. Ogbe**

Department of Earth Sciences, Federal University of Petroleum Resources, PMB 1221, Effurun, Delta State, Nigeria

Received May 7, 2019; Accepted July 15, 2019

Abstract

In order to evaluate and understand transitional events with stratigraphic elements that characterize the close of the Cretaceous and the onset of the Cenozoic in the north-western part of the Niger Delta Basin, where it overlies the Anambra Basin. Cutting samples of sand and shale from a depth range of 1743 – 2655 m of XEN-1 well drilled in the north-western part of the delta were subjected to qualitative lithological, palynological and geochemical analyses, to define paleodepositional settings, age frame and lithostratigraphic profile for the well section. Interpretation of the paleodepositional proxies indicated that the sediments were deposited in fluctuating paleodepositional settings through time between continental to open marine in a cyclic pattern or relative sea-level oscillatory regimes. Sequence stratigraphic interpretation revealed three lowstand systems tracts (LSTs), seven transgressive systems tracts (TSTs), and six highstand systems tracts (HSTs). Age-sensitive palynomorph species suggested a Maastrichtian to Early Miocene age for the sediments. This revealed a major transgressive event that marks the Cretaceous-Tertiary (K-T) transition that ended in the Ypressian (54.6 Ma MFS). Thus, strengthened the age frame of Paleocene-early Eocene for the Imo Formation as suggested by early workers. But in contrast to the regressive model that advances for the deposition of the Ameki Formation by previous studies. The lower lithological unit was redefined to be the product of a still stand sea-level phase. While the upper unit is to be a product of sea-level fall and the base of which is marked by the 47.2 Ma sequence boundary (SB). This study has shown that K-T lithostratigraphic transitional events were controlled essentially by third-order sea-level rise that transcended the K-T boundary, hence characterized by marine shale facies.

***Keywords**: Cretaceous-Tertiary transition; Niger Delta; Ameki Formation; Imo Formations; sequence stratigraphy.*

1. Introduction

Cretaceous stratigraphic events and sequences are contained in two tectonic elements in southern Nigeria. The areas include the Anambra and Dahomey Basins (Fig. 1a). In the Anambra Basin, the stratigraphic pile in the flank areas seems to display stratigraphic signature different from that at the central parts of the basin. Stratigraphically, the Niger Delta Basin rest on the Anambra Basin that is overlying the Abakaliki Basin (Fig. 1b). Older formations of the Niger Delta outcrops in the northern aspects of the delta that falls within the geographic space of the Anambra area. This occurrence has led to serious misconception and misunderstanding among students, academics, and researchers involved in stratigraphic and sedimentological studies in this part of Nigeria. The misunderstanding is hinged on failure to distinguish between geologic (tectonic) and geographic element, hence several formations of the Niger Delta Basin, e.g. the Paleocene Imo, Eocene Ameki, and Oligocene Ogwashi Formations have been erroneously classed as part of the Anambra Basin stratigraphic sequence.

The Atlantic Ocean advanced from the onset of rifting in the Berriasian to open marine conditions in the Albian, at the time depositional of Santo and Campos Basins of Brazil was developing [1], close relatives of southern Nigeria Basins and other West African coastal basins (Figs. 1 and 2). This is attributed to the age of the Asu River Group in Abakaliki sub-basin that is assigned Albian, the oldest subsurface lithostratigraphic unit in southern Nigeria (Fig. 3) [2].

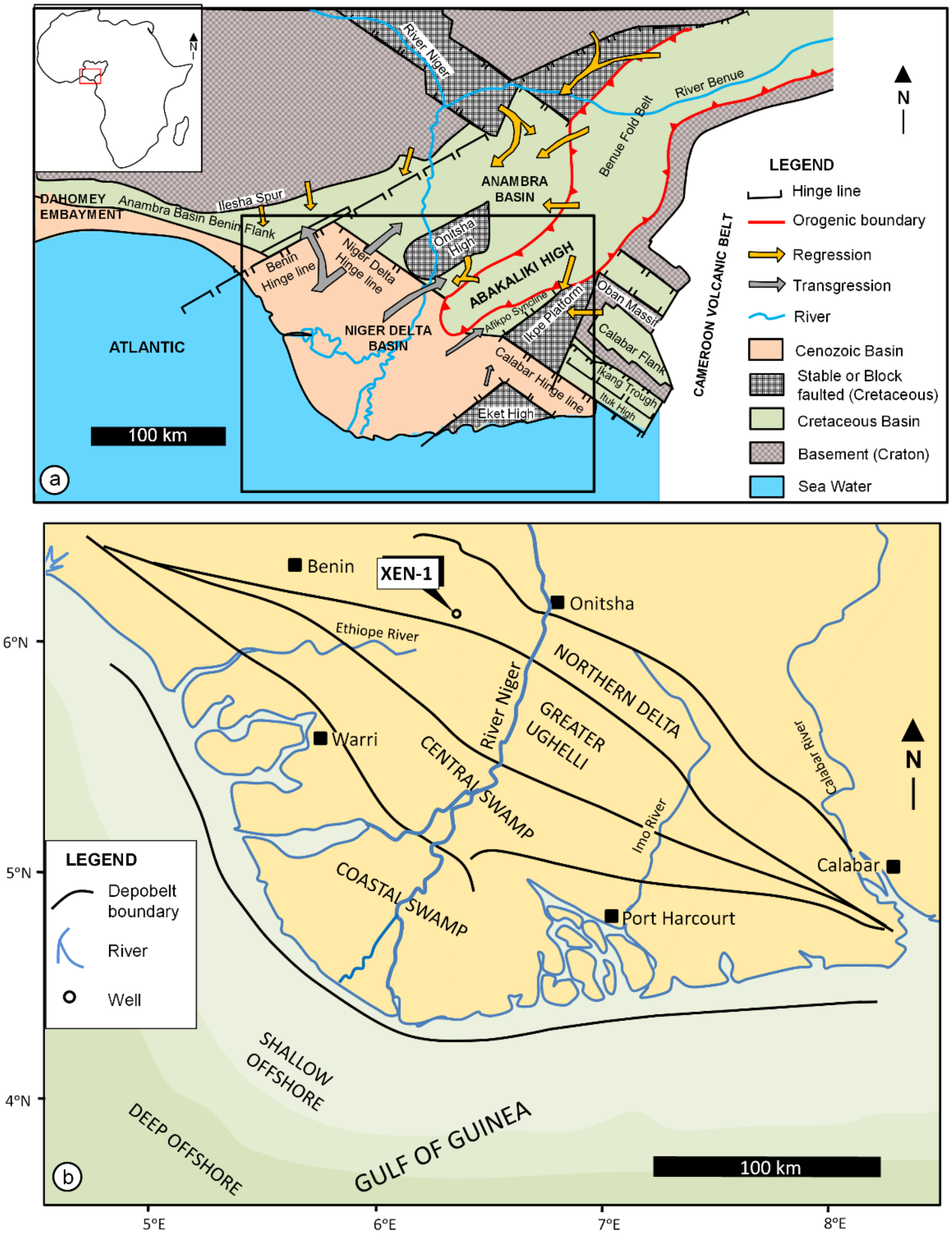

Fig. 1. Location and regional geologic settings of the southern portion (Benue Trough) of Nigeria. (a) Tectonic setting of the Cretaceous and Cenozoic Basins of the Benue Trough showing the boundaries and structural framework of the associated basins (*modified from Murat* [17]; *Ogbe et al.* [18]). Inset map of Africa shows the location of Nigeria and southern Nigeria marked red box. Refer to Fig. 2 for the evolution of the Benue Trough. (b) A simplified Niger Delta map marked black box in Fig. 1b showing the depobelts and XEN-1 well location (*modified from Corredor et al.* [19]). Each depobelt defined by major bounding faults.

It is pertinent to note that the Anambra Basin, adjacent to the Abakaliki sub-basin is strictly a Cretaceous Basin hosting Cretaceous age sediments, while the Niger Delta is a Cenozoic basin containing Cenozoic to Recent sediments (Figs. 1 and 3). The Niger Delta Basin rests unconformably on the Anambra Basin and represents a Cenozoic continuation of southward transportation and deposition of clastics into the coastal Atlantic that commenced since the Late Cretaceous-Early Paleocene (Figs. 1 and 2). Cretaceous sedimentation in southern Nigeria ends and at the Cretaceous-Paleogene boundary popularly known as the Cretaceous-Tertiary (K-T) boundary which may be hosted by the Nsukka Formation that straddles the boundary [3]. Beyond the poor understanding in distinguishing the stratigraphic signatures of both basins, the age range and conditions of deposition call for some adjustments and refinement.

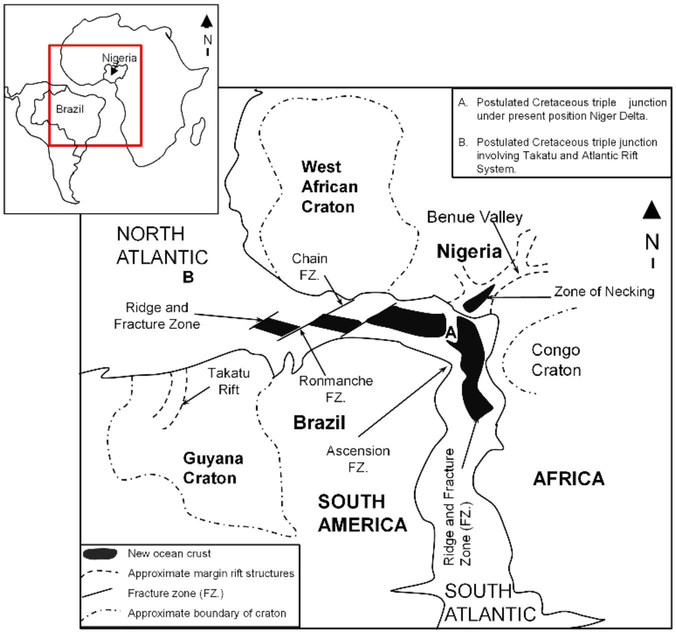

Fig. 2. Schematic diagram showing the development of the Benue Trough and South Atlantic from the onset of rifting in the Early Cretaceous and consequently into open marine conditions *(modified from Burke et al.* [26]), refer to Fig. 1. Note the location of the Nigeria, Brazil, South Atlantic, and Benue Trough marked red box in the inset plate of Africa and South America

SUBSURFACE		SURFACE OUTCROPS			BASIN
Niger Delta Basin Stratigraphy	Oldest known Age	Youngest known Age	Southern Benue Trough	Oldest known Age	
Recent Benin Formation (Afam clay Member)	Oligocene	Plio/Pleistocene	Benin Formation	Miocene	Niger Delta
Recent Agbada Formation	Eocene	Miocene	Ogwashi-Asaba Formation	Oligocene	
		Eocene	Ameki Formation	Eocene	
Recent Akata Formation	Eocene	Lower Eocene	Imo Formation	Paleocene	
		Paleocene	Nsukka Formation	Maastrichtian	Anambra
		Maastrichtian	Ajali Formation	Maastrichtian	
Unknown	Cretaceous	Campanian	Mamu Formation	Campanian	
		Campanian/ Maastrichtian	Nkporo Shale	Santonian	
		Coniacian/ Santonian	Awgu Shale	Turonian	Abakaliki
		Turonian	Eze-Aku Shale	Turonian	
		Albian	Asu River Group	Albian	

Fig. 3. Formations of the Niger Delta Area, Nigeria (Modified from Short and Stauble [2])

Generally and especially in the central northern aspects of the Niger Delta, the Cretaceous-Paleogene transition in the Anambra-Niger Delta province is sedimentologically represented by the Nsukka Formation that unconformably overlies the Ajali Sandstone Formation, and is characterized by sandstone, shale and sub-bituminous coal formed in varied paleodepositional settings ranging from strandplain mash, with occasional fluvial influence to shallow marine [4].

While the Ajali Sandstone Formation is strictly a Cretaceous sedimentological component of the Anambra Basin, the Nsukka Formation straddles the K-T boundary [5] and can partly be ascribed to the Anambra Basin and Niger Delta sequences. Although the many studies on the Cretaceous-Tertiary Boundary (KTB), has left controversies and heated debates on the nature of the events and causal mechanisms of the KTB [6-14], the transition is noted to be heralded by a Late Cretaceous regression and an Early Danian transgression [4-5,15-16]. The two hypotheses advanced so far on the K-T Boundary event are: (1) that the K-T events are the result of catastrophic effects of a large extra-terrestrial body colliding with the earth, and (2) that the K-T extinctions resulted from terrestrial volcanic activities of the Deccan during which gaseous emission affected global climatic system and resulted in annihilation of macro and microfauna, a process which may have been accelerated by a bolide impact at K-T boundary time. Although, Deccan volcanism event could only have caused moderate climatic warming inadequate to drive major sea-level changes [13,16].

This study is aimed at using sequence stratigraphic method to unravel paleosea level signatures prevalent during the Cretaceous-Cenozoic transition in the Anambra-Niger Delta Basin sedimentary pile accessed through a well located in the western parts of the northern depositional belt of the Niger Delta, in order to ascertain the stratigraphic range of the Paleocene Transgressive Event (PTE) in the older stratigraphic sequences of the Niger Delta Basin and to define systems tracts within the Ameki Formation in order to refine and improve on information regarding the depositional condition(s) of the formation. It is expected that this work would provide a basis for further investigation of Cretaceous-Cenozoic sedimentary sequences in similar geologic settings in order to understand sedimentary signatures and events that can offer a better understanding of the end-Cretaceous-Cenozoic transition.

2. Tectonics setting of the Anambra and Niger Delta basins

The Anambra and Niger Delta Basins are both located in Southern Nigeria (Fig. 1). The Niger Delta Basin is located south of the Anambra Basin and situated along the West African coast at the site of a Cretaceous triple junction and lies between longitudes 5° and 8°E and latitudes 3° and 6°N within the coastal area of the Gulf of Guinea (Figs. 1 and 2). Distal aspects of the lithostratigraphic units of the Anambra Basin grade laterally into formations of the Niger Delta at depth.

The Anambra Basin is roughly triangular in shape and covering an area of about 40,000 km^2 [20]. It is bounded at the south by the northern boundaries of the Niger Delta Basin, while the Lower Benue River forms its northern limit (Fig. 1a). The West African Massif and the Abakaliki anticlinorium respectively form the western and eastern boundaries [21]. The basin extends westwards towards Dahomey Basin but separated by the Okitipupa High along the Benin Hinge Line [22], which forms its subsurface boundary to the west (Fig. 1a). The western arm of the Anambra Basin is a narrow tectonic structure that rims the southern limits of the western Basement Complex located in the north of the area (Fig. 1).

The evolution of the Anambra and the Niger Delta Basins is related to the failed arm of a triple junction which evolved during the separation of Africa from South America in the Late Jurassic – Early Cretaceous times (Fig. 2), although the Anambra Basin was formed much later to Paleocene [23-24] and the Niger Delta Basin was formed thereafter in the Paleocene [22]. According to Murat [17] prior to the Santonian thermotectonic event, the megatectonic setting of the southern Benue Trough was characterized by longitudinal fault blocks that preferentially subsided in the eastern half of the trough to become the Abakaliki sub-basin, known as the Southern Benue Trough, while the western parts remained a stable platform until the Santonian. Relative to the western platform area which received thin veneer of clastic and chemical sediments, the subsided eastern part recorded massive clastic sedimentation, thus became the main depocenter (Abakaliki area). The Santonian folding and uplift subsequently caused a flexural inversion that displaced the depocenter to the west and northwest, thereby creating the Anambra Basin. Generally, the thermotectonic basin subsidence in the Southern Benue Trough was by spasmodic mechanism, characterized by the high rate in pre-Albian time, low in Cenomanian, and very high in the Turonian, a phase that is thought to be the initiation of the actual Anambra Basin that climaxed during the Santonian thermotectonic event [25].

The Anambra Basin is sandwiched between the Benue Trough and the Niger Delta Basin in a tied style that is characteristic of West African coastal basins (Figs. 1 and 2) [4]. This probably indicates that a thermal decay occurred after the Santonian thermotectonic event that produced a sagging structure which became the Anambra Basin and continued up to the Paleocene where the formation of the Niger Delta sedimentary pile commenced [4].

Consequently, The Niger Delta builds out into the Atlantic Ocean at the mouth of the Niger-Benue and Cross River drainage systems and extends more than 300km from the proximal to distal ends (Fig. 1) [21]. It prograded from the north to south in the Eocene to Recent, forming successive depositional belts or depobelts: Northern Delta, Greater Ughelli, Central Swamp, Coastal Swamp and Offshore Depoblets (Fig. 1). The Niger Delta Basin contains both sedimentary wedges that are dominated by progradational sequences and major marine transgressive sequences (Fig. 1). Climatic variations, proximity, and nature of sediment source areas and sediment-paleo-circulation pattern influenced the gradual change in the shape of the Cretaceous coastline that developed into a bulge with the growth of the Niger Delta, thereby controlled the extent of incursions of the sea [27]. Rapid subsidence <700 m/Ma and progradation of ≈2 km/Ma along three depo-sitional axes that fed irregular, early delta lobes that eventually coalesced characterized the embryonic delta during the Late Eocene – Middle Miocene [28-30]. Late Oligocene to Middle Miocene delta subsidence remained steady at about 700 m/Ma with increased delta progradation of 8–15 km/Ma [31], Progradation of the delta over a landward dipping oceanic lithosphere has steadily occurred from the Middle Miocene onward [2]. The subsequent lateral merging of active depocenters in the eastern sector resulted in an enlarged delta front, which prograded fast and developed into a convex coastline (Fig. 1).

3. Stratigraphy of the Anambra and Niger Delta Basins

Nwajide [4] concluded that the stratigraphic package of the Anambra Basin that ranged in age from Santonian to Early Paleocene (Fig. 3), was deposited by a major and minor marine transgressive events. The major transgression formed the Nkporo Group, while the minor event formed Coal Measures (Fig. 3) [4,32]. The Nkporo Group (Nkporo Shale and lateral equivalents) occur as the basal units of the basin and overlies an angular unconformity that caps the Abakaliki Basin (Fig. 3) [4]. Stratigraphic units of the Nkporo Group (Lafia, Owelli, Enugu, and Nkporo Shale Formations) are of Campanian age that formed the first depositional cycle of the Anambra Basin (Fig. 3). The younger stratigraphic units of the basin such as the Mamu, Ajali, and Nsukka Formations were deposited in the Danian (Maastrichtian to Early Paleocene) by the minor transgression as the second and last depositional cycle of the basin (Fig. 3)". A detailed description of each of these formations and their age ranges are well documented by earlier workers [4,22,32-40].

Stratigraphic units of the Niger Delta Basin are in both subsurface and outcropping. The outcropping Paleocene-Eocene Imo Formation that is predominantly marine shale occurs in the northern part of the Niger Delta, where it overlies the Nsukka Formation (the youngest unit of the Anambra Basin), is lithostratigraphic equivalent and continuous of the subsurface Akata Formation (Figs. 3 and 4) [2,32,41-44]. The Eocene Ameki Formation composes of grey-green sandy clays, sandy claystone, and sandstone in the Southeastern Nigeria, where it unconformably rests on the Imo Formation is lithostratigraphic equivalent and continuous of the Agbada Formation (Figs. 3 and 4) [17,22,32]. The Ameki Formation was deposited in a deltaic and shallow marine paleoenvironment during the Eocene Regression that affected the Anambra Basin [17,22]. Another cropping unit of the Niger Delta is the Oligocene-Miocene Ogwashi Formation that overlies the Ameki Formation [32]. It is composed of white, blue, and pink clays, cross-bedded sands, carbonaceous mudstones, shales, and seams of lignite, which are inferred to be flood plain environment deposits [4].

The subsurface Akata, Agbada, and overlying Benin Formations are the three main lithostratigraphic units which show a typical offlap sequence, comprising time equivalent proximal-to-distal prograding facies (Fig. 4 and Fig.3). The Akata Formation was deposited in the Early Eocene to Recent and occurs as a bottom set with a thickness that ranges from 600 m to 6000 m that is composed of over 90% prodelta marine shale with less than 10% of sandstone [2]. The Agbada Formation of the Late Eocene to Holocene forms the foreset that is composed of delta front lithofacies of mostly shoreface and shallow marine deposits of alternation of sand and shale of near equal proportion, of a thickness ranging from 3000 m to 4500 m [2,45]. The topset

Benin Formation is an upper delta plain lithofacies that consists of over 90% massive continental sands and gravels with clay intercalations, with a variable thickness which generally exceeds 2100 m and ranges in age from Oligocene – Recent [2,22,44-45].

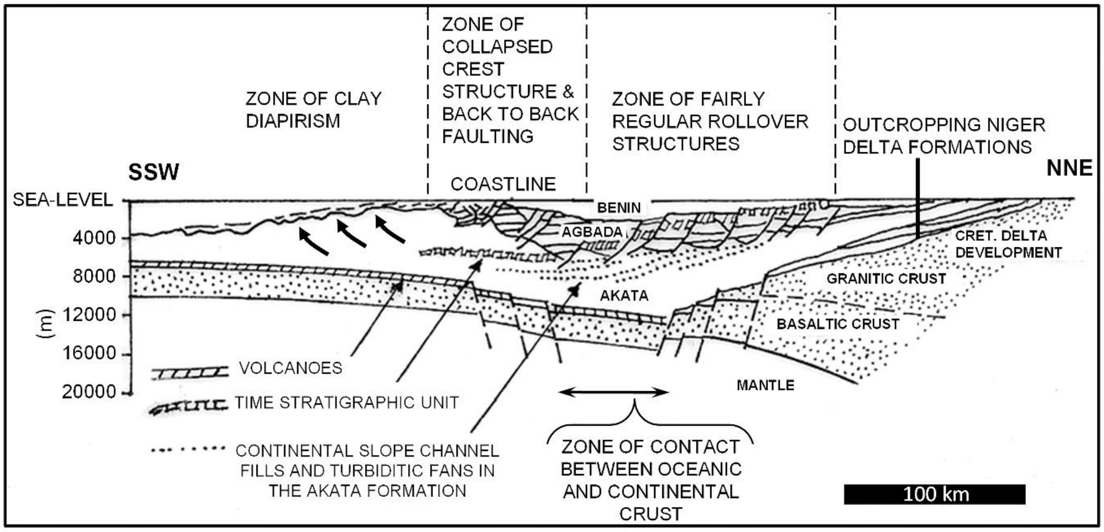

Fig. 4. Schematic stratigraphic cross section of the Cenozoic Niger Delta Basin along depositional dip showing the basin's subsurface and outcropping Formations (*Evamy et al.* [3]). Note the outcropping Cenozoic Niger Delta Formations overlying the Cretaceous sediments of the Anambra Basin in the northern delta

4. Investigative methodology

4.1. Lithofacies and palynological analysis

A total of one hundred and sixty (160) non-composited ditch cutting samples of sand and shale from a depth range of 1743 – 2655 m of the XEN-1 well located in the northwestern Niger Delta Basin (Fig. 1b), were subjected to qualitative whole grain lithological and textural analyses involving stereomicroscopic description to determine gross grain morphology, sorting, color, size distribution, mineralogy and the presence of accessory materials. The well under study belongs to the Shell Petroleum Development Company (SPDC) but is here coded XEN-1well for confidentiality reasons. Generally, the sampling range for lithofacies description is about 5.6 m and an average of 10 m for a palynological purpose. Palynological sample preparation is described in Osokpor and Ogbe [46] in accordance with Traverse [47], while age determination is based on earlier works of the authors [48-49].

4.2. Geochemical analysis

Three subsurface cutting samples retrieved from sections (2380, 2420 and 2545 m) of the Imo Formation in well XEN-1, Northern depobelt, western Niger Delta Basin (Fig. 1b), where geochemically analyzed for biomarker as a complementary proxy for Paleoenvironmental determination in this study. Sediment samples due for analysis were extracted for soluble organic matter using a TECATOR FOSS SOXTEC 2055 extractor during which exhaustive extraction was done for 80 min. at 100°C using dichloromethane. A fractionation of process by column chromatography with 70% silica gel was done for the extracted oils. Elution of the saturate and aromatic hydrocarbons and polar compounds was achieved using n-hexane (20mL), n-hexane/dichloromethane (90:10, v/v/ 40 mL) and DCM/methanol (50:50, 30 mL) respectively.

Saturated hydrocarbon fractions were analyzed by an Agilent 6850 gas chromatography-mass spectrometry (GC-MS) series interfaced with an Agilent 7683 injector series housing an auto-sampler, and equipped with a flame ionization detector. The GC-MS machine, fitted with a capillary column using helium as a carrier gas, was then programmed to run at 35°C to 300°C/min with a flow rate of 1.1mLs/min. Terpanes and steranes were identified using m/z

191 and 217 fragments, respectively. Analyses were carried out at Fugro Robertson Petroleum Geochemistry Laboratory in Llandudno, North Wales United Kingdom.

5. Results

5.1. Lithostratigraphy and biosignals

Lithological characteristics derived through the synthesis of gross lithologic and grain morphologic attributes of well-cutting samples analysis from the well section revealed four main lithotypes (sand, shale, Limestone/lime mud, and coal), and nine lithofacies (very fine – medium sand, medium – coarse sand, coarse sand, sandy limestone, sand shaly limestone, shaly limestone, black coal, carbonaceous shale and sandy shale) displaying a prominent cyclic pattern, a product of probable interplay of auto-allocyclic facies generators (Fig. 5). The lithologic signatures displayed enabled the definition of four lithostratigraphic units in the studied section. These include interbeds of coal and shale punctuated by silty shale intervals at the upper section which occurs as the basal unit and characteristic of the Mamu Formation. The basal unit is overlain by a section composed of thick black shale and is ascribed to the Imo Formation. The Imo Formation is then overlain by limestone lithotype composed of shaly – sandy lime mud facies. The sequence is capped by a section composed of interbeds of sand and shale characteristic of the Agbada Formation.

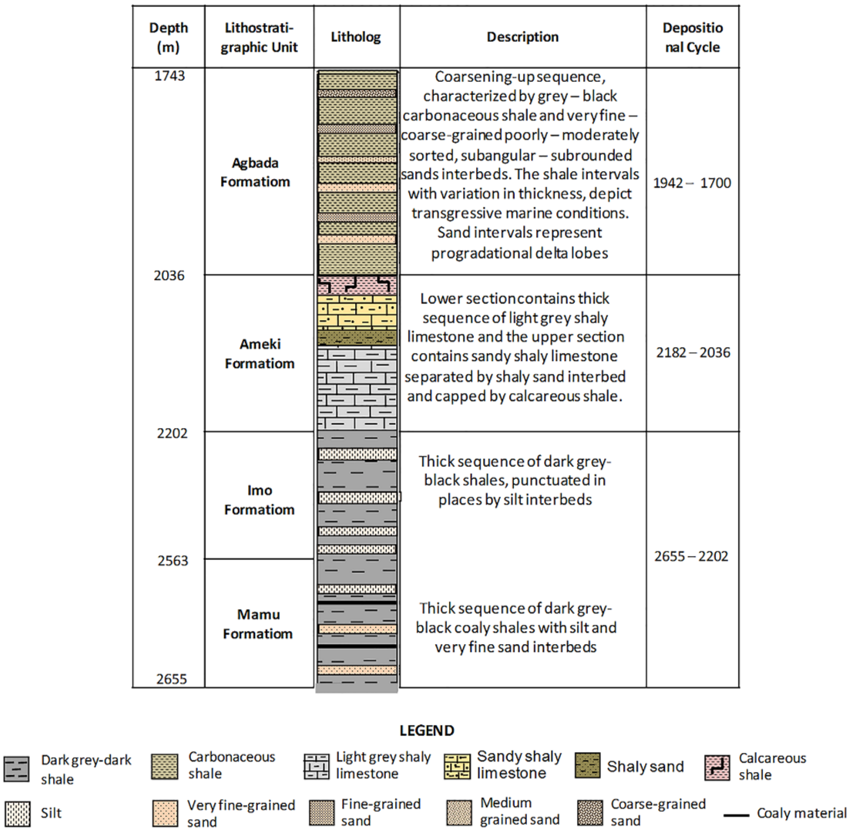

Depth (m)	Lithostratigraphic Unit	Litholog	Description	Depositional Cycle
1743	Agbada Formatiom		Coarsening-up sequence, characterized by grey – black carbonaceous shale and very fine – coarse-grained poorly – moderately sorted, subangular – subrounded sands interbeds. The shale intervals with variation in thickness, depict transgressive marine conditions. Sand intervals represent progradational delta lobes	1942 – 1700
2036	Ameki Formatiom		Lower section contains thick sequence of light grey shaly limestone and the upper section contains sandy shaly limestone separated by shaly sand interbed and capped by calcareous shale.	2182 – 2036
2202	Imo Formatiom		Thick sequence of dark grey-black shales, punctuated in places by silt interbeds	2655 – 2202
2563	Mamu Formatiom		Thick sequence of dark grey-black coaly shales with silt and very fine sand interbeds	
2655				

Fig. 5. Lithologic log of the studied section of the XEN-1 well showing the penetrated depositional cycles and formations with depth

Palynomorphs assemblage dominated by land derived species composed of seventy-six (76) well-preserved pollen, thirty-eight (38) spore, and fifteen (15) dinocyst form species were recovered and identified in selected samples from the well section (Fig. 6). Generally, the dinocyst recovery was poor. Due to the long range of the sporomorph and dinocysts assemblages recovered, the pollen assemblage was solely utilized in age-dating the sediments.

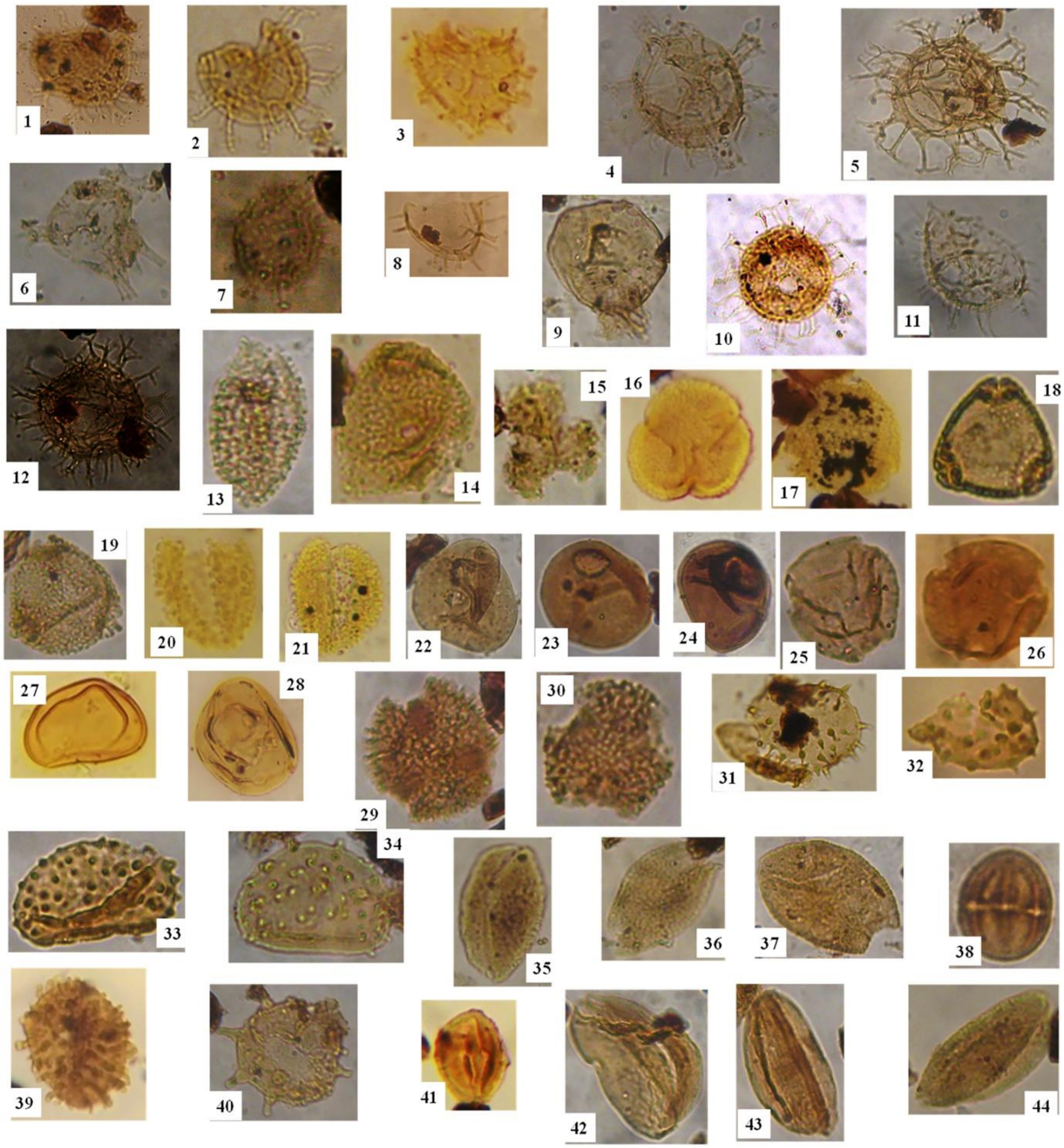

Fig. 6. Some age diagnostic dinocysts and miospore species recovered from XEN-1 well

1. *Hafniasphaera sp.* (L. Maastr.– L. Paleocene), **2.** *Hafniasphaerahyalospinosa.* (L. Maastr. – L. Paleocene), **3**. *Heterosphaeridium sp.* Cookson & Elsenack, 1968 (Sant. – E. Camp. & Oligo), **4.** *Fibrocysta sp.*, **5.** *Spiniferites sp.*, **6.** *Homotriblium sp.*, **7.** *Hystrichosphaeridium sp.*, **8.** *Polysphaeridium sp.* (E. Jurrassic – M. Mio), **9.** *Palynodinium sp.* (L. Cret.), **10.** *Operculodinium centrocarpum.* **11.** *Lingolodinium sp.*, **12.** *Spiniferiteshafnispira*, **13 & 14.** *Arecipitesexilimuratus*, **15.** *Retitricolpites sp.*, **16.** *Perfortricolporitesdigitatus*, **17, 18, 19.** *Retibrevitricolporitesobodoensis*, **20 & 21.** *Racemonocolpiteshians*, **22, 23, 24.** *Monoporitesannulatus*, **25 & 26.** *Psilatricolporitescostatus*, **27 & 28.** *Laevigatosporites sp.*, **29 & 30.** *Gemmatricolporites sp.*, **31.** *Spinozonocolpitesechinatus*, **32.** *Spinozonocolpitesbaculatus*, **33 & 34.** *Verrucatosporitesusmensis*, **35.** *Langapertitesproxapertitiod*, **36.** *Retidiporites sp.*, **37** & **38.** *Sapotaceaepollenites*, **39** & **40**. *Grimsdaleamagnaclavata*, **41.** *Verrutricolporitesscabratus* (L. Miocene), **42.** *Striamonocolpitesundulostriatus*, **43.** *Striamonocolpitesrectostriatus* (Lower Miocene), **44.** *Monocolpopollenitessp* (U. Cret)

5.2. Paleodepositional environment of XEN-1 Well penetrated intervals

The result from the interpretation of paleodepositional environment proxies shows that the sediments were deposited in varying paleodepositional settings through time ranging from continental to open marine in a more or less cyclic pattern occasioned by oscillatory and/or changing relative sea-level. Three major paleodepositional cycles A-C, were established. Sediments in the depth range 2655 – 2202 m (Cycle A), which occupies the lower section of the well and of Maastrichtian – Paleocene age were deposited in a paralic paleoenvironment, probably in a middle - outer neritic zones of the paleo-shelf during the Late Cretaceous to Paleocene transgression that affected the Benin Flank area and created the proto Niger Delta sedimentary pile. This section of the well is composed of black shale devoid of silt, silty shale and coal interbed lithofacies. The black shale is characterized by black coaly and brownish woody fragments suggestive of a transitional fluvio-marine environment [50-51]. This view is strongly supported by biomarker, isoprenoid, and n-alkane data from samples XEN2380, XEN2420, and XEN2545 within this depth range (Fig. 7, Tables 1 and 2).

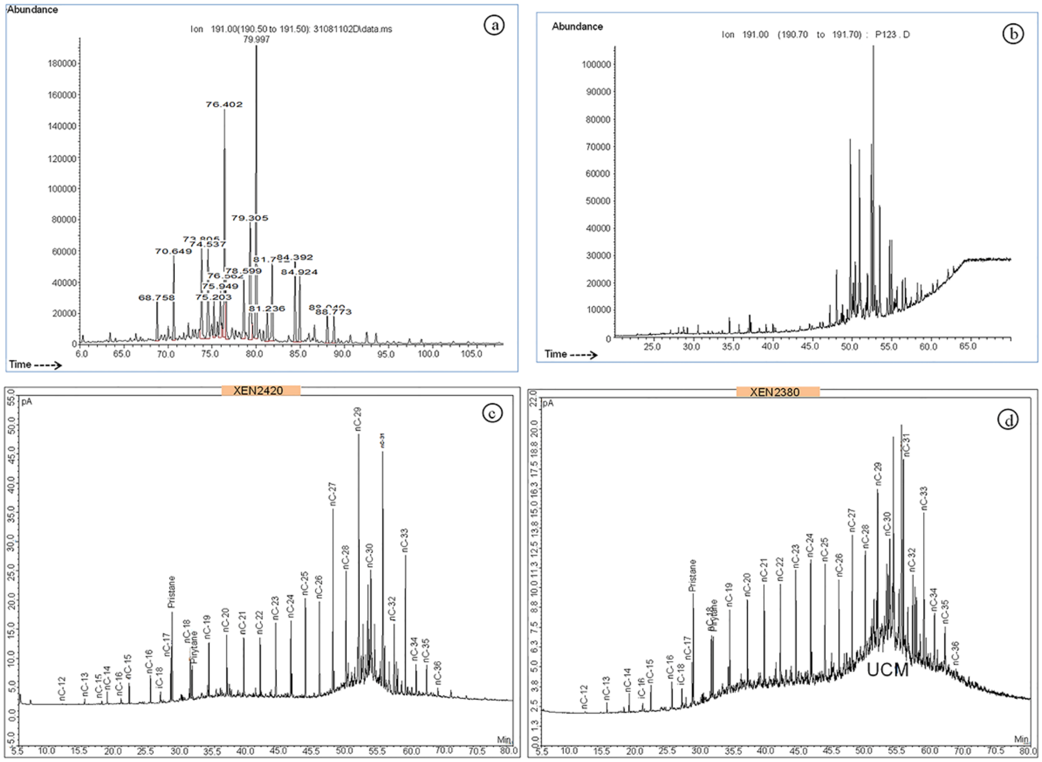

Fig. 7. Chromatogram results of the different samples. (a) High Scan Triterpane mass chromatogram of sample XEN2380. (b) Low Scan Triterpane mass chromatogram of sample XEN2545. (c) Gas Chromatogram for sample XEN2420. (d) Gas Chromatogram for sample XEN2380

The abundance of the C30 pentacyclic triterpanoid, gammacerane, relative to the C30 hopane (Table 1), is a marker for saline environments [52-53]. Within this interval, the Gammacerane index value range from 0.06 to 0.03 (Table 1). This trend ordinarily would indicate a shallowing water condition (Table 2), but the integration of this data with sedimentological and biosignal data reveal a paleosea transgression onto a platform area. Biosignal data of decreasing miospore abundance which indicates a transgression and a bloom of Spiniferites species in this section and known to thrive abundantly in neritic waters [54], supports a deepening trend of the middle neritic condition in the Late Cretaceous to an outer neritic setting in the Paleocene.

Table 1. Paleodepositional environment parameters from the pentacyclic, triterpanes and steranes distribution of the XEN-1 well.

Sample No	Depositional environment S T_7	Salinity T T_{10}
X2380	0.34	0.03
X2545	0.42	0.06

S=(h35S + h35R)/(h34S + h34R) (m/e 191), C_{35}/C_{34} *extended hopane ratio*
T=G/h30 (m/e 191), Gammacerane/hopane ratio (Gammacerane index)

Table 2. Isoprenoid and n-alkane ratios of XEN-1 well

Sample No.	Depositional environment (A) Pr/Ph	Depositional environment (B) $(Pr+nC_{17})/(Ph+nC_{18})$	Depositional environment (C) $\%C_{25}$ + n-alkane	Interpretation
X2380	1.76	1.34	58.30	Shallow marine. Oxic
X2420	2.92	1.18	66.25	Shallow marine and transitional. Oxic

Sediments in **Cycle B** (depth range 2182 – 2036 m), were also deposited in paralic paleodepositional settings although they mark a still stand and a regressive phase of the paleosea, implying that deposition took place in shallower paleobathymetric domains. The lower section is characterized by whitish carbonate (limestone), sandy shale, shaly limestone and calcareous limestone lithofacies of Eocene age that correlates with the lower lithological section of the Ameki Formation, and capped by an upper section, that is composed of sequences of sandy and calcareous shale lithofacies characteristic of the upper lithological section of the Ameki Formation [22].

The biosignal presented by this interval shows an initial increase in total palynomorphs and pollen percentages and a corresponding decrease in sporomorph percentage. This trend signals a flooding and reduced fluvial influx in the lower section, which may have heralded clear coastal water conditions conducive for the development and growth of carbonate depositional systems, and an initial increase and subsequent decrease in sporomorph percentage indicating a shallowing water condition at the upper section.

This position is strengthened by the occurrence of the shallow water dinocysts species, *Multispinula quanta*, and *polysphaeridium sp.* [54], at a depth of 2050 m.

The depth interval 2036 – 1743 m (**Cycle C**) is marked by thick sequences of dark shale with subordinate very fine to medium-grained sand components in some sections and thin fine to coarse-grained sand interbeds. This interval is characterized by increased pollen and reduced spore percentages, which infer probable luxuriant vegetation occasioned by warm paleoclimate associated with a relative rise in sea-level. The inference for this interval is supported by the occurrence of *Operculodinium centrocarpum* a deep water dinocyst species, at 1817 m.

5.3. Sequences stratigraphy

5.3.1. Systems tracts

Four second-order sequences have been established in XEN-1 well. The sequences range from 2655 – 2202 m (Sequence 1 – 4), 2202 – 1945 m (Sequence 5), 1945 – 1758 m (Sequence 6 – 7) and 1758 – 1700 m (Sequence 7).

Lowstand Systems Tract (LST): Three LSTs were identified in the well. The first LST starts from the 47.2 Ma sequence boundary which marks the Lower Lutetian Stage at a depth of 2097 m within the P440 zone [3], and range up to 2036 m, (LST-1) (Fig. 9). The second LST commences at the 32.4 Ma sequence boundary within the P590 zone of Evamy *et al.* [3] at 1942 m and range up to a depth of 1927 m, which is of a Lower Rupelian Stage (Fig. 9). LST-3 commences at 1893 m and range up to 1840 m, marked at the base by the 27.3Ma sequence boundary of Upper Chatian. It falls within the P620 zone of Evamy *et al.* [3]. Paleodepositional environment interpretation for these intervals above shows that the three LSTs were deposited in a near-shore to the shallow marine shelfal paleodepositional environment. Definition of these systems tract is based primarily on biosignal, Lithofacies and overall stacking patterns which show a general progradational trend. The LSTs are characterized by the absence of mangrove pollen species, and an abundance of sporomorphs relative to pollen and thick sand interbeds, a reflection of relatively dry climatic conditions probably signaling a lowering sea-level. Van der Zwan *et al.* [55] reported high run-off and extensive sand deposition to result from dry climatic conditions.

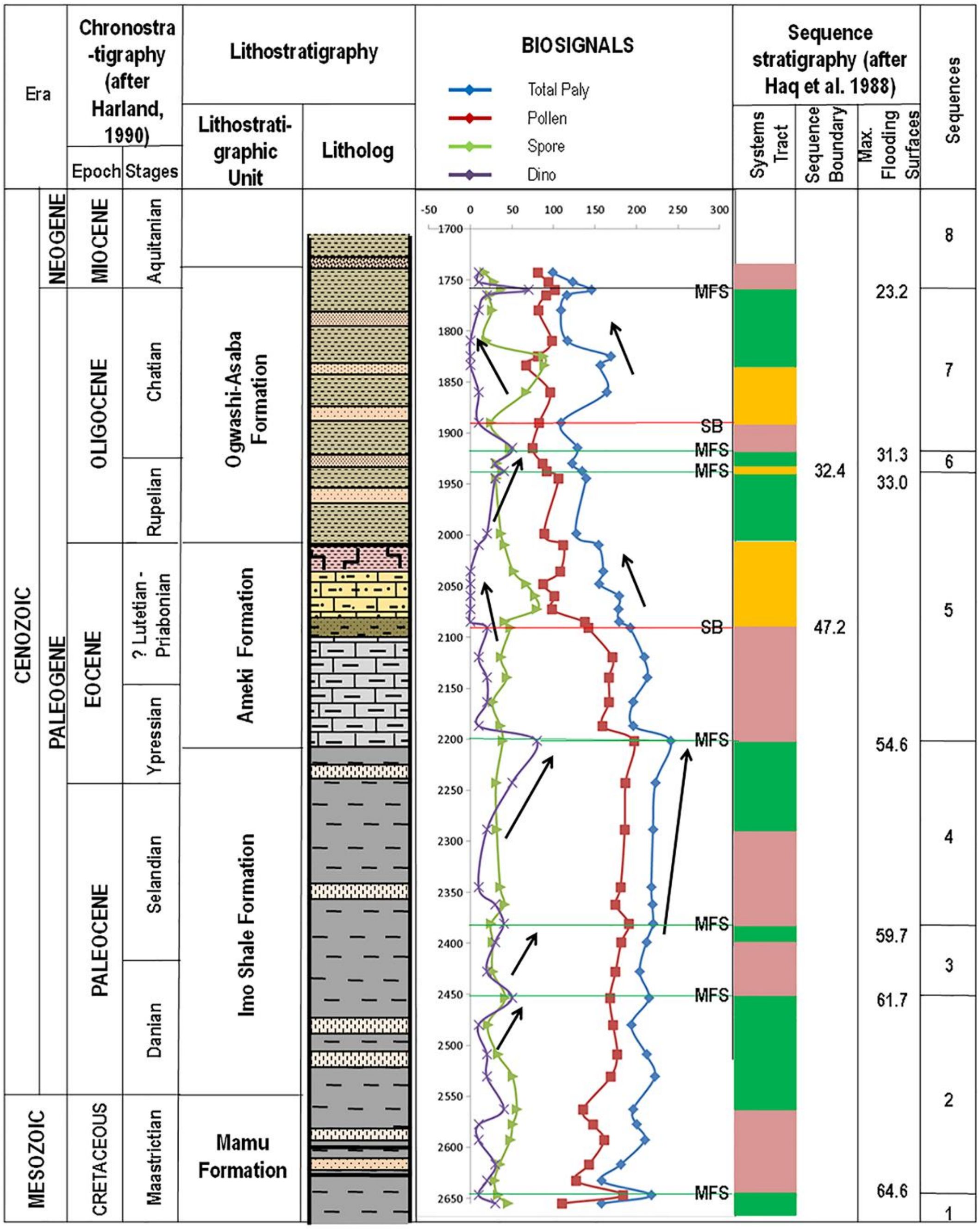

Fig. 8. Quantitative depth plot of biosignals and associated sequence stratigraphic elements correlated with formations and age in the XEN-1 well

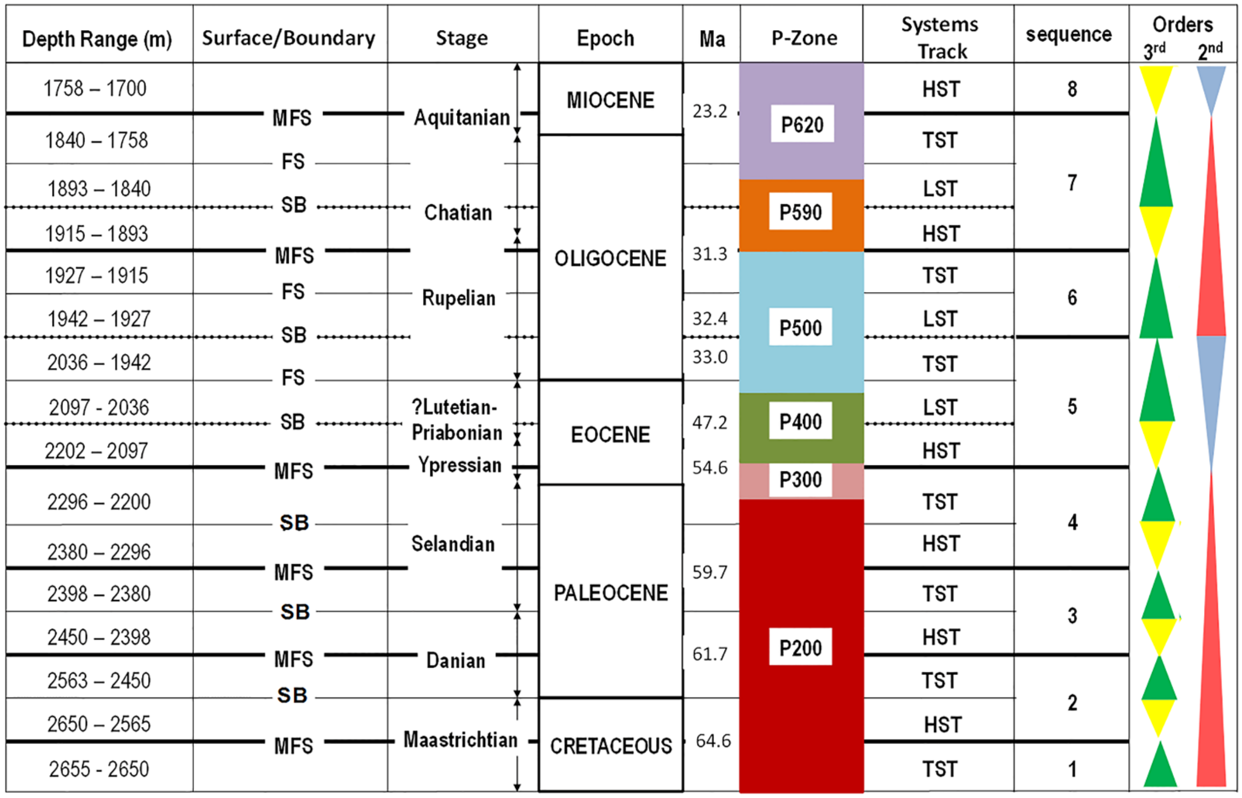

Fig. 9. Sequence stratigraphic summary sheet showing systems tract, major surfaces, Sequence, and P-zones. See Fig. 9, biosignal plot and sequence stratigraphic elements

Low stand systems tract biosignals

LST 1 - Biosignal from LST-1, shows dominance of savanna species (*Retibrevitricolporitesobdoensis, Arecipites sp., Proteacidites sp., Retidiporites sp.* and *Monoporitesannulatus,* etc.) over rainforest species. The interval also displays abundant verrucate spore species sand shallow marine dinocysts assemblages such as *Operculodiniumisrealianium, Polysphaeridium, Lingolodinium,* and *Selenopemphix sp.* (Fig. 6). These signals reveal a climate-driven sea-level change within this interval.

LST-2 - Present savanna ecological group composed of *Graminae, Arecipites sp.*, indeterminate trilete spores, abundant *Laevigotosporites* species, and *Elaesguineensis*, a rainforest species, and freshwater swamp forest groups such as *Racemonocolpiteshians, Retitricolporites sp., Perfortricolpitesdigitatus, Magnatrititeshowardi,* and *Acrostrichumaureum* (Fig. 6). These species occur at different intervals in a cyclical pattern indicating a moderately wet and dry fluctuating paleoclimate in the Lower Oligocene (Mid Rupelian Stage) in this section of the well. The occurrence of *Lingolodinium* and different species of *Spiniferites* characteristic of shallow marine paleoenvironment, confirms a shallow marine paleodepositional setting for this interval.

LST-3 - displays a palynomorph assemblage characterized by initially reduced spore abundance relative to pollen at the lower section and a subsequent increase in spore and a reduction in pollen abundance (Fig. 8). Palynomorph species recovered from this interval include *Racemonocolpiteshians, Retitricolporites sp., Stereisporites sp., Gemmatricolpites,* and *Laevigatosporites sp* (Fig. 6).

Transgressive Systems Tract (TST): Seven TSTs were identified in the well, ranging from 2655 – 2650 m (TST-1), 2563 – 2450 m (TST-2), 2398 – 2380 m (TST-3), 2296 – 2200 m (TST-4), 2036 – 1942 m (TST-5), 1927 – 1915 m (TST-6) and 1840 – 1758 m (TST-7) capped by seven Maximum flooding surfaces.

These systems tracts have been defined based on an overall lithofacies which displays retrogradational parasequence stacking patterns, biosignal trend of high pollen and reduced spore percentages, the dominance of rainforest and freshwater swamp forest pollen species and representative pristine/phytane ratios (Pr/Ph) and biomarker ratio datasets (Table 2). Dense tropical vegetation is indicated by the abundance and increase of tropical rainforest pollen species, which may have evolved by wet and warm tropical climatic conditions. Similar studies in the Campos Basin, Brazil, using dinocysts species, indicated high salinity water and warm tropical climate conditions [56]. These infer warm global paleoclimate that probably occasioned the melting of polar ice which may have led to release of melt waters into the ancient seas with a consequent rise in eustatic sea-level leading to the global transgression that affected both the Anambra and Niger Delta Basins (Fig. 1) and some of their relatives in Brazil (e.g. Espírito Santo and Campos Basins).

5.3.1. Maximum flooding surfaces

The first MFS is established at 2650 m and marks the 64.6 Ma Late Cretaceous marine transgression events that deposited the Mamu Formation. The second MFS is at 2450 m and marks the 61.7Ma flooding event in the Danian stage (Early Paleocene) (Fig. 9). The third MFS is the 59.7Ma surface defined at 2380 m, formed during the Early Selandian Stage. The first three MFSs are within the P200 zone of Evamy *et al.* [3] (Fig. 10). Facies dislocation, which points to an abrupt deepening/shallowing and local palynomorph abundance/reduction appropriately interpreted, have been used to indicate the flooding surfaces of the various TSTs.

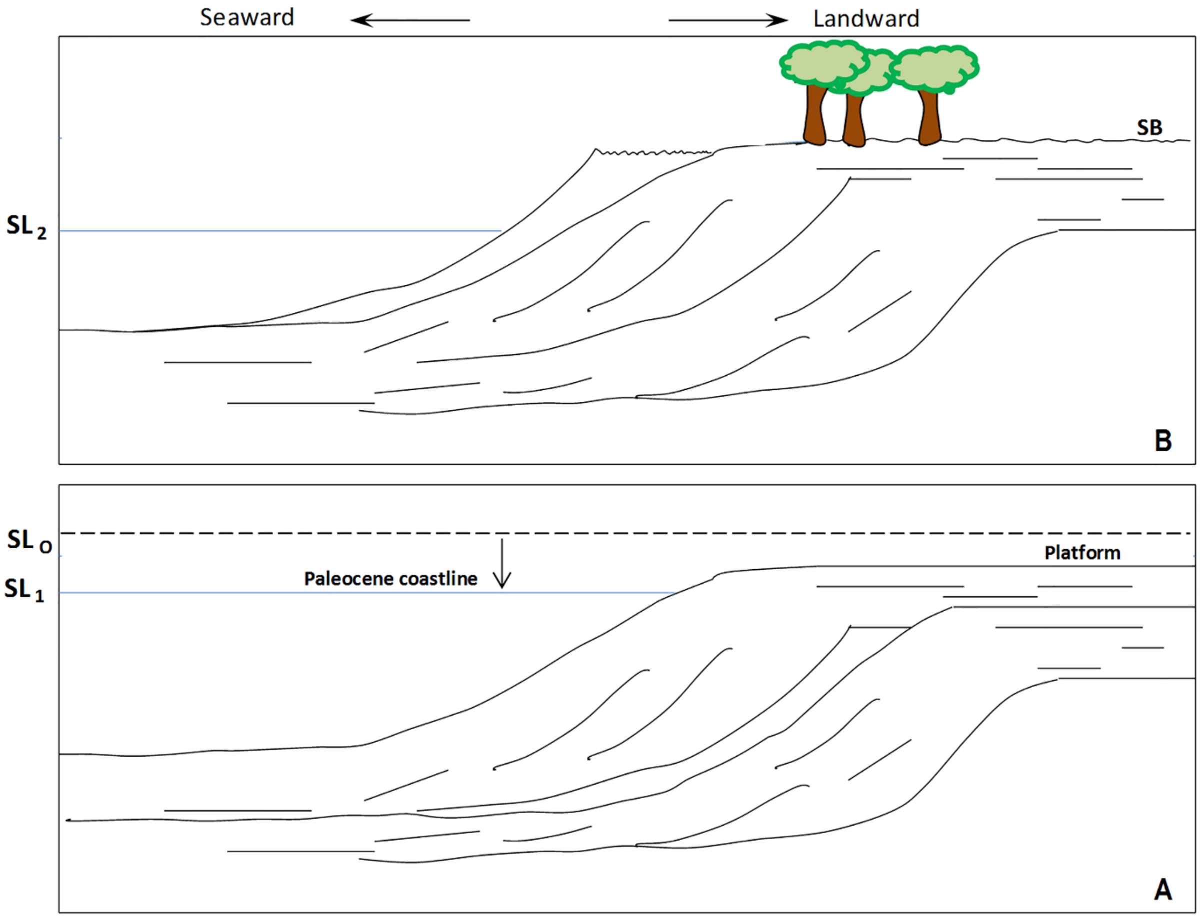

Fig. 10. Eocene-Oligocene paleogeographic conceptual model showing sea-level (SL) cycles during the formation of the Ameki Formation in the Benin Flank area as observed in XEN-1 well. (A) Transgression to highstand showing the relative fall in sea-level. (B) Lowstand, the rate of sedimentation > accommodation

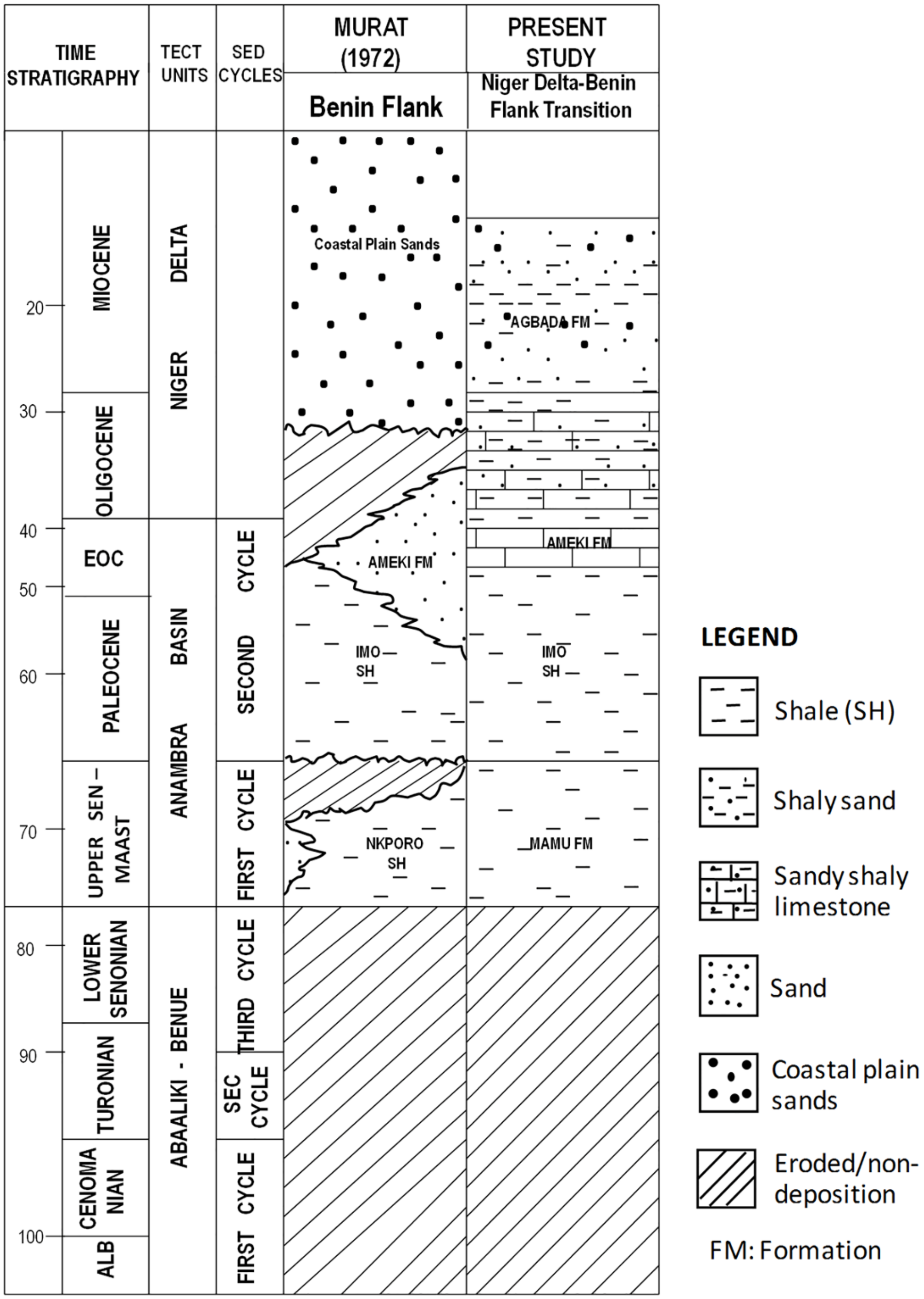

Fig. 11. A comparison of stratigraphic synopsis for Cretaceous and Tertiary formations of Murat [22] and present study in the Niger Delta-Benin Flank Transition from the Xen-1 well penetration

High Stand Systems Tracts: The six High Stand Systems Tracts, (HST) which exhibits a progradational and aggradational stacking pattern were established based on bio- and lithofacies, parasequence stacking pattern, and geochemical data.

Biosignal for these tracts shows a general higher abundance of pollen over spore in all the HSTs. *Spinizonocolpites echinatus* a mangrove forest species occur abundantly. Also, an abundance of *Verrucatosporites usmensis* and *Sporites verrucatus*, spores produced by several families of ferns were recorded, while *Arecipites exilimuratus*, *Laevigatosporites sp.*, and *Psilatricolporites sp.* produced by rainforest and mangrove vegetation (Fig. 6), indicate a warm wet climatic condition which has been variously correlated with sea-level high stand [57]. Shallow marine dinocysts taxa such as *Spiniferites ramosus*, *Homotriblium sp.,* and the freshwater algae *Cymatosphaera* were also recovered. These indicate HST formed in a shallow marine paleoenvironment.

6. Discussion

Results from paleodepositional proxies obtained for the well, indicate deposition in paleodepositional environments ranging from delta plain to shallow marine settings, and assigned ages ranging from Maastrichtian to Early Miocene. Paleodepositional interpretations show a close correlation with relative sea-level changes through time (Figs. 8 and 9), hence instrumental to the nature and type of sedimentary facies and architecture formed.

Results from age determination using an initially generated biozonation scheme for XEN -1 well [48], where the first and last occurrences and ranges of age-diagnostic palynomorphs were drawn, reveal some discrepancies in the age of the Ameki Formation identified in this study and age range presented by Murat [17] and Whiteman [22]. These discrepancies are shown by the sequence stratigraphic interpretations and correlations done for XEN -1 well, (Fig. 8). Integration of palynological signals from the lower sections of the well with lithofacies data, reflects a transgressing sea in a neritic paleoenvironment (Fig. 8) during the Late Cretaceous to Early Tertiary (Maastrichtian – Early Eocene), confirmed by sedimentologic, biosignal and geochemical proxies (Figs. 1, 5, 6, 7 and Tables 1 and 2). Similar sedimentation pattern was observed at the El Kef section by Molina *et al.*, [58], where marine sediments and sedimentation was continuous across the K-Pg boundary.

Lithofacies characteristics correlate the lowermost section of XEN-1 well with the Mamu Shale Formation, while the overlying section correlated with the Imo Formation known to be present in the Benin Flank area [17,22]. These interpretations are supported by palynological age data for this section (Figs. 5 and 11). The salinity index, parameter T10 shows decreasing trend up to the well (Table 1). This trend points to flooding of a platform area where a shallow marine condition probably existed and dilution of seawater was probably caused by fluvial incursion/influence. This view is also affirmed by the isoprenoid and n-alkane ratios for samples XEN2380 and XEN2545 (Figs. 7a and 7b, Table 2). The stratigraphic display revealed in this well supports presentation by Nwajide [4] that the Nsukka Formation is a proximal stratigraphic element, hence disappears in a proximo-distal direction, leaving the more marine Imo Formation resting unconformably on the Mamu Formation.

Towards the close of the Paleocene Transgression, the paleo-sea transgressed onto a sort of platform area (Fig. 10), during which time, strong fluvial influence on coastal deposystems still existed (XEN2420 and XEN2380 %C_{25} + n-alkane) (Figs. 8c and 8d, Table 1), and following which fluvial systems were probably driven landwards and a full marine condition established on the platform area, where carbonate forming biota subsequently thrived, (XEN2380 isoprenoid and n-alkane ratios, Fig. 7a, Tables 1 and 2).

The end-Paleocene transgression is capped by the 54.6 Ma MFS corresponding to Early Ypresian age, marking the end Cretaceous-Tertiary transgression event that affected the Northern Niger Delta Benin Flank area and marked the stratigraphic limit of the Imo Formation. The Imo Formation is overlain by the Ameki Formation in the northern parts of the Niger Delta Basin, interpreted to have been deposited in a deltaic and shallow marine paleoenvironment during the Eocene Regression that affected the coastal areas of southern Nigeria [22]. Murat [17] classed the Paleocene Imo and the Eocene Ameki Formation as part of the Anambra Basin. The Anambra Basin is a Cretaceous tectonic element; hence the stratigraphic limit of the Anambra Basin is the Cretaceous–Paleogene (K-Pg) boundary probably embedded in the lower section of the Nsukka Formation [4].

Systems tracts are predictive [59], and are reflected in the sedimentologic and biosignal characteristics. The transgressive systems tract at the lower section capped by the 54.6 Ma MFS, is overlain by a highstand systems tract interpreted from lithofacies characteristics between 2202 – 2097 m and capped by the 47.2 Ma sequence boundary at 2097 m in the well. Carbonate productivity varies with the sea-level change that can be identified in sequence stratigraphic interpretations of carbonate [60]. Wright and Burchette [60] noted a significant fact, that the bulk of carbonate sediment production occurs in the top 100 m of water column, with by far the highest production rates at depths of less than 20 m of water depth and that if submerged below these depths, rates of carbonate production and the ability of the carbonate system to cope with increases in relative sea-level are significantly impaired.

On most carbonate platforms, sediment production is greatest during sea-level highstands, when the whole platform surface is shallowly submerged (Fig. 10a), then during the intervening LST or transitional phases (Fig. 10b) [61-62], a phenomenon commonly termed 'highstand shedding' [63]. Observations based on sedimentologic, age and sequence stratigraphic interpretations in this present study are consistent with the Burchette and Wright [64], Haak and Schlager [61] and Schlager [62] model for carbonate production. The carbonate facies in XEN-1 well range from 2097 m to 2036 m (≈ 61 m thick). The lower part of this interval overlie the 54.6 MFS of the Early Eocene and is characterized by highstand systems tract carbonate facies, while the upper part is characterized by sandy shale, shaly carbonates and calcareous shale probably formed during carbonate "keep up" phase [65]. The lower part of the carbonate facies interval in XEN-1 well correlates with lithological descriptions of the lower part of the Ameki Formation, while the upper part correlates with the upper part of same formation [17,22]. Deductions based on the above data sets, shows that the lower section of the Ameki Formation in the northwestern area of the Niger Delta was formed in a carbonate platform that was established during a relative sea-level highstand regime in the Late Ypresian to Mid Eocene period (Fig. 10a), while the upper section is a product of a regressive sea level phase, also on a paleo-platform environment following sea-level highstand phase during the Late Eocene to Oligocene period (Figs 9 and 10). This interpretation contrast with conditions of deposition advanced by Murat [17] and Whiteman [22], who showed that the Ameki Formation was solely the product of the Eocene regression event, thus advanced a solely Eocene age for the formation, although Murat [22] without substantiating the Oligocene age limit with biostratigraphic data (Fig. 9), thinks that the age of the Ameki Formation may range from Eocene to Oligocene. Interpretations based on lithofacies and depositional cycles of sequences overlying the Ameki Formation in XEN-1 well shows that the Ameki Formation is overlain by the Agbada Formation. In this well, the section interpreted as corresponding to the Agbada Formation of the Niger Delta, range in age from Early to Late Miocene and overlies the Ameki Formation. This interpretation is also in contrast with interpretations based on Murat [22] stratigraphic synopsis of the Benin Flank, which shows an unconformity spanning the Late Eocene to Oligocene periods over the Ameki Formation and subsequent deposition of the Coastal Plain Sands (Benin Formation) (Fig. 11).

In the central Anambra Basin and eastern areas of the Benin Flank, the Mamu Formation is shown to overlie the Nkporo Shale; while the Ajali Sandstone Formation and Ajali type sandstone in the Fuga area, overlies the Mamu Formation, respectively [4]. A slightly different Late Cretaceous lithostratigraphic succession is observed in the western area of the Benin Flank [17,22]. Murat [22] showed an unconformity overlying the lower Senonian Araromi Shale, correlated with the Nkporo Shale and then deposition of the Paleocene-age Imo Formation (Fig. 11).

In this study, the Late Cretaceous sediments interpreted to correspond with the Mamu Shale are directly overlain by the Imo Formation, with no intervening erosional surface in the form of a sequence boundary or period of non-deposition. Biosignal and lithofacies characteristics from this interval show a Late Cretaceous-Tertiary transgression punctuated by periods of sea-level still stands reflected as highstand systems tracts and renewed rise in sea-levels, reflected as transgressive systems tracts (Fig. 9). Late Cretaceous palynomorphs species abound at the lower section and directly overlain by sediments yielding Early Paleocene species (Fig. 6), which correlates with the Paleocene-age Imo Formation. This fact highlights the limitation of the use of erosional surfaces as sequence boundaries [66], especially in the Niger Delta Basin [44].

7. Conclusions

Data presented in this work has shown that Cretaceous-Tertiary lithostratigraphic transitional events were controlled dominantly by major rising relative sea-level changes that transcended the K-Pg boundary and terminated in the Ypressian, driven by warm climatic conditions. This event created the Late Cretaceous Mamu and Paleocene Imo Formation and was mainly characterized by short sea-level rise pulsations deciphered through systems tract analysis. This could further be used to partly articulate the deposition of the Nsukka Formation in other parts of the Anambra Basin, although not present in this well location.

Integrated sequence stratigraphic results from this study support a Paleocene-Eocene (Ypressian) age range for the Imo Formation. Also, the integrated approach adopted in this work has shed more light on prevalent sea-level conditions under which the Ameki Formation was formed. It shows that the lower lithologic section was formed during a relative sea-level still stand/highstand phase, while the upper lithologic unit was formed as a regressive wedge (LST). The K-T lithostratigraphic transitional events were controlled essentially by third-order sea-level rise that transcended the K-T boundary, hence characterized by marine shale facies.

Acknowledgments

Special thanks to Shell Petroleum Development Company (SPDC) Nigeria for providing the ditch-cuttings of one her wells in the northwestern Niger Delta used for the study and the Tertiary Education Trust Fund (TETFUND) for providing research grants for the laboratory analysis through the Federal University of Petroleum Resources, Effurun (FUPRE) Nigeria. Special thanks to the management and staff of Fugro Robertson Petroleum Geochemistry Laboratory Llandudno, North Wales, United Kingdom, especially Dr. Lucy Costa and Dirby Vosper who have assisted in the geochemical analysis. We also wish to thank the Department of Earth Sciences, FUPRE for making her Laboratories available for the palynological analysis.

References

[1] Wiltshire J and Wright S. Pre-salt of West Africa, twin or distant relative of Brazil sub-surface? Gaffney and Cline Associates, 2016.
[2] Short KC and Stauble AJ. Outline of Geology of Niger Delta. AAPG Bull, 1967; 51: 761-779.
[3] Evamy DD, Haremboure J, Kamerling P, Knaap WA, Molloy FA and Rowlands PH. Hydrocarbon habitat of Tertiary Niger Delta. AAPG Bull, 1978; 62: 1-39.
[4] Nwajide CS. Geology of Nigeria's Sedimentary Basins. CSS Bookshops Ltd, Lagos, Nigeria, 2013.
[5] Mbuk IN, Rao VR and Kumaran KPN. The Upper Cretaceous-Paleocene boundary in the Ohafia-Ozu Abam area, Imo State. J. Mining and Geology, 1985; 22: 105–113.
[6] Alvarez LW, Alvarez W, Asaro F and Michel HV. Extra-terrestrial cause for the Cretaceous–Tertiary extinction: experimental results and theoretical interpretation. Science, l980; 208: 1095–1108.
[7] Bohor BR. A sediment gravity flow hypothesis for siliciclastic units at the K/T boundary, northeastern Mexico. In: Ryder G, Fastovsky D and Gartner S (eds) The Cretaceous–Tertiary Event and other Catastrophes in Earth History. Geol Soc Am, Special Paper, 1996; 307: 183–196.
[8] Keller G, Lopez-Oliva JG, Stinnesbeck W, and Adatt T. Age, stratigraphy, and deposition of near-K/T siliclastic deposits in Mexico: Relation to bolide impact? Geol Soc Am Bull, 1997; 109: 410–428.
[9] Tsujita C. Coincidence in the geological record: from clam clusters to Cretaceous catastrophe. Canad J Earth Sci, 2001; 38: 271–292.
[10] Alvarez W. Comparing the evidence relevant to impacts and flood basalts at times of major mass extinctions. Astrobiology, 2003; 3: 153–161.
[11] Schulte P, Stinnesbeck W, Steuben D, Kramar U, Berner Z, Keller G and Adatte T. Multiple slumped? Chicxulub ejecta deposits with iron-rich spherules and quenched carbonates from the K/T transition, La Sierrita, NE Mexico. Int J Earth Sci, 2003; 92: 114–142.
[12] Keller G, Adatte T, Berner Z, Harting M, Baum G, Prauss M, Tantawy AA and Stueben D. Chicxulub Impact predates K–T boundary: New evidence from Brazos, Texas. Earth and Planet Sci let, 2007; 255(3-4): 339–356.
[13] Schulte P, 40 Others. The Chicxulub asteroid impact and mass extinction at the Cretaceous–Paleogene boundary. Science, 2010; 327: 1214–1218.

[14] Keller G. The Cretaceous–Tertiary Mass Extinction: Theories and Controversies, in, Keller G and Adatte T, eds, The End-Cretaceous Mass Extinction and the Chicxulub Impact in Texas. SEPM Special Publication, 2011; 100: 7–22.

[15] Zachos JC, Arthur MA and Dean WE. Geochemical and paleoenvironmental variations across the Cretaceous/Tertiary boundary at Braggs, Alabama. Paleogeography, Paleoclimatology. Paleoecology, 1989; 69: 245-266.

[16] Self S, Blake S, Sharma K, Widdowson M and Sephton S. Sulfur and chlorine in Late Cretaceous Deccan magmas and eruptive gas release. Science, 2008; 319: 1654–1657.

[17] Murat RC. Stratigraphy and paleogeography of Cretaceous and Lower Tertiary in Southern Nigeria, in, Dessauvagie TFJ, Whiteman AJ, eds, African Geology. University Ibadan Press, Nigeria, 1972; 221– 266.

[18] Ogbe OB, Olobaniyi SB, Ejeh OI, Omo-Irabor OO, Osokpor J, Ocheli A and Overare B. Petrological and structural investigation of rocks around Igarra, southwestern Nigeria. Ife J Sci, 2018; 20 (3): 663–677.

[19] Corredor F, Shaw JH and Bilotti F. Structural styles in the deep-water fold and thrust belts of the Niger Delta. AAPG Bull, 2005; 89: 753–780.

[20] Nwajide CS and Reijers TJA. Sequence architecture in outcrops: examples from the Anambra Basin. NAPE Bull, 1996; 11: 23–32.

[21] Reijers TJA. Selected Chapters on Geology: Sedimentary geology and sequence stratigraphy in Nigeria and three case studies and a field guide. SPDC Corporate reprographic Services, Warri, Nigeria, 1996.

[22] Whiteman AJ. Nigeria: Its Petroleum Geology, Resources, and Potentials. Graham and Trotman, London, 1982.

[23] Agagu O and Ekweozor CM. Source rock characteristics of Senonian shales in the Anambra syncline, southern Nigeria. J Mining and Geology, 1982; 19: 132–140.

[24] Agagu OK, Fayose EA and Petters SW. Stratigraphy and sedimentation in the Senomian Anambra Basin of eastern Nigerian. J Mining and Geology, 1985; 22: 25–36.

[25] Ojoh K. Cretaceous geodynamic evolution of the southern part of the Benue Trough (Nigeria) in the equatorial domain of the south Atlantic: stratigraphy, basin analysis and paleogeography. Bull Centres Recherche Exploration Production, Elf-Aquitane, 1990; 14: 419–442.

[26] Burke K, Dessauvagie TFJ and Whiteman AJ. Openning of the Gulf of Guinea and the Geological History of the Benue Depression and Niger Delta. Nature Physical Sci, 1971; 233: 51-55.

[27] Reijers T.JA, Petters SW and Nwajide, CS. The Niger Delta Basin, in, Selley RC, ed, African basins. Sedimentary Basins of the World (Elsevier, Amsterdam), 1997; 3: 145–168.

[28] Weber KJ and Daukoru E. Petroleum geology of the Niger Delta. Proceedings of the Ninth World Petroleum Congress, 1975; 2: 209–221.

[29] Ejedawe JE. Patterns of incidence of oil reserves in Niger delta basin. AAPG Bull, 1981; 65: 1574–1585.

[30] Ejedawe JE, Coker SJL, Lambert-Aikhionbare DO, Alofe KB and Adoh FO. Evolution of oil-generative window and oil and gas occurrence in Tertiary Niger Delta Basin. AAPG Bull, 1984; 68: 1744–1751.

[31] Knox GJ and Omatsola ME. Development of the Cenozoic Niger Delta in terms of the escalator regression model, in, Proceedings of the KNGMG Symposium 'Coastal Lowlands – Geology and Geotechnology. Kluwer Academic Publishers, 1987; 181–202.

[32] Reyment RA. Aspects of the geology of Nigeria. University of Ibadan press, Nigeria, 1965.

[33] Tattam EM. A Review of Nigerian Stratigraphy. Geol. Surv. Nigeria, 1944; 27-47.

[34] Petters SW. An ancient submarine canyon in the Oligocene-Miocene of the western Niger Delta. Sedimentology, 1984; 31: 805–810.

[35] Petter SW. Foraminiferal biofacies in the Nigerian rift and continental margin delta, in, Oti MN and Postma G, eds, Geology of Delta. A.A. Balkema, Rotterdam, 1995; 219-235.

[36] Nuhu GO. Analytical micropaleontology I interpreting paleoenvironment, stratigraphy and floral province of Upper Cretaceous sediments in the Middle Benue Trough, Nigeria. Abstract, 28th Annual Conference, Nig Mining and Geosci Soc., 1992.

[37] Agumanu AE. Diagenetic processes in sandstones of the Cretaceous southern Benue Trough. Nigeria. J Mining Geology, 1990; 26: 207–224.

[38] Ehinola OA, Ekweozor CM and Simonelt BRT. Geological and geochemical evaluation of Lafia-Obi coal, Benue Trough, Nigeria. NAPE Bull, 2000; 15: 92–104.

[39] Zaborski PMP. The Cretaceous and Paleocene transgressions in Nigeria and Niger. J Mining and Geology, 2000; 36: 153–173.

[40] Okoro AU and Nwajide CS. Petrography and mode of formation of the oolitic ironstone beds in the Campano-Maastrichtian Nkporo Formation in Leru, southeastern Nigeria. Global J. Geol Soc, 2008; 6: 57–62.

[41] Berggren WA. Paleocene biostratigraphy and planktonic foraminifera of Nigeria (West Africa). Proceeds 21st Int Geol Congress, Copenhagen, 1960; 6: 41-55.

[42] Ogbe FGA. Stratigraphy of strata exposed in the Ewekoro quarry, Western Nigeria, in, Dessauvagie TFJ and Whiteman AJ, eds, African Geology, University of Ibadan Press, Nigeria, 1972; 305-322.

[43] Arua AI. Episodic Sedimentation: An example from the Nkporo Shale (Campano-Maastrichtian). J Afri Earth Sci, 1980; 7: 72 –759.

[44] Reijers TJA. Stratigraphy and sedimentology of the Niger Delta. Geologos, 2011; 17 (3): 133–162

[45] Avbovbo AA. Tertiary lithostratigraphy of Niger Delta. AAPG Bull, 1978; 62: 295-306.

[46] Osokpor J and Ogbe OB. Facies evolution, paleodepositional environment and sequence stratigraphy of Tertiary sediments, northwestern Niger Delta Basin. Development J Sci and Tech Res, 2017; 6 (2): 9–24.

[47] Traverse A. Paleopalynology. Unwin Hyman, Boston, 1988.

[48] Osokpor J. Petroleum potentials, paleodepositional environment and sequence stratigraphy of Cretaceous-Tertiary sediments in parts of the Benin Flank & Niger Delta Basins. Unpublished PhD. Thesis, University of Benin, Nigeria, 2013.

[49] Osokpor J, Lucas FA, Osokpor OJ, Overare B and Izeze OE. Palynozonation and lithofacies cycles of Paleogene to Neogene age sediments in PML-1 well, northern Niger Delta Basin. Pacific J Sci and Tech, 2015; 16: 286 – 297.

[50] Sittler C. Illustration de l`histoiregeologique du fosse rhenan et de l`Alsace. – Recording the Rhine graben and Alsace history by sketched cross sections. N. JB. Geology of Paleontology Abh, 1992; 186: 255-282.

[51] Sittler C and Ollivier-Pierre MF. Palynology and palynofacies analysis: Some clues to assess and identify West-European Tertiary depositional environments in terms of relative high or lowstands: Application to the case of three Eocene and Oligocene sections in France. Elf Aquitaine Production F-64018, 1994; 475-487.

[52] Peters KE and Moldovan JM. The biomarker guide interpreting molecular fossils in petroleum and ancient sediments. Prentice-Hall, Englewood Cliffs, NJ, 1993.

[53] Peters KE, Walters CC and Moldowan JM. The biomarker guide: Biomarkers and isotopes in the environment and human history, Cambridge. Cambridge University Press, 2005; 1: 471

[54] Harland R. Distribution maps of Recent dinoflagellate cysts in bottom sediments from North Atlantic Ocean and adjacent seas. Paleontology, 1983; 26: 321-387.

[55] Van der Zwan CJ, Van de Laar JGM, Pagnier HJM and Van Amerom HWJ. Palynological, ecological and climatological synthesis of the Upper Carboniferous of the well De Lutte-06 (East Netherlands). Comptes rendus XII ICC-P, 1993; 1: 167-186.

[56] Santos A, Carvalho MA, de Oliveira AD and Filho JGM. Paleoenvironmental changes and influence on Operculodinium centrocarpum during the Quaternary in the Campos Basin, southwestern Brazil. J South Am Earth Sci, 2017; 80: 255–271.

[57] Poumot C. Palynological evidence for eustatic events in the tropical Neogene. Bulletin des Centers de Recherches Exploration-Production, Elf Aquitaine, 1989; 13: 437-453.

[58] Molina E, Gonzalvo C, Ortiz S, and Cruz LE. Foraminiferal turnover across the Eocene–Oligocene transition at Fuente Caldera, southern Spain: No cause–effect relationship between meteorite impacts and extinctions. Marine Micropaleontology, 2006; 58: 270 – 286.

[59] Posamentier H and Allen G. Siliciclastic sequence stratigraphy – concepts and applications. SEPM Concepts in Sedimentology and Paleontology, 1999; 7: 210

[60] Wright VP and Burchette TP. Shallow-Water Carbonate, in, H. G. Reading, ed., Sedimentary environments: Processes, Facies and Stratigraphy. Blackwell Sci, 1996; 325-394.

[61] Haak AB and Schlager W. Compositional variations in calciturbidites due to sea-level fluctuations, Late Quaternary, Bahamas. Geologische Rundschau, 1989; 78: 477–486.

[62] Schlager W. Depositional bias and environmental change – important factors in sequence stratigraphy. Sedimentary Geology, 1991; 70: 109-130.

[63] Schlager W, Reijmer JJG and Droxler A. Highstand shedding of carbonate platform. J Sedimentary Res, B64, 1994; 270-281.

[64] Burchette TP and Wright VP. Carbonate ramp depositional deposits. Sedimentary Geology, 1992; 79: 3-57.

[65] Schlager W. Carbonate Sedimentology and Sequence Stratigraphy. Tulsa: SEPM (Society for Sedimentary Geology). SEPM Concepts in Sedimentology and Paleontology, 2005; 8: 200.

[66] Galloway WE. Genetic Stratigraphic Sequences in Basin Analysis 1: Architecture and Genesis of Flooding-Surface Bounded Depositional Units. AAPG Bull, 1989; 73 (2): 125–142.

To whom correspondence should be addressed: Dr. Ovie B. Ogbe, Department of Earth Sciences, Federal University of Petroleum Resources, PMB 1221, Effurun, Delta State, Nigeria, ogbe.ovie@fupre.edu.ng

Petroleum and Coal

Article **Open Access**

IMPROVED MODELS FOR THE ESTIMATION OF PVT PROPERTIES OF CRUDE OILS

Arash Kamari [1], Mehdi Sattari [2], Amir H. Mohammadi [2], Deresh Ramjugernath [2**]*

[1] *Department of Geology, Kansas State University, 108 Thompson Hall, Manhattan, KS, 66506, USA*
[2] *Thermodynamics Research Unit, School of Engineering, University of KwaZulu-Natal, Howard College Campus, King George V Avenue, Durban 4041, South Africa*

Received April 10, 2019; Accepted July 1, 2019

Abstract

Reservoir fluid properties, such as oil formation volume factor and bubble point pressure, are vital parameters in many computations associated with petroleum engineering. These computations include hydrocarbon reserve estimation, and consequently, economic efficiency evaluation, fluid flow in porous media, and improved and enhanced oil recovery. Prior to the computations, the pressure-volume-temperature (PVT) properties of reservoir oil must be determined. PVT properties, in turn, are ascertained either by empirical methods, laboratory measurements, or via equations of state. The latter two methods, however, are expensive and time-consuming and require complex calculations. Therefore, it is necessary to develop an accurate and reliable model for the determination of petroleum fluid's physical properties. In this paper, a soft-computing approach is employed to develop efficient models for the calculation of bubble point pressure and oil formation volume factor properties. In pursuit of this goal, a robust mathematical algorithm, namely, gene expression programming (GEP), is applied. Moreover, an extensive databank, covering varied ranges of experimental PVT conditions from different and widespread geological and geographic regions was constructed. The databank includes data on reservoir temperature, gas oil ratio, bubble point pressure, gas gravity, and oil forma-tion volume. In addition, the GEP model results are compared to published data on oil formation volume and bubble point pressure. The results demonstrate close agreement between estimations based on the GEP model and experimental data reported in the literature for both oil formation volume and bubble point pressure properties. Moreover, the results prove that the GEP model, proposed in this study is more accurate and capable than the existing methods, for the determination of both oil formation volume factor and bubble point pressure properties.

Keywords*: Oil formation volume factor; Bubble point pressure; Gene expression programming (GEP); Empirical correlation; PVT properties; Accuracy.*

1. Introduction

The computation of data on oil reservoirs requires detailed and accurate knowledge of the reservoir fluid properties [1]. These properties, which are associated with pressure-volume-temperature (PVT) parameters, are fundamental for undertaking many types of petroleum engineering calculations. In other words, reliable solutions for many petroleum engineering problems are impossible without accurate predictions of the PVT properties of the reservoir fluids [2].

The PVT properties of primary importance for the computation of data are solution gas oil ratio (GOR), bubble point pressure (P_b), gas formation volume factor (GFVF), and oil formation volume factor (OFVF) [3]. These PVT properties are traditionally acquired experimentally by conducting laboratory tests [4]. However, measurement of PVT properties by means of laboratory experiments is expensive and complex because cores or rock samples containing petroleum reservoir fluid are generally from isolated and difficult-to-access well locations [2,5]

Empirical correlations, or models, are employed to avoid time-consuming and costly experimental measurements. A popular method to determine the PVT properties of crude oils is the use of equations of state which are based on a detailed knowledge of the composition of reservoir fluid [6].

Several PVT models have been developed for the determination of the physical properties of reservoir fluids in oil reservoirs over time. Standing [7] and Katz [8] were the first to propose models for the estimation of PVT properties, such as OFVF and bubble point pressure. Standing's [7] model is based on experimental tests conducted on 105 cores from 22 crude oils in California State. Katz's [8] method employs data on bubble point pressure, oil API gravity, gas specific gravity, reservoir temperature and solution gas oil ratio, in order to calculate oil formation volume factor.

Vazquez and Beggs [9] presented a PVT empirical correlation to estimate solution gas–oil ratio, viscosity associated with under-saturated oil reservoirs and oil formation volume factor, based on laboratory measurements of 600 cores collected from various regions of the world. Subsequently, results indicate that their empirical correlation for the estimation of OFVF has an average error of 4.7%.

Glaso [10] performed regression and graphical analyses for oil PVT properties by using data related to 45 core samples, mostly collected from North Sea region. Their results, related to oil formation volume factor and bubble point pressure, display average errors of 1.28 and 20.43 %, respectively.

Al-Marhoun [11] provided an empirical correlation for oil formation volume factor based on experimental PVT data mostly extracted from North America and the Middle East. Dokla and Osman [12] used experimental PVT data from the UAE for the development of bubble point pressure and oil formation volume factor correlations, and Petrosky and Farshad [13] developed under-saturated isothermal oil compressibility, oil formation volume factor, and solution gas–oil ratio correlations using PVT data from the Gulf of Mexico.

Arabloo *et al.* [14] implemented two constrained multivariable search techniques, including a generalized reduced gradient algorithm and successive linear programming, to develop two correlations in order to determine oil formation volume factor and bubble point pressure. To pursue their objective, they utilized experimental data associated with various geographical domains worldwide. Their results indicate that the OFVF and bubble point pressure correlations have average relative errors of 2.24 and 18.9 %, respectively. Recently, smart techniques have been increasingly employed to predict PVT properties [15-18]. However, these methods have some drawbacks: a symbolic equation is not provided; the necessity to use a large dataset as a basis for prediction and; a potential over-fitting problem, in particular for models developed by artificial neural network techniques.

The aim of this work was to propose efficient, accurate and reliable PVT models for determination of oil formation volume factor as well as bubble point pressure, as a function of reservoir temperature, crude oil API gravity and gas specific gravity, and solution gas oil ratio. To this end, a gene expression programming (GEP) [19] strategy was utilized to develop the aforementioned models. In the first step, a large dataset was collected for different oil PVT information related to various geographical regions of the world. Then, the results attained for the newly developed models were compared against actual data, and also, previously reported correlations available in literature. Additionally, the Leverage approach was employed to detect suspended and/, or outlier data points in the dataset. Finally, to evaluate the accuracy and capability performance of the developed models, and to provide a comparative study, a statistical error analysis was performed, in which error parameters and analysis, including a crossplot and error distribution plots, were sketched.

2. Oil PVT properties

A review, dating back to the early 1940s, of published methods for the prediction of oil formation volume factor (OFVF) and bubble point pressure (P_b), indicates the importance of these PVT properties from an industry point of view [14]. By definition, OFVF is the reservoir oil required to produce one barrel (1 bbl) of oil at surface conditions [20]. Additionally, in its original condition, reservoir oil contains some natural gas in solution; consequently, the pressure at which this natural gas begins to come out of solution and forms bubbles is identified as the P_b. As a result, P_b and OFVF are the most vital properties for accurate calculation of hydrocarbon reservoir recoverable reserves, the oil-water flow ratio, reservoir capacity for production of oil, problems related to enhanced and improved oil recovery, and all other issues associated with petroleum engineering computations [9,22-24]. Therefore, developing accurate and efficient models for the determination of P_b and OFVF is a necessary.

As a result, to predict the PVT properties of petroleum reservoir fluids utilizing correlations, field measured data, like reservoir temperature (T_R), reservoir pressure (P_R), crude oil API gravity (API), gas specific gravity or gas relative density (γ_g), and solution gas oil ratio (GOR), are normally required [18]. Hence, reservoir temperature, crude oil API gravity, gas relative density, and solution gas oil ratio are considered as required variables for accurate estimation of P_b and OFVF, in line with the majority of previously published works [7,9,13,25-27] as follows:

$$P_b = f_1(T_R, \gamma_g, GOR, API) \quad (1)$$

$$OFVF = f_2(T_R, \gamma_g, GOR, API) \quad (2)$$

Knowledge of the geographical and geological conditions of reservoir oils is important for proposing PVT correlations because the chemical composition is specific for any crude oil. In other words, obtaining accurate results, by means of PVT correlations, for different crude oils, having different chemical and physical characteristics, is difficult to achieve [28]. Hence, to account for regional characteristics, PVT correlations need to be developed by using comprehensive datasets, which cover a wide range of PVT properties from almost all regions of the world. Hence, the quality and reliability of models, for estimating PVT and thermo-physical properties, are related to the applied database [29-31]. Therefore, about 755 laboratory PVT datasets, covering wide ranges of PVT experimental conditions from a wide spread of geographical and geological regions, were utilized in this study to develop and test the models for the determination of P_b and OFVF.

The dataset used for developing the P_b and OFVF models comprises reservoir temperature (in units of °F), oil formation volume factor at bubble point pressure (in units of bbl/STB), crude oil API gravity, gas gravity, and solution gas oil ratio at bubble point pressure (in units of SCF/STB), which was collected from Moghaddam *et al.* [32], Obomanu and Okpobiri [33], Bello and Villa [34], Omar and Todd [35], Dokla and Osman [12], Al-Marhoun [36], Ghetto and Villa [1], Mahmood and Al-Marhoun [28], and Ostermann *et al.* [23]. Table 1 summarizes the values of minimum, maximum, and average for reservoir temperature, gas oil ratio, oil gravity, bubble point pressure, gas gravity, and oil formation volume factor. The table confirms that the databank collected in this study covers a wide range of PVT properties from volatile oils to heavy crude oils.

Table 1. The minimum, maximum and average values associated with the PVT properties in the databank utilized for proposing the GEP models

	Unit	Min.	Max.	Avg.	Type
Oil formation volume factor, B_{ob}	bbl/STB	1.02	2.92	1.40	Output
Bubble point pressure, P_b	psi	58.02	6 613.82	1 846.05	Output
Gas gravity, γ_g	-	0.52	3.44	1.12	Input
Initial solution gas oil ratio, R_{Si}	SCF/STB	7.08	3 298.66	592.39	Input
Reservoir temperature, T_R	°F	74.00	360.93	207.17	Input
Oil gravity, API	-	6.00	56.80	34.36	Input

3. Developing the GEP models

As already mentioned, a GEP mathematical algorithm was applied, in this study, to develop two models for the determination of PVT properties of reservoir oils, (i.e. oil formation volume factor and bubble point pressure). The GEP [19] approach is a modified version of the genetic algorithm (GA), and genetic programming (GP), which is implemented for solving regression and also classification problems. It employs populations of individuals, which are chosen in keeping with fitness, and presents genetic variation utilizing one and/or more genetic operators [37]. As a comparison, the nature of the individuals is the fundamental difference between GA, GP, and GEP algorithms [19]. Consequently, the individuals in GA, GP and GEP algorithms are: the chromosomes or linear strings of fixed length; the parse trees or nonlinear entities of different shapes and sizes; and the chromosomes or genome and/or linear strings of fixed length, which are subsequently presented as nonlinear entities of different shapes and sizes, respectively [19].

In the GEP [19] algorithm, the structures of the genes allow encoding of any program for effective evolution and development of the solutions [38]. As a result, the GEP [19] mathematical algorithm employs two elements, including the expression tree (ET) and the chromosome. The chromosome has the role of an encoder for the candidate solution, which is translated into an expression tree. Each genetic chromosome involves terminals, including constants and variables; and functions structured in one and/or more genes of equal length [39]. The constants are produced by the GEP algorithm in a range selected by the employer, while the functions and variables are recognized as input data. Additionally, the gene consists of a tail made only of terminals, and a head made of functions, in addition to terminals including variables and constants [39].

The head length (h) is recognized as an input parameter for the GEP mathematical algorithm, while the tail length (t) is expressed as follows:

$$t = h(n-1)+1 \tag{3}$$

where t stands for the tail length of the gene; h shows the head length, and n is the largest arity of the functions utilized in the gene's head.

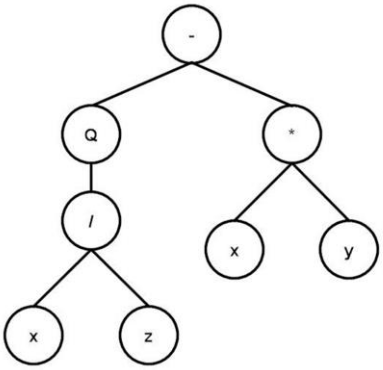

For a better understanding of the GEP procedure, Fig.1 provides an example of a two-gene chromosome composed of four functions, including -, *, / and Q, and also three terminals including x, y, and z, together with its decoded ET, and the corresponding mathematical expression, which is formulated as ($\sqrt{(x/z)}$) - (x*y).

Fig. 1. A typical two-gene chromosome with its corresponding mathematical expression; Q is the square root function

The procedure presented by Ferreira [38] was followed for developing the models, using the GEP algorithm, in order to estimate the OFVF and P_b properties as follows [38]:

I. The initialization of the population of individuals, which is based on counting the random made chromosomes of a certain number of individuals by setting various correlations, as stated;
II. The population of individuals that fits, considering fitness functions (cases);
III. The population of individuals selected, in keeping with their fitness, in order to replicate with modifications;
IV. The implementation of the same procedure, concerning confrontation of the selection environment, the genomes expression, selecting, and duplicating with modification, for the new population of individuals;
V. The repeat of the above stages for a certain number of generations, or until an optimum solution is established (convergence of the algorithm in keeping with the criteria defined).

In order to present capable, and reliable models for the calculation of OFVF and P_b, four input variables are considered. These consist of solution gas oil ratio, gas gravity, oil API gravity, and reservoir temperature. In pursuit of our goal, both datasets related to OFVF and P_b properties are randomly separated into two sub-datasets consisting of the 'Training/Learning' set and the 'Test' set.

In the development of the GEP models, 80% of the main data points related to OFVF and P_b properties, as well as their input parameters, is randomly selected for the 'Training' phase (development of the models), and 20% is assigned for the 'Test' phase (accuracy and capability evaluation), respectively. As a consequence, higher valued input variables may suppress the impact of the smaller ones during the training phase of mathematical algorithms, like in the GEP method. To overcome such an obstacle, and in order to make the GEP algorithm perform for the estimation of both OFVF and P_b properties, all data points should be adequately processed, and well-scaled, prior to input into the GEP.

Although normalization of the data points is not necessary in the estimation process by means of GEP-based methods, better results are normally acquired after normalizing the parameters [40]. Thus, all data points related to the inputs for both OFVF and P_b properties are normalized as follows:

$$r_n = \left(\frac{r}{1.5.xr_{max}}\right)x0.8.+0.1 \qquad (4)$$

where: r_n stands for the data points normalized, r indicates the actual data, and r_{max} is the maximum value of the data [41].

In the next step, the normalized data points are returned to their original values at the end of the modeling process.

4. Results and discussion

4.1. Performance evaluation

Previous research has shown that developing a correlation for bubble point pressure is more complicated than for oil formation volume factor. All of the available correlations for bubble point pressure are less rigorous and precise than those for the estimation of oil formation volume factor [14]. Hence, to obtain robust, reliable, and accurate models for both bubble point pressure and oil formation volume factor, the computational procedure related to the GEP algorithm can be used. In fact, the computational phases, associated with the GEP [38] approach, define the required parameters, which give the most accurate models for both bubble point pressure and oil formation volume factor, on the basis of the introduced variables, consisting of solution gas oil ratio, gas gravity, oil API gravity and reservoir temperature.

In order to increase the accuracy of the GEP model, compared to existing correlations, neutral genes can be added to the model (a newly developed equation), after reaching a reasonable and appropriate number of generations. This is proposed for both of the models related to OFVF and P_b properties.

Moreover, the function, in accordance with the average absolute percent relative error (AAPRE) and correlation coefficient (R2), was chosen to compute the overall fitness of the evolved programs. The program or iterative calculation was undertaken until there was no longer improvement in the precision and capability of the several proposed models, with the various functions utilized. Subsequently, the final equations for both bubble point pressure and oil formation volume factor properties were obtained as follows:

$$B_{ob} = 1 - 0.000081623\,\gamma_g \left[\sqrt{API\,T_R} + \frac{R_{Si}-4.846}{\sqrt{\gamma_g}}\right]\left(0.37658\,\gamma_g - (API - T_R)^{0.3652}\right) \qquad (5)$$

$$P_b = \frac{87.3067 R_{Si}\,T_R\,\left|\gamma_g - 2.95787\right| + 7639.17}{947.493\,\gamma_g + \exp(0.000641267\,API\,T_R) + API\,T_R + 3.59953\,\gamma_g\,R_{Si}} \qquad (6)$$

where: P_b denotes bubble point pressure (psi); B_{ob} stands for OFVF at bubble point pressure (bbl/STB); T_R expresses the reservoir temperature (°F); *API* is the crude oil API gravity; γ_g indicates the gas gravity and R_{Si} shows the solution gas oil ratio at bubble point pressure (SCF/STB).

Having developed the GEP models for the estimation of B_{ob} and P_b properties, an error analysis, including statistical error analysis, in which R2, AAPRE, average percent relative error (APRE), and root mean square (RMSE), and also a graphical error analysis, containing a parity diagram and relative error distribution plot, were performed to evaluate the prediction capability of the models.

Table 2 summarizes the statistical error parameters calculated for the B_{ob} model developed in this study. The results indicate a $R^2 = 0.93$ and an AAPRE = 3.62. The error values show that the newly developed GEP model predicts the oil formation volume factor values reliably within acceptable accuracy.

Table 2. Summarized statistical error parameters including AAPRE, APRE, RMSE and R^2 for the newly developed model for oil formation volume factor as well as the studied correlations resulted from the actual data

Method	AAPRE, %^{a}	APRE, %^{b}	RMSE^c	R$^{2\ d}$
Present study (Eq. (5))	2.17	0.18	0.07	0.93
Arabloo *et al.* model [14]	2.24	-0.04	0.07	0.94
Al-Shammasi model [25]	2.59	-0.92	0.07	0.93
Kartoatmodjo and Schmidt model [26]	2.92	-0.30	0.07	0.93
Frashad *et al.* model [41]	2.94	0.39	0.07	0.93
Al-Marhoun model [36]	3.09	-0.38	0.08	0.93
Standing model [7]	3.36	-1.98	0.08	0.93
Petrosky and Farshad model [13]	3.46	-2.35	0.08	0.93
Omar and Todd model [35]	5.03	2.08	0.12	0.85
Dindoruk and Christman model [42]	5.52	-2.94	0.14	0.83
Vazquez and Beggs model [9]	5.59	3.01	0.13	0.82
Macary and El-Batanony model [27]	9.11	-8.44	0.19	0.85
Abdul-Majeed model [43]	27.77	-27.73	0.40	0.83
Labedi model [44]	37.68	-37.64	0.68	0.93

$$^{a}\ AAPRE\,\% = \frac{1}{n}\sum_{i=1}^{n}|E_i\%| \text{ where } E_i\% = \left[\frac{X_{\text{exp}} - X_{\text{rep./pred}}}{X_{\text{exp}}}\right]\times 100 \Rightarrow i = 1,2,3,\ldots,n$$

$$^{b}\ APRE\,\% = \frac{1}{n}\sum_{i=1}^{n}E_i\%$$

$$^{c}\ RMSE = \sqrt{\frac{1}{n}\sum_{i=1}^{n}\left(X_{i\,\text{exp}} - X_{i\,\text{rep./pred}}\right)^2}$$

$$^{d}\ R^2 = 1 - \frac{\sum_{i=1}^{N}\left(X_{(i)\,\text{exp}} - X_{(i)\,\text{rep./pred}}\right)^2}{\sum_{i}^{N}\left(X_{(i)\,\text{rep./pred}} - averageX_{(i)rep/\,pred}\right)^2}$$

Figure 2 provides a parity diagram and a comparison between the calculated and actual values related to oil formation volume factor data. It is clear, from the figure, that most of the data points are almost placed on the line of Y=X, illustrating that there is an agreement between the newly developed model results and the actual oil formation volume factor data gathered from the literature. In order to illustrate, graphically, capability, and performance of the GEP model in estimating oil formation volume factor, the relative error percentage distribution plot is provided in Fig. 3. As can be seen in Fig. 3, a small margin of error is noticed in relation to Eq. (5).

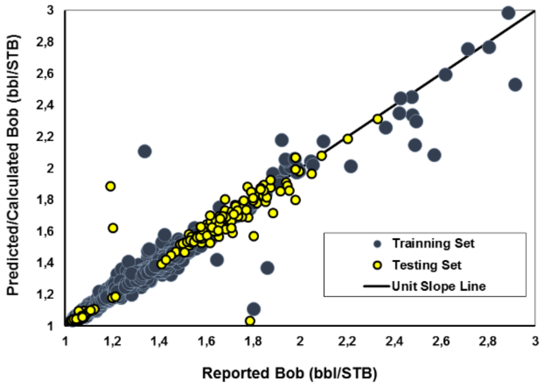

Fig. 2. Parity diagram for the estimated values by the new model and the literature-reported values of the oil formation volume factor

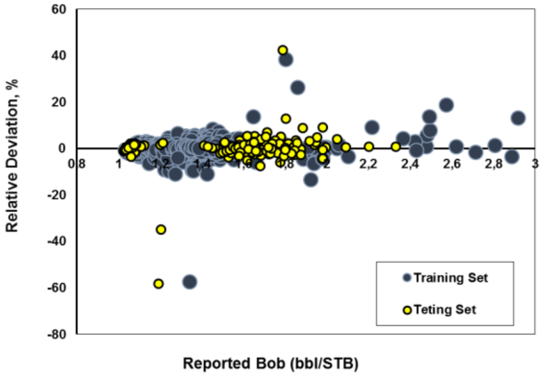

Fig. 3. Relative deviations plot of the oil formation volume factor values obtained by the newly proposed model from the available dataset values

The capability of the model developed for estimation of the oil formation volume factor was then compared with the results of 13 most widely-utilized empirical correlations available in the literature, viz. Arabloo *et al.* [14] model, Al-Shammasi [25] model, Kartoatmodjo and Schmidt [26] model, Frashad *et al.* [41] model, Al-Marhoun [36] model, Standing [7] model, Petrosky and Farshad [13] model, Omar and Todd [35] model, Dindoruk and Christman [42] model, Vazquez and Beggs [9] model, Macary and El-Batanony [27] model, Abdul-Majeed [43] model, and Labedi [44] model.

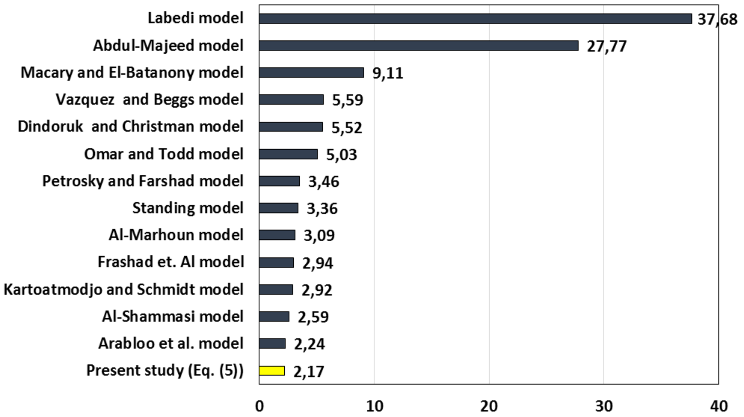

Fig. 4. Graphical comparison between the AAPRE values obtained by the newly model developed in this study for the estimation of oil formation volume factor as well as the corresponding correlations studied

A summary of the comparative study mentioned earlier, in which statistical error parameters were used, is listed in Table 2. It confirms that Eq. (5) shows a better performance for the calculation of oil formation volume factor, compared to the reviewed correlations. An acceptable AAPRE of the estimated values from the actual data was obtained. Moreover, a comparative study in terms of AAPRE is shown in Fig. 4. The bar plots drawn in Fig. 4 illustrate the accuracy of the model developed in this study for estimation of oil formation volume factor which is acceptable when compared with values calculated by other correlations listed.

Table 3 lists the statistical error parameters calculated for the P_b model proposed in the present work. The table reports that the values obtained for AAPRE, APRE, RMSE, and R^2 are 15.3%, 2.23%, 468.11, and 0.88, respectively. These values confirm the accuracy of the model for the estimation of bubble point pressure. Figure 5 is a diagram showing the parity between the calculated and reported values of bubble point pressure data, which illustrates close agreement between the newly developed model results, and the actual bubble point pressure data. Figure 6 presents the relative percentage error distribution plot for the P_b model. The figure indicates a small, existing error range, and a low scatter around the zero error line, for the bubble point pressure data and APRE obtained for the Eq. (6).

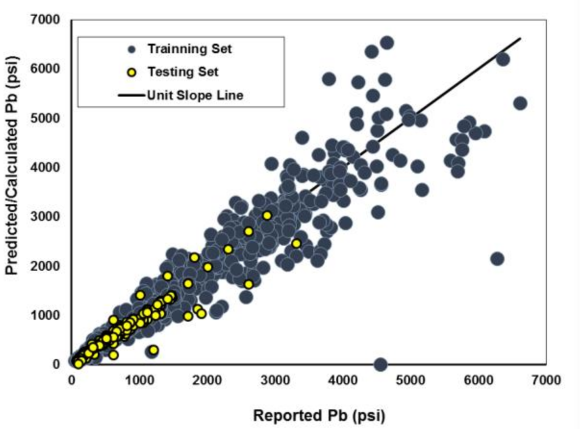

Fig. 5. Parity diagram for the estimated values by the new model and the literature-reported values of the bubble point pressure

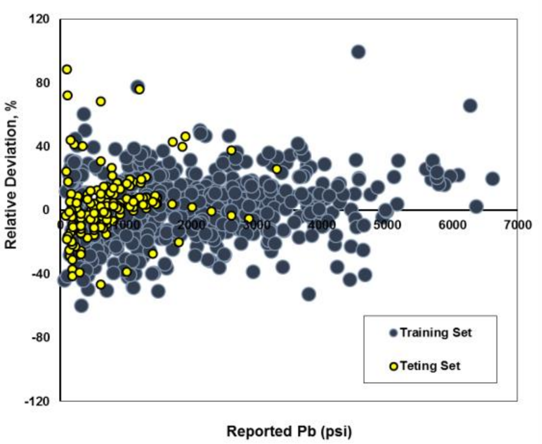

Fig. 6. Relative deviations plot of the bubble point pressure values obtained by the newly proposed model from the available dataset values

Table 3. Summarized statistical error parameters including AAPRE, APRE, RMSE and R^2 for the newly developed model for bubble point pressure as well as the studied correlations resulted from the actual data

Method	AAPRE, %	APRE, %	RMSE	R^2
Present study (Eq. (6))	15.3	2.23	468.11	0.88
Arabloo *et al.* model [14]	18.9	3.2	501.7	0.86
Al-Shammasi model [25]	20.8	−7.6	478.7	0.87
Lasater model [45]	25.5	−8.6	481.5	0.87
Dindoruk and Christman model [42]	25.6	−2.8	510.8	0.86
Valko and Mcain model [46]	25.7	0.1	584.2	0.82
Frashad *et al.* model [41]	25.9	−8.7	507.4	0.85
Velarde *et al.* model [47]	26.9	−2.1	596.6	0.82
Al-Marhoun model [36]	27.9	−4.5	550.8	0.84
Standing model [7]	28.7	−16.4	588.4	0.85
Vazquez and Beggs model [9]	32.3	−24.7	693.9	0.87
Kartoatmodjo and Schmidt model [26]	35.6	−27.2	819.7	0.84
Macary and El-Batanony model [27]	52.9	−38.3	596.4	0.85
Petrosky and Farshad model [13]	90.7	58.7	840	0.85
Yi model [48]	94	94	2 115.2	0.77
Omar and Todd model [35]	361.5	−356.0	11 387.4	0.03
Ikiensikimama and Ogboja model [49]	555.5	−555.5	5 175.9	0.40

Several of the most widely-utilized correlations, related to bubble point pressure property, were provided, including: Arabloo *et al.* [14] model, Al-Shammasi [25] model, Lasater [45] model, Dindoruk and Christman [42] model, Valko and Mcain [46] model, Frashad *et al.* [41] model, Velarde *et al.* [47] model, Al-Marhoun [36] model, Standing [7] model, Vazquez and Beggs [9] model, Kartoatmodjo and Schmidt [26] model, Macary and El-Batanony [27] model, Petrosky and Farshad [13] model, Yi [48] model, Omar and Todd [35] model, and Ikiensikimama and Ogboja [49] model. Table 3 summarizes the statistical error parameters calculated for the aforementioned correlations and the P_b model developed in this study.

As can be seen in the table, the P_b model has better performance in comparison with the reviewed methods. In order to better illustrate the comparison, AAPRE obtained for all methods is shown in Fig. 7. Figure 7 confirms that Eq. (6) is more capable, and accurate, than the other studied correlations for the estimation of bubble point pressure.

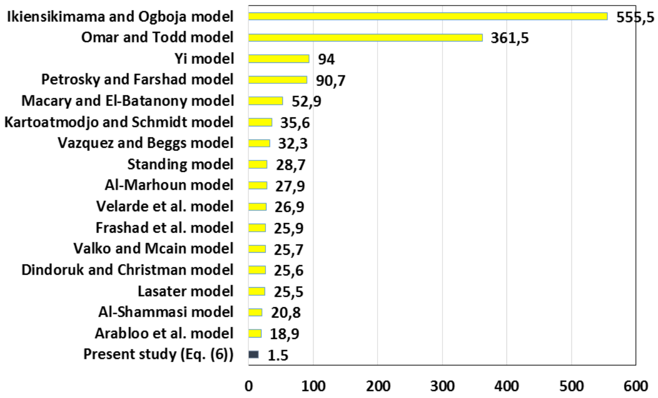

Fig. 7. Graphical comparison between the AAPRE values obtained by the new model developed in this study for the estimation of bubble point pressure as well as the corresponding studied correlations

The results and above discussion confirm that the models proposed in the present study for the evaluation of reservoir oil PVT properties, i.e., oil formation volume factor and bubble point pressure, are more reliable, and accurate than models currently available in the literature. In addition, they can have various potential applications in petroleum engineering, such as in the development of software.

4.2. Detection of outlier data points existing in the dataset

The accurate performance, and capability, of models are improved if outlier data point(s) existing in the datasets are detected and removed, because the results could be sensitive to such data points [50-53]. Hence, the evaluation of datasets, related to both oil formation volume factor and bubble point pressure, is a requisite, since uncertainties affect the accurate performance and capability of the GEP method.

The Leverage value statistics technique was applied for the detection of outlier data points existing in the datasets, associated with both oil formation volume factor and bubble point pressure properties [50,54]. As a result, the detection of the suspended data or outliers is undertaken by means of the Williams plot, based on the H values calculated [51-52]. For more information about the Leverage approach, a detailed definition related to the computational procedure, and the equations for this technique, can be found elsewhere [51-52].

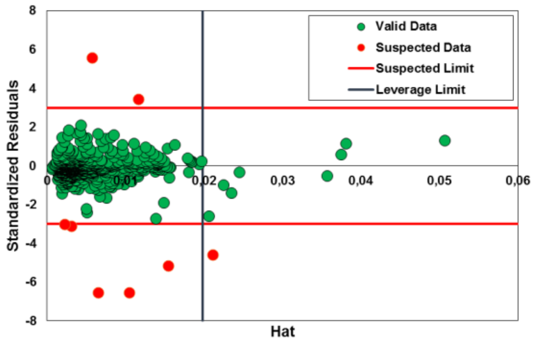

Fig. 8. Detection of the probable outlier and doubtful data of oil formation volume factor and the applicability domain of the proposed GEP model

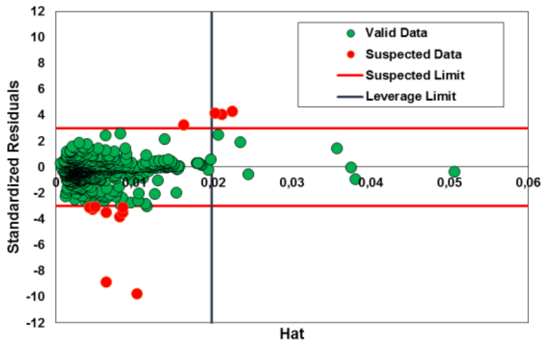

Fig. 9. Detection of the probable outlier and doubtful data of bubble point pressure and the applicability domain of the proposed GEP model

Figures 8 and 9 illustrate the Williams plots for the estimated values of oil formation volume factor and bubble point pressure, respectively, using the newly developed GEP models. As can be seen in these figures, the existence of the majority of data points in the ranges $0 \leq H \leq 0.01984$ and $-3 \leq R \leq 3$ for both of the models developed for oil formation volume factor and bubble point pressure, confirms that the applied models are statistically valid and correct in estimating these oil PVT properties. It should be noted that Figs. 8 and 9 show that there are 12 data points for the oil formation volume factor model, and 13 data points for the bubble point pressure model, compared to their corresponding actual data which are outside of the applicability domain of the GEP models, and could be viewed as outliers with doubtful values.

5. Conclusion

A novel application of the gene expression programming (GEP) method for the modeling of oil PVT properties is presented. A dataset comprising of approximately 755 laboratory PVT datasets, covering wide ranges of PVT experimental conditions from various geographical and geological regions was used for the oil formation volume factor and bubble point pressure of reservoir oil. The variables for the newly-developed models are gas gravity, oil API gravity, initial solution gas oil ratio, and reservoir temperature.

The findings indicate that the new GEP model for the calculation of oil formation volume factor has an AAPRE of 3.62% and a R2 = 0.93, and for bubble point pressure, it is 15.3% and 0.88, respectively.

In order to assess the performance and capability of the equations in estimating both oil formation volume factor and bubble point pressure properties, a comparative study was conducted, against the most widely-utilized correlations available in the open literature. The results obtained confirm that the models presented in this study are rapid to implement, accurate, and more reliable and capable than the available correlations, for the determination of both oil formation volume factor and bubble point pressure properties.

Acknowledgement

This work was based upon research supported by the South African Research Chairs Initiative of the Department of Science and Technology and National Research Foundation.

Nomenclature

GA	*genetic algorithm*
GP	*gene programming*
GEP	*gene expression programming*
ET	*expression tree*
GOR	*gas oil ratio*
OFVF	*oil formation volume factor*
T_R	*reservoir temperature*
P_b	*bubble point pressure*
B_{ob}	*oil formation volume factor at bubble point pressure*
R_{Si}	*initial solution gas oil ratio*
γ_g	*gas gravity*
API	*oil gravity*
R^2	*correlation coefficient*
RMSE	*root mean square errors*
APRE	*average percent relative error*
AAPRE	*average absolute percent relative error*

References

[1] De Ghetto G, and Villa M. Reliability analysis on PVT correlations. European Petroleum Conference 1994. Society of Petroleum Engineers.

[2] Khoukhi A. 2012. Hybrid soft computing systems for reservoir PVT properties prediction. Computers & Geosciences, 2012; 44: 109-119.

[3] Sutton RP, and Farshad F. Evaluation of empirically derived PVT properties for Gulf of Mexico crude oils. SPE Reservoir Engineering, 1990; 5(01): 79-86.

[4] El-Sebakhy EA. Data mining in forecasting PVT correlations of crude oil systems based on Type1 fuzzy logic inference systems. Computers & Geosciences, 2009; 35(9): 1817-1826.

[5] Saleh A, Mahgoub I, and Asaad Y. Evaluation of Empirically Derived PVT Properties for Egyptians Oils. Middle East Oil Show 1987.

[6] Alimadadi F, Fakhri A, Farooghi D, and Sadati H. Using a committee machine with artificial neural networks to predict PVT properties of Iran crude oil. SPE Reservoir Evaluation & Engineering, 2011; 14(01): 129-137.

[7] Standing M. A pressure-volume-temperature correlation for mixtures of California oils and gases. Drilling and Production Practice, 1947: 275-285.

[8] Katz DL. Prediction of the shrinkage of crude oils. Drilling and Production Practice, 1942: 137-147.

[9] Vazquez M, and Beggs HD. Correlations for fluid physical property prediction. Journal of Petroleum Technology, 1980; 32(06): 968-970.

[10] Glaso O. Generalized pressure-volume-temperature correlations. Journal of Petroleum Technology, 1980; 32(05): 785-795.

[11] Al-Marhoun MA. New Correlation for formation Volume Factor of oil and gas Mixtures. Journal of Canadian Petroleum Technology, 1992; 31(3): 22-26.

[12] Dokla ME, and Osman ME. Correlation of PVT properties for UAE crudes. SPE formation evaluation, 1992; 7(1): 41-46.

[13] Petrosky Jr, G, and Farshad F. Pressure-Volume-Temperature Correlations for Gulf of Mexico Crude Oils. SPE Reservoir Evaluation & Engineering, 1998; 1(05): 416-420.

[14] Arabloo M, Amooie M-A, Hemmati-Sarapardeh A, Ghazanfari M-H, and Mohammadi AH. Application of constrained multi-variable search methods for prediction of PVT properties of crude oil systems. Fluid Phase Equilibria, 2014; 363: 121-130.

[15] Boukadi F, Al-Alawi S, Al-Bemani A, and Al-Qassabi S. Establishing PVT correlations for Omani oils. Petroleum science and technology, 1999; 17(5-6): 637-662.

[16] Elsharkawy AM., Modeling the properties of crude oil and gas systems using RBF network, Asia Pacific oil & gas conference 1998, pp. 35-46.

[17] Gharbi RB, and Elsharkawy A. Neural Network Model for Estimating The PVT Properties of Middle East Crude Oils, Middle East Oil Show and Conference 1997. Society of Petroleum Engineers.

[18] Gharbi RB, and Elsharkawy AM. Universal Neural Network Based Model for Estimating The PVT Properties of Crude Oil Systems, SPE Asia Pacific Oil and Gas Conference and Exhibition 1997. Society of Petroleum Engineers.
[19] Ferreira, C., 2001. Gene expression programming: a new adaptive algorithm for solving problems. Complex Systems, 13(2): 87-129.
[20] McCain WD. The properties of petroleum fluids. PennWell Books 1990.
[21] Bandyopadhyay P, and Sharma,A. Development of a new semi analytical model for prediction of bubble point pressure of crude oils. Journal of Petroleum Science and Engineering, 2011; 78(3): 719-731.
[22] Obanijesu E, and Araromi D. Predicting bubble-point pressure and formation-volume factor of Nigerian crude oil system for environmental sustainability. Petroleum Science and Technology, 2008; 26(17): 1993-2008.
[23] Ostermann R, and Owolabi O. Correlations for the reservoir fluid properties of Alaskan crudes, SPE California Regional Meeting 1983. Society of Petroleum Engineers.
[24] Petrosky Jr G, and Farshad F. Pressure-volume-temperature correlations for Gulf of Mexico crude oils, SPE Annual Technical Conference and Exhibition 1993. Society of Petroleum Engineers.
[25] Al-Shammasi A. Bubble point pressure and oil formation volume factor correlations, SPE Middle East oil show & conference 1999, pp. 241-256.
[26] Kartoatmodjo T, and Schmidt Z. Large data bank improves crude physical property correlations. Oil and Gas Journal, 1994; 92(27).
[27] Macary S, and El-Batanoney M. Derivation of PVT correlations for the Gulf of Suez crude oils. Sekiyu Gakkai Shi, 1993; 36(6): 472-478.
[28] Mahmood MA, and Al-Marhoun MA. Evaluation of empirically derived< i> PVT</i> properties for Pakistani crude oils. Journal of Petroleum Science and Engineering, 1996; 16(4): 275-290.
[29] Kamari A, Bahadori A, Mohammadi AH, and Zendehboudi S. A reliable model for estimating a hydrate inhibitor injection rate. Journal of Natural Gas Science and Engineering, 2014; 32(23), 2837-2844.
[30] Kamari A, Gharagheizi F, Bahadori A, and Mohammadi AH. Determination of the equilibrated calcium carbonate (calcite) scaling in aqueous phase using a reliable approach. Journal of the Taiwan Institute of Chemical Engineers, 2014; 45: 1307-1313.
[31] Kamari A, Safirii A, and Mohammadi AH. Compositional Model for Estimating Asphaltene Precipitation Conditions in Live Reservoir Oil Systems. Journal of Dispersion Science and Technology, 2015; 36: 301-309.
[32] Moghadam JN, Salahshoor K, and Kharrat R. Introducing a new method for predicting PVT properties of Iranian crude oils by applying artificial neural networks. Petroleum Science and Technology, 2011; 29(10): 1066-1079.
[33] Obomanu D, and Okpobir, G. Correlating the PVT properties of Nigerian crudes. Journal of energy resources technology, 109(4): 214-217.
[34] Bello O, Reinicke K, and Patil P. Comparison of the performance of empirical models used for the prediction of the PVT properties of crude oils of the niger delta. Petroleum Science and Technology, 2008; 26(5): 593-609.
[35] Omar M, and Todd A. Development of new modified black oil correlations for Malaysian crudes, SPE Asia Pacific oil and gas conference 1993, Society of Petroleum Engineers.
[36] Al-Marhoun MA. PVT correlations for Middle East crude oils. Journal of Petroleum Technology, 1988; 40(05): 650-666.
[37] Mitchell, M., 1998. An introduction to genetic algorithms (complex adaptive systems).
[38] Ferreira C. Gene Expression Programming: Mathematical Modeling by an Artificial Intelligence (Studies in Computational Intelligence). Springer-Verlag New York 2006, Inc., Secaucus, NJ.
[39] Teodorescu L, and Sherwood D. High energy physics event selection with gene expression programming. Computer Physics Communications, 2008; 178(6): 409-419.
[40] Alavi AH, Gandomi,AH, Mousavi M, and Mollahasani A. High-Precision Modeling of Uplift Capacity of Suction. Geomechanics and Engineering, 2010; 2: 253-280.
[41] Frashad F, LeBlanc J, Garber J, and Osorio J. Empirical PVT correlations for Colombian crude oils, SPE Latin America/Caribbean petroleum engineering conference 1996. Society of Petroleum Engineers, Port-of-Spain, Trinidad.
[42] Dindoruk B, and Christman PG. PVT properties and viscosity correlations for Gulf of Mexico oils. SPE Reservoir Evaluation & Engineering, 2004; 7(06): 427-437.
[43] Abdul-Majeed GH, Salman NH, and Scarth B. An empirical correlation for oil FVF prediction. Journal of Canadian Petroleum Technology, 1988; 27(06).

[44] Labedi RM. Use of Production Data to Estimate the Saturation Pressure Solution Gor and Chemical Composition of Reservoir Fluids, SPE Latin America Petroleum Engineering Conference 1990. Society of Petroleum Engineers, Brazil.

[45] Lasater J. Bubble point pressure correlation. J. of Petroleum Technology, 1958; 10(05): 65-67.

[46] Valko P, and McCain Jr W. Reservoir oil bubblepoint pressures revisited; solution gas–oil ratios and surface gas specific gravities. Journal of Petroleum Science and Engineering, 2003; 37(3): 153-169.

[47] Velarde J, Blasingame T, and McCain Jr W. Correlation of Black Oil Properties At Pressures Below Bubble Point Pressure-A New Approach, Annual Technical Meeting. Petroleum Society of Canada 1997.

[48] Yi X. Using wellhead sampling data to predict reservoir saturation pressure, SPE Permian Basin Oil and Gas Recovery Conference 2000, Society of Petroleum Engineers.

[49] Ikiensikimama SS, and Ogboja O. New bubblepoint pressure empirical PVT correlation, Nigeria Annual International Conference and Exhibition 2009. Society of Petroleum Engineers.

[50] Gramatica P. Principles of QSAR models validation: internal and external. QSAR & combinatorial science, 2007; 26(5): 694-701.

[51] Mohammadi AH, Eslamimanesh A, Gharagheizi F, and Richon D. A novel method for evaluation of asphaltene precipitation titration data. Chemical Engineering Science, 2012; 78: 181-185.

[52] Mohammadi AH, Gharagheizi F, Eslamimanesh A, and Richon D. Evaluation of experimental data for wax and diamondoids solubility in gaseous systems. Chemical Engineering Science, 2012; 81: 1-7.

[53] Rousseeuw PJ, and Leroy AM. Robust Regression And Outlier Detection, John Wiley & Sons, Inc. New York, NY, USA 2005, ISBN: 978-0-471-48855-2

[54] Goodall CR. 13 Computation using the QR decomposition. Handbook of Statistics, 1993; 9: 467-508.

To whom correspondence should be addressed: Professor Amir H. Mohammadi, E-mail:amir_h_mohammadi@yahoo.com and Professor Deresh Ramjugernath, Thermodynamics Research Unit, School of Engineering, University of Kwa-Zulu-Natal, Howard College Campus, King George V Avenue, Durban 4041, South Africa, E-mail ramjuger@ukzn.ac.za

Petroleum and Coal

Article **Open Access**

MODELING OF ODOR SUBSTANCE CONCENTRATION IN A CITY TRANSMISSION PIPELINE VIA MERGING GMDH NEURAL NETWORK AND GENETIC ALGORITHM

Farshid Zare'i [1], Allahyar Daghbandan [1], Sajjad Rezaei [2], Amir H. Mohammadi [3]

[1] *Department of Chemical Engineering, University of Guilan, Rasht, Iran*
[2] *Department of Chemical Engineering, Tarbiat Modares University, Tehran, Iran*
[3] *Discipline of Chemical Engineering, School of Engineering, University of KwaZulu-Natal, Howard College Campus, King George V Avenue, Durban 4041, South Africa*

Received April 19, 2019; Accepted July 1, 2019

Abstract

After production and transmission, natural gas is odorized by the injection of mercaptan substances due to safety issues. Mercaptan concentration distribution in transmission pipelines is sometimes non-uniform which fails to meet safety standards of gas companies. Thus, contributing factors including gas flow velocity, distance of city gas station (CGS), pressure, temperature and mass transfer coefficient in mercaptan concentration distribution were determined to attain a uniform distribution. To obtain the odor substance concentration, first, olfactometry operation was conducted at 147 different points in a pipeline with a length of 72 km, faced with non-uniform odor distribution. Then, experimental and computational data were modeled by merging the group method data handling (GMDH) and genetic algorithm with the aim of obtaining efficient polynomial correlation. The modeling results indicate that gas flow velocity and distance from injection points are among the most effective parameters on odorant distribution. Based on the obtained results, the odor substance concentration can be adjusted to the investigated pipeline with the aim of reaching safety standards.

Keywords*: Odor substance; Concentration distribution; Mercaptan; Genetic algorithm; Neural network.*

1. Introduction

In all chemical plants, there are strict regulations regarding health, safety and environment which are referred to as HSE. These regulations also involve gas distribution networks, and since these networks are generally located in residential areas, the odorization process is vitally important. Odorants with low molecular weights in the forms of synthetic chemicals, such as mercaptans and sulfides with molecular weights of about 60 mg/mol, have been used after the Second World War [1].

The need for a gassy odor was heightened with the development of chemical industry and also the hydrocracking units across the world [2]. The minimum natural gas amount that leads to explosion is a concentration between 0.5% and 4.5% which is defined as explosion threshold. Therefore, the minimum odorants should be a specific amount (the gas concentration should be 1% in air) so that the gas can be easily smelled [1]. The different chemical combinations would be selected based on physical and chemical conditions of flow gas and geographical conditions in order to achieve desirable odorant properties and optimize the odorization process performance [1,3]. A study has previously shown that higher operating pressures could increase the possibility of *tert*-butyl mercaptan (TBM) absorption on iron oxide resulting in an increase and a decrease in odor concentration. In addition, low temperature could cause TBM to fade from gas flow [4]. By investigating the fading smell parameters in gas distribution systems, Saadatmand *et al.* [5] found that the gas average temperature rate, gas pressure and flow rate velocity are effective on odor substances concentration distribution. Moreover, according to a study conducted by National Iranian Gas Company (NIGC), odorants adding and fading factors are under the influence of two parameters, a- odorants oxidation in pipelines and b- sedimentation of odor substances during transportation via pipelines. In a study, it was indicated that odorants transfer rate in gas flow depends on injection point distance (odorizer station) and odorants carrying velocity in transfer lines [6].

Group method of data handling (GMDH) has several applications such as modeling the complicated systems, forecasting, data mining of multi-variable processes, pattern recognition, diagnostics and clusterization of data sample [7-12]. Additionally, the forecast about systems behavior which is used in engineering, medicine and economics show successful results [8,11,14]. The GMDH neural networks are created by utility of network structures for GMDH algorithm, and hence, have significant effect on its software and conceptual implementation. Therefore, the use of neural self-organized networks in GMDH algorithm leads to success in different scientific areas such as engineering, science, and economics.

According to the NIGC's HSE standards, odorants concentrations must be in the range of 10 to 20 mg/m^3 for city gas pipelines [15]. The concentration non-uniformity has been observed in some transfer pipelines. This non-uniformity causes two major problems: 1- Odorants high concentrations may lead to environmental damages, and 2- the low concentrations of odorants can lead to a lack of odorants detection when gas leakage occurs (the most important scope of odorization). The correlation between odor substances and concentration distribution factors must be determined in order to monitor the odorant behavior integration of odor substance concentration and achieving determined standards.

The main scope of this study was predicting the odor substance behavior in a pipeline located in northern part of Iran with a length of 72 km, which faced the lack of uniform distribution of odor substances, by merging GMDH neural network and genetic algorithm. Moreover, the effect of different parameters were compared in a big scale of length for a period of one year, and the most significant parameters of inappropriate distribution in pipelines were established by neural network.

2. Material and method

2.1. GMDH neural network

Among different identification algorithms, group method of data handling (GMDH) is a self-organized system in which complicated models are formed step by step based on multiple input initial data and evolved output. The GMDH was introduced by Ivakhneko [13] as a multi-analysis method for modeling and identifying complicated and developed systems. The GMDH can be implemented in modeling without technical information about its algorithm. The main scope of GMDH is to establish an analytical function based on feed forward network, which each of its element is a second-degree transfer function and its coefficients are obtained by recursive method.

The GMDH neural network is a unidirectional network made up of several layers including several neurons with a similar structure of two inputs and one output. The input variables of each neuron, output, or estimated values are selected by each two neurons and are placed in previous layer, so that the main system is remodeled for each N output.

Generally, the systems identification problems are presented so that the unknown function, f, with variables {(xip, xiq), i= 1,2,3,…,N} and corresponding values, yi, such as {(yi), i= 1,2,3,…,N} are established. The f function can be estimated so that the sum of error squares for a sample of input and output data in equation (1) are minimized.

$$\sum_{k=1}^{N}\left[\left(\hat{f}(x_{ki},x_{kj})-y_k\right)^2\right]\rightarrow Min \tag{1}$$

It might be linear or non-linear of input variables in equation (1). The map established between input and output variables by GMDH neural network, is a non-linear function as following [16-17]:

$$\hat{y}=a_0+\sum_{i=1}^{m}a_ix_i+\sum_{i=1}^{m}\sum_{j=1}^{m}a_{ij}x_ix_j+\sum_{i=1}^{m}\sum_{j=1}^{m}\sum_{k=1}^{m}a_{ijk}x_ix_jx_k+\cdots \tag{2}$$

The equation (2) is known as Volterra series functions. The GMDH algorithm is based on decomposition of Volterra series functions to two variables second-degree polynomial. In fact, the scope of this algorithm is finding unknown coefficients (a) in Volterra series functions. Therefore, these coefficients are distributed in decomposed factors by decomposing to two variables second-degree polynomial, so unknown coefficients in this second-degree polynomial are regulated according to equation (3):

$$y_i = f\left(x_{ip},x_{iq}\right) = a_0 + a_1x_i + a_2a_i + a_3x_i{}^2 + a_4x_i{}^2 + a_5x_ix_i \tag{3}$$

The y function has 6 variables, so they must be adjusted so that the desired output {(yi), i= 1,2,3,…,N} would be established for all two variables samples depending on system {(xip, xiq), i= 1,2,3,…,N}. For this reason, the G function will be based on minimum square error according to equation (4) [8].

$$\sum_{k=1}^{N}\left[\left(G\left(x_{ki},x_{kj}\right)-y_k\right)^2\right] \rightarrow Min \tag{4}$$

The equation (5) can be shown as matrix (8) by conditions dominated on problem:

$$Aa = Y \tag{5}$$

$$a = \{a_0,a_1,a_2,a_3,a_4,a_5\}^T \tag{6}$$

$$a = \{y_1,y_2,y_3,\dots,y_N\} \tag{7}$$

$$A = \begin{bmatrix} 1 & x_{1p} & x_{1q} & x_{1p}^2 & x_{1q}^2 & x_{1p}^2x_{1q}^2 \\ 1 & x_{2p} & x_{2q} & x_{2p}^2 & x_{2q}^2 & x_{2p}^2x_{2q}^2 \\ \dots & \dots & \dots & \dots & \dots & \dots \\ 1 & x_{Np} & x_{Nq} & x_{Np}^2 & x_{Nq}^2 & x_{Np}^2x_{Nq}^2 \end{bmatrix} \tag{8}$$

It is necessary to calculate non-square inverse matrix A for solving the equation. So the orthogonal equations solving method is used for calculating non-square inverse matrix A. Therefore, the unknown coefficient vector can be calculated by equation (9).

$$a = (A^T A)^{\pm 1} A^T Y \tag{9}$$

The genetic algorithm as an accidental method in neural network training and linking between the coefficients, has a performance better than methods based on traditional gradient [11].

In most GMDH neural networks, neurons in each layer are connected to same layer's neuron [18]. The encryption scheme in generalizing the neural network GMDH (GS-GMDH) has the ability to express different lengths and sizes in neural networks [12].

2.2. Effective parameters in odor substance concentration

2.2.1. Odor substance oxidation in pipeline

The thiol compounds oxidation is presented by equation (10). The short chains of mercaptans lead to their oxidation in this chemical interaction. The adsorption and desorption power of odorant by gas pipes depends on molecular weight and odor substances structure [19].

$$\mathrm{2R-SH+O_2 \rightarrow R-S-S-R+H_2O} \tag{10}$$

The interaction between odorant molecules and pipelines internal surfaces is shown by equations (11) and (12), in which some odorants will be adsorbed on the internal parts of pipelines. This sweep is continued to achieve a counterpoise, so that the surface adsorption rate and return odorant rate to gas phase are constant. The organosulfurs are more prone to adsorption onto pipe wall in gas flow [19].

$$\mathrm{4Fe+3O_2 \rightarrow 2Fe_2O_3(s)} \tag{11}$$

$$\mathrm{2Fe_2O_3(s)+2RSH(S) \rightarrow RSSR+Fe_2O_3(s)+H_2O} \tag{12}$$

The odorants transfers are based on gas flow velocity in pipelines. This transfer is different based on consumers' consumption and changes in gas flow rates [6].

2.2.2. Modeling of odorant flocculation evaporation in pipeline and its phase change from liquid to gas/vapor

In this model, it is assumed that the odor substances are transported due to high velocity of gas flow and settled in the path due to a decrease in the gas flow velocity, and high molecular weight of mercaptans (about 60 mg/mol) than typical composition of natural gas (about 17.8

mg/mol). If the transfer level is a fraction of the pipe area, which the odorant is settled in it, the odor substance will evaporate in contact with flow gas. Finally, it can be said that $C_A(Z, V, Kc\ (sc, sh))$ is calculated in investigated lines. This model has been investigated with the assumption of the rapid reaction in gas and pipe interface $C_{Ai}=0$, lack of moment interaction, constant mass transfer level at the moment, very low mass transfer between gas mixture components and odor substance concentration in the place of injection C_A, mass transfer coefficient K_d, sectional area of the pipe A, odorant mass accumulation m. Odorant evaporation modeling is shown in Figure 1 and mass transfer equation was solved by equation 13 [6].

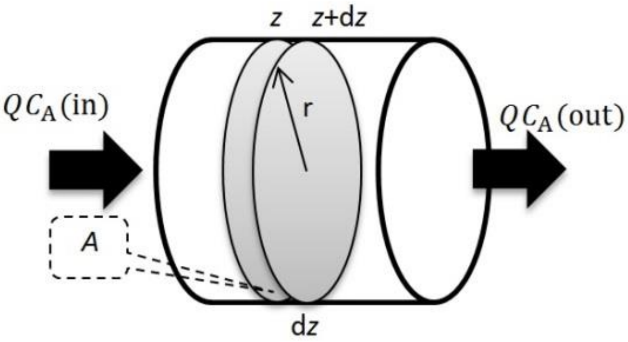

Figure 1. Mass transfer equation in a cross section of pipe with odorant evaporation modeling

$$QC_{A\,in}|_Z - QC_{Aout}|_{Z+\Delta Z} = m = K_d A(C_{Ai} - C_A) \xrightarrow{A=a\Pi Ddz} ln\frac{C_{Ai} - C_{A0}}{C_{Ai} - C_A} = \left[\left(\frac{4\alpha K_d}{VD}\right)Z\right] \quad (13)$$

3. Theory and calculations

After extraction and refining for subscribers' consumption, the natural gas is transferred by City Gas Station (CNG). The odor substance injection place is shown in Figure 2 by red circle, which the gas is odorized for subscribers' safety and identifying gas leakage; then the odor gas is obtained to the subscribers by distribution lines.

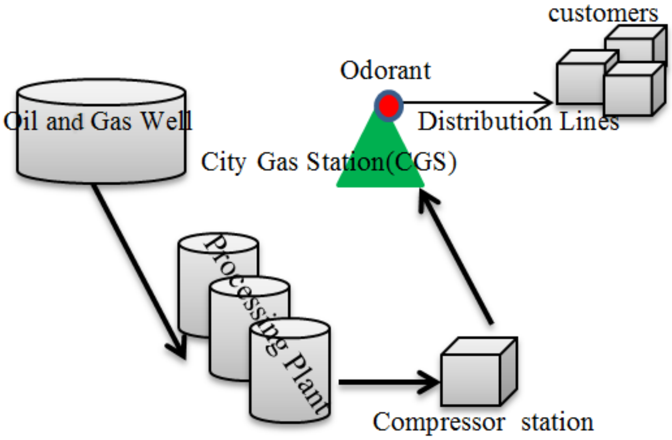

Figure 2. The schematic diagram of natural gas distribution

The gas distribution pipeline, located in a region of the northern part of Iran with a length of 74.4 (km) which was faced with non-uniform mercaptan concentration, is schematically illustrated in Figure 3. This pipeline is between two CGS called feed stations 1 and 2 that are illustrated by green triangles. The electrical pump type odorizer is placed in order for the injecting mercaptan and providing odorant in transfer line. The CGS and TBS stations (gray square) are connected to each other by black lines as pipe; the nominal capacity of the station name is shown at the top of its name. Totally, the investigated line includes 18 stations (12 inches lines are used in stations 4 to 8 and the 16 inches lines are used in other lines). The gas reached to stations in path from both sides of CGS station (indicated by red flash).

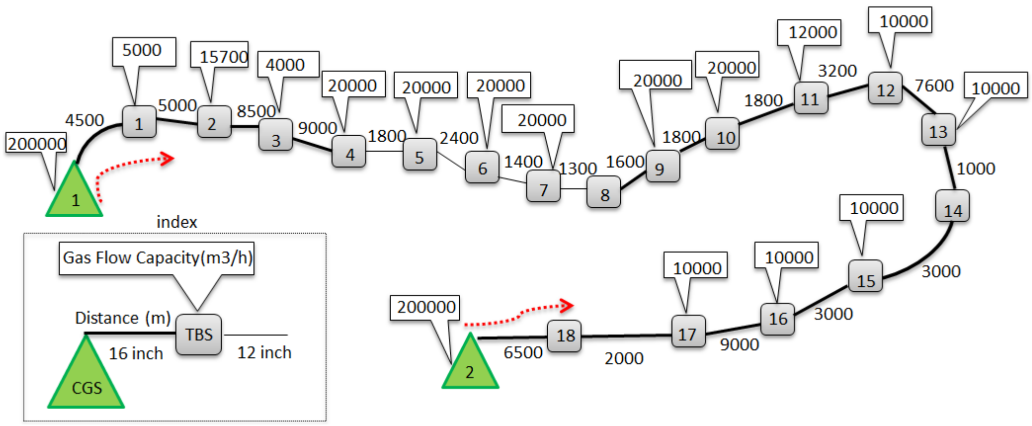

Figure 3. Investigated Nod map in the pipeline

Different points are selected based on possible velocity change in pipe (around TBS station) and different distances to injection point in order to investigate and measure odor substance concentration by an odor handy device. At the beginning of the path in CGS stations, the input temperature and pressure are measured by gage and flow meter, respectively. The mentioned data are entered with gas mixture percentage, distance of measured concentration point (point 2 or exit pipe (i+1)), the pipe effective coefficient (0.9), and pipe diameter as input to system. The velocity , temperature ,density ,reduced pressure, mass transfer coefficient in gas lines, pressure at point 2, Sherwood numbers, Schmidt numbers, Reynolds, fraction co-efficient, mass transfer coefficient at the exit are calculated after entering inputs and using equations of Appendix A (Figure 4).

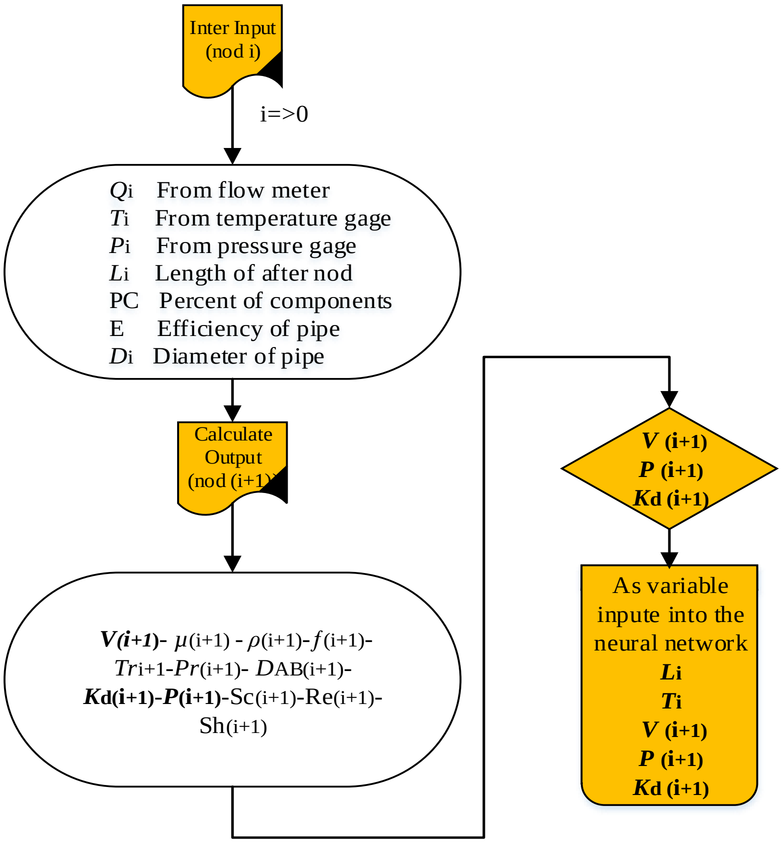

Figure 4. Computation steps of input data to neural network

According to effective parameters on gas concentration distribution in section 2.2, the flow gas velocity, pressure, and mass transfer coefficient variables in measured concentration points with gas average temperature and distance to odor substance variables are effective parameters on odorization. The calculations are done in all 148 investigated systems by entering inputs and calculating outputs, so the input data to neural network is formed. Data are gathered during a year from the hot season (low gas consumption), June and September, to the cold season (high gas consumption), November, December and January. A set of these data is used as input data set to neural network.

4. Results and discussion

Figure 5 presents the measured concentrations of odor substances at different gas temperatures and velocities. Gas temperatures indicate the temperature of the pipeline. The higher gas temperature indicates the lower gas consumption and vice versa. The highest concentration is measured at 293 K, which is in the range of gas velocity in pipeline from 0.58 to 1.59 m/s, which seems to be a low velocity. Moreover, it can be seen that, at low temperatures of 279 and 283 K, the distribution of mercaptan concentration is roughly uniform. This suggests that at velocities between 1.77 and 4.7 m/s, a lower amount of odorants sedimentation through the pipeline meet NIGC standards.

Figure 6 depicts the concentrations of odorants at various temperatures and distances from the injection point, CGS. The highest odorants concentrations are measured at 291 K. At a distance of about 6.8 km from the injection site, mercaptan concentration peaks. This is due to the TBS, which transmits a large volume of gas to the city pipelines reducing its velocity, and increases the time for sedimentation of odor substance. At lower temperatures the effect of distance is insignificant.

According to the influence hypothesis in Section 2.2.b, the odorants mass transfer and its conversion from liquid to gas/vapor is of importance. The distribution of the odorants mass transfer coefficients at different gas concentrations are shown in Figure 7. These data were calculated from the liquid to gas mass transfer equations. Sherwood and Reynolds numbers, diffusion coefficients and other parameters in Appendix A are calculated in order to obtain mass transfer coefficients. This diagram shows that the temperature has a reverse relation with the rate of mass transfer of odor substances.

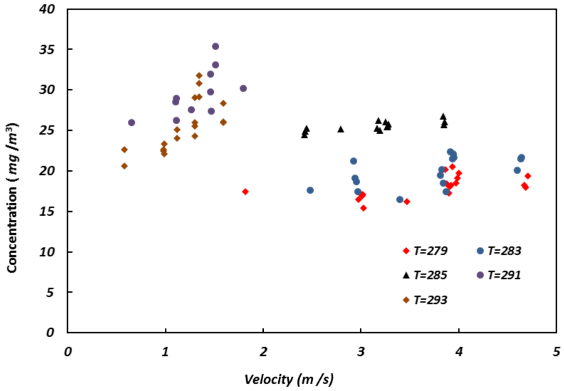

Figure 5. Mercaptan concentrations at various gas temperatures and velocities at real conditions

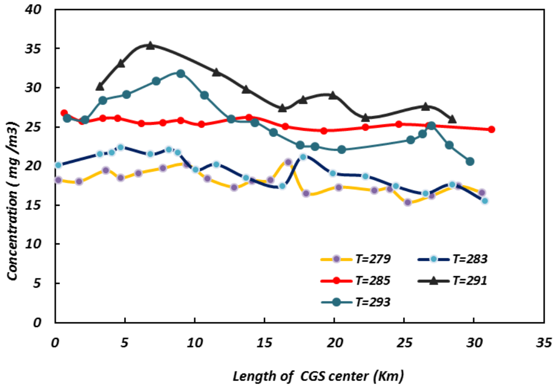

Figure 6. Mercaptan concentrations at different temperatures and distances from CGS.

In Table 1, the maximum, minimum and average of training data (103) and experiment data (45) are indicated.

The genetic parameters, according to Figure 8, are considered in optimization stage for investigated systems. The network forecasting is done in 3 layers to obtain output model.

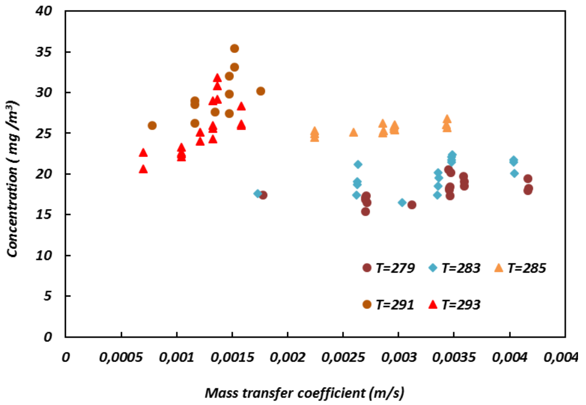

Figure 7. Calculated mercaptan mass transfer coefficients for the conversion from liquid to gas/vapor at various gas concentration

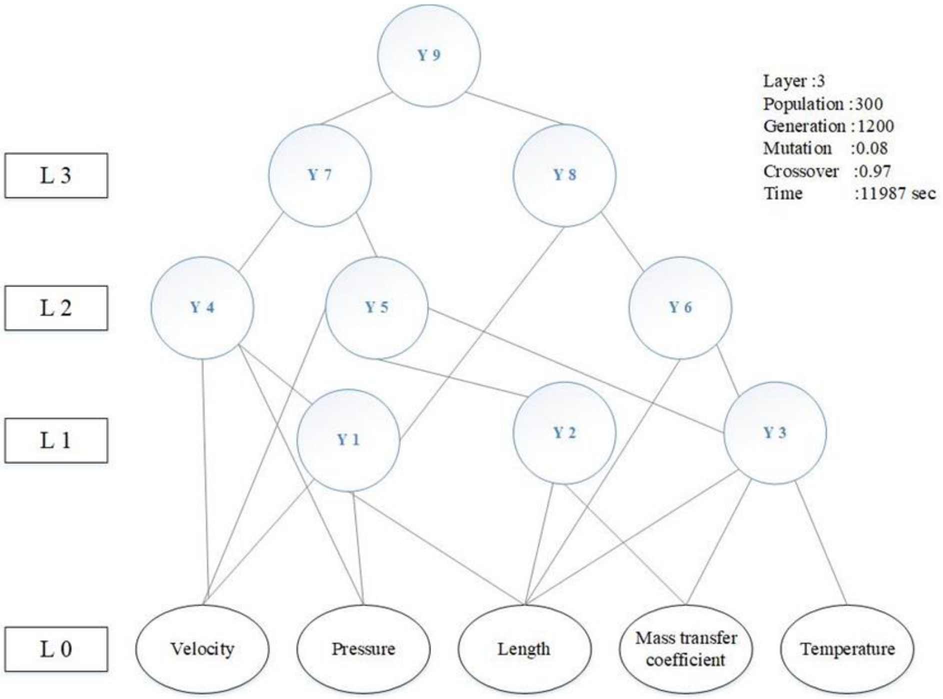

Figure 8. The proposed structure of the GMDH Multi-purpose neural network for estimation of the concentration of odor substance

Table 1. Descriptive statistics of variables used to develop the GMDH

Variable		Train (103 data set)			Test (44 data test)		
		Maximum	Mean	Minimum	Maximum	Mean	Minimum
Input	*V*(*m/s*)	4.703064	2.01229	0.039014	3.999188	2.057561	0.107756
	P(kPa)	1825.125	1794.037	1651.777	1823.673	1788.2	1655.625
	L(km)	39.99542	16.0355	0.214043	0.399	10.868	23.509
	*K*c(m/s)	0.004267	0.001829	0	0.003658	0.001829	0.000305
	T(K)	293.15	286.14	279.15	293.15	285.7722	279.15
Output	*C*A(mol/L)	47.200	23.548	14.000	40.8	23.19027	14.7

The evolutional scheme of neural network structure is used by genetic algorithm with the purpose of designing GMDH network. The genetic algorithm is used for producing initial population, which leads to producing new chromosome. Among these chromosomes the one with less training error and better forecast is selected in order to evaluate the power of obtained model. The error values are indicated in Table 2, which show that the model is reliable (obtained using the equations in Appendix B). After selecting the best chromosome for forecasting model, its polynomial graph is formed based on Table 3 that its value is calculated based on genetic data. The data are divided in two groups in Figure 9 that training data are validated by experimental data, and it is shown that results are acceptable according to formed model.

Table 2. Statistical results for odor substance concentration

	RRSE	AADP (%)	NRMSE	RMSE	MSE	R^2
train	1.219	10.553	0.1107	3.676	13.5157	0.9773
test	1.683	11.561	0.1789	4.671	21.825	0.9618
total	0.367	10.894	0.1204	3.999	15.996	0.9727

Table 3. Model multi-substant equal GMDH (Volttera Series) for estimating odor substant concentration

Basic regression polynomial (Volttera Series)

Y=Y9(Y8(Y6(Y3(5,3),3),Y1(3,2)),Y7(Y5(Y3(5,3),Y2(4,3)),Y4(Y1,1)))

Yi(zj,zk)=a0(i)+a1(i) zj+a2(i)zk+a3(i) zjzj+a4(i) zkzk+a5(i)zjzk

i	a0	a1	a2	a3	a4	a5
1	8.875754	0.475174	1.328846	-0.02348	-0.0067	-0.01743
2	0.191467	-2.88694	36.28694	0.011272	-0.07802	-0.13145
3	47.32473	-0.14197	-4532.79	-0.03862	179084.6	59.23848
4	10.04962	0.191445	-0.14456	0.015436	0.000573	0.006022
5	-15.9467	1.845944	2.108465	0.070071	-0.00816	-0.14609
6	5.664134	-0.06307	0.568644	-0.0478	-0.0707	0.13018
7	22.81855	-0.68887	-0.20673	-0.01632	-0.02877	0.083305
8	22.81855	-0.68887	-0.20673	-0.01632	-0.02877	0.083305
9	-9.20191	4.517381	-2.59854	0.026331	0.161005	-0.20983

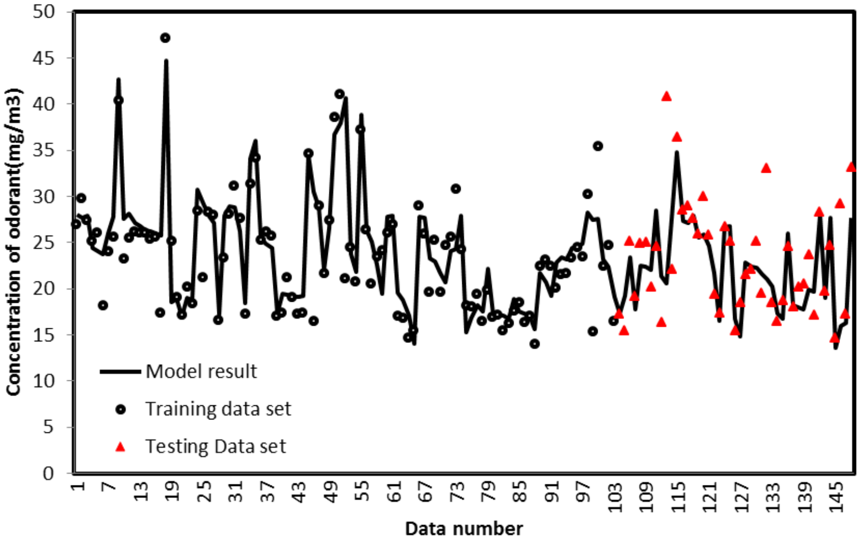

Figure 9. Odor substance amount graph based on the data number. (●) Training data. (▲) Testing data. (—) Data model by combining neural network and genetic algorithm

5. Conclusion

This study was conducted in order to evaluate and forecast the odorization process by the GMDH network. Forecasting results, based on relationship among neurons, show that the most effective parameters on mercaptan concentration distribution are distance from injection point and gas flow velocity. The most significant part of the study indicates that velocity reduction beside TBS stations due to catching a part of flow gas volume (subscribers' consumption) leads to non-uniformity of odor substance concentration, which can be explained by modeling the odor substance flocculation evaporation on pipeline ground. This phenomenon is increased in the hot seasons due to a sharp drop in gas velocity. The selection of odorizers considering stations distance, flow gas capacity, and number of stations must be attained due to non-uniform distribution of odor substances. It was also observed that the problem points in mercaptan distribution path can be identified and increasing or decreasing odorization and achieved safety can be helped by forecasting. Studying the gas pipeline in the region and different temperatures during years can have a significant role in more accurate evaluation of odor substance behavior forecast.

Acknowledgment

The technical support from National Iranian Gas Company is greatly appreciated by the authors.

Nomenclature

ρ	*density(g/m^3)*	P_{pr}	*sub-critical pressure(kPa)*
m	*mass and weight(g)*	Q	*volume flow(m^3/s)*
v	*volume(m^3)*	u	*velocity (m/s)*
G	*specific gravity*	Re	*Reynolds number*
M	*molecular weight(g/mol)*	D	*diameter(cm)*
ν	*viscosity(m^2/s)*	C_A	*odor substance concentration(mol/L)*
T	*temperature(K)*	D_{AB}	*diffusion coefficient(cm^3/s)*
P	*pressure(kPa)*	V_A	*atomic volume per molecule(m^3/kg.atm)*
T_r	*reduced temperature*	Sc	*Schmidt number*
P_r	*reduced pressure*	Sh	*Sherwood number*
T_c	*critical temperature*	K_d	*mass transfer coefficient(m/s)*
P_c	*critical pressure*	E	*efficiency pipeline*
Z	*compressibility factor*	Le	*length of the section(km)*
T_{pr}	*sub-critical temperature(K)&(Rankin)*		

Appendix A. Relations used for calculations in pipelines

$$Q = 737\mathrm{E}\left(\frac{\mathrm{T_b}}{\mathrm{P_b}}\right)^{1.02}\left(\frac{{P_1}^2 - \mathrm{e}^s {P_2}^2}{\mathrm{G}^{0.961} T_f LeZ}\right)^{0.51} D^{2.53} \tag{A .1}$$

$$u = 0.002122\left(\frac{Q_b}{D^2}\right)\left(\frac{P_b}{T_b}\right)\left(\frac{ZT}{P}\right) \tag{A .2}$$

$$P_{\mathrm{avg}} = \frac{2}{3}(P_1 + P_2 - \frac{P_1 \times P_2}{P_1 + P_2}) \tag{A .3}$$

$$\begin{gathered} \mu_g = 10^{-4} K\, exp\left(X\left(\frac{\rho_g}{62.4}\right)^Y\right) \\ K = \frac{(9.4 + 0.02 M_a) T^{1.5}}{209 + 19 M_a + T} \\ X = 3.5 + \frac{986}{T} + 0.01 M_a \\ Y = 2.4 - 0.2X \end{gathered} \tag{A .4}$$

$$\mathrm{T_r} = \frac{\mathrm{T}}{\mathrm{T_c}} \tag{A .5}$$

$$\mathrm{P_r} = \frac{P}{P_c} \tag{A .6}$$

$$\mathrm{T_{pr}} = \frac{T}{T_{\mathrm{c}}} \tag{A .7}$$

$$\mathrm{P_{pr}} = \frac{P}{P_{\mathrm{c}}} \tag{A .8}$$

$$T_{\mathrm{pc}} = \Sigma \mathrm{y_i} T_{\mathrm{c}} \tag{A .9}$$

$$P_{\mathrm{pc}} = \Sigma \mathrm{y_i P_c} \tag{A.10}$$

$$Z = \frac{1}{(\left[1 + \frac{\big(\big(P_{avg} \times 344400 \times (10)^{1.785\mathrm{G}}\big)}{{T_f}^{3.825}}\right])} \tag{A .11}$$

$$D_{AB} = \frac{.001\, T^{1.75}}{P\left[(\sum V_A)^{\frac{1}{3}} + (\sum V_B)^{\frac{1}{3}}\right]}(\frac{1}{M_A} + \frac{1}{M_B})^{\frac{1}{2}} \tag{A .12}$$

$$\frac{D_{AB(1)}}{D_{AB(2)}} = \left[\frac{T_1}{T_2}\right]^{\frac{3}{2}}\left[\frac{P_2}{P_1}\right] \tag{A .13}$$

$$T_c' = \sum x_i T_{ci} \tag{A .14}$$

$$P_c' = \sum x_i P_{ci} \tag{A .15}$$

$$Sc = \frac{\mu}{\rho \mathrm{D_{AB}}} \tag{A .16}$$

$$\begin{gathered} 0.5 \le \mathrm{SC} \le 2000 \\ 3000 \le \mathrm{Re_d} \le 5 \times 10^6 \\ \mathrm{f} = [1.82 \log(\mathrm{Re}) - 1.64]^{-2} \end{gathered} \tag{A .17}$$

$$K_{\mathrm{d}} = \frac{\mathrm{Sh\, D_{AB}}}{\mathrm{d}} \tag{A .18}$$

Appendix B. Statistical analysis

1- Mean Squared Error

$$\text{MSN} = \frac{1}{n}\sum_{i=1}^{n}\left(Y_{(i,exp)} - Y_{(i,model)}\right)^2 \qquad \text{(B .1)}$$

2-Root-Mean Squared Error

$$\text{RMSE} = \sqrt{\frac{1}{n}\sum_{i=1}^{n}\left(Y_{(i,exp)} - Y_{(i,model)}\right)^2} \qquad \text{(B .2)}$$

3- Normalized Root-Mean Squared Error

$$\text{NRMSE} = \left[\frac{1}{n}\sum_{i=1}^{n}\left(Y_{(i,exp)} - Y_{(i,model)}\right)^2\right]^{0.5} \Big/ \left(Y_{(i,exp)} - Y_{(i,model)}\right) \qquad \text{(B . 3)}$$

4-Average Absolute Deviation Percent

$$\text{AADP}(\%) = \frac{100}{n}\sum_{i=1}^{n}\left|\left(Y_{(i,model)}/Y_{(i,exp)}\right) - 1\right| \qquad \text{(B . 4)}$$

5-Root relative-squared error

$$\text{RRSE} = \sum_{i=1}^{n}\sqrt{\left(\frac{\left(\text{Y}_{(\text{i,exp})} - \text{Y}_{(\text{i,model})}\right)^2}{\left(\text{Y}_{(\text{i,model})} - \bar{\text{Y}}\right)^2}\right)} \qquad \text{(B . 5)}$$

6-Coefficient of Determination

$$\text{R}^2 = 1 - \left[\sum_{i=1}^{n}\left(Y_{(i,exp)} - Y_{(i,model)}\right)^2 \Big/ \sum_{i=1}^{n}\left(Y_{(i,exp)}\right)^2\right] \qquad \text{(B . 6)}$$

References

[1] Tenkrat D, Prokes O, Hlincik T. Natural gas odorization. INTECH Open Access Publisher 2010:87-104, DOI: 10.5772/9825.

[2] Parrott KS. Principles of natural gas odorization. International School of Hydrocarbon Measurement, May 2004.

[3] Usher MJ. Odor fade–Possible Causes and Remedies. CSA Gas Measurement School, London 1999.

[4] Andreen BH, Kroencke RL. Stability of mercaptans under gas distribution systems conditions. A.G.A. Operating Section Production Conference 1964.

[5] Saadatmand M, Foroughi H, Dai T, Misra T, Bensabath T, Farnood R. Odor fading in natural gas distribution systems. Process Safety and Environmental Protection, 2015; 94, 131-139.

[6] Talaie M, Shirazi MZ, Gholi Zari N. Investigation on Factors Influencing Non-Uniform Distribution of Mercaptan in Ahvaz Gas Distribution Network and The Applied Remedy for Uniform Mercaptan Distribution, in: Company, N.I.G. (Ed.), Isfahan University 2010, pp. 78-92.

[7] Ardalan H, Eslami A, Nariman-Zadeh N. Piles shaft capacity from CPT and CPTu data by polynomial neural networks and genetic algorithms. Computers and Geotechnics, 2009; 36, 616-625.

[8] Jamali A, Nariman-Zadeh N, Darvizeh A, Masoumi A, Hamrang S. Multi-objective evolutionary optimization of polynomial neural networks for modelling and prediction of explosive cutting process. Engineering Applications of Artificial Intelligence, 2009; 22, 676-687.

[9] Liu G, Kadirkamanathan V. Multiobjective criteria for neural network structure selection and identification of nonlinear systems using genetic algorithms, Control Theory and Applications, IEE Proceedings-. IET, 1999: 373-382.

[10] Nariman-Zadeh N, Atashkari K, Jamali A, Pilechi A, Yao X. Inverse modelling of multi-objective thermodynamically optimized turbojet engines using GMDH-type neural networks and evolutionary algorithms. Engineering Optimization, 2005; 37: 437-462.

[11] Nariman-Zadeh N, Darvizeh A, Ahmad-Zadeh G. Hybrid genetic design of GMDH-type neural networks using singular value decomposition for modelling and prediction of the explosive cutting process. Proceedings of the Institution of Mechanical Engineers, Part B: Journal of Engineering Manufacture, 2003; 217: 779-790.

[12] Nariman-Zadeh N, Darvizeh A, Jamali A, Moeini A. Evolutionary design of generalized polynomial neural networks for modelling and prediction of explosive forming process. Journal of Materials Processing Technology, 2005; 164: 1561-1571.

[13] Ivakhnenko A. Polynomial theory of complex systems. Systems, Man and Cybernetics, IEEE Transactions on, 1971:364-378.

[14] Kondo T, Kondo C, Takao S, Ueno J. Feedback GMDH-type neural network algorithm and its application to medical image analysis of cancer of the liver. Artificial Life and Robotics, 2010; 15: 264-269.

[15] NIGC Odorant to be used for Odorization of Natural Gas. 2009 http://igs.nigc.ir/STANDS/IGS/M-CH-038.PDF.

[16] Farlow SJ. Self-organizing methods in modeling: GMDH type algorithms. CrC Press 1984.

[17] Mueller J-A, Lemke F. Self-organising data mining: an intelligent approach to extract knowledge from data. Pub. Libri 2000, Hamburg.

[18] Nariman-Zadeh N, Darvizeh A, Darvizeh M, Gharababaei, H. Modelling of explosive cutting process of plates using GMDH-type neural network and singular value decomposition. Journal of Materials Processing Technology, 2002 128: 80-87.

[19] Matson MS, Swindell HJ. 2000. Oxidation of mercaptans to disulfides. US Patent number: 6,051,740.

To whom correspondence should be addressed: Mr. Farshid Zare'i, Department of Chemical Engineering, University of Guilan, Rasht, Iran E-mail farshidzarei@msc.guilan.ac.ir
Professor Amir H. Mohammadi, Discipline of Chemical Engineering, School of Engineering, University of KwaZulu-Natal, Howard College Campus, King George V Avenue, Durban 4041, South Africa E-mail amir_h_mohammadi@yahoo.com

Petroleum and Coal

Article **Open Access**

SCALE EFFECTS ON THE HYDRODYNAMICS AND FLOW REGIME TRANSITION OF SLURRY BUBBLE COLUMN: EXPERIMENTAL AND CFD STUDY

*Safaa M.R. Ahmed, Suhaib S. Saleh, Saba A. Gheni**

Department of Chemical Engineering University of Tikrit, Iraq

Received April 21, 2019; Accepted July 1, 2019

Abstract

The Fischer–Tropsch (FT) synthesis on a large scale attracts a lot of attention. It represents a smart innovation to convert low cost natural gas to high-profit fuel and products. Scaling up of such a continuous heterogeneous process needs a very precise determination of hydrodynamic variables with relation to slurry bubble column dimensions and catalyst loading. This study aims to employ a large-scale slurry bubble column in a flow transition study with the aid of computational fluid dynamics. In this study, two flow conditions were considered, periodic and steady state flows. The experimental and computational work have been carried out to study the performance of a scaled-up slurry reactor under the two different modes of operation. The impact of key parameters that enhances or alter the performance of slurry reactor is studied, namely, superficial gas velocity (0.05, 0.1, 0.15, 0.2, 0.25 and 0.35 m/s), solid loading (8, 12 and 15%), and cycle period; short and long periods. A laboratory unit was constructed to conduct this study. A mimic feed and solid loading were used to exclude the impact of chemical reaction and to focus intensively on the hydrodynamics. Air – paraffin oil – silica system was used for the hydrodynamic experiments. The results revealed that the transition flow was accompanied with an observed much lower average liquid flow rate compared to steady state operation at different study conditions of superficial gas velocity average liquid velocity. It also showed that scaling up influenced steady state flow boundaries compared to the same conditions with the lab scale reactor studied previously. On computational part, it was shown that period operation was short and less influent at low liquid flow are and solid loading.

***Keywords**: Slurry bubble column; Large scale; period operation; hydrodynamics; CFD.*

1. Introduction

Slurry bubble column reactors are widely utilized nowadays in several applications in chemical and petrochemical processes. These processes include [1]: oxidation, hydrogenation, chlorination, alkylation, polymerization [2], methanol and Fischer–Tropsch (FT) synthesis [3], membrane technology [4], green technology [5] etc. As the international oil price is increasing obviously, the processes of gas-to-liquid transformation in Fischer–Tropsch (FT) technology has gained a lot of attention and turn into a more feasible industrial process [6]. Also, they become an interesting process for research to increase productivity and upgrade the liquified fuel. Slurry reactors are the heart of Fisher-Tropsch technology; therefore, they evoke a large design effort. Despite slurry column reactor shows excellent efficiency of heat transfer, easiness in construction and maintenance continuous catalyst addition, replacement and withdrawing, and a reasonable rate of mass transfer at the interface along with minimal energy input, its multiphase flow behaviors are very complex, and scale-up effects are significant. Also, although design of reactor and catalyst and progressive development of the process, the application of Fischer Tropsch technology is limited because of the large capital, operational and maintenance costs required for the process compared to the available conventional technologies [6]. Thus, more extensive research is still necessary to develop, design and implement a higher performance slurry column reactor [7]. To develop a precise scale-up of the slurry reactor for Fischer–Tropsch process, it is needed to obtain an appropriate characterization of flow pattern and hydrodynamics such solid, liquid and gas holdups, heat transfer performance, residence time distribution, mass transfer at the interface between gas and liquid along with solid catalyst. All these parameters have to be studied against reactor dimensions (reactor diameter and height) and operating conditions in slurry system such as catalyst loading, operating pressure and superficial gas velocity [8].

The objective of the present study is to describe and evaluate the influence of scale up on the performance of slurry reactor as a function of different key operating variables.

2. Experimental work

In the present work, experiments were carried out in a large scale polymethyl methacrylate column (0.45 m diameter and 2.92 m height) designed and constructed in Chemical Engineering Department University of Missouri Science and Technology, USA. Figure 1 shows the experimental rig and specifications of the components are shown in Table 1.

The system mimic Fischer–Tropsch process consists of C_{10}-C_{12} normal paraffine oil (mixture of decane, undecane, and dodecane, supplied from Sasol Chemicals LLC, (USA) Houston TX), compressed air and silica powder. A 241 holes (3 mm diameter) perforated plate diffuser was used and the holes were arranged in a square pitch configuration. Two mass flow meters were used to control gas and oil flow rates. Three superficial gas velocity were tested; 0.1, 0.15, 0.2, 0.25, 0.3 and 0.35 m/s, and three solid loading were examined; 8, 12 and 15% and a constant liquid flow rate of 0.03 m/s. The silica powder was impregnated with paraffin oil for 24 hrs before operation to ensure complete wetting and adequate liquid distribution at the time of experimentation. Five points were monitored along the height of the column via an optical probe to obtain the hydrodynamic measurements; 14, 28, 42, 56 and 70" at the center of the column with tips facing downwards. The details of this innovative instrument were characterized elsewhere [9]. A time-based gas holdup is obtained by the technique and it is different from the one reported by Xue *et al.* [10], which was based on volume. Thus, the local gas holdup obtained in the present study is defined as [10]:

$$\varepsilon_{g,T} = {}^{T_G}\!/_{T} \qquad (1)$$

where, T_G is the time the probe tip spends in the gas phase (bubbles) and T is the total measuring time [10].

Figure 2 shows an illustration of the probe. To ensure accurate experimentation, the probability distribution analysis was employed at the desired operating conditions of the gas hold up and superficial gas velocity. The percentage of standard deviation was determined at less than 10% for the examined operating conditions.

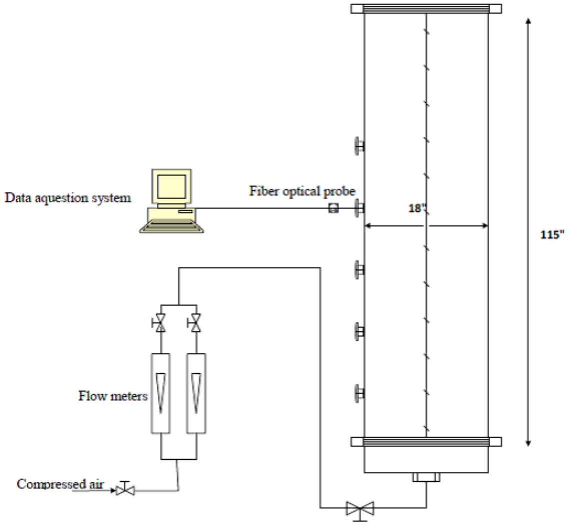

Figure 1. Experimental setup

Table 1. Specifications of experimental setup

Item number	Name	Specifications
1	Slurry bubble column	Vertical polymethylmethacrylate cylinder, 0.45 m diameter, 2.92 m height.
2	Mass flow meters	RS485 flow Range 0-200 L/min, Accuracy ±(2.0+0.5FS) % Response Time ≤2 sec
3	Compressor	Honda GX160 OHV, floating-type, 8-Gallon Twin Tank, 13.7 CFM at 90 Psi
4	Optical probe	Fiber optic cables with glass cores of 200 μm arranged in the geometrical configuration. The bundle is jacketed with four polymer layers.,
5	Computer	Core i5-2450M, hard disk capacity of 1 TB and memory 16 G. 17″ monitor
6	Interface and data logger	SD card logging with Matlab code. Voltage of 0 V to fit into the processing program. Accuracy 0.5%- offset adjustment possible.
7	Gas distributor	Perforated cupper plate (3 mm dia holes, free plate area 0.13%)

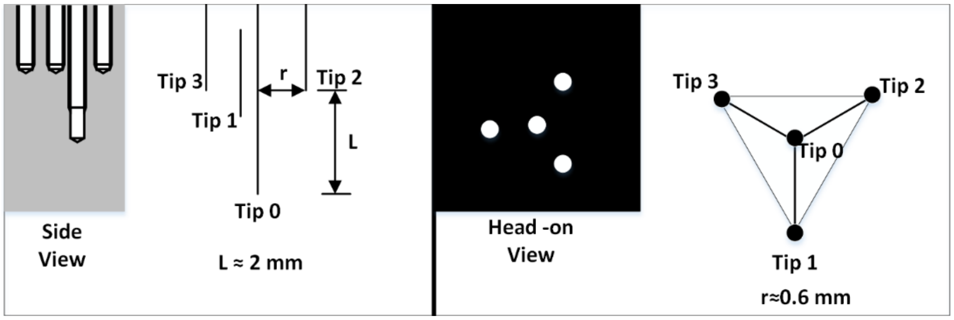

Figure 2. Optical fiber probe [12]

3. Results and discussion

3.1. Steady state operation

In a slurry bubble column, contact between three phases resulted in different flow regimes. Generation of these regimes occur at different flow rates of gas and liquid, flow conditions and physical properties of the interacted materials (gas, liquid and solid). In order to establish a map of transition from homogeneous to heterogeneous regimes, a matrix of experiments was conducted in a broad range of different solid loading and gas flow rates for long cyclic period (steady state operation).

Figure 3 shows the transition boundary from homogeneous to heterogeneous regime as a function of the superficial gas velocity with 8%, 12% and 15% solid loading for air-paraffin oil system. It indicated from Figure 3 that transition from homogeneous at low loading of 8% depends on gas velocity and boarder than the one obtained by Gheni *et al.* [11] with small scale slurry bubble. As solid loading increases to 12%, zone of homogeneous shrinkages and more volume is occupied by clouds and solid. At constant superficial gas velocity of air, a shift towards homogeneous region is observed. As more space is provided in the present work density of solid in this region became less and the homogenous zone gets larger. The flow regimes encountered in the column are established as a result of a balance between the driving forces (inertia and gravity), shear stress and surface tension resisting forces. Thus, adding more solid powder increases surface tension and gravity due to increase of viscosity of slurry system. Also, solid loading incorporates with a low gas flow rate to generate a heavier intertrial force on bubbles flow upward to result in large coalesced bubbles (slugs). The liquid film formed around the bubble in the cylindrical column acquire a uniform thickness because of the circular section and absence of the corners. This gives a reliable mimic accounting for liquid film in slurry bubble system compared to rectangular section mimic reactor utilized elsewhere [12-14] and closer to industrial Fisher Tropsch reactors. The maximum film thickness located at the centerline of the wall in the cross-sectional plane (see Figure 3).

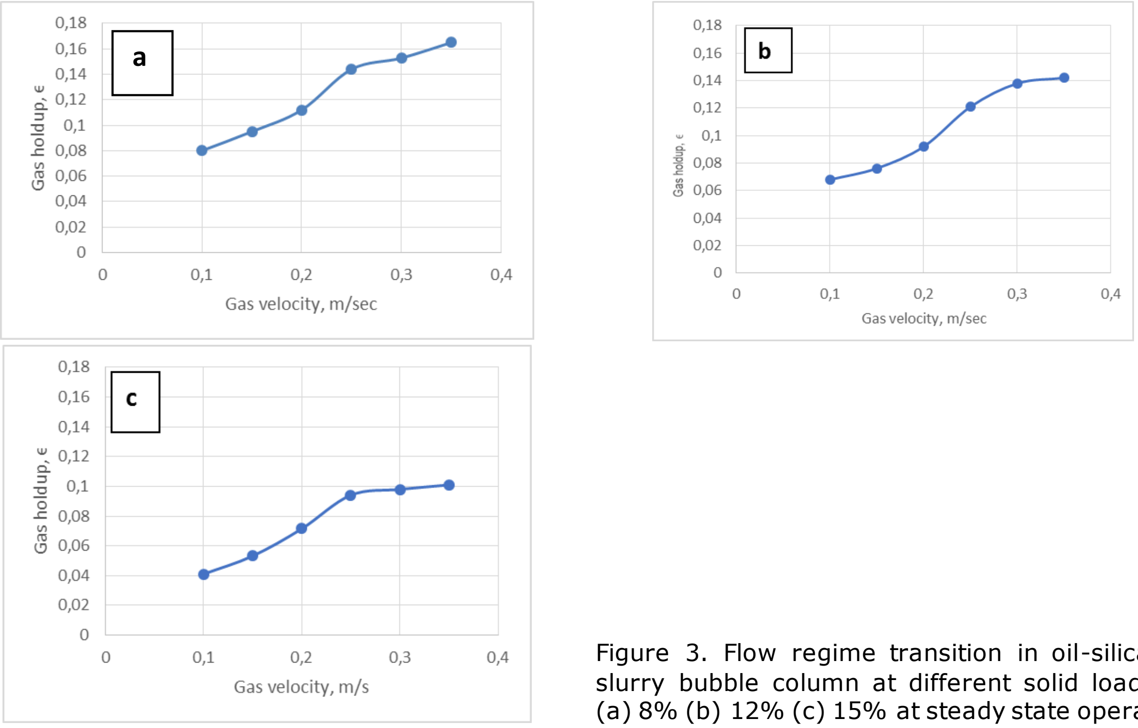

Figure 3. Flow regime transition in oil-silica-air slurry bubble column at different solid loadings (a) 8% (b) 12% (c) 15% at steady state operation

3.2. Periodic operation

One of the main objectives of the present work was to observe the effect of switching liquid flow between ON and OFF modes and cycle period on hydrodynamic parameters of slurry bubble column reactor at a relatively large scale. The periodic parameters were tested under the same conditions examined at steady state study. The unsteady state periodic operation mode has attracted broad attention and a growing interest because many studies have shown the reactor performance can be improved significantly by periodic operation [15-17].

The principle of periodic operation is to force a flowing system to operate continuously in a transient mode rather than relaxing to a steady state [15]. In the present study, the slurry bubble column reactor was operated in a periodic mode at a cyclic period of 5 minute to examine the impact of cyclic operation on hydrodynamics of the slurry bubble column reactor. Figure 4 shows regimes transition at different solid loadings at periodic operation. It is clearly seen that gas holdup obtained at periodic operation is much less than those obtained at steady state. This may attribute to the high surface tension and force of inertia exerted on bubbles dispersed through slurry and they did not let the bubbles to interfere with the oil phase and grow to a larger size bubble. It is also attribute to the short time of contact with oil and residence time in the slurry bubble column. It also shows that operation with higher solid loading resulted in more regimes transitions compared to steady state and instability of operation. However, the low density and moderate density experiments reveal a semi stable transition to heterogeneous flow Although the transition region was boarder, the gas holdup in heterogenous region was almost uniform which is regarded as an important parameter in Fisher Tropsch process. The cyclic operation in slurry bubble column reactor may alter the average interfacial area between gas and liquid, making the determination of mass transfer parameters and experimental acquirement of data in slurry bubble column challenging.

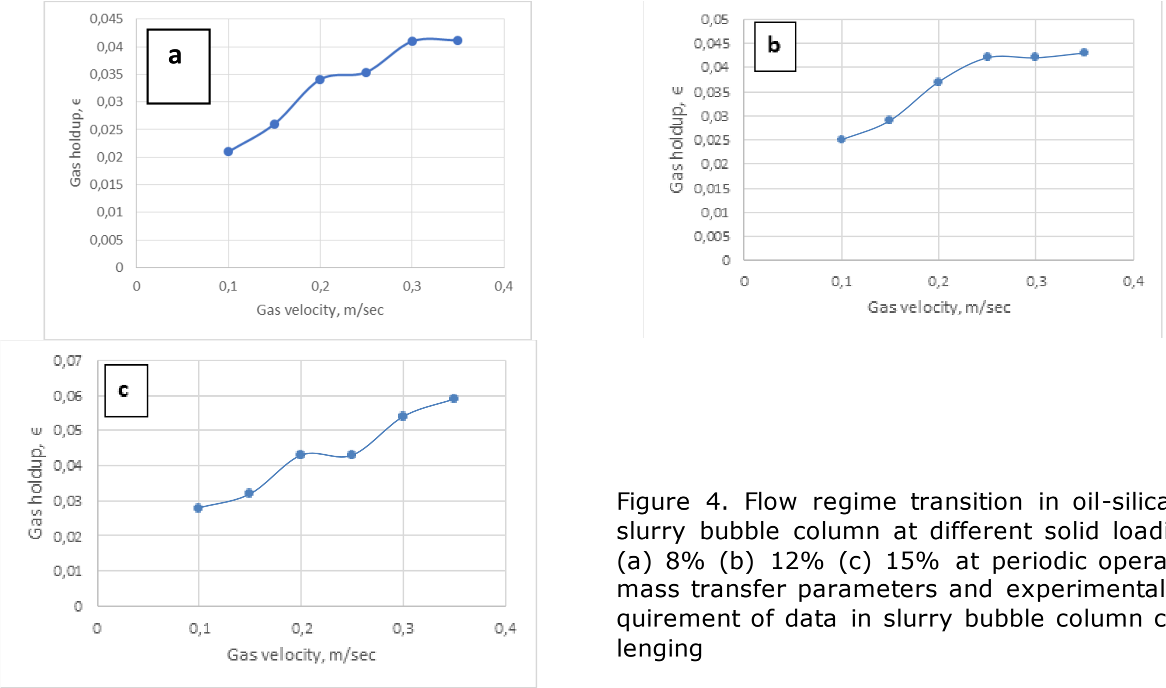

Figure 4. Flow regime transition in oil-silica-air slurry bubble column at different solid loadings (a) 8% (b) 12% (c) 15% at periodic operation mass transfer parameters and experimental acquirement of data in slurry bubble column challenging

3.3. Computation fluid dynamics of the system

In order to validate the experimental observations, computational fluid dynamics (CFD) simulation of a slurry bubble columns operating at steady state and cyclic state is implemented at the examined conditions of this study. A population balance modeling (PBM) was utilized in this part of the study. It has received an unprecedented amount of attention during the past few years from both academic and industrial quarters because of its applicability to a wide variety of particulate processes [18]. To validate the experimental results, PBM was employed and solved numerically using the bubble class method [19]. Figure 5 shows comparison between experimental and simulated results at steady and period states of operation. 12% solid loading and 0.35 gas velocity were chosen as a basis of comparison. It is observed that the local gas holdup for both steady state and simulated results are close at the examined conditions and period results still deviate from both simulated and steady state operations at most of the tested ratios of length to diameter.

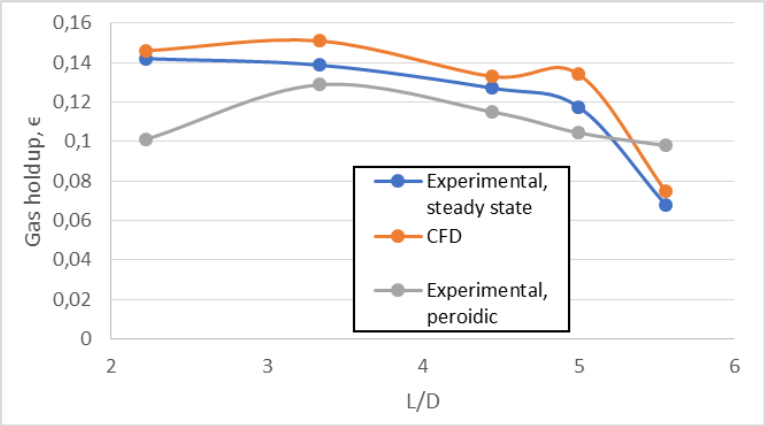

Figure 5. Flow regime transition in oil-silica-air slurry bubble column at 12% solid loadings and 0.35 m/sec gas velocity at steady state and periodic operation compared to CFD simulation at different L/D ratios

4. Conclusions

A large-scale experiment was conducted in a slurry bubble column to visualize and determine the impact of steady state and periodic operation on behavior of paraffin oil-silica powder and air system at different solid loadings and gas flow rates. It was showed that a periodic operation reveals the lowest gas holdup and enhances mixing between phases. It was also shown that regime transition between homogeneous and heterogenous zones are broader than the transition observed previously with water-silica-air system in a small-scale column. The simulated results in CFD showed a good validation of the experimental results of steady state operation and large deviation from the results obtained at periodic operation. Large difference in gas holdup was observed along the height of the column which in turn very influential in industrial applications.

References

[1] Deckwer W-D, Alper E. Katalytische suspensions reacktoren. Chem. Eng. Technol., 1980; 52: 219-228.

[2] Shah YT, Kelkar BG, Godbole SP, Deckwer W-D. Design parameter estimation for bubble column reactors. AIChE J., 1982; 28: 353-379.

[3] Dry ME. The SASOL route to fuels. Chem Tech., 1982; 12: 744-750.

[4] Rahimpour MR, Jokar SM, Jamshidnejad Z. A novel slurry bubble column membrane reactor concept for Fischer–Tropsch synthesis in GTL technology. Chemical Engineering Research and Design. 2012; 90(3):383–396.

[5] Sehabiague L, Basha O, Morsi BI. Recycling of tail gas in Fischer-Tropsch bubble column slurry reactor and its impact on the coal-to-liquid process. In Proceedings of the 30th Annual International Pittsburgh Coal Conference, Beijing, China, 2013.

[6] Nafees A, and Al Hashimi SH. Fischer Tropsch Gas To Liquid Technology (GTL). The Second International Energy 2030 Conference. Abu Dhabi, U.A.E., November 4-5, 2008.

[7] Wang T, Wang J, and Jin Y. Slurry Reactors for Gas-to-Liquid Processes: A Review. Ind. Eng. Chem. Res., 2007; 46 (18): 5824–5847

[8] Krishna R, van Baten J. A Strategy for Scaling Up the Fischer–Tropsch Bubble Column Slurry Reactor. Topics in Catalysis, 2003; 26(1-4): 21-28.

[9] Youssef A and Al-Dahhan MH. Impact of Internals on the Gas Holdup and Bubble Properties of a Bubble Column. Industrial & Engineering Chemistry Research, 2009; 48(17): 8007–8013.

[10] Xue J. Bubble Velocity, Size and Interfacial Area Measurements In Bubble Columns, PhD Dissertation, Washington University, St. Louis 2004.

[11] Ghani SA, Yaqub RJ and Saleh SS. Experimental Study of Volumetric Mass Transfer Coefficients in Slurry Bubble Column Reactor. J. Chem. Eng. Process Technol., 2012; 3: 3

[12] Gheni S, Abdulaziz YI, Al-Dahhan MH. Effect of L/D Ratio on Phase Holdup and Bubble Dynamics in Slurry Bubble Column using Optical Fiber Probe Measurements. International Journal of Chemical Reactor Engineering, 2016; 14. 10.1515/ijcre-2015-0035.

[13] Khodaparast S, Atasi O, Deblais A, Scheid B, and Stone HA. Dewetting of Thin Liquid Films Surrounding Air Bubbles in Microchannels. Langmuir, 2018; 34 (4): 1363–1370.

[14] Ahmed FS, Sensenich BA, Gheni SA, Znerdstrovic D, Al Dahhan MH. Bubble dynamics in 2d bubble column: comparison between high-speed camera imaging analysis and 4-point optical probe. Chemical Engineering Communications, 2015; 202, 1.

[15] Silveston PL, Hanika J. Challenges for the periodic operation of trickle-bed catalytic reactors. Chemical Engineering Science. 2002; 57(16): 3373-3385.

[16] Boelhouwer JG, Piepers HW, and Drinkenburg BAH. Advantages of forced non-steady operated trickle bed reactors. Chem. Eng. Technol,. 2002; 25: 647-650.

[17] Liu G, Duany Y, Wang Y, Wang L. Periodically operated trickle reactor for EAQs hydrogenation: experiments and modeling. Chem. Eng. Sci., 2005; 60: 6270-6278.

[18] Ramkrishna D, Mahoney AW. Population balance modeling. Promise for the future. Chemical Engineering Science, 2002; 57(4): 595-606.

[19] AH Syeda M Boulet, Melchioria T, Lavoie J-M. CFD simulation of a slurry bubble column: Effect of population balance kernels. Computers and Fluids. 2018; 175: 167-179.

To whom correspondence should be addressed: Dr. Saba A. Gheni, Department of Chemical Engineering University of Tikrit, Iraq

Petroleum and Coal

Article **Open Access**

THE EFFECT OF DIFFERENT OPERATION CONDITIONS ON THE RATIO OF CO TO H_2 PRODUCED IN STEAM REFORMING PROCESS

Seyed Javad Ahmadpanah[1], *Saeid Shokri*[2], *Behrouz Nonahal*[3]

[1] *Design and Equipment Technology Division, Research Institute of Petroleum Industry (RIPI), Tehran, Iran*
[2] *Engineering Division, Research Institute of Petroleum Industry (RIPI), Tehran, Iran*
[3] *Petroleum Refining Technology Development Division, Research Institute of Petroleum Industry (RIPI), Tehran, Iran*

Received May 11, 2019; Accepted July 31, 2019

Abstract

Steam reforming of natural gas or naphtha using Nickel-Alumina catalyst is the most important process in the production of synthesis gas ($H_2 + CO_2$) and pure hydrogen. Synthesis gas is a very valuable raw material for the production of various chemicals such as hydrogen, methanol, and ethylene glycol. In this research, by modeling of a steam reforming reactor and using experimental data and solving the equations with the MATLAB software package, the effect of different operational conditions such as the ratio of steam to methane, temperature and pressure of inlet feed to the reactor have been investigated on the rate of produced CO and H_2 along the reactor. The results obtained from the simulation are in agreement with the data extracted from industrial units. The rate of production of CO and H_2 increases with increasing temperature along the reactor due to the endothermic nature of production reactions. Moreover, it was observed that with increasing pressure, according to Le Chatelier's principle, the trend of production reactions tend to the left-hand side and reduction of the rate of products. Hence the rate of produced CO and H_2 has been decreased.

Keywords: *Steam Reforming Process, Heterogeneous Model, Reactor Model, Steam to Methane Ratio.*

1. Introduction

Steam reforming of natural gas is an economical method of producing synthesis gas and generating hydrogen. Natural gas and its conversion to value-added products are of great importance. In this regard, the use of syngas is of great importance in the gas conversion industry. Various chemicals are produced by using syngas along with other related processes. The application of the Fischer-Tropsch synthesis process is to produce heavy hydrocarbons by using natural gas and production of syngas. With respect to increasing oil price and worldwide approach towards producing clean fuels, the Fischer-Tropsch process is justifiable and has attracted many investors. Syngas is a valuable raw material for the production of various chemicals such as methanol synthesis, Fischer-Tropsch synthesis, oxo synthesis, and iron ore regeneration, production of heavy alcohols, esters, ketones and variety of hydrocarbons. Some of these reactions are presented in Table 1 [1-2]:

The Syngas was originally produced from a mixture of coke, air and water vapor and was regarded but one of the most common and economical techniques to convert hydrocarbons since 1930. Within the hydrocarbons, the only production of light hydrocarbons is commercially economic. Production of natural gas, propane, and butane are of great importance, respectively. Nowadays, by using special catalysts, naphtha is regarded as feed. Low price and vast gas reserves, more purity of products, and less formation of coke on the surface of catalyst are the main reasons for natural gas conversion in syngas production. The process of conversion of natural gas is based on the catalytic reaction of hydrocarbon with the aid of a reforming agent at high temperature. This reforming agent can be water vapor, carbon dioxide, oxygen, and or a mixture of them. The combination percentage of produced syngas depends on the type of hydrocarbon, reforming agent and its amount, operational condition, and the type of catalyst.

Table 1. Syngas consumption applications

Row	Process	Reactions
1	Methanol synthesis	$CO + 2H_2 \rightarrow CH_3OH$
2	Ethylene glycol synthesis	$2CO + 3H_2 \rightarrow HOCH_2CH_2OH$
3	Oxo synthesis	$CH_3CH \equiv CH_2 + CO + H_2 \rightarrow CH_3CH_2CH_2CHO \rightleftarrows\rightleftarrows\rightleftarrows\rightleftarrows, CH_3CH(CHO)CH_3$
4	Fischer-Tropsch synthesis	$8CO + 16H_2 \rightarrow C_8H_{16} + 8H_2O$
5	Iron Ore regeneration	$Fe_2O_3 + 1.5(H_2 + CO) \rightarrow 2Fe + 1.5(H_2O + CO_2)$ $Fe_3O_4 + 2(H_2 + CO) \rightarrow 3Fe + 2(H_2O + CO_2)$

The natural gas conversion process is mostly used to produce syngas with a small ratio of H_2/CO [4]. Major operational variables for this process are the ratios of H_2O/CH_4 and CO_2/CH_4 and temperature and pressure, and the major methane consumption reactions in this process are in the form of reactions (I) and (II) shown in Table 2 [5]. It is to be mentioned that the reactions above can be added and rewrite the reactions as (III) or (IV). Reaction (IV) is called dry reforming reaction.

Table 2. Methane reaction in the vapor reforming process

No.	Reactions	$\Delta H^O_{298}\,(KJ/mol)$
I	$CH_4 + H_2O \leftrightarrow CO + 3H_2$	+206.1
II	$CO + H_2O \leftrightarrow CO_2 + H_2$	-41.15
III	$CH_4 + 2H_2O \leftrightarrow CO_2 + 4H_2$	+165.0
IV	$CH_4 + CO_2 \leftrightarrow 2CO + 2H_2$	+247.3

In this research, a one-dimensional heterogeneous model has been used to simulate a reactor of steam reforming unit and model equations solved by MATLAB software with ode 15s command. The simulation results are in agreement with the data extracted from industrial units.

2. Reactions and materials

Three main reactions of the process are as follows:

(I) $MSRCH_4 + H_2O \leftrightarrow CO + 3H_2$

(II) $WGSCO + H_2O \leftrightarrow CO_2 + H_2$

(III) $CH_4 + 2H_2O \leftrightarrow CO_2 + 4H_2$

The experiments were carried out in the presence of Nickel/Alumina (Ni/Al_2O_3) at more than 500°C and pressure of approximately 30 bar and around 400 parallel tubes with an inside diameter of 10 cm and a length of 10 to 12 meters.

Froment *et al.* [9] introduced three reaction equations regarding three steam reforming process of methane (MSR):

1. The rate of transformation of methane to carbon monoxide

$$r_1 = \frac{\frac{k_1}{p_{H_2}^{2.5}}\left(p_{CH_4}p_{H_2O} - \frac{p_{H_2}^3 p_{CO}}{K_1}\right)}{(DEN)^2} \qquad (1)$$

2. The rate of transformation of carbon monoxide to carbon dioxide

$$r_2 = \frac{\frac{k_2}{p_{H_2}}\left(p_{CO}p_{H_2O} - \frac{p_{H_2}p_{CO_2}}{K_2}\right)}{(DEN)^2} \qquad (2)$$

3. The rate of transformation of methane to carbon dioxide

$$r_3 = \frac{\frac{k_3}{p_{H_2}^{3.5}}\left(p_{CH_4}p_{H_2O}^2 - \frac{p_{H_2}^4 p_{CO_2}}{K_3}\right)}{(DEN)^2} \tag{3}$$

$$DEN = 1 + K_{CO}p_{CO} + K_{H_2}p_{H2} + K_{CH_4}p_{CH_4} + \left(\frac{K_{H_2O}p_{H_2O}}{p_{H_2}}\right) \tag{4}$$

The rate of formation of CO and CO_2 and also CH_4 consumption is equal to:

$$R_{CO} = r_1 - r_2 \tag{5}$$

$$R_{CO_2} = r_2 + r_3 \tag{6}$$

$$R_{CH_4} = r_1 + r_3 \tag{7}$$

The constants used in rate equations are obtained by the relations from reference [7]. As stated above, the reactor consists of many parallel tubes with the inside diameter of 10 cm and length of 11 m placed inside the furnace chamber that radiation and convection play the main roles in the heat transfer process.

3. Modeling of steam reforming reactor

In order to model the steam reforming reactor, the assumptions are Steady-state conditions, One-dimensional heterogenic model, Plug flow reactor (with respect to the ratio of length to diameter).

All tubes are considered identical, and only one tube out of 450 is considered for modeling, Heat flux is constant from furnace side along the reactor, Ideal gas flow, Diffusion phenomena is ignored at all reactor directions, Coke formation is ignored. Figure 1 shows a cross-section of a fixed bed tubular reactor for which mass transfer equations, heat transfer, and momentum considered for an element are written for the distance between Z and Z+ ΔZ.

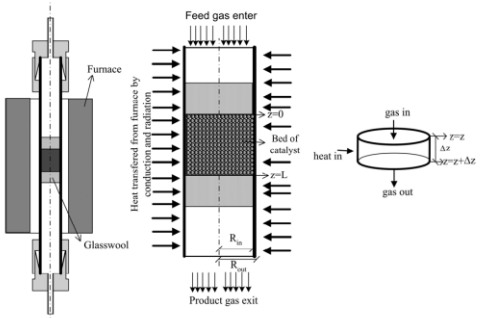

Figure 1 A cross-section of a fixed bed reactor for the transformation of methane to steam

Mass transfer equations can be written as follows:

$$\frac{dX_{CH_4}}{dz} = A_C.\frac{\rho_b.\eta_{CH_4}.R_{CH_4}}{F_{CH_4}^0} \tag{8}$$

$$\frac{dX_{CO_2}}{dz} = A_C.\frac{\rho_b.\eta_{CO_2}.R_{CO_2}}{F_{CH_4}^0} \tag{9}$$

Heat transfer equation can be written as follows:

$$\frac{dT}{dz} = \frac{1}{G_{mass}.Cp_{overall}}.\left(\frac{4H_F}{d_i} + \rho_b \sum_{i=1}^{3}(-\Delta H_i)\eta_i r_i\right) \tag{10}$$

Momentum equation:

$$\frac{dP}{dz} = -\frac{1.75G_S(1-\varepsilon)}{\varphi_S D_p \varepsilon^3 \rho_g} \tag{11}$$

And finally boundary layer condition:

At Z=0: $X_{CH4} = 0$, $X_{CO2} = 0$, $P = P_{IN}$, $T = T_{IN}$

Calculation of partial pressure of fractions in any reactor height (z): With assumption of the preliminary information:

SteamCH_4 molar feed ratio=3.358; H_2/CH_4 molar feed ratio=0.122;
CO_2/CH_4 molar feed ratio=0.056; N_2 CH_4 molar feed ratio=0.164

To calculate partial pressure of fractions following equations are used:

$$\delta = \frac{1 + \theta_{H_2O} + \theta_{CO} + \theta_{CO_2} + \theta_{H_2}}{P_T}$$

$$\theta_j = \frac{F_j^0}{F_{CH_4}^0}, j: CH_4, CO_2, H_2O, CO, H_2, P_T = totalpressure \tag{12}$$

With the above definitions, the partial pressure of fractions is calculated through the following relationships:

$$P_{CH_4} = {(1 - X_{CH_4})}/_{\delta} \quad (13)$$

$$P_{H_2O} = {(\theta_{H_2O} - X_{CH_4} - X_{CO_2})}/_{\delta} \quad (14)$$

$$P_{CO} = {(X_{CH_4} - X_{CO_2})}/_{\delta} \quad (15)$$

$$P_{CO_2} = {(\theta_{CO_2} + X_{CO_2})}/_{\delta} \quad (16)$$

$$P_{H_2} = {(\theta_{H_2} + 3.X_{CH_4} - X_{CO_2})}/_{\delta} \quad (17)$$

$$P_{CO_2} = {\theta_{N_2}}/_{\delta} \quad (18)$$

Having obtained partial pressure, partial molar, and partial mass of fractions can be calculated at any height.

$$y_j = {P_j}/_{p_T}, x_j = {(y_j * MW_j * totalmolarflowrate)}/_{(totalmassflowrate)} \quad (19)$$

In the above relationships, at any (z), total molar flow rate, methane transformation, and carbon dioxide production percentages are obtained by mass equilibrium equations, and the total pressure is obtained through momentum equation. Total mass flow rate is constant and can be used from usual assumptions. The reactions heat at base temperature (298 °K) is given as follows [9]:

$$\Delta_r H^0_{298k.reaction1} = 206310 J.mol^{-1} \quad \Delta_r H^0_{298k.reaction2} = -41200 kJ.mol^{-1}$$

$$\Delta_r H^0_{298k.reaction3} = 165110 kJ.mol^{-1}$$

As is observed, the inlet pressure and temperature are 29 bar and 793.15K. By using HYSYS software, the inlet gas and steam flow rate are obtained as: total mass flow rate=447.6 kg/hr.

The catalyst specifications are: *Dp* = 0.0173 m, (pellet equivalent diameter); ε = Catalyst bed void fraction = 0.6; ρ_b = 1362 kg cat./m^{3}r (catalyst bed density); ρ_s = 2355.2 kg cat./m^{3}s (solid catalyst density); ϕ_s = 0.6563 (pellet sphericity).

By using MATLAB functions, the four differential equations (mass balance, energy, and momentum) have been solved. The differential equations of this model are stiff type, and therefore ode15s order used to solve it.

4. Results and discussion

4.1. The effect of inlet steam to methane ratio (S/C)

The ratio of steam to methane is one of the most important parameters affecting the MSR process. With respect to constant inlet gas flow rate, the change in the ratio of steam to methane is the change in steam flow rate.

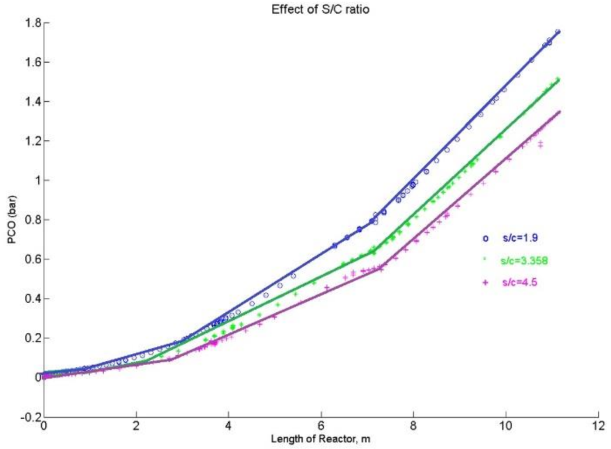

Figure 2 The investigation of the effect of steam to methane ratio on the partial pressure of CO along the reactor

Figure 2 shows the effect of the ratio of steam to methane on the partial pressure of produced CO along the reactor. For three ratios S/C= 2.9, 3.358, and 4.5.

With increasing height, the partial pressure of CO will increase in the first reaction due to production, but with increasing steam to methane ratio, the partial pressure of carbon monoxide decreases.

4.2. The effect of inlet feed temperature:

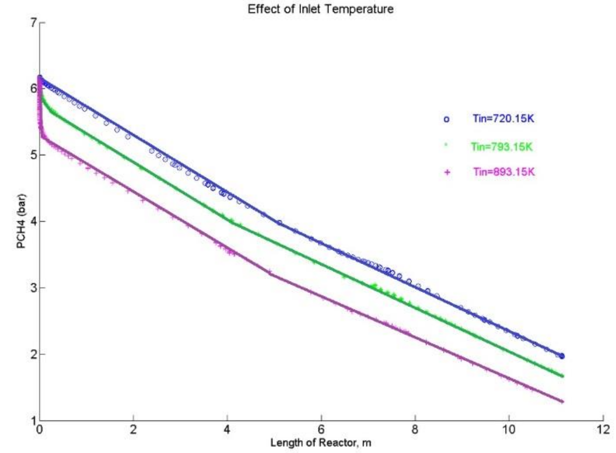

Figure 3. The investigation of the effect of inlet temperature on the partial pressure of CH_4 along the reactor

The primary inlet temperature used in the simulation is 793.15 ºK (52 ºC) that is considered as reference. For comparison of production distribution, two curves have been drawn at two temperatures around 100 ºC higher and lower. Figure 3 shows the effect of inlet temperature on the partial pressure of produced CH_4 along the reactor. For three inlet temperature T_{in}= 720.15, 793.15, and 893.15ºC.

The trends of reduction in the partial pressure of methane along the reactor are similar at all three inlet temperatures. Meanwhile, with increasing temperature, due to the endothermic nature of reactions 1 and 3 in methane transformation, the partial pressure of methane decreases.

Moreover, with increasing reactor height, the partial pressure of CO_2 increases due to advances of reactions 2 and 3. Meanwhile, with increasing inlet temperature, due to the endothermic nature of the dominant reaction in CO_2 production, the partial pressure decreases. Due to a higher concentration of methane, the increasing slope of partial pressure in the beginning 6 meters of the reactor is higher, and in the end sections, the amount of methane for transformation to CO_2 is very low.

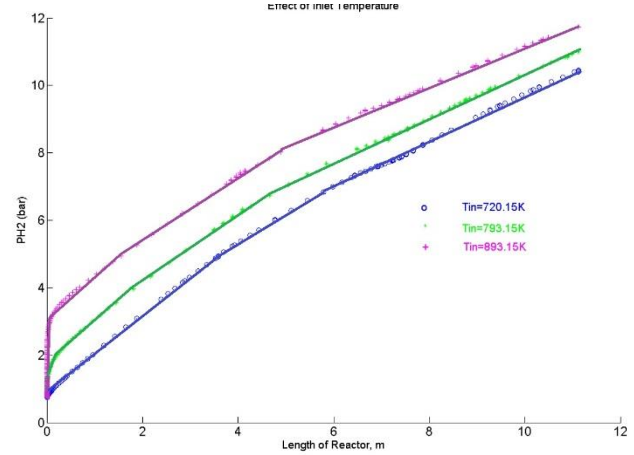

Figure 4. The investigation of the effect of inlet temperature on the partial pressure of H_2 along the reactor

Figure 4 shows the effect of inlet temperature on the partial pressure of produced H_2 along the reactor. For three inlet temperature T_{in}= 720.15, 793.15, and 893.15ºC.

As is observed, with increasing reactor height, the partial pressure of H_2 increases due to advances of reactions 2 and 3. Meanwhile, with increasing inlet temperature, due to the endothermic nature of the dominant reaction in H_2 production, the partial pressure decreases. Also, with increasing reactor height, the partial pressure of CO will increase due to advances of reactions 1 and 3. Furthermore, with increasing inlet temperature, due to the endothermic nature of the dominant reaction in CO production, the partial pressure decreases.

4.3. The effect of inlet pressure

Total inlet pressure used in the simulation is 29 bars that have been considered as reference. Products distribution and process parameters are drawn at two pressures about 10 bars higher and lower.

Figure 5 shows the effect of inlet pressure on methane molar fraction along the reactor. For three inlet pressure P_{in}= 20, 29, and 39 bar:

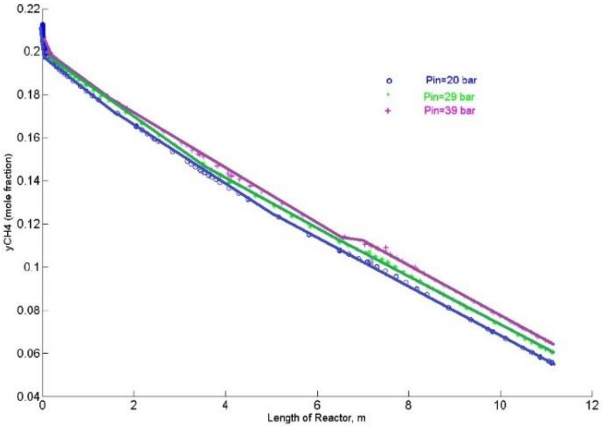

Figure 5. The investigation of the effect of pressure on methane fraction along the reactor

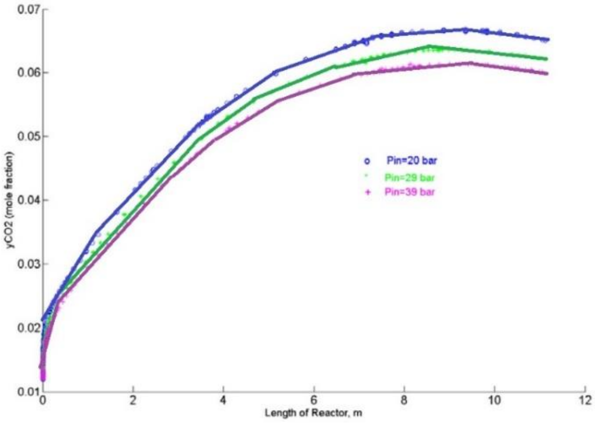

Figure 6. The investigation of the effect of inlet pressure on CO_2 molar fraction along the reactor

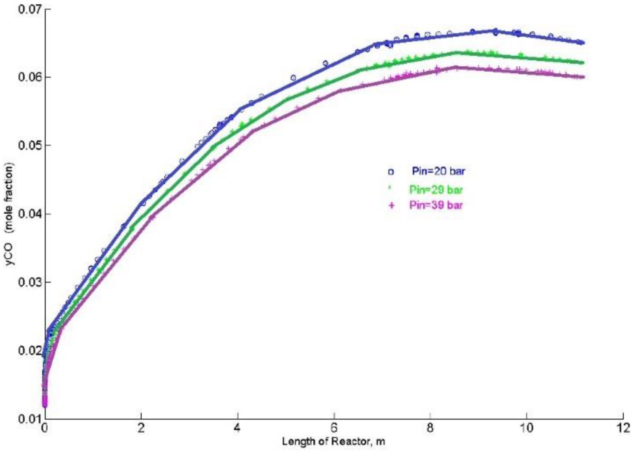

Figure 7. The investigation of the effect of inlet pressure on CO molar fraction along the reactor

The results show that along with the reactor, methane molar fraction decrease due to methane consumption. Meanwhile, the increase or decrease of 10 bars in the inlet pressure, has a negligible effect on methane transformation due to equal stoichiometry of both sides of reactions and the curves do not change much. Therefore, since pressure increase in equilibrium reactions lead to tending the reactions towards fewer moles, reactions tend to the left-hand side, and as a result, less methane is transformed.

(The higher pressure curve is at a higher level). Figure 6, 7 and 8 show the effect of inlet pressure on CO_2, CO and H_2 molar fraction of produced H_2 along the reactor. For three inlet pressure P_{in}= 20, 29, and 39 bar:

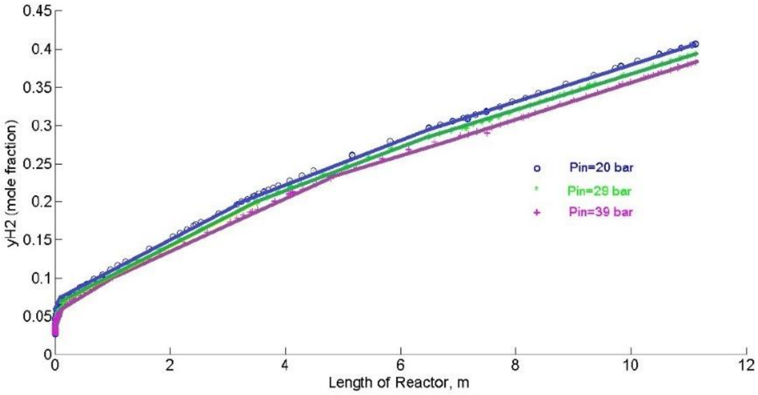

Figure 8. The investigation of the effect of inlet pressure on H_2 molar fraction along the reactor

Along the reactor, the molar fractions of CO, CO_2, and H_2 increase because of the production of CO, CO_2, and H_2. As described earlier, pressure increase works in favor of products transformation to reactants (left-hand side of equilibrium reactions) and therefore decreases.

5. Conclusion

In this research, a one-dimensional heterogeneous model has been used to simulate a reactor of steam reforming unit and model equations solved by MATLAB software with ode 15s command. As it can be observed from the results, along the reactor, the rate of CO and H_2 have been increased due to production reactions, but with increasing the ratio of steam to methane, the rate of CO and H_2 have been decreased due to the reduction of methane as reacting fraction. On the other hand, the rate of production of CO and H_2 increases with increasing temperature along the reactor due to the endothermic nature of production reactions.

References

[1] Chibane L, Djellouli B. Methane Steam Reforming Reaction Behaviour in a Packed Bed Membrane Reactor. International Journal of Chemical Engineering and Applications, 2011; 2(3): 147-156.

[2] Pedernera MN, Pina J, Borio DO, Bucala V. Use of a heterogeneous two- dimensional model to improve the primery steam reformer performance. Chem Eng. J., 2003; 94: 29.

[3] Grevskott S, Rusten T, Hillestad M, Edwin E, Olsvik O. Dynamic simulation of a steam reforming tube with furnace. Chem. Eng. Sci., 2001; 56(2): 597.

[4] Yu YH, Sosna MH. Modeling for industrial heat exchanger type steam reformer. Kor. J.Chem. Eng., 2001; 18(1): 127.

[5] Pina J, Schbib NS, Bucala V, Borio DO. Influence of the heat- flux profiles on the operation of primery steam reformers. Ind. Eng. Chem. Res., 2001; 40: 5215.

[6] Xu J, Froment GF. Methane Steam Reforming Methanation and Water–Gas Shift: Intrinsic Kinetics. AICHE J., 1989; 35(1): 88.

[7] Elnashaie SS,Elshishini SS. Modelling, Simulation and Optimization of Industrial Fixed Bed Catalytic Reactors. Gordon and Breach Sience Publishers S.A. 1993.

[8] Wesenberg MH, Grislingas A, Grevskott S. Modelling of Steam reformer tubes.6th World Congress of Cemical Engineering, 2001; Melbourne, Paper 961.

[9] Froment GF, Bischoff KB. Chemical Reactor Analysis and Design; 2nd Edition, Wiley, Singapore, 1990.

[10] De Groote AM, Froment GF. Reactor Modeling and Simulations in Synthesis Gas Production. Rev. Chem. Eng., 1995; 11(2): 145.

[11] Froment GF, Hofmann PK. Design of Fixed- Bed Gas- Solid Catalytic Reactor in Chemical Reaction and Reactor Engineering; J.J. Carberry and A. Varma (Editors); Marcel Dekker, New York, 1987.

To whom correspondence should be addressed: Dr. Saeid Shokri, Engineering Division, Research Institute of Petroleum Industry (RIPI), 14665-137, Tehran, Iran E-mail shokris@ripi.ir